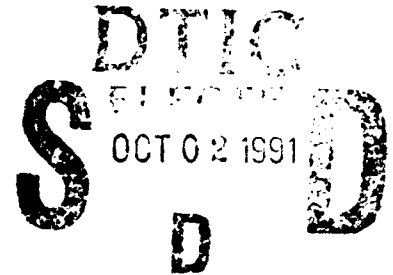


AD-A241 313



Proceedings of Damping '91

**13-15 February 1991
San Diego, California**



(GCA-1 through JCB-17)

August 1991

Final Report for Period February 1989 to February 1991

Approved for public release; distribution is unlimited

Sponsored by:

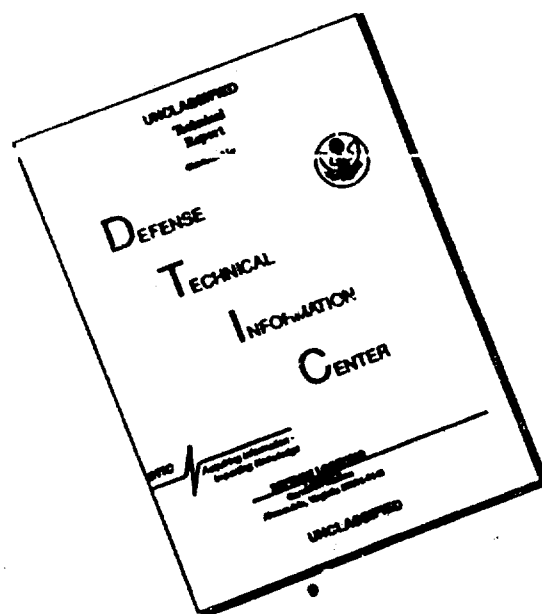
Wright Laboratory

Flight Dynamics Directorate

91-12021



DISCLAIMER NOTICE



THIS DOCUMENT IS BEST QUALITY AVAILABLE. THE COPY FURNISHED TO DTIC CONTAINED A SIGNIFICANT NUMBER OF PAGES WHICH DO NOT REPRODUCE LEGIBLY.

NOTICE

When Government drawings, specifications, or other data are used for any purpose other than in connection with a definitely Government-related procurement, the United States Government incurs no responsibility or any obligation whatsoever. The fact that the government may have formulated or in any way supplied the said drawings, specifications, or other data, is not to be regarded by implication, or otherwise in any manner construed, as licensing the holder, or any other person or corporation; or as conveying any rights or permission to manufacture, use, or sell any patented invention that may in any way be related thereto.

This report is releasable to the National Technical Information Service (NTIS). At NTIS, it will be available to the general public, including foreign nations.

This technical report has been reviewed and is approved for publication.



JEROME PEARSON, Chief
Structural Dynamics Branch



LYNN ROGERS, PhD
Principal Engineer
Structural Dynamics Branch

If your address has changed, if you wish to be removed from our mailing list, or if the addressee is no longer employed by your organization please notify WPAFB, WPAFB, OH 45433-6013 to help us maintain a current mailing list.

Copies of this report should not be returned unless return is required by security considerations, contractual obligations, or notice on a specific document.

REPORT DOCUMENTATION PAGE

1a. REPORT SECURITY CLASSIFICATION Unclassified			1b. RESTRICTIVE MARKINGS			
2a. SECURITY CLASSIFICATION AUTHORITY			3. DISTRIBUTION / AVAILABILITY OF REPORT Approved for public release; distribution unlimited			
2b. DECLASSIFICATION / DOWNGRADING SCHEDULE						
4. PERFORMING ORGANIZATION REPORT NUMBER(S) WL-TR-91-3078, Volume III			5. MONITORING ORGANIZATION REPORT NUMBER(S)			
6a. NAME OF PERFORMING ORGANIZATION Flight Dynamics Directorate Wright Laboratory		6b. OFFICE SYMBOL (If applicable) WL/FIBG		7a. NAME OF MONITORING ORGANIZATION		
6c. ADDRESS (City, State, and ZIP Code) Wright-Patterson AFB, OH 45433-6553			7b. ADDRESS (City, State, and ZIP Code)			
8a. NAME OF FUNDING / SPONSORING ORGANIZATION		8b. OFFICE SYMBOL (If applicable)		9. PROCUREMENT INSTRUMENT IDENTIFICATION NUMBER		
8c. ADDRESS (City, State, and ZIP Code)			10. SOURCE OF FUNDING NUMBERS			
			PROGRAM ELEMENT NO. 62201F	PROJECT NO. 2401	TASK NO. 04	WORK UNIT ACCESSION NO. 23
11. TITLE (Include Security Classification) Proceedings of Damping '91						
12. PERSONAL AUTHOR(S)						
13a. TYPE OF REPORT Final		13b. TIME COVERED FROM FEB 89 TO FEB 91		14. DATE OF REPORT (Year, Month, Day) August 1991		15. PAGE COUNT 518
16. SUPPLEMENTARY NOTATION Pages GCA-1 through JCB-17						
17. COSATI CODES			18. SUBJECT TERMS (Continue on reverse if necessary and identify by block number)			
FIELD	GROUP	SUB-GROUP				
			Vibration Damping, controls/structure interaction.			
19. ABSTRACT (Continue on reverse if necessary and identify by block number) Individual papers of Damping '91 held 13-15 February 1991 in San Diego CA are presented. The subjects included: Viscoelastic Material Testing and Characterization, Passive Damping Concepts, Passive Damping Analysis and Design Techniques, Optimization, Damped Control/Structure Interaction, Viscous Dampers, Friction Damping, Other Vibration Suppression Techniques, Damping Identification and Dynamic Testing, Applications to Aircraft, Space Structures, Marine Structures, Commercial Products, Defense Applications, and Payoffs of Vibration Suppression.						
20. DISTRIBUTION / AVAILABILITY OF ABSTRACT <input checked="" type="checkbox"/> UNCLASSIFIED/UNLIMITED <input type="checkbox"/> SAME AS RPT <input type="checkbox"/> DTIC USERS				21. ABSTRACT SECURITY CLASSIFICATION Unclassified		
22a. NAME OF RESPONSIBLE INDIVIDUAL Dr. Lynn Rogers			22b. TELEPHONE (Include Area Code) (513) 255-6622		22c. OFFICE SYMBOL WL/FIBG	

Workshop Administration

Director

Dr. Lynn C. Rogers
Wright Laboratory
Flight Dynamics Directorate

Technical Chairman

Dr. Conor D. Johnson
CSA Engineering, Inc.

Administrative Chairman

Mrs. Beryl D. Deremigio
CSA Engineering, Inc.

Assistant Administrative Chairman

Ms. Bonnie L. Portis
CSA Engineering, Inc.

Session Chairmen

Mr. Bradley Allen, *CSA Engineering, Inc.*
Capt. Walter Address, *Space Systems Division*
Dr. Mohan Aswani, *Aerospace Corporation*
Capt. Mark Arnold, *Wright Laboratory, Flight Dynamics Directorate*
Mr. Eric Austin, *CSA Engineering, Inc.*
Lt. Col. Ronald L. Bagley, *Air Force Institute of Technology*
Dr. Andrew S. Bicos, *McDonnell Douglas Space Systems Company*
Mr. Daniel Cyphers, *W. J. Schafer Associates, Inc.*
Mr. Eric Dalton, *Teledyne Brown*
Mr. Ralph Dornsife, *US Army / CERL*
Mr. William Driscoll, *3M / Industrial Specialties Division*
Mr. Robert Dunning, *TRW*
Mr. Rod Eddleman, *US Army Strategic Defense*
Mr. Richard Ely, *LTV Aircraft Group*
Dr. James Fanson, *Jet Propulsion Laboratory*
Mr. Bryce Fowler, *CSA Engineering, Inc.*
Dr. Joseph Garibotti, *Ketema, Inc.*
Mr. Russell Gehling, *Martin Marietta Astronautics Group*
Dr. Steven Ginter, *Honeywell Satellite Systems*
Dr. John Gubser, *McDonnell Douglas Missile System Company*
Dr. John Henderson, *Consultant*
Mr. Dennis Hill, *GE Astro Space Division*

Dr. Philip Hipol, *The Aerospace Corporation*
Dr. Robert Holman, *Hughes Aircraft Company*
Mr. J. Warren Hoskins, *Lockheed Missiles and Space Company*
Dr. Roy Ikegami, *Boeing Aerospace*
Dr. Conor Johnson, *CSA Engineering, Inc.*
Mr. Derrick Johnson, *Boeing Aerospace*
Dr. David I. G. Jones, *Wright Laboratory, Flight Dynamics Directorate*
Dr. Edward Kerwin, *Bolt, Beranek and Newman, Inc*
Mr. John Lassiter, *Warner - Robins ALC*
Mr. Paul Lindquist, *Wright Laboratory, Flight Dynamics Directorate*
Lt. John Mackaman, *Wright Laboratory, Flight Dynamics Directorate*
Dr. Ray Manning, *TRW, Space and Technology Group*
Mr. Daniel Morgenthaler, *Martin Marietta Space Systems*
Mr. Ahid Nashif, *Anatrol Corporation*
Mr. Rory Ninneman, *Phillips Laboratory*
Mr. Earl Pinson, *Lockheed Missiles and Space Company*
Mr. Ken Qassim, *Phillips Laboratory*
Mr. Keith Quinn, *Nichols Research Corporation*
Dr. Dantam Rao, *Mechanical Technology, Inc.*
Dr. Wayne Reader, *Vector Research Company, Inc.*
Dr. Kenneth Richards, *Martin Marietta*
Mr. Stanley Sattinger, *Westinghouse Science and Technology Center*
Dr. Daniel Segalman, *Sandia National Laboratories*
Mr. Leonard Shaw, *Wright Laboratory, Flight Dynamics Directorate*
Professor Young Shin, *Naval Postgraduate School*
Dr. Stepan Simonian, *TRW, Space and Technology Group*
Mr. Kevin Slimak, *Phillips Laboratory, Astronautics Directorate*
Dr. Jaak Soovere, *Lockheed Missiles and Space Company*
Mr. Clyde Stahle, *GE Astro Space*
Mr. Ralph Tate, *LTV Aircraft Products Group*
Mr. Roger Thaller, *Aeronautical Systems Division*
Capt. Steven G. Webb, *US Air Force Academy*
Mr. Kenneth R. Wentz, *Wright Laboratory, Flight Dynamics Directorate*
Maj. Stephen Whitehouse, *Wright Laboratory, Flight Dynamics Directorate*
Dr. William Witt, *The CORE Group*
Dr. Y. C. Yiu, *Lockheed Missiles and Space Company*
Mr. Wayne Yuen, *Wright Laboratory, Flight Dynamics Directorate*
Mr. Michael L. Zeigler, *Wright Laboratory, Flight Dynamics Directorate*

FOREWORD

This publication includes individual papers of **Damping '91** held February 13-15, 1991, San Diego, California. The Conference was sponsored by the Wright Laboratory, Flight Dynamics Directorate, Wright-Patterson Air Force Base, Ohio.

It is desired to transfer vibration damping technology in a timely manner within the aerospace community, thereby, stimulating research, development and applications.

Acquisition For	
NTIS CR321	
DTIC 321	
By	
DTIC 321 /	
Availability Codes	
Dist	Availability Code
A-1	Special



TABLE OF CONTENTS

	<u>Paper No.</u>
The F-117 Stealth Aircraft (Keynote Address) Mr. Paul Martin	AAA*
Use of Passive Damping for Aircraft Cabin Noise Control (Invited Speaker) Dr. Leo Butzel	AAB*
The Society of Damping Technology in Japan and its Activities (Invited Speaker) Dr. Yasuo Tokita and Hiroshi Okamura	AAC
<hr/> SESSION BA - Aircraft Applications <hr/>	
Integral Damping Treatment for Primary Aircraft Structures Sal Liguore, Marty Ferman, and Rudy Yurkovich	BAA
An Investigation of Add-on Damping Treatment for Life Extension of the F-15 Upper Outer Wing Skin Michael Parin, V. Levraea, Jr., Dr. Lynn Rogers, and A. Pacia	BAB
Damping Treatments for Aircraft Hardmounted Antennae Ralph E. Tate and Carl L. Rupert	BAC*
<hr/> SESSION BB - Plates and Beams <hr/>	
Examination of Boundary Conditions for Sixth-Order Damped Beam Theory Ralph E. Tate	BBA
The Effect of Compliant Layering on Damped Beams David John Barrett	BBB
The Damping Property of Laminated Steel Sheet after Deep Drawing Hiroshi Okamura	BBC

TABLE OF CONTENTS (continued)

	<u>Paper No.</u>
<hr/> SESSION BC - Analysis and Design I <hr/>	
Practical Design and Analysis of Systems with Fractional Derivative Materials and Active Controls Daniel R. Morgenthaler	BCA
An Implicit Fourier Transform Method for Nonlinear Dynamic Analysis with Frequency Dependent Damping Prof. F. Venancio-Filho and A. M. Claret	BCB
On a Linear Property of Lightly Damped Systems Z. Liang, M. Tong, and G. C. Lee	BCC
<hr/> SESSION CA - Control Structure <hr/>	
Active Vibration Suppression via LQG/LTR: Analytic and Experimental Results for the PACOSS Dynamic Test Article Russell N. Gehling	CAA
H∞ Control for the PACOSS DTA Christopher T. Voth and R. Michael Stoughton	CAB
Active Damping of a Cantilever Beam Dr. Hung V. Vu, Stein Husher, and D. E. Zimmerman	CAC
The Investigation of Large Space Structure Passive Electrodynamic Dampers Dr. Roger Stettner and Dr. Paul Mlakar	CAD
<hr/> SESSION CB - Damping Material and Measurements <hr/>	
A Method for the Measurement of the Complex Compressional Modulus of Thin Layers Dr. Jonathan D. Rogers and Dr. Daniel J. Segalman	CBA*

TABLE OF CONTENTS (continued)

	<u>Paper No.</u>
The Evaluation of Young's Complex Modulus of Viscoelastic Materials Marc Tardif and Prof. Germain Ostiguy	CBB
Role of Morphology in Damping Efficiency Dr. L. H. Sperling, J. J. Fay, and Dr. D. A. Thomas	CBC*
The Thermorheologically Complex Material Lt. Col. Ronald L. Gley	CBD*
<hr/>	
SESSION CC - Analysis and Design 2	
<hr/>	
Methods of Reduction of Wind Induced Dynamic Response in Solar Concentrators and Other Small Lightweight Structures Monte A. McGlaun	CCA
Analysis of a Five-Layer, Viscoelastic, Constrained-Layer Beam Michael A. Falugi	CCB
Dynamics of a Class of Viscously Damped Struts Dr. Y. C. Tiu and Dr. Steven Ginter	CCC
A Study of a Vibration Absorber to Control the Vibration of a Rectangular Plate Akio Sugimoto, Hideo Utsuno, and Toshimitsu Tanaka	CCD
<hr/>	
SESSION DA - Analysis and Testing	
<hr/>	
Impedance Matched Mass-Dampers: A New Approach for Improving Structural Damping Craig Gardner and Prof. Richard H. Lyon	DAA
Analytical and Experimental Modal Analysis of a Two-Tiered Structure Dr. Hung V. Vu, William C. Flynn, and T. K. Vuong	DAB

TABLE OF CONTENTS (continued)

	<u>Paper No.</u>
Development of a Magnetic Suspension System for Reliable Vibration Damping Measurement Dr. Dantam K. Rao	DAC*
<hr/> SESSION DB - Viscoelastic Material <hr/>	
VEM Characterization Program Bryce L. Fowler	DBA
Data Base of the Dynamic Properties of Materials Ahid D. Nashif and Thomas M. Lewis	DBB
Establishing the Validity of the Master Curve Technique for Complex Modulus Data Reduction Dr. S. O. Oyadiji and Prof. G. R. Tomlinson	DBC
<hr/> SESSION DC - Optimization <hr/>	
Integrated Optimization of Composite Structures for Advanced Damped Dynamic Characteristics Dr. Dimitris A. Saravanos and Christos C. Chamis	DCA
An Optimum Design Methodology for Passively Damped Truss Structures Dr. Ray Manning	DCB
On An Application of Complex Damping Coefficients Z. Liang, M. Tong and G. C. Lee	DCC
<hr/> SESSION EA - DAMMPS I <hr/>	
Statistical and Worst Case Evaluation of Orbital Jitter Reduction Using Passive Damping J. Molnar, Dennis Hill, and Clyde Stahle	EAA

*Not available for publication

TABLE OF CONTENTS (continued)

	<u>Paper No.</u>
LMSC DAMMPS Program Status J. Warren Hoskins and Dr. Y. C. Yiu	EAB
Damping of Precision Metal Matrix Trusses Dr. Stepan S. Simonian	EAC
Development of Low Modulus Damping Material for Precision Mounting Platforms Steven Kirshenbaum, Dennis Hill, and Clyde Stahle	EAD
Complex Stiffness Test Data for Three Viscoelastic Materials by the Direct Complex Stiffness Method Bradley R. Allen and Earl Pinson	EAE
SESSION EB - Viscoelastic Material Measurements	
Direct Measurement of the Dynamic Material Properties of Polymers for Low Frequencies Ahid D. Nashif, Thomas M. Lewis, and Paul J. Macioce	EBA
Correlation of Complex Modulus Data by Direct Stiffness and Indirect Resonant Beam Test Techniques T. Lewis, Mona P. Khoury, and Dr. David I. G. Jones	EBB
Constitutive Modeling of Nonlinear Damping Materials Dr. Jerome Sackman, Prof. J. M. Kelly, and A. E. Javid	EBC
Results of a Round Robin Test Series to Evaluate Complex Moduli of a Selected Damping Material Dr. David I. G. Jones	EBD
SESSION EC- Analysis and Design 3	
A Mathematical Framework for the Study of Indirect Damping Mechanisms David L. Russell	ECA*

*Not available for publication

TABLE OF CONTENTS (continued)

	<u>Paper No.</u>
Techniques of Design and Using Viscoelastic Dampers Z. Liang, M. Tong, and G. C. Lee	ECB
Modeling of Constrained Layer Damping in Trusses Dr. Daniel J. Inman, Joseph C. Slater, and W. Keith Belvin	ECC
A Strong Criterion for Testing Proportionally Damped Systems Z. Liang, M. Tong, and G. C. Lee	ECD
<hr/>	
SESSION ED - Applications	
Abbreviated Papers	
The PACOSS Dynamic Test Article Russell N. Gehling	EDA
Retrofitted Damping Treatment for a Three Stage Booster System Dr. Daniel J. Segalman and E. L. Marek	EDB*
Damping Design for a Disk Drive Head Flexure Eric M. Austin, James C. Goodding, and William A. Driscoll	EDC
Damping Jet Engine Front Frame Struts Capt. Vance Johnson, Kurt Nichol, and Dennis Murphy	EDD*
Isolation Joint for Flexural and Compressional Isolation Al Wignall and J. Aron	EDE
Characterization of Viscoelastic Damping in an Antenna Structure Dr. Ephraim Garcia, James M. Argento, and Robert Alan Carlin	EDF
Laminar Blade Damper Michael Koleda	EDG
Experimental Study on Noise Reduction due to Damping Treatments Ken Okada and Junichi Kanazawa	EDH*

TABLE OF CONTENTS (continued)

	Paper No.
<hr/> SESSION FA - DAMMPS 2 <hr/>	
Evaluation of Damping Concepts for Precision Mounting Platforms Dennis Hill, Clyde Stahle, and James Staley	FAA
Synergistic Design of Passive Damping and Metal Matrix Composites Earl D. Pinson, Eric M. Austin, and Michael L. Zeigler	FAB
A Three Element Viscoelastic Isolator Dr. Stepan S. Simonian	FAC
<hr/> SESSION FB - Noise and Acoustics <hr/>	
Integrally Damped Honeycomb Structural Concepts to Increase Noise Transmission Loss Jefferson F. Newton, Dr. Roy Ikegami, and D. J. Carbery	FBA
Reduction of Acoustic Responses Using Viscoelastic Damping Materials Dr. David Chu, C. Stahle, J. Staley, J. Peir, and M. McMeekin	FBB
Design Method of Damping Treatment for Structure-Borne Noise Reduction Iwao Honda, Tadao Nakamura, Yoshihiko Irie, and Kazuo Yamamoto	FBC*
<hr/> SESSION FC - Civil Structures <hr/>	
Earthquake Simulator Testing of Two Damping Systems for Multistory Structures Ian D. Aiken and James M. Kelly	FCA
Correlation of Experimental Results with Predictions of Viscoelastic Damping for a Model Structure T. T. Soong and Dr. Ming Lai	FCB

TABLE OF CONTENTS (continued)

	<u>Paper No.</u>
Damping Capacity of Reinforced Concrete External Beam Column Connections Dr. Alexander G. Tsonos, Ioannis A. Tegos, and Prof. Georgios G. Penelis	FCC*
<hr/> SESSION FD - Analysis and Damping Mechanisms <hr/> Abbreviated Papers	
Eddy Current-based Vibration Damping for Aerospace Structures James Goldie	FDA
The Absolute Value Modal Strain Energy Method Daniel R. Morgenthaler	FDB
An Analytical Model for the Vibration of Viscoelastically Damped Curved Sandwich Beams Dr. Mohan D. Rao and Shulin He	FDC
Bibliography of Environmental Data Measured In-Flight Lt. Col. Raymond F. Hain, III	FDD
General Motion of an Inclined Impact Damper with Friction C. N. Bapat	FDE
The Shock and Vibration Information Analysis Center (SAVIAC) Harold D. Kohn	FDF
<hr/> SESSION GA - Electro-Rheological Fluids and Fluids <hr/>	
The Vibration Damping Effect of an Electrorheological Fluid Stephen A. Austin	GAB
Modelling of Nonlinear Dilatation Response of Fluids Containing Columns Plastic and Shear Relaxation Considered Dr. Bernd Wendlandt	GAC

TABLE OF CONTENTS (continued)

	<u>Paper No.</u>
Electro-Rheological Fluids Characterization by Dynamic Mechanical Thermal Analysis under Applied Fields Dr. R. E. Wetton and Dr. J. C. Duncan	GAD*
<hr/> SESSION GB - Control Structure Interaction 2 <hr/>	
On Piezoelectric Energy Conversion for Electronic Passive Damping Enhancement Dr. Donald L. Edberg, Dr. Andrew S. Bicos, and J. S. Fechter	GBA
The Need for Passive Damping in Feedback Controlled Flexible Structures Dr. Andreas von Flotow and D. W. Vos	GBB
Passive Control of a Flexible Planar Truss Using A Reaction Mass Actuator Capt. Steven G. Webb and Lt. David R. Lee	GBC
<hr/> SESSION GC - Damping Identification <hr/>	
A Identification Technique for Damped Distributed Structural Systems Using the Method of Collocation R. Chander, M. Meyyappa, and S. V. Hanagud	GCA
Correlation Techniques to Determine Model Form in Robust Nonlinear System Realization/Identification Greselda Stry and D. Joseph Mook	GCB
System Level Design and Analysis of Truss Structures Damped by Viscous Struts Dr. Y. C. Yiu	GCC
Damping Ratio Estimates from Autocorrelation Functions Prof. Luigi Balis-Crema and Prof. A. Agneni	GCD

TABLE OF CONTENTS (continued)

	<u>Paper No.</u>
SESSION GD - Damping Materials	
Dynamic Moduli of Fluorocarbon Compounds Dr. Wayne T. Reader and Robert W. Megill	GDA*
Passive Vibration Damping with Noncohesive Granular Materials Dr. Moneh Abdel-Gawad	GDB
VEM Database Program Bryce L. Fowler	GDC
Measurement of the Mechanical Properties of Viscoelastics by the Direct Complex Stiffness Method Bradley R. Allen and Dr. David A. Kienholz	GDD
The Effect of Porosity on the Microstructural Damping Response of a 6061 Aluminum Alloy Jinmin Zhang, M. N. Gungor, and E. J. Lavernia	GDE
Damping Properties of Aliphatic Polyurethanes from 4, 4' - Dicyclohexylmethane Diisocyanate John D. Lee, Gilbert F. Lee, and Bruce Hartmann	GDF
An Apparatus for Measuring the Low Frequency Dynamic Characteristics of Materials Mona P. Khoury and Francis Olivier	GDG
SESSION HA - Composite and Metal Matrix	
Controlling the Damping Behavior of Pitch-based Carbon Fibers Andrew J. Eckel and Steven P. Jones	HAA
Internal Damping of Metal Matrix Composites: A Technical Assessment Jacques E. Schoutens	HAB
Vibration Suppression of Thin-Walled Composite Tubes Using Embedded Viscoelastic Layers F. M. Belknap and Professor J. B. Kosmatka	HAC

*Not available for publication

TABLE OF CONTENTS (continued)

	Paper No.
<hr/> SESSION HB - Tubes and Shells <hr/>	
Directional Damping of the Global Vibration Modes of Tubular Structures by Constrained-Layer Treatments Stanley S. Sattinger	HBA
Damped Response of Viscoelastic Thick Cylinders of Infinite Extent Dr. Hamid Hamidzadeh, D. J. Nunez, and D. E. Chandler	HBB
<hr/> SESSION HC - Circular Plates <hr/>	
Dynamic Analysis of Finite, Three Dimensional, Linear, Elastic Solids with Kelvin Viscoelastic Inclusions: Theory with Applications to Asymmetrically Damped Circular Plates Prof. C. D. Mote, Jr. and I. Y. Shen	HCA
Modal Analysis of Kelvin Viscoelastic Solids Under Arbitrary Excitation: Circular Plates Under Moving Loads I. Y. Shen and Prof. C. D. Mote, Jr.	HCB
Response of a Circular Plate with Patch Damping Prof. Douglas Muster, Mahmoud Mezache, and G. H. Koopmann	HCC
<hr/> SESSION IA - Viscous <hr/>	
Development of the PACOSS D-Strut David Cunningham	IAA
Design, Analysis, and Testing of the PACOSS D-Strut Truss Daniel R. Morgenthaler	IAB
An Advanced D-Strut L. Porter Davis and Dr. Steve Ginter	IAC

TABLE OF CONTENTS (continued)

	<u>Paper No.</u>
Testing of a Viscous Damped Isolator Bradley R. Allen and David Cunningham	IAD
<hr/> SESSION IB - Experimental Measurements <hr/>	
The Effect of Source Impedance on Damping Measurements Using Resonance Dwell Testing Ralph E. Tate	IBA
The Dependency of Vibration Energy Dissipation on the Amplitude of Structural Motion Dale L. Jensen	IBB*
Low-deflection Loss and Hysteresis Measurements on a Spacecraft Test Joint Eric M. Austin, James C. Goodding, and Timothy L. Flora	IBC
Damping Ratio Measurements in Kevlar Sandwich Samples Prof. Luigi Balis-Crema, Prof. A. Castellani, and Prof. A. Agneni	IBD
<hr/> SESSION IC - Metals <hr/>	
Characterization of the Damping Properties of High Damping Alloys Dr. Iain G. Ritchie and Z-L. Pan	ICA
Viscoelastic and Structural Damping Analysis Prof. Harry H. Hilton	ICB
Analysis of Strain Dependent Damping in Metals via Modeling of Material Point Hysteresis Dr. E. J. Graesser and C. R. Wong	ICC
Non-Obstructive Particle Damping Tests on Aluminum Beams Dr. Hagop V. Panossian	ICD

TABLE OF CONTENTS (continued)

	<u>Paper No.</u>
<hr/> SESSION JA - Experimental Measurements of Damping <hr/>	
Complex Dynamic Modulus of Nitinal-reinforced Composites Dr. Amr M. Baz, R. Deigan, and Dr. J. Gilheany	JAA*
Estimation of Nonproportional Damping from Experimental Measurements Dr. T. K. Hasselman and Jon D. Chrostowski	JAB*
Load Unit Deflection Correction for Forced Vibration Test System Kirk R. Biegler	JAC
<hr/> SESSION JB - Friction <hr/>	
An Analytical Approach to Designing Friction Dampers in Turbomachinery Blading Joe Panovsky, D. Hendley, and R. MacKay	JBA
Micro Slip Damping Mechanism in Bolted Joints Prof. M. Groper	JBB*
<hr/> SESSION JC - Analysis and Design 4 <hr/>	
On a Theory of Complex Damping Z. Liang, M. Tong, and G. C. Lee	JCA
An Iterative Method in Dynamic Structural Analyses with Nonproportional Damping Dr. Wan T. Tsai and J.T. Leang	JCB

An Identification Technique for Damped Distributed
Structural Systems Using the Method of Collocation

R. Chander¹, M. Meyyappa² and S.V. Hanagud³

School of Aerospace Engineering
Georgia Institute of Technology
Atlanta, GA 30332

(¹ Currently with Aerostructures, Inc., Arlington, Virginia)

(² Currently with McDonnell Douglas Helicopter Co., Mesa,
Arizona)

(³ Professor)

ABSTRACT

An identification scheme in the frequency domain, suitable for one-dimensional distributed structural dynamic systems with damping is considered. For this purpose, the form of a model representing the behavior of an Euler-Bernoulli beam is assumed to be known in the frequency domain. Also, the response of the system is assumed to be given at discrete locations along the beam. Quintic B-splines are then used to obtain a continuous representation of the response and its derivatives. The system parameters appearing in the governing differential equation are considered to be spatially varying functions. Cubic B-splines are used to approximate the parameter space, and their derivatives are obtained from such approximations. The method of collocation in conjunction with the equation error approach is then used to estimate the unknown parameters, which are the unknown coefficients of the parameter splines. A numerically simulated response of an Euler-Bernoulli beam in the presence of viscous damping is considered to validate the identification scheme. The estimated values of mass, stiffness and damping are discussed.

¹ Aerostructures, Inc.
1725 Jeff Davis Hwy. Suite 704
Arlington, VA 22202.
(703) 979-1600

INTRODUCTION

Damping is inherently present in virtually all types of structures encountered in practice. Hence, an adequate representation of damping and suitable methods to accurately quantify it are essential. In the recent past, there has been an increased interest in the study of distributed damping. For structures that can be modeled as continuous systems, discretization reduces modeling accuracy. In such cases, if the form of a model representing the physical system is known along with the initial and boundary conditions, the actual distributed system itself can be considered without resorting to approximations. A distributed representation is likely to yield more accurate predictions of the system behavior. Identification techniques suitable for distributed structural dynamic systems have been reported in the last decade [References 1-8].

At present, there are only very few techniques available to identify the unknown parameters of distributed structural dynamic systems in the presence of damping. Among these, the finite element and spline-based techniques have received considerable attention. The finite element techniques are primarily concerned with systems that include proportional or general viscous damping. A detailed discussion of such methods is presented in Reference 9. In the spline-based technique, time-domain data of the systems are used. The parameters are considered to be either constant or spatially varying functions, and also include different damping mechanisms [Reference. 5]. Also, in most of the available techniques some of the parameters are assumed to be known a priori.

In this vein, an identification technique that employs frequency domain data is discussed in this paper. For this purpose, the form of a model representing a distributed dynamic system within the framework of the Euler-Bernoulli beam theory was assumed to be known. The damping of the system was included using the linear viscous damping model. Also, the acceleration response was assumed to be given at discrete locations along the beam. The parameters appearing in the model were taken to be spatially varying functions. Quintic and cubic B-splines were then used to obtain approximate representations of the response and parameters, respectively. Their higher order derivatives were then obtained from such representations. These approximate functions were then substituted in the original distributed model, and using the collocation method a set of algebraic equations was obtained. The equation error approach was then used to estimate the unknown parameters, which are the coefficients of the parameter splines. The validity of the identification scheme was demonstrated using numerically simulated data, and the estimated values of mass, stiffness and damping are discussed.

For this purpose, none of the parameters was assumed to be known a priori.

PHYSICAL SYSTEM MODEL

The primary objective of the work presented in this paper was to develop an identification scheme suitable for a one-dimensional dynamic system in the presence of damping. The dynamic system was assumed to be modeled within the framework of the Euler-Bernoulli beam theory. The external damping to the system was included using the linear viscous damping model. A form of the equation governing the behavior of such systems was assumed to be known a priori in the frequency domain and can be written as follows:

$$\frac{d^2}{dx^2} \left[EI(x) \frac{d^2 a^*(x, \omega)}{dx^2} \right] + [j\omega C_v(x) - \omega^2 qA(x)] a^*(x, \omega) = -\omega^2 F(x, \omega) \quad (1)$$

where $a^*(x, \omega)$ is the acceleration response due to the applied forcing function $F(x, \omega)$, x is the axial distance, and ω is the frequency in radians/second. The beam was assumed to be cantilevered at $x=0$ and free at $x=L$, where L is the length of the beam. EI , C_v and ρA are the stiffness, damping and mass distributions, respectively, and were assumed to be continuous functions in x . These are the unknown parameters to be estimated. Also, in equation (1), the initial conditions were taken to be equal to zero.

Due to the popularity of acceleration as the most often measured quantity, it was chosen as the response variable in the model. For identification purposes, it was assumed to be known at as many frequencies as required. In general, it is not possible to have a continuous measurement of the response, hence it was assumed to be known at only a discrete number of locations. From this information, an approximate continuous representation was obtained and used in the identification scheme. To this effect, quintic B-splines were used to obtain a continuous response from the discrete data at each frequency.

Also, each of the parameters appearing in equation (1) was approximated using cubic B-splines due to their continuous nature. The task of parameter identification then reduces to merely estimating the unknown coefficients of the cubic spline functions. The method of collocation in conjunction with an equation error approach was used for this purpose. Frequency response functions at discrete locations along the length of the beam for an impulse load applied at a known location were used as the data in the identification scheme.

It is also assumed that ϕ_1 and ϕ_2 are highest order derivative of the input signal and component wave two and four, respectively. The order of the approximating polynomials are sought to be at least three and four, respectively, with respect to ϕ_1 and ϕ_2 . cubic and quartic approximations are used for ϕ_1 and ϕ_2 respective approximating functions.

RESPONSE REPRESENTATION

The infinite dimensional system response $y(t)$ is estimated by an (N+1) dimensional discrete time model as follows:

$$y[n] = \sum_{k=0}^N a_k y[n-k] + \sum_{k=0}^N b_k x[n-k] \quad (2)$$

or in matrix notation

$$y[n] = \mathbf{a}^T \mathbf{y}[n-1] + \mathbf{b}^T \mathbf{x}[n] \quad (3)$$

where $a_j(x)$ and $b_j(x)$ are the coefficients and \mathbf{a} and \mathbf{b} should satisfy a given set of boundary conditions, and a_0 and b_0 are constants to be determined. The discrete time approximations $\phi_1(x)$ and $\phi_2(x)$ were constructed using the fundamental quarter sine wave basis functions, which are defined below. Reference [2]

$$b_1(x) = \frac{1}{\sqrt{2}} \left[\cos\left(\frac{\pi}{2}x\right) + \cos\left(\frac{3\pi}{2}x\right) + 15\cos\left(\frac{5\pi}{2}x\right) + \dots \right] \quad (4)$$

where

$$x = \frac{t}{T} \quad \text{and } h = \frac{T}{N}$$

Also,

$$x_1 = \frac{t}{T} \quad \text{and } h = \frac{T}{N}$$

and

$$x_2 = \frac{t}{T} \quad \text{and } h = \frac{T}{N}$$

The basis functions $\phi_1(x)$ and $\phi_2(x)$ do not necessarily satisfy the boundary conditions at $t=0$. However, a combination of $\phi_1(x)$ and $\phi_2(x)$ can be used to construct the expressions $\phi_1(x)$ and $\phi_2(x)$ which satisfy the boundary conditions. Though many other approximations are possible, the following

expressions satisfying the cantilevered boundary conditions were used in this paper.

$$\begin{aligned}
 \phi_1(x) &= B_1^5(x) - (9/4)B_{-1}^5(x) + (65/2)B_{-2}^5(x) \\
 \phi_2(x) &= B_2^5(x) - (1/8)B_{-1}^5(x) + (9/4)B_{-2}^5(x) \\
 \phi_N(x) &= B_N^5(x) + (3/2)B_{N+1}^5(x) + B_{N+2}^5(x) \\
 \phi_{N-1}(x) &= B_{N-1}^5(x) - 2B_{N+2}^5(x) \\
 \phi_{N-2}(x) &= B_{N-2}^5(x) - (1/2)B_{N+1}^5(x) \\
 \phi_i(x) &= B_i^5(x), \quad i = 3, 4, \dots, N-3
 \end{aligned} \tag{5}$$

Substituting the expressions for $\phi_i(x)$ from equation (5) in equation (2), for a given set of measured responses at the knot locations $i=0, 1, 2, \dots, N$ at a given frequency, the coefficients $a_i(\omega)$ in equation (2) can be uniquely obtained. The higher order derivatives of the response involved in equation (1) could then be simply obtained by differentiating equation (2) as many times as required.

PARAMETER SPLINES

The unknown structural parameters present in equation (1) were represented as follows.

$$\theta^{(p)}(x) = \sum_{i=0}^M \theta_i^{(p)} C_i(x), \quad p = 1, 2 \text{ and } 3. \tag{6}$$

where $\theta^{(1)}$, $\theta^{(2)}$ and $\theta^{(3)}$ represent EI , C_v and ρA , and $\theta_i^{(1)}$, $\theta_i^{(2)}$ and $\theta_i^{(3)}$ are their corresponding coefficients. The value of M in equation (6) depends on the number of knot locations at which the parameters were identified. For a rapidly varying cross-sectional beam, a large value of M is required for an accurate identification. In the present case, the number of locations at which the parameters were to be identified was taken to be equal to the number of locations at which the response was known. The approximating basis functions $C_i(x)$ were taken to be cubic B-splines and are defined as follows [Reference 10].

$$\begin{aligned}
 C_i^3(x) &= 1/h^3 \left[(x-x_{i-2})_+^3 - 4(x-x_{i-1})_+^3 + 6(x-x_i)_+^3 - \right. \\
 &\quad \left. 4(x-x_{i+1})_+^3 + (x-x_{i+2})_+^3 \right]
 \end{aligned} \tag{7}$$

where

$$(x-x_i)_+^3 = \begin{cases} (x-x_i)^3, & \text{if } x \geq x_i \\ 0, & \text{otherwise} \end{cases}$$

Since the parameter knots were assumed to coincide with that of the response knots, equation (6) could be rewritten as

$$\theta^{(p)}(x) = \sum_{i=1}^{N+1} d_i^{(p)} C_i(x) \quad (8)$$

To obtain a unique solution for the d_i 's in equation (8), the following interpolatory conditions were to be satisfied.

$$\theta^{(p)}(x) = d_{-1}^{(p)} C_{-1}(x) + d_0^{(p)} C_0(x) + \dots + d_{N+1}^{(p)} C_{N+1}(x) \quad \text{at } x = x_0$$

$$\theta^{(p)}(x) = d_{-1}^{(p)} C_{-1}(x) + d_0^{(p)} C_0(x) + \dots + d_{N+1}^{(p)} C_{N+1}(x) \quad \text{at } x = x_1$$

$$\theta^{(p)}(x) = d_{-1}^{(p)} C_{-1}(x) + d_0^{(p)} C_0(x) + \dots + d_{N+1}^{(p)} C_{N+1}(x) \quad \text{at } x = x_{N+1}$$

$$\theta^{(p)}(x) = d_{-1}^{(p)} C_{-1}(x) + d_0^{(p)} C_0(x) + \dots + d_{N+1}^{(p)} C_{N+1}(x) \quad \text{at } x = x_{N+1}$$

(9)

where a " ' " denotes the first derivative with respect to the axial coordinate. Now, define a vector $\{\theta^{(p)}\}$ as

$$\{\theta^{(p)}\} = \left[\theta^{(p)}(x_0), \theta^{(p)}(x_0), \theta^{(p)}(x_1), \dots, \theta^{(p)}(x_N), \theta^{(p)}(x_N) \right] \quad (10)$$

The above vector, which also includes the first derivatives of the parameters at $x=0$ and $x=L$, is the unknown quantity to be identified.

IDENTIFICATION SCHEME

Equation (9) can be written in the matrix form as

$$\{R^{(p)}\} = \{G^{(p)}\} \{P^{(p)}\}$$

or

$$\{d^{(p)}\} = [C^*]^{-1} \{\theta^{(p)}\} \quad (11)$$

Substituting from equation (11) for $\{d^{(p)}\}$, equation (8) and its derivatives were written in the matrix form as

$$\begin{aligned} \theta^{(p)}(x) &= \{C(x)\}^T [C^*]^{-1} \{\theta^{(p)}\} \\ \theta'^{(p)}(x) &= \{C'(x)\}^T [C^*]^{-1} \{\theta^{(p)}\} \\ \theta''^{(p)}(x) &= \{C''(x)\}^T [C^*]^{-1} \{\theta^{(p)}\} \end{aligned} \quad (12)$$

Equation (12) was evaluated at the knot locations $\{x_k\}^T$, and the following equations were obtained.

$$\begin{aligned} \theta^{(p)}(x) &= \{P_k\}^T \{\theta^{(p)}\} \quad \text{at } x=x_k \\ \theta'^{(p)}(x) &= \{Q_k\}^T \{\theta^{(p)}\} \quad \text{at } x=x_k \\ \theta''^{(p)}(x) &= \{R_k\}^T \{\theta^{(p)}\} \quad \text{at } x=x_k \end{aligned} \quad (13)$$

where

$$\begin{aligned} \{P_k\}^T &= \{C(x)\}^T [C^*]^{-1} \quad \text{at } x=x_k \\ \{Q_k\}^T &= \{C'(x)\}^T [C^*]^{-1} \quad \text{at } x=x_k \\ \{R_k\}^T &= \{C''(x)\}^T [C^*]^{-1} \quad \text{at } x=x_k \end{aligned} \quad (14)$$

The dimensions of each of the above vectors is $1 \times (N+3)$.

A term a_{kl}^* was defined as the quantity $a^*(x, \omega)$ in equation (3) evaluated at a given location x_k and frequency ω_1 . Equation (13) was combined with this definition, and equation (1) was rewritten as follows.

$$\begin{aligned} \{P_k\}^T \{\theta^{*(1)}\} (a_{kl}^*)'''' + 2\{Q_k\}^T \{\theta^{*(1)}\} (a_{kl}^*)'''' + \{R_k\}^T \{\theta^{*(1)}\} (a_{kl}^*)'''' + \\ \{P_k\}^T [-\omega_1^2 \{\theta^{*(3)}\} + j\omega_1 \{\theta^{*(2)}\}] a_{kl}^* = F_{kl} \end{aligned} \quad (15)$$

where F_{kl} is the force applied at location x_k and at frequency ω_1 . In equation (15) both a_{kl}^* and F_{kl} are complex quantities. Hence, they could be separated into real and imaginary parts as

$$\begin{aligned} a_{kl}^* &= a_{kl}^R + ja_{kl}^I \\ \text{and} \\ F_{kl} &= F_{kl}^R + jF_{kl}^I \end{aligned} \quad (16)$$

Using the above definition, equation (15) could be finally written as

$$\begin{bmatrix} (R_1)^T_{kl} & -\omega_1 (R_4)^T_{kl} & -\omega_1^2 (R_3)^T_{kl} \\ (R_2)^T_{kl} & \omega_1 (R_3)^T_{kl} & -\omega_1^2 (R_4)^T_{kl} \end{bmatrix} \begin{Bmatrix} \theta(1) \\ \theta(2) \\ \theta(3) \end{Bmatrix} = \begin{Bmatrix} F^R_{kl} \\ F^I_{kl} \end{Bmatrix} \quad (17)$$

where

$$\begin{aligned} (R_1)^T_{kl} &= (P_k)^T (a^R_{kl})'''' + 2(Q_k)^T (a^R_{kl})''' + \\ &\quad (R_k)^T (a^R_{kl})'' \\ (R_2)^T_{kl} &= (P_k)^T (a^I_{kl})'''' + 2(Q_k)^T (a^I_{kl})''' + \\ &\quad (R_k)^T (a^I_{kl})'' \\ (R_3)^T_{kl} &= (P_k)^T (a^R_{kl}) \\ (R_4)^T_{kl} &= (P_k)^T (a^I_{kl}) \end{aligned} \quad (18)$$

Equation (17) was obtained for a single frequency. Similar sets of equations could be written at other frequencies. Combining the different sets at various frequencies, the resulting equations could be written as follows.

$$[C_\theta](\theta) = \{F_\theta\} \quad (19)$$

$[C_\theta]$ is the coefficient matrix of dimension $2(N+3)n \times 3(N+3)$, where n is the number of frequencies used in the estimation. $\{\theta\}$ and $\{F_\theta\}$ are respectively the parameter and force vector of order $3(N+3)$. A least-square solution $\{\theta^*\}$ for equation (19) could be written as follows.

$$\{\theta^*\} = C_\theta^T C_\theta^{-1} C_\theta^T F_\theta \quad (20)$$

NUMERICAL RESULTS

The identification scheme discussed in the previous section was demonstrated using simulated data for a cantilever beam with the following properties.

$$L = 0.61\text{m}$$

$$EI(x) = 18.01 \cdot 10^2 [1 - (x/2L)]^4 \text{ N-m}^2$$

$$\rho A(x) = 4.22 [1 - (x/2L)]^2 \text{ N/m}$$

$$C_V(x) = 17.3 [1 - (x/2L)]^2 \text{ N-sec/m}^2$$

The above parameter distributions correspond to a beam of linearly varying cross section from tip to root, with the dimensions at the tip being half of those at the root. The beam

was subdivided into 12 regions ($N=12$), and an independent finite element program was used to calculate the response at the resulting 13 knots. The assumed impulse was applied at the eighth interior knot x_8 (Figure 1). The first three natural frequencies of the beam determined from the finite element program were found to be 36.9Hz, 155.9Hz and 387.4Hz, respectively. In the identification, the frequency response data in the following frequency bandwidths at 1Hz intervals were used:

25-34Hz and 39-48Hz (regions surrounding the first mode)
144-153Hz and 158-167Hz (regions surrounding the second mode)
376-385Hz and 390-399Hz (regions surrounding the third mode)

Including the data in the immediate vicinity of the modal peaks resulted in less accurate estimates of damping, hence they were omitted. The probable cause for this phenomenon is the fact that the frequency response function tends to vary rapidly around the modal peaks for lightly damped structures, increasing the error in the response close to the peak regions. This in turn could significantly reduce the parameter estimates.

It can be seen from Figures 2-4, that the estimated values are in excellent agreement with the actual values used in generating the frequency response functions at the interior knots. Unacceptable mass and damping estimates at the root location were obtained and are not shown in the figures. This phenomenon may be due to the little or no contribution of these parameter values at the root to the error in satisfying the beam differential equation. Since the parameters are calculated by the subsequent minimization of this error, the procedure yields highly inaccurate estimates at these locations.

SUMMARY AND CONCLUSIONS

A spline based identification technique in the frequency domain that is suitable for damped distributed structural dynamic systems was developed. A beam whose behavior can be modeled within the framework of the Euler-Bernoulli beam theory was considered for the identification scheme. The parameters were allowed to vary linearly along the length of the beam. The infinite-dimensional response and parameter spaces were approximated by quintic and cubic B-splines, respectively. A Galerkin type weighted residual procedure was used to estimate the unknown parameters. Simulated frequency response data for an impulse applied at a known location were used to validate the technique. Acceleration response data around the first three modes of the beam were employed to estimate the mass, stiffness and damping properties. None of the parameters was assumed to be known a priori. The estimated results showed excellent agreement with the actual values at all the interior locations of the beam.

ACKNOWLEDGEMENT

Support for this work from the U.S. Army Research Contract DAAG-29-82-K-0094 is gratefully acknowledged.

REFERENCES

1. Banks, H.T. and Crawley, J.H., "Parameter Estimation for Distributed Systems Arising in Elasticity," Proceedings of Symposium on Engineering Sciences and Mechanics held at National Chang Kung University, People's Republic of China, pp. 153-177, Dec. 1981.

2. Banks, H.T., Rosen, I.G., Wang, C. and Rauch, H.E., "Estimation of Stiffness and Damping in Cantilevered Euler-Bernoulli Beams with Tip Bodies," Proceedings of the 4th IFAC Symposium on Control of Distributed Parameter Systems, pp. 327-332, 1982.

3. Banks, H.T. and Crawley, J.H., "Parameter Identification in Continuum Models," Proceedings of the 1983 American Control Conference, San Francisco, California, June 1983.

4. Banks, H.T. and Crawley, J.H., "Parameter Estimation in Timoshenko Beam Models," Journal of Astronautical Sciences, pp. 381-394, July 1983.

5. Banks, H.T., Fibiano, R.H., Wang, Y., Inman, D.J. and Cudney, H., "Spatial Versus Time Hysteresis in Damping Mechanisms," Proceedings of the 27th IEEE Conference on Decision and Control, pp. 1674-1677, 1988.

6. Baruh, J. and Meirovitch, L., "Parameter Identification of Distributed Systems," Journal of Sound and Vibration, pp. 551-564, 1985.

7. Lee, K.Y. and Hossian, S.A., "Distributed System Approach to Identification of Flexible Structures," Journal of Guidance, Control and Dynamics, pp. 540-548, 1987.

8. Meirovitch, L. and Norris, P., "Parameter Identification in Distributed Spacecraft Structures," Journal of Astronautical Sciences, pp. 341-353, Oct. 1986.

9. Cheng, Y.P., "Frequency Domain Identification of Structural Dynamic Systems with General Damping Matrices," Ph.D Thesis, School of Aerospace Engineering, Georgia Institute of Technology, Atlanta, Georgia, 1987.

10. Prenter, R.M., Splines and Variational Methods, Wiley Interscience, 1975.

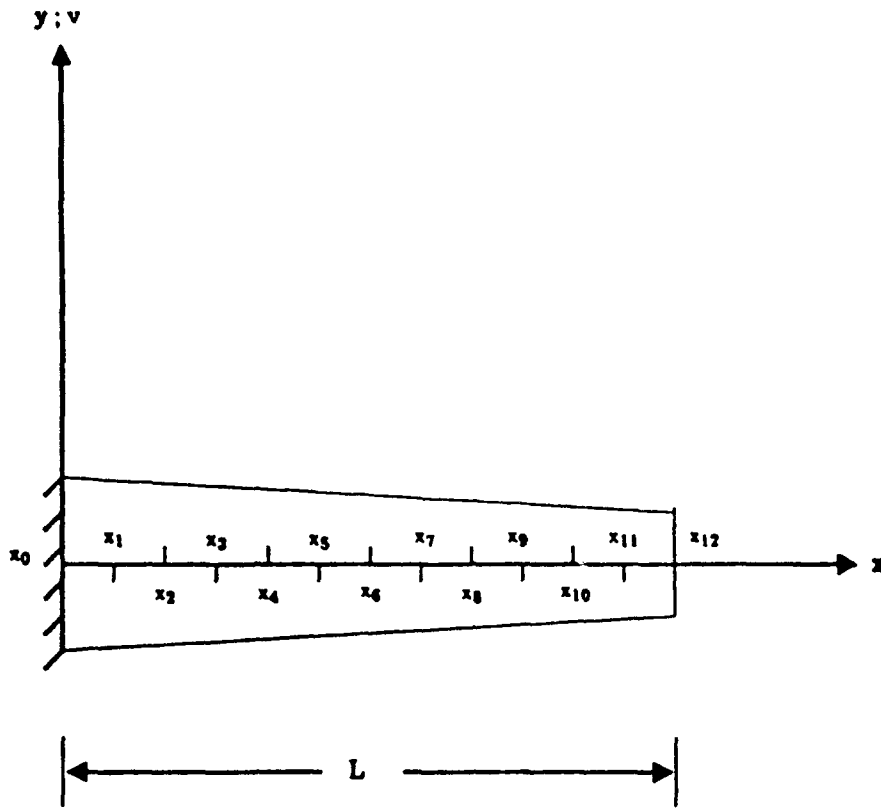


Figure 1 Beam Geometry

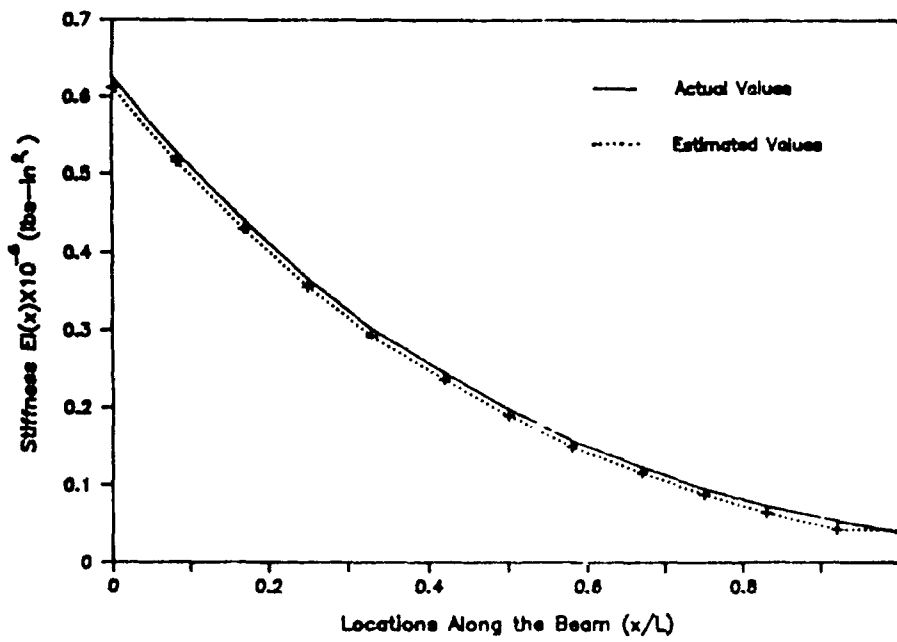


Figure 2 Stiffness Estimates

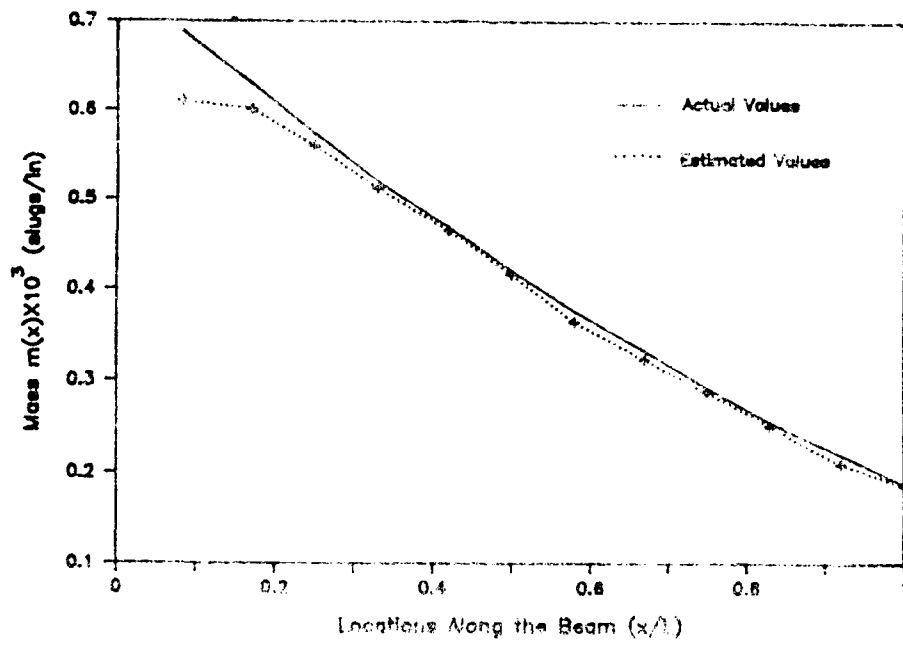


Figure 3 Mass Estimates

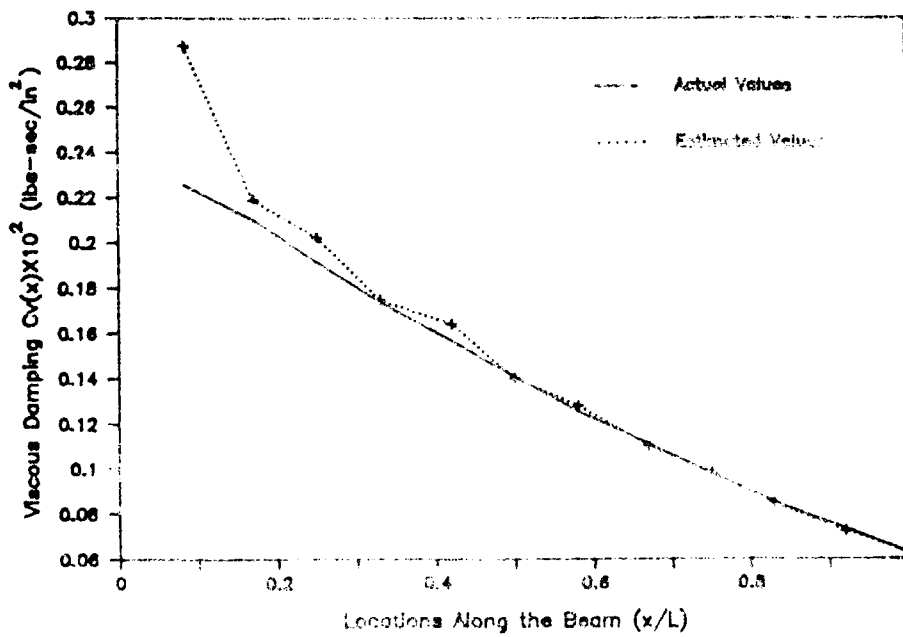


Figure 4 Damping Estimates

Correlation Techniques To Determine Model Form In Robust Nonlinear System Realization/Identification

Greselda I. Stry¹ and D. Joseph Mook²

**Department of Mechanical and Aerospace Engineering
State University of New York at Buffalo
Buffalo, New York 14260
716-636-3058**

ABSTRACT

The fundamental challenge in identification of nonlinear dynamic systems is determining the appropriate form of the model. A robust technique is presented in this paper which essentially eliminates this problem for many applications.

The technique is based on the Minimum Model Error (MME) optimal estimation approach. A detailed literature review is included in which fundamental differences between the current approach and previous work is described. The most significant feature of the current work is the ability to identify nonlinear dynamic systems without prior assumptions regarding the form of the nonlinearities, in contrast to existing nonlinear identification approaches which usually require detailed assumptions of the nonlinearities. Model form is determined via statistical correlation of the MME optimal state estimates with the MME optimal model error estimates. The example illustrations indicate that the method is robust with respect to prior ignorance of the model, and with respect to measurement noise, measurement frequency, and measurement record length.

¹ Graduate Research Assistant; NASA Graduate Researcher

² Assistant Professor

INTRODUCTION

The widespread existence of nonlinear behavior in many dynamic systems is well-documented, e.g. Thompson and Stewart [1]; Nayfeh and Mook [2]. In particular, virtually every problem associated with orbit estimation, flight trajectory estimation, spacecraft dynamics, etc., is known to exhibit nonlinear behavior. Many excellent methods for analyzing nonlinear system models have been developed. However, a key practical link is often overlooked, namely: How does one obtain an accurate mathematical model for the dynamics of a particular complicated nonlinear system? General methods for actually obtaining accurate models for real physical systems are not nearly as widespread or well developed as are the techniques available for analyzing models.

Accurate dynamic models are necessary for many tasks, including basic physical understanding, analysis, performance prediction, evaluation, life cycle estimation, control system design, etc. For example, most filter design assumes white process noise, yet many nonlinear effects are inherently non-zero mean; e.g., quadratic nonlinearities are always positive. In order to obtain a model with truly zero mean process noise for filter design purposes, all of the quadratic terms (and many other nonlinearities) must be well modeled. However, the complexity of many real systems greatly diminishes the possibility of accurately constructing a dynamic model purely from analysis using the laws of physics.

Identification is the process of developing an accurate mathematical model for a system, given a set of output measurements and knowledge of the input. Many well developed and efficient identification algorithms already exist for linear systems (e.g., [3]-[7]). These often may be employed to model nonlinear systems when the system nonlinearities are small, and/or the system operates in a small linear regime. However, linearization does not work well (if at all) in every application, and even when it does provide a reasonable approximation, the approximation is normally limited to a small region about the operating point of linearization. Consequently, there is a real need for nonlinear identification algorithms. If nonlinearities are a predominant part of a system's behavior, using a linear model to describe such a system leads to inconsistencies ranging from inaccurate numerical results to misrepresentation of the system's qualitative behavior. Many important characteristics of nonlinear behavior, such as multiple steady-states, limit cycles, hysteresis, softening or hardening systems, chaos, etc., have no linear equivalent. Since nonlinearities are seldomly easily characterized, identification techniques may prove beneficial in developing accurate mathematical representations of nonlinear systems.

Numerous methods for the identification of nonlinear systems have been developed in the past two decades. Many of these techniques are reviewed in Natke, Juang and Gawronski [8], Billings [9], and Bekey [10]. Most methods fall into one of the following categories:

- describing the nonlinear system using a linear model
- the direct equation approach
- representing the nonlinear system in a series expansion, and obtaining the respective coefficients either by using a regression estimation technique, by minimizing a cost functional,

- by using correlation techniques, or by some other approach
- obtaining a graphical representation of the nonlinear term(s), then finding an analytical model for the nonlinearity

With such diversity of nonlinear identification techniques, the choice of a particular algorithm may be based on criteria such as: the degree to which prior assumptions of the model form affect the user's effort in applying the algorithms; the number of iterations required; the sensitivity to the presence of measurement noise in the data; the number of state measurements needed; whether or not knowledge of the initial conditions is required; the kind of forcing input(s) required or permitted (step, white gaussian noise, sinusoidal, etc.); the ability to handle hysteric or discontinuous nonlinearities; the degree of a priori knowledge of system properties required; and the computational requirements. Most algorithms differ widely in at least some of these comparisons; the choice of a particular technique depends on the needs of the particular application.

Among the methods which linearize the nonlinear system are those presented by Jedner and Unbehauen [11] and Ibanez [12]. Jedner and Unbehauen represent a nonlinear system, which may often operate in small regions around a number of operating points, by an equivalent number of linear submodels. It is assumed that the system operates at only a few points. Although the model may work well for controller design, the points at which the system is operating must be known and the linear models apply only within the operating regions. Ibanez takes a slightly different approach by assuming the system response to be periodic at the forcing frequency. An approximate transfer function is constructed. The transfer function is dependent on the amplitude as well as on the exciting frequency and is valid only within the region of exciting frequencies.

The direct equation approach is used by Yasuda, Kawamura and Watanabe [13], [14]. The input and output measurements of a dynamic process are expressed in a Fourier Series using, for example, an FFT algorithm. The system nonlinearity is represented as a sum of polynomials with unknown coefficients. Applying the principle of harmonic balance, the polynomial coefficients as well as the other system parameters are obtained accurately. Knowledge of the nonlinearity is needed to construct the polynomial. Truncation in the Fourier Series expansion of the input or output may lead to error.

The regression estimation approach is used by Billings and Voon [15] and Greblich and Pawlak [16]. Billings and Voon use the NARMAX model (Nonlinear Auto Regressive Moving Average model with eXogenous inputs) to represent the nonlinear system. A stepwise regression method determines the significant terms in the NARMAX model. Then a prediction-error algorithm provides optimal estimates of the final model parameters. Greblich and Pawlak represent the linear dynamic submodel by an ARMA model and the nonlinearities by a Borel function. A non-parametric kernel regression estimation is employed to obtain the final analytical model.

Kortman and Unbehauen [17] and Distefano and Rath [18] use the minimization of an error cost function as a means of obtaining the coefficients of the functions used to represent the

nonlinearities. The identification of the nonlinear part of the model requires less input and output information as a direct consequence of the sparse nature of the nonlinearities. The parameters of the linear components can be identified in the presence of noise, although a minimum is necessary. Distefano and Rath present a technique for nonlinear identification using an iterative direct identification. In this technique, the measurement of all variables is assumed and the model parameters are obtained through the minimization of an error function. In the second technique, iteration is used to minimize a cost function yielding the system parameters in addition to the state trajectories. In Distefano and Rath's method, a model of the nonlinearities is assumed to be known.

In other techniques, such as statistical linearization, a nonlinear relation is replaced by a linear equivalent gain. Broecker's identification technique of statistical linearization by representing the nonlinearity as a linear combination of a number of arbitrary functions. Correlation techniques are then used to determine the coefficients of these functions. The number and type of functions selected depends on the desired accuracy as well as some knowledge of the system nonlinearity. Reasonable accuracy is obtained in the presence of noise and no iterations are necessary. Although some of the basic properties of the true nonlinear output are preserved, it is limited to only random excitation and steady state conditions and frequency response is required.

In the method of multiple scales (Jan and Mayyappa and Chong [30]), a perturbation solution to the nonlinear equation of motion is obtained. An objective function is built employing an integral least squares approach. The minimization of the functional yields the unknown parameters. Data on only one field variable is necessary, and the method is effective in the presence of high noise. The nature of multiple scales, however, is restricted to systems with small damping and short backslashes and, as in most other methods, the form of the nonlinearity is assumed a priori. The method typically requires some algebraic manipulations which may be quite involved, and these conclusions are only valid for a particular assumed nonlinear form. If the system does not conform to the model, the algorithm must be repeated.

Several techniques do not require a model for a system using the Volterra or Wiener kernels. The Volterra series consists of linear and nonlinear impulse responses of any order of nonlinearity. The Wiener series is also a set of impulse responses, in which the input is white gaussian noise. Marmarelis and Valdes [31] have used the series expansion method to identify the kernels appearing in the Volterra series for a nonlinear system. Chou and Jan [22] use cross-correlation functions and the series expansion method to identify nonlinear models and to show the relative error of the series expansion method. Although weakly nonlinear systems can be approximated by a linear system, for strongly nonlinear systems these series give accurate results. The series expansion method is a method of identifying coefficients. This renders the method useful for identifying nonlinear systems.

Other popular series expansions are the Legendre and Chebyshev series. Legendre (Wang and Jan [23]) and Chebyshev (Horn and Chou [24]) series expansions are used to approximate the nonlinear state equation and the series expansion method is used to identify the coefficients of the nonlinear

system are then estimated using least squares. Even though the algorithm works well in the presence of noise, the nonlinear form must be known a priori.

Methods for the identification of nonlinear systems have also been developed based on the extended Kalman filter. The extended Kalman filter is the linear Kalman filter applied to nonlinear systems by linearizing the nonlinear model into a Taylor series expansion about the estimated state vector. Yun and Shinozuka [25] apply the extended Kalman filter for the parameter estimation of a quadratic term. The state vector is augmented by including the unknown parameters in addition to the state variables. Through a series of iterations, the response, as well as the unknown parameters, are estimated by the Kalman filter. Among its disadvantages are high sensitivity to initial conditions, in particular if the initial conditions are barely known. The nonlinear form must be chosen a priori in order to estimate the corresponding parameter(s).

Hammond, Lo and Seager-Smith [26] use an optimal control technique based on optimal control methods employed for linear system deconvolution. The form of the linear model is assumed to be known as well as the input and the output. A cost functional consisting of the weighted sum of the square of the error (between the actual and estimated output) yields an optimal estimated input. The estimated input and the actual input are used to obtain the nonlinearity as a function of the state variables. Although no previous assumption is made of the nonlinearities, there is no provision to deal with noise.

All of the techniques outlined above have proven useful in certain applications. However, all of them are subject to one or more of the following shortcomings:

1. The form of the nonlinearity (quadratic, cubic, exponential, etc.) must be assumed a priori. This is a very serious drawback, because the identification algorithm can only attempt to find the best model in the assumed form. If the form is assumed incorrectly, the resulting model may be so poor as to be useless, or it may appear to fit the data well enough that the user erroneously concludes that the correct model has been obtained. Also, for many techniques of this type, the effort required to test a given form is considerable, which greatly diminishes the effectiveness since multiple form tests are less likely to be conducted.
2. Techniques which attempt to avoid the problem of a priori model form assumption through the use of series expansions generally eliminate any possibility of understanding the underlying physics. Thus, although a good fit of the data might be achieved using a sufficient number of terms in the series, physical insight is lost. Moreover, large systems and/or particularly complicated behavior may require that a very large number of terms be used to obtain a given level of accuracy.
3. The presence of noise in the measurement data is not rigorously treated, yet noise is generally unavoidable.
4. Initial conditions must be known in order to implement the algorithm.
5. The algorithm can only be implemented if the data is obtained using very specific system excitations.

The algorithm of the current paper compares favorably with existing algorithms in most of

the categories listed above. It is robust with respect to measurement noise; does not require knowledge of the initial conditions; is independent of the forcing (but, like all methods, assumes that it is known); is not computationally prohibitive; and, most importantly, it requires minimal a priori assumptions regarding the form of the model or the system properties. In fact, using the correlation technique outlined in the next section, the algorithm essentially eliminates the need to ever assume the nonlinear model form.

The identification algorithm is based on a combination of Minimum Model Error (MME) state estimation, correlation techniques, and least squares. MME was first described by Mook and Junkins [27]. The MME combines the available measurements and an assumed model of the system to produce optimal estimates of the states and the model error. The assumed model represents an initial attempt to model the system using direct analysis, but may be extremely poor. Given the noisy output measurements of the system, MME estimates the state histories as well as the error in the assumed model. In previous work, the correct form and corresponding parameters of the nonlinear model were then estimated in a trial-and-error fashion, by assuming a nonlinear (in the states) form of the error terms, and then determining the best least-squares fit between the state estimates and the model error estimates. Thus, although the MME portion of the algorithm did not require the model form to be assumed, the subsequent least-squares fit between the state estimates and the model error estimates did. In Mook [28] it was shown that this approach could accurately identify terms in a Duffing oscillator in the presence of noise and sparse measurements. The method worked well even when only a crude model of the dynamic system was assumed, and the error model used for the least-squares fit contained numerous terms in addition to the correct one(s). Later, in Mook and Stry [29], a simple harmonic oscillator with quadratic feedback was simulated on an analog computer. The algorithm was shown to accurately identify the nonlinear model from analog measurements.

In this paper, the identification of the model from the MME-produced state and model error estimates is improved by using correlation techniques to select the form of the correction terms. The correction terms, when added to the initially assumed model, yield the true model of the system. The correction terms may consist of a combination of linear and nonlinear functions. An extensive library of linear and nonlinear functions has been assembled. The correlation technique is used to select the true forms from the library. Even when the true form of the nonlinearity was not present in the library, the correlation technique picks the closest form(s), typically, the first term(s) in the Taylor Series expansion. Once the forms have been selected by the correlation algorithm, least squares is used to determine the model parameters.

IDENTIFICATION ALGORITHM

In this section, the identification algorithm is explained. First, the MME technique is briefly reviewed, and then the correlation technique used to automate the model form determination is explained in detail.

The MME may be summarized as follows (a more detailed explanation may be found

in Mook and Junkins [27]). Suppose there is a nonlinear system whose exact analytical representation is unknown, but for which output measurements are available. Using whatever means are available (analysis, finite elements, etc.), a system model is constructed. As shown in [27]-[29], the MME works well even if this system model is poor. The MME combines the assumed model with the measurements to produce optimal estimates of (i) the state trajectories, and (ii) the error in the model. In the present work, these state and model error estimates are used for system identification.

Consider a forced nonlinear dynamic system which may be modeled in state-space form by the equation

$$\dot{\underline{x}}(t) = A\underline{x}(t) + \underline{F}(t) + \underline{f}(\underline{x}(t), \dot{\underline{x}}(t)) \quad (1)$$

where $\underline{x}(t)$ is the $n \times 1$ state vector consisting of the system states, A is the $n \times n$ state matrix, $\underline{F}(t)$ is an $n \times 1$ vector of known external excitation, and $\underline{f}(\underline{x}(t), \dot{\underline{x}}(t))$ is an $n \times 1$ vector which includes all of the system nonlinearities. State-observable discrete time domain measurements are available for this system in the form

$$\underline{y}(t_k) = \underline{g}_k(\underline{x}(t_k), t_k) + \underline{v}_k, \quad t_0 \leq t_k \leq t_f \quad (2)$$

where $\underline{y}(t_k)$ is an $m \times 1$ measurement vector at time t_k , \underline{g}_k is the accurate model of the measurement process, and \underline{v}_k represents measurement noise. \underline{v}_k is assumed to be a zero-mean, gaussian distributed process of known covariance R_k . The measurement vector $\underline{y}(t_k)$ may contain one or more of the system states. To implement MME, assume that a model, which is generally not the true system model because of the difficulties inherent in obtaining the true system model, is constructed in state-vector form as

$$\dot{\underline{x}}(t) = A\underline{x}(t) + \underline{F}(t) \quad (3)$$

Here, we show a linear model because in practice, linearization is the most common approach to modeling nonlinear systems. MME uses the assumed linear model in Eq. (3) and the noisy measurements in Eq. (2) to find optimal estimates of the states and of the model error.

The model error, which includes the unknown nonlinear terms of the system, is represented by the addition of a term to the assumed linear model as

$$\dot{\underline{x}}(t) = A\underline{x}(t) + \underline{F}(t) + \underline{d}(t) \quad (4)$$

where $\underline{d}(t)$ is the $n \times 1$ model error to be estimated along with the states.

A cost functional, J , that consists of the weighted integral square of the model error term plus the weighted sum square of the measurement-minus-estimated measurement residuals, is formed:

$$J = \sum_{k=1}^M \left\{ [\underline{y}(t_k) - \underline{g}_k(\hat{\underline{x}}(t_k), t_k)]^T R_k^{-1} [\underline{y}(t_k) - \underline{g}_k(\hat{\underline{x}}(t_k), t_k)] \right\}$$

$$J = \int_{t_0}^{t_f} \underline{d}(\tau)^T W \underline{d}(\tau) d\tau \quad (5)$$

where M is the number of measurement times, $\underline{z}(t_k)$ is the set of measurements at time t_k and W is a weight matrix to be determined.

J is minimized with respect to the model error term, $\underline{d}^T \underline{z}$. The necessary conditions for the minimization lead to the following two point boundary value problem (TPBVP) (see Giering [30]),

$$\dot{\underline{z}}(t) = A\underline{z}(t) + \underline{F}(t) + \underline{d}(t) \quad (5a)$$

$$\dot{\underline{\lambda}}(t) = -A^T \underline{\lambda}(t) \quad (5b)$$

$$\underline{d}(t) = -\frac{1}{2} W \underline{\lambda}(t) \quad (5c)$$

$$\underline{\lambda}(t_k^+) = \underline{\lambda}(t_k^-) + 2H_k R_k^{-1} \underline{y}(t_k) - \underline{g}_k(\underline{z}(t_k), t_k) \quad (5d)$$

$$H_k = \frac{\delta \underline{g}}{\delta \underline{z}} \Big|_{\underline{z}(t_k), t_k}$$

$$\underline{z}(t_0) = \underline{z}_0 \quad \text{or} \quad \underline{\lambda}(t_0) = 0 \quad (5e)$$

$$\underline{z}(t_f) = \underline{z}_f \quad \text{or} \quad \underline{\lambda}(t_f) = 0 \quad (5f)$$

where $\underline{\lambda}(t)$ is a vector of costates (Lagrange multipliers). Its integration, along with that of the model error are produced by the solution of this two point boundary value problem. The estimates depend on the particular value of W . The solution is repeated until a value of W is obtained which produces state estimates which satisfy the performance constraint specified next.

According to the covariance constraint, the measurement noise and the measurement residual covariance matrix must match the measurement model and the covariance matrix. This may be written as

$$\underline{y}(t_k) - \underline{g}_k(\underline{z}(t_k), t_k)^T \underline{y}(t_k) - \underline{g}_k(\underline{z}(t_k), t_k) = R_k \quad (6)$$

During the minimization, the weight W is varied until the state estimates satisfy the covariance constraint, i.e., the left hand side of Eq. (6) is approximately equal to the right hand side. The model error is, therefore, the minimum adjustment to the model to make the estimated states to predict the measurements with approximately the same covariance as the measurement error.

The TPBVP represented by Eqs. (5a) to (5f) contains jump discontinuities and, consequently, in the model error. As evident from Eq. (5d), the size of the jump is directly proportional to the measurement residual at each measurement time. The more the measurements, the larger the jump size. A multiple shooting algorithm, developed by the author [31], converts this jump-discontinuous TPBVP into a set of linear algebraic equations which can be solved using any linear equation solver. Multiple shooting also facilitates the analysis of a large number of measurements, by processing the solution at the end of every measurement.

Correlation is a measure of the relationship that exists between two variables. The more highly correlated two variables are, the more closely will their values, or possibly correspond to

a change in the other variable. The cross-correlation coefficient between two discrete variables, say x and y , is defined as (see Newland [32] or Witte [33])

$$C(x, y) = \frac{\sum_{i=1}^n (x_i - \bar{x})(y_i - \bar{y})}{\sigma_x \sigma_y n} \quad (7)$$

where n is the number of data points and the overbar denotes the mean of those n points. σ_x is the standard deviation of the variable x and is defined as

$$\sigma_x = \sqrt{\frac{\sum_{i=1}^n (x_i - \bar{x})^2}{n}}$$

$C(x, y)$ is a measure of the linear relationship between variables x and y . The value of $C(x, y)$ lies in the range $-1 < C(x, y) < 1$. If, for instance, changes in the value of x correspond to perfectly predictable (linearly) changes in the value of y , where the changes in both variables are of the same sign, then the value of $C(x, y)$ is 1. If the changes are of opposite sign but still perfectly predictable, then the value of $C(x, y)$ is -1. If changes in the values of x and y tend to correspond in sign but are not perfectly predictable, then $0 < C(x, y) < 1$. If changes in the values of x and y tend to be of opposite sign but are not perfectly predictable, then $-1 < C(x, y) < 0$. If there is no linear relationship between the values of x and y , then $C(x, y) = 0$. For example, suppose x and y are multiples of each other, $x = K * y$, where K is an arbitrary constant of proportionality. Then

$$C(x, y) = \frac{\sum_{i=1}^n K(x_i - \bar{x})^2}{\sum_{j=1}^n K(x_j - \bar{x})^2} = 1.0 \quad (8)$$

The true functional form of the model error can be found by calculating the correlation of the MME model error estimates with functions of the MME state estimates. If the functional form of the actual system is used, and if the estimates from MME are perfect, then $C(x, y) = 1.0$. Thus, an algorithm may be constructed which performs nonlinear system identification by (i) utilizing the MME to process the available measurements and the initial model in order to produce state estimates and model error estimates, and (ii) testing the correlation between the state estimates and the model error estimates using a "sufficient number" of functional forms so that the actual form is included among those tested. The MME does not require that the correct form of the model be known a priori. The correlation tests may be performed using an existing library of nonlinear functional forms, without input from the user. Thus, if the library is complete (in the sense that it contains the actual model form), the identification of the nonlinear model is accomplished, yet at no point in the algorithm is the user required to assume the correct model form.

The success of the algorithm is determined by the ability of the MME to produce accurate state and model error estimates, and by the completeness of the library of nonlinear functions to be used in the correlation test. We now address these issues in order.

The MME has been shown to consistently produce state and model error estimates of high accuracy in the presence of high measurement noise, low measurement frequency, and poor

initial model [27-29]. Generally, however, some noise is still present in both the state estimate and the model error term, although these noise levels are considerably less than the noise in the original data. Let the model error term be given by $x_{\text{correction}} = x + \xi$ where ξ is the noise. The cross-correlation between the error term and the test function y becomes

$$C(x, y) = \frac{\sum_{i=1}^n (x_i - \bar{x})(y_i - \bar{y}) + \sum_{j=1}^n \xi(y_j - \bar{y})}{n\sigma_y \sqrt{\sigma_x^2 + \frac{1}{n} \sum_{k=1}^n (2\xi(x - \bar{x}) + \xi^2)}} \approx 1.0 \quad (9)$$

As long as the noise is negligible all terms containing ξ are small and affect the result only slightly. Thus, the correlation calculated for the actual function is close to, but not exactly equal to, 1, while the correlation calculated for incorrect terms remains close to 0. If the level of noise is excessive, say, of comparable magnitude to one or more of the actual nonlinear model terms, then the ability of the correlation test to distinguish this term from similar terms may be greatly reduced or eliminated. However, subsequent least-squares fit of the terms has, in every case tested, correctly selected the actual nonlinear function from among those which the correlation test could not distinguish. An example of this is shown in the next section.

The issue of completeness of the library is now addressed. The error term may be composed of more than one function from the library, or the actual function may be missing from the library. Consider first the case where the actual error is a combination of library terms, say, two terms. The error term may be written $x_{\text{correction}} = x_1 + x_2$ and the cross-correlation has the form

$$C(x, y) = \frac{\sum_{i=1}^n (x_{1i} - \bar{x}_1)(y_i - \bar{y}) + \sum_{j=1}^n (x_{2j} - \bar{x}_2)(y_j - \bar{y})}{n\sigma_y \sqrt{\sigma_{x_1}^2 + \sigma_{x_2}^2 + \frac{1}{n} \sum_{k=1}^n 2(x_{1k} + \bar{x}_1)(x_{2k} + \bar{x}_2)}} \quad (10)$$

The cross-correlation is highest for the term which constitutes the largest part of the error. Thus, it is desirable to execute the algorithm iteratively. The library term which constitutes the largest portion of the actual model error is identified first and then added to the MME model. The entire process (including MME) is then repeated, so that new state and model error estimates are obtained (note that the change in state estimates should be minimal, while the change in model error estimates should be a large reduction in magnitude). The largest term remaining in the model error is identified in each pass, then added to the initial MME model.

An alternative to iterative application of the algorithm is to test the correlation of combinations of the library functions. An algorithm can be constructed which tests every possible combination of the functions explicitly contained in the library. This approach has not been attempted in the examples which follow.

If the actual model error is not present in the library, then test cases show that the highest correlation values are calculated for the terms in the series expansion of the actual function. Thus, for example, if the actual model error was of the form $\sin(x)$, but $\sin(x)$ was not present in the library, the correlation coefficients are highest for the terms x , x^3 , x^5 , etc. However, the test described by Eq. 7 is very fast, so the library may contain a very large number of terms.

EXAMPLES

For illustrative purposes, the true system was chosen as a simple harmonic oscillator with various forms of nonlinear feedback. The true system can be modeled as

$$\begin{pmatrix} \dot{x} \\ \dot{v} \end{pmatrix} = \begin{pmatrix} 0 & 1 \\ -1 & 0 \end{pmatrix} \begin{pmatrix} x \\ v \end{pmatrix} + \begin{pmatrix} 0 \\ f(x, v) \end{pmatrix} \quad (15)$$

where x is position, v is velocity and the dot indicates differentiation with respect to time. For simplicity, the system was unforced. The term $f(x, v)$ represents the nonlinear terms to be identified by the MME-based identification algorithm. Measurements were generated from the true system, Eq. (15), with different kinds of nonlinear functions $f(x, v)$. The ability of the identification algorithm to identify the model with no prior knowledge of $f(x, v)$ is tested. Table 1 shows the functions used in each simulation. Note that the unknown error term may be a combination of linear and nonlinear functions. Table 1 also shows the initial conditions and the amount of noise used to generate measurements for each test. The noise levels represent the percentage of the peak system response (actual percentages are higher for the majority of the measurements since the response is only at peak amplitude for brief periods).

Table 1
SUMMARY OF TEST CASES

TEST #	TRUE ERROR: $f(x, v)$	$x(0)$	$v(0)$	NOISE
1	$3.0 * x * x$	0.175	0	0
2	$-0.1 * x * x * v$	0.175	0	0
3	$-0.5 * \cos(x) * \cos(v)$	0.175	0	0
4	$-1.0 * v * \sin(x)$	0.175	0	0
5	$-1.0 * x * x - 0.25 * v$	0.350	0	0
6	$-1.0 * x * x * x - 0.1 * \tan(v)$	0.873	0	0
7	$-1.0 / \cos(x) - 1.0 * \sin(v)$	1.750	0	0
8	$3.0 * x * x$	0.175	0	10%
9	$-1.0 * x * x - 0.25 * v$	0.350	0	10%
10	$-1.0 * x * x * x - 0.1 * \tan(v)$	0.873	0	10%

The assumed model used for the MME analysis consisted of the undamped linear oscillator part of the system,

$$\begin{pmatrix} \dot{x} \\ \dot{v} \end{pmatrix} = \begin{pmatrix} 0 & 1 \\ -1 & 0 \end{pmatrix} \begin{pmatrix} x \\ v \end{pmatrix} \quad (16)$$

For each test, 200 measurements of position were obtained from the digital simulation of Eq. (15) at a sampling rate of 10 Hz. The functional form of the dynamic error, $f(x, v)$, was determined solely from the least-squares fit of the functions identified during the correlation tests on the MME state and model error estimates obtained using only the model in Eq. (16).

A library of functions was built consisting of approximately 300 of the most commonly found nonlinear and linear forms. For a particular test, after the model error term was found from MME, it was correlated with each one of the functions in the library. The correlation test of the entire library of functions did not take more than a few seconds to execute, since the calculations are simple. The functional form of the unknown nonlinear term was chosen as the one for which the absolute value of the cross-correlation coefficient was closest to 1. Table 2 shows the results for all 10 tests, including the true dynamic error, the highest cross-correlation coefficient obtained, the corresponding functional form, and the respective coefficient computed from the least squares fit. The star (*) indicates tests performed from noisy measurements.

Table 2.
IDENTIFICATION RESULTS FOR EACH TEST CASE

TEST#	TRUE ERROR(S)	C(d(t),f)	SELECTED	L.S.
1	$3.0*x*x$	0.999	$x*x$	2.99
2	$-0.1*x*x*v$	0.999	$x*x*v$	-0.10
3	$-0.5*cos(x)*cos(v)$	0.999	$cos(x)*cos(v)$	-0.49
4	$-1.0*v*sin(x)$	0.999	$v*sin(x)$	-1.00
5	$-1.0*x*x$	0.999	$x*x$	-0.99
	$-0.25*v$	0.746	v	-0.24
6	$-1.0*x*x*x$	0.936	$x*x*x$	-1.00
	$-0.1*tan(v)$	0.999	$tan(v)$	-0.10
7	$-1.0/cos(x)$	0.927	$1/cos(x)$	-0.99
	$-1.0*sin(v)$	0.999	$sin(v)$	-1.00
8*	$3.0*x*x$	0.797	$x*x$	3.12
9*	$-1.0*x*x$	0.937	$x*x$	-0.90
	$-0.25*v$	0.772	v	-0.22
10*	$-1.0*x*x*x$	0.838	$x*x*x$	-0.98
	$-0.1*tan(v)$	0.583	$tan(v)$	-0.10

For tests 1, 2, 3, and 4, the exact form of the nonlinearity was contained in the library and the measurements did not contain noise. The calculated value of $C(d(t), f)$ was 1 for the true forms. In test 8, the library contained the exact form of the nonlinearity but the measurements contained significant noise. The correlation for the correct term was much higher than for any other term, but was approximately 0.8 instead of 1 due to the noise. In the cases where the

error term consisted of two functions but the measurements were noise-free (tests 5, 6 and 7), $C(d(t), f)$ was close to one for both functions after applying the algorithm iteratively as described in the previous section.

When noise and more than one function was present in the dynamic error term (tests 9 and 10), the maximum value of the cross-correlation coefficients dropped significantly and in some cases did not immediately identify the actual form over other similar forms. As an example, Table 3 shows the top five cross-correlation values for the identification of the $\tan(v)$ term in test case 10. Note that the functions with the highest cross-correlation values are all similar in form to $\tan(v)$, and the corresponding correlation coefficients are of similar magnitude. Since $C(d(t), f)$ did not clearly identify $\tan(v)$ as the missing term, the five functions yielding the highest $C(d(t), f)$ values were individually least-squares fit to the model error term. In all cases (i.e., repeating this test for a number of different random noise samples), the function with the smallest least squares error cost was the correct function ($\tan(v)$). Thus, the least-squares fit of the parameters to the functional forms also serves as a second test if the correlation test is inconclusive due to high noise levels.

Table 3.
HIGHEST CROSS-CORRELATION COEFFICIENTS
OBTAINED FOR THE TAN(V) TERM OF TEST CASE 10

FUNCTION	C(d(t),f)	L.S.	L.S. cost
$\tan(v)$	0.583	-0.104	0.588
v	0.584	-0.119	0.623
$v*\cos(x)*\cos(v)$	0.584	-0.150	0.659
$v*\cos(x)$	0.586	-0.126	0.607
$\sin(v)*\cos(x)$	0.586	-0.133	0.621

The number of data points used in the MME algorithm was irrelevant as long as there were enough points to reasonably span the qualitative aspects of the system (e.g., sinusoidal terms cannot be identified if the data only spans a small fraction of the period).

If the exact functional form of the dynamic error term was not in the function library, the correlation procedure would pick the first term in the Taylor Series expansion of the exact form. For example in a test case where the dynamic error term corresponded to $x*\sin(v)$ and $x*\sin(v)$ was deleted from the library, the function with the largest $C(d(t), f)$ was $x*v$. Similarly, in several examples which are not shown the magnitude of the states, x and v , were small. Thus, the trigonometric functions of position and velocity were approximately equal to the first term in their Taylor Series expansions, i.e., $\cos(x) \approx 1.0$, $\sin(x) \approx x$, $\cos(v) \approx 1.0$ and $\sin(v) \approx v$. In these cases, assumptions of linearity are clearly valid, and are not of interest in the present work.

SUMMARY AND CONCLUSIONS

In this paper, an algorithm based on the MME estimation technique, coupled with correlation tests and least squares, has been developed for identification of nonlinear systems. The results of the examples indicate that the correlation technique applied to the MME-produced state and model error estimates enables the form of the model to be accurately determined, thus eliminating the requirement that the form be assumed a priori. Once the form is determined, the least-squares fit provides excellent parameter identification. In cases of high noise, where the correlation test may not be able to distinguish the actual form from similar forms, the least-squares fit also proved to be a reliable second test for determining the actual form.

At no point in the algorithm is the user required to assume the form of the model, representing a tremendous advantage over existing techniques, including the previous MME-based work. The MME does not require an accurate model in order to produce accurate state and model error estimates, and the correlation tests are automatically performed on a large existing library of functions. Additional functions and more sophisticated methods of combining existing functions can be added to the correlation testing portion of the algorithm (the authors are currently pursuing this), virtually eliminating the likelihood that the actual model error terms are not tested.

REFERENCES

1. Thompson, J.M.T., and Stewart, H.B., *Nonlinear Dynamics and Chaos*, Wiley, New York, 1986.
2. Nayfeh, A. H., and Mook, D. T., *Nonlinear Oscillations*, Wiley, New York, 1979.
3. Ibrahim, S.R., and Mikulcik, E.C., "A Method for the Direct Identification of Vibration Parameters from the Free Response," *Shock and Vibration Bulletin*, No. 47, Pt. 4, pp. 183-198, Sept. 1977.
4. Rajaram, S., and Junkins, J.L., "Identification of Vibrating Flexible Structures", *AIAA Journal of Guidance, Control, and Dynamics*, Vol. 8, No. 4, pp. 463-470, July-Aug. 1985.
5. Hendricks, S.L., et. al., "Identification of Mass, Damping, and Stiffness Matrices for Large Linear Vibratory Systems", *AIAA Journal of Guidance, Control, and Dynamics*, Vol. 7, No. 2, pp. 244-245, March-April 1984.
6. Chen, J.C., et.al., "Direct Structural Parameter Identification by Modal Test Results", *24th Structures, Structural Dynamics, and Materials Conference*, Pt. 2, 1983.
7. Juang, J.-N., and Pappa, R.S., "An Eigensystem Realization Algorithm (ERA) for Modal Parameter Identification and Model Reduction", *AIAA Journal of Guidance, Control, and Dynamics*, Vol. 8, No. 5, pp. 620-627, Sept.-Oct. 1985.
8. Natke, H.G., Juang, J.-N., and Gawronski, W., "Identification of Nonlinear Mechanical Systems: A Brief Review," NASA Langley Research Center, Hampton, VA, U.S.A. .
9. Billings, S.A., "Identification of Nonlinear Systems-a Survey," *IEE Proc.*, Vol. 127, Pt. D, No. 6, 1980, pp.272-285.
10. Bekey, G.A., "System Identification-an Introduction and a Survey," *Simulation*, October 1970, pp. 151-166.

11. Jedner, U., and Unbehauen, H., "Identification of a Class of Nonlinear Systems by Parameter Estimation of a Linear Multi-Model," *IMACS, Modeling and Simulation for Control of Lumped and Distributed Parameter Systems*, June 3-6, 1986, pp. 11-15.
12. Ibanez, P., "Identification of Dynamic Parameters of Linear and Non-Linear Structural Models from Experimental Data," *Nuclear Engineering and Design*, Vol. 25, 1973, pp. 32-41.
13. Yasuda, K., Kawamura, S., and Watanabe, K., "Identification of Nonlinear Multi-Degree-of-Freedom Systems (Identification Under Noisy Measurements)," *JSME International Journal*, Vol. 3, No. 1, 1988, pp. 502-509.
14. Yasuda, K., Kawamura, S., and Watanabe, K., "Identification of Nonlinear Multi-Degree-of-Freedom Systems (Presentation of an Identification technique)," *JSME International Journal*, Vol. 3, No. 1, 1988, pp. 8-14.
15. Billings, S.A., and Voon, W.S.F., "A Prediction-Error and Stepwise Regression Estimation Algorithm for Nonlinear Systems," *Int. J. Control*, Vol. 44, No. 3, 1986, pp. 803-822.
16. Greblick, W., and Pawlak, M., "Hammerstein System Identification by Non-Parametric Regression Estimation," *Int. J. Control*, Vol. 45, No. 1, 1987, pp. 343-354.
17. Kortmann, M., and Unbehauen, H., "Application of a Recursive Prediction Error Method to the Identification of Nonlinear Systems Using the Weiner Model," *IMACS, Modeling and Simulation for Control of Lumped and Distributed Parameter Systems*, June 3-6, 1986, pp. 3-9.
18. Distefano, N., and Rath, A., "System Identification in Nonlinear Seismic Dynamics," *Computer Methods in Applied Mechanics and Engineering*, Vol. 5, 1975, pp. 353-372.
19. Broersen, P.M.T., "Estimation of Parameters of Non-Linear Dynamical Systems," *Int. J. Non-Linear Mechanics*, Vol. 9, 1974, pp. 355-361.
20. Hanagud, S.V., Meyyappa, M., and Craig, J.I., "Method of Multiple Scales and Identification of Nonlinear Dynamical Systems," *AIAA J.*, Vol. 23, No. 5, 1985, pp. 802-807.
21. Marmarelis, P.Z., and Udwadia, F.E., "The Identification of Building Structural Systems-PartII: The Nonlinear Case," *Bulletin of the Seismological Society of America*, Vol. 66, 1979, pp. 153-171.
22. Chen, H., Ishii, N., and Suzumura, N., "Structural Classification of Non-Linear Systems by Input and Output," *Int. J. Systems Sci.*, Vol. 17, No. 5, 1986, pp. 741-774.
23. Wang, M.L., and Chang, R.Y., "Model Reduction and Control System Design by Shifted Legendre Polynomial Functions," *A.S.M.E. J. Dynam. Sys. Meas. Control*, Vol. 105, 1983, pp. 52-55.
24. Horn, I-R., and Chou, J-H., "Analysis and Identification of Non-Linear Systems via Shifted Jacobi Series," *Int. J. Control*, Vol. 45, No. 1, 1987, pp. 279-290.
25. Yun, C-B., and Shinozuka, M., "Identification of Nonlinear Structural Dynamic Systems," *J. Struct. Mech.*, Vol. 8, No. 2, 1980, pp. 187-203.
26. Hammond, J.K., Lo, H.R., and Seager-Smith, E.J., "Identification of Nonlinearities in Vibrating Systems Using Optimal Control Techniques," *IMAC*, 1987, pp. 1467-1473.
27. Mook, D.J., and Junkins, "Minimum Model Error Estimation for Poorly Modeled Dynamic Systems", *AIAA Journal of Guidance, Control, and Dynamics*, Vol. 11, No. 3, 1988, pp. 256-261.

28. Mook, D.J., "Estimation and Identification of Nonlinear Dynamic Systems," *AIAA Journal*, Vol. 27, No. 7, 1989, pp. 968-974.
29. Mook, D.J., and Stry, G.I., "An Analog Experimental Study of Nonlinear System Identification," to appear, *Nonlinear Dynamics*.
30. Geering, H.P., "Continuous Time Optimal Control Theory for Cost Functionals Including Discrete State Penalty Terms," *IEEE Trans. A. C.*, Vol. AC-21, 1976, pp. 86-869.
31. Mook, D.J., and Lew, J-H., "Solution of Linear Two-Point Boundary Value Problems with Jump Discontinuities," to appear in the *IEEE Trans. A.C.* .
32. Newland, D.E., "(An Introduction to) *Random Vibrations and Spectral Analysis*," 3rd. ed., Longman, Great Britain, 1980, pp. 29.
33. Witte, R.S., "*Statistics*," Holt, Rinehart and Winston, New York, USA, 1980, pp. 75.

SYSTEM LEVEL DESIGN AND ANALYSIS OF TRUSS STRUCTURES DAMPED BY VISCOUS STRUTS

Y. C. Yiu

Structural Dynamics, Space Systems Division, Dept. 62-18, B/104
Lockheed Missiles & Space Company, 1111 Lockheed Way, Sunnyvale, CA 94089
Telephone : 408-742-4048

ABSTRACT

A procedure is presented to design passive damping into large truss structures using viscously damped struts to enhance vibration attenuation or stability of controls system. A method is derived from the equations of motion using Rayleigh-Ritz method to relate the approximate contributions of a viscously damped strut to the system level modal damping ratios and frequencies. Strut placement locations, the total number of struts required and the damping characteristics of struts can be easily identified and calculated. The procedure consists of three steps: 1) extract structural characteristics from the undamped baseline finite element model, 2) on a mode by mode basis, perform damping design using the derived equations to meet system level requirements and 3) update finite element model to include damping mechanism and perform verification analysis using complex eigensolution.

INTRODUCTION

Truss systems are often used for large space structures because of weight efficiency. These structures often have many flexible modes within the disturbance and control bandwidth. For stringent performance requirements, tight joints are required for precision truss structures. The intrinsic structural damping associated with this type of structure may be very low (less than 0.1% equivalent viscous damping¹) and the dynamic responses under operational forces can be significantly amplified. Passive vibration control is a cost effective and reliable way to suppress dynamic responses and also provide additional stability margin to the controls system. Struts with good stiffness and damping characteristics can significantly enhance the performance of this class of structure.

Struts with imbedded viscoelastic materials have been successfully designed, tested, and integrated into truss structures^{2,3}. Viscoelastic materials are often frequency and temperature dependent⁴. However, design procedure and approximate analytical methods⁵ for this type of structure have been quite well established. Test results from demonstration structural articles compared favorably with analytical prediction³.

Precision struts with build-in fluid viscous damping chamber have been built and tested. They were demonstrated to be quite effective in provided stiffness and damping⁶. This class of struts can be characterized by a small number of frequency independent physical parameters. The dynamics of this class of struts is well understood⁷. The analytical methods for structures with viscous damping, though more complicated and not commonly used, has a solid mathematical foundation. This paper presents a simple three-step procedure to design viscously damped struts into a large truss structure. Based on the baseline undamped structural model, the most effective strut placement locations, the key stiffness and damping strut parameters and the number of struts required are determined. Only simple design iterations are required to optimize the design. The engineering design is then verified by the rigorous analytical method.

ANALYSIS OF DAMPED STRUCTURES

It is essential to understand the analysis of a damped structure before designing such a structure to meet the design objectives. A complex structure is modeled by a finite element model with $n \times n$ matrices. The governing differential equations of a structure with viscous damping are given by:

$$M \ddot{u} + C \dot{u} + K u = p g(t) \quad (1)$$

The damping matrix is due to viscous dashpots in the structure. The intrinsic damping is assumed to be negligible or added at the modal level. It is unlikely that the dashpot locations and characteristics result in a damping matrix which is mass or stiffness proportional, or satisfies Caughey's orthogonality condition⁸. Classical normal modes do not provide uncoupled scalar equations to Equation (1). The solution to Equation (1) is often obtained in the first order form by rewriting the equation as:

$$\begin{bmatrix} C & M \\ M & 0 \end{bmatrix} \begin{bmatrix} \dot{u} \\ \ddot{u} \end{bmatrix} + \begin{bmatrix} K & 0 \\ 0 & -M \end{bmatrix} \begin{bmatrix} u \\ \dot{u} \end{bmatrix} = \begin{bmatrix} p \\ 0 \end{bmatrix} g(t) \quad (2)$$

In order to uncouple the matrix equation, a complex eigenvalue problem for the large $2n \times 2n$ matrices⁹ must be solved.

$$\lambda_i \begin{bmatrix} \mathbf{C} & \mathbf{M} \\ \mathbf{M} & \mathbf{0} \end{bmatrix} \begin{bmatrix} \phi_u \\ \phi_{u,i} \end{bmatrix} + \begin{bmatrix} \mathbf{K} & \mathbf{0} \\ \mathbf{0} & -\mathbf{M} \end{bmatrix} \begin{bmatrix} \phi_u \\ \phi_{u,i} \end{bmatrix} = \begin{bmatrix} \mathbf{0} \\ \mathbf{0} \end{bmatrix} \quad (3)$$

Both the eigenvalues and eigenvectors are complex. The corresponding undamped natural frequencies and modal damping can be computed from the complex eigenvalues:

$$\omega_i = \sqrt{\lambda_i^R{}^2 + \lambda_i^I{}^2} \quad (4a)$$

$$\xi_i = \frac{-\lambda_i^R}{\omega_i} \quad (4b)$$

The modal damping is embedded in the real part of the eigenvalue. For a passive stable system, the real parts of the eigenvalues are always non-positive. The introduction of viscous dampers in the finite element model also results in the presence of overdamped modes with zero vibratory frequencies and large damping coefficients. The techniques in selecting an accurate and efficient algorithm for complex eigensolution computation is quite important but *not elaborated upon here*.

This procedure is mathematically rigorous and gives the correct solution to Equation (1). However, it is quite computationally intensive for large structures. Also, from the design point of view, it does not offer much insight into the behavior of the structures, and does not help synthesizing and optimizing passive damping design for structure. However, once the damping design is complete, the complex eigensolution should be performed to verify the passive damping design.

TRUSS STRUCTURES

If a undamped truss structure has n degrees of freedom, the equations of motion are given by:

$$\mathbf{M}_{11} \ddot{\mathbf{u}}_1 + \mathbf{K}_{11} \mathbf{u}_1 = \mathbf{p} g(t) \quad (5)$$

The small amount of intrinsic damping in the structure is inserted at the modal level. A few elastic struts are replaced by viscously damped struts to enhance the damping in the structure. For design purposes, it is assumed that the truss behavior is governed by the axial properties of the struts. Then, a typical viscous strut can be characterized by a three-node model with an internal dashpot⁷. The modified structure requires additional degrees of freedom to model the dashpots in the finite element model. Let the additional nv degrees of freedom be represented by \mathbf{u}_2 . The governing differential equations are now given by:

$$\begin{bmatrix} \mathbf{M}'_{11} & \mathbf{0} \\ \mathbf{0} & \mathbf{M}'_{22} \end{bmatrix} \begin{bmatrix} \dot{\mathbf{u}}_1 \\ \dot{\mathbf{u}}_2 \end{bmatrix} + \begin{bmatrix} \mathbf{C}'_{11} & \mathbf{C}'_{12} \\ \mathbf{C}'_{21} & \mathbf{C}'_{22} \end{bmatrix} \begin{bmatrix} \dot{\mathbf{u}}_1 \\ \dot{\mathbf{u}}_2 \end{bmatrix} + \begin{bmatrix} \mathbf{K}'_{11} & \mathbf{K}'_{12} \\ \mathbf{K}'_{21} & \mathbf{K}'_{22} \end{bmatrix} \begin{bmatrix} \mathbf{u}_1 \\ \mathbf{u}_2 \end{bmatrix} = \begin{bmatrix} \mathbf{p} \\ \mathbf{0} \end{bmatrix} g(t) \quad (6)$$

Equation (6) describes the behavior of a structure yet to be designed. The damping design will entail the locations, number, mass, damping and stiffness properties of the viscous struts. Unlike the viscoelastic struts, all the structural properties specified in Equation (6) are frequency

independent. Using engineering assumptions, a design procedure can be derived to approximate the solution to these governing equations.

In order to utilize the information of the baseline structure to help the damping design, it is important to recast Equation (6) into the same number of degrees-of-freedom as the baseline structure. Assuming the mass at the internal degrees of freedom of the struts is small and the internal dynamics of the struts is not important to the solution, then for a harmonic force input this condition is summarized as.

$$\begin{bmatrix} \mathbf{M}'_{11} & \mathbf{0} \\ \mathbf{0} & \mathbf{M}'_{22} \end{bmatrix} \begin{bmatrix} \dot{\mathbf{u}}_1 \\ \dot{\mathbf{u}}_2 \end{bmatrix} + \begin{bmatrix} \mathbf{C}'_{11} & \mathbf{C}'_{12} \\ \mathbf{C}'_{21} & \mathbf{C}'_{22} \end{bmatrix} \begin{bmatrix} \dot{\mathbf{u}}_1 \\ \dot{\mathbf{u}}_2 \end{bmatrix} + \begin{bmatrix} \mathbf{K}'_{11} & \mathbf{K}'_{12} \\ \mathbf{K}'_{21} & \mathbf{K}'_{22} \end{bmatrix} \begin{bmatrix} \mathbf{u}_1 \\ \mathbf{u}_2 \end{bmatrix} = \begin{bmatrix} \mathbf{p} \\ \mathbf{0} \end{bmatrix} e^{i\omega t} \quad (7a)$$

$$\mathbf{M}'_{22} = \mathbf{0} \quad (7b)$$

The \mathbf{u}_2 degrees of freedom can be condensed out by using the second matrix equation of Equation (7a):

$$\mathbf{u}_2 = (i\omega \mathbf{C}'_{22} + \mathbf{K}'_{22})^{-1} (i\omega \mathbf{C}'_{21} + \mathbf{K}'_{21}) \mathbf{u}_1 \quad (8)$$

Backsubstitute \mathbf{u}_2 into the first matrix equation of Equation (7a) and collecting terms, Equation (7a) can now be represented by:

$$\tilde{\mathbf{M}} \ddot{\mathbf{u}}_1 + \tilde{\mathbf{K}} \mathbf{u}_1 = \mathbf{p} e^{i\omega t} \quad (9a)$$

In this form, the stiffness matrix is complex:

$$\tilde{\mathbf{K}} = \tilde{\mathbf{K}}^R + i \tilde{\mathbf{K}}^I \quad (9b)$$

It is also a function of both the stiffness and damping characteristics of the struts (\mathbf{u}_2 degrees of freedom). Despite the dissimilarity in appearance, Equations (7) and (9) are identical descriptions of the same system. Equation (7) is the preferred form for analytical computation while Equation (9) is very useful to guide the damping design. For damping design, there is no need to form $\tilde{\mathbf{K}}$ explicitly. Instead, the contribution of each strut element to $\tilde{\mathbf{K}}$ is evaluated individually. The contribution of each strut to system level damping can be assessed through its contribution to $\tilde{\mathbf{K}}^I$.

STRUT CHARACTERISTICS

In order to design damping at the system level, the damping and stiffness characteristics of the damped struts must be totally understood. A class of viscously damped struts can be represented by three frequency independent parameters⁷ as shown in Figure 1.

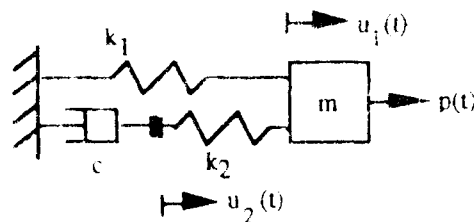


Figure 1. 3-Parameter 2 DOFs Viscous Strut Model

The dynamic characteristics of this class of strut were derived based on a similar method such that the results can be used for system level damping design. The stiffness and damping characteristics of the struts are summarized here. The strut is represented by a complex stiffness:

$$k = k^R (1 + i \eta) \quad (10a)$$

where,

$$k^R = k_1 \left[\frac{\kappa^2 k_1^2 + (1 + \kappa)(c\omega)^2}{(c\omega)^2 + \kappa^2 k_1^2} \right] \quad (10b)$$

$$\eta = \frac{\alpha^2 (c\omega) k_1}{\kappa^2 k_1^2 + (1 + \kappa)(c\omega)^2} \quad (10c)$$

$$\kappa = \frac{k_2}{k_1} \quad (10d)$$

Normalized design curves, optimum strut damping and damping bandwidth can be found in Reference 7. The maximum loss factor, η_{op} , is governed by κ only:

$$\eta_{op} = \frac{\kappa}{2\sqrt{1 + \kappa}} \quad (11a)$$

and the frequency at which this maximum loss occurs, ω_{op} , is governed by the damping coefficient:

$$\omega_{op} = \frac{\kappa}{\sqrt{1 + \kappa}} \frac{c}{k_1} \quad (11b)$$

A simple 3-parameter viscous strut model allows a simple strut representation for system level design and a simple strut performance specification for component level design.

APPROXIMATE ANALYSIS OF DAMPED STRUCTURES

From a practical standpoint, if a few struts are replaced by damped struts to increase system damping, say to around 10%, the basic undamped structural characteristics should not be changed significantly. Based on this assumption, the Rayleigh-Ritz method can be used to compute the approximate solution to Equation (1)¹⁰. This not only expedites the computation significantly but it also provides a direct physical insight into the "modal" damping synthesis of the structure. The undamped normal modes are used as the basis vectors (generalized coordinates):

$$\mathbf{u} = \sum_{i=1}^m \phi_i q_i = \Phi \mathbf{q} \quad (12)$$

where the eigenvalue problem is performed at a selected frequency of interest:

$$\tilde{\mathbf{K}}^R \phi_i = \bar{\omega}_i^2 \tilde{\mathbf{M}} \phi_i \quad (13)$$

In practice, the mode shapes of the baseline structure are used to start the design process. Then Equation (9) is approximated by:

$$\Phi^T \tilde{\mathbf{M}} \Phi \ddot{\mathbf{q}} + \Phi^T \tilde{\mathbf{K}} \Phi \mathbf{q} \approx \Phi^T \mathbf{p} g(t) \quad (14)$$

For design purposes, assume the coupling between generalized coordinate does not significantly affect the dynamic response. The approximate uncoupled equations of motion are therefore:

$$\phi_i^T \tilde{\mathbf{M}} \phi_i \ddot{q}_i + \phi_i^T \tilde{\mathbf{K}} \phi_i q_i = \phi_i^T \mathbf{p} g(t) \quad (15a)$$

$$\left[(-\omega^2 \phi_i^T \tilde{\mathbf{M}} \phi_i + \phi_i^T \tilde{\mathbf{K}}^R \phi_i) + i (\phi_i^T \tilde{\mathbf{K}}^I \phi_i) \right] q_i e^{i\omega t} \approx \phi_i^T \mathbf{p} e^{i\omega t} \quad (15b)$$

The equivalent "modal" characteristic of the generalized coordinate can be found by equating the complex stiffness to a single degree of freedom system at resonance frequency:

$$\left[(-\omega^2 + \omega_o^2) + i (2\xi_o \omega \omega_o) \right] q_o e^{i\omega t} = \frac{p}{m} e^{i\omega t} \quad (16)$$

The "modal" frequency of the modified structure can therefore be approximated by:

$$\bar{\omega}_i = \sqrt{\frac{\phi_i^T \tilde{\mathbf{K}}^R \phi_i}{\phi_i^T \tilde{\mathbf{M}} \phi_i}} \quad (17)$$

but the change in structural weight of the struts with respect to the overall structural and non-structural weight is often very small such that $\phi_i^T \tilde{\mathbf{M}} \phi_i \approx 1$. The equivalent damping near resonance can therefore be approximated by:

$$\xi_i = \frac{1}{2} \frac{\phi_i^T \tilde{\mathbf{K}}^I \phi_i}{\bar{\omega}_i^2} \quad (18)$$

ELEMENT MODAL CONTRIBUTION

Based on this approximate analysis method, it is possible to assess the contribution of a viscous strut at a given location to the system level damping and stiffness change. Decompose the global stiffness into element stiffness contributions (ne = number of elastic elements and nv = number of damped struts):

$$\tilde{\mathbf{K}} = \left(\sum_{j=1}^{ne} \mathbf{k}_j + \sum_{j=1}^{nv} \mathbf{k}^R_j(\omega) \right) + i \sum_{j=1}^{nv} \eta_j(\omega) \mathbf{k}^R_j(\omega) \quad (19)$$

The "modal" stiffness is given by:

$$\bar{\omega}_i^2 = \phi_i^T \left(\sum_{j=1}^{nc} \mathbf{k}_j + \sum_{j=1}^{nv} \bar{\mathbf{k}}_j^R(\omega) \right) \phi_i \quad (20)$$

The normalized "modal" stiffness contribution of the j-th viscous strut to the system is given by:

$$\epsilon_{ij} = \frac{\phi_i^T \bar{\mathbf{k}}_j^R \phi_i}{\bar{\omega}_i^2} \quad (21a)$$

The normalized "modal" stiffness contribution is also identical to the "modal" strain energy (MSE) ratio:

$$\epsilon_{ij} = \frac{w_{ij}}{\sum_j w_{ij}} = \frac{\frac{1}{2} \phi_i^T \bar{\mathbf{k}}_j^R \phi_i}{\frac{1}{2} \bar{\omega}_i^2} \quad (21b)$$

The "modal" damping ratio contribution of the j-th viscous strut to the system is given by:

$$\xi_{ij} = \frac{\eta_j}{2} \frac{\phi_i^T \bar{\mathbf{k}}_j^R \phi_i}{\bar{\omega}_i^2} = \frac{\epsilon_{ij} \eta_j}{2} \quad (22)$$

The system level damping from all the viscous struts is therefore simply given by:

$$\xi_i = \frac{1}{2} \sum_{j=1}^{nv} \epsilon_{ij} \eta_j \quad (23)$$

The assumptions used in deriving these approximations provides a very simple concept for damping design. It is clear from Equation (23) that there are three key parameters in system level modal damping design: the strut locations, ϵ_{ij} , the strut loss factors, η_j , and the total number of viscous struts, nv . For a given mode, the strut location with the highest strain energy ratio is the most effective location in providing damping. This location has the maximum relative displacement, hence relative velocity, to activate the viscous damper. The strut with higher loss factor also provides higher system level damping. The contribution of each damped strut to the system level damping is proportional to the strut loss factor and the modal strain energy ratio. System level damping can also be increased by incorporating more struts. Of course, as the most effective locations are occupied, the effectiveness of an additional strut is diminishing as the modal strain energy ratio is declining.

SYSTEM LEVEL DAMPING DESIGN PROCEDURE

In the beginning of a design cycle, the baseline structure is modeled and analyzed. The performance of the structure is not satisfactory and higher damping is required in a few modes to reduce the dynamic responses or stabilize the control system. Consequently modal damping ratios are specified as design requirements. The modal properties of the baseline structural model can be used to start the design process. The modal strain energy ratio of each strut member is computed:

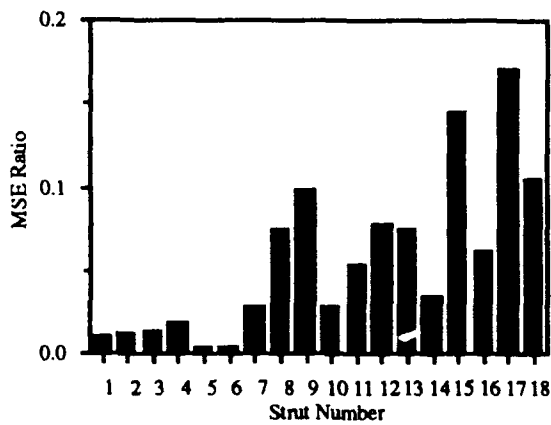


Figure 2 Modal Strain Energy Distribution

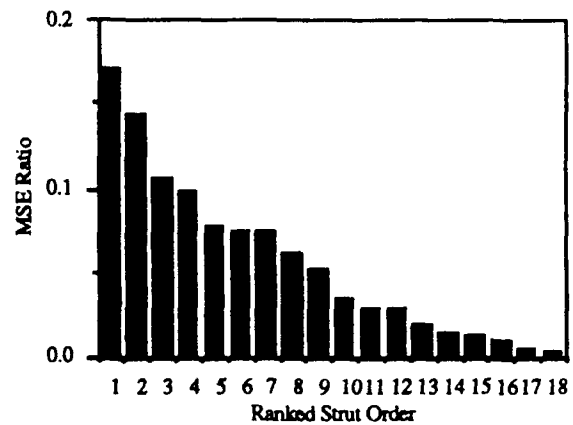


Figure 3 Rank Modal Strain Energy

$$\epsilon_{ij} = \frac{\phi_i^T k_j \phi_i}{\tilde{\omega}_j^2} \quad (24)$$

A typical modal strain energy distribution is shown in Figure 2. For the mode of interest, rank strut members in descending order of modal strain energy ratios as shown in Figure 3. The order of the struts should be noted as shown in Table 1.

Table 1 Strut Modal Strain Energy Data

Strut Order	1	2	3	4	5	6	7	8	9	10	11	12
Strut No.	17	15	18	9	12	8	13	16	11	14	7	10
MSE	0.170	0.143	0.105	0.098	0.077	0.073	0.073	0.061	0.052	0.034	0.027	0.027
Cum MSE	0.170	0.314	0.418	0.516	0.593	0.666	0.739	0.800	0.852	0.886	0.914	0.941

If only one type of strut, with component loss factor η , is used, compute the cumulative sum of the the ranked modal strain energy ratios:

$$\epsilon_{i1} = \sum_{j=1}^l \epsilon_{ij} \quad (25)$$

A typical plot of the cumulative strain energy of the ranked struts is shown in Figure 4.

Assuming a realistic strut loss factor, and working with realistic static and dynamic strut stiffnesses, find the suitable k_1 and k_2 by using Equations (10) and (11). Determine the frequency characteristics of the strut by defining the c parameter in Equation (11b). Iterate if necessary to optimize the strut design. Compute the dynamic stiffness and loss factor at the frequencies of interest. A typical strut loss factor curve is shown in Figure 5.

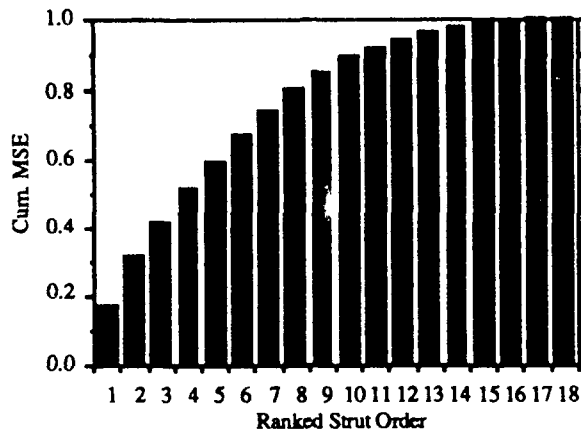


Figure 4 Cumulative Strut Modal Strain Energy

The system level modal damping for J number of struts is given by:

$$\xi_{ij} = \frac{\eta}{2} \epsilon_{il} \quad (26)$$

The system level damping is a product of strut loss factor and contributions from participating struts, i.e. higher strut damping requires less members and vice versa. Iterate to determine the necessary component loss factor and number of struts to meet the design requirement on a mode by mode basis. Candidate struts for each modes are identified.

Candidate struts from all the modes are included in the final design to meet the design requirements. The modal strain energy ratios, ϵ_i , of these struts are computed as shown in Figure 6. The approximate system level damping is given by:

$$\xi_i = \frac{1}{2} \eta \epsilon_i \quad (27)$$

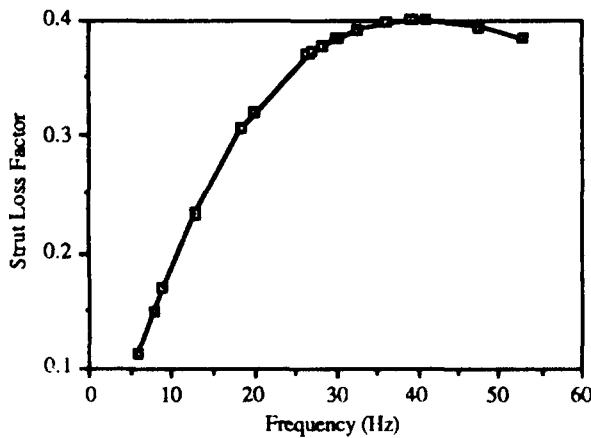


Figure 5 Strut Loss Factor vs Frequency

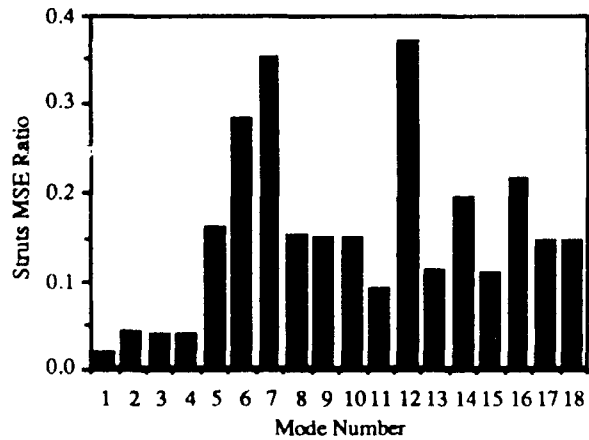


Figure 6 Struts MSE Ratio vs Mode Number

The system level damping is a product of the strut loss factor at the modal frequency and the participation of the selected struts at the system level. The modal strain energy ratios with respect to frequency are shown in Figure 7. The system level damping curve, Figure 8, is simply the product of Figures 6 and 7.

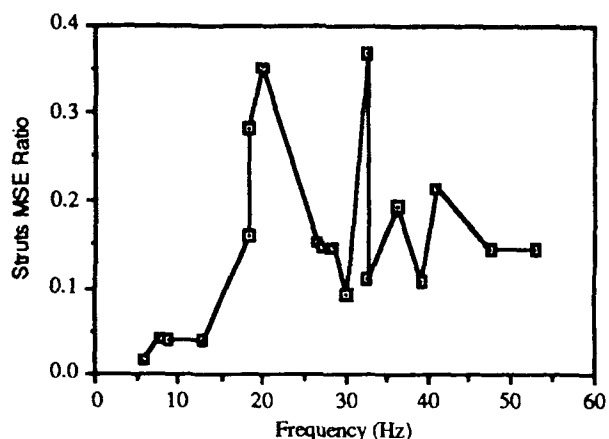


Figure 7 Struts MSE vs Frequency

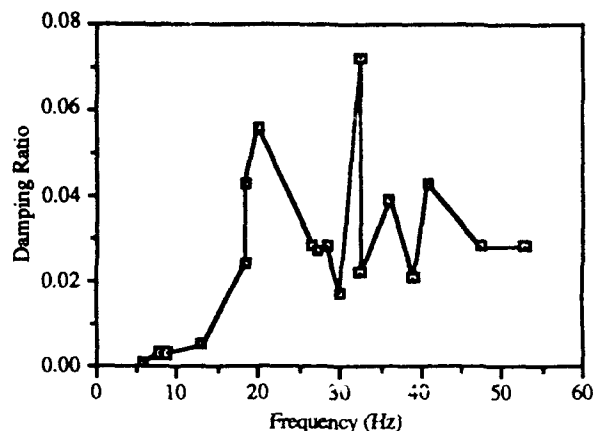


Figure 8 Predicted System Level Damping

The approximate system frequencies can be predicted by considering the "modal" stiffness contribution of the viscous struts and the relative change in dynamic axial stiffness:

$$\tilde{\omega}_i = \sqrt{1 + \left(\frac{k^R}{k_o} - 1\right)\epsilon_i} \omega_i \quad (28)$$

As can be seen from the derivation of this procedure, quite a few assumptions were used in order to establish this simple procedure. As in any design process, iterations are required to refine the initial design. The number of struts and the strut parameters may be optimized. Also, for better damping prediction at different frequency ranges, the baseline finite element model can be updated to reflect the dynamic strut stiffness in accordance with Equation (10b) so that the strain energy distribution is better represented at the frequency ranges of interest. The effect of modal damping coupling can also be evaluated if necessary. However, it may be more expedient to let the verification analysis provide the final verdict. Generally speaking, if the damping is well distributed, it is closer to a proportional damping case. However, if only a few dampers are used to provide a substantial amount of damping to the system, the damping matrix can be quite non-proportional. If the strut placement also changes the mode shapes of the structure substantially, the original mode shapes are not a good approximation. An updated finite element model should be used as the baseline model.

When a good, practical and balanced damping design is in hand, the finite element model is updated to include all the viscous struts which are modeled by elastic and viscous elements as shown in Equation (6). This model removes all the assumptions imposed during the design process and provides the best engineering predictions of the behavior of the structure damped by viscous struts. The system damping and frequencies of the passively damped structure can be computed from the complex eigenvalues using Equations (4a) and (4b). The verification analysis is an important step to the design process.

There can be many variations to the method presented. Different struts with different stiffness and damping characteristics can be added to the structure due to the geometric difference of struts to be replaced. If damping is to be optimized over a wide frequency range, struts with different

frequency characteristics can be used. However, the basic principles are still the same. The procedure can be modified to accommodate such special circumstances. A summary of the design and analysis procedure is provided in Table 2.

Table 2. Summary of Design and Analysis Procedure

1. Understand damping design requirements.
2. Perform eigenvalue analysis of baseline structural model to get ω_i and ϕ_i .
Compute modal strain energy ratios of strut members, ϵ_{ij} .
3. Rank strut members in descending order of modal strain energy ratios for modes of interest.
4. Compute cumulative sum of the ranked modal strain energy ratios, ϵ_{i1} , for modes of interest.
5. Assume a physically achievable strut loss factor, η_j . Estimate required dynamic stiffness. Iterate to find the k_1 , k_2 and c parameters to obtain static stiffness, maximum loss factor and frequency characteristics of struts. Compute the loss factors at the frequencies of interest, $\eta(\omega_i)$.
6. Find the number of struts required to meet the damping requirements for the given modes. For each mode, locate the struts. The set of viscous struts is all the members required for all the modes.
7. Compute the modal strain energy ratios of the set of viscous struts, ϵ_i .
8. Compute the predicted system level damping, $\eta(\omega_i)\epsilon_i$.
9. Iterate upon the number of struts, strut locations, and strut parameters as necessary.
10. Iterate upon the accuracy of mode shapes and modal strain energy distributions at selected frequencies if necessary.
11. Update finite element model to include dashpots and perform complex eigenvalue problem to verify damping design.
12. Iterate as necessary to correct for any deficiency from complex eigensolution.

TRUSS DESIGN EXAMPLE

A small example is included here to illustrate the method. A 3 bay truss with 13 nodes and 60 active degrees of freedom is used. The first two bending modes of the structure are 21.3 Hz. The goal is to design 5% viscous damping into the system. For the mode of interest, a bottom longeron member has significant amount of modal strain energy. One damped strut is used to replace the original strut. The damped strut is designed to have $k_1 = 110,491$ lb/in, $k_2 = 114,955$ lb/in, $c = 839.88$ lb-sec/in. This corresponds to a loss factor of 0.36 in the member at the frequency of interest. The updated finite element model now has 122 equations in the first order form. The solution from the complex eigenvalue problem is summarized in the Table 3. The results are very satisfactory considering that only very little amount of computation required to arrive at this design.

Experience in working with large truss structures showed that the design procedure is quite effective and the design prediction and analytical solution are often quite close.

Table 3 Comparison of Design Prediction and Analytical Solution

Parameters	Design Goal	Eigensolution	Error
Frequency	21.3 Hz	21.95 Hz	3%
Damping	5%	5.45%	9%

CONCLUSION

A comprehensive design and analysis method for integration of viscously damped struts into large precision truss structure is presented. The method is based on an approximate solution to the governing differential equations using the Rayleigh-Ritz method. Simplification to a practical design procedure is facilitated by making relevant engineering assumptions for the struts and the truss behavior. The method effectively uses the modal data from the baseline structural model. A simple design procedure is use to determine the strut placement locations, the strut stiffness and damping parameters, and number of struts required to meet the design objectives. Upon completion of a damping design, a rigorous verification analysis is performed to check the passive design. Therefore all the assumptions used in the design process will not affect the accuracy of the analytical prediction. The method is simple, efficient and accurate, and has been used for large structures with good success.

NOMENCLATURE

Symbols

C, c	=	viscous damping matrix, coefficient
g	=	forcing function
i	=	imaginary unit, $\sqrt{-1}$
I	=	identity matrix
K, k	=	stiffness matrix, stiffness coefficient, strut axial stiffness
M, m	=	mass matrix, mass
p	=	spatial force vector
t	=	time, second
u	=	displacement vector
w	=	element strain energy
β	=	non-dimensional frequency parameter for viscous strut
ϵ	=	strain energy ratio
ϕ, Φ	=	eigenvectors, eigenvector matrix
η	=	loss factor
κ	=	non-dimensional stiffness ratio viscous strut
ξ	=	viscous damping ratio
λ, Λ	=	eigenvalue, eigenvalue matrix
ω	=	forcing frequency or natural frequency when used with index, radian/second
\sim	=	denoting modified elements

Subscripts

i	=	for the i -th mode
j	=	the j -th strut element
l	=	number of viscous struts in descending order of modal strain energy
m	=	number of modes in solution
o	=	single degree of freedom system, pertaining to original component
op	=	condition at maximum loss factor
v	=	viscoelastic
u	=	displacement
\dot{u}	=	velocity
ξ	=	damping ratio
1	=	baseline degrees of freedom, or outer spring of viscous strut
2	=	additional degrees of freedom for dashpots, or inner spring of viscous strut

Superscripts

I	=	Imaginary
R	=	Real
T	=	matrix transpose

REFERENCES

1. J.L. Fanson, G.H. Blackwood and C.-C. Chu, 'Active Member Control of Precision Structures', *AIAA/ASME,ASCE,AHS/ASC 30-th Structures, Structural Dynamics, and Materials (SDM) Conference*, 1989, Mobile, Alabama.
2. White, C.W., 'Viscoelastic Component Damper Design Problems', *Damping 1986*, AFWAL-TR-86-3059, Flight Dynamics Laboratory, Air Force Wight Aeronautical Laboratories (1986).
3. Johnson, C.D., and Kienholz, D.A., 'Design and Testing of a Sixty-Foot Damped Generic Space Truss', *Damping 1986*, AFWAL-TR-86-3059, Flight Dynamics Laboratory, Air Force Wight Aeronautical Laboratories (1986).
4. Nashif, A.D., D.I.G. Jones, and J.P. Henderson, *Vibration Damping*, John Wiley & Sons (New York, 1985).
5. Johnson, C.D., and Kienholz, D.A., 'Finite Element Prediction of Damping in Structures with Constrained Viscoelastic Layers', *AIAA Journal* Vol 20, No. 9 (Sept. 1982).
6. E. Anderson, M. Trubert, J. Fanson, and P. Davis, 'Testing and Application of a Viscous Passive Damper for Use in Precision Truss Structure', *AIAA/ASME,ASCE,AHS/ASC 32-th Structures, Structural Dynamics, and Materials (SDM) Conference*, 1991, Baltimore, Maryland.
7. Y.C. Yiu and S.D. Ginter, 'Dynamics of a Class of Viscously Damped Struts', *Damping '91 Conference*, February 1991, San Diego, California.
8. Caughey, T.K., 'Classical Normal Modes in Damped Linear Systems' *Journal of Applied Mechanics*, Vol. 27, 1960, pp 269-271.
9. Hurty, W.C. and Rubinstein, M.F., *Dynamics of Structures*, Prentice-Hall, Inc., 1964.
10. Y.C. Yiu, 'Design and Analysis of Viscoelastic Struts for Large Space Structures', *Damping '89 Conference*, February, 1989, West Palm Beach, Florida.

DAMPING RATIO ESTIMATES FROM AUTOCORRELATION FUNCTIONS

A.Agneni and L.Balis Crema

Università di Roma "La Sapienza"
Dipartimento Aerospaziale
Via Eudossiana, 16 - Roma (Italy)
FAX No. (6) 4819473

ABSTRACT

The paper deals with the possible overestimation of the damping ratio, when evaluated from autocorrelation functions in the time domain, because of a bias caused by a triangular window.

Some theoretical considerations permitted to evaluate a lower bound for the sampling period over which it has been possible to estimate the damping ratio with acceptable errors and therefore to limit the effects of the above said bias.

Several numerical examples singled out its possible effects on the modal parameter estimations and gave quantitative evaluations of it. Firstly numerical data regarded single degree of freedom systems in function of the sampling period, afterwards two modes have been considered. This last example is also presented with a high random noise added to the original impulse response, and that because the autocorrelation permits to clean up the noisy signal. In addition when more modes are present in the baseband the problem could become critical: in fact the mode with the highest time constant and therefore, in general, the one with the lowest frequency, is exposed to bias errors which, in case of a large oversampling, become completely unacceptable.

Nomenclature

f_n	natural frequency (Hz)
$h[n]$	sampled impulse response
m	lag index
n	index of samples
$w[n]$	sampled triangular window
E	expectation value
M	maximum number of lag points
N	number of points contained in the impulse response
R	residue magnitude
T_s	sampling period (s)
$(T_s)_{lim}$	limit sampling period (s)
$\rho_h[m]$	sampled autocorrelation function relative to $h[n]$
$\hat{\rho}_h[m]$	estimated autocorrelation sequence
ϵ_f	error in the natural frequency estimation
ϵ_R	error in the residue magnitude estimation
ϵ_ζ	error in the damping ratio estimation
ζ	viscous damping ratio
σ	decay rate (rad/s)
τ_c	time constant (s)
τ_{lim}	limit time (s)
ω_d	damped angular frequency (rad/s)
ω_n	natural angular frequency (rad/s)

1. Introduction

Correlation functions play an important role in diverse areas of science and technology, in particular they are commonly utilized in Modal Analysis to obtain Frequency Response Functions (FRFs) [1 to 4]. Besides, Autocorrelation Functions (AFs), derived from Impulse Responses (IRs), could be used to get modal parameters, i.e. natural frequencies and damping factors, directly in the time domain. This approach can turn out to be useful when the impulse responses are corrupted by a very high additive random noise [5], as it happens for data gathered from flight tests; in fact, evaluating autocorrelation functions, it is possible to remove an uncorrelated noise present in the original impulse response.

Autocorrelation functions are generally estimated by a relationship that introduces a bias consisting in a triangular window around the origin of the time axis.

For a sampled signal, the maximum time lag - given by the sampling period times

the number of points whereof the signal is shifted with respect to the origin - where the autocorrelation is estimated from the available data, must satisfy some constraints. It not only ought to be of the order of one tenth of the data block length in order to avoid instability in Power Spectral Density estimates [6], but it must be also chosen in such a way that the exponentially decaying envelope of the autocorrelation is smaller than the contribution of the triangular window. So if the number of the lag points is determined in function of the available number of the total points of the original IR, the sampling period, in addition to the Shannon condition, that determines an upper limit, must also satisfy a lower limit, which permits to estimate the damping ratio with acceptable errors.

In this paper the evaluation of the above said parameter is derived, for each mode, from the instantaneous envelope and phase of the autocorrelation function, which in turn are obtained via the Hilbert transform [7,8].

2. Theoretical considerations

In order to discuss our subject, let us consider the impulse response - sampled over N points - of a real mode derived from a single degree of freedom system:

$$h[n] = R e^{-\sigma(nT_s)} \sin[\omega_d(nT_s)] \quad 0 \leq n \leq (N-1) \quad (1)$$

where n is the sample index, T_s is the sampling period, σ is the decay rate and ω_d is the damped angular frequency.

The autocorrelation sequence can be estimated by the following relationship:

$$\hat{\rho}_h[m] = \left[\frac{1}{N} \right] \sum_{n=0}^{N-m-1} h[n] h[n+m] \quad (2)$$

valid for 0 ≤ m ≤ (N-1), where m indicates the number of lag points of which one sequence is shifted with respect to the other (the time lag is therefore given by mT_s).

Since the autocorrelation is an even function:

$$\rho_h[-m] = \rho_h[m] \quad (3)$$

and in addition we are only interested in the sequence relative to m > 0, Eq. (2) is completely sufficient for our purpose.

Although the relationship above mentioned is frequently utilized, in fact it provides a true autocorrelation sequence (the matrix formed with its elements results to be always positive semidefinite), this estimate is biased by the triangular window:

$$w[m] = \left[1 - \frac{m}{N} \right] \quad (4)$$

As for $N \rightarrow \infty$ the window is identically equal to the unit, the autocorrelation estimate (2) results asymptotically unbiased [9,10]. Thus the expectation of the estimated sequence is given by the product of the actual autocorrelation times the window:

$$E \{ \hat{\rho}_h[m] \} = \rho_h[m] \cdot w[m] \quad (5)$$

If the maximum lag index M is small enough in comparison with N , the estimate given by Eq. (2) is an acceptable approximation of $\rho_h[m]$ and, under proper conditions [5], it can be written as follows:

$$\hat{\rho}_h[m] \cong \left[\frac{1}{NT_s} \right] \frac{R^2 \omega_d e^{-\sigma(mT_s)}}{4\sigma \sqrt{\sigma^2 + \omega_d^2}} \cdot \cos \left[\omega_d(mT_s) - \arctan \left[\frac{\sigma}{\omega_d} \right] \right] \quad (6)$$

When the viscous damping model is adopted, the decay rate and the damped angular frequency can be written as follows:

$$\sigma = \zeta \omega_n \quad (7)$$

and

$$\omega_d = \omega_n \sqrt{1 - \zeta^2} \quad (8)$$

where ζ is the damping ratio, thus relation (6) reduces to:

$$\hat{\rho}_h[m] \cong \left[\frac{1}{NT_s} \right] \frac{R^2 \sqrt{1 - \zeta^2} e^{-\sigma(mT_s)}}{4\zeta \omega_n} \cdot \cos \left[\omega_d(mT_s) - \arctan \left[\frac{\sigma}{\omega_d} \right] \right] \quad (9)$$

Besides, if the damping ratio is small such that its square value is negligible with respect to the unit, relationship (9) is further simplified:

$$\hat{\rho}_h[m] \cong \frac{R^2}{4NT_s\sigma} e^{-\sigma(mT_s)} \cdot \cos\left[\omega_d(mT_s)\right] \quad (10)$$

in fact, the damped and the natural frequencies are practically equal and for the above said position:

$$\arctan\left[\frac{\zeta}{\sqrt{1-\zeta^2}}\right] \cong \arctan(\zeta) \cong 0 \quad (11)$$

Actually, owing to the presence of the bias mentioned above, the decaying of the function results greater than the one due to the exponential term appearing in relations (6), (9) and (10). Because our interest is devoted to estimate the decay rate, or better the damping ratio, it is necessary that the contribution of the triangular window is negligible with respect to the one of the exponential decay. A limit time (τ_{lim}) can be derived from the following relationship (Fig.1):

$$e^{-\sigma\tau_{lim}} = \left(1 - \frac{\tau_{lim}}{T}\right) \quad (12)$$

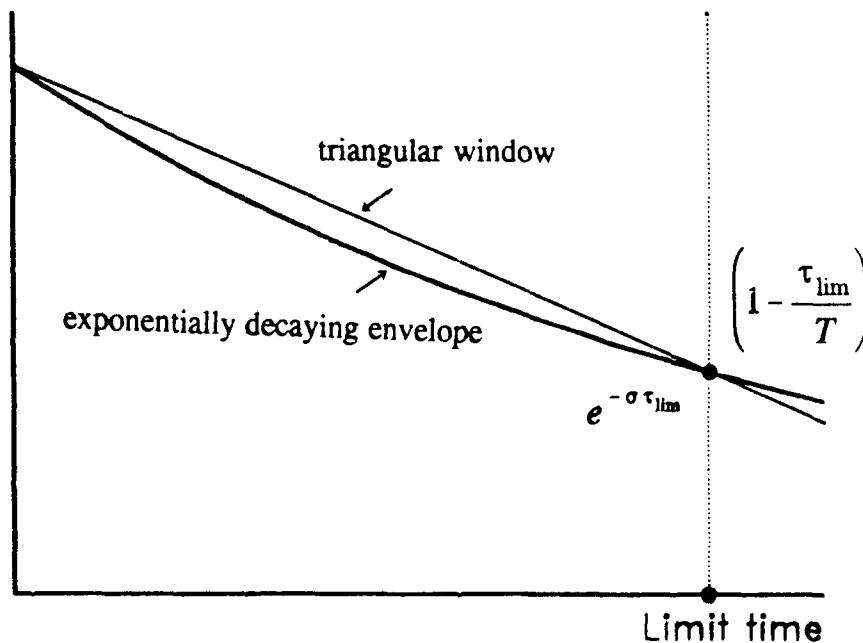


Figure 1 - Limit time evaluated at the maximum time lag.

that - in function of the sampling period, of the maximum number of lag points and of the total number of samples - becomes:

$$e^{-\sigma M T_s} = \left(1 - \frac{M}{N} \right) \quad (13)$$

Performing the natural logarithm, it is possible to derive a relation between the system time constant ($\tau_c = 1/\sigma$) and τ_{lim} :

$$\frac{\tau_{\text{lim}}}{\tau_c} = - \ln \left(1 - \frac{M}{N} \right) \quad (14)$$

Therefore the limit time ought to be in the order of $[(1/10)\tau_c]$ or less, supposing M much lower than N , so that the contribution of the triangular window is small enough. Thus the limit sampling period, evaluated for the maximum value of the lag points, is given by:

$$(T_s)_{\text{lim}} = - \left(\frac{\tau_c}{M} \right) \ln \left(1 - \frac{M}{N} \right) \quad (15)$$

Since τ_c is unknown "a priori", it is necessary to have a rough knowledge at least of its order of magnitude, anyway once the natural frequency and the damping ratio have been estimated, it is possible to check the limit sampling, in fact if $(T_s)_{\text{lim}}$, evaluated introducing into relationship (15) the estimated time constant, is not sufficiently less than the sampling period actually employed, a longer T_s must be used.

When several modes are contained within the baseband, $(T_s)_{\text{lim}}$ is constrained by the highest time constant, that is - supposing the damping ratio almost equal for each mode - by the mode with the lowest natural frequency.

3. Numerical tests

Data sequences presented in the following numerical simulations are formed by 4096 points, whereas the number of lag points of the autocorrelation function has been chosen equal to 512 in order to get the Hilbert transform by a standard FFT software.

All the impulse responses considered hereafter have the same amplitude: $R=10$, even when two modes are presented.

In Tab.1 estimates from the autocorrelation of an impulse response representing a real mode with a very low natural frequency and a light damping ratio (the input modal parameters are: $f_n=0.71$ Hz and $\zeta=0.003$) are shown:

Table 1 - Modal parameter estimates from a highly truncated impulse response versus the sampling period.

T_s (s)	R	$ \epsilon_R $ (%)	f_n	$ \epsilon_f $ (%)	ζ	$ \epsilon_\zeta $ (%)
0.150	10.00047	$0.47 \cdot 10^{-2}$	0.71	$0.46 \cdot 10^{-3}$	$0.30002 \cdot 10^{-2}$	$0.59 \cdot 10^{-2}$
0.100	10.00142	$0.14 \cdot 10^1$	0.71	$0.47 \cdot 10^{-3}$	$0.30007 \cdot 10^{-2}$	$0.23 \cdot 10^{-1}$
0.050	10.04965	0.50	0.71	$0.62 \cdot 10^{-3}$	$0.30406 \cdot 10^{-2}$	1.35
0.030	10.32771	3.28	0.71	$0.17 \cdot 10^{-3}$	$0.33171 \cdot 10^{-2}$	10.57
0.020	10.80397	8.04	0.71	$0.34 \cdot 10^{-3}$	$0.39330 \cdot 10^{-2}$	31.10
0.015	11.25559	12.56	0.70996	$0.51 \cdot 10^{-2}$	$0.47019 \cdot 10^{-2}$	56.73
0.010	11.95407	19.54	0.70973	$0.39 \cdot 10^{-1}$	$0.64287 \cdot 10^{-2}$	114.29

Since the baseband is 2 (Hz), the sampling period must be less than 0.195 (s), because a sampling factor equal to 2.56 has been considered. On the other hand T_s should be greater than the limit time 0.0195 (s), derived from Eq.(15). Actually up to $T_s=0.050$ (s) errors on ζ are negligible, on the contrary for decreasing sampling periods higher and higher damping ratios have been obtained, owing to the presence of the triangular window.

The amplitude R has been achieved through estimates of the decay rate and of initial values of the autocorrelation function, Eq.(10).

Natural frequencies have been instead evaluated with immaterial errors for all the cases presented.

The truncation at the end of the maximum time lag does not affect the modal parameter estimates, in fact they have been carried out in the time domain with the Hilbert approach [7,8] (Appendix).

The same case is also shown in Tab.2, where estimates have been carried out in the frequency domain, using 400 spectral lines, with the commercial software SMS Modal 3.0 [11]:

Table 2 - Damping ratio estimations in the frequency domain.

T_s (s)	0.150	0.100	0.050	0.030	0.020	0.015	0.010
ζ	0.00300	0.00300	0.00305	0.00337	0.00404	0.00490	0.00703
$ \epsilon_f $ (%)	-	-	1.67	12.33	34.67	63.33	134.33

Errors on the damping ratio are in agreement with the ones obtained by the time approach: the FRF results to be biased, in fact the triangular window, due to the uncertainty principle [12,13], broadens the peaks and therefore an overestimation of ζ occurs. For the first two sampling periods no errors could be evaluated because of the limited number of decimal digits provided by the software outputs.

Amplitudes have not been reconstructed because they are not only altered by the errors on the decay ratio estimates, but they are also modified by the effects due to the truncation of the autocorrelation function at the end of its observation time [14].

Another example, with a greater decay rate ($f_n=8.25$ Hz and $\zeta=0.01$), is presented in Tab.3:

Table 3 - Estimates from a higher decay rate impulse response.

T_s (s)	R	$ \epsilon_R $ (%)	f_n	$ \epsilon_f $ (%)	ζ	$ \epsilon_f $ (%)
0.020	10.00123	$12.33 \cdot 10^{-1}$	8.24959	$0.50 \cdot 10^{-2}$	$0.10001 \cdot 10^{-1}$	$0.14 \cdot 10^1$
0.010	10.00031	$0.31 \cdot 10^{-2}$	8.24959	$0.50 \cdot 10^{-2}$	$0.10001 \cdot 10^{-1}$	$0.90 \cdot 10^{-2}$
0.005	10.00083	$0.83 \cdot 10^{-2}$	8.24958	$0.50 \cdot 10^{-2}$	$0.10002 \cdot 10^{-1}$	$0.17 \cdot 10^{-1}$
0.001	10.21345	2.13	8.25043	$0.52 \cdot 10^{-2}$	$0.10544 \cdot 10^{-1}$	5.44
0.0008	10.28766	2.88	8.24636	$0.44 \cdot 10^{-1}$	$0.10940 \cdot 10^{-1}$	9.40
0.0005	10.54330	5.43	8.28293	0.34	$0.12641 \cdot 10^{-1}$	26.41
0.0003	12.76663	27.67	8.20648	0.53	$0.21966 \cdot 10^{-1}$	119.66

In this case a baseband of 10 (Hz) has been considered, therefore the Shannon sampling period is equal to $T_s=0.039$ (s), on the contrary the limit sampling time equals 0.0005 (s). As in the first Table, errors on ζ increase as the sampling time lowers and unacceptable values have been obtained for T_s equal or less than the limit value. The order of magnitude of ϵ_f is similar to the one gained for the first example.

In the next Table two modes in the baseband of 10 (Hz) have been considered; modal parameter estimates achieved from autocorrelation functions of impulse responses with the same amplitudes and the same natural frequencies of the previous examples,

but with the damping ratio equal to 0.003 for both the modes, are shown (Tab.4):

Table 4 - Modal parameter evaluations for two modes present in the same baseband (10 Hz) versus the sampling period.

T_s	mode	R	$ \epsilon_R $ (%)	f_n	$ \epsilon_f $ (%)	ζ	$ \epsilon_\zeta $ (%)
0.035	1st	10.19364	1.94	0.71	-	$0.31820 \cdot 10^{-2}$	6.07
	2nd	10.00335	$0.33 \cdot 10^{-1}$	8.24995	$6.06 \cdot 10^{-4}$	$0.30006 \cdot 10^{-2}$	$0.21 \cdot 10^{-1}$
0.030	1st	10.32731	3.27	0.71	-	$0.33169 \cdot 10^{-2}$	10.56
	2nd	10.01256	0.13	8.24993	$8.49 \cdot 10^{-4}$	$0.30025 \cdot 10^{-2}$	$0.85 \cdot 10^{-1}$
0.025	1st	10.52615	5.26	0.71	-	$0.35444 \cdot 10^{-2}$	18.15
	2nd	10.00393	$0.39 \cdot 10^{-1}$	8.24990	$1.21 \cdot 10^{-3}$	$0.30009 \cdot 10^{-2}$	$0.30 \cdot 10^{-1}$
0.020	1st	10.80372	8.04	0.71	-	$0.39328 \cdot 10^{-2}$	31.10
	2nd	10.00082	$0.82 \cdot 10^{-2}$	8.24989	$1.33 \cdot 10^{-3}$	$0.30003 \cdot 10^{-2}$	$0.88 \cdot 10^{-2}$
0.015	1st	11.26584	12.66	0.70996	$5.63 \cdot 10^{-3}$	$0.47096 \cdot 10^{-2}$	56.99
	2nd	9.97821	0.22	8.24984	$1.94 \cdot 10^{-3}$	$0.29935 \cdot 10^{-2}$	0.22
0.010	1st	11.97794	19.78	0.70973	$3.80 \cdot 10^{-2}$	$0.64517 \cdot 10^{-2}$	115.06
	2nd	9.95462	0.45	8.25002	$2.42 \cdot 10^{-4}$	$0.29848 \cdot 10^{-2}$	0.51

For sampling period up to the limit value 0.0195 (s), due to the first mode (i.e. the one with the lowest decay rate), errors on ζ increase to about 30% for the first mode, whereas they remain negligible for the second mode. In any case errors on natural frequencies are always irrelevant and therefore the ones on the amplitude are practically related to the errors on the correspondent ζ 's. Obviously for shorter T_s 's, errors on the damping ratios of the first mode result higher and higher, whereas for the second mode they always remain small. Due to the presence of more modes in the baseband, and since the Hilbert transform approach works on the single mode, a suitable filter must be applied. In particular, an adaptable cosine tapered filter has been used: its width has been chosen taking into account the shift of the peaks in the frequency domain, owing to the different sampling periods. Estimates from the previous two modes, when they are added to an uncorrelated random noise, with zero mean and standard deviation equal to 50% of the common impulse response amplitude, are shown in Tab.5 (Fig.2 shows the time history relative to $T_s=0.02$, whereas its autocorrelation is presented in Fig.3):

Table 5 - Effect of a high random noise on parameter estimates of the modes presented in Tab.4.

T_s	mode	R	$ \epsilon_R $ (%)	f_n	$ \epsilon_f $ (%)	ζ	$ \epsilon_\zeta $ (%)
0.020	1st	9.97203	0.28	0.71019	$2.63 \cdot 10^{-2}$	$0.32681 \cdot 10^{-2}$	8.94
	2nd	12.32280	23.22	8.25263	$3.19 \cdot 10^{-2}$	$0.34667 \cdot 10^{-2}$	15.96
0.015	1st	11.54107	15.41	0.71043	$6.06 \cdot 10^{-2}$	$0.48112 \cdot 10^{-2}$	60.37
	2nd	9.32304	6.77	8.25823	$9.98 \cdot 10^{-2}$	$0.24305 \cdot 10^{-2}$	18.98
0.010	1st	11.68375	16.84	0.70958	$5.92 \cdot 10^{-2}$	$0.60516 \cdot 10^{-2}$	101.72
	2nd	8.69748	13.03	8.24198	$9.72 \cdot 10^{-2}$	$0.24436 \cdot 10^{-2}$	18.55

In this case the effect of the added noise, on the damping ratio estimations, is especially significant for the second mode because its impulse response is more rapidly damped out. Besides, even if the residues of the two modes are equal, the initial amplitudes of the autocorrelation functions - derived by filtering - result to be completely different: in fact - for the sake of simplicity - considering each mode independently and not taking account of the cross-correlation terms, autocorrelation amplitudes are inverse functions, being all the other values common, of the relative decay rates and so the second mode could have a much smaller amplitude than the first one: see Figs.4 and 5 for the filtered autocorrelation functions and Figs.6 and 7 for the relative envelopes.

4. Conclusions

In the use of an approach based on autocorrelation functions of impulse responses in order to obtain - in the time domain - the modal parameters, a possible source of error in the damping ratio estimation is connected with a bias due to a triangular window positioned around the time axis origin. Owing to this bias, it is necessary to evaluate - for example at the maximum time lag where the autocorrelation function is calculated - a minimum sampling period (lower limit), suitable to analyze the signal and in particular to estimate the decay rate and consequently the damping ratio. Although the value of this sampling period is a function of the unknown signal time constant, nevertheless it is possible, starting from an its first estimate, to update the value of the sampling period and so to eliminate bias errors. In this way, the peculiar advantages deriving from the use of autocorrelation functions - especially if evaluated from highly

noisy impulse responses - to estimate modal parameters, and in particular damping ratios, can be thoroughly exploited.

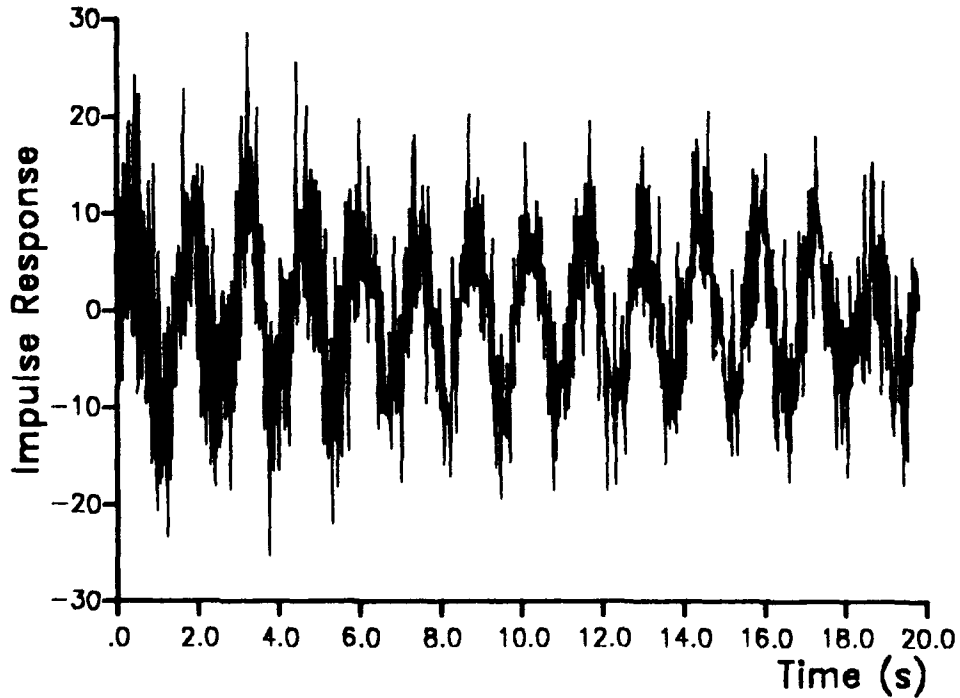


Figure 2 - Impulse response of Tab.5, relative to $T_s=0.02$ (s), contaminated by a random noise.

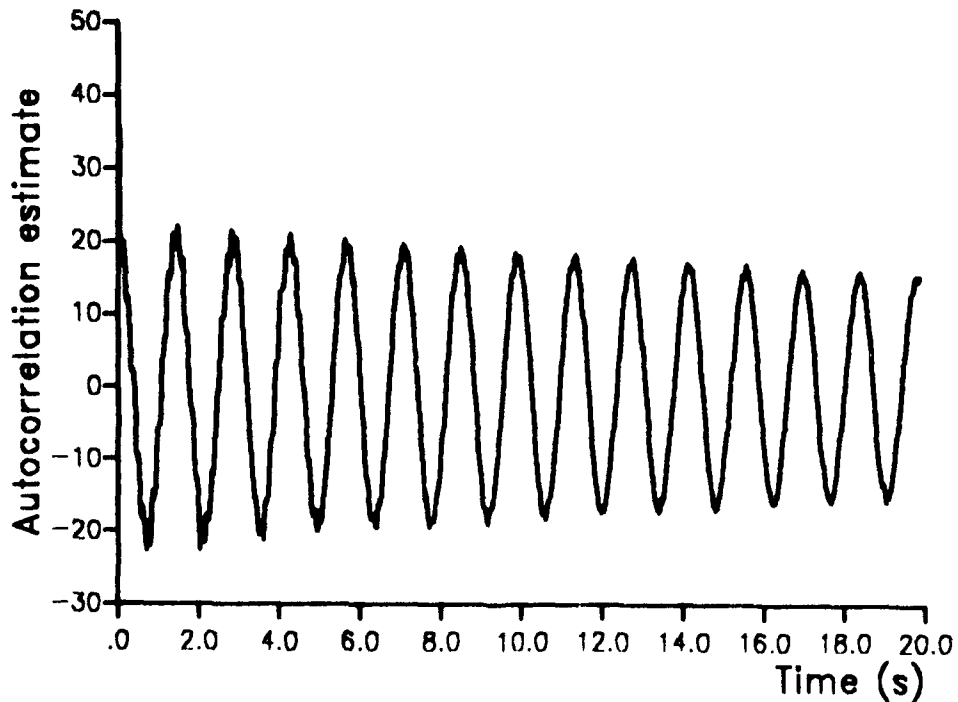


Figure 3 - Autocorrelation estimate of the time history presented in the previous Fig.

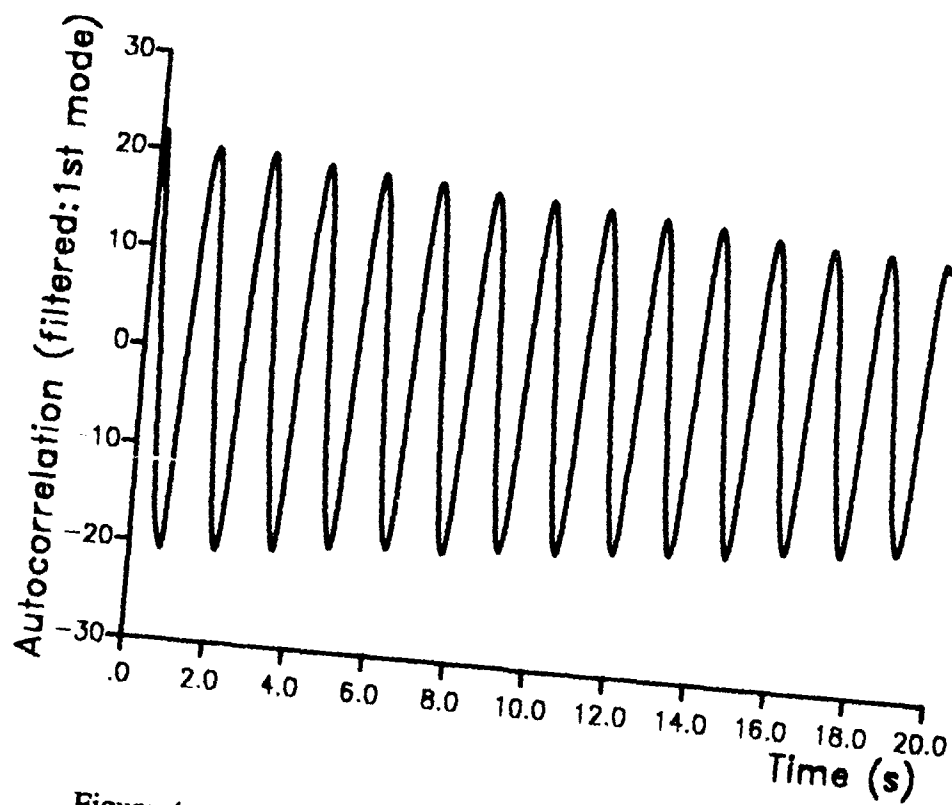


Figure 4 - Filtered autocorrelation function of the first mode.

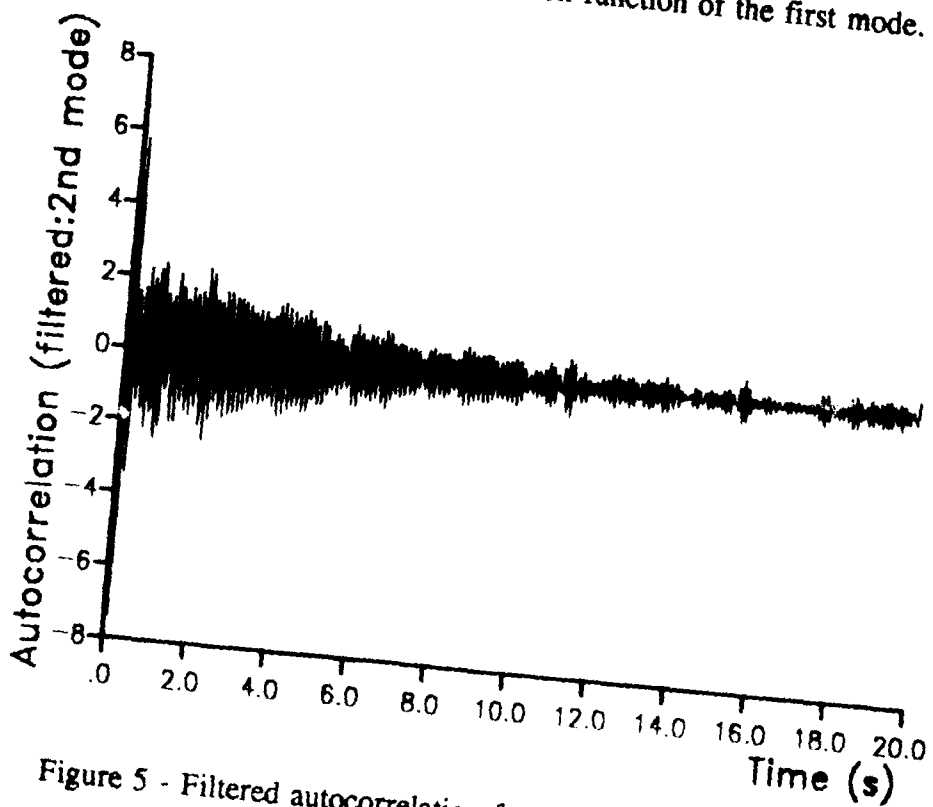


Figure 5 - Filtered autocorrelation function of the second mode.

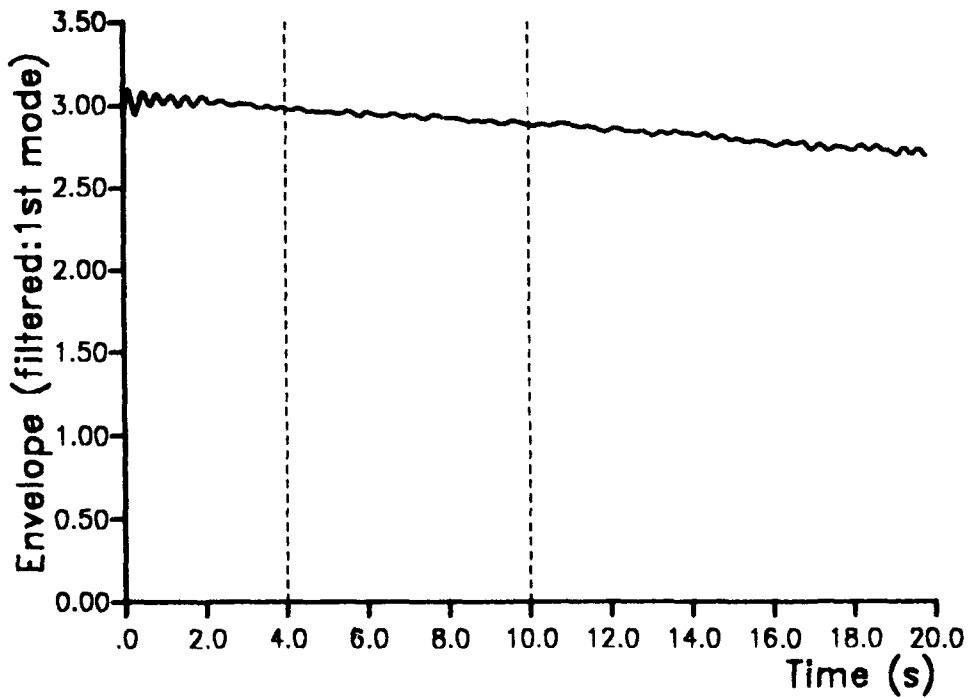


Figure 6 - Envelope relative to the first mode (semi-log plane):the vertical dashed lines contain the points used in the least squares regression.

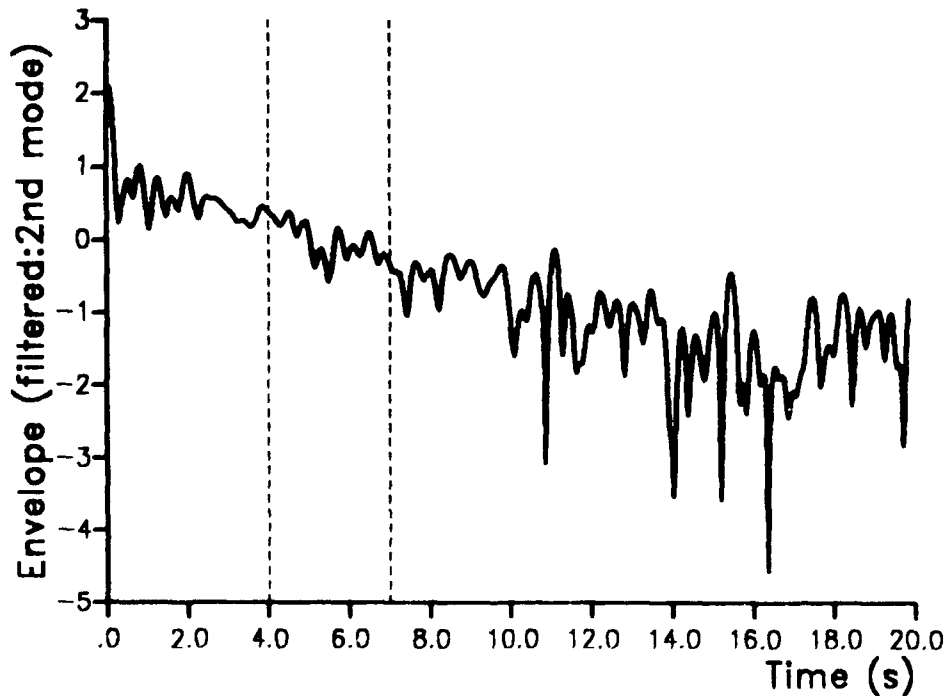


Figure 7 - Envelope of the second mode in the semi-log plane:the points used in the least squares regression are contained within the dashed lines.

Acknowledgments

The authors wish to thank Dr. A. Paolozzi for his helpful support.

This paper was sponsored both by the M.P.I. research project: "Stima del fattore di smorzamento da segnali molto rumorosi" and by the C.N.R. grant CTB 88.03112.11: "Tecniche di identificazione modale di una struttura aeronautica".

References

- [1] R.K. Otnes and L. Enochson: *Digital Time Series Analysis*
J. Wiley & Sons, New York 1972, pp.323-345.
- [2] J.S. Bendat and A.G. Piersol: *Random Data: analysis and measurement procedures*
Wiley-Interscience, New York 1971, pp.136-167.
- [3] B.L. Clarkson and C.A. Mercer: *Use of cross correlation in studying the response of lightly damped structures to random forces*
AIAA Journal, vol.3, n.12, 1965, pp.2287-2291.
- [4] F. Kandianis: *Frequency response of structures and the effects of noise on its estimates from the transient response*
Journal of Sound and Vibration, 15(2), 1971, pp.203-215.
- [5] A. Agneni: *Modal parameter estimates from autocorrelation functions of highly noisy responses*
(to be published)
- [6] S.L. Marple Jr.: *Digital Spectral Analysis with Applications*
Prentice Hall Inc., Englewoods Cliffs 1987, p.149-150.
- [7] A. Agneni, L. Balis Crema: *Damping measurements from truncated signals via Hilbert transform*
Mechanical System and Signal Processing, 3(1), 1989, pp.1-13.
- [8] A. Agneni, L. Balis Crema: *Analytic signals in the damping coefficient estimation*
Proc. Int. Conf.: "Spacecraft Structures and Mechanical Testing", Noordwijk, The Netherlands, 1988.
ESA SP-289, pp.133-139.
- [9] S.L. Marple Jr.: *Digital Spectral Analysis with Applications*
Prentice Hall Inc., Englewoods Cliffs 1987, p.146-149.

- [10] M.Kunt: *Traitement numérique des signaux*
Dunod, Lousanne 1981, pp.251-257.
- [11] Structural Measurement Systems (SMS), Modal Analysis System. Operating Manual "Theory of Operation", 1985, ch.12, pp.12-25 to 12-33.
- [12] A.A.Kharkevich: *Spectra and Analysis*
Consultant Bureau, New York 1960, pp.62-73.
- [13] A.Papoulis: *The Fourier Integral and its Applications*
McGraw-Hill, New York 1962, pp.62-74.
- [14] A.Agneni, L.Balis Crema, A.Paolozzi: *Impulse response identification of SDOF systems from time-truncated signals*
(to be presented at: 9th International Modal Analysis Conference (IMAC), Firenze, April 14-18, 1991).
- [15] E.Bedrosian: *The analytic signal representation of modulated waveforms*
Proc. IRE, 50, 1962, pp.2071-2076.
- [16] E.Bedrosian: *A product theorem for Hilbert transform*
Proc. IEEE, 51, 1963, pp.868-869.

Appendix: Hilbert transform and modal parameter estimation

The time sequence (10) can be considered as an amplitude modulated signal with the carrier equal to the damped angular frequency and the modulating signal equal to the decaying exponential function: $[R^2/(4NT_s\sigma)] \exp(-\sigma mT_s)$. Since the spectrum of this last function is unbounded, relationship (10) and:

$$\hat{\rho}'_h[m] \cong \frac{R^2}{4NT_s\sigma} e^{-\sigma(mT_s)} \cdot \sin \left[\omega_d (mT_s) \right] \quad (\text{A.1})$$

are not strictly a pair of Hilbert transforms. Nevertheless, under proper conditions [8], the Bedrosian theorem [15,16] can be applied at least in the limit sense, thus the complex signal:

$$\begin{aligned}
z[m] &= \frac{R^2}{4NT_s\sigma} e^{-\sigma(mT_s)} \left\{ \cos \left[\omega_d (mT_s) \right] + j \sin \left[\omega_d (mT_s) \right] \right\} = \\
&= \frac{R^2}{4NT_s\sigma} e^{-\sigma(mT_s)} e^{j\omega_d(mT_s)}
\end{aligned} \tag{A.2}$$

can be considered as analytic.

It is easy to recognize that the magnitude of $z[m]$ represents the modulating function, whose decay rate could be directly estimated from the straight line:

$$\ln |z[m]| = \ln \left[\frac{R^2}{4NT_s\sigma} \right] - \sigma m T_s \tag{A.3}$$

whereas its argument is the instantaneous phase, the slope of which gives the damped angular frequency:

$$\text{Arg} \{ z[m] \} = \omega_d m T_s \tag{A.4}$$

Consequently, it is possible to achieve the natural angular frequency:

$$\omega_n = \sqrt{\sigma^2 + \omega_d^2} \tag{A.5}$$

and the damping ratio:

$$\zeta = \frac{\sigma}{\omega_n} \tag{A.6}$$

The residue magnitude R can be evaluated introducing the known values and the estimate of σ , achieved from the envelope, into the initial amplitude of Eq.(10).

Good estimates of the parameters mentioned above can be gained performing least squares regressions on the two straight lines represented by Eqs.(A.3) and (A.4).

DYNAMIC MODULI OF FLUOROCARBON COMPOUNDS

Wayne T. Reader¹
Vector Research Co., Inc.
Bethesda, MD

Robert W. Megill
E. J. Dupont de Nemours & Co.

ABSTRACT

Viscoelastic polymers are frequently used to eliminate harmful or annoying noise fields in an environment which contains solvents or gases at elevated temperatures. The frequency range over which the particular polymer performs as a sound isolator, an absorber, or a damper may vary by orders of magnitude. Hence, a polymer family which is resistant to many common solvents and exhibits high loss factors distributed over several frequency decades covering the audio band should find many applications. Fluorocarbon elastomers such as copolymers of vinylidene fluoride and hexafluoropropylene are such a family. Presented in this paper will be the results of an initial examination of the dynamic moduli, consisting of the elastic and loss components, of six different commercially available family members. The magnitude of the peak loss factor is found to vary between approximately 1.1 to 1.4, and its location by more than two decades in the frequency domain.

**FULL PAPER NOT AVAILABLE FOR
PUBLICATION**

¹Vector Research Co., Inc., Suite 1200, 6903 Rockledge Drive, Bethesda, MD 20817, (301) 493-5500

Passive Vibration Damping with Noncohesive Granular Materials

M. Abdel-Gawad
Rockwell International Science Center
Thousand Oaks, CA 91360
(805-373-4220)

Abstract

Dynamical systems comprised of noncohesive solid particles offer a promising approach for passive vibration damping as an alternative where viscous or viscoelastic materials become ineffective at high or low temperatures or in a hostile environment. We are employing a vibrating bar apparatus to understand damping mechanisms in such systems and to identify important parameters for use in the design of efficient methods for controlling damaging vibrations in high speed aircraft and Large Space Structures. In systems involving solid particles rubbing and colliding with each other, loss of mechanical energy can be substantial but the mechanisms are complex and not fully understood. The material parameters we have been studying include grain size and shape, intrinsic grain density, packing density, and friction coefficient. Measurements on a variety of noncohesive granular materials show that damping is both frequency and amplitude dependent which indicates the combined effects of frictional and viscous-like damping mechanisms. Considerable mechanical energy loss results from friction by particle sliding, rolling and by transfer of inertia at collisions between the grains. Relatively low packing densities and fine grain size seem to be favorable properties for maximizing vibration energy losses, at least for the materials examined and in the frequency range, strain amplitudes and vibration modes employed. Microstructures which enhance internal surface area and resistance to compaction are favorable properties for promoting high mechanical energy loss. A full understanding of the mechanisms may provide the data necessary for designing and manufacturing damping materials tailored for use in applications where conventional viscoelastic materials are ineffective.

Introduction

Potentially destructive vibrations often take place in aerospace structures and components. Vibration induced cracks occur in the aircraft affecting structural elements, aircraft skin and antennas. When aircraft operate at very low temperatures conventional damping materials based on viscous or viscoelastic mechanisms are transformed from their rubbery or transitional state into their glassy state where they lose their effectiveness. Serious cracks have been known to develop in aerospace components operating at high temperatures and hostile environments. Vibration problems are also anticipated in advanced launch systems and are pervasive in many other industrial applications. The use of noncohesive granular materials as a damping medium offers a promising approach for damping vibrations in situations where conventional materials cannot be used.

The objectives of this work are to a) understand damping mechanisms in oscillating particles set in motion by a vibrating structure, b) identify critical parameters needed for design of effective damping systems, and c) acquire the knowledge necessary for recognizing potential applications and limitations of this technique.

This work is based on two studies performed independently at the Rockwell Science Center (1-3) and Rocketdyne divisions (4). We learned from previous studies on elastic wave attenuation in rocks with a wide range of cohesiveness that damping increases substantially with the increase in crack density and inversely with the strength of bonding at grain interfaces. The presence of even small amounts of water adsorbed on silicate grains causes considerable weakening of the interface bond and dramatically increases the damping factor ($1/Q$). Damping mechanisms in semi-consolidated materials were found to be complex, involving both internal friction and viscoelastic-like effects. In noncohesive materials with solid particles rubbing on and colliding with each other, loss of mechanical energy can be substantial; but the effects of various parameters on damping are complex and often work in opposite directions. This paper reports progress toward understanding the effects of some microstructural parameters on damping in relation to frequency and strain amplitude.

Measurements and Techniques

This study draws upon damping measurement techniques and research experience developed over the last ten years at Rockwell Science Center to characterize the dynamic mechanical properties of aerospace and aerospace materials. Figure 1 shows a schematic

of a vibrating bar apparatus and measurement system we currently use for making damping and modulus measurements on composite materials. A Hewlett-Packard computer is used to control the experiment and is programmed to allow the selection of input voltage and frequency range parameters and for measurements at high temperatures and controlled environment. The system tracks and digitizes the resonance peaks, and calculates the loss factor $1/Q$ from the width of the resonance curve measured at $1/2$ of the maximum amplitude and is given by

$$1/Q = \omega_2 - \omega_1 / \omega_r$$

where Q is the quality factor, ω_r is the resonant frequency in forced vibration, and ω_1 , ω_2 are the frequencies at which the amplitude of the vibration has fallen to $1/2$ of the maximum value.

In these experiments the forced vibrating bar apparatus was used to measure the damping factor Q^{-1} of a three-layer rectangular bar geometry. The composite bar consists of two identical constraining copper bars rigidly mounted on the vibrating bar device and separated by a space in which the test damping material is placed. The metal bars are 10 cm long, 2.5 cm wide and 0.06 cm thick and are separated by a spacing of 0.6 cm. The geometry is that of a damping layer sandwiched between two constraining metal layers Figure 2. The damping test material is contained in a tailored bag of thin mylar film placed between the two metal bars. The mylar bag had a small effect on damping of the composite bar and this was taken into consideration when making comparisons between measurements made with and without the damping layer.

The theoretical basis of damping in multi-layer beams was discussed by Ross, Ungar, and Kerwin (5). A method for determining the damping properties in various multi-layer geometries is described by Nashif et al (6), and in ASTM Standard Method E756-83 (7).

Figures 3-7 illustrate the effects of some microstructural parameters on damping ($1/Q$) of the composite bar system using a variety of damping materials. The measurements were made on the fundamental mode in a free-free end-loaded geometry in flexure. A rotor with calibrated weights rigidly clamped to the ends of the specimen provided a means for varying the resonance frequency. A full description of this technique was given by Papadakis (8).

Figure 3 is a plot of $1/Q$ for four damping materials representing a range of packing densities. Diatomaceous earth (DE) with the lowest density shows superior damping compared to the high density nickel particles (Ni). The 1 micron zirconia (ZR) also shows excellent damping. The four points, collectively labeled GL, represent crushed glass beads with different packing densities. In this case, however, the observed differences in damping may not be

little or no energy. Adjacent to these are areas of relatively high damping caused by particle rotation and frictional sliding (12,13).

Energy dissipation caused by friction is a complex function of many variables including a) the number of contacts per unit volume which is dependent on grain size and coordination number (packing density), b) normal stresses at points of contacts, which is also a function of packing density, c) the shear stress at the sliding interface, and d) the effective friction coefficient which is a function of the intrinsic friction coefficient of the material (usually measured on two smooth surfaces) modified by the presence of asperities (grain shape).

In more loosely compacted material the grains lose energy both by friction and collision. The latter mechanism becomes more dominant at low packing densities. In the collision dominant regime viscous-like damping results from losses during momentum transfer (14). In this case particle inertia and frequency of collisions are major contributors to energy loss. At high packing density the particle velocity, inertia and number of collisions are reduced due to the increased stiffness and resistance to deformation.

Figure 9 illustrates a rheological model of particle interactions in a system where both elastic and viscous normal forces and tangential frictional forces simultaneously take place (15). The model (16) for granular flow which is based in part on the early work of Bagnold (14) on shearing of solid spheres dispersed in a Newtonian fluid. The model considers the total stress as the sum of two parts,

$$\sigma_{\text{total}} = \sigma(C)_{\text{Coulomb}} + \lambda(C) \rho D^2 (dU/dy)^2$$

rate-independent
dry friction part

rate-dependent
viscous part

where C is the solids fraction,

dU/dy is the rate of shear strain,

λ is the linear grain concentration coefficient, defined as the ratio grain diameter/mean free dispersion distance,

$\lambda = 1/(C_0/C)^{1/2} - 1$ where C_0 is the maximum possible static volume concentration,

ρ is mass density of particle material,

D is mean particle diameter.

Noncohesive granular materials are not Newtonian fluids and their flow models cannot quantitatively describe the complex movements of oscillating particles. However, the relationships identified above provide some insights of the mechanisms involved.

The term $\lambda(C)$ relates to the packing density; the strain shear rate (dU/dy) is equivalent to frequency. The role of grain diameter D is more complex because it enters into the viscous part and also in the friction part of the total energy dissipated. Fine grained particles have higher surface area per unit mass and therefore produce higher levels of grain to grain friction than the coarse grained particles. The role of the intrinsic grain density ρ in relation to vibration modes is also unclear and must be investigated by further studies.

With these qualifications in mind, the granular flow model is qualitatively synergistic with energy dissipation in oscillating particles. In both processes the rate-independent, strain dependent part of damping can be ascribed to dry Coulomb friction and the 'viscous' contribution results from momentum transfer during collisions between particles. At high values of solids fraction (high compaction) and low shear rates the rate-independent term is dominant, whereas at low packing densities and high shear rates the collisional transfer term prevails.

This is qualitatively consistent with our data whereby high levels of damping are associated with low packing densities. The observed behavior of strain amplitude dependence together with frequency dependence of damping ($1/Q$) indicates that both frictional and viscous-like processes are involved. Diatomaceous earth, the most effective damping material found so far in this study, possesses several of the favorable microstructural properties discussed above. It consists of siliceous skeletal remains of marine microorganisms (diatoms). In addition to fine grain size with high internal surface area, diatomaceous earth has high resistance to compaction. These properties are favorable for high damping and the excellent filtration properties for which this material is very well known.

Summary and Conclusions

Laboratory studies on a variety of noncohesive granular materials show that damping is both frequency and amplitude dependent which indicates the combined effects of frictional and viscous-like damping mechanisms. Considerable mechanical energy loss results from friction by particle sliding, rolling and by transfer of inertia at collisions between the grains. Relatively low packing densities and fine grain size seem to be favorable properties for maximizing vibration energy losses, at least for the materials examined and in the frequency range, strain amplitudes and vibration modes employed. Microstructures which enhance internal surface area and resistance to compaction are favorable properties for promoting high mechanical energy loss. The effects of other parameters such as intrinsic grain density, grain shape, and the

presence of very small amounts of adsorbed fluids need to be further investigated. Quantitative modeling of the complex mechanisms involved is a challenging task necessary for optimizing design of damping materials tailored for specific vibration problems. Full understanding of these mechanisms will also be useful in developing internally damped alloys and composite materials.

Acknowledgements

This work was done on Rockwell International Science Center IR&D funds. The author thanks H. V. Panossian of Rockwell Rocketdyne Division for discussions during the initial stages of this research.

References

1. Abdel-Gawad, M., L. Bivins, J. Bulau, B. R. Tittmann, and M. Vassiliou, Seismic Absorption Mechanisms in Sedimentary Rocks, Final Report (M. Abdel-Gawad editor), Rockwell International Science Center Report SC5851.FR submitted to Petroleum Company Consortium, pp.64, 1989.
2. Tittmann, B. R., M. Abdel-Gawad, C. Salvado, J. Bulau, L. Ahlberg and T. W. Spencer, A Brief Note on the Effect of Interface Bonding on Seismic Dissipation, Proc. Lunar Sci. Conf. 12th, 1737-1754, 1981.
3. Tittmann, B. R., J. R. Bulau, and M. Abdel-Gawad, The Role of Viscous Fluids in the Attenuation and Velocity of Elastic Waves in Porous Rocks, in Physics and Chemistry of Porous Media, D.L. Johnson and P. N. Sen Editors, Schlumberger-Doll Research-1983, AIP Conf. Proceedings 107, p. 131-143, 1984.
4. Panossian, H. V., and D. L. Bice, Non-obstructive Particle Damping Tests on Aluminum Beams, paper presented at the "DAMPING '91 Conference sponsored by the Air Force Wright Laboratory, Feb. 13-15, 1991, San Deigo, California.
5. Ross, D , E.E. Ungar, and E. M. Kerwin, Jr., Damping of plate flexural vibrations by means of viscoelastic laminate- Structural Damping, ASME, New York, pp. 49-88, 1959.
6. Nashif, A. D., D. I.G. Jones, and J. F. Henderson, Vibration damping, John Wiley & Sons, New York, 451 pp., 1985.
7. ASTM, Standard method for measuring vibration damping properties of materials, ASTM E756-83, 1983.
8. Papadakis, E. P., Balanced resonator for infrasonic

- measurements of Young's Modulus and damping in flexure, J. of Testing and Evaluation , V. 1, No. 2, p. 126-132, 1973.
9. Cundall, P. A. and O.D.L Strack, Model of microscopic mechanisms in granular material, in J. T. Jenkins and M. Satake (editors) Mechanics of Granular Materials: New Models and constitutive relations, Elsevier Science publishers, Amsterdam, pp. 137-149, 1983.
10. Walton, O. R., Particle -dynamics calculations of shear flow, in J. T. Jenkins and M. Satake (editors) Mechanics of Granular Materials: New Models and constitutive relations, Elsevier Science publishers, Amsterdam, pp. 327-338, 1983.
11. Campbell, C. S., and C.E. Brennen, Computer simulation of shear flows of granular material, in J. T. Jenkins and M. Satake (editors) Mechanics of Granular Materials: New Models and constitutive relations, Elsevier Science publishers, Amsterda., pp. 313-326, 1983.
12. Oda, Masanobu, J. Konishi and S. Nemat-Nasser, Experimental micromechanical evaluation of the strength of granular materials: effects of particle rolling, in J. T. Jenkins and M. Satake (editors) Mechanics of Granular Materials: New Models and constitutive relations, Elsevier Science publishers, Amsterdam, pp. 21-30, 1983.
13. Kanatani, Ken-ichi, Mechanical properties of ideal granular materials, in J. T. Jenkins and M. Satake (editors) Mechanics of Granular Materials: New Models and constitutive relations, Elsevier Science publishers, Amsterdam, pp. 235-244, 1983.
14. Bagnold, R. A., Experiments on a gravity free dispersion of large solid spheres in a Newtonian fluid under shear. Proc. R. Soc. London, Ser. A225, pp 49-63, 1954.
15. Walton, O., Particle dynamics modeling of geological materials, Lawrence Livermore National Laboratory Report. UCRL-52915, 1980.
16. Savage, S., Granular flow down rough inclines - review and extension, in J. T. Jenkins and M. Satake (editors) Mechanics of Granular Materials: New Models and constitutive relations, Elsevier Science publishers, Amsterdam, pp. 261-282, 1983.

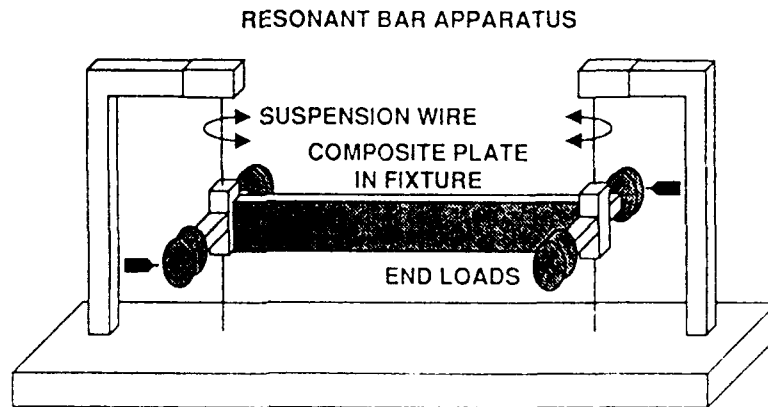
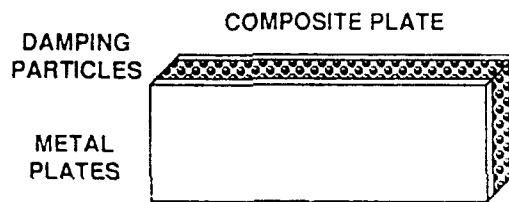
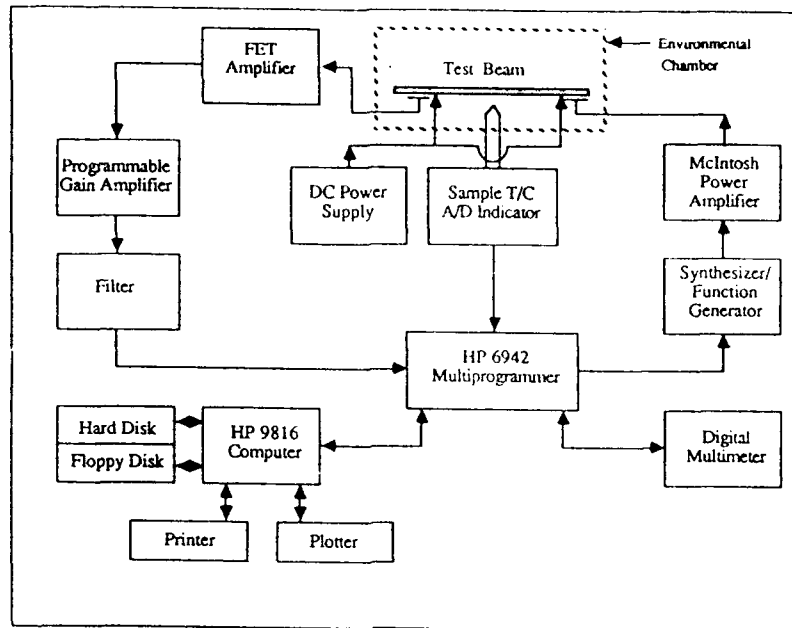


Figure 1- Vibrating Bar Apparatus and Measurement System Schematic

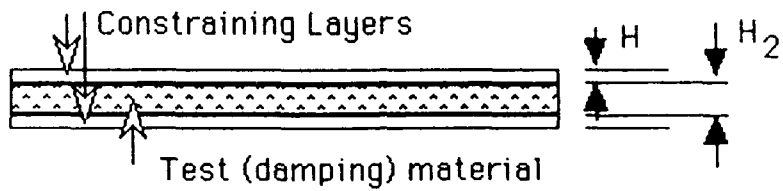


Figure 2. Three-Layer Geometry of Composite Test Bar.

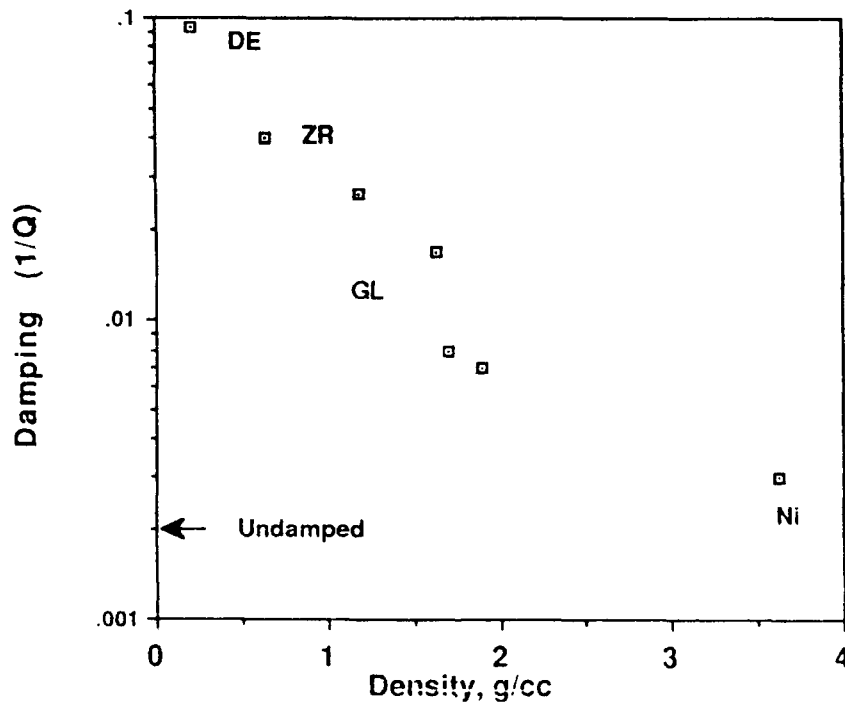


Figure 3. Damping versus Packing Density- DE: Diatom.Earth, ZR: 1-micron zirconia, GL: glass (4 points), Ni: Nickel.

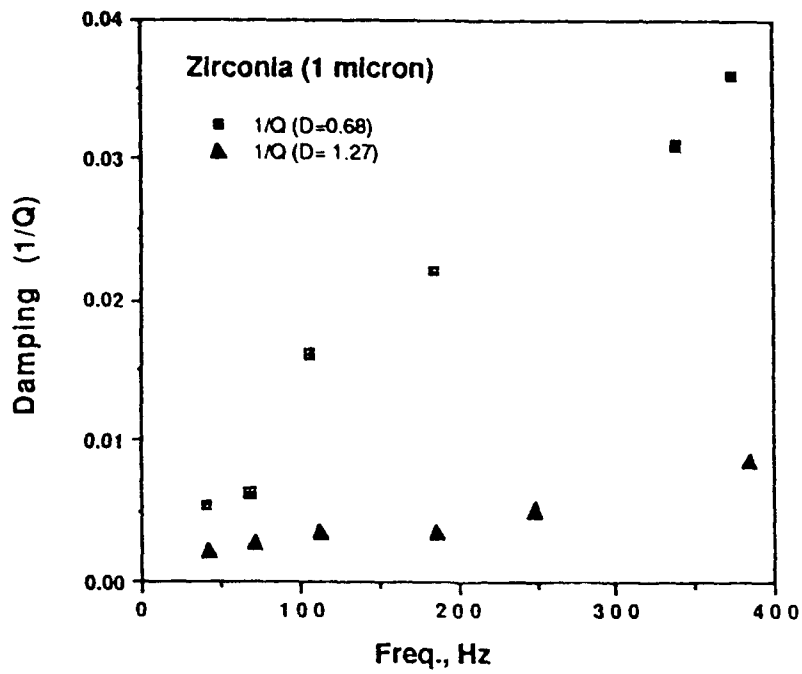


Figure 4. Frequency and Packing Density Dependence of $1/Q$.

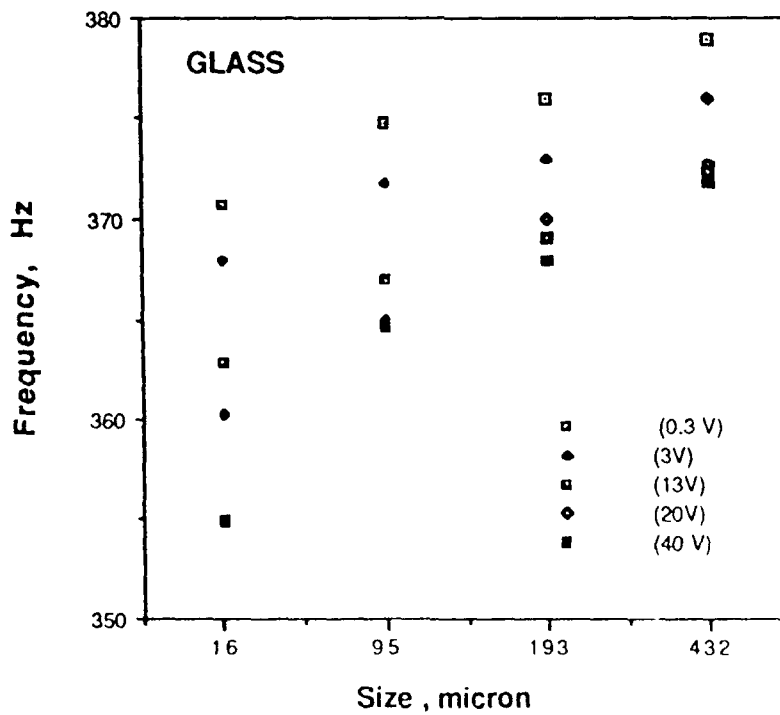


Figure 5. Frequency, Grain Size and Amplitude Dependence.

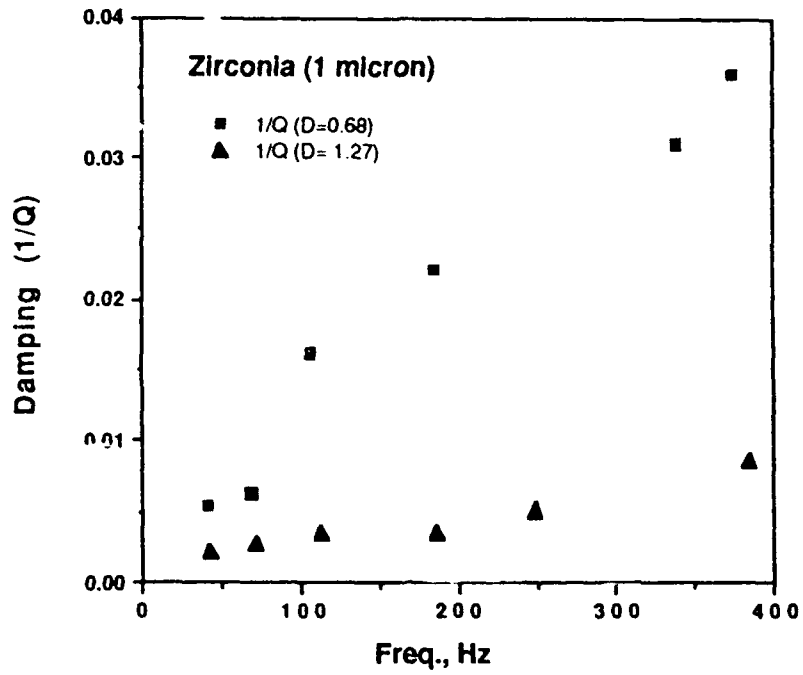


Figure 4. Frequency and Packing Density Dependence of $1/Q$.

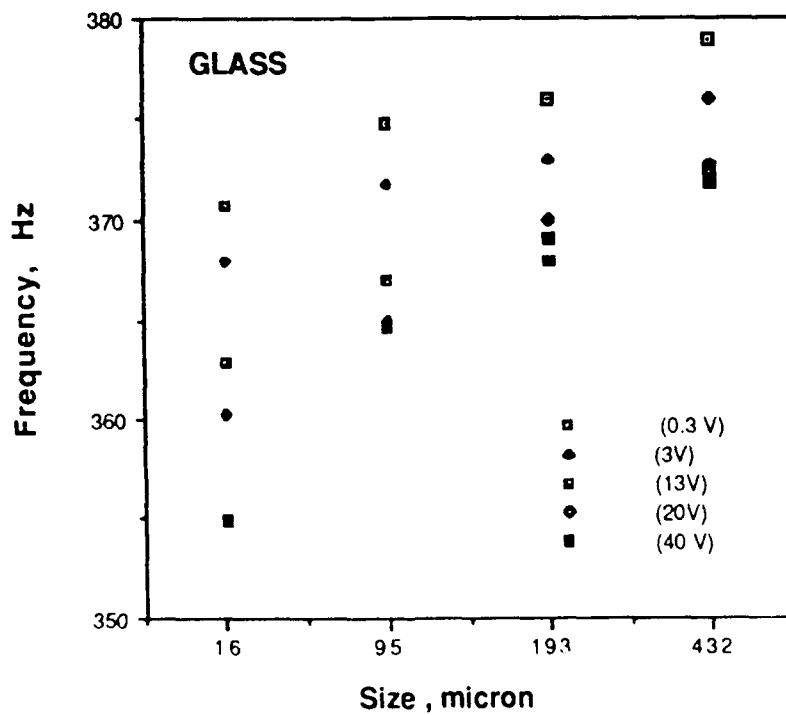


Figure 5. Frequency, Grain Size and Amplitude Dependence.

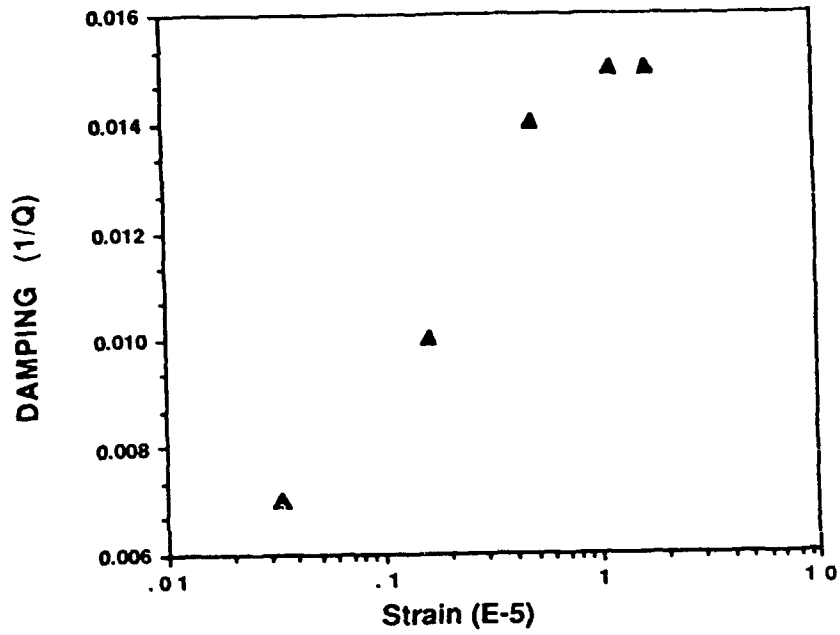


Figure 6. Damping Dependence on Strain Amplitude.

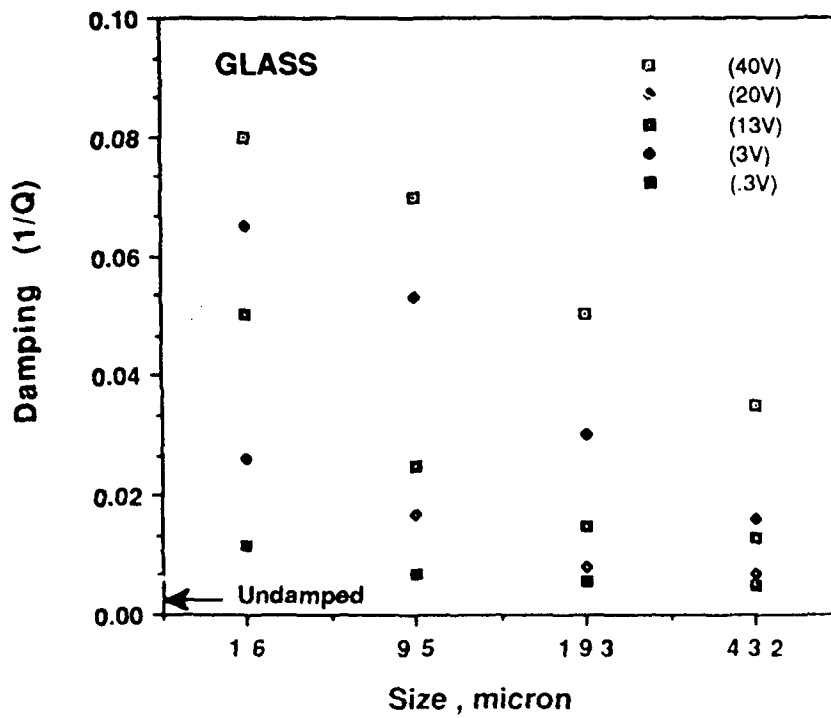


Figure 7. Damping, Grain Size and Amplitude Relations.

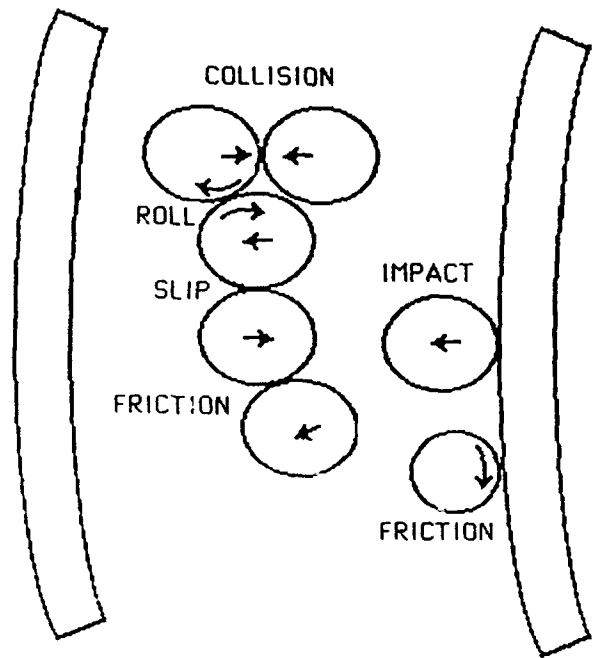


Figure 8. Energy Dissipation Mechanisms in Grains Oscillating Between Beams Vibrating in Flexure.

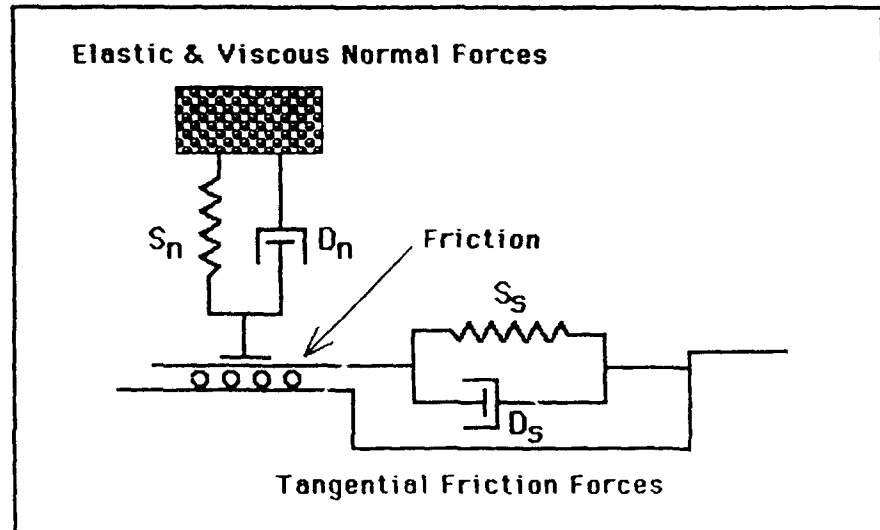


Figure 9. Rheological Model of Intergranular Contact Forces (after Walton, 1980).

VEM DATABASE PROGRAM

Bryce L. Fowler¹
CSA Engineering, Inc.
Palo Alto, CA

ABSTRACT

A three-tiered implementation of a viscoelastic material (VEM) database under development is described. Using low-level calls, searches for characterized VEM's may be conducted based on property constraints (e.g., modulus and loss factor at certain temperature and frequency) and/or other criteria (e.g., available thicknesses, type, etc.).

1. A graphical front end program that runs on a Macintosh personal computer is being written. It will be dynamically linked to VEM characterization and testing programs for data sharing.
2. A stand-alone program for UNIX machines using X windows is being written. Reports will be in the form of tables and X-Y plots. A similar program to run under MS-DOS is also being developed concurrently.
3. A VEM database engine which may be compiled and run on any computer that supports ANSI FORTRAN 77 is described. The engine consists of FORTRAN callable subroutines that search a VEM database created by a librarian program using VEM characterization data files.

¹CSA Engineering, Inc., 560 San Antonio Road, Suite 101, Palo Alto, CA 94306, (415) 494-7351

Payoffs of a VEM database

- **Engineers have access to a larger set of up-to-date information**
- **The search-tabulate-analyze design cycle is much faster, more accurate, and spans more materials**
- **Centralized storage and distribution of information**

User Community

- **A materials reference program must meet the requirements of the user community**
 - **Testers**
 - **Characterizers**
 - **Designers**
 - **Fabricators**
- **These groups obviously have very different interests and requirements**

User Community

Designers:

- Must search through material data for simultaneous occurrences of T , f , G , η
- Must tabulate material properties for analysis
- Need various other properties
 - Is material available in
 - sheets (available thicknesses)
 - liquid
 - Is material qualified for
 - outgassing
 - cohesion

User Community:

Testers and Characterizers:

- **Need to trace VEM batches, test configuration, etc. (audit trail)**
- **Need place to store and order test data and characterizations**

User Community:

Fabricators:

- **Handling**
 - **VEM's, constraining layers, adhesives, sealers**
- **Application**
 - **Contamination, environment control**
- **Quality control**
 - **Testing of treatment to determine bond quality**

Database Fields

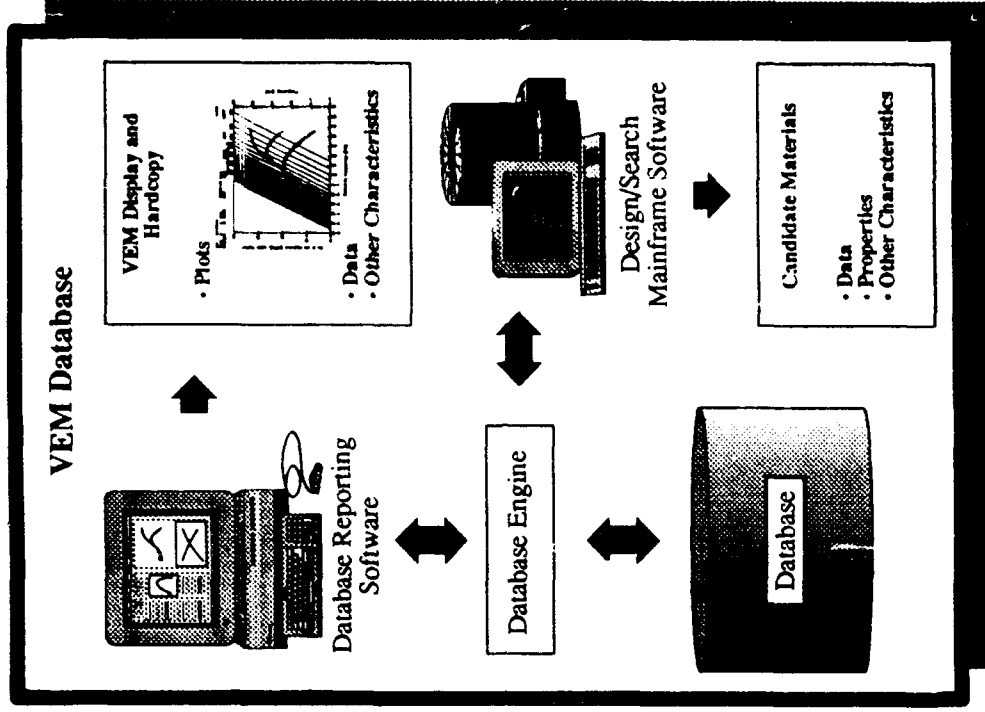
- **Measured Properties**

(All are temperature and/or frequency dependent)

- Shear modulus
- Loss factor
- Poisson's ratio
- Outgassing characteristics
- Creep characteristics
- Non-linear effects
- Pre-load effects
- Strain effects

- **Other Properties/Information**

- Sources
- Availability
- Type (adhesive, rubber, etc.)
- Available forms (liquid, sheets, etc.)
 - Thicknesses
- Density
- Application techniques
- Test conditions and apparatus
- Environmental resistance
- Cost
- Quality of data



VEM Database Mainframe Module

- **Database file architecture – FORTRAN 77 direct access**
 - **(EXP) file holds experimental data and characterization parameters**
 - **(INF) file hold all other material information**
- **Command line interface with batch capability**
- **Data import and export in ASCII**
- **Linkable to other software projects**

Current Implementation

- File storage
- Command-line interface with batch
- Data import from ASCII
- Command List

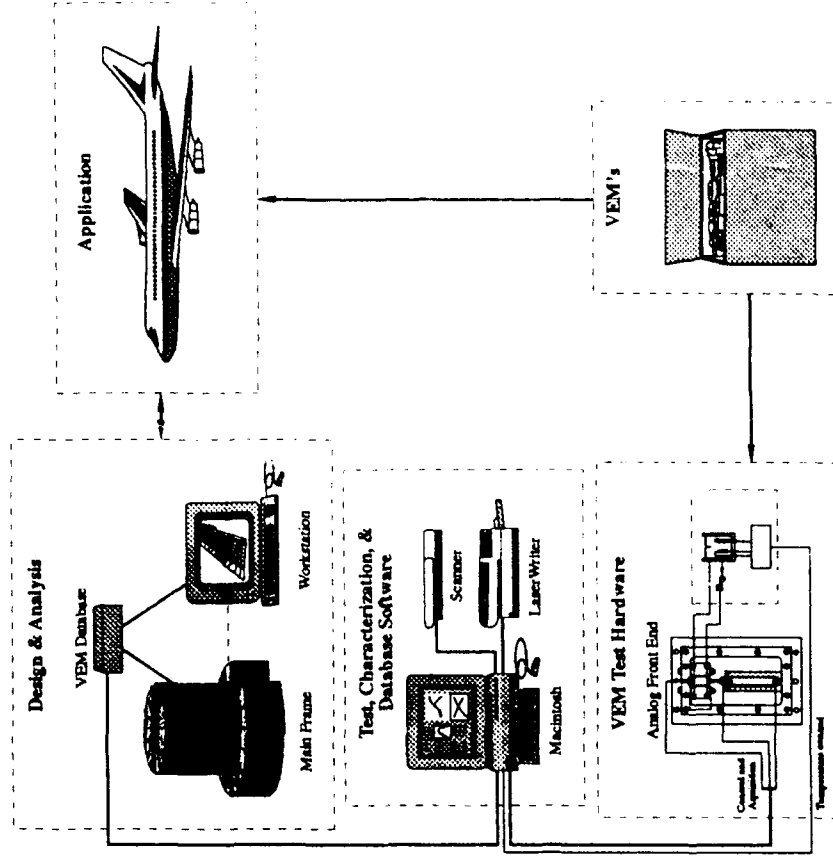
EXIT
@<filename>.IND
OPEN <database>
CLOSE <database>
IMPORT <filename>.DAT <database>
DELETE <material name>
SHOW FILES
SHOW FILE <database>
SHOW REPORTS
SHOW REPORT <report number>
SHOW POINTS
SHOW POINT <point number>
SET PROMPT <prompt string>
SET UNITS '<ENGLISH>' or '<SI>'
SET POINT <point number> [<temperature> <frequency>
<shear mod low> <shear mod high>
<eta low> <eta high>]
MATCH POINTS <point numbers> [OR <point numbers>]
EXPORT REPORT <report number> <filename>
EXPORT MATERIAL <material name> <filename>

Example

```
VEM Database v1.00
VEM_DB* OPEN VEMFILE
VEM_DB-Warning-VEMFILE.EXP not found
Create new database file? Y
VEM_DB-Info-'VEMFILE' created
VEM_DB* IMPORT C1002
VEM_DB-Info-File C1002.DAT added to VEMFILE
VEM_DB* IMPORT ISD113
VEM_DB-Info-File ISD113.DAT added to VEMFILE
VEM_DB* SET POINT 1
Enter temperature: 295
Enter frequency: 100
Enter lower modulus: 2
Enter upper modulus: 100
Enter lower loss factor: .5
Enter upper loss factor: 2
VEM_DB* SET POINT 2
Enter temperature: 295
Enter frequency: 1000
Enter lower modulus: 10
Enter upper modulus: 200
Enter lower loss factor: .5
Enter upper loss factor: 2
VEM_DB* MATCH POINTS 1, 2
VEM_DB-Info- 1 material found
VEM_DB* SHOW REPORT
Reports:
      1
VEM_DB* SHOW REPORT 1
Materials in Report 1
      EAR C1002
VEM_DB* EXPORT REPORT 1 VEMFILE
VEM_DB* EXIT
Exiting VEM_LB
```

Integration on Macintosh

- Test, characterization, and database programs run on same platform
- Graphical windowing interface
- High-resolution hardcopy
- Connectivity



MEASUREMENT OF THE MECHANICAL PROPERTIES OF VISCOELASTICS BY THE DIRECT COMPLEX STIFFNESS METHOD

Bradley R. Allen¹
CSA Engineering, Inc.
Palo Alto, CA

David A. Kienholz
CSA Engineering, Inc.
Palo Alto, CA

ABSTRACT

Accurate material properties are essential for the design of viscoelastic damping treatments and material properties are often the predominant error source process when modal strain energy techniques are implemented.

The trade-offs between various test techniques are discussed with primary emphasis on a system developed at CSA Engineering for direct complex stiffness measurements on viscoelastic materials. Issues such as analog front-end design, temperature control, and system software are discussed.

¹CSA Engineering, Inc., 560 San Antonio Road, Suite 101, Palo Alto, CA 94306, (415) 494-7351

**Measurement of the Mechanical Properties of Viscoelastics
by the Direct Complex Stiffness Method**

Bradley R. Allen
David A. Kienholz
CSA Engineering, Inc.

Presented February 15, 1991
Damping '91, San Diego, CA

**Measurement of the Mechanical
Properties of Viscoelastics by the Direct
Complex Stiffness Method**

Damping Designer Needs Accurate Material Properties

- **Moduli and loss factor**
- **Typically want shear properties**
- **Need properties across broad ranges of temperature and frequency**
- **Material property accuracy is often the limiting factor in current damping design**
 - **Wide scatter common in viscoelastic test data**

Damping Designer Needs Accurate Material Properties

Methods for Dynamic Mechanical Testing of Viscoelastics

- **Resonant methods**
 - material properties extracted from resonant system
 - cantilever beam tests
- **Nonresonant methods**
 - material properties calculated from specimen stiffness
 - measurements performed below resonant frequencies of test specimen
 - Direct Complex Stiffness test method

Methods for Dynamic Mechanical Testing of Viscoelastics

- **Resonant tests imply stiffness from the natural frequency of a resonant system; the loss factor is extracted from the modal damping.**
- **With direct stiffness method (DCS), stiffness of specimen is the real part of the complex stiffness and loss factor is calculated from the phase angle between force and displacement.**

CSA Prefers DCS for Most Aerospace Applications

- **No modeling assumptions**
 - often introduce random and/or bias errors
- **Excellent accuracy and repeatability**
 - accuracy limited by
 - instrumentation
 - fixture design
- **Resonant tests least accurate at highest damping levels**

CSA Prefers DCS for Most Aerospace Applications

- **Damping measurements become difficult as modal damping becomes large; however, modeling errors increase as strain energy in the viscoelastic is reduced. The combination of these effects make it difficult to obtain accurate measurements at the center of transition on many materials.**

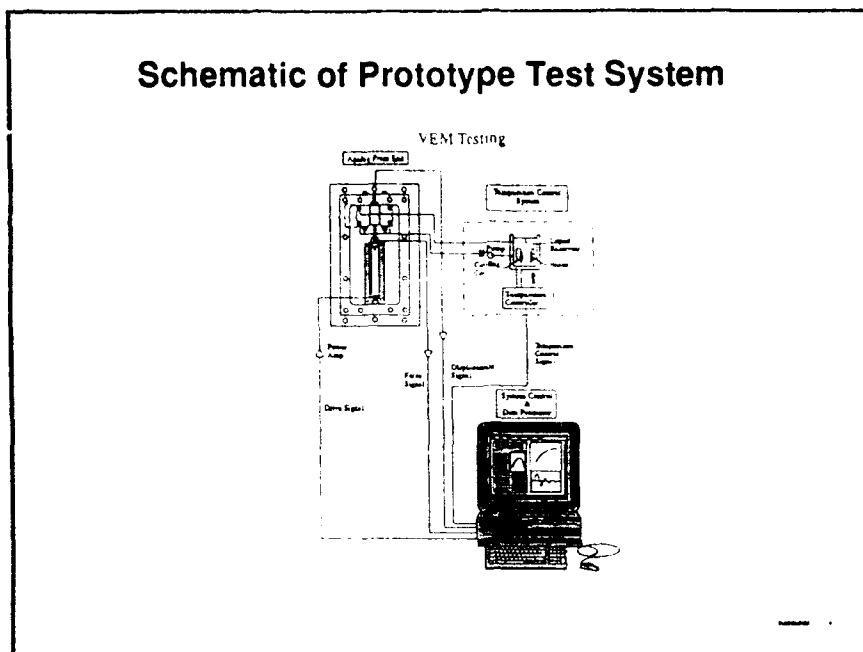
Current Prototype Employed by CSA Engineering



Current Prototype Employed by CSA Engineering

- **Viscoelastic specimen is in dual shear.**
- **Cooling and heating are provided by liquid convection.**
- **Exterior box dimensions are 15" x 11" x 6"**

Schematic of Prototype Test System



Schematic of Prototype Test System

- Macintosh computer controls entire data acquisition process.

Capabilities of New System

- 150 lbf
- 0.1 to 1000 Hertz bandwidth
- -85 to 500 F temperature control
- Wider dynamic range of stiffness
- Fast-Fourier transform analyzer
- Computer controlled data acquisition
- Characterization and data acquisition software run concurrently

Capabilities of New System

- **Peak capacity of driver is 150 lbf with a 0.1 to 500 Hz broad band excitation.**
- **Temperature accuracy is plus or minus one degree Fahrenheit.**
- **Fast-Fourier Transform used to process data. Both random and sine excitation are available.**
- **Macintosh windowing environment allows data acquisition program to run concurrently with characterization software, and its tasks such as wicket plot display can be performed during data acquisition.**

Computer Controlled Data Acquisition

- **Automated test capability**
- **Sophisticated post-processing capabilities**
- **Error tracking routines in data acquisition and post-processing**
 - **inertia contaminated data**
 - **machine compliance**
 - **impure shear**
- **Exporting to characterization and database software**

Computer Controlled Data Acquisition

- **Data acquisition, temperature control, and post-processing are performed through a single Macintosh computer interface.**

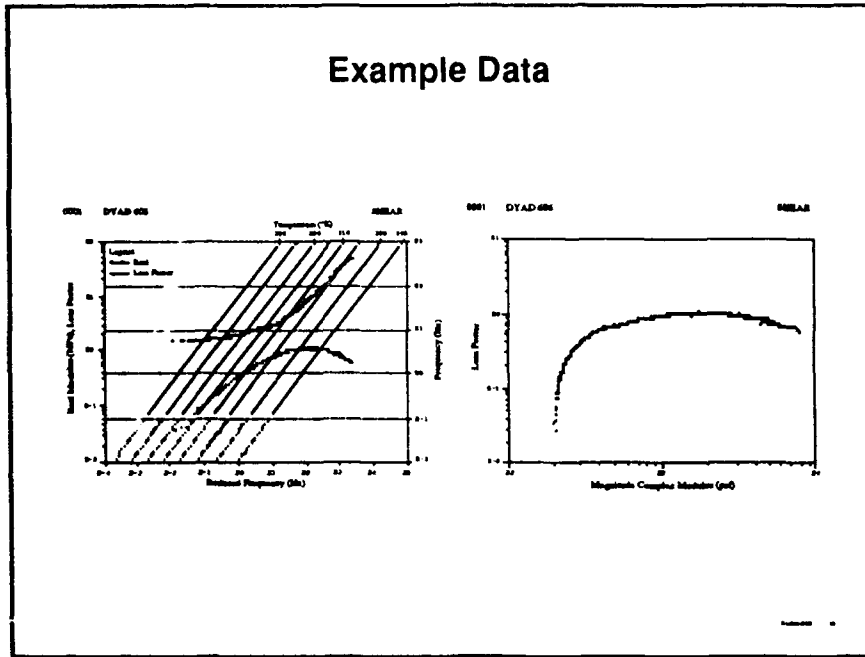
**Primary Design Objectives are
Material Characterization**

- Extended dynamic range of specimen stiffness to accommodate many materials and strain levels
- Wide temperature band
- Error tracking
- Computer controlled data acquisition
- Short data acquisition time

**Primary Design Objectives are
Material Characterization**

- Moduli of viscoelastic materials often change by greater than 1000:1 through transition. Therefore, the dynamic range of stiffness for the test machine is extremely important for broad band characterization.

Example Data



Example Data

- Data shown was collected at only 8 isotherms and was thinned to display approximately one in four data points.

THE EFFECT OF POROSITY ON THE MICROSTRUCTURAL DAMPING RESPONSE OF A 6061 ALUMINUM ALLOY

J. Zhang¹, M. N. Gungor² and E. J. Lavernia¹

¹ Department of Mechanical and Aerospace engineering
University of California at Irvine
Irvine, CA 92717

² Westinghouse Science and Technology Center
1310 Beulah Road, Pittsburgh, PA 15235

ABSTRACT

There is a strong experimental evidence suggesting that the presence of pores or cavities in a microstructure may play an important role in the damping response of a material. The present paper reports on the results of a systematic study of the effects of micrometer-sized pores on the damping response of 6061 aluminum alloy. Spray atomization and deposition processing was selected for the present study as a result of its ability to produce a material with a pre-determined amount of non-interconnected, micrometer-sized pores or cavities. Furthermore, by using this synthesis approach, the amount and distribution of pores present in the material may be systematically altered through variations in the processing parameters. 6061 Al alloy was selected for the present study because it has been widely used in structural applications, and because its damping behavior has been studied previously. The damping measurements were accomplished on cantilever beam specimens by using the free vibration decay logarithmic decrement and the resonant vibration half band width techniques. The present results suggest that there is a correlation between the damping response of the material and the amount of porosity present in the microstructure. The damping capacity, logarithmic decrement δ , of the as-spray deposited material increased from 1.8 to 2.9% as the amount of porosity increased from 4 to 10%. A correlation between the magnitude of the damping capacity and the average pore diameter was also noted. Overall, the damping response of the spray deposited materials is higher than that reported by other investigators using the same alloy.

¹J. Zhang
Materials Section
Department of Mechanical and Aerospace Engineering
University of California, Irvine, CA 92717
(714) 856-8583

1. INTRODUCTION

The effective utilization of advanced metals and alloys in structural applications that require minimal sound and vibration transmission is often limited by our current understanding of the factors that govern their microstructural damping response. The microstructural damping capacity of a material - referred to hereafter simply as damping capacity - may be defined as its ability to dissipate elastic strain energy, although plasticity may be involved at large strain amplitudes. The dissipation of elastic strain energy in the microstructure typically occurs through a combination of several mechanisms, which include: 1) relaxation of point defects, 2) macro-thermoelasticity, 3) micro-thermoelasticity, 4) Eddy-current effects, 5) Snoek effect, 6) stress-induced ordering reactions, and 7) electronic effects^[1, 2]. In addition, the dissipation of elastic strain energy may be affected by discontinuities that may be present in the microstructure, such as grain boundaries and pores or cavities.^[3-5]

There is a strong experimental evidence suggesting that the presence of pores or cavities in the microstructure may play an important role in the damping response of a material. Shimizu^[3], for example, showed that the damping behavior of a carbon/epoxy composite could be modified either by adding a certain amount of flexibilizer or by foaming the epoxy matrix. His results demonstrated that the damping behavior of the carbon/epoxy composite samples was strongly influenced by the resulting porous microstructure that was induced during the foaming of the matrix. In related studies, Klimentos and McCann^[4] investigated the relationship among compressional wave attenuation, porosity, clay content, and permeability in sandstones. In their study, they measured the attenuation coefficients of compressional waves of sandstone samples containing pores filled with clay and saturated with fluid. Their results showed that the logarithmic decrement (δ) of the samples at 1000 kHz and 40 MPa was related to porosity (P , in %) and clay content inside pore (C , in %) by $\delta = aP + bC - c$, where a , b and c are positive constants. They also noted that there was no apparent correlation between attenuation and mean grain size for their samples. Nielsen^[5] developed a theoretical model to estimate the complex modulus of porous and impregnated materials (e.g. cement) and viscoelastic porous materials. Rice^[6] also proposed a theoretical model to predict the effects of porosity and grain size on the tensile modulus, strength and fracture energy of ceramics.

Despite the aforementioned results which suggest that the presence of pores and cavities in the microstructure may have a strong influence on the overall damping response of a material, the understanding of the precise role played by pores and cavities in damping behavior is not clearly

understood. This lack of knowledge may limit efficient applications of certain advanced materials in damping-critical structures, since these materials often exhibit some amount of porosity. One of such class of materials includes, for example, that produced by powder metallurgical means (e.g., consolidating fine powders into bulk preforms).^[7-8] Therefore, the objective of the present work is to provide insight into the effects of porosity on the damping behavior of structural aluminium alloys. Spray atomization and deposition processing was selected for the present study as a result of its ability to produce a material with a pre-determined amount of non-interconnected, micrometer-sized pores or cavities.^[9-15] Furthermore, by using this synthesis approach, the amount and distribution of porosity present in the material may be systematically altered through variations in the processing parameters. Aluminum alloy 6061 was selected for the present study because it has been widely used in structural applications, and because its damping behavior has been studied previously.^[2,16,17]

2. EXPERIMENTAL

2.1 MATERIAL SYNTHESIS

The aluminum alloy used in the present study was a commercial quality 6061 aluminum alloy, with the following nominal compositions: 0.6% Si, 0.28% Cu, 1.0% Mg, 0.2% Cr, and balance Al (in wt. %). Spray atomization and deposition processing involves the energetic disintegration of the molten 6061 alloy into micrometer-sized droplets by high velocity inert gas jets (N₂ was used in the present study), followed by deposition on a water cooled Cu substrate. The rapidly quenched, partially solidified droplets impact, first on the deposition surface, and subsequently on each other, and collect into a preform whose microstructure is largely dictated by the solidification conditions during impact. A diagram of the experimental apparatus used in the present study is shown in Figure 1. The geometry of the spray deposited material, which normally exhibits a contour akin to the Gaussian distribution of droplets impacting on the substrate,^[9-13] was readily modified in the present study by displacing the substrate during deposition. In order to avoid extensive oxidation of the 6061 Al matrix during processing, the environmental chamber was evacuated to a pressure of 0.2 kPa, and backfilled with inert gas to pressure of 0.1 MPa prior to melting and atomizing the material. A more detailed discussion of the spray atomization and deposition experiments can be found elsewhere^[9-15].

Two spray atomization and deposition experiments using 6061 Al were conducted for the present study. The primary experimental variables used during each experiment are shown in Table 1. The parameters in this table show that the metal to gas mass flow ratio, $J_{\text{metal}}/J_{\text{gas}}$, was the

only variable altered during the experiments. The effects of the melt to gas mass flow ratio used in Experiment 132, relative to that used in Experiment 134, on the resulting microstructure will be discussed in a subsequent section.

Table 1 Experimental Variables Used in the Study

Experiment number	132	134
Alloy	6061 Al	6061 Al
Atomization pressure	1.21 MPa	1.21 MPa
Atomization gas	nitrogen	nitrogen
Flight distance	40.64 cm	40.64 cm
Pouring temperature	750 °C	750 °C
Ratio of melt to gas mass flow rates	2.29	1.97

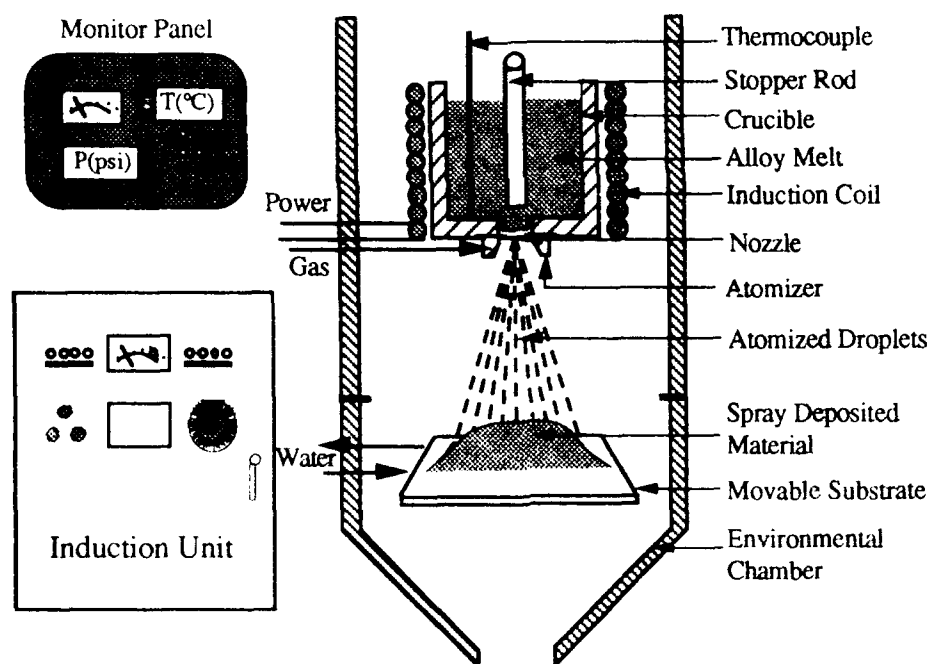


Figure 1. Schematic diagram showing spray atomization and deposition processing.

2.2 STRUCTURAL CHARACTERIZATION

The geometry of the spray atomized and deposited material is shown schematically in Figure 2. In this figure, the orientation of the Z axis was selected to lie in the height direction, whereas the orientation of the X and Y axes were chosen to lie in the short transverse and long

transverse directions, respectively. Cantilever beam specimens for damping characterization studies and samples for porosity analyses were simultaneously removed by sectioning the as-spray deposited material into rectangular bars. The following procedure was adopted in order to keep track of the precise location of each sample within the spray deposited material. The central core of the deposit was first sectioned into a block with the following approximate dimensions: 15 cm long x 7 cm wide x 6 to 8 cm high. This block was subsequently sectioned into several layers (usually 5 to 7 layers numbered with 1, 2, 3...7 from the bottom to the top) along the height direction, and

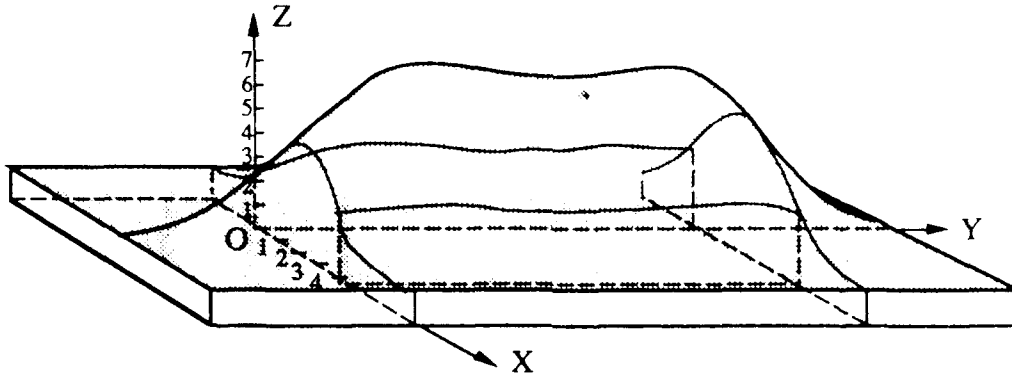


Figure 2. Schematic diagram showing the geometry of the as-spray deposited 6061 aluminum alloy.

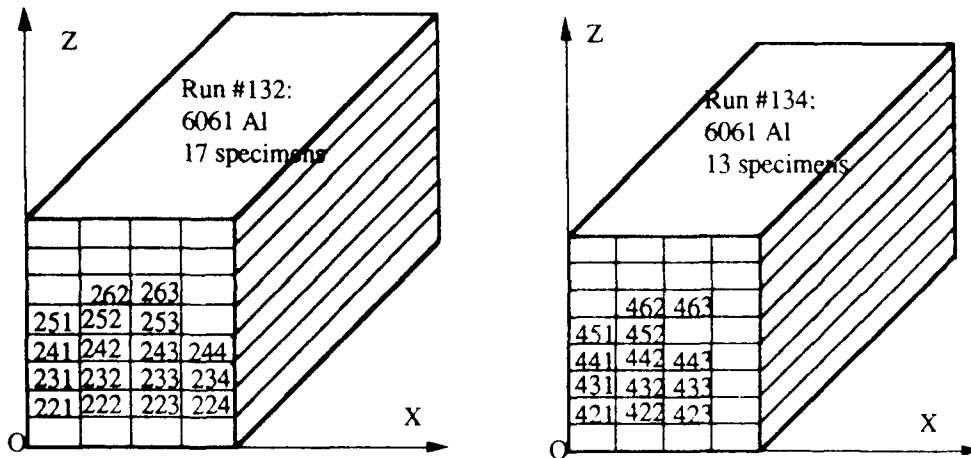


Figure 3. Schematic diagram showing position of samples within the as-spray deposited material.

each layer was then divided into rectangular samples (3 to 4 samples numbered 1, 2, 3 and 4). This procedure is shown schematically in Figure 3, for Experiments 132 and 134. In this figure, the relative location of each rectangular specimen inside the spray deposited block is designated by a number. Every rectangular sample was subsequently divided into two pieces; one was used for the damping measurements, and the other for porosity analyses (see Figure 4). This procedure

allowed careful analysis of the microstructure present in the damping specimens, since the microstructure of spray atomized and deposited materials has been reported to change with spray deposition thickness (Z axis), but remain relatively constant along the longitudinal dimension (Y axis) (18, 21).

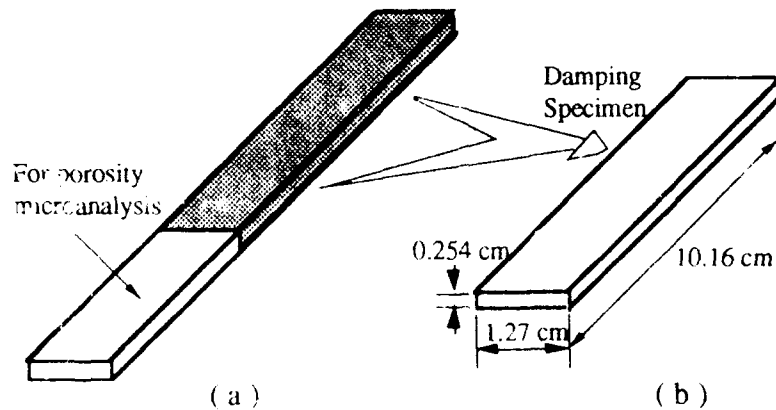


Figure 4. Schematic diagram showing specimen configuration and geometries.

2. POROSITY CHARACTERIZATION

Quantitative characterization of the porosity present in the spray deposited materials was accomplished by means of density measurements and computerized analysis of metallographic samples using an Imageset image analyzer. The density measurements were conducted in accordance with ASTM B311-83 Standard, based on Archimedes' principle. In this procedure the weight of each specimen in the air and in liquid was obtained by using a Fisher Scientific A-250 electronic balance. The liquid used in the present study was ethylene glycol with a density of 1.117 g/cm^3 at room temperature (25°C). Accordingly, the density of specimen is calculated from the following equation

$$\rho_s = m_{sa} \rho_l / (m_{sa} - m_{sl}) \quad (1)$$

where ρ_s and ρ_l denote the density of the specimen and the liquid, respectively, and m_{sa} and m_{sl} denote the mass of specimen in air and in liquid, respectively. It then follows that the amount of porosity present in each spray deposited sample can be determined by

$$P = (\rho_{Al} - \rho_s) / (\rho_{Al} - \rho_{gas}) \quad (2)$$

where P denotes volume fraction of porosity present in sample material, ρ_{Al} represents the theoretical density of 6061 Al, and ρ_{gas} represents the density of any inert gas present inside the pores. In the present study, the density of extruded 6061 Al was used as the theoretical density, ρ_{Al} , and determined according to the following procedure. A 2.54 diameter cylinder was removed

from the as spray deposited 6061 Al, and extruded at 400 °C into a rod with a diameter of 1.27 cm; the extrusion pressure used was 27.58 MPa. The density of the extruded material was then determined according to Eq. (1) as $\rho_{Al} = 2.73 \text{ g/cm}^3$. This value compares favorably with the measured density of 2.72 g/cm³ for as-received 6061 Al. In view of the fact that the magnitude of ρ_{gas} is substantially smaller than that corresponding to ρ_{Al} , Eq. (2) is simplified, and P is calculated from the following equation

$$P = (\rho_{Al} - \rho_s) / \rho_{Al} \quad (3)$$

While the total amount of porosity present in the spray deposited materials was determined using the above described procedure, the distribution of pore sizes was quantitatively characterized for each specimen by using image analysis in combination with a Nikon Epiphot optical microscope and a Macintosh IIfx computer. An adaptor was utilized in the present work to transmit images from the optical microscope directly to the computer, where the size distribution of pores was readily established. This procedure allowed the characterization of a large number of metallographic samples, accurately and efficiently.

2.4 DAMPING MEASUREMENTS

The cantilever beam technique was used in the present study to characterize the microstructural damping response of the spray deposited materials. In this technique, one end of a rectangular specimen was fixed in place while the opposite end was allowed move freely to respond to a mechanically induced displacement or vibration. The damping capacity of the material was then determined from the resulting displacement spectrum, by utilizing the logarithmic decrement and the half power band width analysis methodologies. In the logarithmic decrement method, a history of amplitude versus time during a free vibration of the cantilever beam specimen was recorded by an oscilloscope through an optical displacement transducer. By measuring the amplitude decay (Figure 5), the logarithmic decrement δ can be evaluated by

$$\delta = (1/n) \ln (A_i / A_{i+n}) \quad (4)$$

where A_i and A_{i+n} are the amplitudes of the i^{th} cycle and the $(i+n)^{\text{th}}$ cycle at times t_i and t_2 , respectively, separated by n periods of oscillation.

The half power band width methodology is based on a forced vibration test in which the specimen was vibrated by a shaker which was driven by an amplified signal from a white noise generator. In this technique the resonant frequency peak is distinguished by recording the vibration amplitude as a function of frequency. The damping loss factor, η , may then be

calculated from the vibration spectrum, recorded by an FFT signal analyzer through an optical transducer using the following equation

$$\eta = (f_1 - f_2) / f_r \quad (5)$$

where f_1 , f_2 and f_r are shown in Figure 6. Finally, the logarithmic decrement, δ , and the loss factor, η , can be checked by the following relationship^[2]

$$\eta = \delta / \pi \quad (6)$$

All of the damping data used in the present study was derived from experiments performed at the Westinghouse Science and Technology Center (Pittsburgh, PA).

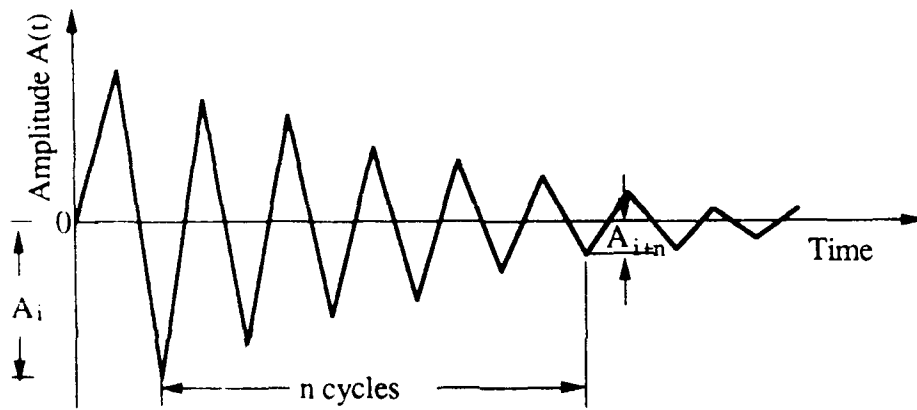


Figure 5. Schematic diagram of free vibration decay^[2]

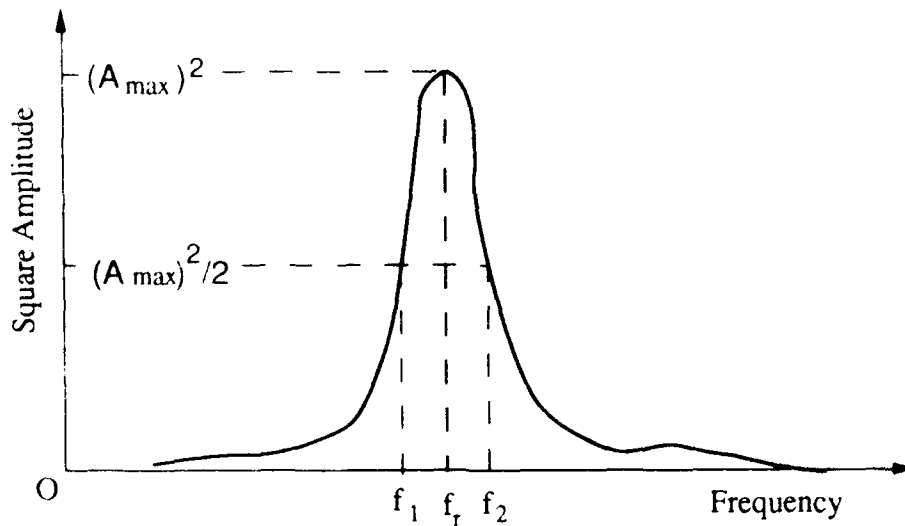


Figure 6. Schematic diagram showing Lorentzian Peak^[2]

3. RESULTS

3.1 POROSITY AND MICROSTRUCTURE

Table 2 shows the density, ρ_s , and the amount of porosity, P, of the as-deposited 6061 Al specimens, calculated from Equations (1) and (3), respectively. The results shown in Table 2 correspond to the various locations within the spray deposited materials, as designated in Figure 3.

Table 2. Density and Porosity of As-Spray Deposited 6061 Al

Deposit	¹ Sample	m_{sa} (g)	m_{sl} (g)	ρ_s (g/cm ³)	P (%)
132	222	8.5844	4.8565	2.5606	6.20
132	242	8.5541	4.8380	2.5597	6.23
132	252	8.6848	4.9720	2.6011	4.72
132	234	8.3702	4.7875	2.5980	4.83
134	422	8.0587	4.4268	2.4674	9.61
134	442	7.5877	4.2314	2.5139	7.91
134	452	8.3760	4.6700	2.5132	7.94
134	433	8.3339	4.6130	2.4906	8.77

¹Sample location is shown in Figure 3.

Optical microscopy was conducted on Keller's etched coupons of the as-spray deposited materials and two examples, corresponding to Experiments 132 and 134, are shown in Figures 7 and 8 respectively. The presence of numerous pre-solidified droplets in the microstructure precluded a precise quantitative assessment of the grain size. However, a large number of observations revealed that the as-spray deposited grain size ranges from 15 to 49 μm with a average of 32 μm for Deposit 132 and from 10 to 35 μm with a average of 22 μm for Deposit 134. In addition, it is worth noting that the microstructure remained relatively constant throughout the entire specimen length of the as-spray deposited materials. The evolution of microstructure during spray atomization and deposition has been addressed by numerous investigators, and the interested reader is encouraged to consult the available scientific literature.^[10-15, 18]

The size distribution of the pores present in the samples from Deposits 132 and 134 are shown in Figures 9 and 10, respectively. In order to quantify the size distribution and morphology of the pores, optical metallography samples were studied using image analysis, in combination with a Nikon Epiphot optical microscope and a Macintosh IIfx computer. The results are shown in Table 3, where the total amount of porosity present in the samples, as inferred from image analysis, is compared to that obtained using Archimedes' principle. Also shown in Table 3 is the average diameter of the pores present in the as-spray deposited microstructure, as determined from

image analysis. It is worth noting that each data point shown in Table 3 was determined by examining 2-3 viewing areas. This procedure increased the accuracy of the measured values. In general, comparison of the amount of porosity present in the spray deposited materials determined using image analysis and Archimede's principle revealed a relatively good agreement between both techniques.

Table 3 Porosity of As-Deposited 6061 Al by Image Analysis

Run	¹ Sample	P (%) by Image	P (%) by Archimede's	² d (μm)
132	222	6.45	6.20	5.38
132	242	6.90	6.23	3.96
132	252	4.80	4.72	2.36
132	234	3.78	4.83	1.91
134	422	10.12	9.61	9.30
134	442	8.99	7.91	7.32
134	452	7.42	7.94	5.51
134	433	9.48	8.77	5.50

¹Sample location is shown in Figure 3.

²Average pore diameter as determined from image analysis.

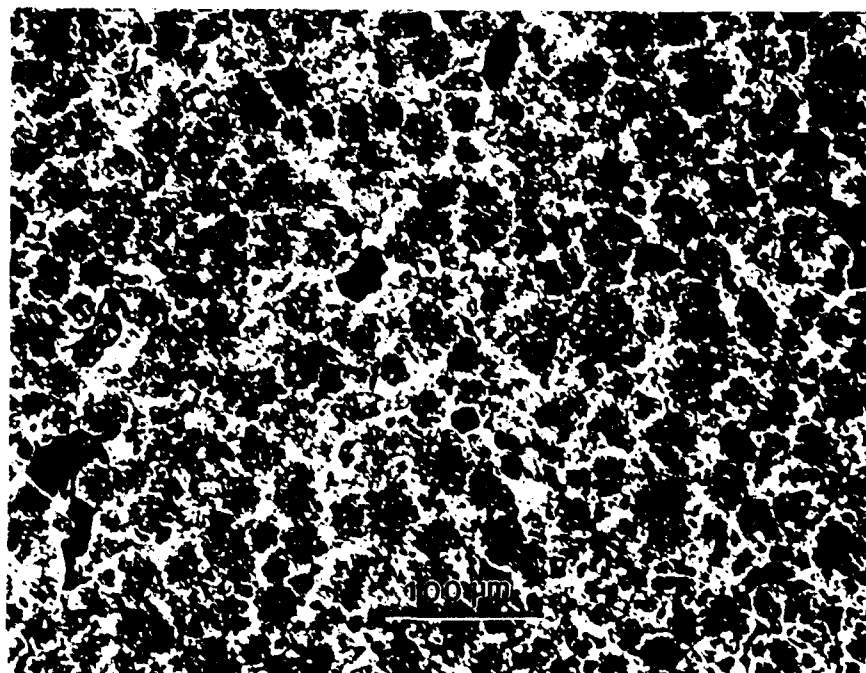


Figure 7. Optical micrograph showing the typical grain and pore morphology present in Deposit 132.

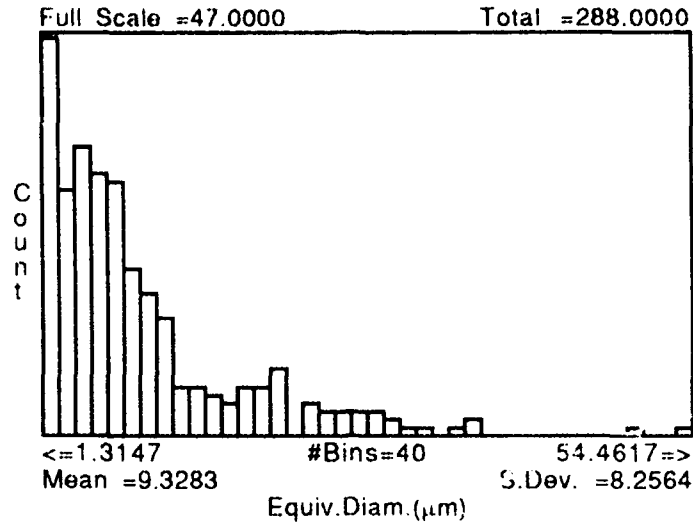


Figure 10. Distribution of pore sizes present in sample 422 (see Figure 3) from Deposit 134.

3.2 DAMPING CAPACITY

The damping response of the spray deposited materials, as determined from the experimental data in combination with Equations (4) and (5), are summarized in Table 4. Also shown in this table is the Lorentzian peak frequencies for each of the samples tested. It is worth noting that the free decay vibration tests were performed at a frequency of 220 Hz in order to allow comparison of the present data to that obtained by other investigators. Comparison of the values of the logarithmic decrement, δ , to those of the loss factor, η , using Eq. (6) suggests good agreement between the logarithmic decrement and the half power band width analysis methodologies. One notable exception to this observation is the result obtained for sample 442, which show that the loss factor for this sample was abnormally high (1.7). This was attributed to difficulties with the experimental measurements.

Table 4. Damping Capacity of As-Spray Deposited 6061 Al.

Deposit	Sample	δ (%)	f_r (Hz)	η (%)
132	222	2.0	294.50	0.7
132	242	1.9	292.00	0.6
132	252	1.9	300.25	0.6
132	234	2.0	287.50	0.7
134	422	2.9	280.75	0.8
134	442	2.6	261.25	1.7
134	452	1.8	281.25	0.8
134	433	2.3	280.50	0.8

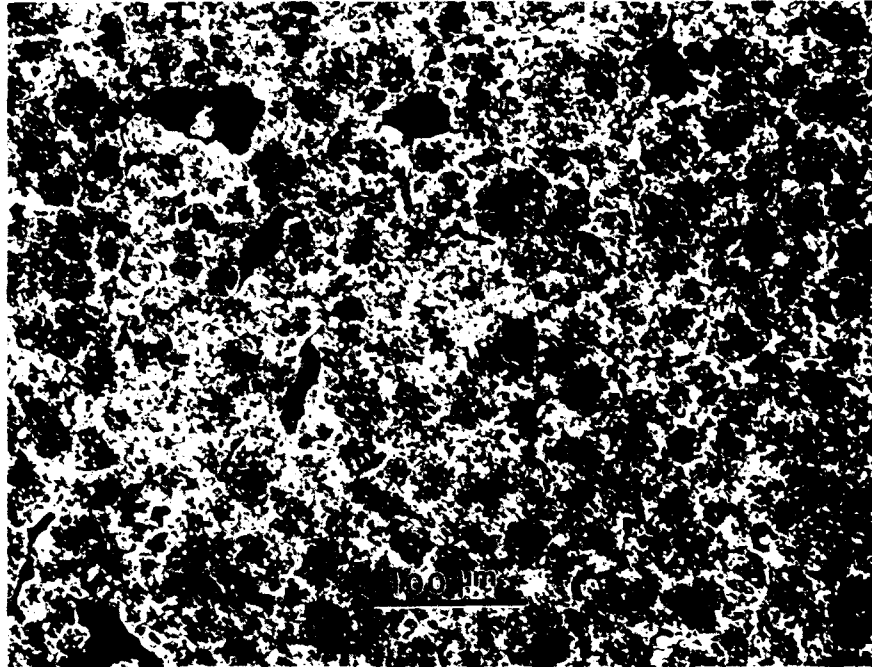


Figure 8. Optical micrograph showing the typical grain and pore morphology present in Deposit 134.

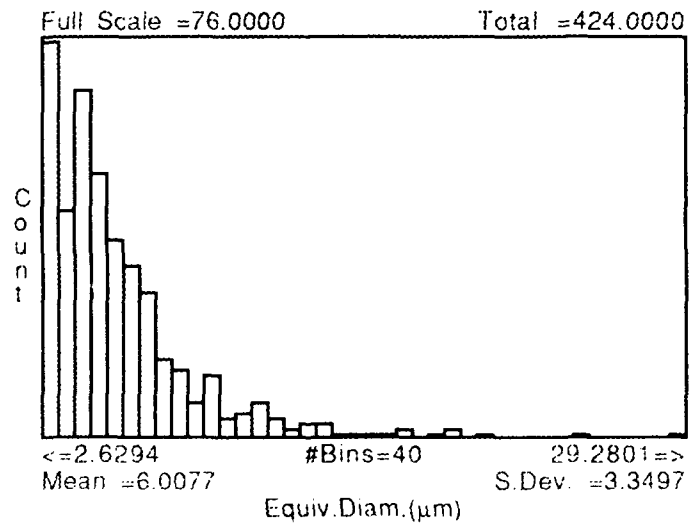


Figure 9. Distribution of pore sizes present in sample 222 (see Figure 3) from Deposit 132.

4. ANALYSIS AND DISCUSSION

In order to discuss the effects of porosity on damping behavior it is first necessary to provide some background information on the factors that govern the formation of pores during spray atomization and deposition. This background information will also provide a basis for the discussion on the differences in the size and distribution of pores present in the materials obtained from Experiments 132 and 134. It is worth noting that since the present results showed that there was a relatively close correlation between the amount of porosity present and the average pore size (see Table 3), in the discussion that follows average pore size and amount of porosity may be thought of as interchangeable terms.

An important microstructural characteristic frequently associated with the microstructure of the as-spray atomized and deposited materials is the presence of a finite amount of non-interconnected pores.^[9-15, 18, 22] The overall amount of porosity present in spray atomized and deposited materials depends on: (a) the thermodynamic properties of the material, (b) the thermodynamic properties of the gas, and (c) the processing parameters. Under conditions typical for aluminum alloys, for example, the amount of porosity present in spray atomized and deposited materials has been reported to be in the 1 to 10% range.^[13, 14, 18] This is consistent with the results of the present study which showed the porosity levels in the 4 to 10% range. Furthermore, the present results also revealed that the size distribution of pores was skewed (see Figures 11 and 12), with an average pore diameter in the 6 to 10 μm range. It has been suggested that the origin of porosity in spray atomized and deposited materials may be attributed to one or a combination of the following mechanisms: (a) gas rejection, (b) solidification shrinkage, (c) interparticle porosity. The first mechanism, gas rejection, is anticipated as a result of the limited solid solubility of inert gases in most structural materials. As the temperature of the material decreases during solidification, any amount of gas that might have dissolved during the melting and superheating stage will be rejected into the matrix, leading to the formation of gas pores. However, results obtained using fast neutron activation analyses show that spray atomized and deposited materials exhibit extremely low levels of dissolved gases, suggesting that this mechanism is not as important as originally suggested.^[23] In addition, in view of the irregular morphology of the pores, it is highly improbable that a large proportion of the porosity originates from the rejection of entrapped gases, since gas porosity generally exhibits a spheroidal morphology (see Figures 7 and 8).

The formation of shrinkage porosity is generally associated with sluggish solidification kinetics, such as those present during ingot casting. In view of the limited amount of liquid phase present under normal spray atomization and deposition conditions, it is unlikely that solidification

shrinkage plays an important role in the formation of the observed pore distribution.^[13, 14, 21] It is worth noting, however, that if the spray atomization and deposition conditions are such that there is an excessive amount of liquid phase present at the deposition surface, this mechanism may play a significant role in the formation of porosity. The presence of excess amount of liquid phase during impact may develop as a result of (a) coarse droplet sizes, (b) high deposition temperatures, and (c) remelting of solid phases caused by high spray enthalpies.^[13, 14] Under these conditions, the atomization gas may interact with the molten metal, leading to the formation of large amounts of porosity.

The available experimental evidence suggests that a large proportion of the porosity that is generally observed in spray atomized and deposited materials may be attributed to the third mechanism, interparticle porosity. As the droplets descend, first on the deposition surface, and eventually on each other, they overlap leaving micrometer-sized cavities in between. In spite of the large amount of turbulence present, the relatively rapid drop in temperature during deposition prevents any liquid phase present from filling all of the cavities, leading to the formation of irregular pores. This mechanism is consistent with the observed correlation between deposition conditions such as spray density, powder size, and the amount of porosity present throughout the deposit. For example, the higher density associated with the central region of the deposit may be attributed to the elevated mass flux of droplets in this region of the spray, relative to the periphery.^[19] These droplets contain elevated fractions of liquid phase, effectively filling the interstices between droplets. Regarding the variations in density as a function of thickness, the present results show that the highest amount of porosity present in the spray deposited materials was present in the samples closest to the water cooled substrate (samples 222 and 422 in Table 3). This is consistent with the initially high rates of heat extraction experienced by the region of the deposit in close proximity to the substrate. In contrast, the high amount of porosity generally observed in the periphery of the samples (samples 234 and 433) results from a large proportion of small, presolidified droplets that tend to segregate to this region. It is noticed that under the processing conditions where deposited droplets are allowed to solidify completely before the arrival of more droplets, interlayer porosity will also develop at the original droplet boundaries.

In order to establish a relationship between the amount of porosity present and the processing parameters, it is useful to consider the factors governing the atomization stage of the process. The disintegration of a molten metal by high energy gas jets (atomization) is complex and only portions of it have been addressed from a theoretical viewpoint.^[24] The work of Lubanska^[25] has shown that the disintegration of liquids by high velocity jets obeys a simple correlation. A slightly modified form of the original correlation has been shown to represent the

results of molten metal atomization experiments reasonably well.[12, 20, 21] According to the modified Lubanska's correlation, the mass mean droplet diameter (i.e., the opening of a screening mesh which lets through 50 percent of the mass of the powder resulting from an atomization experiment), d_{50} is given by:

$$d_{50} = K_d [(\mu_m d_o \sigma_m / \mu_g V_{ge}^2 \rho_m) (1 + J_{melt} / J_{gas})]^{1/2} \quad (7)$$

where K_d is an empirically determined constant with a value between 40 and 400 (a value of 51.7 was selected for the conditions used in the present study, since this has been shown to yield a good correlation between theory and experiment^[26]); μ_m , σ_m , ρ_m , and J_{melt} are the viscosity, surface tension, density and mass flow rate of the melt, respectively; μ_g , V_{ge} , and J_{gas} are the viscosity, velocity and mass flow rate of the atomizing gas, respectively; and d_o is the diameter of the metal delivery nozzle. Expressions for the flow rates can be obtained as functions of the process parameters from Bernoulli's equation in the case of the metal^[27] and from theory of compressible flow^[28] in the case of the gas. The mass mean droplet diameter of the powder size distribution (d_{50}) for both experiments was computed from Eq. (7), using the processing parameters and physical constants corresponding to each experiment (see Tables 1 and 5). Eq. 7 predicts d_{50} values of 108 μm and 98 μm for Experiments 132 and 134, respectively. These results are consistent with the higher densities that were noted for Experiment 132, relative to those of Experiment 134, since a smaller droplet diameter will dissipate thermal energy more effectively, thereby leading to a greater extent of pre-solidification prior to impact.

Table 5 Computational Results of d_{50} for Two Deposits of 6061 Al

Gas: Nitrogen		Melt: 6061 Al		
$\mu_g = 1.54 \times 10^{-4} \text{ g/cm}\cdot\text{s}$		$\mu_m = 1.3 \times 10^{-2} \text{ g/cm}\cdot\text{s}$		
$\rho_{gas} = 3.375 \times 10^{-3} \text{ g/cm}^3$		$\rho_m = 2.385 \text{ g/cm}^3$		
$V_{ge} = 3.232 \times 10^4 \text{ cm/s}$		$\sigma_m = 914 \text{ g/s}^2$		
$K_d = 51.7$				
Deposit	d_o	J_{gas}	J_{melt}	d_{50}
132	0.3048 cm	9.87 g/s	22.58 g/s	108 μm
134	0.2794 cm	9.87 g/s	19.46 g/s	98 μm

The damping capacity of the as-spray atomized and deposited 6061 Al obtained in the present study is summarized in Table 6, where the values of the logarithmic decrement, δ , are compared to the results obtained by other investigators using the same alloy. The values of the

logarithmic decrement, δ , shown in Table 6 were the average of the four samples investigated for each deposit (see Table 4). The results show that the value of δ of the spray atomized and deposited 6061 Al is higher than those reported by other investigators. The damping response of the spray atomized and deposited 6061 Al is thought to be derived from two factors: a) the presence of a finite amount of micrometer-sized pores, and b) a fine grained microstructure. In the discussion that follows, this suggestion is discussed in reference to results reported by other investigators.

Table 6. Comparison of Damping Behavior of 6061 to Results of other Studies.

Processing	Ref.	Experiment	Frequency	Amplitude	δ (%)
As-Deposited Run 132	This work	Cantilever beam	220 Hz	---	1.95±.05
As-Deposited Run 134	This work	Cantilever	220 Hz	---	2.40±.47
6061-T6	[16]	Cantilever	500 Hz	---	0.62
6061-T6	[17]	Cantilever	15 Hz	---	1.82
6061-T651	[2]	Cantilever	19.8 Hz	6-20x10 ⁶ ε	0.65

Previous studies^[3-5] have demonstrated that the damping capacity of an impregnated porous material increases with the amount of porosity, concomitant with a drop in elastic modulus and strength. This observation is substantiated by the results obtained in the present study, as shown in Figure 11. The results shown in this figure suggest that the value of the logarithmic decrement, δ , increases with the percent of porosity present in the microstructure. The dissipation of elastic energy in porous materials has been rationalized in terms of a mechanism known as *mode conversion*.^[29-31] From a macroscopic viewpoint, every point inside a cantilever beam specimen under lateral vibration will move in a transverse direction. Hence, every crystal or grain deforms in tension due to the transverse motion of the specimen and in shear due to the non-uniform deformation along longitudinal direction of the cantilever beam. In a porous metal, the tensile deformation may be converted into shear deformation at the boundaries of pores. The shear deformation may furthermore produce viscoelastic flow that is most readily achieved at the pore boundaries. The viscous flow is then converted to heat by molecular collisions or dislocations. The production of either thermal energy or dislocations are both beneficial to internal friction or material damping according to thermodynamics^[32] and Granato-Lücke dislocation theory^[33,34], respectively. The eventual result of these serial conversions is the decay of vibration inside the porous material.

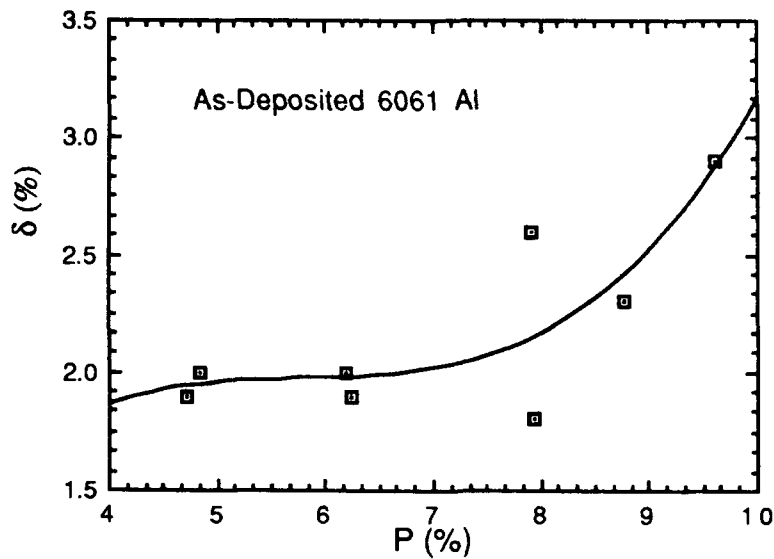


Figure 11. Relationship between damping capacity and porosity for as-deposited 6061 Al alloy.

Substantial mode conversion may be also reached when there is a certain medium inside the pores.^[29] In the spray atomized and deposited 6061 material, and as discussed in a previous section, the low solubility of the atomizing gas may lead to the formation of pores containing a partial pressure of inert gas. In this case, the motion of the inert gas relative to the porous framework material will be high, since the porous material is rigid in comparison with the inert gas. As a consequence, there will be an impedance mismatch to vibration movement between the inert gas and the as-spray deposited metal. This mismatch may change the deformation field in the neighboring metal region and therefore lead to secondary shear deformation in the neighboring metal, increasing the density of dislocations, and thereby the damping due to internal friction.

Damping associated with grain boundary relaxation, anelasticity or viscosity in the polycrystalline metals has been described by Zener,^[35] Lazan^[1] and Nowick^[36], respectively. In polycrystalline metals there exist amorphous grain boundaries that display viscous-like properties. The viscous flow at grain boundaries will convert mechanical energy produced under cyclic shear stress into thermal energy, as a result of internal friction. The thermal energy will then be dissipated by the conductivity of metal and the heat exchange with the surroundings. The energy absorbed in grain boundaries not only depends on the magnitude of the shear stress and the anelastic shear strain, but also is proportional to the grain boundary area per unit volume, i.e., inversely proportional to grain size. In view of these results, the fine grained microstructure of the

spray atomized and deposited material may also play an important role in the dissipation of elastic strain energy. More detailed microstructural characterizations are currently under way in order to provide experimental basis for these suggestions.

5. CONCLUSIONS

In summary, the results of the present work show that the presence of micrometer-sized pores increases the damping capacity of the as-spray atomized and deposited 6061 Al alloy. Furthermore, the results of damping characterization studies show that the value of δ of the spray deposited 6061 Al is higher than the results reported by other investigators using the same alloy. The damping characteristics of the spray deposited material obtained in the present work is thought to be derived from two factors: a) the presence of a finite amount of micrometer-sized pores, and b) a fine grained microstructure. This suggestion was discussed in light of the relevant damping mechanisms. Further work is continuing in this area in order to ascertain the mechanisms that are responsible for the observed damping behavior.

6. ACKNOWLEDGEMENTS

The authors wish to acknowledge the Office of Naval Research (Grant No.: N00014-90-J-1923 to the University of California at Irvine, and Grant No.: N00014-90-C-0211 to the Westinghouse Science and Technology Center) for financial support. In addition, the authors would also like to express their gratitude to Catherine Wong of David Taylor Research Center, for her able technical assistance and valuable discussions; to E. S. Diaz of the Westinghouse Science and Technology Center and to I. Sauer of the University of California at Irvine for their assistance with the experimental part of this study; and to Y. Wu of the University of California at Irvine for his many insightful discussions.

REFERENCES

1. B.J. Lazan, Damping of Materials and Members in Structural Mechanics, Pergamon Press, Oxford, 1968.
2. G.G. Wren and V.K. Kinra, Damping in Metal Matrix Composites, Technical Report of Texas A&M University, 1990.
3. K. Shimizu, Composite Materials: Mechanics, Mechanical Properties and Fabrication, ed. by K. Kawata and T Akasaka, Japan Society for Composite Materials, Tokyo, 1981, p. 111.
4. T. Klimentos and C. McCann, Geophysics, **55**(8), Aug. 1990, p. 998.

5. L.F. Nielsen, J. of the American Ceramics Society, **67**(2), 1984, p. 93.
6. R.W. Rice, Materials Science and Engineering, **A112**, 1989, p. 215.
7. S.M. Kaufman and S. Mocarski, Inter. J. of Powder Metallurgy, **7**, 1971, p. 19.
8. S.M. Kaufman, Inter. J. of Powder Metallurgy, **8**, 1972, p. 183.
9. P. S. Grant, W. T. Kim, B. P. Bewlay and B. Cantor, Scripta Metallurgica, **23**, 1986 p.1651.
10. A. L. Moran, and W. A. Palko, Journal of Metals, **40** (12),1988, p. 12.
11. P. Mathur, D. Apelian and A. Lawley, Acta Metallurgica, **37**, 1989, p.429.
12. E. Gutierrez, E. J. Lavernia, G. Trapaga, J. Szekely and N. J. Grant, Met. Trans., **20A**, 1989, p.71.
13. E.J. Lavernia, Inter. J. of Rapid Solidification, **5**, 1989, p. 47.
14. M. Gupta, F.A. Mohamed, and E.J. Lavernia, Inter. J. of Rapid Solidification, 1991, in press.
15. E.J. Lavernia, T. Ando and N.J. Grant, Proc. of ASM's 1986 International Conference on Rapidly Solidified Materials, San Diego, 1986, p. 29.
16. R.B. Bhagat, M.F. Amateau and E. C. Smith, Cast Reinforced Metal Composite, ed. by S.G. Fishman and A.K. Dhingra, ASM International, Materials Park, Ohio, 1988, p. 399.
17. M.S. Misra and P.D. LaGreca, Proc. of Vibration Damping 1984 Workshop Proceedings, AFWAL-TR-84-3064, Long Beach, Ca., Feb. 1984, p. U-1.
18. B.P. Bewley and B. Cantor, Proc. of 1st Inter. Conf. on Rapidly Solidified Materials, ed. by P. Lee and R. Carbonara, ASM International, Materials Park, Ohio, 1986, p.15.
19. V.G. McDonell, E.J. Lavernia and G.S. Samuelsen, Synthesis and Analysis in Materials Processing: Advances in Characterization and Diagnostics of Ceramic and Metal Particulate Processing, ed. by E.J. Lavernia, H. Henein and I. Anderson, The Metallurgical Society, 1989, p.30.
20. E.J. Lavernia et al., Proc. of the 1987 Annual Powder Metallurgy Conference and Exhibition, Progress in Powder Metallurgy, **43**, 1987, p. 683.
21. E. Gutierrez, E.J. Lavernia, G. Trapaga, J. Szekely and N.J. Grant, Met. Trans., **20A**, 1989, p. 71.
22. R. Vetter, L. Z. Zhuang, I. Majewska-Glabus and J. Duszczyk, A Modified Spray Deposition Model Verified with Ni₃Al-Cr Intermetallic Alloys," Scripta Metall. et Mater., **24** (11), in press, 1990.
23. K. Ogata, E. J. Lavernia, G. Rai and N. J. Grant, International Journal of Rapid Solidification, **2** (1), 1986, p. 21.
24. T. Mikami, R.G. Cox and S.G. Mason, Int. J. Multiphase Flow, **2**, 1975, p. 113.
25. H. Lubanska, J. Metals, **22**, 1970, p. 45.

26. X. Zeng, Thesis for Master of Science in Engineering, University of California, Irvine, 1991.
27. G.H. Geiger and D.R. Poirier, Transport Phenomena in Metallurgy, Reading, MA, Addison-Wesley, 1973, p. 134.
28. A.H. Shapiro, The Dynamics and Thermodynamics of Compressible Fluid Flow, I, New York, NY, Ronald Press, 1953, p. 85.
29. Jacek Jarzynski, Sound and Vibration Damping with Polymers, American Chemical Society, Washington, DC, 1990, p.167.
30. R. D. Corsano et al., Ibid, p.208.
31. W.M. Madigosky and K.P. Sharnhorst, Ibid, p.228.
32. D. Zhang and B.I. Sandor, Fatigue Fract. Engng. Mater. Struc., **13**(5), 1990, p.497.
33. A. Granato and K. Lucke, J. of Appl. Phy., **27**(6), 1956, p.583.
34. A. Granato and K. Lucke, J. of Appl. Phy., **27**(7), 1956, p.789.
35. C. Zener, Elasticity and anelasticity of Metals, The University of Chicago Press, Chicago, IL., 1948, p.147.
36. A.S. Nowick and B.S. Berry, Anelastic Relaxation in Crystalline Solids, Academic Press, New York, 1972, p. 436.

**DAMPING PROPERTIES OF ALIPHATIC POLYURETHANES FROM
4,4'-DICYCLOHEXYLMETHANE DIISOCYANATE**

John D. Lee, Gilbert F. Lee, and Bruce Hartmann

Nonmetallic Materials Branch, Code R31
Naval Surface Warfare Center, White Oak
Silver Spring, MD 20903-5000

Abstract

Polyurethanes cover a wide range of damping properties depending in large part on their two-phase morphology. Hard segment crystallinity was proposed to be the dominant factor in determining these properties. The evidence for this conjecture came from a comparison of a system in which hard segment crystallinity was present with a system where crystallinity was inhibited by using a different chain extender. To verify our assumption, in this work crystallinity was inhibited not by changing the chain extender but by changing the diisocyanate from the aromatic 4,4'-diphenylmethane diisocyanate or MDI to the cycloaliphatic 4,4'-dicyclohexylmethane diisocyanate or H₁₂MDI. Prepolymers of poly(tetramethylene ether glycol) (PTMG) of four different molecular weights (650, 1000, 2000, 2900) with H₁₂MDI were synthesized and chain extended with 1,4 butanediol. Measurements of the dynamic mechanical properties of these materials verified the assumption that hard segment crystallinity is the dominant factor in determining the damping characteristics of polyurethanes. All non-crystalline hard segment systems have very similar properties regardless of the diisocyanate type or the chain extender type.

10901 New Hampshire Ave., Silver Spring, MD 20903 301-394-1199

INTRODUCTION

Polyurethanes are widely used in many damping applications, but the large number of possible chemical compositions makes it difficult to know which one to choose for a particular application without a tedious trial and error evaluation program. For this reason, it is desirable to be able to determine general rules governing the behavior of these materials, which allows one to predict which materials will be useful for a given application. For some applications, a high, narrow loss factor is required while for others a low, broad loss factor is needed.

It was suggested in our earlier work¹ that the presence of hard segment crystallinity has a dominant effect in determining damping properties. It was found that polyurethanes with hard segment crystallinity have higher rubbery modulus and lower, broader loss factors than those lacking crystallinity. In that work, crystallinity occurred when a chain extender without pendant groups was used while the substitution of a chain extender with pendant groups inhibited crystallinity. It was proposed that the difference between the two cases was a result of the presence or absence of hard segment crystallinity and should be independent of the chain extender if some other way could be found to control crystallinity.

The chain extender without pendant groups used previously was 1,4-butanediol or BDO. Due to the simple, regular structure of this material, all the polymers made using it were found to develop hard segment crystallinity. By contrast, a chain extender with pendant methyl groups, 2,2-dimethyl-1,3-propanediol or LMPD, hinders hard segment orientation and inhibits crystallinity¹.

The present work was undertaken in an attempt to verify the importance of crystallinity by examining a system similar to the previous one but one in which crystallinity is controlled not by the chain extender but by the diisocyanate. If our assumption is correct, the same chain extender that gave rise to high rubbery modulus and low, broad loss factor will have low modulus and high, narrow loss factor if crystallinity can be inhibited.

The diisocyanate used earlier with both of the above chain extenders was 4,4'-diphenylmethane diisocyanate (MDI). In the present work, a cycloaliphatic diisocyanate, H₁₂MDI, will be substituted. H₁₂MDI is a cycloaliphatic diisocyanate composed of a mixture of the three geometric isomers: trans-trans, trans-cis, cis-cis. While the MDI based polyurethanes can form a well defined crystalline hard segment as we have previously seen, hard segment crystallinity is inhibited in H₁₂MDI based polymers due to the presence of these three isomers. Our supposition is that the same qualitative properties will be obtained by varying the diisocyanate portion rather than the chain extender portion provided that hard segment crystallization can be inhibited (i.e. morphology is more important than chemistry).

The remainder of this paper will discuss the synthesis of the polyurethanes, the thermal analysis to determine transition temperatures, the dynamic mechanical analysis to determine damping characteristics, and the conclusions reached. It will be verified that the presence or absence of hard segment crystallinity is the dominant factor in determining the qualitative form of the dynamic mechanical properties, independent of the specific diisocyanate or chain extender.

SYNTHESIS

All the polymers synthesized were based on the same polyglycol used previously, poly(tetramethylene ether) glycol or PTMG (DuPont Terathane). Nominal molecular weights of PTMG were 650, 1000, 2000, and 2900. In the earlier study, an aromatic diisocyanate was used, 4,4'-diphenylmethane diisocyanate or MDI (Dow Isonate 2125M). In the present work a cycloaliphatic diisocyanate, 4,4'-dicyclohexylmethane diisocyanate or H₁₂MDI (Mobay Desmodur W), was used. This material is about 65 percent cis-trans, 30 percent trans-trans, and 5 percent cis-cis isomer. The three isomers are illustrated in Figure 1.

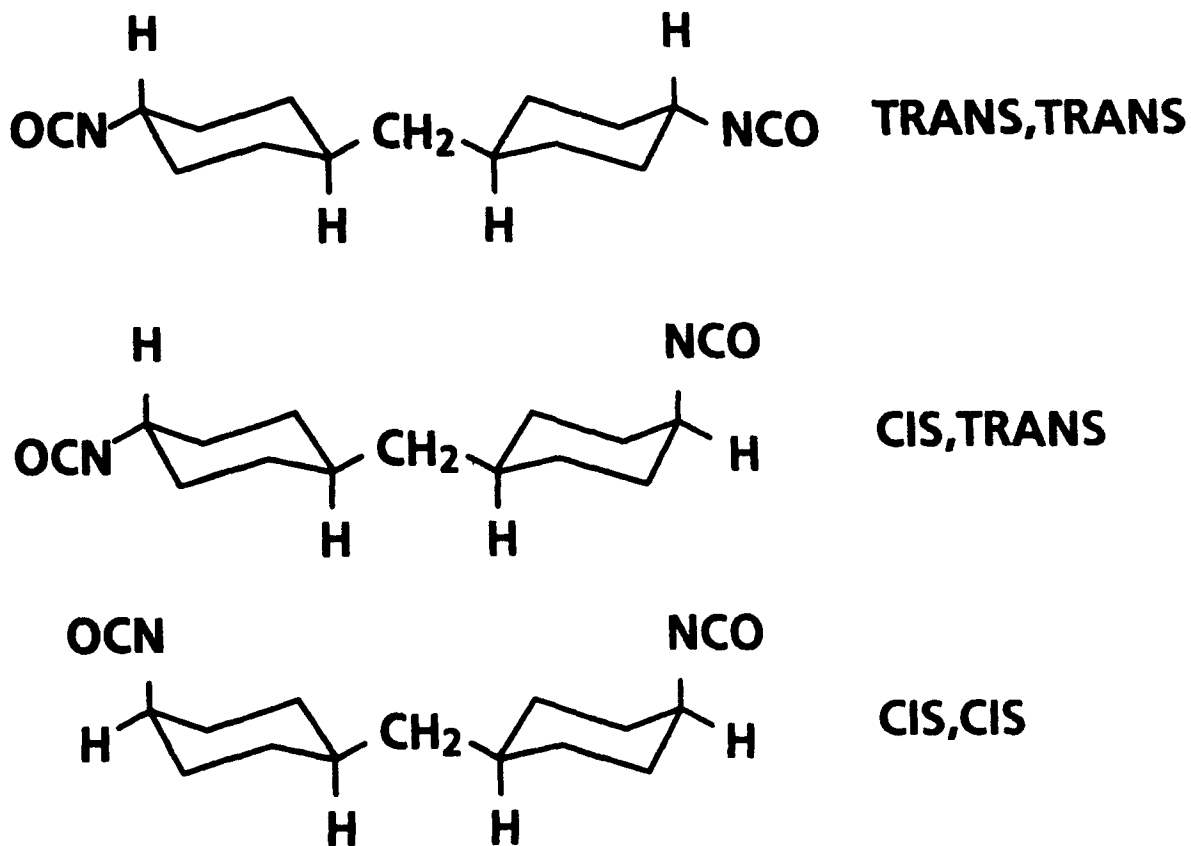


Figure 1. Isomers of H₁₂MDI

All of the above polyglycols were reacted with H_{12} MDI under nitrogen using 1 mole of PTMG and 3 moles of H_{12} MDI to form prepolymers. The reaction temperature was kept between 75 and 80°C for at least two hours after the addition of polyglycol was complete. A small amount of dibutyl tin dilaurate (Air Products DABCO T-12) catalyst was used to speed up the reaction between the polyglycol and the diisocyanate. This mixture was then degassed and stored under nitrogen until further use.

The PTMG/ H_{12} MDI prepolymer was chain extended with BDO. Figure 2 shows the structures of PTMG, MDI, H_{12} MDI, BDO, and DMPD. The prepolymer was heated to 80°C and degassed then chain extended with BDO. The BDO was added and mixed under vacuum at high speed using a laboratory mechanical mixer for about three minutes. The polymer was poured into a pre-heated Teflon coated mold at 100°C. The isocyanate index was 1.05, which ensures that there is 5 percent excess diisocyanate for crosslinking during the cure. All of the samples were cured at 100°C for 16 hours. Then the samples were equilibrated at room temperature and 50 percent RH for a minimum of two weeks before dynamic mechanical analysis.

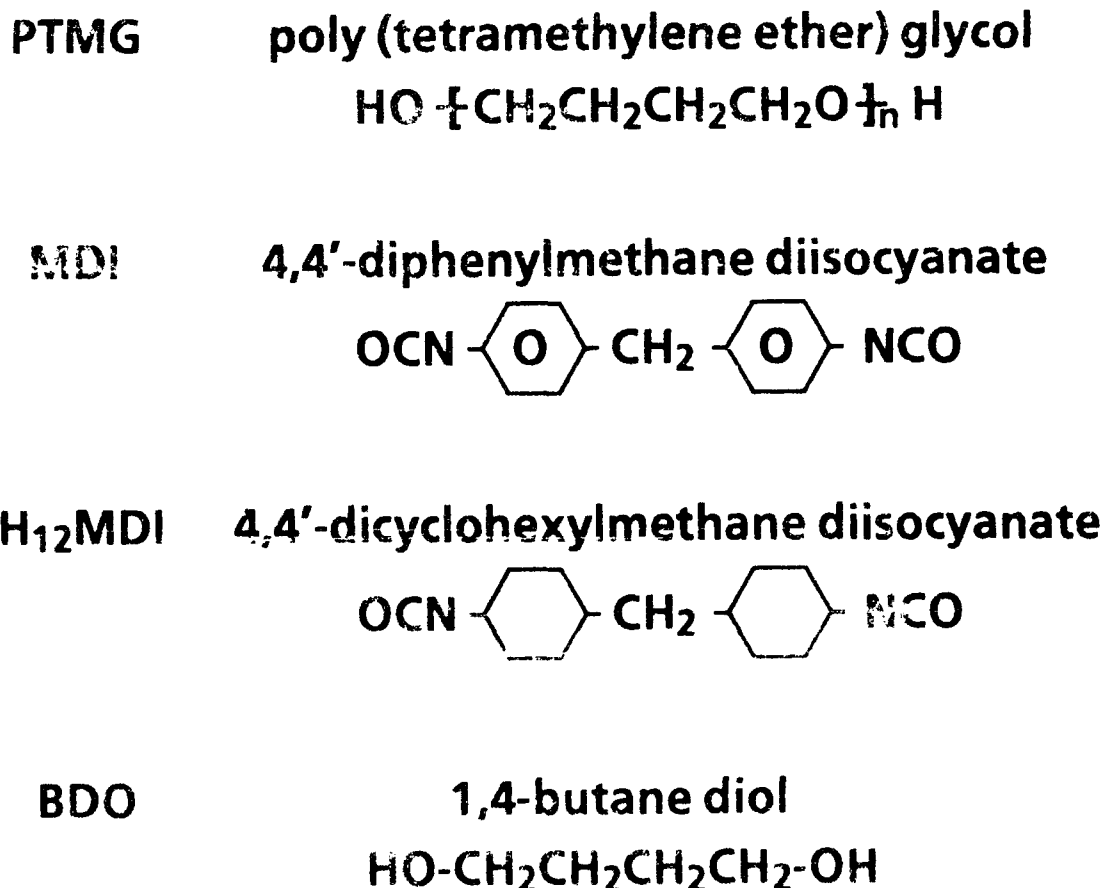


Figure 2. Chemical Structures of Components

EXPERIMENTAL

THERMAL ANALYSIS

A DuPont 9900 Thermal Analyzer was used in conjunction with a 910 DSC (differential scanning calorimeter) module to obtain thermograms. Samples (15-20 mg) were cut from the test bars used for the dynamic mechanical measurements and placed in aluminum test pans for analysis. Measurements were carried out in a argon atmosphere at a scanning rate of 10°C/min. Two runs were made on each sample, each from -170 to 250°C.

Thermograms were analyzed to determine the glass transition temperature in the soft segment, $T_g(ss)$, the melting temperature in the hard segment, $T_m(hs)$, and the melting temperature in the soft segment, $T_m(ss)$, if any. In addition, the heat of fusion was determined whenever crystallinity was present.

DYNAMIC MECHANICAL ANALYSIS

Dynamic mechanical properties were obtained using the resonance apparatus previously described¹. In this apparatus, Figure 3, modulus and loss factor were obtained over a frequency range of about two decades for temperatures from -60 to 70°C. All data will be presented at a reference temperature of 25°C.

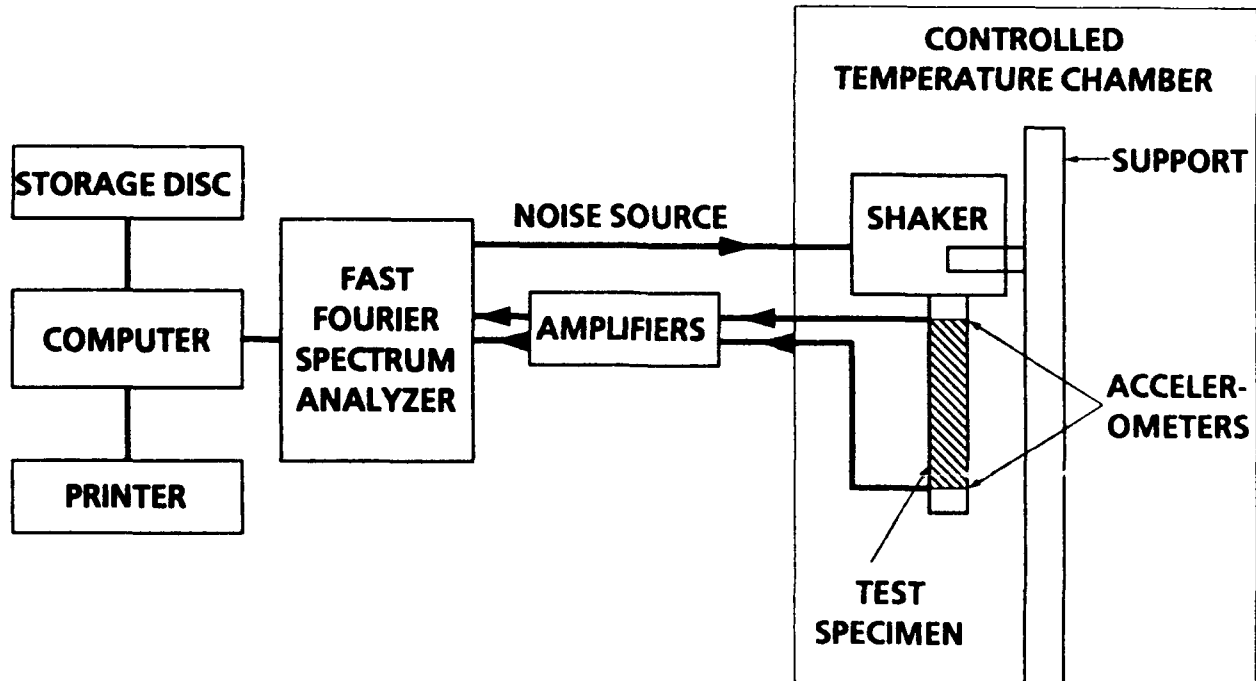


Figure 3. Resonance Apparatus

Measurements were made at 5 degree temperature intervals and the sample was equilibrated for twenty minutes at each interval before measurement. This data was shifted, using the time-temperature superposition principle to form master curves of

modulus and loss factor as a function of frequency over a very wide frequency range at a reference temperature of 25°C. Measurements and data analysis were carried out in the same fashion as the earlier work¹.

RESULTS AND DISCUSSION

Transition temperatures were determined from DSC thermograms. A typical example of the results obtained is shown in Figure 4, where we have compared the data for PTMG 1000/H₁₂MDI/BDO with that PTMG 1000/MDI/BDO. As can be seen, there is a well developed melting peak for the MDI based polymer, indicating that hard segment crystallinity was present, but no crystallinity is seen in the H₁₂MDI based polymer.

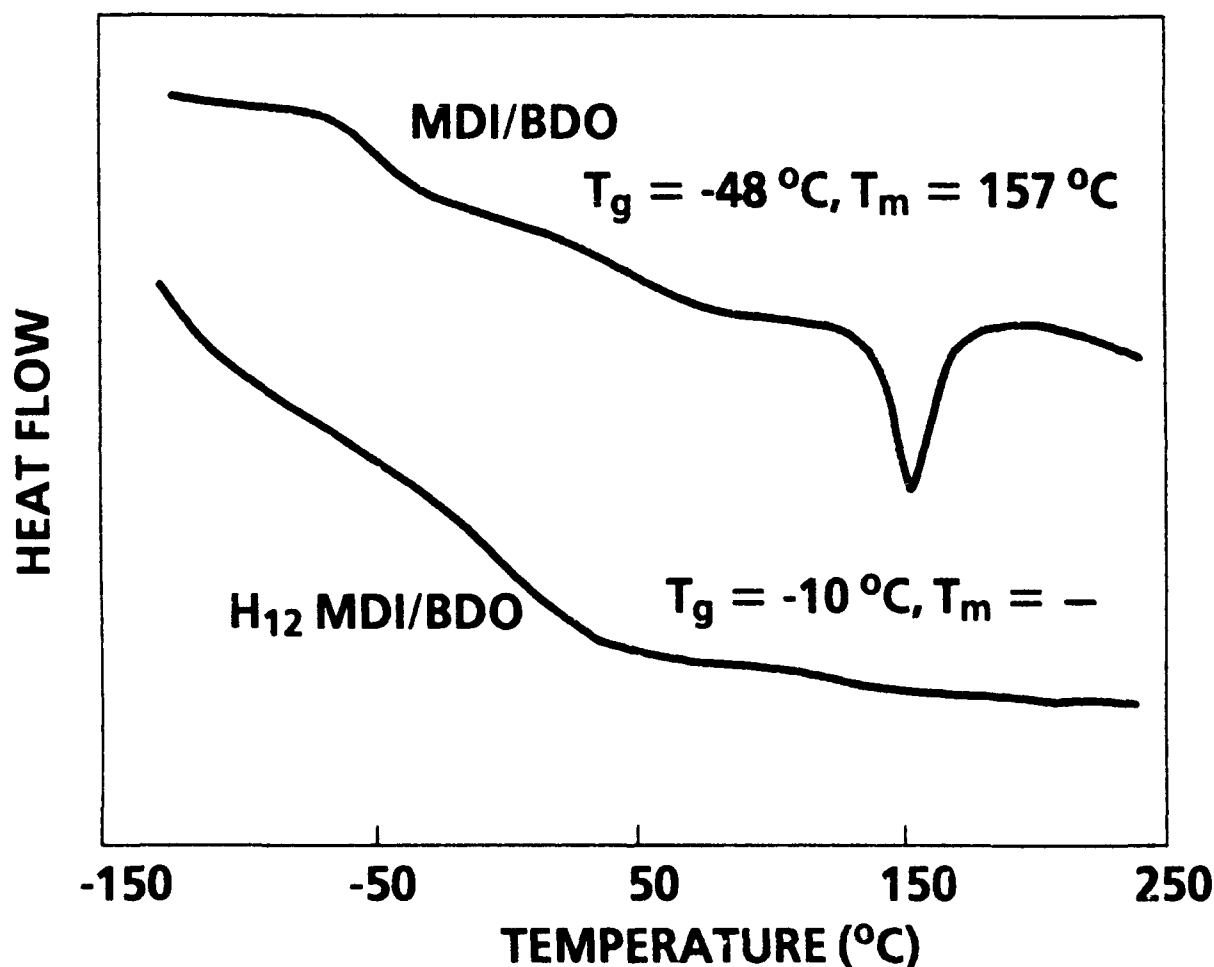


Figure 4. DSC Thermograms of PTMG 1000 Polymers

Thermograms for the other molecular weights were analyzed in a similar manner, and the transition temperatures obtained are listed in Table 1. Densities of the H₁₂MDI polymers and the analogous MDI based polymers are also listed in Table 1.

Table 1. Transition Temperatures and Densities for PTMG 650-2900/H₁₂MDI/BDO and PTMG 650-2900/MDI/BDO

	T _g (ss) °C	T _m (hs) °C	T _m (ss) °C	Density g/cm ³
PTMG 650/H ₁₂ MDI/BDO	13	152	--	1.096
PTMG 1000/H ₁₂ MDI/BDO	-10	--	--	1.075
PTMG 2000/H ₁₂ MDI/BDO	-68	--	--	1.040
PTMG 2900/H ₁₂ MDI/BDO	-71	--	18	1.027
PTMG 650/MDI/BDO	-24	160	--	1.174
PTMG 1000/MDI/BDO	-48	157	--	1.139
PTMG 2000/MDI/BDO	-66	184, 197	2	1.080
PTMG 2900/MDI/BDO	-71	191, 198	10	1.056

ss - soft segment

hs - hard segment

In comparing the results for the two systems, the glass transition temperature for the PTMG 2900/H₁₂MDI/BDO polymer is identical to that for the analogous MDI based polymer and the value for PTMG 2000/H₁₂MDI/BDO polymer is nearly the same as the analogous MDI based polymer. For the lower molecular weight PTMG, however, the H₁₂MDI based polymers have significantly higher glass transition temperatures than the analogous MDI based polymers. For PTMG molecular weight of 1000, the T_g for H₁₂MDI based polymer is 38 degrees higher than the MDI based polymer. while T_g for PTMG 650/H₁₂MDI/BDO polymer is 37 degrees higher than the analogous MDI based polymer. Since, for these systems, the lower the PTMG molecular weight the higher the hard segment concentration, it follows that the cycloaliphatic diisocyanate has the most effect in those polymers with the higher hard segment concentration. This increase in T_g is presumably a result of phase mixing of the hard segment into the soft segment.

We notice that hard segment crystallinity has been inhibited in the H₁₂MDI polymers with the exception of the lowest molecular weight, where there is a small amount of hard segment crystallinity. The heat of fusion for the 650 MW polymer is 7 J/g compared with 20 J/g for the analogous value for an MDI system². Thus we expect the slightly crystalline PTMG 650/H₁₂MDI/BDO polymer to behave similar to the non-crystalline PTMG 650/MDI/DMPD polymer, though with a slightly higher rubbery modulus and lower, broader loss factor. This behavior is, in fact observed¹. The non-crystalline PTMG 1000/H₁₂MDI/BDO polymer should be very close in behavior to the non-crystalline PTMG 1000/MDI/DMPD polymer, and this is also found experimentally¹.

Finally, we observe that soft segment crystallinity occurs for the PTMG 2900 polymers which we have seen before. When the

soft segment gets long enough, soft segment crystallinity occurs regardless of the hard segment. Based on our previous experience, there is likely some soft segment crystallinity in the PTMG 2000 polymers that does not appear in the DSC at a scanning rate of 10°C/min but which does appear when sufficient time for annealing is allowed, as in the dynamic mechanical measurements where the sample is equilibrated at each temperature interval. The step-wise isothermal dynamic mechanical measurements are made in steps of five degrees with an equilibration time of 20 min after each step. The equivalent heating rate is then 0.25°C/min.

Density values determined by water displacement (ASTM Method D 792) are also listed in Table 1. It can be seen that, for both systems, the polymer density decreases as the molecular weight of the PTMG increases. Since the higher the PTMG molecular weight, the higher the soft segment concentration, the decrease in density is a soft segment concentration effect. For any given PTMG molecular weight, the density of the MDI polymer is about 5 percent higher than the analogous H₁₂MDI polymer, due to the hard segment crystallinity in the MDI based polymers.

Dynamic mechanical modulus results for PTMG 650/H₁₂MDI/BDO and PTMG 1000/H₁₂MDI/BDO are shown in Figure 5.

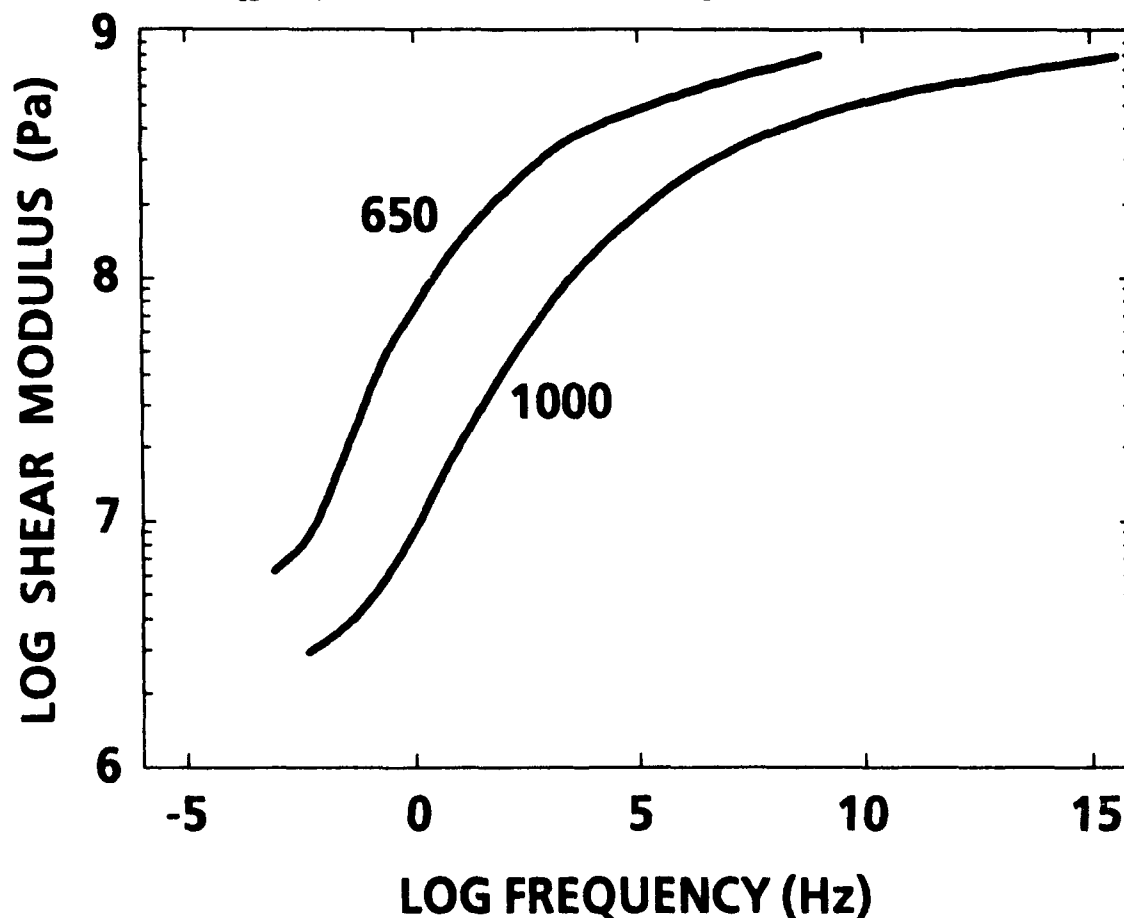


Figure 5. Shear Modulus for PTMG 650 and 1000/H₁₂MDI/BDO

The PTMG 2000 polymer was not thermorheologically simple so that master curves could not be generated. This behavior is probably due to a small amount of soft segment crystallinity which occurs during the slow heating cycle of the dynamic mechanical testing but which is not seen in the more rapid scanning used in the DSC. For the PTMG 2900 polymer, definite soft segment crystallinity was present even in the DSC thermogram and again the data could not be shifted.

Looking more closely at the modulus results (Figure 5), the glassy modulus of both polymers is about 1 GPa, typical for polyurethanes regardless of chemical composition. The rubbery modulus, however, shows much more variation with the chemistry and morphology of the particular system. Both molecular weights tend asymptotically to a rubbery modulus of about 2 MPa, the same as the PTMG/MDI/DMPD systems. In fact, the PTMG/H₁₂MDI/BDO data is very close to the PTMG/MDI/DMPD system. In contrast, both these polymers are qualitatively different than the PTMG/MDI/BDO system where the rubbery modulus tended to about 20 MPa, as can be seen in Figure 6, where a comparison is made for the three PTMG 1000 polymers.

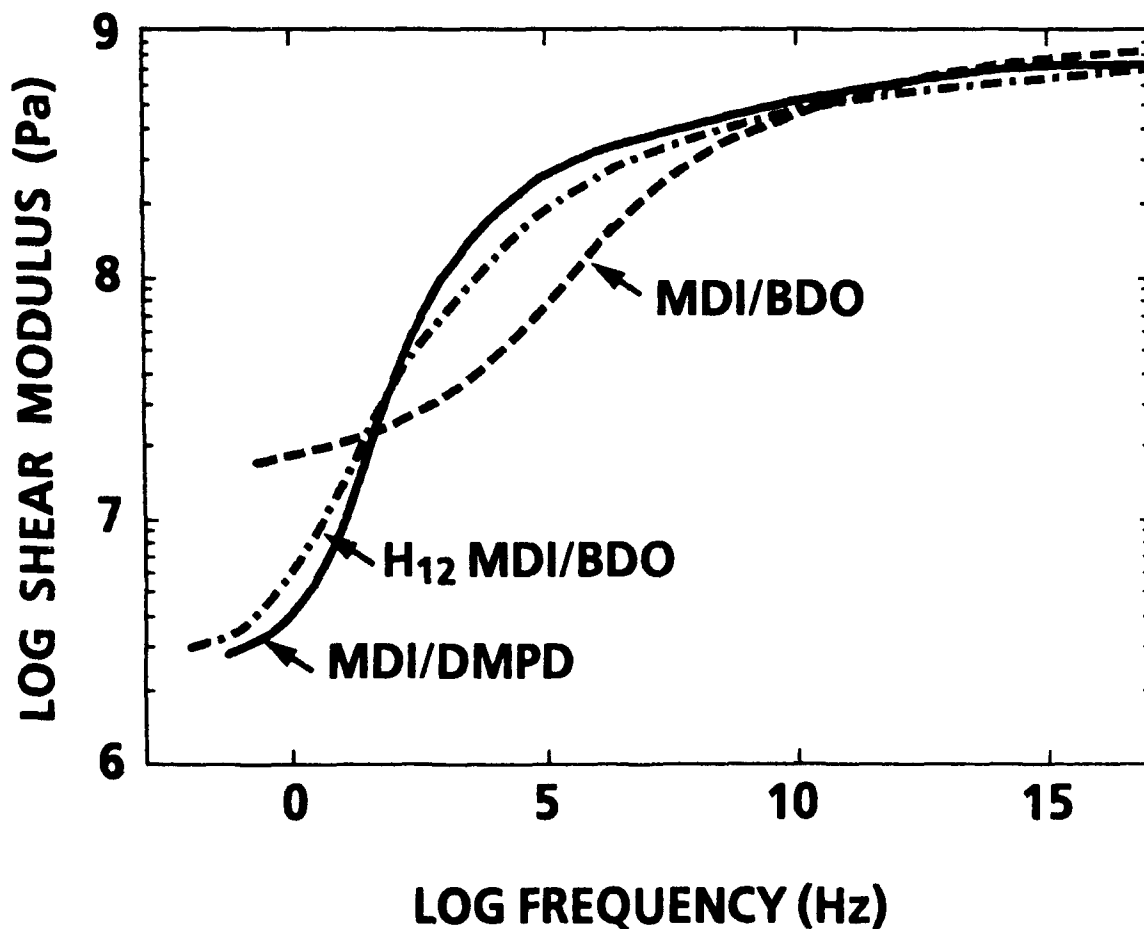


Figure 6. Shear Modulus for PTMG 1000/MDI/BDO, PTMG 1000/MDI/DMPD, and PTMG 1000/H₁₂MDI/BDO

Note that the two polymers with very similar modulus values (MDI/DMPD and H₁₂MDI) have rather different chemistry. What they have in common is that they have no hard segment crystallinity. The polymer without hard segment crystallinity (MDI/BDO) has very different modulus values. These observations are in agreement with our supposition that hard segment crystallinity dominates the dynamic mechanical properties not chain extender or diisocyanate type.

The loss factor data for the two H₁₂MDI polymers is shown in Figure 7.

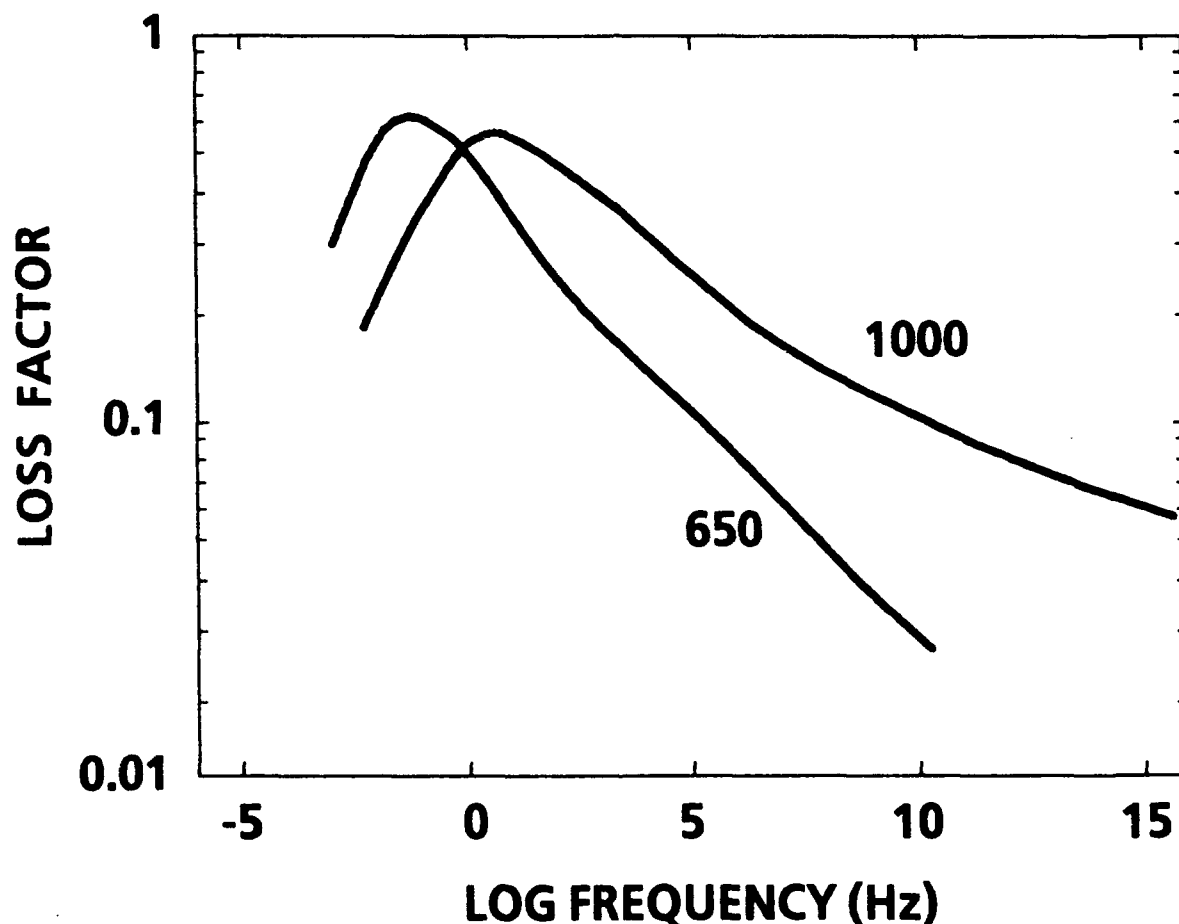


Figure 7. Loss Factor for PTMG 650 and 1000/H₁₂MDI/BDO

Both polymers have a relatively high loss factor, about 0.8, and the maximum values occur about three decades of frequency apart. The T_g values for these polymers differ by 23°C, and a difference of 7°C/decade is typical for polymers in general.

Further confirmation of the effect of hard segment crystallinity is observed in the loss factor data, Figure 8, where a comparison is made for the three PTMG 1000 polymers. The PTMG/H₁₂MDI/BDO data is very close to the PTMG/MDI/DMPD, both having a peak loss factor of about 0.8, but these polymers are qualitatively different than the PTMG/MDI/BDO, with a peak loss

factor of about 0.3. Once again, morphology is more important than chain extender or diisocyanate type.

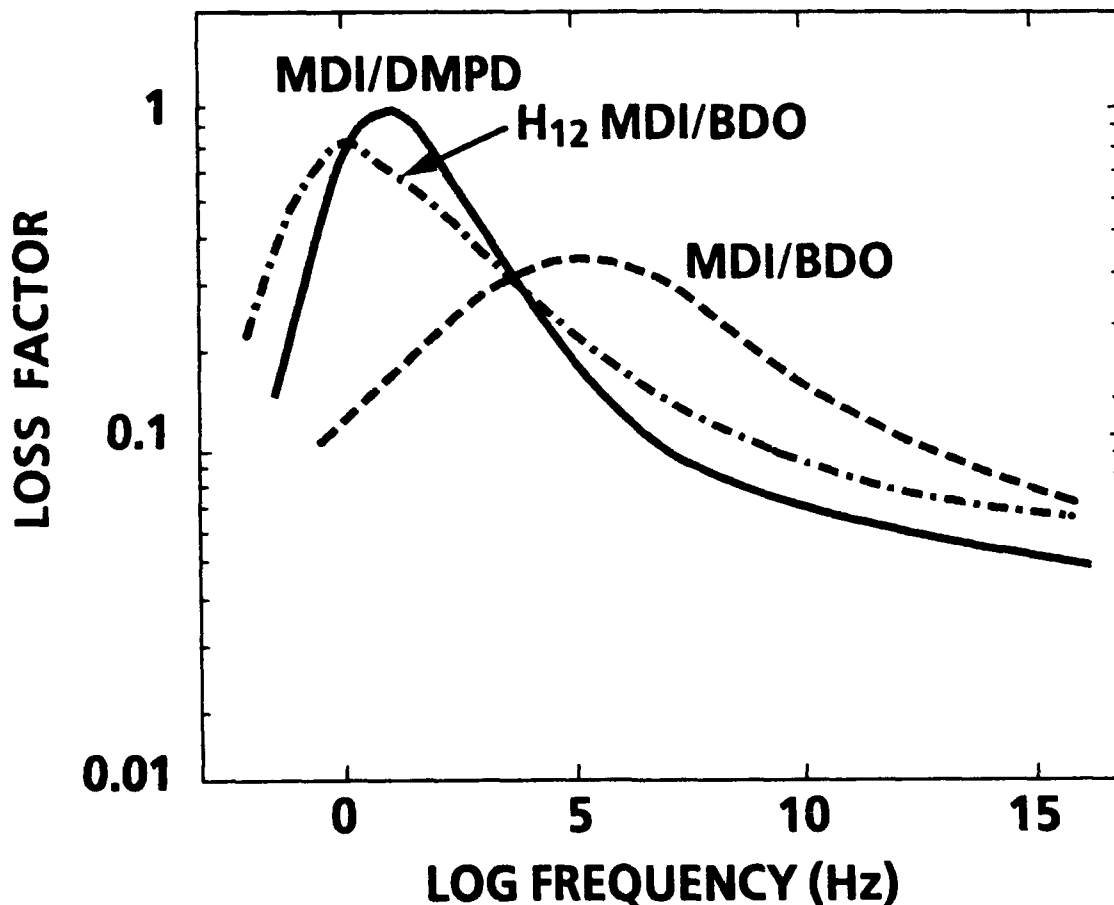


Figure 8. Loss Factor for PTMG 1000/MDI/BDO, PTMG 1000/MDI/DMPD, PTMG 1000/H₁₂MDI/BDO

CONCLUSIONS

Thermal and dynamic mechanical measurements were made on a series of polyurethanes based on cycloaliphatic diisocyanate and the results obtained compared to similar data on the aromatic analog. The results confirm our hypothesis that the presence or absence of hard segment crystallinity is the dominant factor in determining the qualitative form of the dynamic mechanical properties, independent of the specific diisocyanate or chain extender. The following specific conclusions were reached:

- Hard segment crystallinity is the dominant factor in determining the dynamic mechanical properties of polyurethanes
- Regardless of the chain extender or diisocyanate, high loss is obtained if crystallinity is avoided
- Regardless of the chain extender or diisocyanate, low rubbery modulus is obtained if crystallinity is avoided

ACKNOWLEDGEMENT

This work was sponsored by the NSWC Independent Research Program.

REFERENCES

1. J. V. Duffy, G. F. Lee, J. D. Lee, and B. Hartmann, in Sound and Vibration Damping with Polymers, R. D. Corsaro and L. H. Sperling, eds, ACS Books, Washington, 1990, pp 281-300.
2. B. Hartmann and G. F. Lee, *J. Noncryst. Solids*, in press.
3. W. M. Madigosky and G. F. Lee, *J. Acoust. Soc. Amer.*, 73, 1374 (1983).

AN APPARATUS FOR MEASURING THE LOW FREQUENCY DYNAMIC CHARACTERISTICS OF MATERIALS.

Francis OLIVIER* and Mona KHOURY

Centre d'Etudes et de Recherches pour la Discretion Acoustique des Navires (CERDAN)
DCN Toulon, 83800 Toulon Naval, FRANCE

INTRODUCTION

The TNO Institute of Applied Physics at Delft (TPD Netherland) has developed an apparatus for the evaluation of dynamic stiffnesses of resilient mounts and flexible hosepipes (see reference) used in automotive or shipboard machinery. It exploits accelerometric transfer measurements and, as main advantages, allows to work under static preload with a hydraulic jack, and over six possible degrees of freedom. We have adapted it to the characterization of the intrinsic properties of materials in a low frequency range (from 100 Hz up to about 2 kHz) through the longitudinal bulk $M = \lambda + 2\mu$ and the shear $G = \mu$ complex moduli.

In that paper we describe this apparatus, its main characteristics and performances. We also present some results and explain its limitations in order to propose some improvements. They show how the TPD bench may be considered as an interesting and complementary device for the knowledge of foam and composite rubbery materials, at low frequencies, under varying conditions of static pressure.

* E.ternal consulting engineer from STERIA for CERDAN; telephone : (33) 94-02-50-53

I - GENERAL WORKING PRINCIPLES

I - 1 General description

The TPD apparatus is a steel made heavy framework composed of a lower bench supporting an arch which carries a hydraulic jack (figure 1-a). It has sufficiently large dimensions to receive metal masses of several hundreds kilograms, that one can isolate from the structure by hanging them on resilient mounts. Usual work needs to superpose two masses related together by the element to be tested like a resilient mount or a flexible hose. Generally these masses have a circular shape; they are chosen within a set of several steel or aluminium masses which inertial characteristics and internal eigenfrequencies are perfectly known. So one can build a discrete mass-stiffness-mass system (figure 1-b), isolated by suspensions judiciously chosen between a set of known mounts, and obviously much less stiff than the element to test. By changing masses and isolators stiffnesses, we are able to control the working frequency broadband while satisfying the "isolated discrete system" assumption. In special cases, this broadband may go from a few tens of hertz up to about 2 kHz.

For vibratory testing of elastic mounts or flexible hosepipes, it is often interesting to put them in real working situation. This is the reason why the TPD bench includes a jack and a hydraulic circuit, both hand generated with their own pump. With the first, one can apply a static loading that simulates a real structure or a machine which may weigh up to a hundred tons. The second allows filling a flexible pipe with a liquid pressure.

The mass-stiffness-mass system is aligned along the vertical z-axis. The horizontal plane will be noted xy. The excitations are applied with two electrodynamic shakers, symmetrically mounted on a transversal bar (y) which is perpendicular to the main frontbeam (x). They attack the upper mass, named input mass and pointed out by index 1. The vibration goes through the element to test, down to the lower output mass pointed out by the index 2.

I - 1 Vibratory equations for the 6 degrees of freedom system

One can consider that the mount to test behaves like a pure stiffness if one admits the following realistic assumptions :

- its mass is negligible compared to the masses 1 and 2;
- its dimensions are much smaller than the wavelength (especially for low frequencies),
- it presents a linear behavior for vibrations having little displacements.

Writing Hooke's law between the two bounds of the specimen and generalizing it to the six possible degrees of freedom, one can define its stiffness 12x12 matrix [K] as :

$$\{F\} = [K] \cdot \{X\} \quad \text{or} \quad \begin{pmatrix} F_1 \\ F_2 \\ F_3 \\ F_4 \\ F_5 \\ F_6 \end{pmatrix} = \begin{bmatrix} K_{11} & K_{12} \\ K_{21} & K_{22} \\ K_{31} & K_{32} \\ K_{41} & K_{42} \\ K_{51} & K_{52} \\ K_{61} & K_{62} \end{bmatrix} \cdot \begin{pmatrix} X_1 \\ X_2 \\ X_3 \\ X_4 \\ X_5 \\ X_6 \end{pmatrix} \quad (1)$$

- $\{F_i\}$ force vector on node i , with 6 components : 3 forces F_x, F_y, F_z , and 3 torques M_x, M_y, M_z ;
- $\{X_i\}$ displacement vector on node i , with 6 components : 3 translations x, y, z , and 3 rotations $\theta_x, \theta_y, \theta_z$;
- $[K_{11}]$ et $[K_{22}]$ input (respectively output) stiffness matrix for blocked output (respectively blocked input);
- $[K_{12}]$ et $[K_{21}]$ input (respectively output) transfer matrix for blocked output (respectively blocked input).

This matrix contains all the mount characteristic stiffnesses. From now on it will be the unknown of our general problem. We will consider all of its elements as complex values which imaginary parts reveal the eventual presence of damping.

Using that formulation, one can write the dynamic equation of the two-nodes discrete system :

$$[M] \{\ddot{X}\} + [K] \{X\} = \{F_e\} \quad (2)$$

where $\{F_e\}$ is the six components external force vector applied to the input mass with the two shakers, and $[M]$ is the inertial tensor on both nodes. If we consider the two masses as punctual, that is if the two junction nodes merge into the centers of gravity of the masses, then $[M]$ is a diagonal matrix which twelve diagonal elements may be written as : $m_1, m_1, m_1, J_{x1}, J_{y1}, J_{z1}, m_2, m_2, m_2, J_{x2}, J_{y2}, J_{z2}$. For example, J_{yi} is the moment of inertia of node i ($i=1$ or 2) around the y rotation axis.

In practice, we do not use the whole formulation in every cases. Except for inertias, all the involved variables may depend on frequency so that it would be too long to process them all systematically. To lighten the problem formulation, one can take advantage of the symmetry properties of matrix $[K]$ due to the reciprocity theorem. Therefore we are allowed to concentrate only on the output mass movements and to consider that $[K_{21}]$ and $[K_{22}]$ contain the whole characteristic stiffness informations about the specimen. Moreover, since we apply excitations to the input node (mass $n^{\circ}1$), the equation of the output node becomes simpler setting its second member to zero :

$$[M_2] \{\ddot{X}_2\} + [K_{21}] \{X_1\} + [K_{22}] \{X_2\} = \{0\} \quad (3)$$

To go on into simplifications, another working fundamental assumption is to suppose the output blocked. In practice, we realize that condition by using an output mass much heavier than the input one (for example $m_1 = 50$ kg and $m_2 = 450$ kg). In the following paragraph, we will verify the validity of such an approximation which intends to eliminate a third term in equation (3) and reduce it to:

$$[M_2] \{\ddot{X}_2\} + [K_{21}] \{X_1\} = \{0\} \quad (4)$$

From this equation we can notice that the unknown is restricted to $[K_{21}]$ and deduce two important remarks that will affect the experimental aspect of our method. First, since external forces have disappeared we will not have to measure them. The measurements will be reduced to displacements or accelerations, and this leads to the second remark. The "blocked output" hypothesis may seem quite paradoxal because, strictly, we should measure zero output accelerations! In fact the assumption remains true if one satisfies the following compromise : output accelerations must be measurable, that means stronger than the background noise, but much weaker than the input ones (about 20 dB).

The transfer matrix $[K_{21}]$ is generally not fullfilled. It may present many zero elements, depending on the specimen shape. This represents a considerable advantage for our method, because we may reduce the number of unknowns from it. In other words, symmetries may occur in the mount shape, which tend to separate coupled degrees of freedom. Therefore the formulation becomes simpler and, for example, in case of a specimen having three planes of symmetry xy, xz and yz, equation (4) becomes :

$$\begin{pmatrix} m_2 \ddot{X}_2 \\ m_2 \ddot{Y}_2 \\ m_2 \ddot{Z}_2 \\ \ddots \\ J_{x2} \ddot{\theta}_{x2} \\ \ddots \\ J_{y2} \ddot{\theta}_{y2} \\ \ddots \\ J_{z2} \ddot{\theta}_{z2} \end{pmatrix} = \begin{bmatrix} K(1,1) & 0 & 0 & 0 & K(1,5) & 0 \\ 0 & K(2,2) & 0 & K(2,4) & 0 & 0 \\ 0 & 0 & K(3,3) & 0 & 0 & 0 \\ 0 & K(2,4) & 0 & K(4,4) & 0 & 0 \\ K(1,5) & 0 & 0 & 0 & K(5,5) & 0 \\ 0 & 0 & 0 & 0 & 0 & K(6,6) \end{bmatrix} \begin{pmatrix} X_1 \\ Y_1 \\ Z_1 \\ \theta_{x1} \\ \theta_{y1} \\ \theta_{z1} \end{pmatrix} \quad (5)$$

I - 3 Tension-compression equations along z axis.

By construction, the experimental mounting privileges vertical (z) tension-compression vibrations within all other degrees of freedom. Equation (5) shows that this "dof" is not coupled with any other one, so that it becomes very easy to write this two-nodes reduced system equations for harmonic vibrations :

$$\begin{aligned} m_1 \ddot{Z}_1 + K(Z_1 - Z_2) &= F_e \exp(i\omega t) \\ -K(Z_1 - Z_2) + m_2 \ddot{Z}_2 &= 0 \end{aligned} \quad (6)$$

where $K = K(3,3)$. The two angular eigen frequencies are given by :

$$\omega^2 = 0 \quad \text{et} \quad \omega^2 = K \left(\frac{1}{m_1} + \frac{1}{m_2} \right) \quad (7)$$

and since $\ddot{Z} = -\omega^2 Z$, both displacements are written as :

$$Z_1 = F_e \frac{K + m_2 \omega^2}{\omega^2 (m_1 m_2 \omega^2 - K (m_1 + m_2))} \quad \text{et} \quad Z_2 = F_e \frac{K}{\omega^2 (m_1 m_2 \omega^2 - K (m_1 + m_2))} \quad (8)$$

The output/input ratio leads to :

$$\frac{Z_2}{Z_1} = \frac{K}{K - m_2 \omega^2} = \frac{1}{1 - \frac{m_2}{K} \omega^2} = \frac{\ddot{Z}_2}{\ddot{Z}_1} \quad (9)$$

From transfer function (9) we can observe that, for a given specimen stiffness, the heavier the output mass the weaker its acceleration is, compared to the input mass one. This contrast increases with frequency and for small stiffnesses. This illustrates the previous paragraph purpose and shows how the question of signal to noise ratio may appear. For that reason, we will probably have to deal with high frequency limitations. Moreover we can notice that the stiffness K may be approximated by :

$$K = - m_2 \omega^2 \frac{\ddot{Z}_2}{\ddot{Z}_1} \quad (10)$$

with a negligible error when $m_2 \omega^2 / K \gg 1$. Therefore, simply multiplying the accelerometric transfer function by $-m_2 \omega^2$, provides directly a good estimation of the stiffness. To evaluate the specimen damping, we just have to take the complex K phase information into account.

We just saw that signal to noise ratio problem could cause the high frequency limits of our approach. Other reasons may be :

- unsatisfaction of the "discrete system" assumption at the eigenfrequencies neighbourhood;
 - bad isolation of the tension-compression degree of freedom which may get coupled with other ones like rotation, in case of small defects or weak dissymmetries in the mounting.
- According to (9), the low frequency limit will be given by :

$$f = \frac{1}{2\pi} \sqrt{\frac{K}{m_2}} \quad (11)$$

These considerations we just made about tension-compression may be applied to the other degrees of freedom in the same way. But neither the involved stiffnesses and inertial terms, nor the frequency limitations therefore, would be the same.

I - 4 Experimental processing.

Measuring the accelerometric transfer function between the two masses in the conditions described above, needs a good experimental care.

To guarantee that the degrees of freedom are sufficiently uncoupled from each other, all the transducers, shakers as well as sensors, are used by pairs, geometrically symmetric or antisymmetric mounted depending on the dof (figure 1-b). That kind of rig allows spurious movement cancellation and desired movement extraction. Each pair needs twin transducers, very well calibrated in modulus and phase, so that their signal

may be added or subtracted without distortion. These operations are made by two analog electronic devices (see the right part of figure 1-b) :

- the VCCD (Vibration Component Cancellation Device) splits the input amplified signal into two in-phase or phase opposite components which feed the two electrodynamic shakers (Denitron);

- the ASD (Additive Subtractive Device) gives on output the half-sum or half-difference (following the operator choice) of both input signals coming from a pair of sensors.

For vertical tension-compression (z axis), both vibrators are fed by the same signal, and the ASD compute the half-sum of the amplified signal outcoming from the pairs of accelerometers.

About signal processing, we usually estimate transfer function (9) with a HP 6532 numeric analyser, which can also provide the excitation signal. To optimize the Fourier analysis in the point of view of signal to noise ratio, we use a slowly swept sine which may require about seven minutes acquisition time when working from 0 to 2 kHz with a 2.5 Hz resolution. This quite long analysis allows the output signal to come into view from the background noise level, while avoiding at the same time, the injection of a too powerful excitation which could introduce undesirable non linear behaviour. Then we satisfy the following compromise : noise level $< Z_2 \ll Z_1$.

The digitalized transfer function migrates out from the analyzer into the memory of a HP 9000 computer which makes post-processings like, for example, the multiplication by $-m_2\omega^2$ and the graphics too. A complete software program manages the whole tests over many kinds of specimen like mounts, hoses and pipes. It can also process a matrix treatment to separate coupled degrees of freedom.

To insure that the experimental conditions fulfill the working assumptions described in the paragraph above, we generally add complementary measurements to the main transfer function. They are (figure 2) :

- the measurement of both input and output masses acceleration spectra, to verify that the level of the second is effectively about 20 dB lower than the level of the first; we can also see if they are eventually polluted by a spurious movement.

- the measurement of this spurious degree of freedom to diagnostic and correct it;

- the measurement of the bench acceleration spectrum, below the output mass; it must be at least 10 dB lower than the output mass level for the discrete system to be well isolated. Because of a bad resilient suspension, it could happen that the output mass might be excited not only by the specimen but through the isolation mount too. Indeed an acoustical channel links it to the input mass : it goes up through the upper mount to the jack, then from the jack down to the lower part of the bench and up again through the lower mounts to the mass. This case may occur if, for example under very heavy static loadings, the resilient mounts lose their efficiency because of smashing or their own degradation.

Moreover, we can use many different amplification gains on the excitation signal, to verify that the specimen has effectively a linear vibratory behavior in Hooke's law.

II - USING TPD BENCH AS A VISCOANALYZER

II - 1 Measurement of longitudinal and transverse moduli

We have explained how to measure the dynamic stiffnesses of a resilient specimen. Now we are going to describe a derivated usage of TPD bench, specifically destined to the evaluation of the M longitudinal bulk (plane wave) and G transverse (shear) moduli which are characteristic of the material the specimen is made of. Elasticity theory says that those two parameters are sufficient to completely define an isotropic material. This may be extended to viscoelastic materials by considering their moduli as complex values. From now on, we will not speak of a mount to test anymore, but of a material specimen, and our objectives will not be anymore to evaluate only global parameters like stiffnesses, but to obtain a material intrinsic information, which does not depend on the mount shape.

This special utilization of the apparatus is particularly well adapted to the characterization of materials like natural or synthetic rubbers, foams and many of their derivated composites which may contain inclusions or internal structures. As main advantage it provides directly the viscoelastic moduli we use to deal with in acoustical modeling, either with Lamé coefficients in tridimensional elasticity equations, or through the sound celerities of longitudinal and transversal waves :

$$M = \lambda + 2\mu ; G = \mu \Rightarrow c_L = \sqrt{\frac{\lambda + 2\mu}{\rho}} \text{ et } c_T = \sqrt{\frac{\mu}{\rho}} \quad (12)$$

In that point of view, the direct method we recommend here is much more appropriate than the usual viscoelastic measurement devices like rheovibrons or viscoanalysers, which generally try to estimate Young's and shear moduli, E and G , through the observation of beams working in tension-compression, torsion or flexion. In using the equations linking the elastic moduli to each other, a simple analytical calculation of the relative error is sufficient to convince oneself about it . If we deduce M from experimental values of E and G , we obtain :

$$M = G \left(\frac{4G - E}{3G - E} \right) \Rightarrow \frac{dM}{M} = \frac{dG}{G} - \frac{EG}{(3G - E)(4G - E)} \left[\frac{dG}{G} - \frac{dE}{E} \right] \Rightarrow$$

$$\frac{\Delta M}{M} = \left(1 + \frac{EG}{(3G - E)(4G - E)} \right) \frac{\Delta G}{G} + \frac{EG}{(3G - E)(4G - E)} \frac{\Delta E}{E} \quad (13)$$

By another way using Young's modulus and Poisson ratio ν we have :

$$M = E \frac{(1 - \nu)}{(1 + \nu)(1 - 2\nu)} \Rightarrow \frac{\Delta M}{M} = \frac{\Delta E}{E} + \frac{2\nu^2(2 - \nu)}{(1 - \nu^2)(1 - 2\nu)} \frac{\Delta \nu}{\nu} \quad (14)$$

The materials we are used to study, generally have quite strong Poisson coefficients between 0.4 and 0.5. A well-known consequence of that fact is the following inequality :

$$G = \frac{E}{2(1+\nu)} \Rightarrow 2.8 G \leq E \leq 3 G \quad (15)$$

In expressions (13) and (14) of $\Delta M/M$, the presence of $(1-2\nu)$ or $(3G-E)$ in the denominators shows how a small error in evaluating E and/or ν may be amplified on M :

$$\begin{aligned} - \nu = 0.4 &\Rightarrow \frac{\Delta M}{M} = 5 \frac{\Delta G}{G} + 4 \frac{\Delta E}{E} = \frac{\Delta E}{E} + 3 \frac{\Delta \nu}{\nu} \\ - \nu = 0.45 &\Rightarrow \frac{\Delta M}{M} = 10 \frac{\Delta G}{G} + 9 \frac{\Delta E}{E} = \frac{\Delta E}{E} + 8 \frac{\Delta \nu}{\nu} \end{aligned} \quad (16)$$

Figure 3 illustrates the consequence of that fact on the longitudinal wave celerity. An error of 1% in the measurement of E or G may produce an error of 10% or 20 % on M . 1% is a quite optimistic error because many viscoelastic devices have very poor accuracy which sometimes lead to aberrations like $E > 3 G$!

II - 2 Specific tool for measuring $M = \lambda + 2\mu$.

For measuring a material longitudinal bulk modulus, we most often use square panel shaped samples, from 30 to 50 mm thick, with 100 mm, 200 mm or 300 mm sides. Other tests also work with cylinders of same thickness and nominal diameters of 80 mm or 140 mm. These dimensions are needed with an accuracy of ± 3 mm, so that the specimen can fit a metal box which encloses it and blocks lateral displacements. By pressing weakly on its sides and lubricating the lateral contact faces with a silicon oil, we are sure to block both static and dynamic displacements along x and y axis; this also allows free tangential sliding parallel to z axis. The blocking box is made of a steel circular plate which supports a square framework with two fixed faces and two moving ones which may be actionned with a screw. This tool weight is about 50 kg and is not negligible so that it must be added to the output mass. To apply the excitation correctly, a metal piston of lightly smaller section compared to the specimen, is put between its upper face and the input mass (figure 4).

This care we take in the mounting, insures the dynamic condition which is said of "plane deformation". Along the vertical z axis, the stress-strain relation for the specimen considered as an element of volume, may be written as :

$$\sigma_{zz} = \mu (\epsilon_{xx} + \epsilon_{yy}) + (\lambda + 2\mu) \epsilon_{zz} \quad (17)$$

Since the tool cancels the lateral displacements one can merge :

- the z stress into the output inertial force divided by the sample section S ;
- the z strain into the gradient of z displacements divided by the sample thickness h .

Then, using (10) and (17) one can write :

$$\lambda + 2\mu = \frac{\sigma_{zz}}{\epsilon_{zz}} = \frac{m_2 \dot{Z}_2 / S}{(Z_2 - Z_1) / h} = K(3,3) \frac{h}{S} \quad (18)$$

Therefore we can see that the measurement of the longitudinal bulk modulus only requires to correct the stiffness $K(3,3)$ with the shape factor h/S which is very easy to evaluate because the specimen shape cannot change. In addition to the good control of boundary conditions, this is a second advantage of the method. For data processing the estimation of M requires to apply this second coefficient to the accelerometric transfer function besides the factor $-m_2\omega^2$ already used for the estimation of the stiffness. The obtained value (figure 5) may be complex in case of damping, and may depend on frequency if the material exhibits a dispersive behavior.

II - 3 Static preloading configuration.

The TPD bench allows the testing of materials under static preloading which may be useful for certain applications. Under pressure the materials behave differently : their internal static stress state makes them look like other materials with a weakly higher density (a few percent) but much stronger elastic moduli. The relationship between pressure and those moduli is generally not linear and depends a lot on the kind of considered material. For homogeneous materials the molecular interactions are changed. For composites or foams the internal structures are affected.

To simulate the working under static pressure we use the hydraulic jack. A force ring gives the value of the injected force up to 100 tons, and therefore, dividing it by section S , the value of the static pressure. Because of the blocking framework, S does not change. The thickness h may eventually diminish under the effect of smashing : anyway its new value can be easily measured by comparison with its initial state. As it was said before, the specimen shape remains the same and the shape factor is calculated as before.

Some aspects may change on the experimental point of view. Since the specimen stiffness increases (figure 1-b), so does the low frequency limit and the accelerometric contrast fades between input and output masses on one hand, and between the output mass and the lower part of the bench on the other hand. So the isolation mounts are generally removed into more resisting ones which support heavy preloading and are consequently less efficient. Coupling with other dof may also become more embarrassing and pollute the measurements. Only the signal to noise ratio takes advantage of that configuration. Nevertheless one can observe that the experimental conditions get globally worse (figures 2-c and 2-d) but the measurement remains always possible for static pressures less than 20 bars.

About static preloading configuration, an important remark must be done. The static stress we apply is not isotropic but axial. Therefore, the stress state inside the

specimen is not isotropic either. Indeed, for a material with a static Poisson ratio ν , its components are :

$$\sigma_{xx} = \sigma_{yy} = \sigma_{zz} \frac{\nu}{1 - \nu} \quad (19)$$

For instance the blocking frame reaction is 66% of preloading if $\nu = 0.4$ and 82% if $\nu = 0.45$. So there is some ambiguity in interpreting the results obtained in such a configuration, mixing static and dynamic considerations.

If the dynamic modulus variation is due to the isostatic stress state, we probably underestimate the real value of M that the material would present under isotropic preloading (in a fluid for instance). Nevertheless equation (19) shows that the materials with a strong Poisson ratio like rubbers, are not very affected. About materials with weak Poisson ratio like rubbery foams, one can imagine that their compressibility makes the Poisson ratio increase under the effect of heavy preloading. The Poisson ratio of a foam is rather low at atmospheric pressure because of the bubbles it contains. A static smashing may fill those cavities where the material will not expand anymore : so it becomes less compressible. To conclude, we can say that the error must probably decrease as the static pressure increases, and be more sensitive for the lighter loadings which unfortunately, are the conditions we are most often used to deal with.

II - 4 Shear measurement

Measuring the shear modulus G can be done in a way similar to that used for the longitudinal bulk modulus. It only needs to work along the horizontal x axis instead of the vertical z axis (figure 6-a). We then look after evaluating $K(1,1)$ which may be obtained by transposing the relations concerning $K(3,3)$ (cf. §I-3). The application of the shape factor remains the same because the equation linking the dynamic stiffness to the characteristic modulus is of the same kind as (18) :

$$G = \mu = \frac{\sigma_{zx}}{\epsilon_{zx}} = \frac{m_2 \ddot{X}_2 / S}{(X_2 - X_1) / h} = K(1,1) \frac{h}{S} \quad (20)$$

If the measurement principle does not make any difficulty, on the other hand the experimental conditions are much less easy. The shear mounting presents some specificities very different from those of vertical tension-compression, which involve difficulties on several aspects.

First, the pairs of transducers must be horizontally positioned, diametrically and phase opposite. Since the shear modulus of a material is always much weaker than the longitudinal one, the global shear stiffness of a specimen is much lower too. Therefore the acceleration transmitted through the specimen to the output mass has a lower level, and the signal risks to be drowned very soon at a few hundred Hz, into the background noise. In such a case we will have to use a lighter output mass (figure 6-b).

Another problem is that the panel cannot be held in the blocking frame because the definition of shear requires to keep its edges free. As a consequence we lose some control on the boundary conditions and the shape factor when we want to work under heavy static preloading. If not enclosed in a box, the sample can expand on its sides : then its thickness strongly decreases, its section increases and its lateral faces round off, so that the shape factor becomes uneasy to evaluate. A second consequence is the difficulty to well isolate the shear degree of freedom, even without static preload. Indeed, the lack of signal mentioned above may lead to amplify the excitation signal. Then the x displacements tend unfortunately to get coupled with the rotation around y axis, especially for the highest frequencies (figure 6-b). To improve this particular point two solutions are possible.

The first one is to mount a special rig that would be mechanically and geometrically symmetric toward the medium plane which horizontally cuts the input upper mass through the middle (figure 6-a). But we then need a second twin specimen and a second mass identical to the lower one which movements would balance and cancel the rotation degree of freedom. But for practical reasons of heaviness and overcrowding this solution cannot be applied.

The second one keeps the original rig and concerns the measurement post-processing. Since a spurious rotation may occur we can take it into account by exciting it deliberately and measuring it. Then a matrix treatment may allow the separation of the different stiffness terms involved in the problem. Let us consider the output mass movements with both coupled degrees of freedom ; if m is its mass and J its moment of inertia around the y axis shifted to the junction point with the sample, then following (5) one can write :

$$\begin{aligned} m \ddot{X}_2 &= K(1,1) X_1 + K(1,5) \theta_{y1} \\ J \ddot{\theta}_{y2} &= K(5,1) X_1 + K(5,5) \theta_{y1} \end{aligned} \quad (21)$$

We do not have to measure an accelerometric transfer function anymore, but directly all the accelerations involved in (21), using for instance an electrical reference. These measurements must be done a first time by exciting the shear translation of the input mass (figure 6-a), and a second time by exciting its rotation applying a torque around y axis (figure 7-b). To do this we just have to put both electrodynamic shakers in the same vertical position used for tension-compression, but in that case they are fed with two phase-opposite signals (antisymmetric mounting). Then we are able to build a linear system of 4 equations and 4 unknowns which are the stiffness terms. A software program makes the matrix processing which has to provide these complex values versus frequency. It often happens that the sample has a horizontal (xy) plane of symmetry : in such cases the calculation should yield this property of the stiffness matrix with $K(1,5) = K(5,1)$. For practical reasons this method has not been tested yet for the shear modulus evaluation, but we know from elsewhere that it already works for resilient mounts testing at low frequencies.

CONCLUSION

We have described in that paper a derivated utilization of TPD bench in order to characterize the elastic properties of materials like rubbers and foams at low frequencies. This apparatus gives reliable results especially on the longitudinal bulk modulus under different conditions of static pressure. The shear measurements are not completely satisfying yet but there are some solutions to improve them.

Another interesting direction of investigation is to test the behavior of the measurements for various materials especially viscoelastic ones which may exhibit strong damping (phase sensibility) and frequency dispersion (magnitude sensibility) in their transition region. Naturally the big dimensions of the TPD bench prohibit testings versus temperature like many viscoanalysers focused on the temperature-frequency equivalence law. But, even at room temperature, the possibility of working under different static pressures, with many kind of rubbers and composites, makes this special apparatus an efficient way of knowing those materials, complementary of other devices like viscoanalyzers and acoustic impedance tubes.

Reference

"Handbook on the measurement of sound transfer functions of flexible".
J.G. van Bavel, Department of Ship Acoustics, TNO Institute of Applied Physics, Delft, Netherlands.

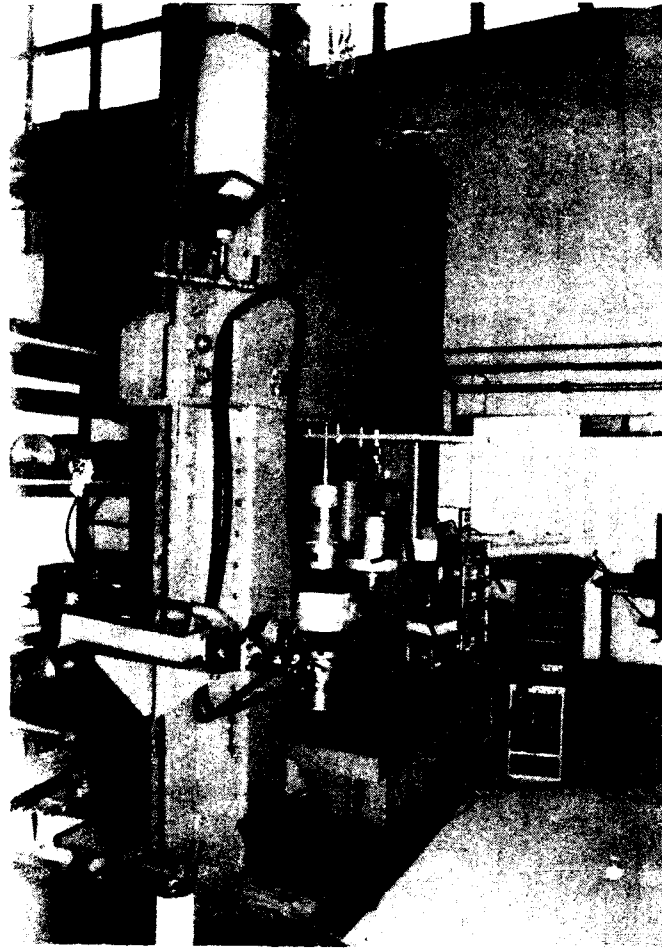


Figure 1-a : general view of TPD bench.

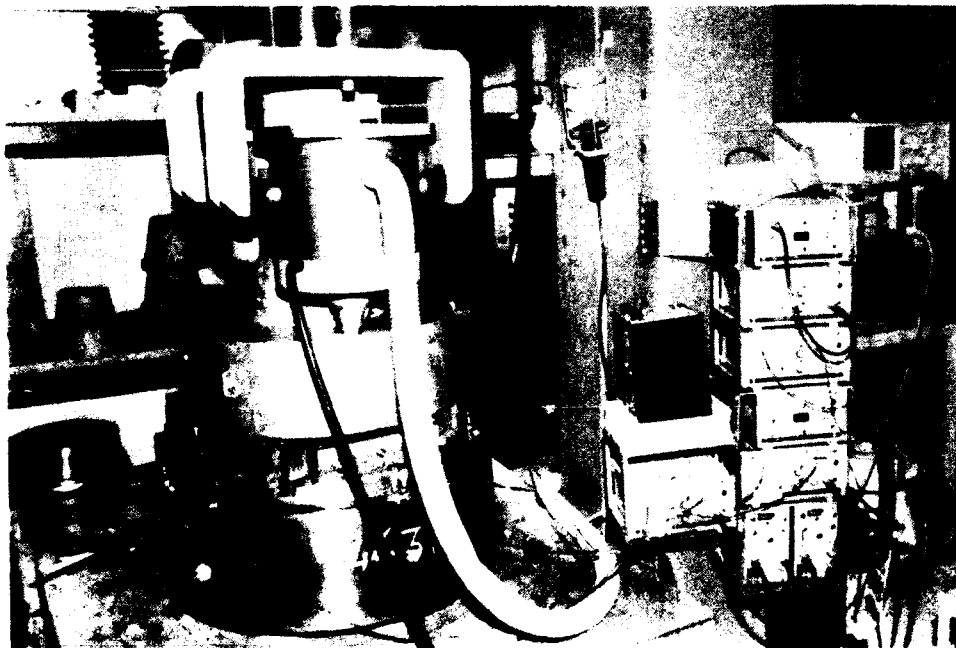
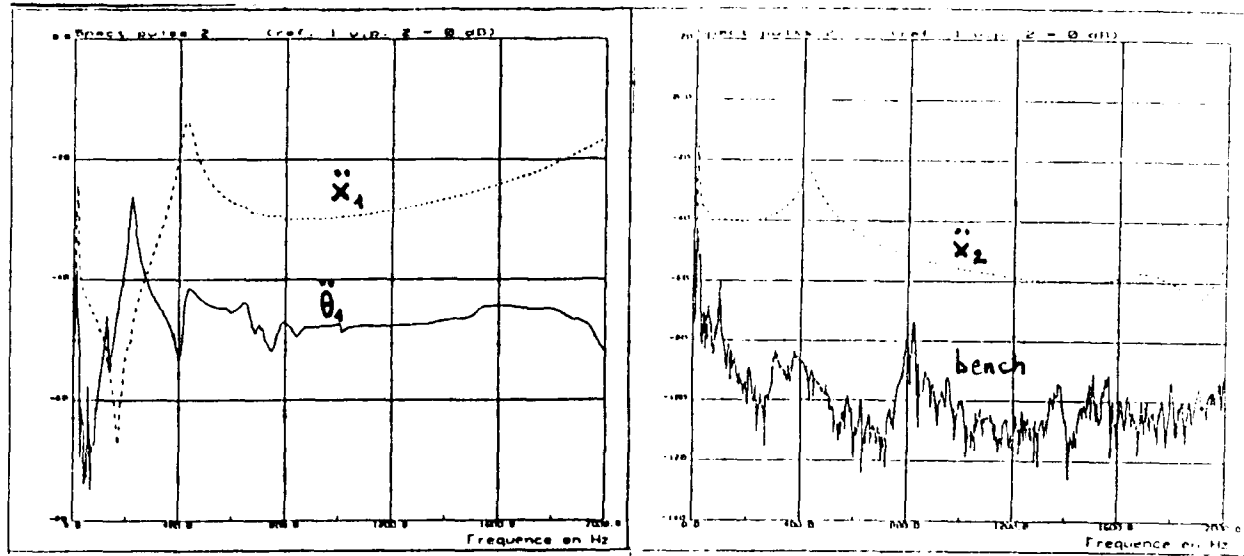
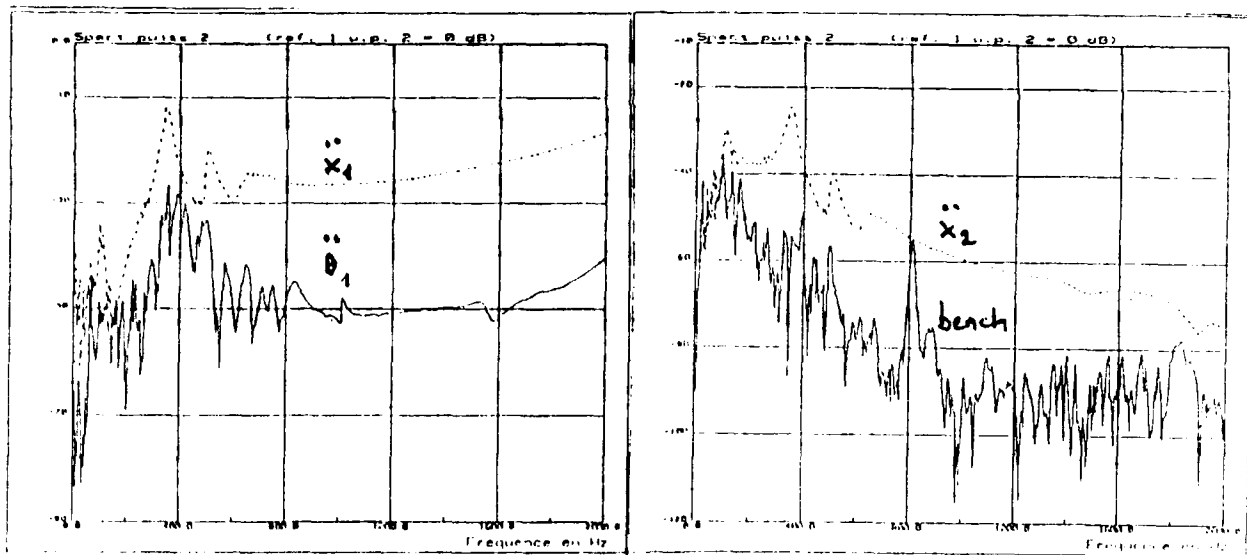


Figure 1-b : measurement rig with diametrically opposite transducers (see lower mass) connected to analog additives and subtractive devices (ASD and VCCD on the right part of the picture).



(a)

(b)



(c)

(d)

Figure 2 : control measurements for vertical tension-compression.

(a) input mass acceleration and spurious rotation; (b) output mass and lower part of the bench accelerations (the contrast checks the good isolation of the mounting).

(a) and (b) curves come from a testing under a static preloading of 1 bar; (c) and (d) are obtained for a preloading of 11 bars : one can notice the degradation on the experimental conditions.

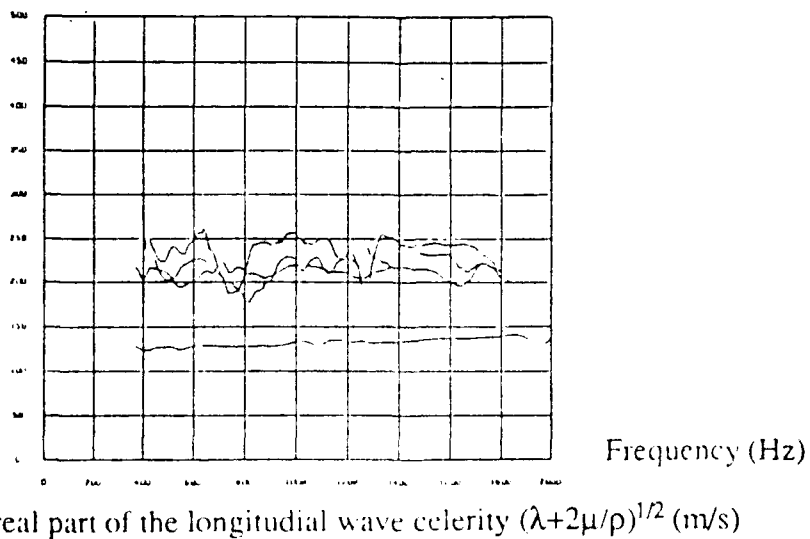
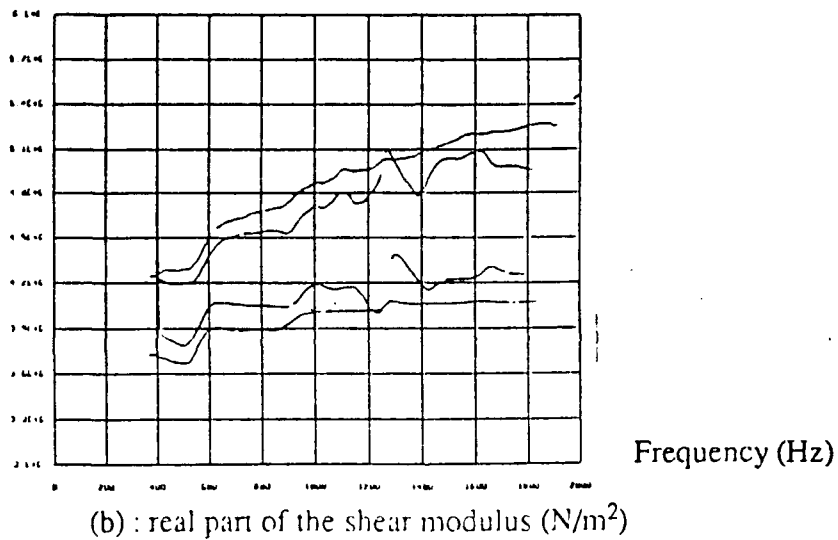
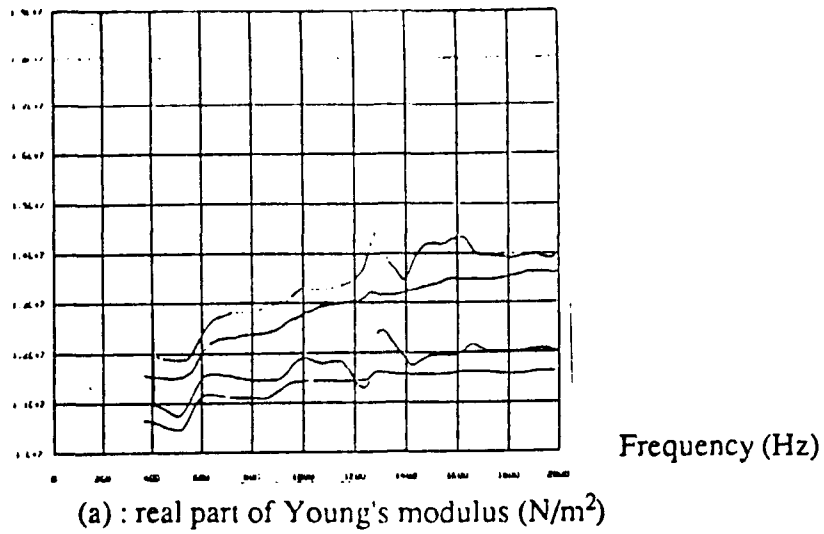


Figure 3 : visco-analyser results for 4 cases of temperature and pressure. The specimen is a small beam in tension-compression for Young's modulus measurement (a), in torsion for the shear modulus (b). Using relations between elastic constants one deduce the longitudinal wave celerity (c).

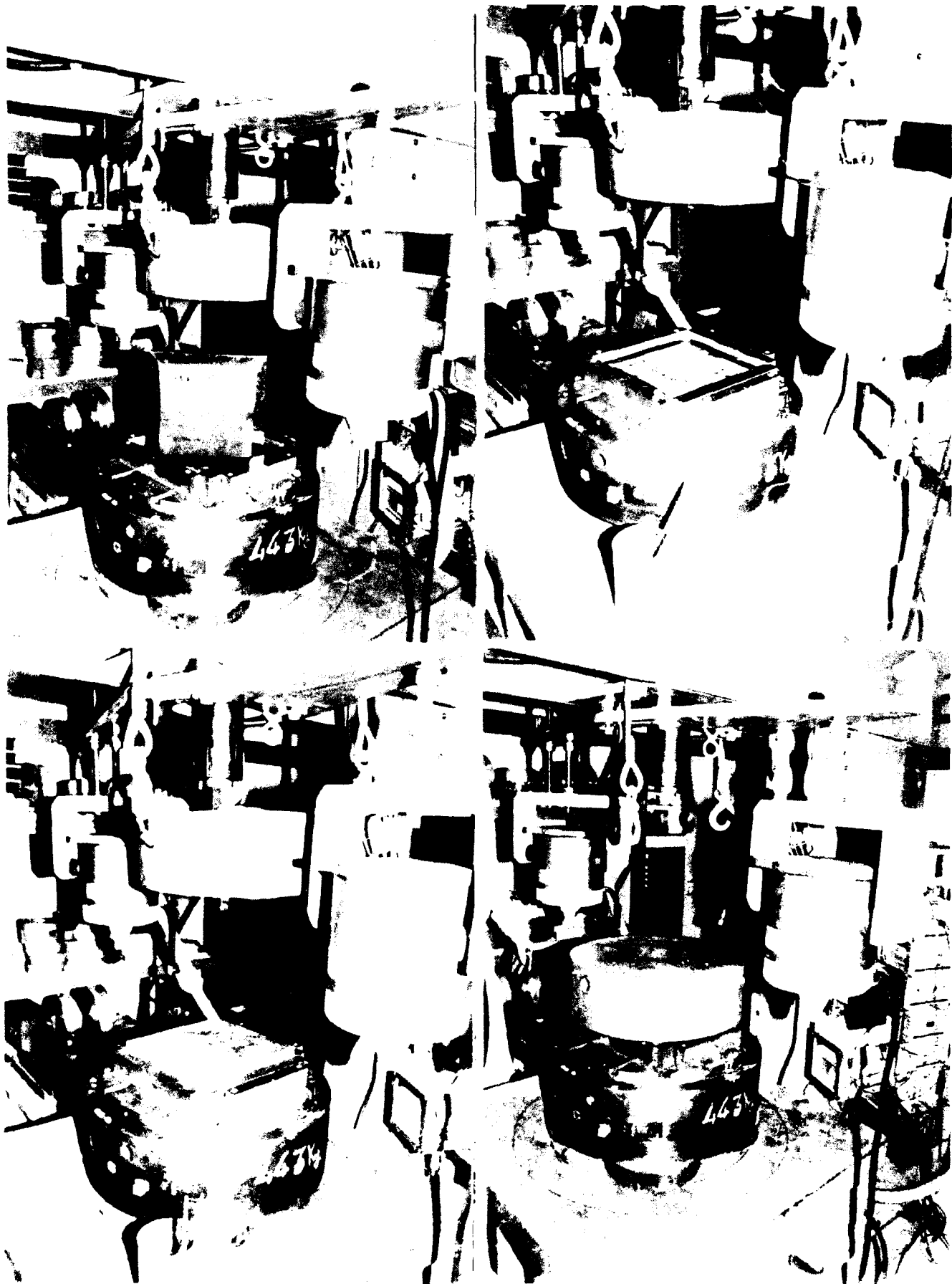


Figure 4. installation of the square panel specimen. The square blocking framework (a) encloses the specimen (b). Then we superpose the plane excitation piston (c) and the input upper mass (d).

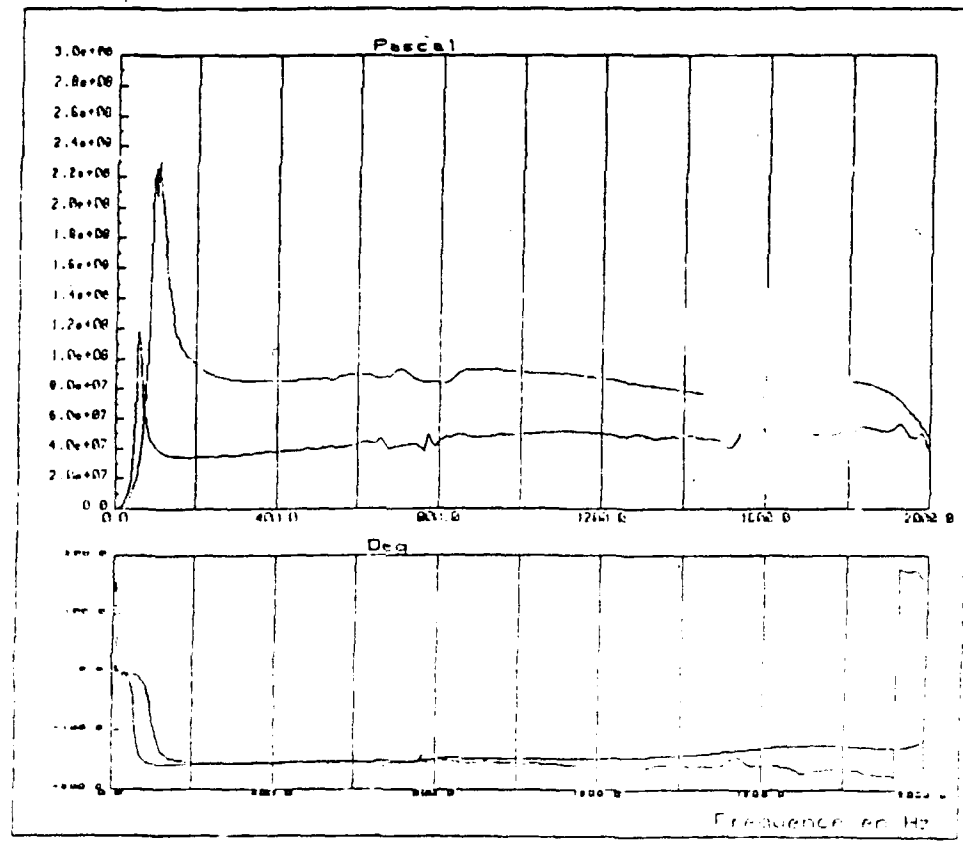
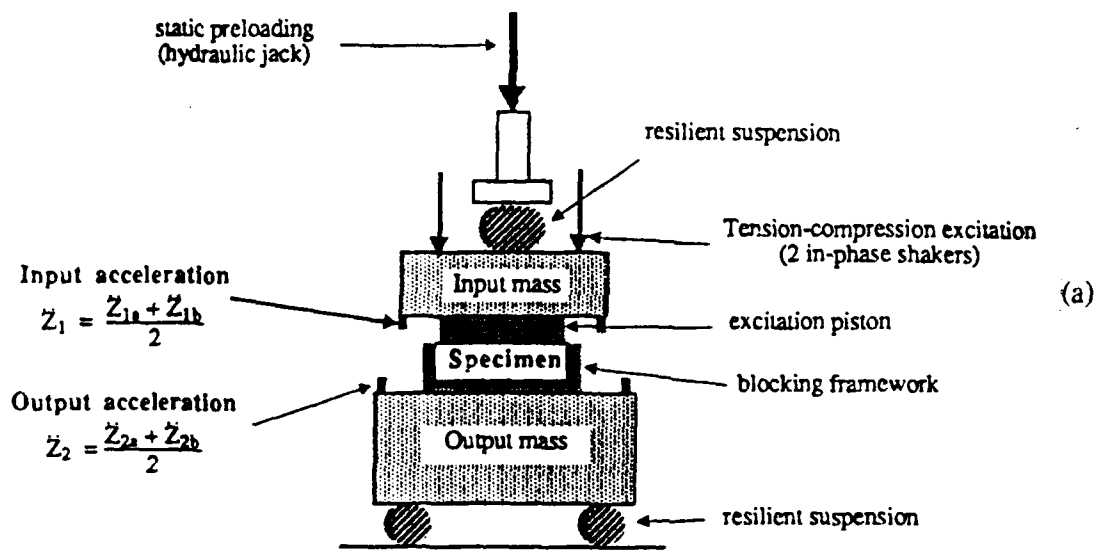


Figure 5 : measurement of the longitudinal bulk modulus $\lambda+2\mu$ (N/m^2). (a) : experimental mounting. (b) : resulting curves for a material under 1 bar and 8 bars static pressures. One can notice the significant flat part of the curves, the limiting low frequency resonance peak, and the 180° constant phase due to a sign error (true value 0°). Presence of damping would smooth the peak and shift the phase.

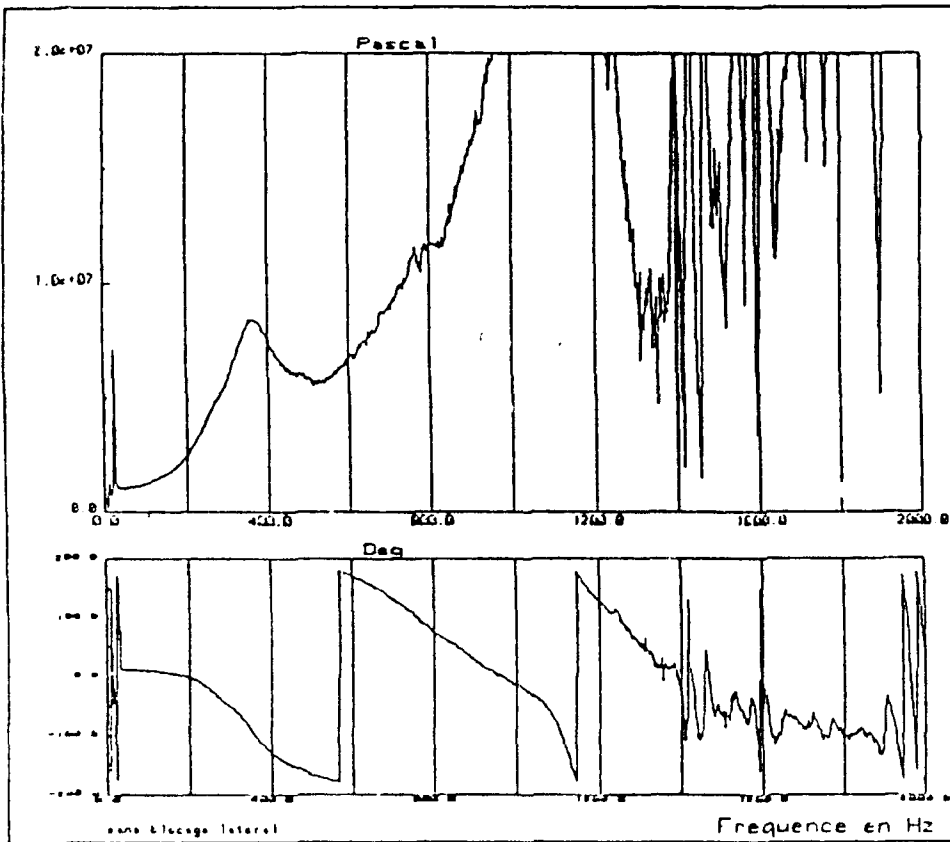
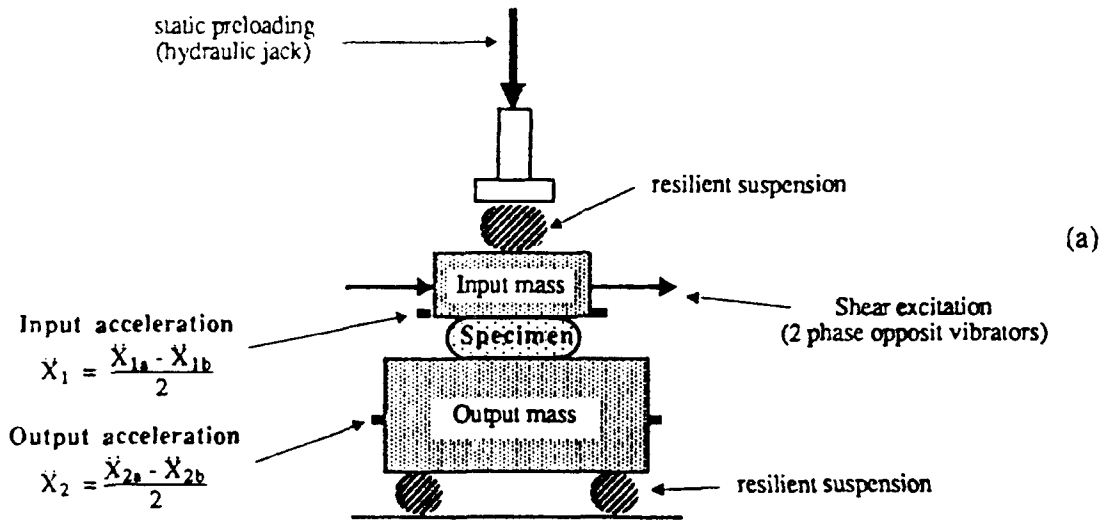


Figure 6 : measurement of the shear modulus (N/m^2). (a) : experimental mounting. (b) : resulting curve for a material at atmospheric pressure. One can notice the very low resonance peak due to a too heavy output mass. Background noise and spurious rotation peaks pollute this measurement from a hundred Hz.

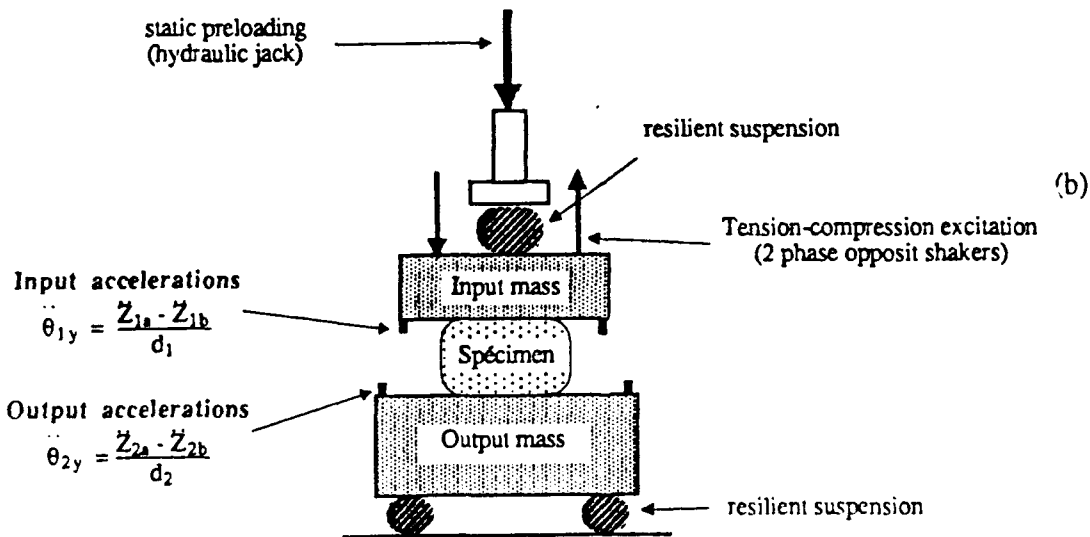
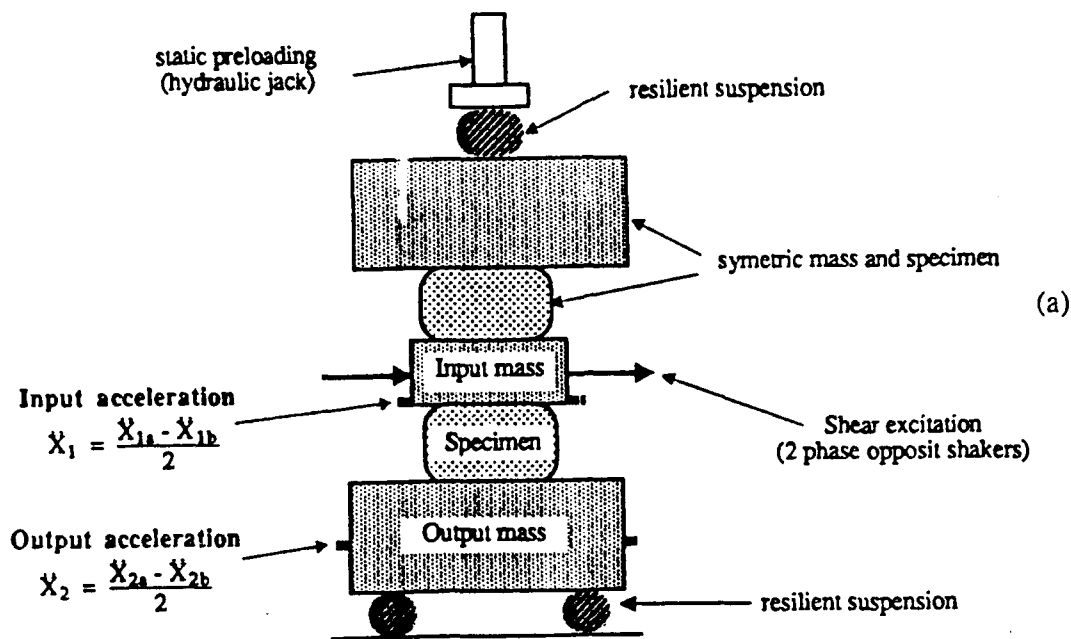


Figure 7 : (a) symmetric mounting for the shear modulus measurement. (b) mounting for the rotation stiffness measurement : it is the same as tension-compression but with phase opposite transducers.

CONTROLLING THE DAMPING BEHAVIOR OF PITCH-BASED CARBON FIBERS

*Andrew J. Eckel**

National Aeronautics and Space Administration
Lewis Research Center
Cleveland, OH 44135

and

Steven P. Jones

Clemson University
Clemson, SC 29632

The damping capacity of intercalated graphite fibers has been found to be significantly greater than that of pristine fibers. An effort is discussed to control and optimize the damping behavior via intercalation. A resonant flexural free decay test method was used to measure the damping of single pristine and intercalated pitch-based carbon fibers (Thornel P100). The fibers were tested in high vacuum, at temperatures from 77 K to 675 K, and at frequencies from 50 to 2000 hz. The fibers were intercalated by two methods. The resulting damping capacities are compared and contrasted. The effects of changes in the intercalation processes are discussed as a means of controlling the fiber damping capacity. In addition, the retention of increased damping capacity following thermal cycling was measured and is discussed.

* NASA Lewis Research Center, MS 106-1, 21000 Brookpark Rd., Cleveland, OH 44135, ph. (216) 433-8185

BACKGROUND

$$\zeta_{\text{composite}} = \zeta_{\text{fiber}} \frac{E_{\text{fiber}}}{E_{\text{composite}}} + \zeta_{\text{matrix}} \frac{E_{\text{matrix}}}{E_{\text{composite}}}$$

- ▶ **UNIQUE FACILITY FOR MEASUREMENT OF DAMPING CHARACTERISTICS OF SINGLE FILAMENT FIBERS.**
- ▶ **COOPERATIVE RESEARCH WITH SPARTA, INC. SHOWED DAMPING CAN BE INCREASED SIGNIFICANTLY USING INTERCALATED FIBERS.**
- ▶ **TECHNOLOGICALLY SIGNIFICANT DAMPING PEAK OBSERVED IN TEMPERATURE RANGE OF INTEREST FOR VAPOR BROMINATED P100 FIBERS.**

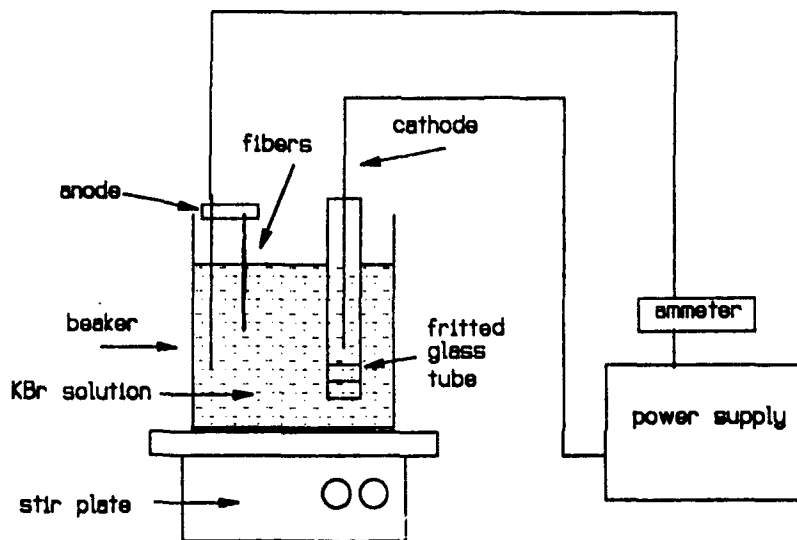
The majority of intrinsic material damping in polymer and metal matrix composites is contributed by the fibers rather than the matrix damping properties. Increased damping can reduce or eliminate vibration loads and reduce acoustic noise. Additionally, passive damping, via fibers in composites, is an important attribute for many space structures and could alleviate the need for more complex active damping mechanisms. A flexural free decay fiber test facility enables the measurement of the damping characteristics of single filament fibers [1]. This is beneficial for both providing constituent data for modelling composite behavior and allowing direct and simple measurement of changes in fiber damping behavior resulting from chemical or physical treatments.

Using the facility, Lesieutre et al [2-4] measured the damping characteristics of various graphite fibers and demonstrated that the damping capacity of pitch-based graphite fibers can be significantly increased by intercalation treatments. The authors reported a damping capacity peak on the order of 3 percent, in a narrow temperature range, for P100 fibers intercalated via a bromine vapor treatment.

CURRENT WORK

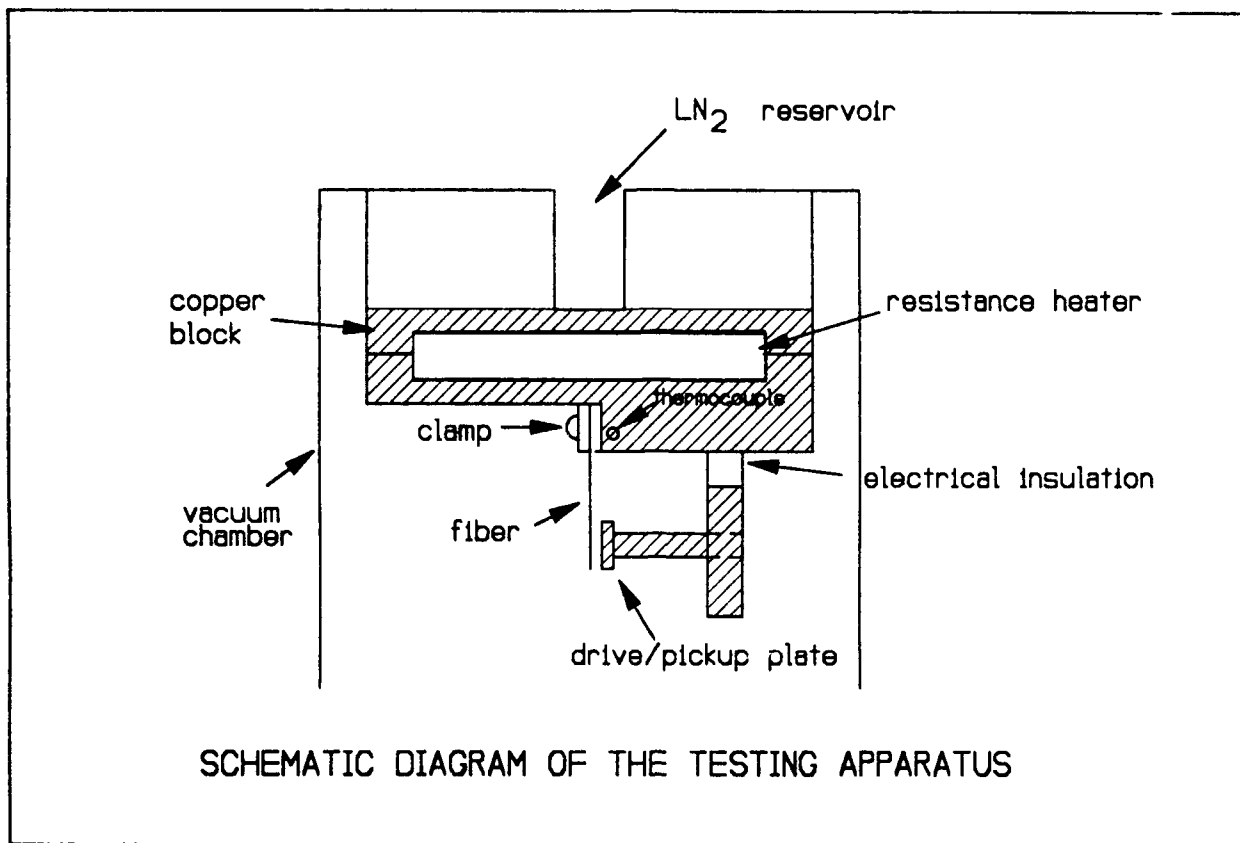
- **TO EVALUATE THE DAMPING BEHAVIOR OF P100 FIBERS INTERCALATED ELECTROCHEMICALLY.**
- **TO ASSESS AND DEMONSTRATE THE FEASIBILITY OF TAILORING FIBER DAMPING PROPERTIES VIA ELECTROCHEMICAL INTERCALATION.**

Ho and Chung [5] demonstrated that P100 fibers can be intercalated by both vapor and electrochemical methods. Since electrochemical methods allow greater control of intercalation parameters, this study is being undertaken to evaluate the damping differences between vapor brominated and electrochemically brominated P100 fibers. Comparison of damping from the two methods and the greater control of the electrochemical technique may allow determination of the mechanisms at work that result in various damping behavior. This work-in-progress paper summarizes the research to date and demonstrates the feasibility of tailoring fiber damping properties via electrochemical intercalation.



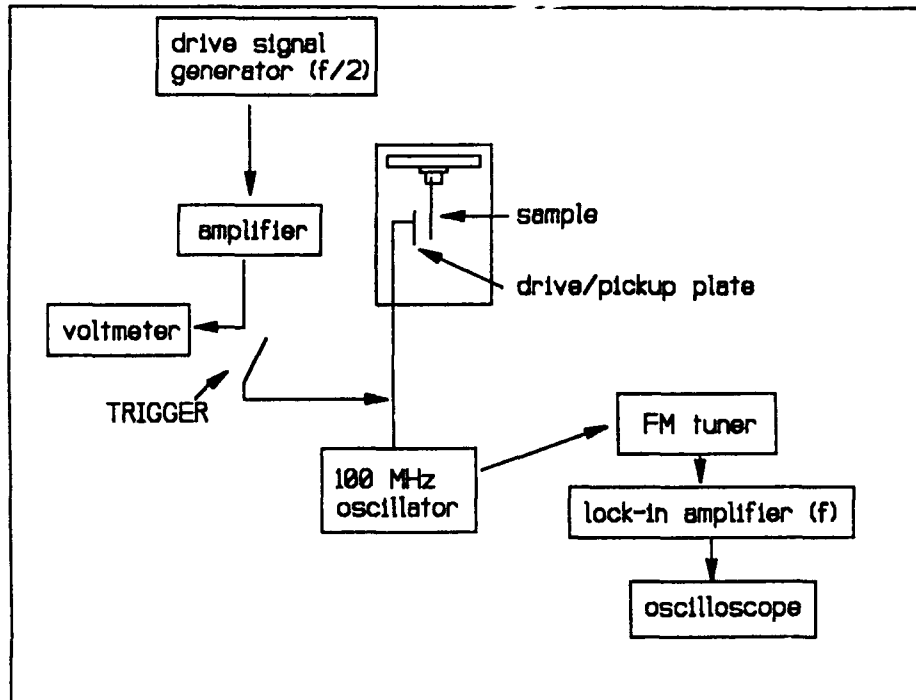
SCHEMATIC DIAGRAM OF INTERCALATION PROCESS

The intercalation process used was similar to the one used by Ho and Chung [5], with some minor modifications. Pristine P100 graphite fibers, unsized and continuous filaments, were used in this study. Fiber tows of approximately 2000, 10 μm diameter filaments were suspended in a saturated aqueous potassium bromide solution. A constant current was then passed through the tow and platinum fixture. The fixture, with tow, was removed from the solution at specific time increments (25, 49, 80, and 100 h.) After each removal, the tow was thoroughly rinsed with deionized water, and allowed to dry overnight in air at room temperature.



Individual fibers were removed from fiber tows and mounted in tantalum tabs following the procedure described by Lesieutre et al [2,4]. The mounted fiber specimen was clamped to a copper block which served as both a seismic and a thermal mass. The temperature of the block was controlled by pouring liquid nitrogen into a reservoir on the top, initially cooling to 77 K (-196 C) and then slowly heating to 673 K (400 C) by adjusting the current through an embedded resistive heater. A thermocouple attached to the block near the fiber root measured the temperature. The combination of high fiber longitudinal thermal conductivity and slow heating rates (2 K/min) ensured that the fiber temperature was effectively that measured by the thermocouple. Data points were taken usually every 15-20 K, depending on the situation. The drive/pickup plate was mechanically attached to the specimen mounting block, but was electrically insulated from it. The entire block was placed inside a vacuum chamber (10^{-4} to 10^{-6} torr) to eliminate the effects of air damping, which was significant on these fibers.

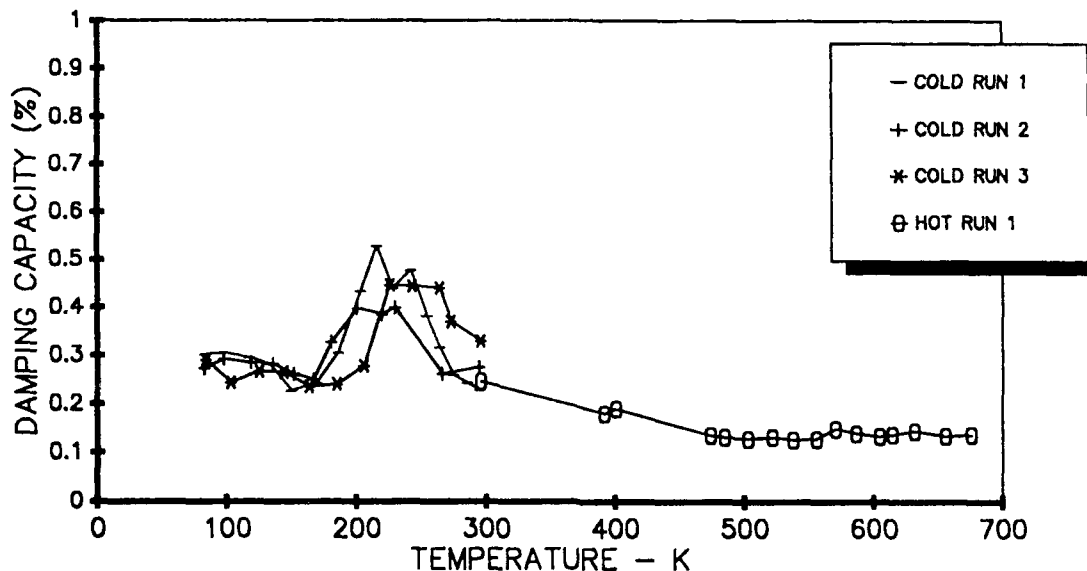
ELECTRONICS SCHEMATIC



The fiber was driven electrostatically at one of its resonant flexural frequencies, f_n , by applying an alternating voltage at $f_n/2$ between the fiber and an adjacent drive plate [1]. The fiber-plate separation was adjusted by a screw type manipulator attached to the drive plate. Specimen vibration amplitude was controlled by the output voltage from the drive amplifier. Strain amplitudes at the fiber root surface were on the order of 10^{-6} , and no significant amplitude-dependence of damping was observed for amplitudes near this level.

Specimen motion was detected by placing the fiber-plate capacitor into the tank circuit of a 100 MHz RF oscillator. Fiber vibrations produced an oscillating capacitance which directly modulated the RF oscillator via a half-wavelength coaxial cable. A commercial FM tuner detected these modulations and converted them back to an audio signal with frequency f_n and amplitude directly proportional to that of specimen vibration. Damping was determined by disconnecting the drive signal (triggering the signal) and allowing the fiber resonant vibrations to decay freely. The decaying signal was displayed on an oscilloscope and recorded photographically. Damping values are calculated from free decay data and are reported as damping capacity ($\psi = \Delta w/w =$ relative vibration energy lost per cycle).

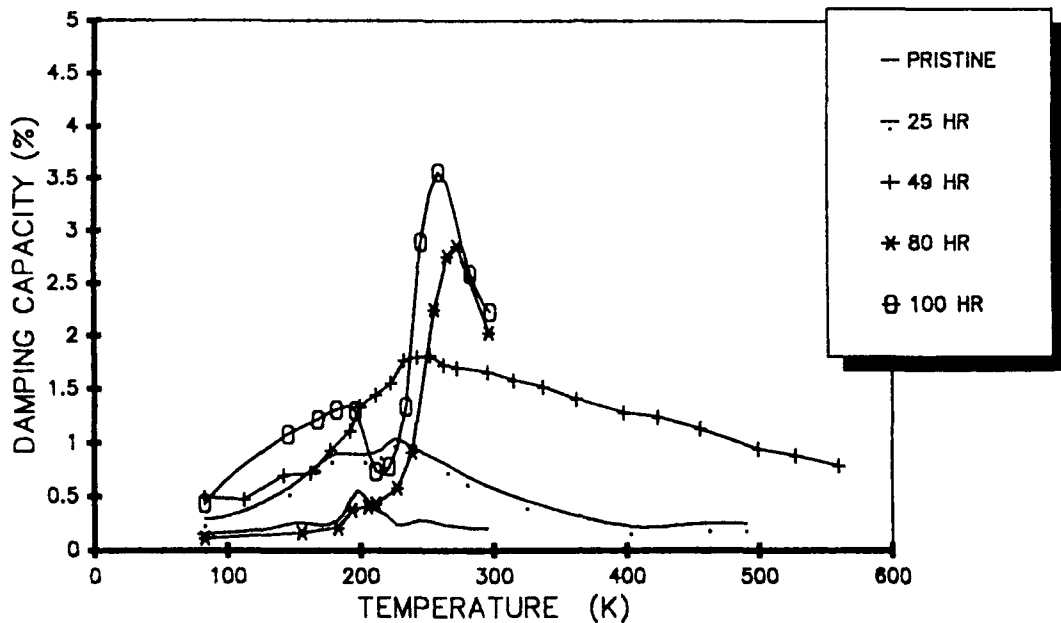
DAMPING BEHAVIOR OF PRISTINE P100 GRAPHITE FIBERS



Various treatments were performed on *pristine P100* graphite fibers to determine their effects on damping behavior. These included vacuum cycling, thermal cycling, and exposure to air and nitrogen gas. These were performed since they are typical of treatments the fibers may see during composite processing.

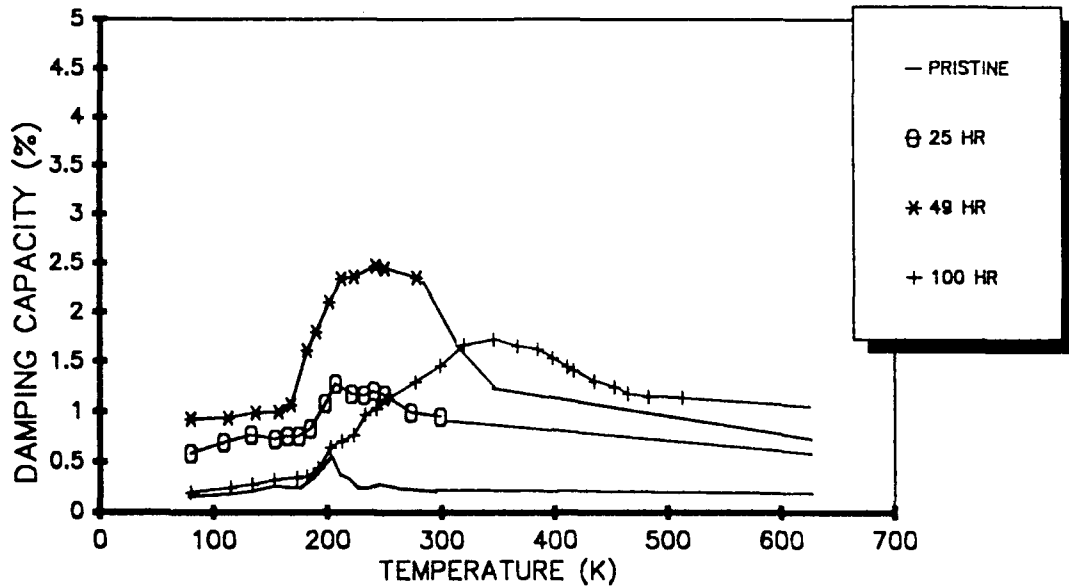
Upon heating from liquid nitrogen to room temperature (cold run 1) the *pristine P100* fiber exhibited a damping peak at 213 K (-60 C) which is small in magnitude, with ψ about 0.5%. The thermal cycling included runs to elevated temperatures (673 K [400 C], hot run 1) and back to cold temperatures (77 K [-196 C], cold run 2). During this thermal cycling, the damping peak location remained the same at 213 K (-60 C), and the peak height remained virtually unchanged at 0.5%. Also, the third cold temperature run (cold run 3) was conducted after the test chamber was brought up to atmospheric pressure in air for 24 h and then re-evacuated. There was no change with any of these treatments to the damping of the *pristine* fibers. The next treatment was exposure to gaseous nitrogen (not shown). After evacuation, the vacuum chamber was back filled with gaseous nitrogen for 18 hours. Damping data was then taken on the fiber. The damping peak again occurred at a temperature in the vicinity of 213 K (-60 C) and had a peak height of 0.45%. This value is almost identical to the *pristine* fibers. Also, the baseline remained around 0.18%, similar to the *pristine* fiber. It can then be concluded that these basic treatments to the *pristine* fibers do not introduce significant changes in damping behavior.

COMPARISON OF P100 GRAPHITE FIBERS BROMINATED AT 50 μ A



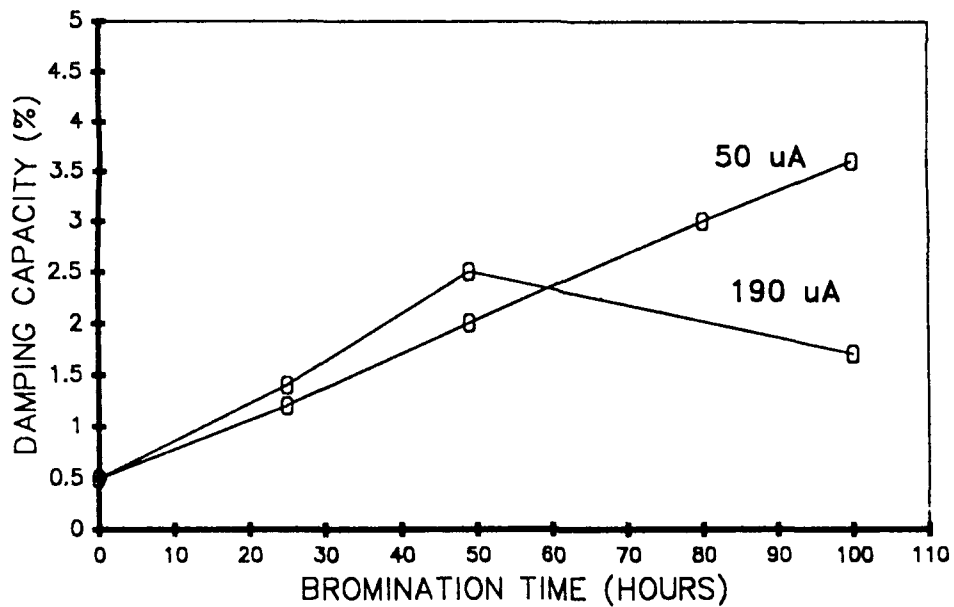
To determine the effects of electrochemical bromination parameters, a current of 50 microamperes (μ A) was selected and the fibers were brominated for 25, 49, 80, and 100 h. The damping peaks increased in magnitude, as well as shifting to higher temperatures, as bromination times increased. The 100 hour test showed the highest peak magnitude, $\psi_{\max} = 3.6\%$, at 253 K (-20 C). The peaks shift to higher temperatures as a result of increased concentrations of bromine added to the fiber. In addition, all of the 50 μ A samples showed a second, smaller peak between 133 and 183 K (-140 C and -90 C.) This peak is quite small in magnitude, except for the 100 hour test, in which the peak has a magnitude of approximately 1.4% and occurs at 183 K (-90 C.)

COMPARISON OF P100 GRAPHITE FIBERS BROMINATED AT 190 μ A



The next step was to determine if increased currents and corresponding increases in bromine concentration would further improve the damping behavior of the fibers (actual determination of bromine mass and mass distribution in single fibers is difficult and has not yet been done.) The current was increased to 190 μ A and fibers were brominated through a similar cycle as the 50 μ A samples. The damping continually increased until the 49 h point where it had a peak of 2.5%. Temperatures at which damping peaks occurred increased as the bromination time increased. At 100 h, the peak magnitude decreased to 1.7% and the temperature of the peak was 60 C. No explanation for this behavior is provided, although work is still proceeding. The baseline itself also had a value 5 times that exhibited by pristine graphite fibers, measuring approximately 1.0%.

PEAK MAGNITUDES OF BROMINATED P100 GRAPHITE FIBERS
ELECTROCHEMICALLY INTERCALATED



The peak magnitudes of damping for the electrochemically intercalated fibers generally increased with time of bromination. Work is continuing to evaluate a broader range of currents and investigate the decrease in damping for the 100 hour bromination treatment at 190 μ A.

CONCLUSIONS

- P100 GRAPHITE FIBERS INTERCALATED ELECTRO-CHEMICALLY DEMONSTRATE SIGNIFICANT INCREASES IN DAMPING VALUES OVER PRISTINE FIBERS.
- THE DAMPING CHARACTERISTICS OF P100 GRAPHITE FIBER CAN BE TAILORED BY ELECTROCHEMICAL INTERCALATION.
- THE HIGHEST DAMPING OBSERVED TO DATE (~ 3.5%) IS OBTAINED AT LOWER INTERCALATION CURRENTS AND LONGER TIMES.
- ADDITIONAL STUDY IS NEEDED TO RESOLVE MECHANISMS FOR DAMPING BY BROMINE INTERCALATION.

- [1] J.A. DiCarlo and J.E. Maisel, "Measurement of the time Dependent Dynamic Mechanical Properties of Boron/Aluminum Composites." p 201-27 in Fifth Conference on Composite Materials: Testing and Design. ASTM-STP-674, Amer. Soc. for Test Materials, Philadelphia, Pa., 1979
- [2] G.A. Lesieutre, A.J. Eckel, and J.A. DiCarlo "Temperature Dependent Damping of Some Commercial Graphite Fibers" Metal Matrix, Carbon and Ceramic Matrix Composites, NASA CP-3018, 125-133, 1989.
- [3] G.A. Lesieutre, A.J. Eckel, and J.A. DiCarlo "Increased Graphite Fiber Damping via Intercalation" pp. GDA1-GDA9 in Proceedings of Damping '89, WRDC-TR-89-3116, Vo. II, 1989.
- [4] G.A. Lesieutre, A.J. Eckel, and J.A. DiCarlo "Damping of Bromine-Intercalated P100 Graphite Fibers" Accepted for publication in Carbon February, 1991.
- [5] C.T. Ho and D.D.L. Chung "Carbon Fibers Brominated by Electrochemical Intercalation" Carbon, Vol 28,4 521-528 (1990).

INTERNAL DAMPING OF METAL MATRIX COMPOSITES: A TECHNICAL ASSESSMENT

Jacques E. Schoutens
MMCIAC
Kaman Sciences Corporation

ABSTRACT

Internal damping in metal matrix composites (MMC) is of interest to engineers and designers of large space structures, in applications where dynamic dimensional stability is important, and in the control and damping of vibrations in space structures. Theories of current interest used to understand and explain internal damping in MMCs are discussed briefly, and experimental data for some fibers and MMC systems are presented. Some general conclusions close this paper.

INTRODUCTION

Damping of structures has two sources: external and internal. External sources of damping include the effects of fluids such as drag in a liquid or in a gas, loss of energy at supports or joints due to friction or transmission into supporting structures, and active and passive damping control systems. Internal sources of damping include a number of effects. At low levels of stress, the damping behavior of metals and metal matrix composites is governed by micromechanisms causing anelastic behavior. At high levels of stress [1,2] internal damping occurs by mechanisms leading to hysteretic response. Internal damping in metals has been used as a method of studying atomic motion at low stress levels. This has provided insight into fundamental mechanisms in diffusion, ordering, interstitial and substitutional solid solutions, and estimates of dislocation densities. For engineering applications, damping data have been obtained at intermediate and high strain levels (> 50 microstrain) to develop insight into energy dissipation mechanisms and fatigue life of metal components. As is well-known, the interface between a fiber and the matrix is a unique site of reaction layers, residual stresses, microvoids, dislocation structures, impurities, disbonds, and other defects. It has been postulated, and to some extent verified, that the interface is also a source of energy dissipation, and considerable efforts have been expended in attempting to identify and model these sources [3]. It should be borne in mind that selecting materials for effective damping must take account of the space environment (zero gravity, high vacuum, and thermal fluctuations between -160 to $+160^{\circ}\text{C}$), and candidate materials must exhibit high damping at low frequencies (0.1 to 10 Hz) [2] and at strain levels on the order of 50 microstrain.

This paper presents a brief discussion of currently used theories of internal damping in MMCs, and presents some of the available data on internal damping of these advanced materials. For more details, the reader is referred to reference 4 or 5.

816 State Street, P.O. Box 1479, Santa Barbara, CA 93102-1479, (805)963-6426.

THEORY

The methods for measuring damping in metals and metal matrix composites span some seventeen orders of magnitudes in frequency, from about 10^6 Hz to 100 GHz. There are four major categories covering this range: quasi-static methods, subresonance methods, resonance methods, and high frequency wave propagation methods [5]. The quasi-static method is of no interest in this paper, and the high-frequency range will not be discussed because it is used mainly to measure dynamic moduli and other phenomena [8].

The damping properties of a material are variously referred to as specific damping capacity, loss factor, loss angle, quality factor, and log decrement. These quantities are all related as follows [4,5]

$$\Psi = 4\pi\xi = 2\pi Q^{-1} = 2\pi\eta = 2\pi\tan\phi = 2\zeta \quad (1)$$

where Ψ is the specific damping capacity (SDC), ξ is the damping ratio, Q is the quality factor, η is the loss factor, ϕ is the loss angle and ζ is the logarithmic decrement. Most of the data presented in this paper will be in terms of the specific damping capacity.

The methods used to measure damping properties are discussed in detail in reference [4]. Suffice it here to mention that they include the cantilever beam method, free-free flexure method, torsion-tension method, free fall method, piezoelectric ultrasonic composite oscillation technique (PUCOT) [5], and the method of wave propagation. These methods give slightly different results; consequently, data must be corrected accordingly [4,5]. Damping factors are measured as a function of strain amplitude, temperature or frequency.

The following summarizes the various damping mechanisms and the theories used to explain these mechanisms. Note that some theories predict certain behavior fairly well in a particular range of interest, but by and large, theoretical models used to predict damping behavior are rather primitive, particularly for MMCs. Little or no theoretical work has been done for the fiber/matrix interface.

Matrix Metal. Damping in the matrix metal can occur from any one or all of the following mechanisms: point defect damping, dislocation damping, grain boundary damping, and thermoelastic damping.

A point defect in a crystal can be a vacancy or extra atom either in the crystal lattice or as an impurity atom. This alters the crystal, thereby lowering the crystal symmetry, termed a defect symmetry. The criterion for the existence of point defect damping is that there must be more than one distinguishable orientation of the defect. The elastic distortion surrounding the defect causes the point defect to interact with the crystal lattice, behaving as an elastic dipole. Different defects will interact differently causing some redistribution of the orientation of the point defects. The point defect damping mechanism. For models with a crystal lattice, the following types of defects having non-symmetrical strain fields give rise to

damping [5]: interstitial impurities, vacancy-impurity pairs, and divacancies. Spherically symmetric strain fields do not cause damping. The first of these defects give rise to Snoek relaxation, and the second to Zener relaxation. Snoek relaxation is expected to contribute to damping in MMCs with bcc crystal lattices, and Zener relaxation contributes to internal friction in alloys [4,5] of fcc, bcc, and hcp structure.

Dislocation damping plays an important role in crystalline MMCs. This damping mechanism involves the motion of dislocations which lag behind the applied stress. In some metals (Cu for example) the application of stress will also cause the generation or multiplication of dislocations. Damping occurs when dislocations are hindered in their motion by obstacles such as point defects. There are two relevant mechanisms in MMCs; relaxation or resonance absorption (Zener), and hysteresis losses. Granato and Lucke [4,5,7] developed a model for dislocation damping that is based on the vibrating string model, where the string is the dislocation motion while pinned at both ends by defects. This is an important model because it has been used to calculate mobile dislocation densities and the spacing between impurity atoms on dislocation lines from measurements of strain amplitude dependent damping [5].

Zener [6] predicted that grain-boundary relaxation occurs by viscous sliding between adjacent grains. Nowick and Berry [7] show that the viscous slip model predicts a relaxation that is essentially independent of grain size, as long as the grain size is less than the specimen diameter. A satisfactory quantitative theory of grain-boundary relaxation is not yet available [5].

Thermoelastic damping is the result of coupling between the conjugate pair stress and strain, and the conjugate pair temperature and entropy, as for example during expansion where the specimen length can be changed by stretching or by heating. This means that a change in entropy with respect to stress ($T=\text{const.}$) is equal to the change in strain with respect to temperature (constant stress), and is identical to the coefficient of thermal expansion [5]. When a beam, plate, or rod vibrates, relaxation takes place under inhomogeneous stress. Bending of isotropic materials induces uniaxial strain which varies linearly with distance from the neutral axis. As the beam vibrates, an alternating temperature gradient is set up across the beam, and relaxation occurs by heating and heat transfer across the specimen. In the case of longitudinal thermal currents induced by vibrations, Nowick and Berry [7] showed that this kind of damping is negligibly small at frequencies below 100 MHz.

Fiber. Only limited experimental results and theoretical modeling have been reported. The fiber is usually assumed to be a perfectly elastic material contributing little or no damping to MMCs [9]. Internal damping in boron fibers and whiskers was studied experimentally and theoretically using torsional oscillations [10-12]; Postnikov et al [13] using bending oscillations in the kHz range studied the internal friction in boron fibers. These researchers obtained dynamic modulus data as a function of temperature. Internal friction in boron fibers is characterized by a peak between 530 and 630°C. Models published so far treat continuous fibers as a single material, which clearly is not correct. Continuous fibers are built up on a substrate of either tungsten or carbon; the outer surface of the fiber is coated, sometimes with an elastically compliant coating and/or a reaction barrier.

Fiber/Matrix Interface Damping. The presence of an interface and/or a reaction layer between fiber and matrix raises the possibility of introducing a controlled source of damping in metal matrix composites. Modeling of the effects of damping on MMCs by Nelson and Hancock [15] predicted the interface friction slip. Their model consisted of a frictional energy loss at the interface and viscoelastic energy dissipation in the matrix when the composite is subjected to cyclic tensile loading. Good agreement with experiment was noted for a model consisting of discontinuous, aligned fibers, loaded along the fiber direction. Transverse loading of a linearly elastic material with rigid cylindrical reinforcement was modeled by Kishore et al. [16,17], in which no slip, slip, and interface separation could be introduced; only frictional losses were considered. The loss factor, not surprisingly, was found to depend on fiber volume fraction, coefficient of friction at the interface, load amplitude and constraint stresses at the interface. Whisker or particulate reinforced matrix may exhibit increased specific damping capacity due to stress concentrations near the ends of the reinforcement; stress concentration results in increased dislocation density. Ledbetter and Datta [18] modeled the internal friction for scattering of stress waves by elastic particles dispersed in the matrix, and predicted an increase in friction with increasing particle concentration, increase in particle characteristic length, reduction in aspect ratio, and increases in the difference between particle and elastic stiffness. A more recent model proposed by Ledbetter et al [8] suggested an approach followed up by Schoutens [14] with a simple model based on the thickness of the reaction layer. No results were obtained because of the difficulty in assigning some damping properties and friction coefficients for the reaction layer. Modeling of damping caused by the presence of discontinuous fiber reinforcement in a metal matrix indicates that damping is increased by an increase in the fiber-end gap dimension, for a given fiber volume fraction, and a decreasing fiber aspect ratio [19]. Differences in the coefficient of thermal expansion between reinforcement and matrix produces residual stresses which produce dislocation substructure. Damping increases with increasing dislocation density. The amount of damping produced by these dislocations can be calculated with the Granato-Lucke theory [4]. The role of residual stresses at the interface has been verified by experiments [2]. These test results show that stress-relieved and T6 stress-relieved P55/6061 Al specimens exhibit lower specific damping capacity than the as-fabricated specimens. However, heat treatment is in the primary recrystallization range, and recrystallization is known to reduce damping by decreasing the dislocation density in the matrix, and by increasing the size of grains. Stress-relieved specimens showed nearly strain-amplitude-independent damping response even at intermediate strain amplitudes, while as-fabricated specimens showed strain-amplitude-dependent behavior. When stress-relieved specimens were reheated to 540°C (close to the consolidation temperature) and slowly cooled to room temperature, measurements showed damping values consistent with as-fabricated specimens.

Combined Mechanisms. In the absence of detailed theories to predict the specific damping capacity of MMCs, it is tempting to use the rule of mixtures to predict properties from those of the constituents. In this way, the specific damping capacity is predicted from the sum of specific damping capacity of constituents weighed by their fraction in the composite. The fraction of damping due to the interface reaction layer is also included in this sum. The matrix damping, is the sum of contributions from dislocations, point defects, grain boundaries and other relevant effects. This approach generally over simplifies the problem considerably, and in consequence cannot be considered as reliable. Hashin [20] showed how the correspondence principle may be used to relate the effective viscoelastic functions for composites to the effective

moduli. This method has resulted in reasonably good predictions of specific damping of MMCs [5].

For many MMCs, one or two damping mechanisms usually dominate for a given combination of strain amplitude, temperature and frequency. Predictions from dislocation damping (Granato-Lucke model) and thermoelastic damping (Zener relaxation) have turned out to be useful. For predicting damping from constituent properties, Hashin's correspondence principle has been useful [5].

INTERNAL DAMPING DATA

Internal damping data has been reported most often as specific damping capacity Ψ (SDC) in percent, and less often as the loss or quality factor. Damping is generally shown as a function of strain amplitude, frequency, or temperature. For example in pure aluminum, the damping capacity shows very little dependence on strain amplitude until the strain amplitude reaches approximately 10^{-4} , and beyond this point the damping capacity rises fairly steeply. Damping capacity, as we will show, varies also as function of frequency. The damping capacity also rises with increasing temperature, sometimes exhibiting a maximum. Table 1 presents the damping capacity of unreinforced structural materials. MMCs have a damping capacity in the 0.1% to 30% range at frequencies ranging from approximately 1 Hz to a few kHz.

Table 1 - Specific Damping Capacity (Ψ) for Some Unreinforced Structural Materials

Material	Ψ (%)	Frequency Range
403 SS Nivco NiTi Cast iron Cast Pure Mg	6-40	kHz
2024 T3 6061 T6 1020 Steel	0.4-3	Hz-kHz
310 SS Ti-6Al-4V	0.1 - 0.2	40 kHz
Brass MMCs	~ 0.06 ~ 0.1 - 30	kHz Hz-kHz

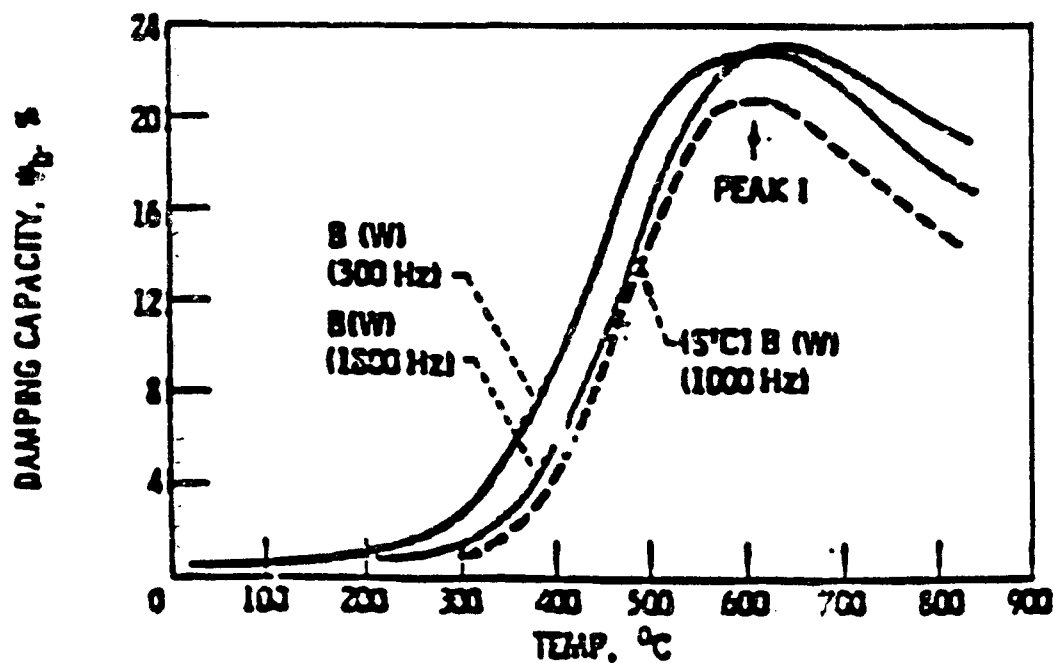


Figure 1 Damping Capacity of boron fiber and silicon carbide coated boron fibers [9]

Figure 1 shows the damping capacity of boron fiber and of silicon-carbide-coated boron fibers, as a function of temperature. Both filaments were produced on a tungsten core. The data were obtained at 300 and 1500 Hz for the boron fiber and at 1000 Hz for the SiC-coated boron fiber (Borsic). DiCarlo and Williams [9] noted that the damping capacity decreased with heat treatment cycles. The damping agrees with measurements on boron fibers made in the Soviet Union [10-13]. Borsic exhibits a consistently lower damping capacity over most of the temperature range of interest, compared to uncoated boron fibers. At 600°C, the damping of both fibers is approximately a factor of 20-23 higher than at room temperature. The prediction of the maximum damping capacity made by Postnikov et al. [13] is approximately a factor of 10 below measured values.

Figure 2 shows the damping capacity of silicon carbide fiber as a function of frequency and Figure 3 shows the damping capacity of the same fiber as function of temperature. Figure 3 we see a sharp rise in the damping capacity with a rise in temperature. Figure 2 shows that there is a significant effect on the damping capacity of the fiber due to thermoelastic effects. This effect rises above the damping capacity due to the microstructure. The peak damping capacity is at about 2500 Hz, where it has increased by a factor of about four above that of due to the microstructure. The curve seems to be fairly broad, ranging from approximately 200 Hz to 50 kHz. A similar but broader peak as a function of temperature has been reported for bromide treated pitch-base carbon fibers [21]. SiC fiber damping capacity is considerably lower than for boron fiber, by a factor of 10-12.

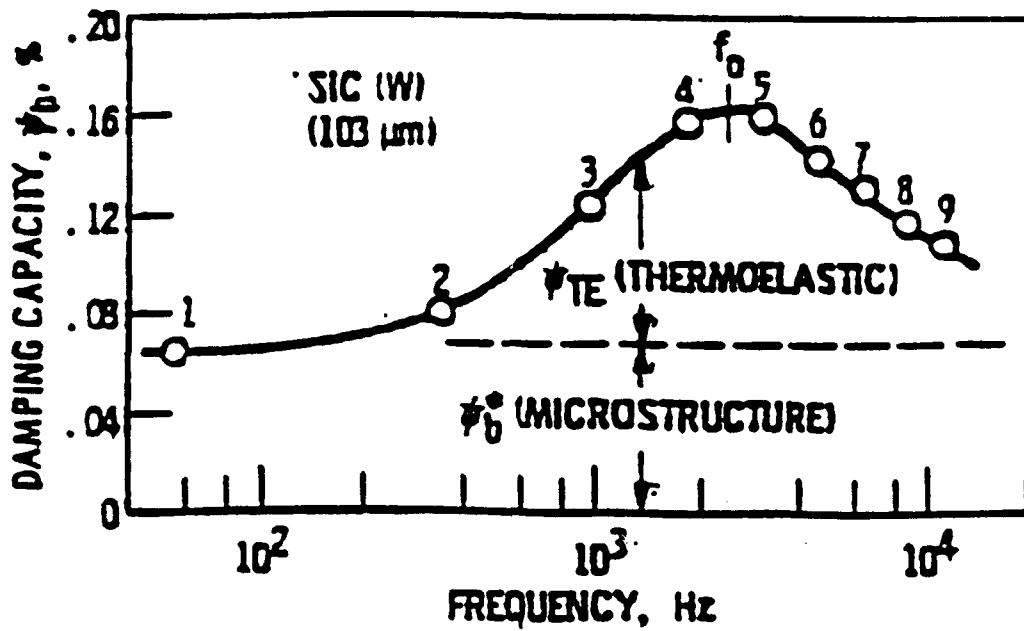


Figure 2 Damping capacity of SiC fiber at 26°C for the first nine flexural tones. Fiber diameter 103 μm . Core: tungsten [9].

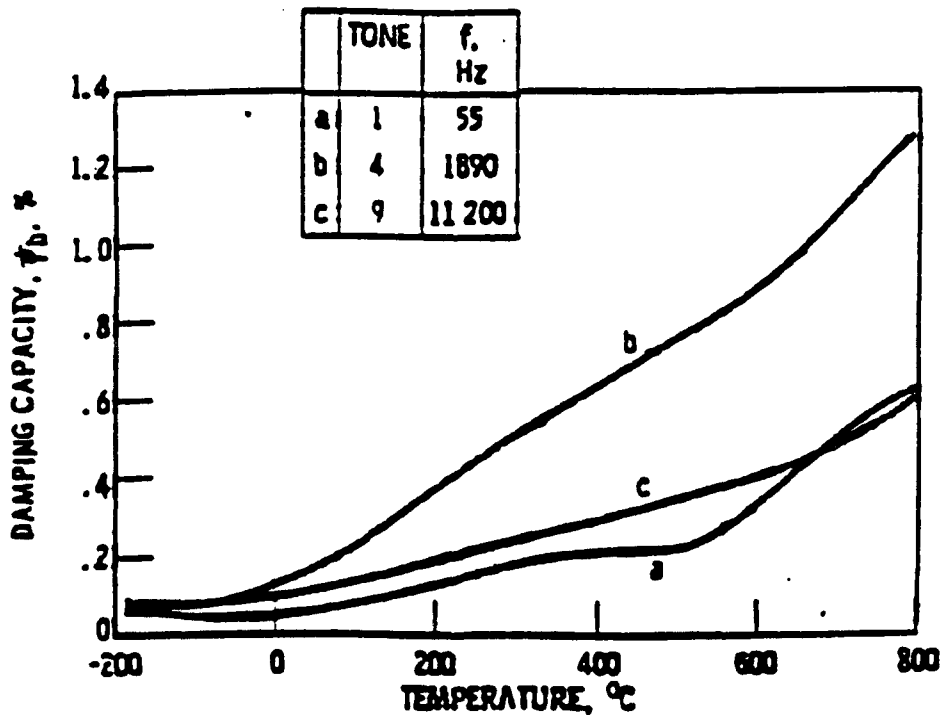


Figure 3 Damping capacity of SiC fiber at three flexural tones. Fiber diameter is 103 μm . Core: tungsten [9].

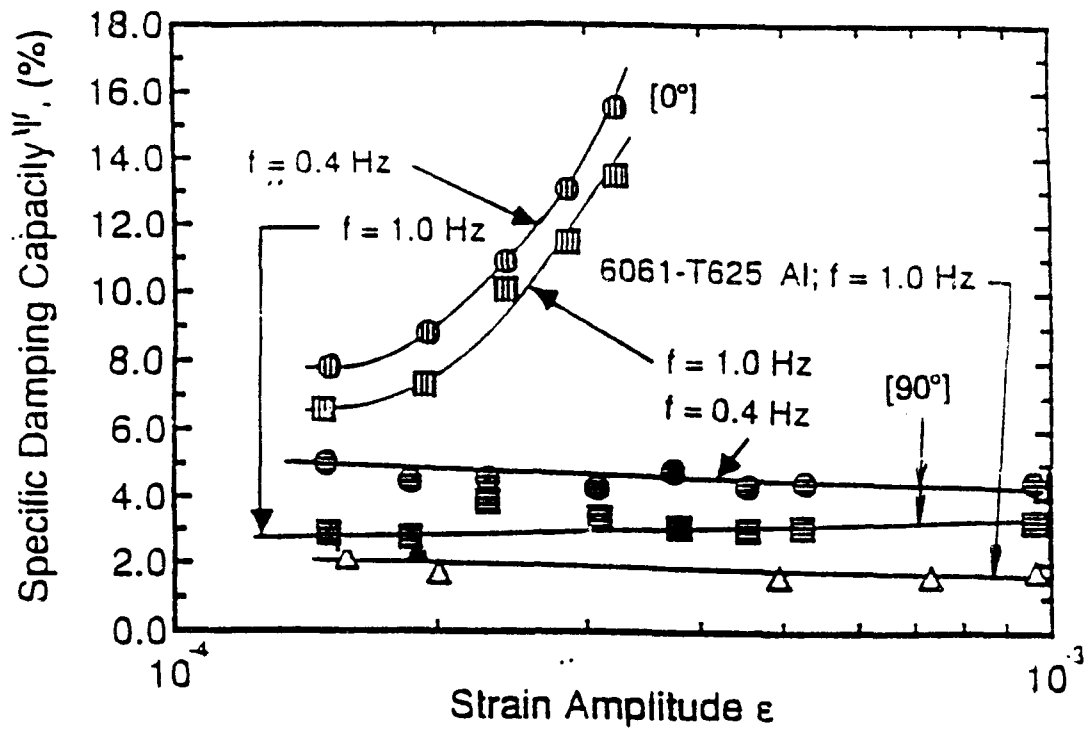


Figure 4 Damping capacity of P55Gr/6061 Al composites for $[0^\circ]$ and $[90^\circ]$ fiber orientation [2]. (Tension-Tension Fatigue Test)

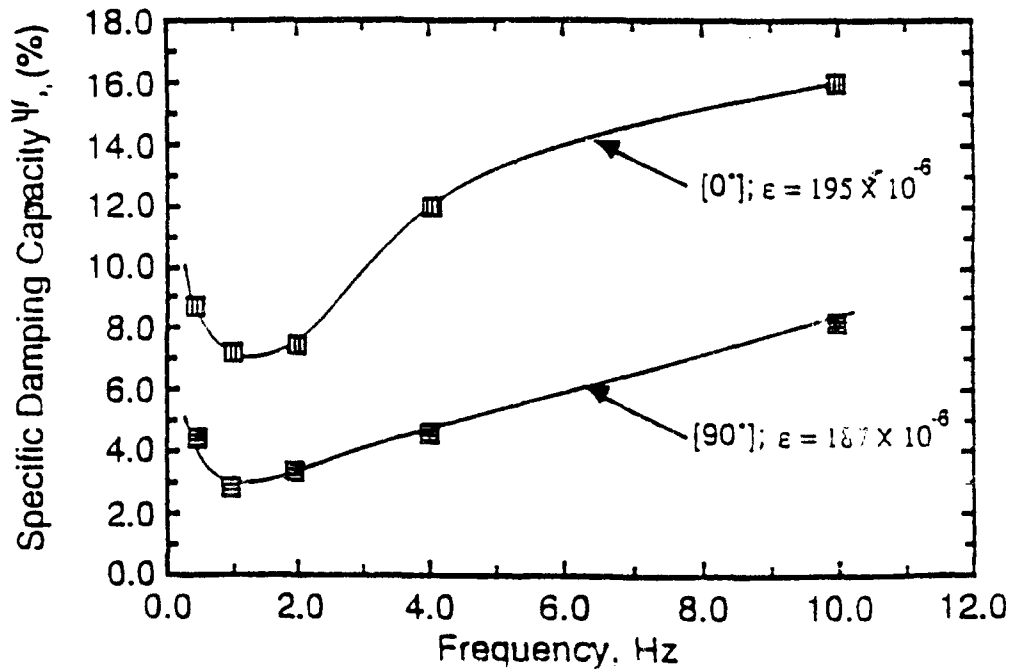


Figure 5 Damping capacity of P55Gr/6061 Al as a function frequency for $[0^\circ]$ and $[90^\circ]$ fiber orientation. (Tension-Tension Fatigue Test) [2].

Figure 4 shows the damping capacity of P55/6061 aluminum composite as a function of strain amplitude and for two ply orientations. Measurements were performed in a tension-tension fatigue test. These data were obtained at frequencies of 1 Hz and 0.4 Hz. This frequency range also corresponds to a frequency range where the damping capacity is a minimum. Note that the $[0^\circ]$ orientation gives a fairly fast rising damping capacity with only modest increases in strain amplitude. Conversely, the $[90^\circ]$ orientation remains fairly constant with strain amplitude.

Figure 5 shows the damping capacity of P55Gr/6061 aluminum as a function of frequency for two ply orientations, $[0^\circ]$ and $[90^\circ]$; the data were obtained from tension-tension fatigue tests at approximately 190 microstrain. Note the minima in these curves at approximately 1 Hz, and the fact that the longitudinal data ($[0^\circ]$) exhibits a higher damping capacity than the transverse data ($[90^\circ]$) by about a factor of two.

Figure 6 shows the damping capacity of P55Gr/Mg - 0.6 at. % Zr as a function of temperature. The material was tested in the as-cast condition, and the result of several indicated heat treatments are shown. The measurements were made at 0.1 microstrain. The damping capacity exhibits a peak at approximately 200°K, and a minimum at about 300-400°K. As indicated, this peak has been attributed by Misra and co-workers [22] to a phase transition in the graphite fibers from a rhombohedral phase to a hexagonal close-packed phase. The difference in the damping capacity between the maximum and minimum values is approximately 36%. Overall the damping capacity of this kind of graphite/magnesium composite is not very high, only 0.8-0.9%.

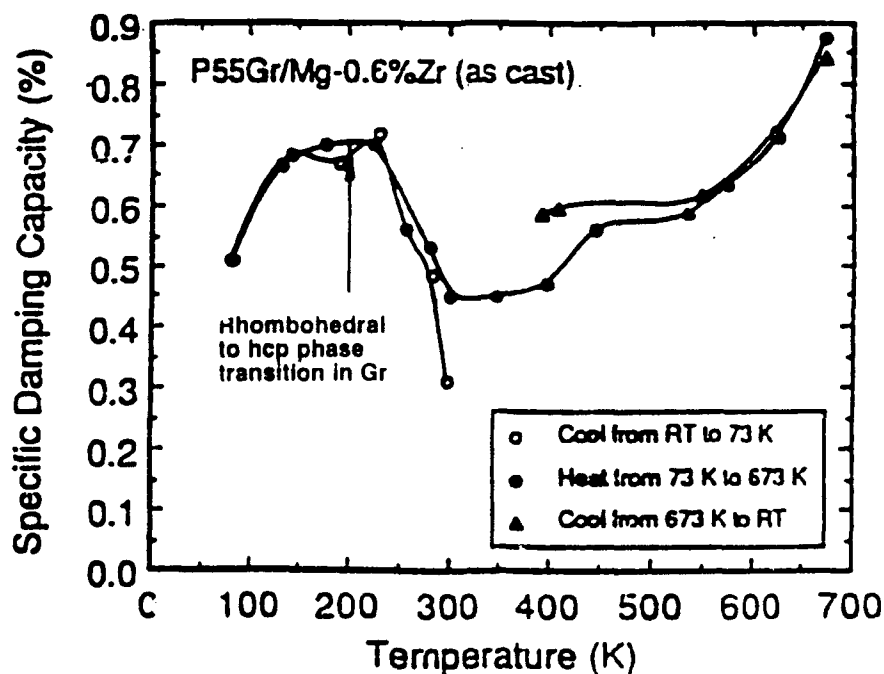


Figure 6 Damping capacity of as-cast Gr/Mg-0.6 at. % Zr as a function of temperature [22].

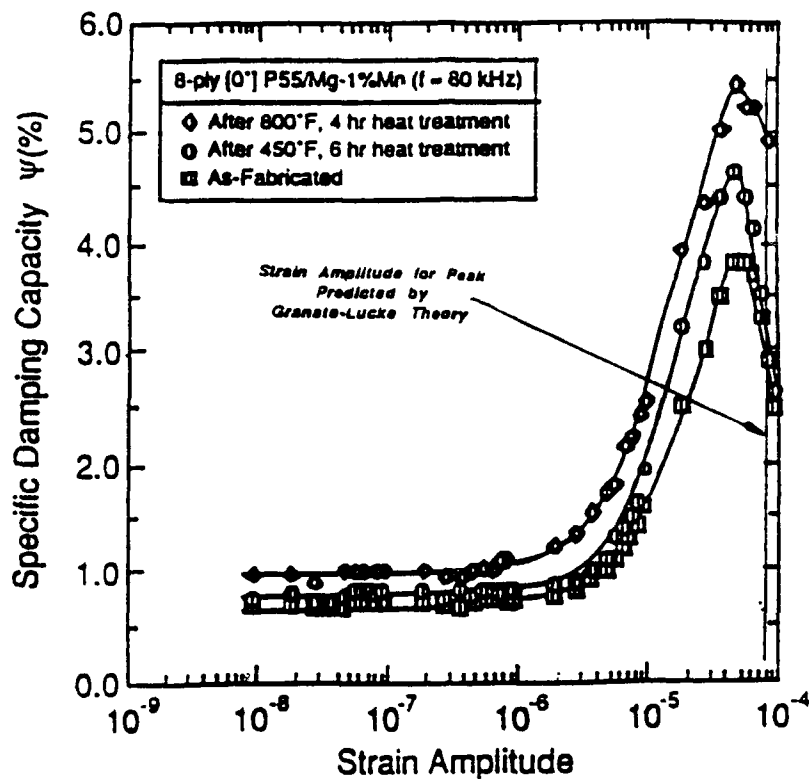


Figure 7 Damping capacity of P55Gr/Mg-1 at.% Mn as a function of strain amplitude [22].

Figure 7 shows the damping capacity of P55Gr/Mg - 1 at.% Mn as a function of strain amplitude. The data are for the as-fabricated condition, and for two types of heat treatment. Unlike the aluminum matrix, heat treatment causes a modest rise in damping capacity. For all three conditions the damping capacity increases from about one percent to about five percent at strain amplitudes greater than 2×10^{-6} , and decreases again following the peaks at about 5×10^{-5} . The Granato-Lucke theory was used to predict the strain amplitude at which the damping capacities are a maximum: at 80 microstrain.

The axial damping capacity of silicon-carbide-fiber-reinforced titanium for the indicated values of the fiber volume fraction is shown in Figure 8. The vertical scale was expanded relative to the horizontal scale, creating the impression that the damping capacity undergoes large variations with small temperature changes. Predicted values based on a model by DiCarlo et al. [23] are plotted on the bottom graph for frequency values of 1200 and 2000 Hz. These predictions are quite low, increasing only marginally with increasing frequency and temperature.

These computed curves testify not only to the inadequacies of current models, but also to our lack of fundamental understanding of the damping mechanisms in metal matrix composites.

The damping properties of SiC particulate- and whisker-reinforced aluminum material are shown in Tables 2 and 3. The damping capacity and the frequency at which these data were obtained are shown at the extreme right in these tables. For constant fiber volume concentration, both SiC particulate- and whisker-reinforced aluminum exhibit damping capacity

Table 2 Specific damping capacity of SiC_p/Al and SiC_w/Al [24].

Fiber	Matrix	Fiber Vol. (%)	Elastic Mod. (msi)		Density (g/cm ³)	Freq. (Hz)	Ψ (%)
			Trans.	Long.			
SiC _p	CT90 Al	20	17.1	17.1	2.962	62.25	3.98
SiC _p	CT90 Al	20	17.8	17.8	2.962	111.00	3.20
SiC _w	2024 Al	20	15.4	15.4	2.962	53.25	4.72
SiC _w	2024 Al	20	16.3	16.3	2.962	110.00	3.05

Table 3 Specific damping capacity for SiC_p/6061 and SiC_w/6061 composites [25].

Material	Fiber Vol. (%)	Elastic Mod. (msi)	Ultimate Strength (ksi)	Elongation to Failure (%)	Freq. (Hz)	Ψ (%)
SiC _w /6061-T6(L)*	17	14.7	73	2.1	32.1	1.571
SiC _p /6061-T6(L)*	20	15.2	70	4.5	120.0	2.890
SiC _p /6061-T6(L)*	30	17.5	77	3.0	20.1 104.7	2.325 0.817
SiC _p /6061-T6(T)**	30	17.5	77	3.0	105.4	0.942

* Extended and cross-rolled sheet, L=longitudinal to the extension direction. The mechanical properties for the 20 v/o SiC_p/6061 composites are those for the T6 condition. However, the damping measurements are given for the composites in the F condition.

** Rolled sheet.

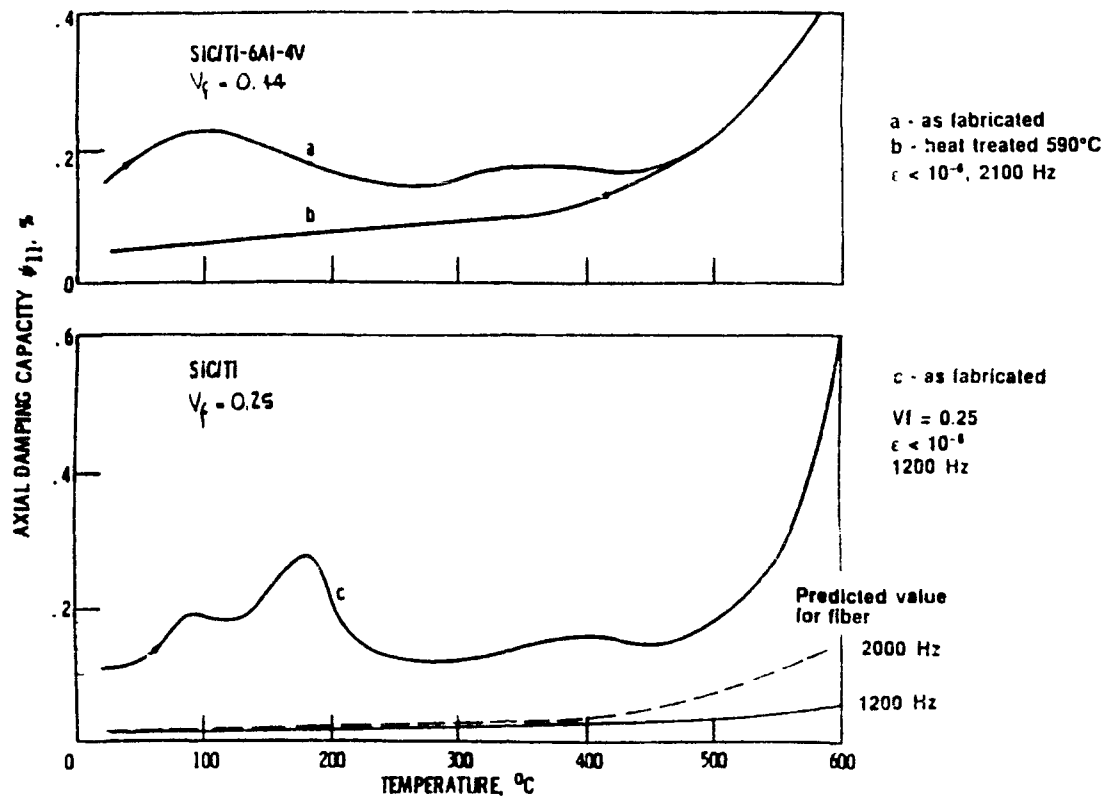


Figure 8 Axial damping capacity of SiC fiber reinforced Ti-6Al-4V [23].

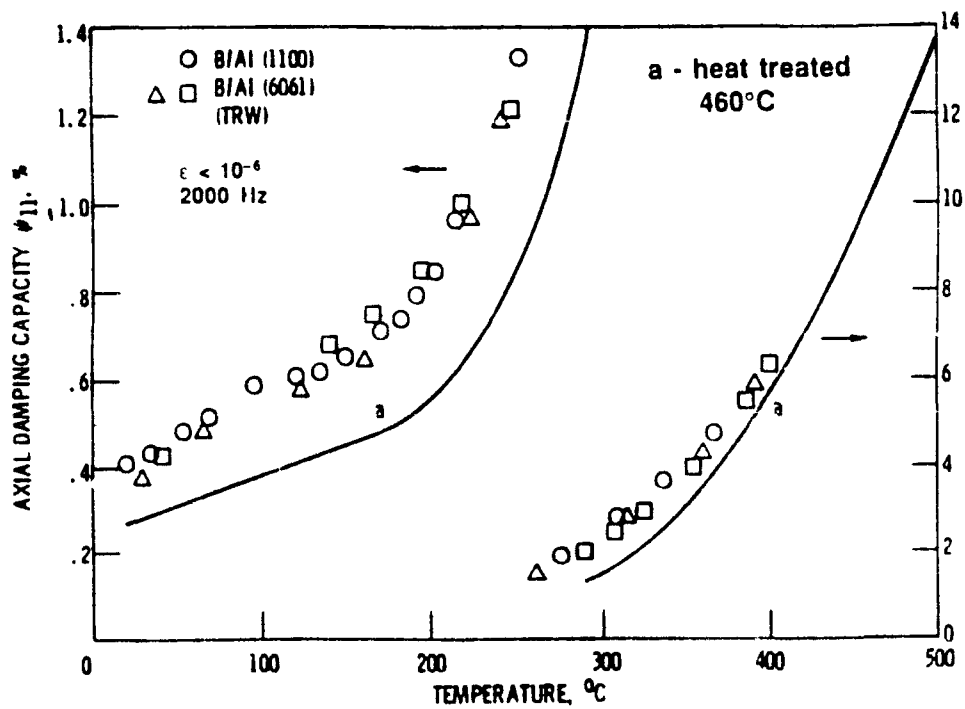


Figure 9 Axial Damping Capacity of B/1100 Al and B/6061 Al [23].

of about 3 to 5 percent which does not appear to depend on matrix type. Table 3 shows a significant reduction in damping capacity due to a change in the orientation of the specimens. These variations taken collectively may be due to process variations, reinforcement concentration, and testing frequency.

Figure 9 presents axial damping capacity of B/1100 Al and B/6061 Al. Two scales are used to show the large change in Ψ with temperature. These measurements were made at less than one microstrain and at 2000 Hz. The B/6061 Al material was fabricated by TRW, Inc. The solid curve represents the same material after subjecting it to a heat treatment at 460°C. The heat treatment is in the primary recrystallization range of aluminum. Recrystallization is known to reduce damping (by decreasing the dislocation density in the matrix), and to increase the matrix grain size. No systematic studies of the effects of heat treatment on boron/aluminum materials seem to have been carried out.

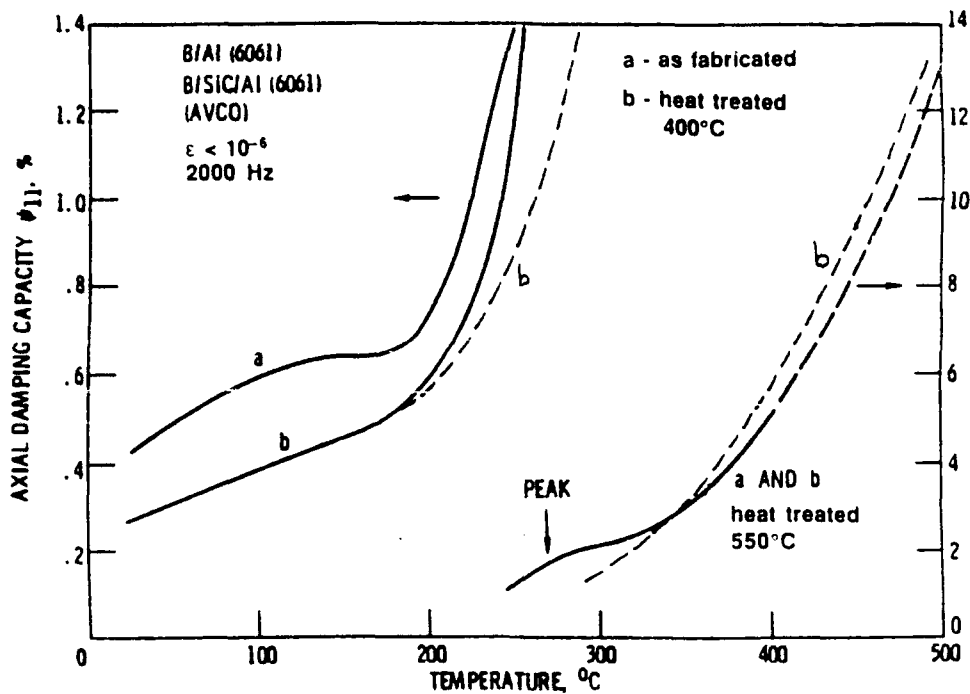


Figure 10 Axial Damping Capacity of B/6061 Al and Borsic/6061 Al [23].

The effects of a SiC coating on boron fiber (Borsic) used in reinforcing 6061 Al is shown in Figure 10. This material was fabricated by Avco, now H.R. Textron. Note that the heat treatments reduce the damping capacity of the composite: this is caused by a reduction in dislocations in the matrix near each fiber by grain growth due to recrystallization. The dashed curves labeled c are the curves labeled a in Figure 9. The other dashed curve on the left and curve c are for damping of Borsic/6061 Al specimens after heat treatment to 550 °C. These data were obtained at 2000 Hz and 1 microstrain [4,23]. The duration and cooling mode of these specimens were not reported [5].

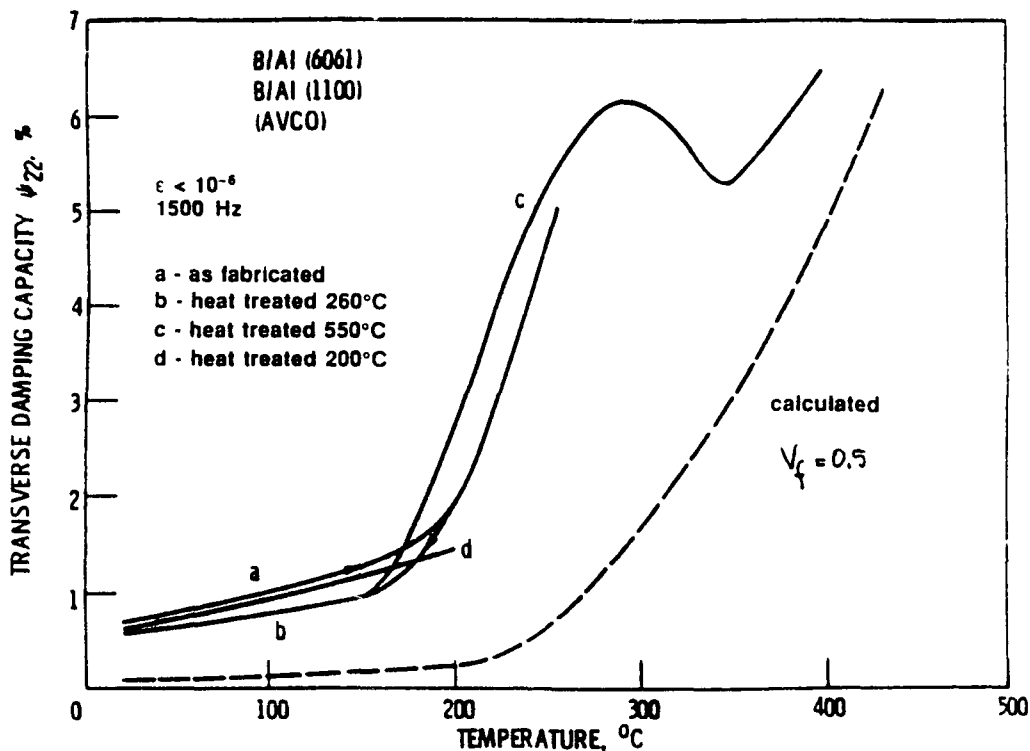


Figure 11 Transverse Damping of B/1100 Al and B/6061 Al. Curves a to c are for B/6061 Al and curve d is for B/1100 Al [23].

The transverse damping capacity of B/1100 Al and B/6061 Al are shown in Figure 11. The figure shows the results of various heat treatments, which do not appear to affect the damping capacity. The calculated transverse damping capacity of B/6061 Al with a fiber volume fraction of 0.5 is shown as a dashed line. The difference in the maximum and the minimum of the damping capacity exhibited by curve c amounts to only 15 percent.

Figure 12 summarizes the specific damping capacity of MMCs discussed above, as a function of temperature. The dark heavy line is the damping capacity of pure aluminum shown for reference. The dashes represent the damping capacity of fibers alone. This shows the strong anelastic effect on the damping capacity of boron and Borsic fibers compared to SiC fibers shown near the bottom of the graph. The difference in the damping capacity between these two types of fibers is approximately a factor of 20-30 at about 600°C. Enhancement in damping capacity of pitch-base carbon fiber has been reported elsewhere [21], and has not been added to Figure 12. The relatively large damping capacity of boron fiber is responsible for the observed large damping capacity of boron-aluminum composites. Note the low damping capacity, less than 1 percent, of Gr/Mg and SiC_r/Ti composites, while that of B/6061 Al is almost as high as the boron fiber itself.

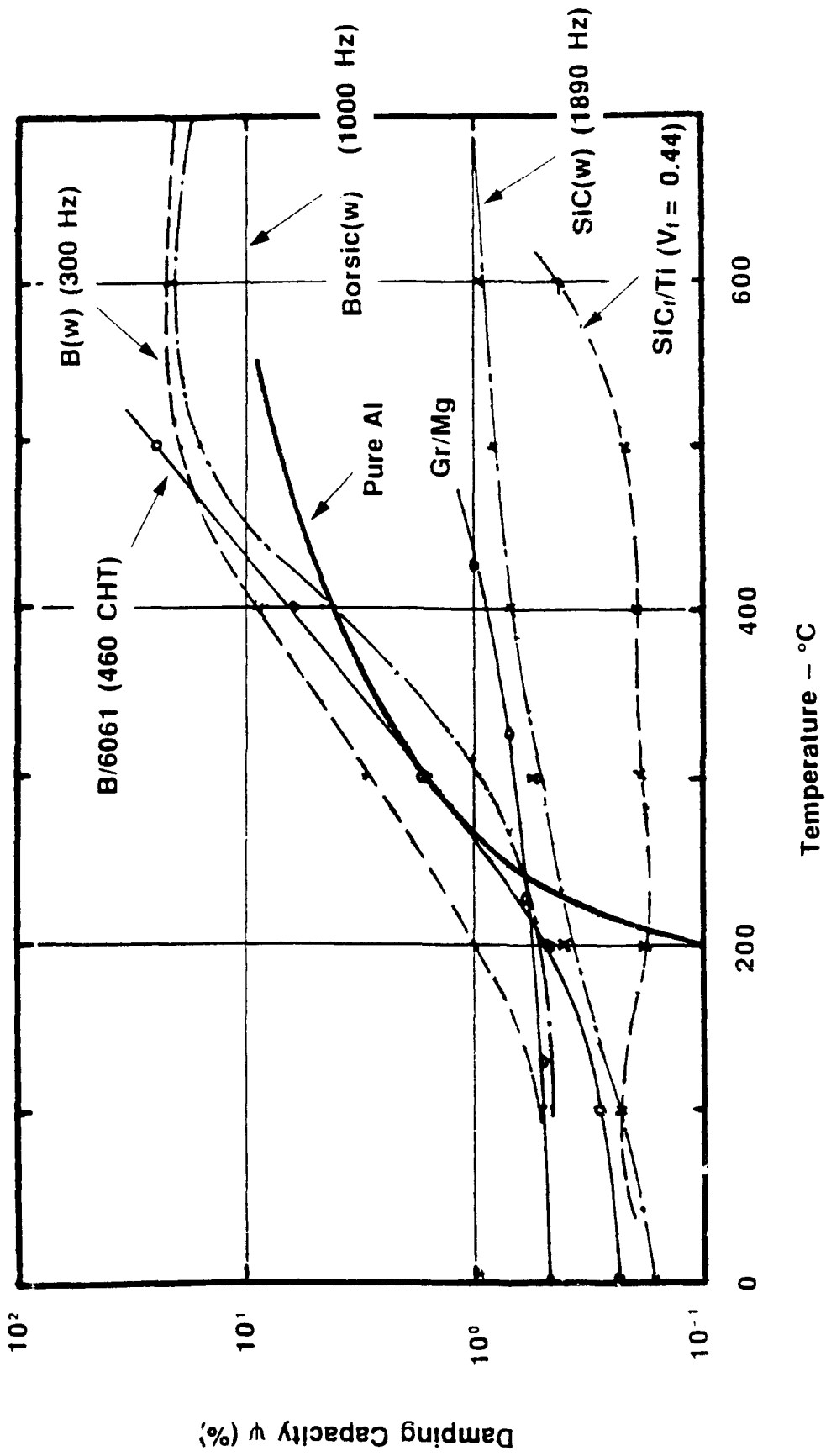


Figure 12 Summary of the Specific Damping Capacity of Some MMCs as a Function of Temperature.

Figure 13 presents a summary of specific damping capacity as a function of strain amplitude of the MMCs previously discussed. The damping capacity of pure aluminum is shown for reference. The short dashed lines represent computational predictions made with various models [5] for Gr/Mg and Gr/Al. Some of these computations included the effects of residual stresses resulting both from the difference in the coefficient of thermal expansion between fiber and matrix, and from the fiber anisotropy. Although some of these predictions agree well with measurements, that of the Gr/Mg composite does not. All the data presented in Figures 1 through 11 are represented as cross-hatched areas. Note the behavior of P55Gr/Mg - 1 at. % Mn. The damping capacity exhibits the kind of rise with increasing strain amplitude exhibited by pure aluminum, but at approximately 1.5 orders of magnitude lower strain amplitude.

A comparison of the loss factors of various materials and metal matrix composites is shown in Figure 14. Two conclusions are obvious from this figure: the damping capacity of MMCs is not better than conventional unreinforced metals, and viscoelastic materials exhibit the greatest damping. This suggests that for a material to simultaneously achieve high stiffness, high strength, and high damping capacity, the material should combine MMCs with viscoelastic materials. This is nothing new!

GENERAL CONCLUSIONS

As already mentioned, the most striking observation is that the damping capacity of metal matrix composites is not very good, certainly no better than unreinforced metals, except perhaps at elevated temperatures and high strain amplitudes. Dislocation substructures surrounding reinforcements tend to impart strain independent behavior to reinforced aluminum. From preliminary work reported elsewhere [21], it appears that the damping capacity of carbon-fiber-reinforced metals may be improved, but at present it remains in doubt that such improvements would raise the composite damping capacity much beyond unreinforced metals. MMCs do exhibit a somewhat equal or better damping capacity than low atomic number alloys, such as aluminum or titanium, making MMCs attractive for space structures. Nonetheless, significant increases in the damping capacity of dimensionally critical space structures must be obtained by other methods as is discussed by some other papers in these proceedings.

An important problem in assessing the state of art is the database; at present it is small and this author is unaware of any systematic efforts to compile these data. Thus, one finds oneself in the ironic situation of needing a larger database to understand the potential of these materials with regards to damping capacity. At the same time the great expectation that MMCs would exhibit high damping capacity having failed to materialize resulted in funding reduction to study these material properties. If any recommendation is to be made it is that fundamental work in understanding the physics of MMCs subjected to time-varying loads should continue with carefully planned experiments.

The theoretical analysis and model development for describing and predicting the intrinsic (or internal) damping behavior of MMCs is at present rather primitive. There are a number of microscopic models [5] used to explain and even predict performance, but they exhibit poor reliability when fiber and matrix material properties are changed. Model calculations in B/Al,

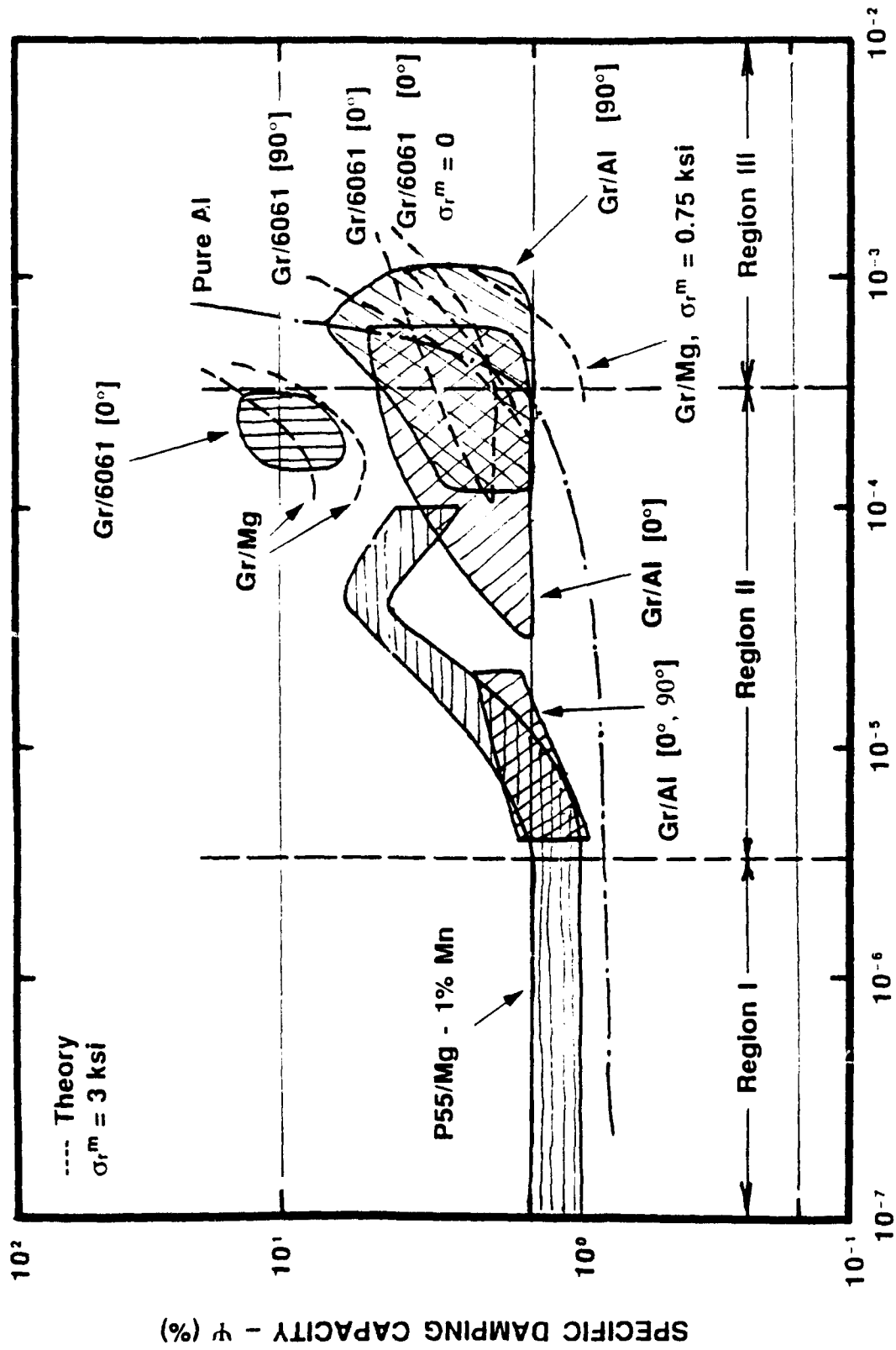


Figure 13 Summary of Specific Damping Capacity of Some MMCs as a Function of Strain Amplitude.

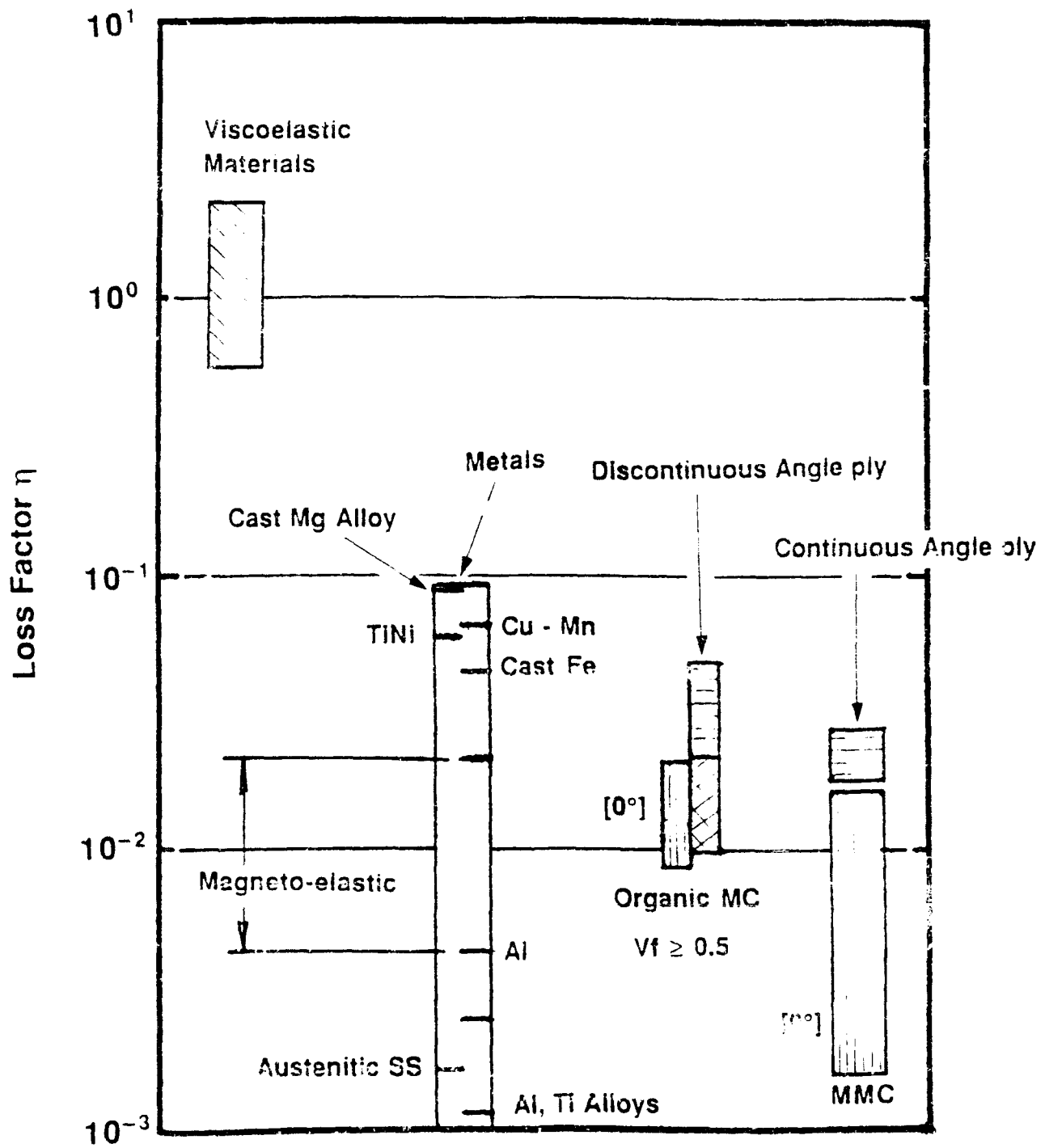


Figure 14 Loss Factor Comparisons for Various Materials [2].

for example, have predicted damping capacity values much lower than observed, implying a lack of fundamental understanding of the damping mechanisms of these complex advanced materials. Modeling of fiber damping has been fairly well developed in the Soviet Union relative to the US, but even this modeling is not enough. Theoretical analysis must consider the fiber as a composite consisting of a core (tungsten or carbon or something else) surrounded by the fiber material with an outer surface of a reaction barrier coating and/or a compliant coating. The analytical machinery is well developed and there are numerous papers available describing the application of linear elastic theory to cylindrical problems of this type. To set the stage for systematic theoretical analysis and model development, a review of theoretical work in this area should be carried out so others, including newcomers, would have a sensible place to start for developing new ideas and approaches. Any new developments in the theoretical analysis of the damping capacity of MMCs must include the phenomenology of the interface.

It is obvious from the small amount of data presented in this paper that boron fibers exhibit high damping capacity and appear to dominate the damping capacity in aluminum reinforced with boron. The SiC coating on these fibers appears to decrease the damping capacity slightly. Damping capacity of boron fibers is distinctly superior to that of SiC fibers. Damping capacity of other fibers of interest (Al_2O_3 , TiB_2 , B_4C coated boron), with the possible exception of carbon fibers [21], seems not to have received attention. Silicon carbide fiber on a tungsten core has a damping capacity well below boron fibers, by as much as a factor of 20-30.

Observations of the small database available indicates that the damping capacity of MMCs appears to be dependent on process method, fiber content, frequency, temperature, heat treatment, and strain amplitude. Strain amplitude in a certain range of values (10^{-5} - 10^{-3}) has a strong effect on damping capacity. This is generally believed to be due to the Zener relaxation effect, and dislocation structures can be explained to some extent by means of the Granato-Lucke theory.

Heat treatment has an effect on damping capacity in a way that is not understood. Theoretical understanding in this case appears difficult and testing various hypotheses could prove very expensive as large numbers of specimens would need to be tested and microscopically examined. Nevertheless, present observations of the effects of heat treatment on damping indicate that heat treatment decreases damping in fibers and aluminum, but increases it in carbon-fiber-reinforced magnesium.

"Someday all will be well" is our hope

"All is well today" is illusion

Voltaire, 1722.

References

1. R.L. Sheen, Experimental Measurements of Material Damping for Space Structures in Simulated Zero-G, M.S. Thesis, MIT, December 1983.
2. S.P. Rawal, T.H. Armstrong, and M.S. Misra, Interfaces and Damping in Metal Matrix Composites, Final Report, Martin Marietta Denver Aerospace, Denver, Co, December 1986
3. M.S. Misra, S.P. Rawal, and J.H. Armstrong, Damping Characteristics in Metal Matrix Composites, Technical Report, Martin Marietta Denver Aerospace, Denver, Co, November
4. J.E. Schoutens, Internal Damping in Metal Matrix Composites, MMCIAC, Kaman Sciences Corp., Santa Barbara, CA 93102, Rept. No. 720, 1990
5. A. Wolfenden and T.M. Wolla, Dynamical Mechanical Properties, in Metal Matrix Composites: Mechanisms and Properties, R. K. Everett and R. J. Arsenault, Eds., Academic Press, New York, 1991, p.287.
6. C. Zener, Phys. Rev., 60 (1941) p.906.
7. A.S. Nowick and B.S. Berry, Anelastic Relaxation in Crystalline Solids, Academic Press, New York, 1972.
8. H.M. Ledbetter, M. Lei, and M.W. Austin, Young Modulus and Internal friction of a Fiber-Reinforced composite, J. Appl. Phys., 59(6) (1986)p.1972.
9. J. DiCarlo and W. Williams, Dynamic Modulus and Damping of Boron, Silicon Carbide, and Alumina Fibers, Ceramic Engineering and Science Proceedings, Vol. 1 (1980) p.671.
10. G.N. Dugladze, G.Sh. Darsavelidze, and G.V. Tsagareishvili, High-Temperature Internal Friction in Boron Fibers, Soobsch. Akad. Nank Gruz, SSR, 70 (1) (1973) p.141.
11. G.Sh. Darsavelidze, et al., Temperature Dependence of the Internal Friction of Coated Boron Whiskers, Goobshck. Akad. Nank Gruz, 89(2) (1978) p.421.
12. G.V. Tragareishvili, et al., Internal Friction in Boron Whiskers, Boron-Production, Structures, and Properties, Nanka, Moscow, 1974.
13. V.S. Postnikov, et al., Mechanism of Absorption of Elastic Energy in Boron Fibers, Soviet Powder Metallurgy and Metal Ceramics, 22, no. 9 (249), September 1983, p.773.

14. J.E. Schoutens, Review of Some Recent Developments in the Physics of Metal Matrix Composite Materials, MMCIAC Report no. 803, 1990.
15. D.J. Nelson and J.W. Hancock, J. Mater. Sci., 13 (1978) p.2429.
16. N.N. Kishore et al., J. Reinf. Plas. Comp., 1 (1982) p.40.
17. N.N. Kishore et al., J. Reinf. Plas. Comp., 1 (1982) p.64.
18. H. M. Ledbetter and S.K. Datta, Vibration Damping Workshop 1984, AFWAL-TR-84, pp.W1-W8, Wright Patterson AFB, OH, 1984.
19. S.I. Hwang and R.F. Gibson, J. Eng. Mater. and Tech., 109 (1987) p47.
20. Z. Hashin, Trans. ASME, 32 (1965) p.630.
21. A.J. Eckel and Steven P. Jones, Controlling the Damping Behavior of Pitch-Based Carbon Fibers, these Proceedings.
22. M.S. Misra, Damping Characteristics of Metal Matrix Composites, Letter Report, Martin Marietta, Denver, CO, Report no. MCR-85-721, Issue 9, 1988.
23. J.A. DiCarlo and J.E. Maisel, High Temperature Dynamic Modulus and Damping of Aluminum and Titanium Matrix Composites, NASA TM 79080, 1980.
24. F.D. Ross and L. Rubin, Acoustic Attenuation of Metal Matrix Composites, The Aerospace Corporation, Report no. SD-TR-82-62 (MMC 701706), August 1982.
25. M.S. Misra and P.D. LaGreca, Damping Behavior of Metal Matrix Composites, Martin Marietta, Denver, CO, DTIC no. ADP004704.

Vibration Suppression of Thin-Walled Composite Tubes Using Embedded Viscoelastic Layers

Frank M. Beiknap
Composite Optics, Inc.
San Diego, California

and
J. B. Kosmatka
Department of Applied Mechanics and Engineering Science
University of California
San Diego, California 92093

Abstract

This paper documents the design and fabrication of a thin-walled composite tube consisting of inner and outer graphite shells with a viscoelastic layer between the shells to provide damping. The graphite shells are fabricated from fabric and unidirectional tape with ply orientations that cause the shells to counter-rotate in opposite directions when subjected to bending or extension. The counter-rotation of inner and outer shells provides a large shear area at the viscoelastic layer, therefore optimizing the damping. Stiffness characteristics of a laminated tube are used to determine ply orientations to maximize damping and structural stiffness. Details of the tube construction are described along with design issues of incorporating viscoelastic layers in a composite laminate. Tests results of the tube with an embedded viscoelastic layer are compared to those of a tube constructed from the same laminate without the damping layer.

Introduction

The need for lightweight, high-strength structures often leads to various vibration problems. Advanced composites offer high stiffness-to-weight ratios, but the levels of structural damping remain relatively low. Viscoelastic materials, which are also lightweight, offer vibration attenuation, but cannot be used as structural elements because of their low stiffness properties. Hybrid composite structures are being designed with layers of viscoelastic materials strategically embedded in composite laminates to control motion due to the vibration.

One example of a hybrid composite structure, that can provide high damping levels, is a thin-walled composite tube consisting of a viscoelastic layer embedded between inner and outer graphite/epoxy shells. The graphite/epoxy shells are fabricated from woven cloth and unidirectional tape. The plies of the unidirectional tape are oriented so the fibers wrap

spirally around the inner shell, and wrap in an opposite (or opposing) spiral in the outer shell. The application of either an extensional, bending, or shear load to the tube ends will produce relative twisting between the inner and outer shells since the shells are rotating in opposite directions. This relative twisting will induce significant shear strain levels in the viscoelastic material, thus producing a large amount of useful structural damping.

If the inner and outer shells of the tube were made of an isotropic material, then the application of either an axial or flexure load would produce tube extension or bending, respectively, but with no relative twisting. This bending-action will produce very low shear levels within the viscoelastic core away from the neutral axis. Studies have shown [1,2] that the effectiveness of this type damping treatment is extremely limited due to the small shear-strain areas. Because the two shells of the current composite design are rotating in opposite directions, shear strain is produced in the entire viscoelastic layer. This large shear area is due to the mechanical advantage of the relative rotational of the two shells acting independently.

The application of an axial load on a tube with isotropic shells would produce shear in the viscoelastic layer if the two shells are only coupled in the axial direction by the viscoelastic layer. This load path will result in high damping but the tube will have low structural stiffness in the axial direction due to the soft viscoelastic layer. The soft core material will react in series with the two stiffer shells resulting in a low system stiffness. Other designs have incorporated the use of viscoelastic layers with composite shells but still requiring one shell to be the primary structural member [3]. With the current composite design developed in the present paper, the two shells twist oppositely when subjected to loading which causes both shells to experience the same length change. Thus, the ends of both shells are coupled in the axial direction and they support the entire axial load without the soft viscoelastic core reducing the system stiffness. Only the rotational degree-of-freedom at both ends of the tube needs to remain unconstrained leaving the axial stiffness unaffected.

The application of damping to spacecraft structures has significant impacts on increased reliability and reduced costs associated with launch and extended operation [4]. The material selection for the current composite design is based upon possible applications for satellite systems. The matrix system used in the graphite/epoxy material must be capable of withstanding the temperature extremes associated with space environments. The viscoelastic material must also be compatible with this resin system. Another area of concern is the possibility of contamination by these types of materials in a space environment.

The graphite material is a fiber type T-300 pre-impregnated with a Hysol #934 resin system that cures at 350 degrees Fahrenheit. The viscoelastic damping material is 3M Scotchdamp SJ-2015X Viscoelastic Polymer Type 1210. This material is provided by 3M Corporation in a standard thickness of 10 mils (.010 inches). The stiffness properties for the viscoelastic material are provided by 3M product information [5]. Outgassing tests were

conducted by the Boeing Aerospace Company [6] on this material and proved it to be acceptable for space applications. A series of structural tests were conducted to verify that the chemical composition of the viscoelastic material did not reduce the mechanical properties of the graphite/epoxy material [7].

Theoretical Development

The stiffness properties of a laminated composite tube are studied so that the ply orientations which maximize the extension-torsion coupling and shear strain in the viscoelastic layer can be determined. Consider a long slender beam of length L acted upon by end forces and moments. A Cartesian coordinate system (x,y,z) and corresponding displacements (u,v,w) are defined where x and y define the cross-section plane and z defines the axial direction. See Fig.1 for further details. The displacement field of a point on the deformed beam can be written in its most general form by assuming that it is a linear combination of global functions that represent extension, bending, and twisting of the tube and local functions that represent generalized warping of the cross-section;

$$\begin{aligned}
 u(x,y,z) &= u_0(z) - y\theta_0(z) + \psi_x(x,y), \\
 v(x,y,z) &= v_0(z) + x\theta_0(z) + \psi_y(x,y), \\
 w(x,y,z) &= w_0(z) - x\theta_y(z) + y\theta_x(z) + \psi_z(x,y).
 \end{aligned}
 \tag{1.a-c}$$

where u_0 , v_0 , and w_0 represent z -dependent displacements in the x , y , and z directions, respectively, ϕ_x , ϕ_y , and θ_0 represent rotations about the x , y , and z axes respectively, and ψ_x , and ψ_y represent warping within the cross-section plane and ψ_z is the warping out of the cross-section plane. Assuming a two-dimensional strain state, one can derive the final form of the z -dependent functions as:

$$\begin{aligned}
 u_0(z) &= \frac{\kappa_x}{2} z^2, & \theta_x(z) &= \kappa_y z, \\
 v_0(z) &= -\frac{\kappa_y}{2} z^2, & \theta_y(z) &= \kappa_x z, \\
 w_0(z) &= e z, & \theta_0(z) &= \theta z,
 \end{aligned}
 \tag{2.a-f}$$

where e , κ_x , κ_y , and θ represent the extension strain, the bending curvatures of the beam in the x - z and y - z planes, and the elastic twist per unit length, respectively. The six strain components of the beam, which

fully account for warping (deformation) within the cross-section, are calculated using Eqns. (1) and (2)

$$\begin{aligned} \epsilon_{xx} &= \psi_{x,x}, & \gamma_{yz} &= x\theta + \psi_{z,y}, \\ \epsilon_{yy} &= \psi_{y,y}, & \gamma_{xz} &= -y\theta + \psi_{z,x}, \\ \epsilon_{zz} &= e - x\kappa_x + y\kappa_y, & \gamma_{xy} &= \psi_{x,y} + \psi_{y,x}. \end{aligned} \quad (3.a-f)$$

The determination of local cross-section deformation functions (ψ_x , ψ_y , ψ_z) is based upon using a separation of variables solution technique combined with the Ritz method assuming that the warping functions can be expressed as a linear combination of unknown functions that are proportional to the axial strain, bending curvatures, and twist rate, i.e.:

$$\begin{aligned} \psi_x &= e \psi_x^{(1)} + \kappa_x \psi_x^{(2)} + \kappa_y \psi_x^{(3)} + \theta \psi_x^{(4)} \\ \psi_y &= e \psi_y^{(1)} + \kappa_x \psi_y^{(2)} + \kappa_y \psi_y^{(3)} + \theta \psi_y^{(4)} \\ \psi_z &= e \psi_z^{(1)} + \kappa_x \psi_z^{(2)} + \kappa_y \psi_z^{(3)} + \theta \psi_z^{(4)}. \end{aligned} \quad (4.a-c)$$

Since the geometry and material properties of the tube are constant with respect to the z-axis, the current problem reduces to a two-dimensional elasticity problem, where the only unknowns are the warping functions. Since these functions are only dependent upon the cross-section coordinates (x,y), this elasticity problem can be solved by developing special two-dimensional finite elements for studying the cross-section warping behavior. Each lamina (including the viscoelastic layer) is discretized into a series of subregions (finite elements) where the warping within each subregion is described using a bi-quadratic isoparametric interpolation function:

$$\begin{aligned} \psi_x &= [N(x,y)]_i^t \Psi_x^i \\ \psi_y &= [N(x,y)]_i^t \Psi_y^i \\ \psi_z &= [N(x,y)]_i^t \Psi_z^i. \end{aligned} \quad (5.a-c)$$

The strains are written in matrix form in terms of the unknown displacement functions and the axial strain, bending curvatures, and twist rate:

$$\{\epsilon\} = [B] \{\Psi\} + f_b \{b\} \quad (6.a)$$

where

$$[B] = \begin{bmatrix} N(x,y)_{,x} & 0 & 0 \\ 0 & N(x,y)_{,y} & 0 \\ 0 & 0 & 0 \\ 0 & 0 & N(x,y)_{,y} \\ 0 & 0 & N(x,y)_{,x} \\ N(x,y)_{,y} & N(x,y)_{,x} & 0 \end{bmatrix} \quad (6.b)$$

$$\{\Psi\}^T = \left\{ \{\Psi_x\}, \{\Psi_y\}, \{\Psi_z\} \right\} \quad (6.c)$$

$$[fb] = \begin{bmatrix} 0 & 0 & 0 & 0 \\ 0 & 0 & 0 & 0 \\ 1 & -x & y & 0 \\ 0 & 0 & 0 & x \\ 0 & 0 & 0 & -y \\ 0 & 0 & 0 & 0 \end{bmatrix} \quad (6.d)$$

and

$$\{b\}^T = \left\{ e, \kappa_z, \kappa_y, \theta \right\} \quad (6.e)$$

The principle of minimum potential energy is given as

$$\delta\Pi = \sum_{i=1}^n \delta U^{(i)} - \delta W_e^{(i)} = 0 \quad (7)$$

where n is the number of subregions, $dU^{(i)}$ is the variation of the strain energy with respect to the unknown local deformations of the i^{th} subregion given by

$$\delta U^{(i)} = \int_0^L \int_{A^{(i)}} \left\{ \delta \epsilon^{(i)} \right\}^T [C^{(i)}] \left\{ \epsilon^{(i)} \right\} dA^{(i)} dz \quad (8.a)$$

and $\delta W_e^{(i)}$ is the variation of the work of external forces of the i^{th} subregion that results from the applied tractions on the beam ends. This virtual work expression will reduce to zero since both the stresses and the local cross section deformations are assumed to be independent of the axial coordinate (z). A set of linear algebraic equations for determining the local cross section deformations in terms of $\{b\}$ is obtained by substituting Eqns. (6) and (8.a) into Eq. (7) and carrying out the integration over the beam volume. Writing this set of equations for the i^{th} subregion:

$$[K^{(i)}]\{\psi^{(i)}\} + [F_b^{(i)}]\{b\} = \{0\} \quad (9)$$

where the stiffness matrix is defined as

$$[K^{(i)}] = L \int_{A^{(i)}} [B^{(i)}]^T [C^{(i)}] [B^{(i)}] dA^{(i)} \quad (10 a)$$

and the force matrix is presented as

$$[F_b^{(i)}] = L \int_{A^{(i)}} [B^{(i)}]^T [C^{(i)}] \{f_b\} dA^{(i)} \quad (10 b)$$

Since both the stiffness matrix ($[K^{(i)}]$) and the force matrix ($[F_b^{(i)}]$) are linearly dependent upon the beam length (L), then the calculated local deformations functions are length independent and (L) can be dropped from the above equations. Unit solutions for the local deformations (ψ_x, ψ_y, ψ_z) can be calculated for each of the four cases of $\{b\}$ by setting the appropriate value in the array $\{b\}$ equal to unity and the remaining three to zero. Thus, the calculated deformation functions can be written in matrix form as

$$\{\psi^{(i)}\} = [\overline{\psi^{(i)}}]\{b\} \quad (11)$$

where each of the four columns of $\{\psi^{(i)}\}$ are the unit local deformations associated with the four cases of $\{b\}$. Thus, the calculated functions for the first case represent the local deformations as a result of applied unit axial strain (e) with dimensional units of length per unit axial strain. Similarly, the second and third cases define the local deformation associated with applied bending curvatures (κ_x, κ_y) with dimensional units of length per unit bending curvature. Finally the fourth case describes the local deformation from applied twist rate (θ) with dimensional units of length per unit twist rate. Similarly, the stress components of the i^{th} subregion can be expressed in terms of a set of unit stresses and $\{b\}$ by substituting Eqns. (15) and (9) into (2.a)

$$\{\sigma^{(i)}\} = [\overline{\sigma^{(i)}}]\{b\} \quad (12)$$

where

$$[\overline{\sigma^{(i)}}] = [C^{(i)}] [B^{(i)}] [\overline{\psi^{(i)}}] + f_b \quad (13)$$

Finally, the calculated stress components are substituted into the four cross-section equilibrium equations in order to express $(e, \theta, \kappa_x, \kappa_y)$ in terms of the applied axial force, twist moment, and bending moments:

$$\begin{aligned} \int_A \sigma_{zz} dA &= P, & \int_A x \sigma_{zz} dA &= -M_y, \\ \int_A y \sigma_{zz} dA &= M_x, & \int_A (y \tau_{xz} - x \tau_{yz}) dA &= M_z, \end{aligned} \quad (14)$$

Numerically integrating the stress over each subregion that comprises the cross-section allows one to study the extension-bend-twist coupling behavior of the constrained tube;

$$\begin{bmatrix} K_{11} & K_{12} & K_{13} & K_{14} \\ K_{12} & K_{22} & K_{23} & K_{24} \\ K_{13} & K_{23} & K_{33} & K_{34} \\ K_{14} & K_{24} & K_{34} & K_{44} \end{bmatrix} \begin{pmatrix} e \\ \kappa_x \\ \kappa_y \\ \theta \end{pmatrix} = \begin{pmatrix} P \\ M_y \\ M_x \\ M_z \end{pmatrix} \quad (15)$$

Inverting the above relationship, one can study the coupling behavior of an unconstrained bar:

$$\begin{bmatrix} a_{11} & a_{12} & a_{13} & a_{14} \\ a_{12} & a_{22} & a_{23} & a_{24} \\ a_{13} & a_{23} & a_{33} & a_{34} \\ a_{14} & a_{24} & a_{34} & a_{44} \end{bmatrix} \begin{pmatrix} P \\ M_y \\ M_x \\ M_z \end{pmatrix} = \begin{pmatrix} e \\ \kappa_x \\ \kappa_y \\ \theta \end{pmatrix} \quad (16)$$

Applying an axial force (P) produces extension as well as bending and twist that satisfy:

$$\frac{\kappa_x}{e} = \frac{a_{12}}{a_{11}}, \quad \frac{\kappa_y}{e} = \frac{a_{13}}{a_{11}}, \quad \frac{\theta}{e} = \frac{a_{14}}{a_{11}}. \quad (17)$$

Formulation of Ply Orientation

The cross-section stiffness properties for the tube are examined as a function of the unidirectional tape ply angles ϕ . The ply angle ϕ is defined as zero when the fibers in the ply align with the axial direction (z) of the tube. For stability purposes with this design, the fabric plies are maintained with the fibers oriented at both 0 and 90 degrees. The stiffness properties of the composite tube are sensitive to the orientation of the unidirectional

tape ply angles ϕ . As expected, the torsional stiffness (GJ) of the tube is maximized with ply angles of ± 45 degrees and minimized at 0 and 90 degrees. Both the axial stiffness (EA) and bending stiffness (EI) are maximized with ply angles at 0 degrees and minimized at 90 degrees. A graphical depiction of this ply angle sensitivity is illustrated in Figure 2. Torsional, axial, and bending stiffness are plotted as a function of the unidirectional ply angles ϕ .

The coupling of twist to applied extension is evident by the a_{14} term within [a]. The coupling of twist to extension is maximized when the unidirectional tape plies are oriented at an angle of 30 degrees. At this ply angle, the tube undergoes a large amount relative twist displacement, but the tube also suffers a significant reduction in both axial and bending stiffness. Since the tube is designed to have a primary load path in the axial direction, the axial stiffness needs to be monitored as well as the extension-twist coupling. Optimizing the shear between the two shells while maintaining structural stiffness is accomplished by comparing the extension-twist/extension ratio of the composite tube for varying ply angles ϕ . The value of a_{14}/a_{11} is the ratio of extension-twist coupling to extensional stiffness. The extension-twist/extension ratio versus ply orientation is plotted in Figure 3. This ratio is extremely sensitive to ply orientation and is maximized at an angle of 15 degrees.

To evaluate the effect the ply angle has on the damping of the tube, the shear stress within the viscoelastic must be examined. The maximum shear stress shown in Figure 4 as a function of ϕ is at a maximum for a 25 degree ply angle. But once again, optimizing the damping using this method would result in a penalty in structural stiffness. The amount of damping provided through matrix shear deformation of just the graphite/epoxy plies was not considered within this study. The orientation of the plies without a viscoelastic layer provides a supplemental damping mechanism to the laminate [8]. This effect is not accounted for in this analysis since its contribution will be small for a fiber-dominated design such as this one.

Tube Construction

The number of plies in the laminate were determined before the the cross-section properties was analyzed for various ply angles. The types of materials and placement within the laminate were chosen for their desired characteristic behavior. Figure 5 depicts the order of ply sequencing within the entire laminate. The fabric material is placed in the inner and outer most plies of the laminate to provide hoop stiffness to the structure. The hoop stiffness is required because of the low transverse tension capabilities of the viscoelastic layer in the center of the laminate. Large relative displacements between the inner and outer shells in the radial direction will result in a delamination at the graphite-to-viscoelastic interface.

Two plies of the unidirectional tape are used in each of the shells next to the viscoelastic layer. The use of unidirectional graphite material ensures the properly designed extension-bend-twist coupling behavior necessary to maximize damping and yet maintain structural stiffness. For this particular phase of the study, no other combinations of ply distribution or materials were examined.

The mandrel for the lay-up is a 60 inch long by 2.5 inch outer diameter solid aluminum round bar. The mandrel is hand polished to remove any surface imperfections then a releasing agent applied. The first ply is the fabric pre-cut to the required size. The next two plies are the unidirectional tape cut in a manner that maintains continuous fibers the length of the tube. The width of the unidirectional tape is the circumference of the mandrel including preceding plies times an angle of 15 degrees. When these fibers are then placed at 15 degrees to the tube's longitudinal axis and spirally wrapped, the edges of the ply come into contact with one another.

The fabric and two plies of tape create the inner shell of the tube. The unbalanced laminate of this shell will result in the extension-bend-twist coupling that is desired for this design. For this particular application, the viscoelastic damping layer is applied directly to the graphite/epoxy material before it is cured. The damping material selected acts as though it is a pressure-sensitive adhesive and requires only nominal pressure at room temperature to effect a good bond. Special care is required when handling the damping layer to avoid creating a void between this material and the graphite/epoxy layers. To reduce the tackiness of the viscoelastic layer, the damping material should be cooled to 30 degrees Fahrenheit before handling it.

The construction of the outer shell is accomplished the same way as the inner shell. The width of the unidirectional tape and fabric takes into account the increase in the circumference due to the additional preceding plies. The angle of orientation for the unidirectional fibers is in the *opposite direction of those for the inner shell*. This ensures that the outer shell extension-bend-twist coupling is in the opposite direction from the inner shell.

Once the final ply of the laminate is applied, the tube is wrapped with a teflon film. A layer of shrink wrap tape is applied in a spiral manner to provide uniform pressure during the cure cycle. The shrink wrap and teflon film are perforated to allow excess resin to bleed out of the laminate. A bleeder cloth is wrapped around the tube to absorb any excess resin during the cure cycle.

The cure cycle consists of an increase in temperature from room temperature to 350 degrees Fahrenheit in one hour. The cure temperature of 350 degrees is then held for an additional two hours. The reduction in temperature back to room ambient requires one more hour. The part is

removed from the oven then cooled in a freezer to contract the size of the aluminum mandrel. The composite tube then easily slides off the cold mandrel.

Test Results

A design study was conducted to compare a baseline design without viscoelastic material to the composite construction with the damping layer. The plies of graphite/epoxy fabric and tape are identical for the two laminates. The only difference between the two designs is the absence of the damping layer in the baseline configuration. Other studies^[9] have been conducted to analyze the effects of embedded damping layers but they examined the effects of replacing stiffness material with damping material. By maintaining the same number and orientation of plies within the laminates of both tube designs, the direct effect of embedding a damping layer can be quantified.

Measurements were made by the impact-hammer modal-test method with the specimen suspended in the near free-free boundary condition. To simulate the free-free boundary condition, the tubes are suspended in the vertical position by a string. Damping is measured using the half-power band-width method.

The first natural frequencies are similar for the tubes with or without the viscoelastic core. The first mode for the tube without the viscoelastic core is 455 Hertz, while the tube with the viscoelastic core is 400 Hertz. Damping in the first mode for the tube without the viscoelastic core is 0.6 percent. A damping value of 4.3 percent is present in the first mode of the tube with the embedded viscoelastic layer. Frequencies and damping measurements for the axial modes will not be made until end fittings are fabricated to couple the stiffness of the two shells with the viscoelastic core. It is important to note that the tube is designed in a state of axi-symmetric extension, but tested in a state of bending. Comparable results are expected for the load case of extension as obtained from the bending test.

Conclusions

The analytical techniques described in this paper enabled the placement of a viscoelastic core and ply orientations of two shells, optimizing the damping in combination with overall structural stiffness. The test results show a reduction of frequency from 455 to 400 Hertz with the addition of the viscoelastic layer. A majority of the reduction can be attributed to the increase in the mass of the tube from the additional material. The evaluation of the ply orientations within the composite design allows effective use of the damping material with the smallest penalty in stiffness. For a small reduction in stiffness, the damping in the first mode is increased over 7 times by optimizing ply angles and embedding a viscoelastic layer.

References

- 1) Lall, A. K., Asnani, N. T. and Nakra, B. C., "Damping Analysis of Partially Covered Sandwich Beams." Journal of Sound and Vibration, 1988, Vol. 123 No. 2, pp. 247-259.
- 2) Johnson, C. D., Kienhol' D. A. and Rogers, L. C., "Finite Element Prediction of Damping in Beams with Constrained Viscoelastic Layers." Shock and Vibration Bulletin, No. 51, May 1981, pp. 78-81.
- 3) Bronowicki, A. J. and Diaz, H. P., "Analysis, Optimization, Fabrication and Test of Composite Shells with Viscoelastic Layers." paper presented at the Damping '89 Conference, West Palm Beach, Florida, Feb. 1989, pp. GCA1-GCA21.
- 4) Stahle, C. V. and Staley, J. E., "Application of Damping to Spacecraft Structures," 29th National SAMPE Symposium, April 3-5, 1984, pp. 185-194.
- 5) 3M Product Information, Scotchdamp SJ-2015X Type 1210, Structural Products Department, St. Paul MN.
- 6) Ikegami, R., Johnson D. W., Walker, W. J., and Beck, C. J., "The Application of Viscoelastic Passive Damping To Satellite Equipment Support Structures," Journal of Vibration, Acoustics, Stress, and Reliability in Design, 1985, pp. 1-8.
- 7) Belknap, F. M., "Vibration Reduction of Composite Structures Using Constrained Layer Damping Techniques," Proceedings of the 32nd AIAA/ASME/AHS/ACSE Structures, Structural Dynamics, and Materials Conference, 1991, pp 2391-2396.
- 8) Andriulli, J. B., "Measured Damping and Modulus of Composite Cylinders." paper presented at the Damping '89 Conference, West Palm Beach, Florida, Feb. 1989, pp. BCC1-BCC26.
- 9) Barrett, D. J., "A Design for Improving the Structural Damping Properties of Axial Members." paper presented at the Damping '89 Conference, West Palm Beach, Florida, Feb. 1989, pp. HCB1-HCB18.

Figure 1. Coordinate System

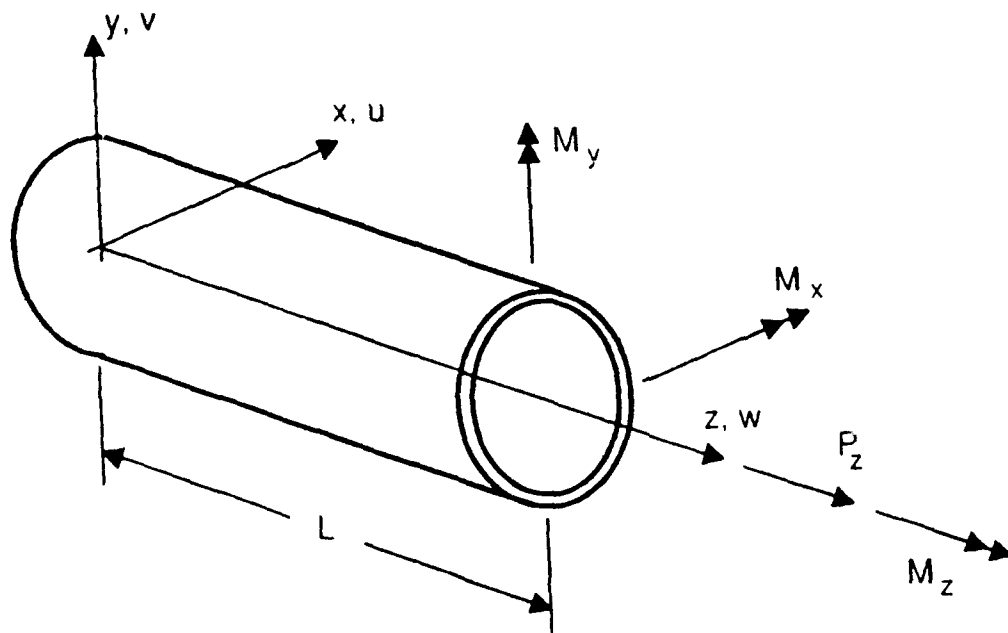


Figure 2. Torsional, Axial, and Bending Stiffness versus Unidirectional Ply Angle

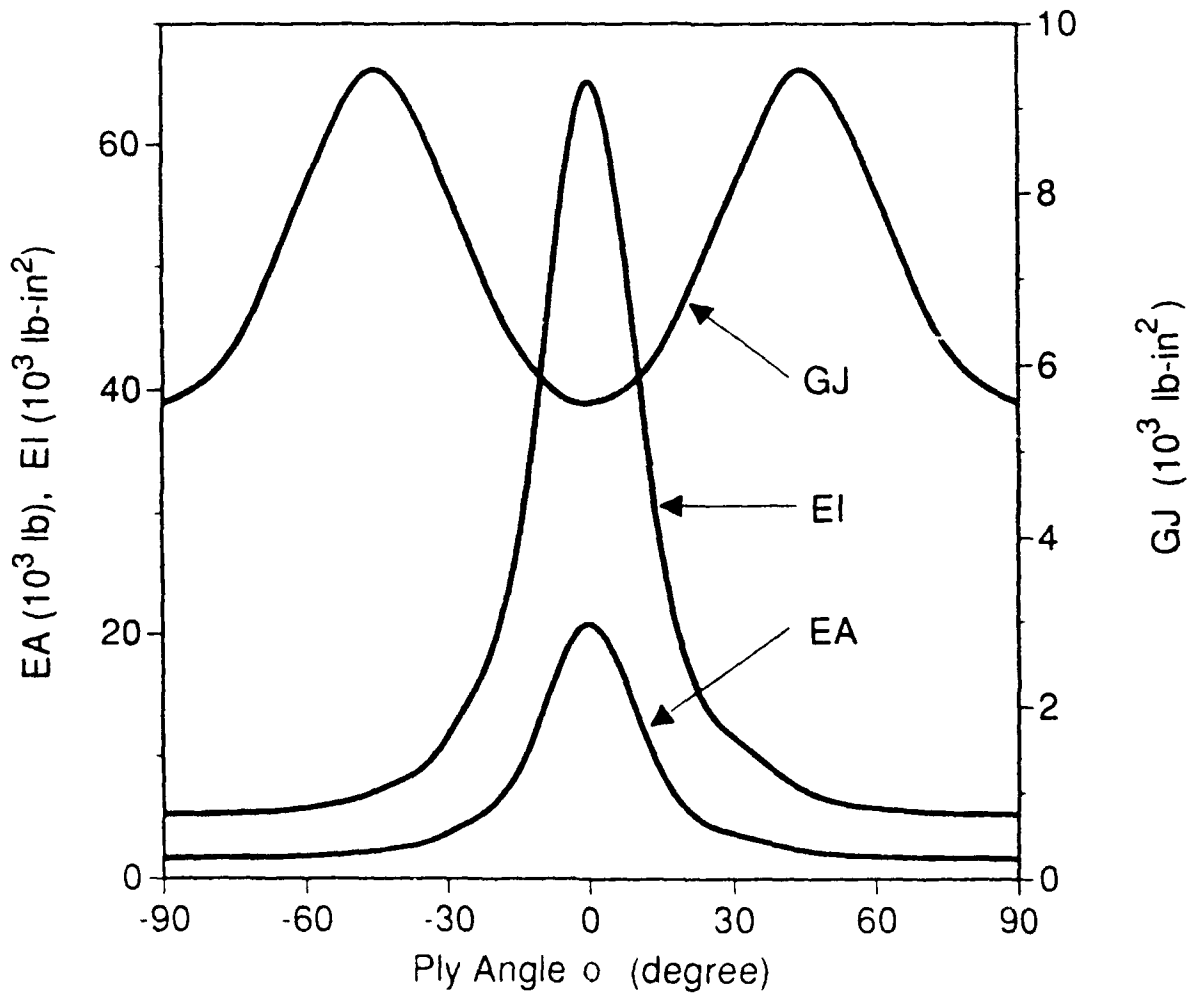


Figure 3. Extension-Twist/Extension Ratio versus Unidirectional Ply Angle

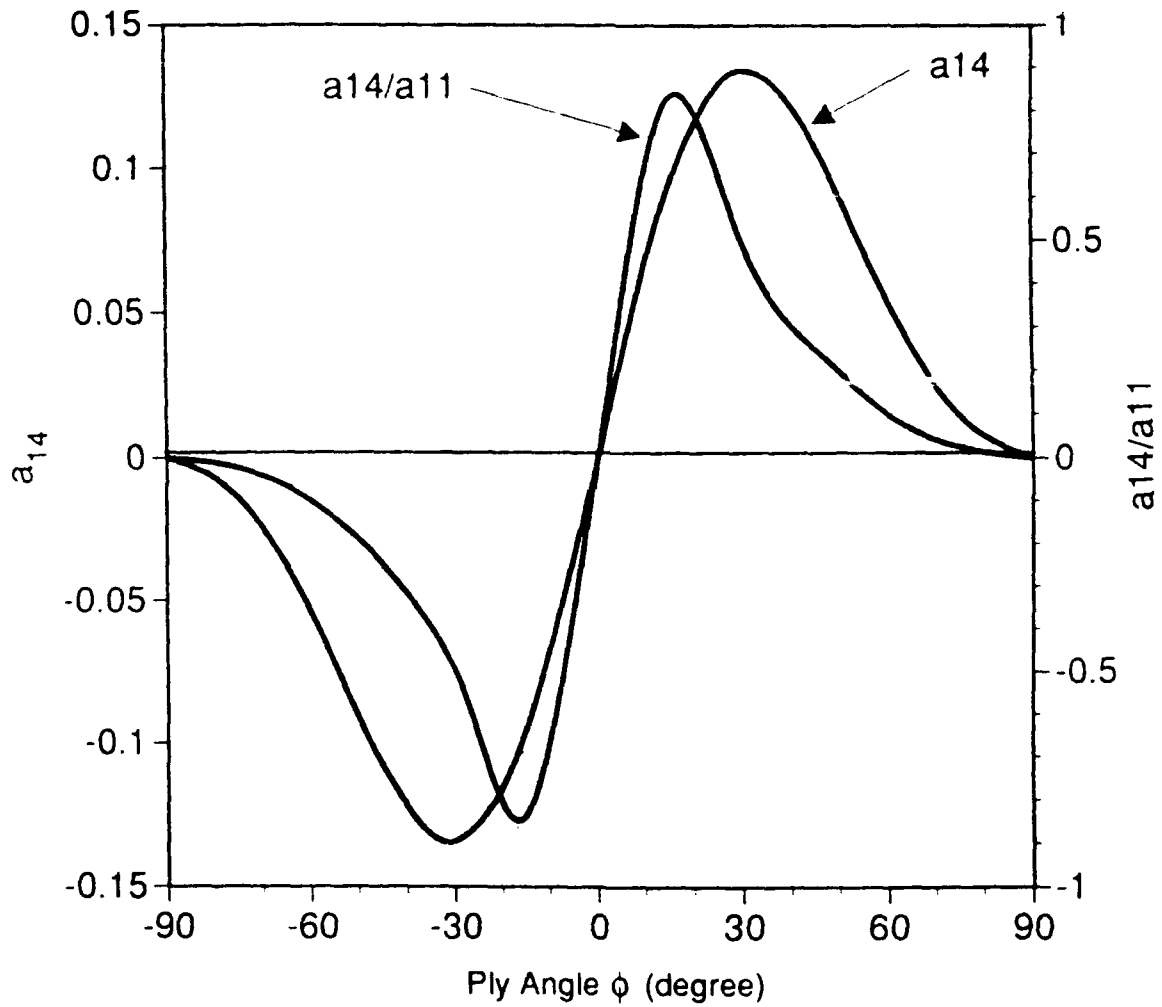


Figure 4. Maximum Shear Stress in Core versus Unidirectional Ply Angle

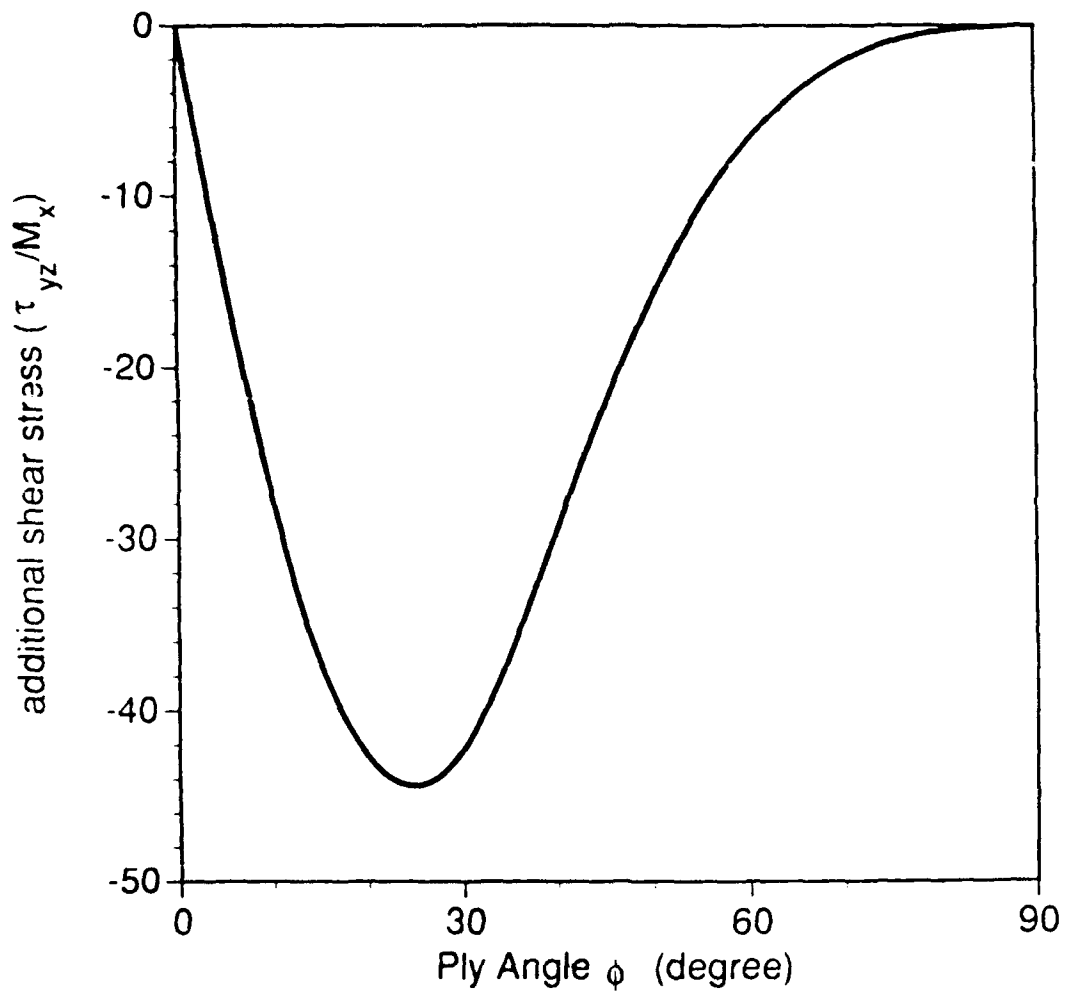
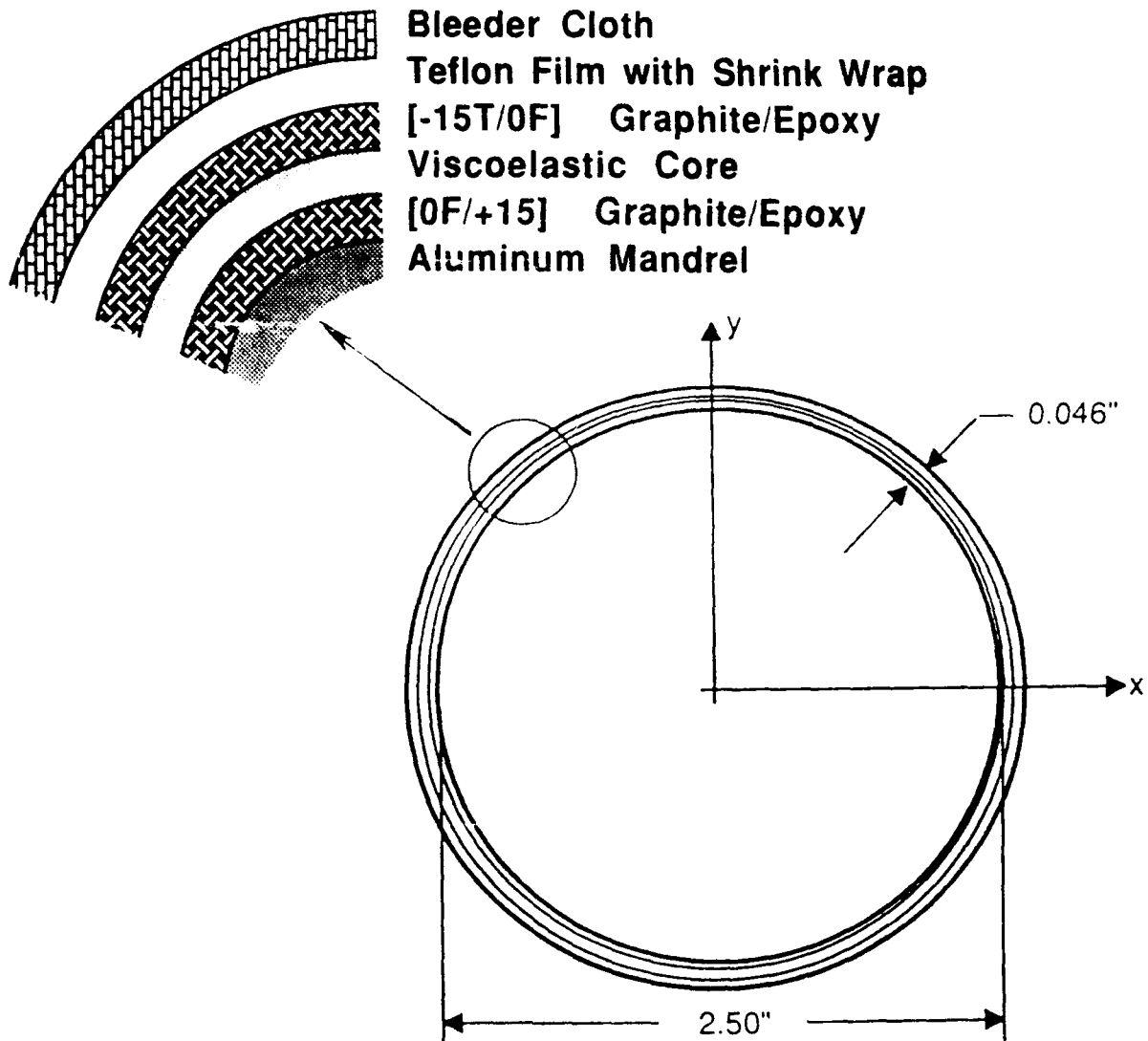


Figure 5. Ply Sequencing of Laminate



DIRECTIONAL DAMPING OF THE GLOBAL VIBRATION MODES OF TUBULAR STRUCTURES BY CONSTRAINED-LAYER TREATMENTS

S. S. Sattinger

Mechanics & Tribology Department
Westinghouse Science & Technology Center*

ABSTRACT

Among the types of vibration modes that may need to be damped in thin-walled structures are those involving low-order, long-wavelength bending, torsion, or extension. These modes are characterized by vibratory stresses that are uniform or nearly uniform through the thickness of the wall. Although more commonly used for the control of panel bending, shell bending, and other local modes, segmented constrained-layer damping treatments can also provide effective damping for the control of such global vibrations. Methods described for the prediction of global-mode damping include new interpretations of closed-form solutions generated previously by Torvik. A finite-element implementation of the strain-energy principle of Ungar and Kerwin is also described. The axial length of the structure spanned by a single segment of damping treatment has been assumed much smaller than a vibration wavelength at the frequencies of interest, making static or quasi-static analyses useable. Damping loss factors calculated by each of these methods compare well with measurements on an assembly of damped, hollow, rectangular-cross-section beams.

INTRODUCTION

A need often arises to design passive vibration-damping treatments that can reduce responses of several classes of vibration modes of a given structure. Specifically, the low-frequency, long-wavelength, global bending modes, the torsional modes, and possibly even the axial modes of a thin-walled tube may all need to be damped. All of these global modes can play major roles in the transmission of low-frequency noise and vibration, and their responses are often difficult to control.

Effective applications of constrained-layer treatments to damp local plate-bending and shell-bending modes, (Figure 1b), are common. However, the use of these treatments to damp the global beam-bending modes of tubular structures, (Figure 1a), and their torsional and axial modes, is not frequently reported. A previous paper [1] showed that a given constrained-layer treatment, properly designed, can provide effective damping of the global bending modes, concurrent with high damping of the local plate- or shell-bending modes, of open- or closed-section, thin-walled beams. Segmentation of the constraining layers was shown to be vital in obtaining such combinations of global- and local-mode damping performance.

*Pittsburgh, PA 15235, (412) 256-1327

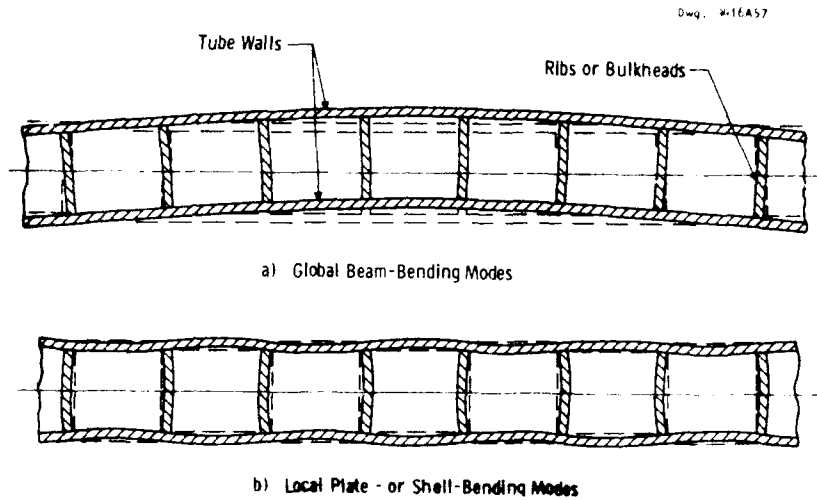


Figure 1 - Global vs. local bending modes of vibration in a thin-walled tubular structure

Constrained-layer treatments may also be required to damp the global modes of more complex structures in which each component simultaneously undergoes several different directions of vibration. One example would be the combined bending and torsion in members of a machinery support structure vibrating as illustrated in Figure 2. If the damping performance can be separately predicted for each direction of vibration in each component, the overall system damping values for combined modes of the entire structure can then be determined.

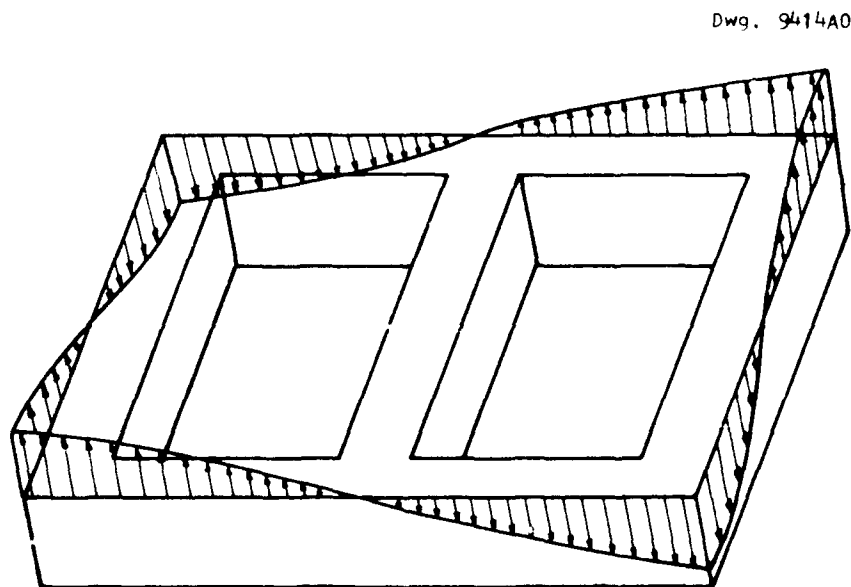


Figure 2 - Displacement shape for a combined torsional and bending vibration mode of a machinery support structure comprised of tubular members

This paper demonstrates that a given constrained-layer treatment can be effective in simultaneously damping the global bending, torsion, and axial vibrations of a tubular structural component. Methods are described for predicting or estimating the damping values for the individual directions of

vibration, including new interpretations of closed-form analyses performed previously by Torvik [2] and finite-element implementations of the strain energy principle of Ungar and Kerwin [3]. Experimental results on a damped box-beam test assembly, confirming the validity of these methods, are also given. Applications are primarily to closed tubular cross-sections, although the cross-section may be of almost any shape.

PREVIOUS ANALYSES OF DAMPING TREATMENT SEGMENTATION

The Ross-Ungar-Kerwin theory [4] is the basis of a method that is widely used for the design of constrained-layer treatments to damp flexural vibration waves in plates and beams. However, its application is valid only in cases where both the damping treatment and damped member are continuous or where any cuts between adjacent damping treatment segments happen to coincide with nodal points in a standing wave.

Parfitt [5] extended the Ross-Ungar-Kerwin theory to cases where the damping treatment is cut at uniform intervals along the length of a vibrating beam. Parfitt found that the low-frequency (long-wavelength) damping performance was dramatically improved by such axial segmentation, and he derived an expression for the optimum spacing of cuts in terms of the thicknesses and moduli of the constraining layer and the constrained VEM layer. Assuming constant VEM properties, the optimum segmentation would provide, at very low frequencies, damping performance almost as high as the peak damping of the continuous treatment. In this derivation the damping treatment was assumed sufficiently compliant to have no influence on the strain distribution in the base structure and to acquire negligibly small amounts of stored strain energy.

In a similar derivation of damping performance and optimum segment length by Plunkett and Lee [6], the same assumption of damping treatment compliance was made. Kress [7] derived an expression for optimum segment length which is sensitive to the properties of the base structure in addition to those of the damping layers.

Torvik [2] analyzed two different cases of quasi-static vibratory loading of constrained-layer-damped structural members, both of which can be applied to the global-mode damping of tubular structures having segmented damping treatments. Both of these analyses account for strain energy stored in all components of the system and are therefore applicable to stiff damping treatments such as are used in the experiments described later. These analyses are described and interpreted for use in global-mode damping applications in the next section.

DAMPING PERFORMANCE PREDICTION METHODS FOR GLOBAL MODES

Three alternate approaches for predicting or estimating the global-mode damping performance of segmented constrained-layer treatments on tubular structures are described below.

Closed-Form, Quasi-Static Solution for Vibratory Flexure

Torvik [2] analyzed the case of quasi-static moment loading of a finite-length cantilever beam covered by a single segment of constrained-layer treatment which is built-in at the root end and free at the opposite end as

shown in the uppermost view in Figure 3. Flexure in both the base member and the constraining layer is modeled using Bernoulli-Euler beam theory. The solution is also directly applicable to a free-free, moment-loaded beam of twice the length of the cantilever beam.

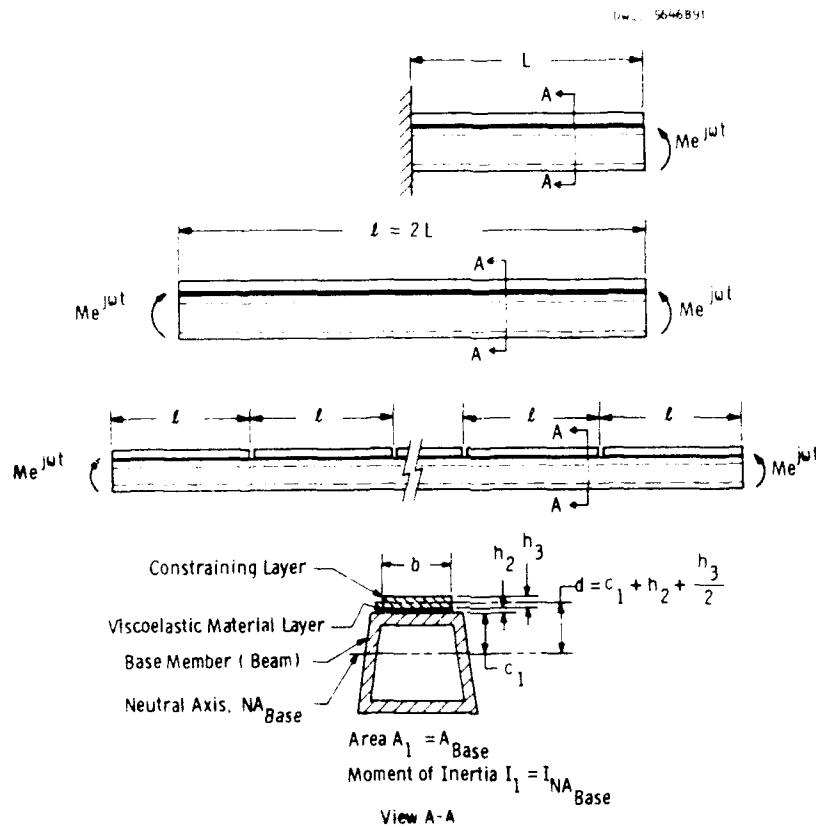


Figure 3 - One-side-damped cases represented by Torvik's closed-form, quasi-static solution for vibratory flexure

For sufficiently long wavelengths, the beam analyzed can also be viewed as a building block of a long, continuous vibrating beam of the same cross-section, damped by a segmented treatment as shown in a lower view in Figure 3. This analysis applies only to the installation of damping treatment on a planar surface that is oriented parallel to the neutral surface of the base member, but, as indicated by Figure 4, it can also be interpreted as applicable to structures that have symmetric cross-sections and are damped on two sides.* Torvik's analysis applies to the dynamic vibratory case, i.e., to the case in which there are transverse vibratory inertia forces, provided that the instantaneous standing-wave bending-moment distribution is nearly constant over the length of beam covered by each segment. That is, the bending wavelength must be long in comparison with the segment lengths.

*Setting area A_1 equal to infinity models the condition of zero extension at the base member centroid, brought about by symmetry.

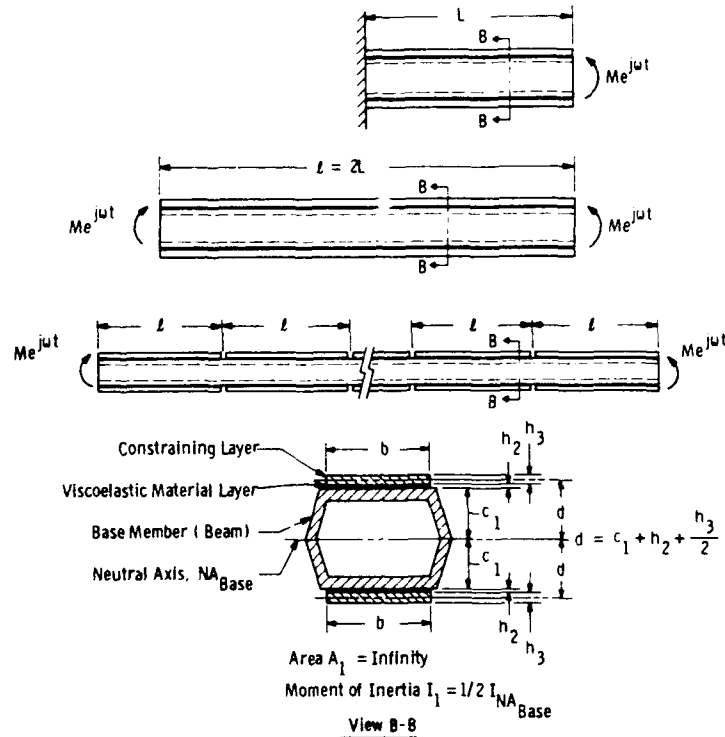


Figure 4 - Two-sides-damped cases represented by the closed-form, quasi-static solution for vibratory flexure

Torvik developed expressions for stored and dissipated energy leading to the following closed-form expression for system damping in flexure:

$$\eta_f = \frac{\eta_2 G_2 d^2}{h_2 \left[E_1 I_1 + \frac{E_3 b h_3^3}{12(1-\nu_3^2)} \right]} \cdot \frac{F(\theta)}{\text{Re} \left[\frac{L \tanh \theta}{\theta} - \frac{gL^3}{\theta^3} (\tanh \theta - \theta) \right]} \quad (1)$$

where η_f = flexural damping loss factor = 2 x percent critical damping /100, and

$$g = \frac{G^* b}{h_2} \left[\frac{1}{E_1 A_1} + \frac{1}{E_3 b h_3} \right]$$

$$F(\theta) = - \frac{1}{2} \frac{\text{Im} [\tan(i\theta) / (i\theta)]}{\text{Re} [\theta] \text{Im} [\theta]}$$

$$\theta = \left\{ \frac{G^* b L^2}{h_2} \left[\frac{1}{E_1 A_1} + \frac{1}{E_3 b h_3} + \frac{d^2}{E_1 I_1 + \frac{E_3 b h_3^3}{12(1-\nu_3^2)}} \right] \right\}^{1/2}$$

where $G^* = G_2(1 + j\eta_2) =$ complex shear modulus of the VEM

$$j = \sqrt{-1}$$

$E =$ Elastic tensile modulus

Subscript 1 denotes the damped member

Subscript 2 denotes the VEM layer

Subscript 3 denotes the constraining layer

Re (z) denotes the real component of the complex quantity z

Im (z) denotes the imaginary component of the complex quantity z

and all other symbols are defined in Figures 3 and 4. In contrast with Torvik's original development for a solid rectangular cross-section, these results are expressed here in terms of the properties of arbitrarily-shaped base member cross-sections for greater generality.

Closed-Form Quasi-Static Solution for Vibratory Extension

For thin-walled tubular structure cross-sections, the distribution of global-mode vibratory bending stresses is nearly uniform through the thickness of the wall. Under these conditions, which are illustrated in Figure 5, the bending-mode damping can be estimated by applying a solution of quasi-static extensional loading of a constrained-layer-damped structural member, derived by Torvik as an adaptation of an earlier analysis of lap joints by Avery [8]. This solution is also directly useable for predicting the damping of axial modes, and, as shown later, the torsional-mode damping values can also be reasonably close to the extensional damping value in some instances.

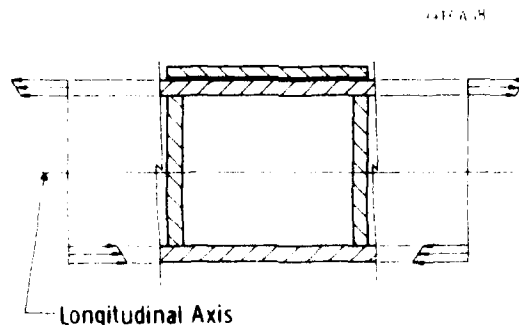


Figure 5 - Instantaneous stress distribution in a region of a damped tubular component undergoing global bending vibration, showing that the walls are in a state of extensional stress that is nearly uniform through the thickness

Torvik addressed the case of a member built-in at one end and covered by a single segment of damping treatment which is built-in at the root end and

free at the loaded end. This case is shown in the uppermost view of Figure 6. The solution also applies directly to a free-free, extensionally loaded bar of twice the length of the built-in bar, which is the case pictured in the middle view of Figure 6. Good agreement between calculated and measured extensional damping performance in constrained-layer-damped bars was obtained in an earlier study by the author [9].

Key assumptions in Torvik's derivation are that plane cross-sections in the damped member and in the constraining layer remain plane and translate without rotating. While this pure-translational deformation assumption does not apply in a strict sense, it is a good approximation to the actual conditions in a tubular structure in bending. Torvik derived the following formula for damping under vibratory extension:

$$\eta_e = \frac{\eta_2 G_2 b L^2}{E_1 A_1 h_2} \cdot \frac{F(\beta)}{\left[\frac{1}{\frac{E_3 h_3 b}{E_1 A_1} + 1} \right] + \frac{G_2 b L^2}{E_1 A_1 h_2} \operatorname{Re} \left[\frac{(1+j\eta_2) \tan(j\beta)}{j\beta^3} \right]} \quad (2)$$

where η_e = extensional damping loss factor

$$F(\beta) = - \frac{1}{2} \frac{\operatorname{Im}[\tan(j\beta)/(j\beta)]}{\operatorname{Re}[\beta] \operatorname{Im}[\beta]}$$

$$\beta = \left\{ \frac{G^* b L^2}{h_2} \left[\frac{1}{E_1 A_1} + \frac{1}{E_3 b h_3} \right] \right\}^{1/2}$$

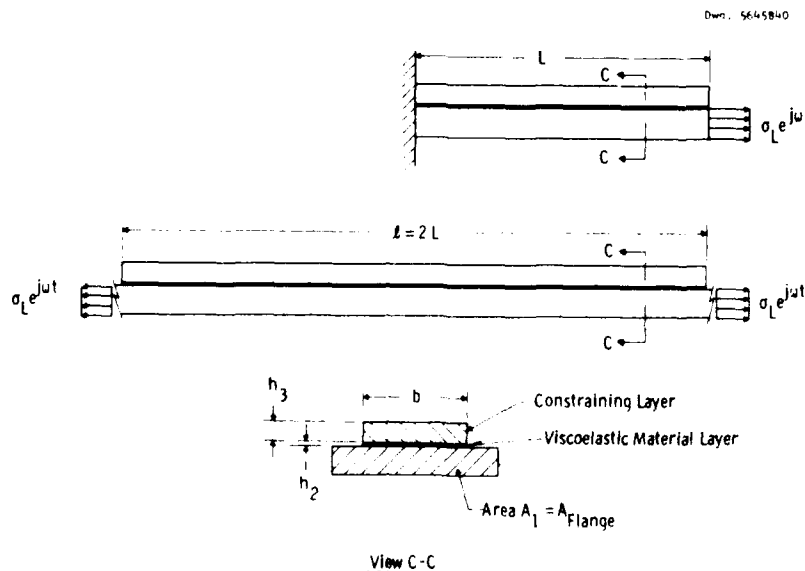


Figure 6 - The case of quasi-static, vibratory extension, analyzed earlier by Torvik, as applied to the portion of a structure wall beneath one segment of damping treatment

and all other quantities are defined in conjunction with Equation 1 above, or in Figure 6. Whereas Torvik assumed all three layers to be of equal width, which vanished in the formula he derived, his formula has been re-expressed here in terms of damping treatment width, b , and damped member area, A_1 , to apply to situations where the surface area is partially covered by the damping treatment.

In a separate treatment of the subject of segmentation, Kerwin and Smith [10] stated that achievable loss factors in extension are lower than those in flexure for a given system cross-section. This rule decidedly holds true for solid damped-member cross-sections.* However, as demonstrated in a later section, the difference diminishes for hollow cross-sections, and in the limit of beams whose section properties are dominated by flat, widely spaced parallel flanges, the optimum global bending loss factor tends toward equality with the optimum extensional loss factor.

To the extent that strain energy is stored in other regions of the tubular structure that are untreated, the extensional damping calculated in this manner will overestimate the true overall global-bending-mode loss factor. The experimental results in a later section demonstrate, however, that the extensional damping estimate can be reasonably close to the true bending-mode damping value for rectilinear-cross-section, thin-walled tubular beams having segmented damping treatment on all panels.

Finite-Element Modeling

In recent years there have been many applications of the finite-element method to predictions of constrained-layer damping performance. In many cases these predictions have made direct use of the strain-energy principle of Ungar and Kerwin [3], which is expressed symbolically as

$$\eta_s = \frac{\sum_j \eta_j U_j}{\sum_j U_j} \quad (3)$$

where η_s = system damping loss factor

U_j = strain energy in the j th region or component of the system in a given mode of vibration

η_j = the damping loss factor of the j th region or component.

The modeling to be described here is one such application.

The prediction of global-mode damping performance of segmented treatments introduces no new kinds of finite-element modeling requirements but may, if wavelengths are sufficiently long, offer the analyst the option to perform a static analysis in lieu of a dynamic one. Major incentives for choosing the finite-element approach for bending-mode damping predictions in preference to the previously-described closed-form methods might be curvature, slope, or irregularities such as cut-outs in the structure walls, which could

*A rule of thumb is that optimum flexural loss factors are roughly a factor of three times larger than the corresponding optimum extensional loss factors for solid cross-sections.

invalidate the use of the latter methods. In the case of torsional modes, no closed-form solutions appear to be available as alternates to finite-element modeling.

The finite-element modeling described here is an adaptation of an earlier approach of Killian and Lu [11] in which short, offset beam elements are used in lieu of brick elements to represent the VEM layer. Although originally used in conjunction with the direct frequency-response method using a complex-modulus representation for the VEM, this approach also lends itself to elastic modeling of the VEM layer using the modal strain energy principle. As in all other elastic-modeling implementations, which are quite common in finite-element predictions of constrained-layer damping, the results are approximations in that real-valued deformation shapes are generated in lieu of complex shapes. All modeling described here has been performed using the WECAN finite-element modeling program [12].

GLOBAL-MODE DAMPING EXPERIMENTS ON A TUBULAR STRUCTURE

Figure 7 is a photograph of an all-steel box-beam test assembly specially designed and constructed to verify global-mode damping

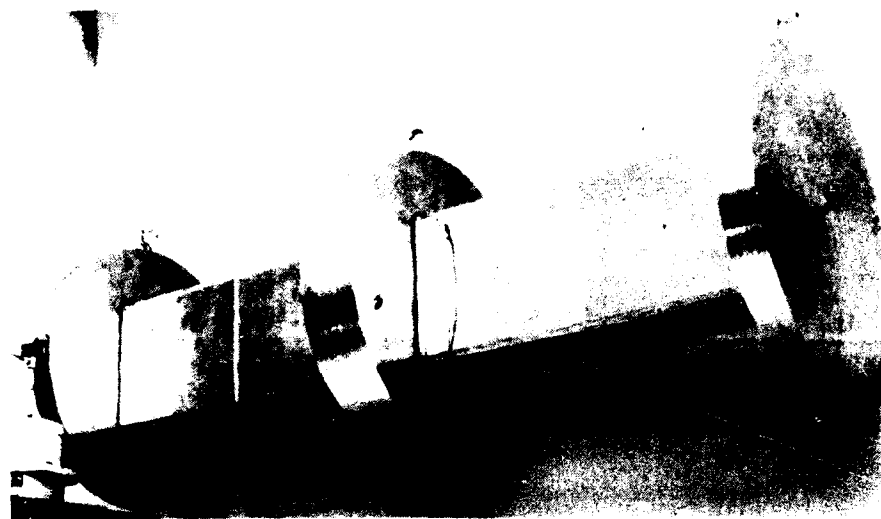


Figure 7 - Mass-loaded box-beam test assembly, with segmented damping treatment in place, undergoing torsional damping measurements

performance predictions, generated by each of the methods described above, for individual directions of vibration. The tubular portions represent the construction of the larger machinery support structure pictured in Figure 2, but with a one-dimensional configuration, it would be possible to measure the individual damping values without coupling among the various directions of vibration. The three solid circular discs made it possible to use a compact test configuration by providing mass and inertia loadings simulating reactions that would be present in a continuous beam of much greater length. Figure 8 shows the design details and illustrates that, in general, the cuts between damping treatment segments need not coincide with the placement of ribs or stiffeners. The next section addresses the fact that damping treatment was applied on all four sides of the rectangular-cross-section beams, whereas the closed-form solution for flexure applies to cases where only one or two sides are damped.

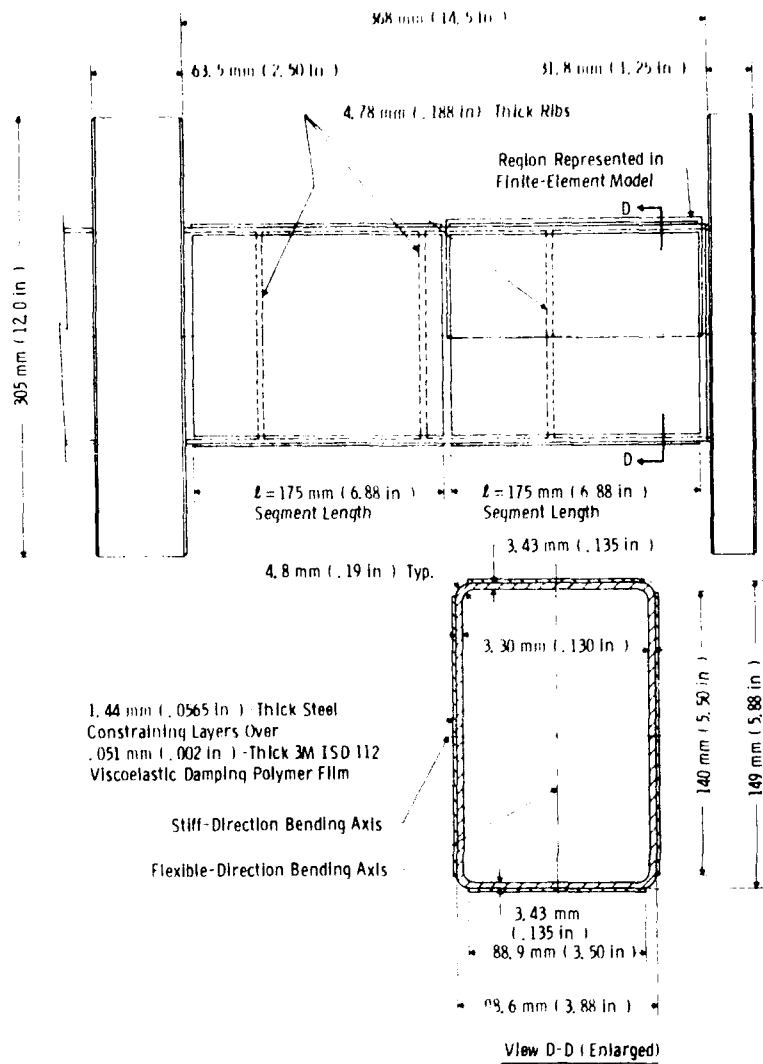


Figure 8 - Design details of the box-beam test assembly

The beams were fabricated by bevel-welding ribs of cold-rolled steel between short sections cut from 152 mm x 102 mm x 4.8-mm wall (6 in x 4 in x 3/16-in wall) structural-steel rectangular tubing. Flat surfaces were machined on the beam-wall exteriors before the weld-attachment of the discs and the installation of the damping treatment. Because of weld distortion there were sizeable variations in wall thickness, and the thickness values shown represent averages after machining. The total mass of the damped assembly was 91.6 kg (202lb), of which the undamped beams comprised 15.3 kg (33.7 lb) and the damping treatment comprised 3.6 kg (8.0 lb).

The damping treatment was installed in segments of 1.44 mm (0.0565 in)-thick constraining layer over 0.051mm (0.002 in)-thick 3M ISD 112 viscoelastic damping polymer, giving a fairly large stiffness ratio ($E_{3h_3}/E_{1h_1} = 0.43$). Both sides of the damping polymer layers were bonded to the adjacent steel surfaces using 3M 1838 epoxy structural adhesive. Care was taken to avoid adhesive bridging between the constraining layer segments and the base structure. All damping performance calculations were performed using the frequency-dependent VEM property values plotted in Figure 9. These

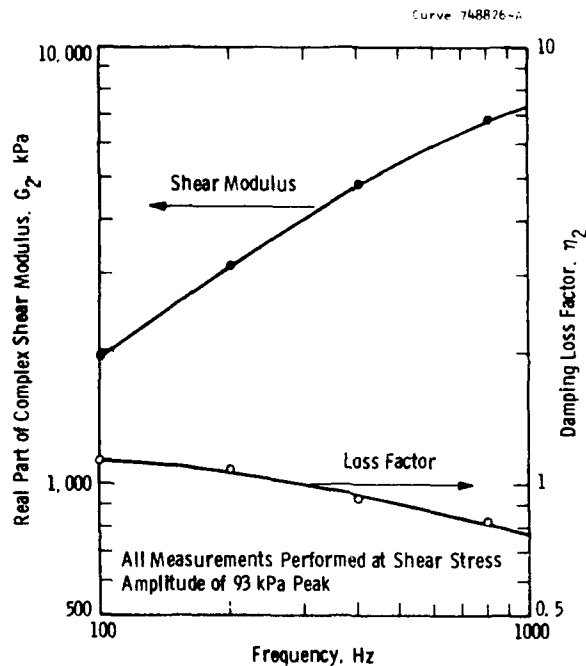


Figure 9 - Properties used in modeling the 3M ISD 112 constrained damping layers at the 22°C (72°F) test conditions

properties were measured on a different lot of the same damping polymer using a previously described measurement technique [13]. The extent of lot-to-lot variation in properties is not known.

The various bending and torsional modes of the assembly before and after installation of the damping treatment were individually excited in sinusoidal dwells using an eccentrically positioned shaker. Measurements of the higher-frequency axial modes were also performed by driving on the center axis. The damping values were measured by means of rates of decay from these dwells at shaker cutoff. All tests were performed at approximately 22°C (72°F) room temperature.

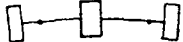
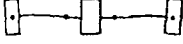
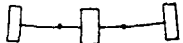
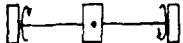
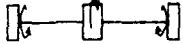
COMPARISON OF CALCULATIONS AND MEASUREMENTS

Table 1 lists measured natural frequency and damping values for the global modes of the test assembly before and after the installation of damping treatment. The results show that the damping due to the add-on treatment far exceeded the inherent damping of the base structure. The increases in natural frequencies show that the net effect of the damping treatment installation was to increase the dynamic stiffnesses in greater proportion than the increase in mass.

Although damping treatment was installed on all four sides of the beam portions, calculations using the closed-form solution for flexure with damping treatment on only two sides are nonetheless useful. Table 2 compares calculations for two different choices of area moment of inertia, one choice being half that of the full base-member cross-section as per Figure 4, and the other being that of only one of the two "flanges" (sides oriented parallel to the neutral axis). The former choice produces a lower bound to the true damping, because the damping contribution of the treatment on the sides perpendicular to the neutral axis is not taken into account. By the strain-

Table 1

Measured Natural Frequencies and Damping Values for Global Vibration
Modes of the Mass-Loaded Box-Beam Test Assembly

Mode Type	Mode Identity and Shape	Undamped Configuration		Damped Configuration		
		Natural Frequency, Hz	Damping Loss Factor	Natural Frequency, Hz	Damping Loss Factor	
Flexible-Direction Beam Bending	1st Mode		218	0.00088	230	0.043
	2nd Mode		669	0.00085	712	0.041
	3rd Mode		845	0.00088	896	0.036
	4th Mode		987	0.00070	1052	0.043
Stiff-Direction Beam Bending	1st Mode		305	0.00088	324	0.039
	3rd Mode*		1145	P	1229	P
	4th Mode		1360	P	--	--
Torsional	1st Mode		357	0.0010	383	0.052
	2nd Mode		511	0.0010	558	0.049
Axial	1st Mode		942	0.0031	1005	0.035
	2nd Mode		1323	0.0030	1387	0.028

* Indicates point of minimum motion amplitude.

P Indicates measurement rejected as invalid due to coupling with local bending modes of beam wall panels.

* A stiff-direction bending mode analogous to the second flexible-direction mode could not be identified but is believed to have existed at a frequency coincident with the first extensional mode.

energy principle, the latter choice should predict the true damping if the ratio of VEM strain energy to total strain energy in the sides perpendicular to the neutral axis were equal to the corresponding ratio in the flanges. However, the results of finite-element modeling, discussed below, indicate that in both the flexible and stiff bending directions, the fraction of VEM to total strain energy in the perpendicular sides is somewhat less than that in the flanges. Therefore the use of only the flange moment of inertia produces an upper bound to the true damping in instances where the thicknesses are nearly constant throughout the beam cross-section.

Figure 10 plots the calculated closed-form flexural damping values from Table 2 together with a curve of calculated extensional damping. Frequency affects all of these calculations only to the extent that it governs the VEM properties. The extensional damping curve has been generated using, for a base member, a flange having 3.35 mm (0.132 in) thickness, which represents a weighted average of the thicknesses of the four sides. This simplified approach can be taken because the stiffness ratio, E_3h_3/E_1h_1 , is nearly constant around the periphery. The base member width has been regarded as equal to that of the damping treatment, but to account for the incomplete coverage, an area ratio of 0.875 has been used to pro-rate the resultant loss

Table 2

Damping Values Calculated for Mass-Loaded Box-Beam Test Assembly
Using Closed-Form Solution for Vibratory Flexure

Mode Type	Mode Identity	Natural Frequency, Hz	Damping Loss Factor*	
			Using Moment of Inertia of Full Cross-Section	Using Moment of Inertia of Flanges Only
Flexible- Direction Bending	1st Mode	230	0.0530	0.0639
	2nd Mode	712	0.0411	0.0491
	3rd Mode	896	0.0381	0.0454
	4th Mode	1052	0.0359	0.0428
Stiff- Direction Bending	1st Mode	324	0.0417	0.0564

* Calculated in accordance with Equation (1) and Figure 4 using VEM properties at damped natural frequency for each mode. Resultant loss factors have been pro-rated by a 0.949 length ratio to account for incomplete coverage by the treatment.

factors. The fact that the extensional loss factor curve is bounded from above and below by the calculated flexural damping values illustrates its usefulness as an estimator of global bending-mode damping. The peak in the extensional damping curve is due to the occurrence of an optimum combination of G_2 , h_2 , and l for the specific E_1, h_1, E_3 , and h_3 values used.

Also included in Figure 10 are the results of quasi-static finite-element modeling of damping under both directions of pure bending-moment loading and under torsional and axial loading. Figure 11 depicts the 1/8-region finite-element mesh that modeled one of the tubular portions of the assembly (see also Figure 8) and shows how these loading conditions were simulated by imposing constant or linearly-varying displacement distributions on one of the ends while the opposite end was restrained. The VEM layer was modeled elastically. The storage modulus and loss factor values used were based on an arbitrarily-chosen frequency of 340 Hz for all loadings. The computed damping loss factors have been reduced by an empirically derived factor of 1/1.2. This factor corrects for the use of elastically calculated deflection shapes to compute the strain energies in a viscoelastically damped structure having a VEM loss factor of about 1.0.

The closeness among the finite-element results for the various directions of vibration adds further validity to the notion of using an extensional damping calculation to estimate the global bending-mode damping. Furthermore, these finite-element results are in very close proximity to the closed-form solution results. It seems at first surprising that the torsional damping is in such close proximity to that of the other directions. However, Figure 12 illustrates that the pure-shear deformation of the individual panels under torsion produces an extensional deformation of damped panel slices oriented at 45° to the tube axis, and that the effective lengths of these slices are comparable to the axial lengths of the segments.

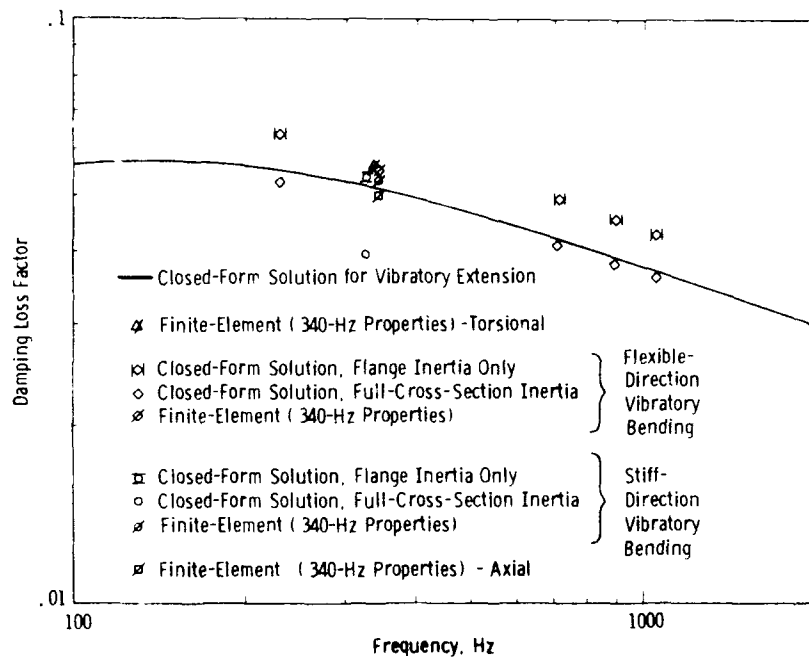


Figure 10 - Calculated damping performance for the box-beam test assembly

Finally, Figure 13 compares the closed-form extensional damping calculation with measured damping values for the global bending and extensional modes. There is considerable scatter in the measurements, but their trends appear reasonably well predicted by the extensional damping curve. The scatter may be partly attributed to the earlier-mentioned irregularities in wall thicknesses of the beam portions. In addition, transverse shear forces were undoubtedly present in some of the global bending modes, and these may have influenced the overall damping values differently for each of the modes.

DISCUSSION

The fact that the damping performance values plotted in Figures 10 and 13 are in the proximity of a peak is the result of the combination of damping treatment design parameters having been nearly optimized. This combination is particularly sensitive to the segment length parameter, l . The optimum global-mode loss factors are considerably smaller than the optimum loss factors for local-mode plate bending with this treatment (which would be in the vicinity of 0.15), but they do, nonetheless, represent useful and effective damping.

Circumferential segmentation of the damping treatment can play an important role in achieving good global-mode damping performance. Without segmentation circumferentially, the damping treatment would be forced to conform to the bending curvature of the base structure (compatible deformations) by way of transverse normal forces, and the VEM layer would sustain very little shear deformation as a result. This situation may be visualized by imagining the four circumferential damping treatment segments of the test assembly to be connected together rigidly at the corners as the beam sections undergo bending. This circumferential segmentation was the subject of an earlier analysis of damped, circular-cross-section tubes by the Russian authors Vinogradov and Chernoberevskii [14]. The conclusion of their study

was that the bending loss factors of tubes having axially continuous constrained-layer treatments can be substantially increased by slitting the constraining layer lengthwise into a number of arc-shaped segments. Especially for long axial segment lengths, the same result should apply to axially segmented treatments.

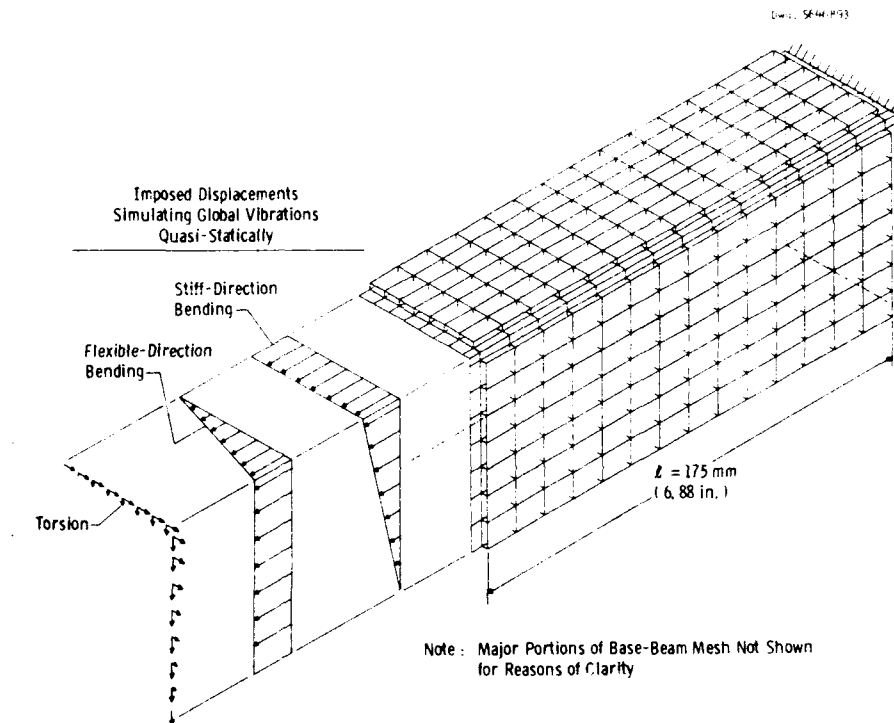


Figure 11 - Finite-element model of a one-eighth portion of one of the damped tubular portions of the box-beam test assembly

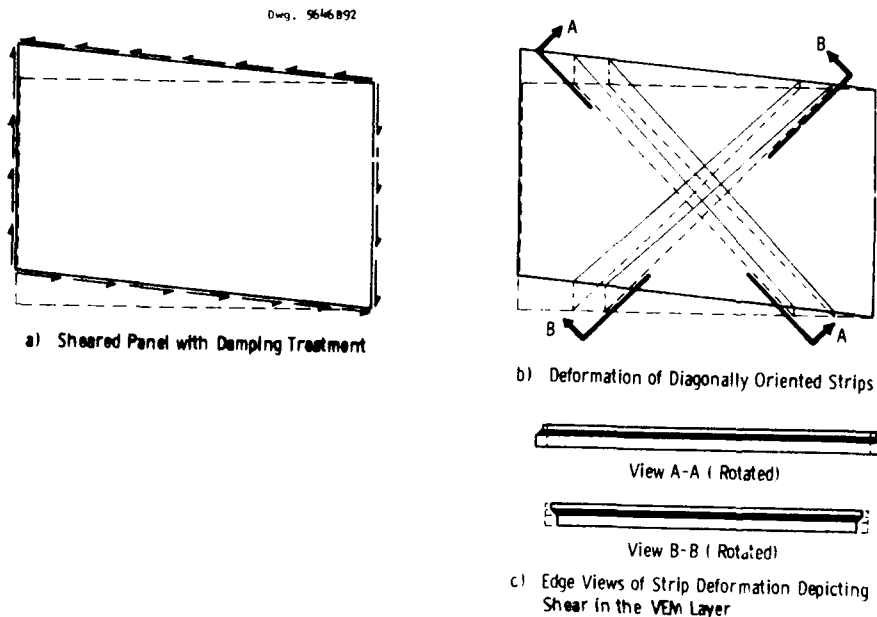


Figure 12 - Deformation of a damped box-beam panel under torsion-induced shear stress

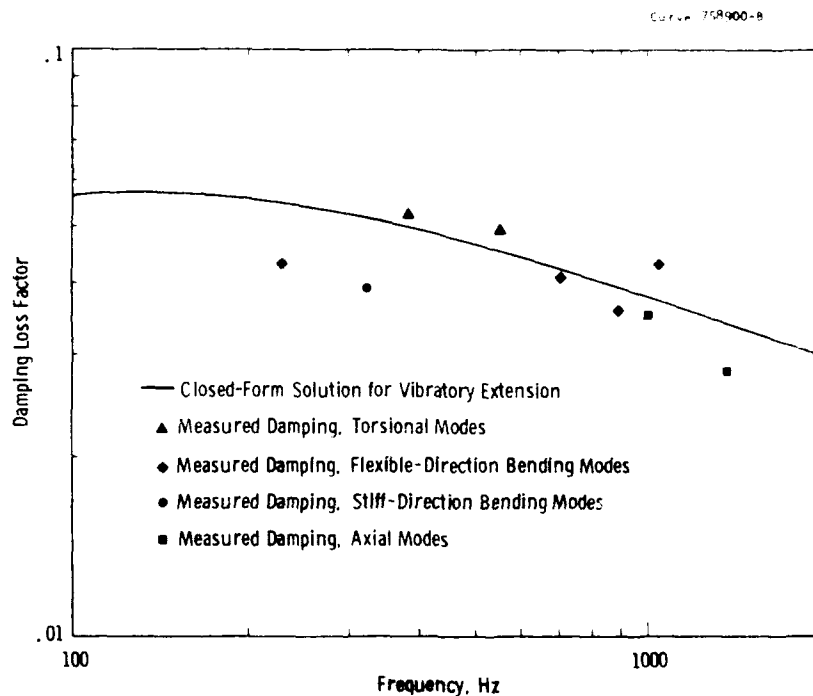


Figure 13 - Measured vs. calculated damping performance for the box-beam test assembly

If distinctly different values of damping are predicted for each direction of vibration in each component, the overall system damping value for each mode of a complex structural assembly can be predicted by using impedance or energy methods. Finite-element structural analysis codes such as MICA [15] enable the user to specify individual damping values corresponding to each degree of freedom of the beam elements used to model the components of a given structure, and a system damping loss factor is predicted by the code for each mode of the assembly.

CONCLUSIONS

A given constrained-layer treatment can be simultaneously effective in damping the global bending, torsion, and axial vibrations of a tubular structural component. The effective damping of the global modes requires the use of relatively stiff treatments, and axial subdivision of the treatment into segments of optimum length is vitally important. However, circumferential subdivision can also play an important role, especially for long axial segment lengths.

Torvik's closed-form, quasi-static solutions for the flexural and extensional vibrations of damped members are well-suited for performance estimates on these configurations. The use of finite-element modeling for this purpose may be warranted in cases where curvature, slope, or irregularities in the beam walls would invalidate the closed-form solutions.

The experiments on the damped, hollow, rectangular-cross-section beam assembly demonstrate the usefulness of each of these methods for calculating global-mode damping performance. Although derived for members damped on sides that are parallel to the neutral axis, the quasi-static flexural damping

prediction method is useable for performance estimates on rectangular-cross-section, tubular components having damping treatment on all sides. Measured and finite-element-calculated damping values for all global modes of the assembly agreed closely with the quasi-static extensional damping calculations, underscoring the usefulness of the latter method as a simple, but reasonably accurate, performance estimator.

ACKNOWLEDGEMENTS

The support of Dr. L. K. H. Lu of the Westinghouse Marine Division, sponsor of this work, is appreciated. J. P. Condle, K. B. Wilner, D. V. Wright, and J. A. Zaldonis of the Westinghouse Science & Technology Center are thanked for their contributions.

REFERENCES

1. Sattinger, S. S., "Constrained-Layer Damping of Global Bending Vibration Modes of Thin-Walled Beams," *Vibration Control of Mechanical, Structural, and Fluid-Structural Systems*, PVP-Vol. 202, ASME, 1990, pp. 45-53.
2. Torvik, P. J., "The Analysis and Design of Constrained Layer Damping Treatments," *Damping Applications for Vibration Control*, AMD-Vol. 38, ASME, 1980, pp.85-112.
3. Ungar, E. E. and Kerwin, E. M., Jr., "Loss Factors of Viscoelastic Systems in Terms of Energy Concepts," *Journal of the Acoustical Society of America*, Vol. 34, 1962, pp. 954-957.
4. Ross, D., Ungar, E. E., and Kerwin, E. M., Jr., "Damping of Plate Flexural Vibrations by Means of Viscoelastic Laminae," *Structural Damping*, Section III, J. E. Ruzicka, ed., ASME, 1959, pp. 49-87.
5. Parfitt, G. C., "The Effect of Cuts in Damping Tapes," *Fourth International Congress on Acoustics*, Copenhagen, August 1962, pp. 21-28.
6. Plunkett, R. and Lee, C. T., "Length Optimization for Constrained Layer Damping," *Journal of the Acoustical Society of America*, Vol. 48, No.1 (Part 2), July 1970, pp. 150-161.
7. Kress, G., "Improving Single-Constrained-Layer Damping Treatment by Sectioning the Constraining Layer," *The Role of Damping in Vibration and Noise Control*, DE-Vol.5, ASME, 1987, pp. 41-48.
8. Avery, C. P., "An Investigation of Longitudinal Shear Distribution and Damping in a Viscoelastic Adhesive Lap Joint," *U. S. Air Force Wright Air Development Division Technical Report No. WADD TR 60-687*, November 1960.
9. Sattinger, S. S., "A Study of Extensional Damping Performance Discrepancies in Certain Constrained-Layer Treatments," *The Role of Damping in Vibration and Noise Control*, DE-Vol.5, ASME, 1987, pp. 33-40.

10. Kerwin, E. M., Jr., and Smith, P. W., Jr., "Segmenting and Mechanical Attachment of Constrained Viscoelastic Layer Damping Treatments for Flexural and Extensional Waves," U. S. Air Force Flight Dynamics Laboratory Vibration Damping Workshop, Long Beach, CA, February 1984, pp.KK-1 - KK-24.
11. Killian, J. W. and Lu, Y. P., "A Finite Element Modeling Approximation for Damping Material Used in Constrained Damped Structures," Journal of Sound and Vibration, Vol. 97, No. 2, 1984, pp. 352-354.
12. "WECAN- Westinghouse Electric Computer Analysis, User's Manual," W. E. Stillman, Editor, Revision X, June 1, 1988, Vols. 1-4.
13. Sattinger, S. S., "Direct Method for Measuring the Dynamic Shear Properties of Damping Polymers," Chapter 5 of Sound and Vibration Damping with Polymers, R. D. Corsaro and L. H. Sperling, eds., American Chemical Society Symposium Series, No. 424, pp. 79-91, 1990.
14. Vinogradov, B. D. and Chernoberevskii, V. V., "Damping of Tubes by a Constrained Coating," Soviet Physics Acoustics, Vol. 26, No. 4, 1980, pp328-330.
15. Yu, I. W., Bartolomeo, D. R., and Akey, J. G., "MICA- Mechanical Impedance Computer Program," Westinghouse R&D Report No. 85-1J7-IMPED-R1, January 1986.

Damped Response of Visco-Elastic Thick Cylinders of Infinite Extent

H.R. Hamidzadeh, D.J. Nunez and D.E. Chandler

Department of Mechanical Engineering
South Dakota State University

ABSTRACT

Harmonic responses of viscoelastic thick circular cylinders of infinite extent, subjected to harmonic radial and tangential boundary stresses are considered. In development of an analytical solution two dimensional elastodynamic theory is employed and the viscoelastic material for the medium is allowed by assuming complex elastic moduli. The solution provides stresses and displacements at any point in the medium in terms of boundary stresses. The resonant frequencies for different circumferential flexural (lobar) modes and their corresponding thickness modes are computed and satisfactorily compared with an available solution. The present solution is not limited to thin shells, and it equally treats thick cylinders with any values of hysteretic damping. Also, several design charts for estimation of resonant frequencies for a wide range of thickness ratio are developed.

¹Crothers Engineering Hall SDSU, Brookings, SD 57007:
(605) 688-5319

INTRODUCTION

The trend towards dissipating vibratory energy in cylindrical structures when subjected to circumferential flexural vibrations requires application of viscoelastic materials with high strength. Although many cylindrical structures can be analyzed using the theory of thin shells, thicker cylinders with hysteretic damping have to be studied using the general theory of elasticity with complex moduli. The first investigators to study the vibrations of an infinitely long traction-free hollow cylinder were Greenspon (1957), and Gazis (1958). Armenakas et al (1969), in particular, considered the transmission of elastic energy by means of elastic waves, and formulated the eigenvalue problem for stress free cylindrical surfaces. He presented tables of natural frequencies for different ratios of mean radius/thickness and for different numbers of circumferential wave numbers. McNiven, Shah and Sackman (1966) considered the axisymmetric vibrations of hollow cylinder utilizing "Three Modes Theory". Gladwell and Vijay (1975) studied the three dimensional vibrations of a finite length circular cylinder with traction free boundaries, using a finite element approach. Svardh (1984) investigated wave propagation in a semi-infinite, hollow, elastic circular cylinder with traction-free lateral surface initially at rest and subjected to transient end loadings. Hutchinson (1980) developed a series solution of the general three dimensional equation of linear elasto-dynamic problem. Hutchinson and El-Azhari (1986) extended Hutchinson's work in solid cylinders to include free hollow cylinders with finite length. Singal and Williams (1988) studied free vibrations of thick circular cylindrical shells and rings using the energy method and obtained a frequency equation to provide resonant frequencies for breathing and beam type modes. They also conducted experimental investigations to assess the validity of their analysis.

The present study involve the development of an analytical solution to the harmonic response of infinitely long cylindrical structure with internal damping subjected to flexural vibrations around the circumference.

GOVERNING ELASTO-DYNAMIC EQUATIONS

For the isotropic homogeneous elastic medium shown in Figure 1,

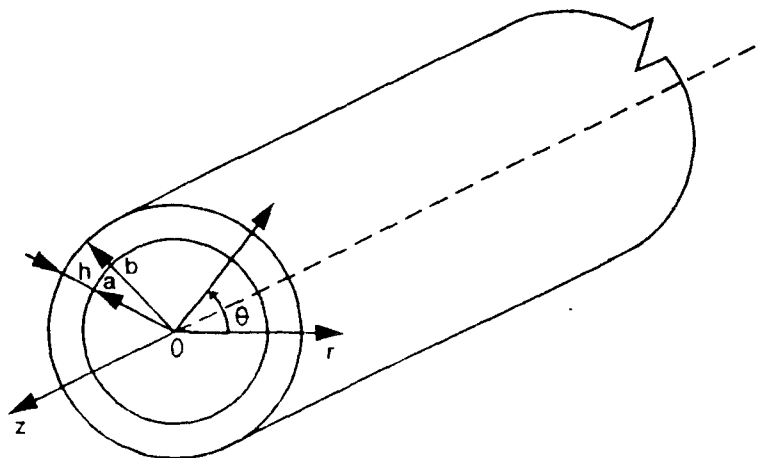


Figure 1. Reference coordinates and dimensions

the governing equation of motion in terms of harmonic radial and tangential displacements amplitudes u and v are:

$$-\rho p^2 u r - (\lambda + 2G) r \frac{\partial}{\partial r} e - 2G \frac{\partial}{\partial \theta} \omega_z \quad (1-a)$$

and

$$-\rho p^2 v - (\lambda + 2G) \frac{1}{r} \frac{\partial}{\partial \theta} e + 2G \frac{\partial}{\partial r} \omega_z \quad (1-b)$$

where:

$$e = \frac{\partial u}{\partial r} + \frac{1}{r} \frac{\partial v}{\partial \theta} \quad (2-a)$$

and

$$\omega_z = \frac{1}{2} \left[\frac{\partial v}{\partial r} + \frac{v}{r} - \frac{1}{r} \frac{\partial u}{\partial \theta} \right] \quad (2-b)$$

e and ω_z are the volumetric strain and elastic rotation about z axis.
 u and v are radial and tangential displacement amplitudes.
 p is the frequency of the harmonic excitation.
 G and λ are shear modulus and Lamé's elastic constant.
 ρ is the density of the medium.

Differentiating equations (1-a) and (1-b) with respect to r and θ and adding them together yields:

$$-\rho p^2 r e - (\lambda + 2G) \left[r \frac{\partial^2}{\partial r^2} e + \frac{\partial}{\partial r} e + \frac{1}{r} \frac{\partial^2}{\partial \theta^2} e \right] \quad (3-a)$$

Differentiating equations (1-a) and (1-b) with respect to θ and r , after arranging the results, yields:

$$-\rho p^2 r \omega_z - G \left[\frac{1}{r} \frac{\partial^2}{\partial \theta^2} \omega_z + \frac{\partial}{\partial r} \omega_z + r \frac{\partial^2}{\partial r^2} \omega_z \right] \quad (3-b)$$

Introducing two parameters β^2 and μ^2 such that

$$\beta^2 = \frac{\rho p^2}{\lambda + 2G} \quad (4-a)$$

$$\mu^2 = \frac{\rho p^2}{G} \quad (4-b)$$

Substituting β^2 and μ^2 in equation (3-a) and (3-b) they become:

$$r^2 \frac{\partial^2}{\partial r^2} e + r \frac{\partial}{\partial r} e + r^2 \beta^2 e - \frac{\partial^2}{\partial \theta^2} e \quad (5-a)$$

$$r^2 \frac{\partial^2}{\partial r^2} \omega_z + r \frac{\partial}{\partial r} \omega_z + r^2 \mu^2 \omega_z - \frac{\partial^2}{\partial \theta^2} \omega_z \quad (5-b)$$

Considering the boundary conditions, the solution to these equations are:

$$e(r, \theta) = \sum_{n=0}^{\infty} e_n(r, \theta) \quad (6-a)$$

$$\omega_z(r, \theta) = \sum_{n=0}^{\infty} \omega_{zn}(r, \theta) \quad (6-b)$$

where:

$$e_n(r, \theta) = \beta^2 [A_n J_n(\beta r) + B_n Y_n(\beta r)] \cos(n\theta) \quad (7-a)$$

$$\omega_{zn}(r, \theta) = \mu^2 [C_n J_n(\mu r) + D_n Y_n(\mu r)] \sin(n\theta) \quad (7-b)$$

J_n and Y_n are first and second kinds of Bessel functions of n^{th} order.

MODAL DISPLACEMENT AND STRESS COMPONENTS

Substituting equations (7) into equations (1), modal displacement components will become:

$$u_n(r, \theta) = -\beta [A_n J_n(\beta r) + B_n Y_n(\beta r)] \cos(n\theta) + (2n/r) [C_n J_n(\mu r) + D_n Y_n(\mu r)] \cos(n\theta) \quad (8-a)$$

$$v_n(r, \theta) = n/r [A_n J_n(\beta r) + B_n Y_n(\beta r)] \sin(n\theta) - 2\mu [C_n J_n(\mu r) + D_n Y_n(\mu r)] \sin(n\theta) \quad (8-b)$$

Amplitude of stresses on the plane normal to the radial axis in the elastic medium, in terms of volumetric strain ϵ and elastic rotation ω_z are:

$$\sigma_{rr} = \lambda \epsilon + 2G \frac{\partial}{\partial r} u \quad (9-a)$$

$$\tau_{r\theta} = 2G \left[\frac{\partial}{\partial r} v - \omega_z \right] \quad (9-b)$$

substituting from equations (8) and (7) into (9), component of stresses will be presented as:

$$\sigma_{rrn}(r, \theta) = [A_n E_n(r) + B_n F_n(r) + C_n G_n(r) + D_n H_n(r)] \cos(n\theta) \quad (10-a)$$

$$\tau_{r\theta n}(r, \theta) = [A_n E_n^*(r) + B_n F_n^*(r) + C_n G_n^*(r) + D_n H_n^*(r)] \sin(n\theta) \quad (10-b)$$

In the above equations, E_n , F_n , G_n , H_n , E_n^* , F_n^* , G_n^* , and H_n^* are functions of Bessel functions, where:

$$E_n(r) - \beta^2 \lambda J_n(r\beta) - 2G\beta^2 J''(r\beta) \quad (11-a)$$

$$F_n(r) - \beta^2 \lambda Y_n(r\beta) - 2G\beta^2 Y''_n(r\beta) \quad (11-b)$$

$$G_n(r) - 4Gn\mu/r J'_n(r\mu) - 4Gn/r^2 J_n(r\mu) \quad (11-c)$$

$$H_n(r) - 4Gn\mu/r Y'_n(r\mu) - 4Gn/r^2 Y_n(r\mu) \quad (11-d)$$

$$E_n^*(r) - 2G\beta n/r J_n(r\beta) - 2Gn/r^2 J_n(r\beta) \quad (11-e)$$

$$F_n^*(r) - 2G\beta n/r Y'_n(r\beta) - 2Gn/r^2 Y_n(r\beta) \quad (11-f)$$

$$G_n^*(r) - -4G\mu^2 J''(r\mu) - 2G\mu^2 J_n(r\mu) \quad (11-g)$$

$$H_n^*(r) - -4G\mu^2 Y''(r\mu) - 2G\mu^2 Y_n(r\mu) \quad (11-h)$$

Functions $J_n'(x)$, $J_n''(x)$, $Y_n'(x)$ and $Y_n''(x)$ are first and second derivative of $J_n(x)$ and $Y_n(x)$ with respect to x .

MODAL HARMONIC RESPONSE

Considering the boundary stresses in inner and outer surfaces these stresses can be presented as:

$$\begin{bmatrix} E_n(a) & F_n(a) & G_n(a) & H_n(a) \\ E_n^*(a) & F_n^*(a) & G_n^*(a) & H_n^*(a) \\ E_n(b) & F_n(b) & G_n(b) & H_n(b) \\ E_n^*(b) & F_n^*(b) & G_n^*(b) & H_n^*(b) \end{bmatrix} \begin{Bmatrix} A_n \\ B_n \\ C_n \\ D_n \end{Bmatrix} = \begin{Bmatrix} \sigma_{rr}(a) \\ \tau_{r\theta}(a) \\ \sigma_{rr}(b) \\ \tau_{r\theta}(b) \end{Bmatrix} \quad (12-a)$$

or

$$T_n a_n = \sigma_n \quad (12-b)$$

where.

σ_n is a vector containing radial and shear stresses on the inner and outer surface of the medium.

a_n is a vector containing arbitrary constants.

T_n is a square matrix containing the coefficients in terms of Bessel functions.

To provide displacement and stress components at any point in the cylinder, equations (8) and (10) can be arranged in the following matrix equation.

$$\begin{Bmatrix} U_n(r, \theta) / \cos(n\theta) \\ V_n(r, \theta) / \sin(n\theta) \\ \sigma_{rrn}(r, \theta) / \cos(n\theta) \\ \tau_{r\theta n}(r, \theta) / \sin(n\theta) \end{Bmatrix} = \begin{bmatrix} -\beta J_n(\beta r) & -\beta Y_n(\beta r) & \frac{2n}{r} J_n(\mu r) & \frac{2n}{r} Y_n(\mu r) \\ \frac{n}{r} J_n(\beta r) & \frac{n}{r} Y_n(\beta r) & -2\mu J_n(\mu r) & -2\mu Y_n(\mu r) \\ E_n(r) & F_n(r) & G_n(r) & H_n(r) \\ E_n^*(r) & F_n^*(r) & G_n^*(r) & H_n^*(r) \end{bmatrix} \begin{Bmatrix} A_n \\ B_n \\ C_n \\ D_n \end{Bmatrix} \quad (13-a)$$

The above matrix equation can be abbreviated as:

$$R_n(r) - S_n(r) a_n \quad (13-b)$$

where:

$R_n(r)$ is a vector containing components of radial and tangential displacement and stress.

$S_n(r)$ is a coefficient square matrix.

Arranging equation (12-b) and (13-b) they result in

$$D_n(r) R_n(r) - \sigma_n \quad (14)$$

where:

$$D_n(r) - T_n S_n^{-1}(r) \quad (15)$$

For given lobar boundary stress components, Equation (14) can provide the displacement and stress components at any point in the medium.

RESULTS AND DISCUSSION

The frequency response for different lobar modes of vibrations can be computed for any cross sectional geometry of the elastic or viscoelastic cylinders. Figure 2 illustrates the lobar vibration forms for the first three modes. Computations were conducted to determine the resonant responses of the first three lobar modes ($n = 2$ to 4) and five of their corresponding thickness modes ($m = 1$ to 5). Results presented in Figure 3 provide the non-dimensionalized resonant frequency (frequency factor) versus thickness ratio for the lobar modes ($n = 2, 3$ and 4) of elastic cylinder. Figure 3 demonstrate coupling between the different thickness modes, at particular thickness ratios. These results are computed for Poisson's ratio = 0.33.

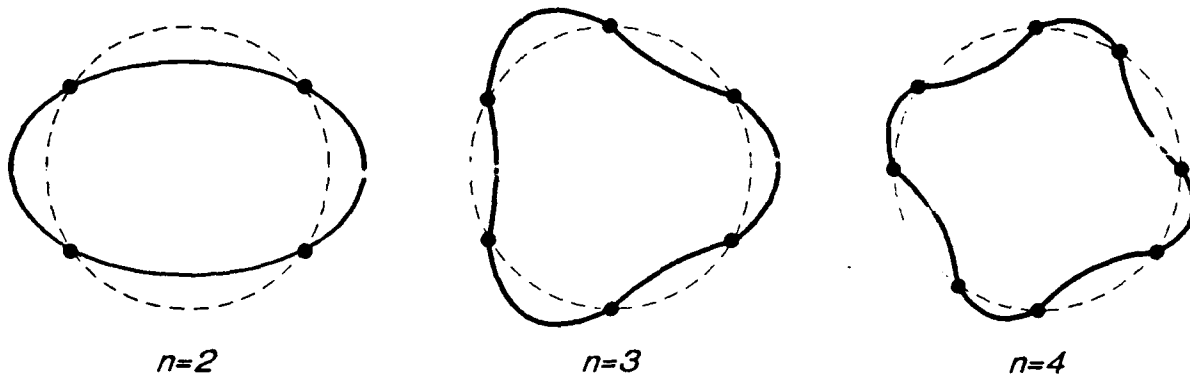


Figure 2. Lobar Vibration Forms

To verify the validity of the present results, computed resonant frequency were compared with Armenakas et al (1969) results. The comparison of the results for different thickness ratios indicates satisfactory agreement between them. It is believed that the present results are more accurate than Armenakas' results. This is due to the fact that in his computation, only a few terms in expansion of the Bessel functions are assumed, however, the present results are obtained by utilizing higher accuracy for the Bessel functions of complex arguments.

Table 1. Comparison of present resonant frequency factors with Armenakas (1969) natural frequency factors for different thickness ratios

n,m	h/a = 0.1276		h/a = 0.1739		h/a = 0.1978	
	Present	Armenakas	Present	Armenakas	Present	Armenakas
2,1	0.0101	0.010	0.0175	0.0176	0.0230	0.0223
2,2	0.2408	0.2414	0.1800	0.1763	0.3600	0.3604
3,1	0.0240	0.0270	0.0480	0.0490	0.5078	0.6152
3,2	0.3360	0.3411	0.4440	0.4530	0.5040	0.5084
4,1	0.0530	0.523	0.0910	0.0914	0.1140	0.1145
4,2	0.4440	0.4442	0.5880	0.5895	0.5600	0.6611

Frequency responses of maximum radial displacement for a cylinder having thickness ratio of 0.5 and poisson's ratio of 0.25, subjected to harmonic radial stress from inside, for three damping factors of $\eta = 0.2, 0.05$ and 0.1 are presented in Figure 4.

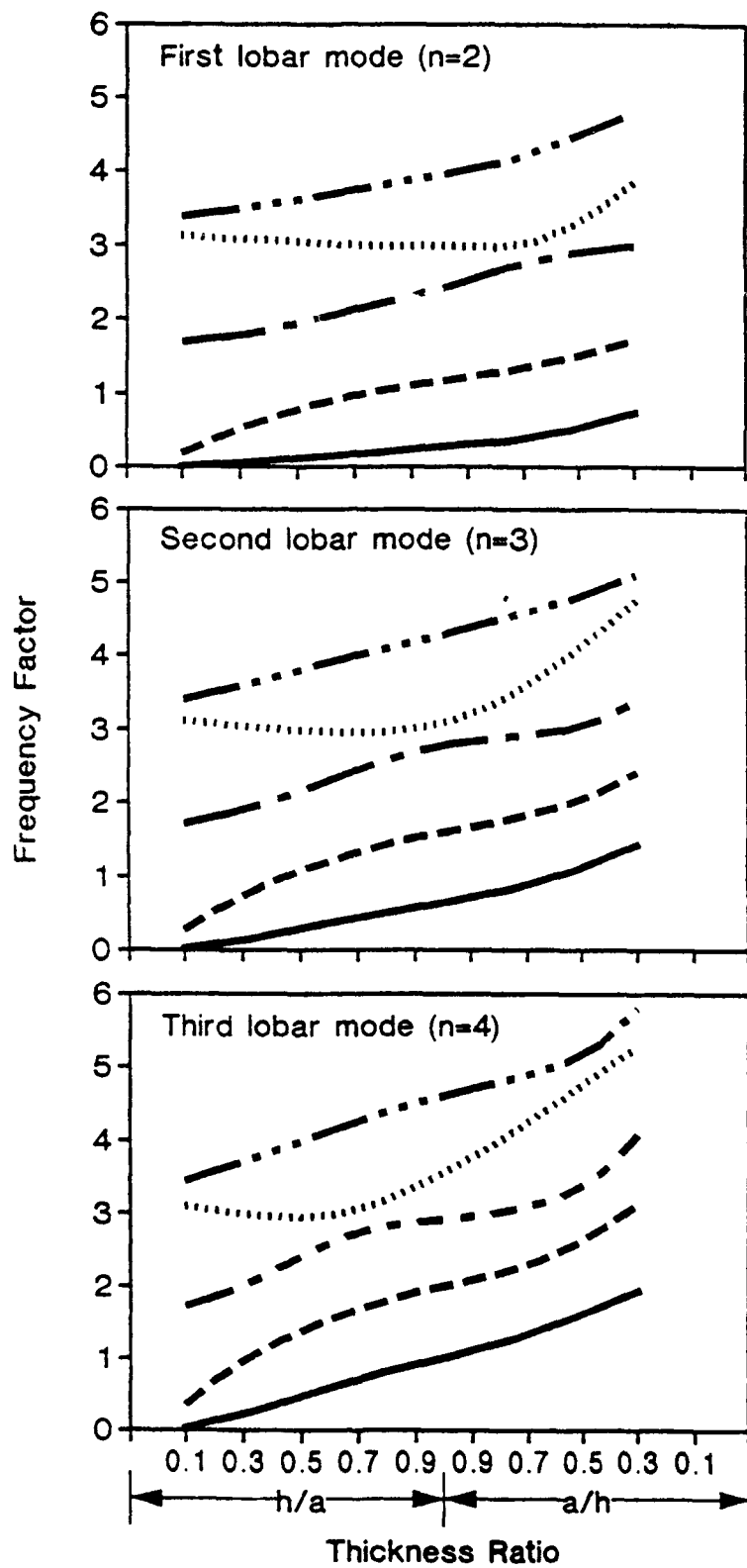


Figure 3. First five resonant frequency factors for different thickness ratio

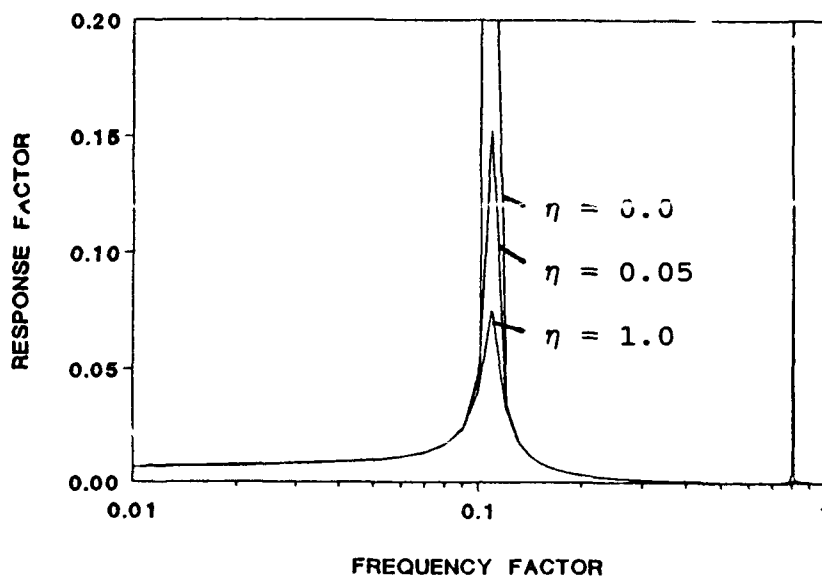


Figure 4. Frequency response of a point with maximum radial displacement on a cylinder having thickness ratio of $h/a = 0.5$ and Poisson's ratio of 0.25. Excited by a harmonic internal radial stress with an amplitude of 10^4 psi for three different damping factors.

CONCLUSIONS

Harmonic lobar vibrations of thick viscoelastic cylinders were considered and a general solution based on two dimensional wave propagation was developed. Design charts for estimation of the Non-dimensional resonant frequencies were provided and results were compared with available data and satisfactory agreement was established.

REFERENCES

- Armenakas, A. E., Gazis, D. C. and Hermann, G., "Free Vibrations of Circular Cylindrical Shells", Oxford: Pergamon Press, 1968.
- Gazis, D. C., "Exact Analysis of the Plane-Strain Vibrations of Thick-Walled Hollow Cylinders", Journal of the Acoustical Society of America, Vol. 30, pp 786-796, 1958.
- Gladwell, G. M. and Vijay, D. K., "Natural Frequencies of Free Finite-Length Circular Cylinders", Journal of Sound and Vibration, Vol. 42, pp. 387-397, 1975.

Greenspan, J. E., "Flexural Vibrations of a Thick Wall Circular Cylinder According to the Exact Theory of Elasticity", Journal of Aerospace Sciences, Vol. 27, pp 1365-1373, 1957.

Hutchinson, J. R., "Vibrations of Solid Cylinders", ASME Journal of Applied Mechanics, Vol. 47, pp. 901-907, 1980.

Hutchinson, J. R. and El-Azhari, S. A., "Vibrations of Free Hollow Circular Cylinders", ASME Journal of Applied Mechanics, Vol. 53, pp. 641-646, 1986.

Mc Niven, H. D., Shan, A. E. and Sackman, J. L., "Axially Symmetric Waves in Hollow Elastic Rods", Journal of the Acoustical Society of America 40, pp. 684-691, 1966.

Singal, R. K. and Williams, K., "A Theoretical and Experimental Study of Vibrations of Thick Circular Cylindrical Shells and Rings", ASME Journal of Vibrations, Acoustics, Stress and Reliability in Design, Vol. 110, pp. 533-537, 1988.

Svardah, P. A., "Three-Dimensional Analysis of Axisymmetric Transient Waves in Hollow Elastic Cylinders", ASME Journal of Applied Mechanics, Vol. 51, pp. 792-796, 1984.

**Dynamic Analysis of Finite, Three Dimensional, Linear,
Elastic Solids With Kelvin Viscoelastic Inclusions:
Theory with Applications to
Asymmetrically Damped Circular Plates**

I. Y. Shen †
and
C. D. Mote, Jr.

Department of Mechanical Engineering
University of California, Berkeley
Berkeley, CA 94720
U. S. A.

ABSTRACT

Eigensolutions and Green's functions of finite, three dimensional, linear, elastic solids with Kelvin viscoelastic inclusions are analyzed. The eigensolutions satisfy a set of integral equations expressing the reciprocal theorem of viscoelasticity. Successive approximations to these integral equations lead to asymptotic solutions and an iteration scheme for the eigensolutions. The Green's function is also determined through the integral equation approach. Finally, the vibration of Kirchhoff circular plates with evenly spaced, radial, viscoelastic inclusions, which cause some of the repeated vibration modes to split into distinct ones, is analyzed both analytically and numerically for the eigensolutions and the Green's function.

† (415) 642-6371

1. Introduction

Tuned dampers and surface damping treatments are commonly used damping designs [1-3]. The tuned damper can be a one degree of freedom system consisting of a mass and a viscoelastic element attached to the structures to be damped [4, 5]. They can also be viscoelastic links connecting complex structures. When the structures vibrate, the tuned dampers dissipate energy. The surface damping treatments include thin layers of viscoelastic materials bonded onto surfaces of the structures [6, 7]. The vibration energy is dissipated via cyclic bending or shearing of the viscoelastic layers. A review of surface damping treatment is given by Torvik [7].

An alternative damping design is to replace part of an elastic structure by a viscoelastic component. For instance, slots and holes filled with viscoelastic material can reduce vibration of circular saws. The holes and slots can be arranged so that the viscoelastic material is significantly strained when the structure vibrates in particular modes. The damping design procedure, however, is one of trial and error; dynamic analysis of such designs has not been presented.

The purpose of this paper is to provide a dynamic analysis of damping designs through viscoelastic inclusions. The damped structure is modeled as a finite, three dimensional, linear, elastic solid containing Kelvin viscoelastic inclusions. Eigensolutions and Green's functions of the damped structure are determined analytically and numerically. Special attention is given to degenerate systems, like axisymmetric circular plates, that occur when the corresponding, homogeneous, linear, elastic solid (without inclusions) possesses repeated eigenvalues.

According to the reciprocal theorem of viscoelasticity (Section 7.3 of [8]), the eigensolutions satisfy a set of regular, homogeneous, Fredholm integral equations of the second kind. Successive approximations to the integral equations yield perturbation formulas and a numerical iteration scheme for the eigensolutions. The real and imaginary parts of each eigenvalue represents the modal damping coefficient and the damped natural frequency, respectively. The eigenfunctions may or may not be complex depending on the geometry and the viscosity of the inclusions. The Green's function is also determined through the integral equation approach.

The analysis is illustrated on the transverse vibration of a classical circular plate with evenly spaced, radial, viscoelastic inclusions. The perfect plate is axisymmetric and spectrally degenerate. The perturbation theory for degenerate systems predicts that some of the repeated vibration modes split into two distinct ones when the inclusions are introduced. Perturbed eigensolutions are also derived explicitly. In addition, eigensolutions and Green's functions at two different excitation frequencies are predicted numerically. The numerical results show that vibration modes with higher natural frequencies possess greater damping and the nodal curves may be time dependent.

2. Formulation

Consider a homogeneous, isotropic, linear, elastic solid containing Kelvin viscoelastic inclusions shown as System 1 in Fig. 1(a). The elastic solid occupies a finite, three

dimensional region $\tau^{(1)}$ with Lamé constants λ_0, μ_0 and density ρ_0 . The perfectly bonded viscoelastic inclusions occupy a not necessarily small region τ_c with Lamé constants λ'_0, μ'_0 , density ρ'_0 , and Kelvin damping coefficients λ_0^*, μ_0^* .

The response of System 1 is equivalent to that of System 2 in Fig. 1(b) which consists of an inhomogeneous Kelvin viscoelastic solid occupying a region $\tau (\equiv \tau^{(1)} \cup \tau_c)$ with stiffness $\lambda(\mathbf{r}), \mu(\mathbf{r})$, density $\rho(\mathbf{r})$, and damping $\lambda^*(\mathbf{r})$ and $\mu^*(\mathbf{r})$ [9]

$$\lambda(\mathbf{r}) = \lambda_0 - \lambda_1 J(\mathbf{r}), \quad \mu(\mathbf{r}) = \mu_0 - \mu_1 J(\mathbf{r}), \quad \rho(\mathbf{r}) = \rho_0 - \rho_1 J(\mathbf{r}) \quad (1a)$$

$$\lambda^*(\mathbf{r}) = \lambda_0^* J(\mathbf{r}), \quad \mu^*(\mathbf{r}) = \mu_0^* J(\mathbf{r}) \quad (1b)$$

where

$$J(\mathbf{r}) = \begin{cases} 1 & \mathbf{r} \in \tau_c \\ 0 & \mathbf{r} \in \tau^{(1)} \end{cases} \quad (1c)$$

and

$$\lambda_1 = \lambda_0 - \lambda'_0, \quad \mu_1 = \mu_0 - \mu'_0, \quad \rho_1 = \rho_0 - \rho'_0 \quad (1d)$$

The constitutive equation of System 2 is then

$$\tau_{ij}(\mathbf{w}; \lambda, \mu, \lambda^*, \mu^*) = \lambda \delta_{ij} \epsilon_{kk}(\mathbf{w}) + 2\mu \epsilon_{ij}(\mathbf{w}) + \lambda^* \delta_{ij} \dot{\epsilon}_{kk}(\mathbf{w}) + 2\mu^* \dot{\epsilon}_{ij}(\mathbf{w}) \quad (2a)$$

where the infinitesimal strain $\epsilon_{ij}(\mathbf{w})$ and the infinitesimal strain rate $\dot{\epsilon}_{ij}(\mathbf{w})$ associated with the displacement field $\mathbf{w}(\mathbf{r}, t)$ are

$$\epsilon_{ij}(\mathbf{w}) = \frac{1}{2} (w_{i,j} + w_{j,i}), \quad \dot{\epsilon}_{ij}(\mathbf{w}) = \frac{1}{2} (\dot{w}_{i,j} + \dot{w}_{j,i}).$$

When the displacement and stress fields are both harmonic, i.e., $\mathbf{w}(\mathbf{r}, t) = \mathbf{u}(\mathbf{r})e^{v t}$ and $\tau_{ij}(\mathbf{w}; \lambda, \mu, \lambda^*, \mu^*) = \sigma_{ij}(\mathbf{u}, v; \lambda, \mu, \lambda^*, \mu^*)e^{v t}$, (2a) implies

$$\sigma_{ij}(\mathbf{u}, v; \lambda, \mu, \lambda^*, \mu^*) = \lambda \delta_{ij} \epsilon_{kk}(\mathbf{u}) + 2\mu \epsilon_{ij}(\mathbf{u}) + v [\lambda^* \delta_{ij} \epsilon_{kk}(\mathbf{u}) + 2\mu^* \epsilon_{ij}(\mathbf{u})] \quad (2b)$$

In addition, the reciprocal theorem is (Section 7.3 of [8])

$$\begin{aligned} & \int_{\sigma_2} \sigma_{ij}(\mathbf{u}, v; \lambda, \mu, \lambda^*, \mu^*) n_j u'_i d^2 \mathbf{r} - \int_{\tau} \frac{d}{dx_j} [\sigma_{ij}(\mathbf{u}, v; \lambda, \mu, \lambda^*, \mu^*)] u'_i d^3 \mathbf{r} \\ &= \int_{\sigma_2} \sigma_{ij}(u', v; \lambda, \mu, \lambda^*, \mu^*) n_j u_i d^2 \mathbf{r} - \int_{\tau} \frac{d}{dx_j} [\sigma_{ij}(u', v; \lambda, \mu, \lambda^*, \mu^*)] u_i d^3 \mathbf{r} \\ &= \int_{\tau} \sigma_{ij}(\mathbf{u}, v; \lambda, \mu, \lambda^*, \mu^*) \epsilon_{ij}(\mathbf{u}') d^3 \mathbf{r} = \int_{\tau} \sigma_{ij}(u', v; \lambda, \mu, \lambda^*, \mu^*) \epsilon_{ij}(\mathbf{u}) d^3 \mathbf{r} \\ &= \int_{\tau} I(\mathbf{u}, \mathbf{u}'; \lambda, \mu) d^3 \mathbf{r} + v \int_{\tau} I(\mathbf{u}, \mathbf{u}'; \lambda^*, \mu^*) d^3 \mathbf{r} \end{aligned} \quad (3)$$

with

$$I(\mathbf{u}, \mathbf{u}'; \lambda, \mu) = \int_{\tau} [\lambda \epsilon_{kk}(\mathbf{u}) \epsilon_{kk}(\mathbf{u}') + 2\mu \epsilon_{ij}(\mathbf{u}) \epsilon_{ij}(\mathbf{u}')] d^3 \mathbf{r}$$

where $\mathbf{u}(\mathbf{r})e^{v t}$ and $\mathbf{u}'(\mathbf{r})e^{v t}$ are two harmonic displacement fields satisfying zero displacements on σ_1 .

3. Eigensolutions

Exact Solutions. The complex-valued eigenfunction $\boldsymbol{\psi}(\mathbf{r}) \equiv \{\psi^{(1)}(\mathbf{r}), \psi^{(2)}(\mathbf{r}), \psi^{(3)}(\mathbf{r})\}^T$ and the corresponding complex eigenvalue ν of system 2 under zero body force and vanishing surface tractions satisfy

$$\frac{d}{dx_j} [\sigma_{ij}(\boldsymbol{\psi}, \nu; \lambda, \mu, \lambda^*, \mu^*)] = \nu^2 \rho(\mathbf{r}) \psi^{(i)}(\mathbf{r}), \quad i = 1, 2, 3 \quad (4)$$

with boundary conditions

$$\boldsymbol{\psi}(\mathbf{r}) = \mathbf{0}, \quad \text{on } \sigma_1 \quad (5a)$$

$$\sigma_{ij}(\boldsymbol{\psi}, \nu; \lambda, \mu, \lambda^*, \mu^*) n_j = 0, \quad \text{on } \sigma_2, \quad i = 1, 2, 3 \quad (5b)$$

in the unprimed system. The complex-valued Green's function $\mathbf{G}^k(\mathbf{r}|\mathbf{r}_0)$ of System 3†, shown in Fig. 1(c) under an interior concentrated force $\delta(\mathbf{r}-\mathbf{r}_0)e^{i\nu t}$ acting in direction x_k ($k=1, 2, 3$), is represented in the primed system. Therefore, $\mathbf{G}^k(\mathbf{r}|\mathbf{r}_0) \equiv [G_1^k(\mathbf{r}|\mathbf{r}_0), G_2^k(\mathbf{r}|\mathbf{r}_0), G_3^k(\mathbf{r}|\mathbf{r}_0)]^T$ satisfies

$$\frac{d}{dx_j} [\sigma_{ij}(\mathbf{G}^k(\mathbf{r}|\mathbf{r}_0), \nu; \lambda_0, \mu_0, 0, 0)] - \rho_0 \nu^2 G_i^k(\mathbf{r}|\mathbf{r}_0) = -\delta_{ik} \delta(\mathbf{r}-\mathbf{r}_0), \quad i, k = 1, 2, 3 \quad (6)$$

with boundary conditions

$$\mathbf{G}^k(\mathbf{r}|\mathbf{r}_0) = \mathbf{0}, \quad \text{on } \sigma_1, \quad k = 1, 2, 3 \quad (7a)$$

$$\sigma_{ij}(\mathbf{G}^k(\mathbf{r}|\mathbf{r}_0), \nu; \lambda_0, \mu_0, 0, 0) n_j = 0, \quad \text{on } \sigma_2, \quad i, k = 1, 2, 3 \quad (7b)$$

With the unprimed solution specified by (4), (5a,b), and the primed by (6), and (7a,b), the equalities in (3) give the following integral equations governing the free vibration of System 2 [9]:

$$\begin{aligned} \boldsymbol{\psi}^k(\mathbf{r}_0) &= H[\mathbf{G}^k(\mathbf{r}|\mathbf{r}_0), \boldsymbol{\psi}(\mathbf{r})] \\ &\equiv \nu^2 \int_{\tau} \rho_1 J(\mathbf{r}) \boldsymbol{\psi}(\mathbf{r}) \cdot \mathbf{G}^k(\mathbf{r}|\mathbf{r}_0) d^3\mathbf{r} - \nu \int_{\tau} I(\mathbf{G}^k(\mathbf{r}|\mathbf{r}_0), \boldsymbol{\psi}(\mathbf{r}); \lambda_0^* J(\mathbf{r}), \mu_0^* J(\mathbf{r})) d^3\mathbf{r} \\ &\quad + \int_{\tau} I(\mathbf{G}^k(\mathbf{r}|\mathbf{r}_0), \boldsymbol{\psi}(\mathbf{r}); \lambda_1 J(\mathbf{r}), \mu_1 J(\mathbf{r})) d^3\mathbf{r}, \quad k = 1, 2, 3 \end{aligned} \quad (8)$$

$\mathbf{G}^k(\mathbf{r}|\mathbf{r}_0)$ is seldom known for numerical or perturbation evaluation of (8). An orthonormal eigenfunction expansion of $\mathbf{G}^k(\mathbf{r}|\mathbf{r}_0)$ is

$$\mathbf{G}^k(\mathbf{r}|\mathbf{r}_0) = \sum_{n=1}^{\infty} \frac{\boldsymbol{\phi}_n^k(\mathbf{r}_0)}{\nu^2 + \omega_n^2} \boldsymbol{\phi}_n(\mathbf{r}), \quad k = 1, 2, 3 \quad (9)$$

where ω_n and $\boldsymbol{\phi}_n(\mathbf{r}) \equiv [\phi_n^1(\mathbf{r}), \phi_n^2(\mathbf{r}), \phi_n^3(\mathbf{r})]^T$ are the n -th eigensolution‡ of System 3 with orthonormality

$$\int_{\tau} \rho_0 \boldsymbol{\phi}_n(\mathbf{r}) \cdot \boldsymbol{\phi}_m(\mathbf{r}) d^3\mathbf{r} = \delta_{nm} \quad (10a)$$

† System 3 is defined by a perfect, homogeneous, linear, elastic solid *without* viscoelastic inclusions occupying the same domain τ and satisfying boundary conditions (5a,b).

‡ ω_n and $\boldsymbol{\phi}_n(\mathbf{r})$ are real, because the eigenvalue problem associated with System 3 is self-adjoint.

$$\int_{\tau} I(\phi_n(\mathbf{r}), \phi_m(\mathbf{r}); \lambda_0, \mu_0) d^3\mathbf{r} = \omega_n^2 \delta_{nm} \quad (10b)$$

Substitution of (9) into (8), recalling the definition of $J(\mathbf{r})$ in (1c), and discarding index k give

$$\psi(\mathbf{r}_0) = \sum_{n=1}^{\infty} \frac{\phi_n(\mathbf{r}_0)}{v^2 + \omega_n^2} U(\psi(\mathbf{r}), \phi_n(\mathbf{r}); v) \quad (11a)$$

where

$$U(\psi(\mathbf{r}), \phi_n(\mathbf{r}); v) = v^2 \langle \psi | \phi_n \rangle_{\rho_1} - v \langle \psi | \phi_n \rangle_{I^*} + \langle \psi | \phi_n \rangle_I \quad (11b)$$

with

$$\langle \psi | \phi_n \rangle_{\rho_1} \equiv \int_{\tau_c} \rho_1 \psi(\mathbf{r}) \cdot \phi_n(\mathbf{r}) d^3\mathbf{r} \quad (12a)$$

$$\langle \psi | \phi_n \rangle_{I^*} \equiv \int_{\tau_c} I(\psi(\mathbf{r}), \phi_n(\mathbf{r}); \lambda_0^*, \mu_0^*) d^3\mathbf{r} \quad (12b)$$

$$\langle \psi | \phi_n \rangle_I \equiv \int_{\tau_c} I(\psi(\mathbf{r}), \phi_n(\mathbf{r}); \lambda_1, \mu_1) d^3\mathbf{r} \quad (12c)$$

In addition, (11a) is homogeneous allowing normalization of $\psi(\mathbf{r})$ such that

$$\psi(\mathbf{r}) = T_1[\psi, v] = \phi_n(\mathbf{r}) + \sum'_m \frac{U(\psi, \phi_m; v)}{v^2 + \omega_m^2} \phi_m(\mathbf{r}), \quad \sum'_m \equiv \sum_{\substack{m=1 \\ m \neq n}}^{\infty} \quad (13a)$$

when

$$v^2 = T_2[\psi, v] = -\omega_n^2 + U(\psi, \phi_n; v) \quad (13b)$$

The $\psi(\mathbf{r})$ and v of (13a,b) are the eigensolutions of System 2 (and hence System 1). In Appendix A, T_1 and T_2 in (13a,b) are shown to be contraction mappings for sufficiently small τ_c and their contraction constants α_1 and α_2 are also estimated. The convergence of the infinite series in (13a) is also shown in the Appendix A.

As $\tau_c \rightarrow 0$, $U(\psi, \phi_m; v)$ vanishes if the solution is regular. Otherwise, it is singular. Singular solutions are not discussed here.

Perturbation Solutions. For regular and nondegenerate solutions, first order perturbation is obtained by replacing $\psi(\mathbf{r})$ and v on the right hand side of (13a,b) by $\phi_n(\mathbf{r})$ and $i\omega_n$. The n -th eigenfunction $\psi_n(\mathbf{r})$ is

$$\psi_n(\mathbf{r}) = \phi_n(\mathbf{r}) + \sum'_m \frac{d_{nm}^*}{\omega_m^2 - \omega_n^2} \phi_m(\mathbf{r}) + O(\tau_c^2) \quad (14a)$$

where

$$d_{nm}^* = U(\phi_n, \phi_m; i\omega_n) = -\omega_n^2 \langle \phi_n | \phi_m \rangle_{\rho_1} - i\omega_n \langle \phi_n | \phi_m \rangle_{I^*} + \langle \phi_n | \phi_m \rangle_I$$

The n -th eigenvalue v_n is

$$v_n = \sqrt{-\omega_n^2 + d_{nn}^*} + O(\tau_c^2) \\ = -\frac{1}{2} \langle \phi_n | \phi_n \rangle_{I^*} + i \left\{ \omega_n + \frac{1}{2\omega_n} \left[\omega_n^2 \langle \phi_n | \phi_n \rangle_{\rho_1} - \langle \phi_n | \phi_n \rangle_I \right] \right\} + O(\tau_c^2) \quad (14b)$$

where the branch selected for the square root satisfies $\lim_{\tau_c \rightarrow 0} v_n = i\omega_n$ for a regular solution. If the inclusion is dissipative $\langle \phi_n | \phi_n \rangle_{J^*} > 0$, and if it is elastic $\langle \phi_n | \phi_n \rangle_{J^*} = 0$.

Degeneracy occurs when any ω_n is repeated. The contraction mappings in (13a,b) are valid if the initial trials $[v]^{(0)}$ and $[\psi(\mathbf{r})]^{(0)}$ for the iteration of v_n and $\psi_n(\mathbf{r})$ satisfy $[v^2]^{(0)} \neq -\omega_n^2$. Otherwise, the denominators of the terms containing the repeated eigenvalues in (13a) vanish and the iteration fails. A perturbation theory for degenerate systems is presented in Appendix B.

1. Green's Functions

Exact Solutions. The Green's function of System 1, excited by a concentrated force $\delta(\mathbf{r}-\mathbf{r}_1)e^{v t}$ acting in the direction x_l ($l=1,2,3$), is $\mathbf{R}^l(\mathbf{r}|\mathbf{r}_1)$ in the unprimed system. $\mathbf{R}^l(\mathbf{r}|\mathbf{r}_1)$ and v satisfy

$$\frac{d}{dx_j} [\sigma_{ij}(\mathbf{R}^l(\mathbf{r}|\mathbf{r}_1), v; \lambda, \mu, \lambda^*, \mu^*)] - v^2 \rho(\mathbf{r}) R_i^l(\mathbf{r}|\mathbf{r}_1) = -\delta_{il} \delta(\mathbf{r}-\mathbf{r}_1), \quad i, l = 1, 2, 3 \quad (15)$$

and boundary conditions

$$\mathbf{R}^l(\mathbf{r}|\mathbf{r}_1) = 0, \quad \text{on } \sigma_1, \quad l = 1, 2, 3 \quad (16a)$$

$$\sigma_{ij}(\mathbf{R}^l(\mathbf{r}|\mathbf{r}_1), v; \lambda, \mu, \lambda^*, \mu^*) n_j = 0, \quad \text{on } \sigma_2, \quad i, l = 1, 2, 3 \quad (16b)$$

The Green's function $\mathbf{G}^k(\mathbf{r}|\mathbf{r}_0)e^{v t}$ of System 3 is in the primed system. Then $\mathbf{R}^l(\mathbf{r}|\mathbf{r}_1)$ satisfies the integral equation

$$\mathbf{R}_k^l(\mathbf{r}_0|\mathbf{r}_1) = \mathbf{G}_k^l(\mathbf{r}_1|\mathbf{r}_0) + H[\mathbf{G}^k(\mathbf{r}|\mathbf{r}_0), \mathbf{R}^l(\mathbf{r}|\mathbf{r}_1)], \quad k, l = 1, 2, 3 \quad (17)$$

where $R_k^l(\mathbf{r}_0|\mathbf{r}_1)$ is the k -th element of the Green's function $\mathbf{R}^l(\mathbf{r}|\mathbf{r}_1)$ ($k=1,2,3$), and $H[\cdot, \cdot]$ is the integral operator defined in (8).

The eigenfunction expansion in (9) converts (17) into

$$\begin{aligned} \mathbf{R}^k(\mathbf{r}_0|\mathbf{r}_1) &= \mathbf{G}^k(\mathbf{r}_0|\mathbf{r}_1) + T_3[\mathbf{R}^k(\mathbf{r}|\mathbf{r}_1), v] \\ &\equiv \mathbf{G}^k(\mathbf{r}_0|\mathbf{r}_1) + \sum_{m=1}^{\infty} \frac{U(\mathbf{R}^k(\mathbf{r}|\mathbf{r}_1), \phi_m(\mathbf{r}); v)}{v^2 + \omega_m^2} \phi_m(\mathbf{r}_0) \end{aligned} \quad (18)$$

in which the symmetry $G_i^k(\mathbf{r}_1|\mathbf{r}_0) = G_k^i(\mathbf{r}_0|\mathbf{r}_1)$ has been used. T_3 is a contraction mapping for sufficiently small τ_c (see Appendix A); therefore, iteration of (18) converges to $\mathbf{R}^l(\mathbf{r}|\mathbf{r}_1)$.

Perturbation Solution. Use of $\mathbf{G}^k(\mathbf{r}|\mathbf{r}_1)$ for $\mathbf{R}^k(\mathbf{r}|\mathbf{r}_1)$ in $T_3[\cdot, v]$ yields a first order perturbation

$$\mathbf{R}(\mathbf{r}_0|\mathbf{r}_1) = \mathbf{G}(\mathbf{r}_0|\mathbf{r}_1) + \sum_{m,n=1}^{\infty} \frac{U(\phi_n, \phi_m; v)}{(v^2 + \omega_m^2)(v^2 + \omega_n^2)} \phi_m(\mathbf{r}_0) \phi_n^T(\mathbf{r}_1) + O(\tau_c^2) \quad (19)$$

where $\mathbf{R} \equiv [\mathbf{R}^1, \mathbf{R}^2, \mathbf{R}^3]$ and $\mathbf{G} \equiv [\mathbf{G}^1, \mathbf{G}^2, \mathbf{G}^3]$ are Green's matrices and the superscript T denotes the transpose. The perturbation solution (19) is valid only when v is far from $\pm i\omega_k$ (and therefore v_c) avoiding the small divisors in (19) and resonance. The perturbation formulas at resonance can be obtained through an approach similar to that shown in Appendix B, they are not discussed here.

5. Circular Plates with Evenly Spaced, Radial, Viscoelastic Inclusions

Consider the transverse vibration of a Kirchhoff circular plate of uniform thickness h with k evenly spaced, radial, Kelvin viscoelastic inclusions each spanning a small angle ϵ and located at $\bar{\theta}_i = \frac{2\pi}{k}i$, $i=1,2,\dots,k$ from $r=r_0$ to $r=b$. The inner and outer rim at $r=a$ and $r=b$ are free, clamped, or simply supported. The eigensolutions and the Green's function of the asymmetrically damped circular plate are evaluated by the methods derived previously.

Axisymmetric Circular Plates. Let $\omega_{m,\pm n}$ and $\Phi_{m,\pm n}(r)$ be the eigensolutions of an axisymmetric circular plate with n nodal diameters and m nodal circles. When $n=0$, the eigenfunctions are axisymmetric; i.e.,

$$\Phi_{m0}(r) = R_{m0}(r) \quad (20a)$$

When $n > 0$, the eigenfunctions

$$\Phi_{mn}(r) = R_{mn}(r) \cos(n\theta + \alpha_{mn}) \quad (20b)$$

$$\Phi_{m,-n}(r) = R_{mn}(r) \sin(n\theta + \alpha_{mn}) \quad (20c)$$

correspond to repeated eigenvalues $\omega_{mn} = \omega_{m,-n}$. In (20a,b,c), α_{mn} is an arbitrary constant and $R_{mn}(r)$ is a linear combination of Bessel's functions satisfying boundary conditions at both rims and the orthonormality conditions

$$\int_A \rho_0 h \Phi_{mn}(r) \Phi_{pq}(r) dA = \delta_{mp} \delta_{nq}, \quad m, p = 0, 1, 2, \dots, \infty, \quad n, q = 0, \pm 1, \pm 2, \dots, \pm \infty$$

$$\int_A I(\Phi_{mn}(r), \Phi_{pq}(r); D_0, \sigma_0) dA = \omega_{mn}^2 \delta_{mp} \delta_{nq}, \quad m, p = 0, 1, 2, \dots, \infty, \quad n, q = 0, \pm 1, \pm 2, \dots, \pm \infty$$

with the bilinear operator

$$I(u, v; D_0, \sigma_0) = D_0 \left[\nabla^2 u \nabla^2 v + 2(1-\sigma_0) \left\{ \left(\frac{1}{r} \frac{\partial^2 u}{\partial r \partial \theta} - \frac{1}{r^2} \frac{\partial u}{\partial \theta} \right) \left(\frac{1}{r} \frac{\partial^2 v}{\partial r \partial \theta} - \frac{1}{r^2} \frac{\partial v}{\partial \theta} \right) \right. \right. \\ \left. \left. - \frac{1}{2} \left[\left(\frac{1}{r} \frac{\partial u}{\partial r} + \frac{1}{r^2} \frac{\partial^2 u}{\partial \theta^2} \right) \frac{\partial^2 v}{\partial r^2} + \left(\frac{1}{r} \frac{\partial v}{\partial r} + \frac{1}{r^2} \frac{\partial^2 v}{\partial \theta^2} \right) \frac{\partial^2 u}{\partial r^2} \right] \right\} \right]$$

h , D_0 , ρ_0 , and σ_0 are the thickness, flexural rigidity, density, and Poisson ratio of the axisymmetric plate.

Perturbation Solutions. According to the perturbation theory for degenerate problems in Appendix B, the k viscoelastic inclusions affect the plate eigenfunctions $\Phi_{m,\pm n}(r)$ corresponding to eigenvalue $\omega_{mn} = \omega_{m,-n}$ through

$$\langle \Psi_{mn} | \Phi_{pq} \rangle_{\rho_1} = \sum_{j=1}^k \int_{\bar{\theta}_j - \frac{\epsilon}{2}}^{\bar{\theta}_j + \frac{\epsilon}{2}} \int_{r_0}^b \rho_1 h \Psi_{mn}(r) \Phi_{pq}(r) r dr d\theta$$

$$\langle \Psi_{mn} | \Phi_{pq} \rangle_{I^*} = \sum_{j=1}^k \int_{\bar{\theta}_j - \frac{\epsilon}{2}}^{\bar{\theta}_j + \frac{\epsilon}{2}} \int_{r_0}^b I(\Psi_{mn}, \Phi_{pq}; D_0^*, \sigma_0^*) r dr d\theta$$

and

$$\langle \Psi_{mn} | \Phi_{pq} \rangle_I = \sum_{j=1}^k \int_{\bar{\theta}_j - \frac{\epsilon}{2}}^{\bar{\theta}_j + \frac{\epsilon}{2}} \int_{r_0}^b I(\Psi_{mn}, \Phi_{pq}; D_1, \sigma_1) r dr d\theta$$

with D_0^* , σ_0^* derived from λ_0^* , μ_0^* in (1b) and D_1 , σ_1 derived from λ_1 , μ_1 in (1d), respectively. For example, to transform $\langle \Psi_{mn} | \Phi_{pq} \rangle_{\rho_1}$ above to the asymptotic form (B-1a), define

$$\Pi(\theta) = \int_{r_0}^b \rho_1 h \Psi_{mn}(r) \Phi_{pq}(r) r dr \quad (21a)$$

and

$$\Gamma(\theta) = \int_0^\theta \Pi(\phi) d\phi \quad (21b)$$

Therefore,

$$\langle \Psi_{mn} | \Phi_{pq} \rangle_{\rho_1} = \sum_{j=1}^k [\Gamma(\bar{\theta}_j + \frac{\epsilon}{2}) - \Gamma(\bar{\theta}_j - \frac{\epsilon}{2})]$$

Use of the Taylor expansion around $\theta = \bar{\theta}_j$ gives

$$\langle \Psi_{mn} | \Phi_{pq} \rangle_{\rho_1} = \epsilon \sum_{j=1}^k \left[\Pi(\bar{\theta}_j) + \frac{\epsilon^2}{24} \frac{d^2 \Pi(\bar{\theta}_j)}{d\theta^2} + \dots \right] \quad (22)$$

Compare (22) with (B-1a) to obtain

$$\langle \Psi_{mn} | \Phi_{pq} \rangle_{\rho_1}^{(0)} = \sum_{j=1}^k \int_{r_0}^b [\rho_1 h \Psi_{mn}(r) \Phi_{pq}(r)]_{\theta=\bar{\theta}_j} r dr, \quad \langle \Psi_{mn} | \Phi_{pq} \rangle_{\rho_1}^{(1)} = 0, \dots \quad (23a)$$

Similarly,

$$\langle \Psi_{mn} | \Phi_{pq} \rangle_I^{(0)} = \sum_{j=1}^k \int_{r_0}^b [I(\Psi_{mn}, \Phi_{pq}; D_0^*, \sigma_0^*)]_{\theta=\bar{\theta}_j} r dr, \quad \langle \Psi_{mn} | \Phi_{pq} \rangle_I^{(1)} = 0, \dots \quad (23b)$$

and

$$\langle \Psi_{mn} | \Phi_{pq} \rangle_I^{(0)} = \sum_{j=1}^k \int_{r_0}^b [I(\Psi_{mn}, \Phi_{pq}; D_1, \sigma_1)]_{\theta=\bar{\theta}_j} r dr, \quad \langle \Psi_{mn} | \Phi_{pq} \rangle_I^{(1)} = 0, \dots \quad (23c)$$

With $\langle \Psi_{mn} | \Phi_{pq} \rangle_{\rho_1}^{(i)}$, $\langle \Psi_{mn} | \Phi_{pq} \rangle_I^{(i)}$, and $\langle \Psi_{mn} | \Phi_{pq} \rangle_I^{(i)}$ ($i=0, 1, \dots$) in (23a,b,c), the results derived in Appendix B can be applied directly. From (B-5) in Appendix B the following coefficients are needed for the explicit expression of $\Psi_{mn}(r)$.

$$d_{rs}^{pq(0)} = \sum_{j=1}^k \int_{r_0}^b [-\rho_1 h \omega_{mn}^2 \Phi_{rs}(r) \Phi_{pq}(r) - i \omega_{mn} I(\Phi_{rs}, \Phi_{pq}; D_0^*, \sigma_0^*) + I(\Phi_{rs}, \Phi_{pq}; D_1, \sigma_1)]_{\theta=\bar{\theta}_j} r dr$$

$$e_{rs}^{pq(0)} = \sum_{j=1}^k \int_{r_0}^b [2i \omega_{mn} \mu_{mn} \rho_1 h \Phi_{rs}(r) \Phi_{pq}(r) - \mu_{mn} I(\Phi_{rs}, \Phi_{pq}; D_0^*, \sigma_0^*)]_{\theta=\bar{\theta}_j} r dr$$

$$d_{rs}^{pq(1)} = e_{rs}^{pq(1)} = 0, \dots$$

For each pair of repeated eigensolutions (m, n) and $(m, -n)$, the unperturbed eigenfunctions are specified via diagonalization of the matrix

$$D^{(0)} \equiv \begin{bmatrix} d_{mn}^{mn(0)} & d_{mn}^{m,-n(0)} \\ d_{m,-n}^{mn(0)} & d_{m,-n}^{m,-n(0)} \end{bmatrix} = \begin{bmatrix} A_{mn}^{mn}\theta_{11} - B_{mn}^{mn}\theta_{22} & (A_{mn}^{mn} + B_{mn}^{mn})\theta_{12} \\ (A_{mn}^{mn} + B_{mn}^{mn})\theta_{12} & A_{mn}^{mn}\theta_{22} - B_{mn}^{mn}\theta_{11} \end{bmatrix}$$

where A_{mn}^{pq} and B_{mn}^{pq} are complex coefficients given by

$$A_{mn}^{pq} = -\rho_1 h \omega_{mn}^2 \int_{r_0}^b R_{mn}(r) R_{pq}(r) r dr$$

$$+ (D_1 - i \omega_{mn} D_0^*) \int_{r_0}^b \left(\frac{d^2}{dr^2} + \frac{1}{r} \frac{d}{dr} - \frac{n^2}{r^2} \right) R_{mn}(r) \left(\frac{d^2}{dr^2} + \frac{1}{r} \frac{d}{dr} - \frac{q^2}{r^2} \right) R_{pq}(r) r dr$$

$$- [D_1(1-\sigma_1) - i \omega_{mn} D_0^*(1-\sigma_0^*)] \int_{r_0}^b \left[\frac{d^2 R_{mn}(r)}{dr^2} \left(\frac{1}{r} \frac{d}{dr} - \frac{q^2}{r^2} \right) R_{pq}(r) \right. \\ \left. + \frac{d^2 R_{pq}(r)}{dr^2} \left(\frac{1}{r} \frac{d}{dr} - \frac{n^2}{r^2} \right) R_{mn}(r) \right] r dr$$

$$B_{mn}^{pq} = -2 [D_1(1-\sigma_1) - i \omega_{mn} D_0^*(1-\sigma_0^*)] \int_{r_0}^b \left[\left(\frac{n}{r} \frac{d}{dr} - \frac{n}{r^2} \right) R_{mn}(r) \right] \left[\left(\frac{q}{r} \frac{d}{dr} - \frac{q}{r^2} \right) R_{pq}(r) \right] r dr$$

and

$$\theta_{11} = \sum_{j=1}^k \cos^2 n(\bar{\theta}_j + \alpha_{mn}) = \begin{cases} \frac{k}{2}, & 2n \neq M(k) \\ \frac{k}{2}(1 + \cos 2\alpha_{mn}), & 2n = M(k) \end{cases}$$

$$\theta_{22} = \sum_{j=1}^k \sin^2 n(\bar{\theta}_j + \alpha_{mn}) = \begin{cases} \frac{k}{2}, & 2n \neq M(k) \\ \frac{k}{2}(1 - \cos 2\alpha_{mn}), & 2n = M(k) \end{cases}$$

$$\theta_{12} = \sum_{j=1}^k \sin n(\bar{\theta}_j + \alpha_{mn}) \cos n(\bar{\theta}_j + \alpha_{mn}) = \begin{cases} 0, & 2n \neq M(k) \\ \frac{k}{2} \sin 2\alpha_{mn}, & 2n = M(k) \end{cases}$$

in which $2n = M(k)$ means $2n$ is an integer multiple of k . Following Appendix B, the unperturbed eigenfunctions $\Phi_{mn}(r)$ and $\Phi_{m,-n}(r)$ require $D^{(0)}$ to be diagonal; i.e., $\theta_{12} = 0$, or equivalently,

$$\alpha_{mn} = \begin{cases} 0, \frac{\pi}{2}, \pi, \frac{3\pi}{2}, \dots, & \text{if } 2n = M(k) \\ \text{arbitrary}, & \text{if } 2n \neq M(k) \end{cases}$$

In the sequel, $\alpha_{mn} = 0$ when $2n = M(k)$. If $2n \neq M(k)$, α_{mn} can be shown to be arbitrary at least up to the second order. Therefore

$$D^{(0)} = \begin{cases} \begin{bmatrix} \frac{k}{2}(A_{mn}^{mn} - B_{mn}^{mn}) & 0 \\ 0 & \frac{k}{2}(A_{mn}^{mn} - B_{mn}^{mn}) \end{bmatrix}, & 2n \neq M(k) \\ \begin{bmatrix} kA_{mn}^{mn} & 0 \\ 0 & -kB_{mn}^{mn} \end{bmatrix}, & 2n = M(k) \end{cases}$$

For the α_{mn} classified above, the repeated $\Phi_{m,\pm n}(r)$ evolve into two distinct groups depending on the number of nodal lines n and the number of inclusions k that are spaced equally on the circular plate. Application of the perturbation formulas in Appendix B gives the following results.

The eigenfunctions $\Psi_{m,\pm n}(r)$ of the asymmetric plate remain arbitrarily positioned and the eigenvalues remain repeated (to the first order) if $2n \neq M(k)$, $n \neq 0$:

$$v_{mn} = v_{m,-n} = i\omega_{mn} - i \frac{\epsilon k}{4\omega_{mn}} (A_{mn}^{mn} - B_{mn}^{mn}) + O(\epsilon^2) \quad (24)$$

Note that $v_{m,\pm n}$ are not imaginary because A_{mn}^{mn} and B_{mn}^{mn} are complex. The complex eigenfunctions, perturbed to first order, are

$$\begin{aligned} \Psi_{mn}(r) &= R_{mn}(r) \cos(n\theta + \alpha_{mn}) \\ &- \frac{\epsilon k}{2} \left[\sum_{q=M(k)-n} \bar{\sum} \frac{A_{mn}^{pq} + B_{mn}^{pq}}{\omega_{mn}^2 - \omega_{pq}^2} \Phi_{pq}(r) + \sum_{q=M(k)+n} \bar{\sum} \frac{A_{mn}^{pq} - B_{mn}^{pq}}{\omega_{mn}^2 - \omega_{pq}^2} \Phi_{pq}(r) \right] + O(\epsilon^2) \end{aligned} \quad (25a)$$

$$\begin{aligned} \Psi_{m,-n}(r) &= R_{mn}(r) \sin(n\theta + \alpha_{mn}) \\ &+ \frac{\epsilon k}{2} \left[\sum_{q=M(k)-n} \bar{\sum} \frac{A_{mn}^{pq} + B_{mn}^{pq}}{\omega_{mn}^2 - \omega_{pq}^2} \Phi_{p,-q}(r) - \sum_{q=M(k)+n} \bar{\sum} \frac{A_{mn}^{pq} - B_{mn}^{pq}}{\omega_{mn}^2 - \omega_{pq}^2} \Phi_{p,-q}(r) \right] + O(\epsilon^2) \end{aligned} \quad (25b)$$

with α_{mn} arbitrary up to the first order perturbation, and $\bar{\sum}_{q=M(k)-n}$ denotes double summation on integers $p \geq 0$ and $q > 0$ with $q = M(k) - n$ and $(p, q) \neq (m, n)$.

The eigenfunctions $\Psi_{m,\pm n}(r)$ are termed split modes if $2n = M(k)$, $n \neq 0$, because the complex eigenvalues are distinct:

$$v_{mn} = i\omega_{mn} - i \frac{\epsilon k}{2\omega_{mn}} A_{mn}^{mn} + O(\epsilon^2) \quad (26a)$$

$$v_{m,-n} = i\omega_{mn} + i \frac{\epsilon k}{2\omega_{mn}} B_{mn}^{mn} + O(\epsilon^2) \quad (26b)$$

The corresponding complex eigenfunctions, perturbed to the first order, are

$$\Psi_{mn}(r) = R_{mn}(r) \cos n \theta$$

$$- \left\{ \begin{array}{l} \epsilon k \sum_{q=M(k)+\frac{k}{2}}^{\infty} \frac{A_{mn}^{pq} \Phi_{pq}(r)}{\omega_{mn}^2 - \omega_{pq}^2}, \quad n \neq M(k) \\ \epsilon k \left[\sum_{p=0}^{\infty} \frac{A_{mn}^{p0} \Phi_{p0}(r)}{\omega_{mn}^2 - \omega_{p0}^2} + \sum_{q=M(k)}^{\infty} \frac{A_{mn}^{pq} \Phi_{pq}(r)}{\omega_{mn}^2 - \omega_{pq}^2} \right], \quad n = M(k) \end{array} \right\} + O(\epsilon^2) \quad (27a)$$

$$\Psi_{m,-n}(r) = R_{mn}(r) \sin n \theta + \epsilon k \sum_{q=M(k)+n}^{\infty} \frac{B_{mn}^{pq} \Phi_{p,-q}(r)}{\omega_{mn}^2 - \omega_{pq}^2} + O(\epsilon^2) \quad (27b)$$

The eigenfunctions $\Psi_{m0}(r)$ are not axisymmetric to first order perturbation:

$$\Psi_{m0}(r) = R_{m0}(r) - \epsilon k \left[\sum_{p \neq m}^{\infty} \frac{A_{m0}^{p0} \Phi_{p0}(r)}{\omega_{m0}^2 - \omega_{p0}^2} + \sum_{p=0}^{\infty} \sum_{\substack{q=1 \\ q=M(k)}}^{\infty} \frac{A_{m0}^{pq} \Phi_{pq}(r)}{\omega_{m0}^2 - \omega_{pq}^2} \right] + O(\epsilon^2) \quad (28)$$

with eigenvalue

$$v_{m0} = i \omega_{m0} - i \frac{\epsilon k}{2 \omega_{m0}} A_{m0}^{m0} + O(\epsilon^2) \quad (29)$$

where $\sum_{\substack{q=1 \\ q=M(k)}}^{\infty}$ denotes the summation on the positive integer q with $q = M(k)$.

Numerical Solutions. The eigensolutions and Green's functions of a circular plate with three equally spaced, radial, Kelvin viscoelastic inclusions are computed numerically by the perturbation iteration method (13a,b) and (18). The inclusions are thin sector bars extending from $r/b = 0.75$ to $r/b = 1$. The angle ϵ spanned by each inclusion is 0.035 rad ($\approx 2.0^\circ$). The material properties satisfy

$$\frac{\rho_0'}{\rho_0} = \frac{E_0'}{E_0} = 0.5; \quad \sigma_0' = 0.3; \quad \xi = \frac{E_0^*}{E_0} \sqrt{\frac{E_0 h^2}{4 \rho_0 b^4}} = 0.05; \quad \sigma_0^* = 0.3$$

Eigenfunctions with 0 to 20 nodal diameters and 0 and 1 nodal circles are used in the series in (13a) and (18). In calculating the eigensolutions of the asymmetrically damped plate,

the iteration converges if the differences in $|v_{mn}| \equiv \left| v_{mn} \sqrt{\frac{4 \rho_0 b^4}{E_0 h^2}} \right|$ and in $||\Psi_{mn}(r)||^2 \equiv ||\sqrt{\rho_0 h b^2} \Psi_{mn}(r)||^2$ between successive iterations are less than 10^{-6} and 10^{-10} , respectively.

The upper bounded estimates of the contraction constants α_1 and α_2 in Appendix A are calculated in advance to guarantee convergence. For a 3-inclusion plate, calculation shows that $\alpha_1, \alpha_2 < 1$ for modes up to 7 nodal diameters and zero nodal circles. For these modes, the perturbation iteration is guaranteed contractive and convergent. For modes (0, 11), (0, 12) and (0, 13) $\alpha_1 = 24.3, 14.5,$ and 17.7 , but the iteration converges; the results are shown in

Table 1.

The normalized complex eigenvalues $\bar{\nu}_{mn}$ of the 3-inclusion plate are listed in Table 1. The exact eigenvalues of the axisymmetric plates are also listed for reference. The results in Table 1 show the split in $\Phi_{mn}(r)$ when $2n = M(k)$. In addition, Table 1 shows that damping coefficient $-\text{Re}[\bar{\nu}_{mn}]$ and damping ratio $\zeta_{mn} = -\frac{\text{Re}[\bar{\nu}_{mn}]}{\text{Im}[\bar{\nu}_{mn}]}$ both increase as $\text{Im}[\bar{\nu}_{mn}]$ increases.

For example, $\zeta_{0,13} = 4.54\%$ while $\zeta_{01} = 0.05\%$. This suggests that the damped circular plate possesses large stability margins for high frequency modes.

The eigenfunctions of the damped circular plate are characterized by nodal lines that periodically shift their positions at twice the characteristic frequency. The evolution of the nodal lines of (0, 12) cosine mode is shown in Fig. 2 for one-half of a period.

The loci of eigenvalues $\bar{\nu}_{mn}$ with respect to ξ on the complex $\bar{\nu}$ plane from three to six nodal diameter modes are shown in Fig. 3. Bifurcations occur for split modes 3^c , 3^s , 6^c , and 6^s as predicted by (26a,b).

Green's Functions. The Green's function $R(r|r_0)$ of the asymmetrically damped circular plate under harmonic excitation is also found by the perturbation iteration method. Two Green's function displacement contours are shown in Fig. 4 and 5. In Fig. 4 the load is applied on an antinodal line of the unperturbed modes with circumferential distribution $\sin 3\theta$, $\sin 9\theta$, ..., and $\cos 5\theta$, $\cos 12\theta$, The perturbation iteration terminates when difference in $\| \frac{Eh^3}{4b^2} R(r|r_0) \|^2$ between consecutive iterations is less than 10^{-7} . In Fig. 5 the excitation frequency is near the 3 nodal diameter cosine mode resonance (cf. Table 1).

6. Conclusions

1. Explicit perturbation formulas and a numerical iteration scheme are developed to determine eigensolutions and Green's functions for finite, three dimensional, linear, elastic solids containing Kelvin viscoelastic inclusions under the condition that the solutions are regular at the inclusions. The perturbed eigensolutions are represented in a convergent series of orthonormal eigenfunctions of the perfect elastic solid. The perturbation iteration generates results to the precision required provided the perfect solid solutions are known.

2. Perturbation analyses show that all vibration modes are damped by a viscoelastic inclusion. The damping of the n -th vibration mode is determined by $\langle \phi_n | \phi_n \rangle$, which cannot vanish. The viscosity of the inclusions affects natural frequencies through second order perturbation.

3. Circular plates with k evenly spaced, sector, Kelvin viscoelastic inclusions are studied by this technique for eigensolutions and Green's functions. The repeated eigensolutions $\Phi_{mn}(r)$ with m nodal circles and n nodal diameters of the corresponding, axisymmetric, circular plate split into two distinct eigensolutions when $2n$ is an integer multiple of k . Otherwise, $\Phi_{mn}(r)$ remain repeated. Numerical results show that vibration modes with higher natural frequencies possess relatively greater damping ratios. The location of the nodal curves of the perturbed eigenfunctions on the plate changes periodically at twice the eigenfrequency.

Appendix A

This appendix shows that T_1 and T_2 in (13a,b) and T_3 in (18) are contraction mappings for sufficiently small τ_c , and determines an upper bound to the contraction constant of each mapping. The convergence of the series in T_1 and T_3 is also discussed.

Mapping T_1 . Substitute (13b) into (13a) and recall $U(\psi, \phi_m; \nu) = O(\tau_c)$ to give

$$\psi(\mathbf{r}) = \phi_n(\mathbf{r}) + \sum'_m \frac{U(\psi, \phi_m; \nu)}{\omega_m^2 - \omega_n^2 + U(\psi, \phi_n; \nu)} \phi_m(\mathbf{r}) \quad (\text{A-1a})$$

$$= \phi_n(\mathbf{r}) + \sum'_m \frac{U(\psi, \phi_m; i\omega_n)}{\omega_m^2 - \omega_n^2} \phi_m(\mathbf{r}) + O(\tau_c^2) \quad (\text{A-1b})$$

Equation (A-1b) is shown to be a contraction mapping up to $O(\tau_c)$ under the strain energy norm

$$\|\mathbf{x}\|_{SE} = \sqrt{\int_{\tau} I(\mathbf{x}, \bar{\mathbf{x}}, \lambda_0, \mu_0) d^3\mathbf{r}} \quad (\text{A-2})$$

where $\bar{\mathbf{x}}$ is the complex conjugate of \mathbf{x} . Consider the first order mapping T_1^* defined by

$$T_1^* \psi = \phi_n(\mathbf{r}) + \sum'_m \frac{\omega_n^2 \langle \psi | \phi_m \rangle_{\rho_1} + i\omega_n \langle \psi | \phi_m \rangle_{I^*} - \langle \psi | \phi_m \rangle_I}{\omega_n^2 - \omega_m^2} \phi_m(\mathbf{r}) \quad (\text{A-3})$$

then

$$\|T_1^* \psi_1 - T_1^* \psi_2\|_{SE}^2 = \sum'_m \left| \frac{\omega_n^2 \langle \psi_1 - \psi_2 | \phi_m \rangle_{\rho_1} + i\omega_n \langle \psi_1 - \psi_2 | \phi_m \rangle_{I^*} - \langle \psi_1 - \psi_2 | \phi_m \rangle_I}{\omega_n^2 - \omega_m^2} \right|^2 \omega_m^2 \quad (\text{A-4})$$

Because every ψ is normalized according to (13a), the eigenfunction representation

$$\psi_1 - \psi_2 = \sum'_k a_k \phi_k(\mathbf{r}) \quad (\text{A-5})$$

implies that $\|\psi_1 - \psi_2\|_{SE}^2 = \sum'_k \omega_k^2 |a_k|^2$ and

$$\|T_1^* \psi_1 - T_1^* \psi_2\|_{SE}^2 = \sum'_m \left| \frac{\omega_m}{\omega_n^2 - \omega_m^2} \sum'_k a_k (\omega_n^2 d_{km} + i\omega_n f_{km} - e_{km}) \right|^2 \quad (\text{A-6})$$

where $d_{km} = \langle \phi_k | \phi_m \rangle_{\rho_1}$, $f_{km} = \langle \phi_k | \phi_m \rangle_{I^*}$, and $e_{km} = \langle \phi_k | \phi_m \rangle_I$. With the Schwartz inequality

$$\left| \sum'_k a_k (\omega_n^2 d_{km} + i\omega_n f_{km} - e_{km}) \right|^2 \leq \sum'_k \left| \frac{\omega_n^2 d_{km} + i\omega_n f_{km} - e_{km}}{\omega_k} \right|^2 \|\psi_1 - \psi_2\|_{SE}^2 \quad (\text{A-7})$$

(A-6) is reduced to

$$\|T_1^* \psi_1 - T_1^* \psi_2\|_{SE}^2 \leq \alpha_1 \|\psi_1 - \psi_2\|_{SE}^2 \quad (\text{A-8a})$$

with

$$\alpha_1 = \sum'_m \sum'_k \left| \frac{\omega_n^2 d_{km} + i\omega_n f_{km} - e_{km}}{[1 - (\omega_n/\omega_m)^2] \omega_k \omega_m} \right|^2 \quad (\text{A-8b})$$

$\alpha_1 < 1$ is a sufficient condition for the contraction mapping (A-1b) to first order of τ_c .

Mapping T_2 . Substitute (13a) into (13b) and retain terms up to $O(\tau_c)$

$$v^2 = -\omega_n^2 + U(\phi_n(r), \phi_n(r); v) + O(\tau_c^2)$$

Then

$$\begin{aligned} v_2^2 - v_1^2 &= (v_2^2 - v_1^2) \left[\langle \phi_n | \phi_n \rangle_{\rho_1} - \frac{1}{v_1 + v_2} \langle \phi_n | \phi_n \rangle_{I^*} \right] + O(\tau_c^2) \\ &= (v_2^2 - v_1^2) \left[d_{nn} + i \frac{f_{nn}}{2\omega_n} \right] + O(\tau_c^2) \end{aligned}$$

where $v_1, v_2 = i\omega_n + O(\tau_c)$ has been used. Therefore, T_2 is a contraction mapping up to $O(\tau_c)$ if

$$\alpha_2 = \left| d_{nn} + i \frac{f_{nn}}{2\omega_n} \right| < 1 \quad (\text{A-9})$$

Mapping T_3 . The proof that T_3 is contractive follows that given for T_1^* because T_3 is the same form as T_1^* with \sum'_m and $i\omega_n$ replaced by $\sum_{m=1}^{\infty}$ and v .

$$\alpha_3 = \sum_{m=1}^{\infty} \sum_{k=1}^{\infty} \left| \frac{v^2 d_{km} - v f_{km} + e_{km}}{[1 + (v/\omega_m)^2] \omega_k \omega_m} \right|^2 \quad (\text{A-10})$$

$\alpha_3 < 1$ is a sufficiency condition that T_3 is contractive.

Convergence. The convergence of the orthonormal eigenfunction series in (13a) and (18), according to the Riesz-Fisher theorem, is determined by the series

$$S \equiv \sum'_m \left| \frac{v^2 \langle \psi | \phi_m \rangle_{\rho_1} - v \langle \psi | \phi_m \rangle_{I^*} + \langle \psi | \phi_m \rangle_1}{v^2 + \omega_m^2} \right|^2 \quad (\text{A-11})$$

Apply the parallelogram law twice to (A-11)

$$S \leq 2 \sum'_m \left| \frac{v^2 \langle \psi | \phi_m \rangle_{\rho_1}}{v^2 + \omega_m^2} \right|^2 + 4 \sum'_m \left| \frac{v \langle \psi | \phi_m \rangle_{I^*}}{v^2 + \omega_m^2} \right|^2 + 4 \sum'_m \left| \frac{\langle \psi | \phi_m \rangle_1}{v^2 + \omega_m^2} \right|^2 \quad (\text{A-12})$$

Furthermore, the Schwartz inequalities associated with the inner products $\langle \cdot | \cdot \rangle_{\rho_1}$, $\langle \cdot | \cdot \rangle_{I^*}$, and $\langle \cdot | \cdot \rangle_1$ give

$$\begin{aligned} S \leq 2 \sum'_m \left[\frac{v^2 \| \phi_m \|_{\rho_1}}{v^2 + \omega_m^2} \right]^2 \| \psi \|_{\rho_1}^2 \\ + 4 \sum'_m \left[\frac{v \| \phi_m \|_{I^*}}{v^2 + \omega_m^2} \right]^2 \| \psi \|_{I^*}^2 + 4 \sum'_m \left[\frac{\| \phi_m \|_1}{v^2 + \omega_m^2} \right]^2 \| \psi \|_1^2 \end{aligned} \quad (\text{A-13})$$

where $\| \cdot \|_{\rho_1}$, $\| \cdot \|_{I^*}$, and $\| \cdot \|_1$ are the natural norms

$$\|\phi_m\|_{\rho_1}^2 \leq \frac{|\rho_1|}{\rho_0} \int_{\tau} \rho_0 \phi_m \cdot \phi_m d^3r = \frac{|\rho_1|}{\rho_0}$$

$$\|\phi_m\|_{I'}^2 \leq c_1 \int_{\tau} I(\phi_m, \phi_m; \lambda_0, \mu_0) d^3r = c_1 \omega_m^2$$

and

$$\|\phi_m\|_{I''}^2 \leq c_2 \int_{\tau} I(\phi_m, \phi_m; \lambda_0, \mu_0) d^3r = c_2 \omega_m^2$$

where $c_1 = \text{Max} \left[\frac{|\lambda_0^*|}{\lambda_0}, \frac{|\mu_0^*|}{\mu_0} \right]$, and $c_2 = \text{Max} \left[\frac{|\lambda_1|}{\lambda_0}, \frac{|\mu_1|}{\mu_0} \right]$. Therefore,

$$S \leq 2 \frac{|\rho_1|}{\rho_0} \sum_m \left[\frac{v^2}{v^2 + \omega_m^2} \right]^2 \|\psi\|_{\rho_1}^2 + 4c_1 \sum_m \left[\frac{v\omega_m}{v^2 + \omega_m^2} \right]^2 \|\psi\|_{I'}^2 + 4c_2 \sum_m \left[\frac{\omega_m}{v^2 + \omega_m^2} \right]^2 \|\psi\|_{I''}^2 \quad (\text{A-14})$$

The three infinite series in (A-14) converge if the Green's function representation (9) exists. If ψ is regular, then $\|\psi\|_{\rho_1}$, $\|\psi\|_{I'}$, and $\|\psi\|_{I''}$ are finite. Therefore, the series in (A-11) converges for it is monotonically increasing and bounded above by the RHS of (A-14). The convergence of the orthonormal eigenfunction series in (13a) and (18) is guaranteed by the Riesz-Fisher theorem.

Appendix B

Assume that the first β eigenvalues of a finite, elastic solid without inclusions (System 3 in Fig. 1(c)) are repeated and the remainder are distinct. The perturbation formulas (14a,b) are not valid for the eigenfunctions $\Psi_n(\mathbf{r})$ ($n \leq \beta$) because small divisors appear for the repeated eigensolutions in (14a).

Let ϵ be a dimensionless, small parameter measure of the inclusions (e.g., volume ratio of the inclusions to the solid). Being defined on the small inclusion domain τ_c , $\langle \Psi_n | \Phi_m \rangle_{\rho_1}$, $\langle \Psi_n | \Phi_m \rangle_{j^*}$, and $\langle \Psi_n | \Phi_m \rangle_j$ can be expanded in asymptotic series of ϵ ; i.e.,

$$\langle \Psi_n | \Phi_m \rangle_{\rho_1} = \int_{\tau_c} \rho_1 \Psi_n(\mathbf{r}) \cdot \Phi_m(\mathbf{r}) d^3\mathbf{r} = \epsilon \sum_{i=0}^{\infty} \epsilon^i \langle \Psi_n | \Phi_m \rangle_{\rho_1}^{(i)} \quad (\text{B-1a})$$

$$\langle \Psi_n | \Phi_m \rangle_{j^*} = \int_{\tau_c} I(\Psi_n, \Phi_m; \lambda_0^*, \mu_0^*) d^3\mathbf{r} = \epsilon \sum_{i=0}^{\infty} \epsilon^i \langle \Psi_n | \Phi_m \rangle_{j^*}^{(i)} \quad (\text{B-1b})$$

and

$$\langle \Psi_n | \Phi_m \rangle_j = \int_{\tau_c} I(\Psi_n, \Phi_m; \lambda_1, \mu_1) d^3\mathbf{r} = \epsilon \sum_{i=0}^{\infty} \epsilon^i \langle \Psi_n | \Phi_m \rangle_j^{(i)} \quad (\text{B-1c})$$

where $\langle \Psi_n | \Phi_m \rangle_{\rho_1}^{(i)}$, $\langle \Psi_n | \Phi_m \rangle_{j^*}^{(i)}$, and $\langle \Psi_n | \Phi_m \rangle_j^{(i)}$ are coefficients of the asymptotic series. These coefficients can be determined explicitly by expanding the integrals $\int_{\tau_c} (\dots) d^3\mathbf{r}$ into series of ϵ and comparing these series with those in (B-1a,b,c). This process is illustrated in Section 5 when obtaining (23a). Therefore,

$$U(\Psi_n, \Phi_m; v_n) = \epsilon \sum_{i=0}^{\infty} \epsilon^i [v_n^2 \langle \Psi_n | \Phi_m \rangle_{\rho_1}^{(i)} - v_n \langle \Psi_n | \Phi_m \rangle_{j^*}^{(i)} + \langle \Psi_n | \Phi_m \rangle_j^{(i)}]$$

Assume also that the eigenfunction $\Psi_n(\mathbf{r})$ and the eigenvalue v_n take the asymptotic series representations

$$\Psi_n(\mathbf{r}) = \Phi_n(\mathbf{r}) + \epsilon \sum_j' a_{nj} \Phi_j(\mathbf{r}) + \epsilon^2 \sum_j' b_{nj} \Phi_j(\mathbf{r}) + \dots \quad (\text{B-2a})$$

$$v_n = i\omega_n + \epsilon\mu_n + \epsilon^2\lambda_n + \dots \quad (\text{B-2b})$$

or

$$v_n^2 = -\omega_n^2 + \epsilon(2i\omega_n\mu_n) + \epsilon^2(2i\omega_n\lambda_n + \mu_n^2) + \dots \quad (\text{B-2c})$$

Equation (13a) for the exact mode shape $\Psi_n(\mathbf{r})$ ($n \leq \beta$) is then rearranged as

$$\begin{aligned} \Psi_n(\mathbf{r}) = & \Phi_n(\mathbf{r}) + \sum_{\substack{m=1 \\ m \neq n}}^{\beta} \frac{\sum_{i=0}^{\infty} \epsilon^i [v_n^2 \langle \Psi_n | \Phi_m \rangle_{\rho_1}^{(i)} - v_n \langle \Psi_n | \Phi_m \rangle_{j^*}^{(i)} + \langle \Psi_n | \Phi_m \rangle_j^{(i)}]}{2i\omega_n\mu_n + \epsilon(2i\omega_n\lambda_n + \mu_n^2) + \dots} \Phi_m(\mathbf{r}) \\ & + \sum_{m=\beta+1}^{\infty} \frac{U(\Psi_n, \Phi_m; v_n)}{v_n^2 + \omega_m^2} \Phi_m(\mathbf{r}), \quad n \leq \beta \end{aligned} \quad (\text{B-3})$$

where the troublesome small divisors in (13a) are addressed by the second term on the right of (B-3), which contains an order ϵ^0 term $d_{nm}^{(0)} \equiv -\omega_n^2 \langle \Phi_n | \Phi_m \rangle_{\rho_1}^{(0)} - i\omega_n \langle \Phi_n | \Phi_m \rangle_{j^*}^{(0)} + \langle \Phi_n | \Phi_m \rangle_j^{(0)}$ ($n, m \leq \beta$). In order that the perturbed mode shape $\Psi_n(\mathbf{r})$ remains nearby the unperturbed

$\phi_n(\mathbf{r}), n=1, 2, \dots, \beta$ must be specified such that $\mathbf{D}^{(0)} \equiv [d_{nm}^{(0)}] (n, m \leq \beta)$ is a diagonal matrix. The specification of $\phi_n(\mathbf{r}), n=1, 2, \dots, \beta$ is unique only when all the diagonal elements of $\mathbf{D}^{(0)}$ are distinct. Otherwise, those $\phi_n(\mathbf{r})$ corresponding to the repeated diagonal $d_{nn}^{(0)}$ can be arbitrarily chosen within any orthogonal transformation.

With diagonal $\mathbf{D}^{(0)}$, (B-1), and (B-2a,b), equations (13a,b) for the exact $\psi_n(\mathbf{r})$ and v_n ($n \leq \beta$) become

$$\begin{aligned} \psi_n(\mathbf{r}) = & \phi_n(\mathbf{r}) + \sum_{\substack{m=1 \\ m \neq n}}^{\beta} \frac{\phi_m(\mathbf{r})}{2i\omega_n\mu_n} \left\{ \epsilon \left[\sum_{j=\beta+1}^{\infty} a_{nj} d_{jm}^{(0)} + a_{nm} d_{mm}^{(0)} + e_{nm}^{(0)} + d_{nm}^{(1)} \right] + \right. \\ & \epsilon^2 \left[\sum_j' a_{nj} (d_{jm}^{(1)} + e_{jm}^{(0)}) + e_{nm}^{(1)} + d_{nm}^{(2)} - \left(\frac{\lambda_n}{\mu_n} + \frac{\mu_n}{2i\omega_n} \right) d_{nm}^{(1)} + \right. \\ & \left. \left. [b_{nm} - \left(\frac{\lambda_n}{\mu_n} + \frac{\mu_n}{2i\omega_n} \right) a_{nm}] d_{mm}^{(0)} + \sum_{j=\beta+1}^{\infty} [b_{nj} - \left(\frac{\lambda_n}{\mu_n} + \frac{\mu_n}{2i\omega_n} \right) a_{nj}] d_{jm}^{(0)} \right] + O(\epsilon^3) \right\} \\ & + \sum_{m=\beta+1}^{\infty} \frac{\phi_m(\mathbf{r})}{\omega_m^2 - \omega_n^2} \left\{ \epsilon d_{nm}^{(0)} + \epsilon^2 \left[\sum_j' a_{nj} d_{jm}^{(0)} + d_{nm}^{(1)} + e_{nm}^{(0)} - \frac{2i\omega_n\mu_n}{\omega_m^2 - \omega_n^2} d_{nm}^{(0)} \right] + O(\epsilon^3) \right\} \end{aligned} \quad (\text{B-4a})$$

and

$$v_n^2 = -\omega_n^2 + \epsilon d_{nn}^{(0)} + \epsilon^2 \left[\sum_{j=\beta+1}^{\infty} a_{nj} d_{jn}^{(0)} + d_{nn}^{(1)} + e_{nn}^{(0)} \right] + O(\epsilon^3) \quad (\text{B-4b})$$

where

$$\left. \begin{aligned} d_{pq}^{(i)} &= -\omega_n^2 \langle \phi_p | \phi_q \rangle_{\rho_1}^{(i)} - i\omega_n \langle \phi_p | \phi_q \rangle_j^{(i)} + \langle \phi_p | \phi_q \rangle_l^{(i)} \\ e_{pq}^{(i)} &= 2i\omega_n\mu_n \langle \phi_p | \phi_q \rangle_{\rho_1}^{(i)} - \mu_n \langle \phi_p | \phi_q \rangle_l^{(i)} \end{aligned} \right\} n \leq \beta, i=0, 1, 2, 3, \dots, \infty \quad (\text{B-5})$$

First Order Perturbation. Comparison of (B-4a,b) with (B-2a,c) to the first order of ϵ implies

$$\mu_n = \frac{d_{nn}^{(0)}}{2i\omega_n} = -\frac{1}{2} \langle \phi_n | \phi_n \rangle_l^{(0)} + \frac{i}{2\omega_n} \left[\omega_n^2 \langle \phi_n | \phi_n \rangle_{\rho_1}^{(0)} - \langle \phi_n | \phi_n \rangle_l^{(0)} \right] \quad (\text{B-6a})$$

and

$$a_{nm} = \begin{cases} \frac{d_{nm}^{(0)}}{\omega_m^2 - \omega_n^2}, & \text{for } n \leq \beta, m > \beta \\ \frac{\sum_{j=\beta+1}^{\infty} a_{nj} d_{jm}^{(0)} + e_{nm}^{(0)} + d_{nm}^{(1)}}{d_{nn}^{(0)} - d_{mm}^{(0)}}, & \text{for } n, m \leq \beta \end{cases} \quad (\text{B-6b})$$

If $\mu_n \neq \mu_m$, the perturbation a_{nm} ($n, m \leq \beta$) is well defined by (B-6b). If $\mu_n = \mu_m$, a_{nm} , $\phi_n(\mathbf{r})$, and $\phi_m(\mathbf{r}), n, m \leq \beta$, must be determined by higher order perturbations.

Second Order Perturbation. Assume that μ_n are repeated for all $n=1,2,\dots,\beta$. The procedure shown below can also be applied to the case when some of the μ_n , $n=1,2,\dots,\beta$, are repeated. Select the unperturbed orthogonal eigenfunctions $\phi_n(\mathbf{r})$, $n=1,2,\dots,\beta$, such that the matrix $\mathbf{P}^{(1)} \equiv [p_{rs}]$ ($r,s \leq \beta$) with

$$p_{rs} = \sum_{j=\beta+1}^{\infty} \frac{d_{rj}^{(0)} d_{js}^{(0)}}{\omega_j^2 - \omega_n^2} + e_{rs}^{(0)} + d_{rs}^{(1)}, \quad (n \leq \beta) \quad (\text{B-7})$$

is diagonal. Comparison of (B-4a,b) with (B-2a,c) to the second order perturbation ϵ^2 gives

$$\lambda_n = \frac{p_{nn} - \mu_n^2}{2i\omega_n} = \frac{1}{2i\omega_n} \left[\sum_{j=\beta+1}^{\infty} a_{nj} d_{jn}^{(0)} + e_{nn}^{(0)} + d_{nn}^{(1)} + \left[\frac{d_{nn}^{(0)}}{2\omega_n} \right]^2 \right] \quad (\text{B-8a})$$

as well as the following relations between a_{nm} and b_{nm}

$$b_{nm} = \frac{1}{\omega_m^2 - \omega_n^2} \left[\sum_{\substack{j=1 \\ j \neq n}}^{\beta} a_{nj} d_{jm}^{(0)} + p_{nm} - d_{nn}^{(0)} a_{nm} \right] \quad (\text{B-8b})$$

for $n \leq \beta, m > \beta$, and

$$\sum_j' a_{nj} (e_{jm}^{(0)} + d_{jm}^{(1)}) + \sum_{j=\beta+1}^{\infty} b_{nj} d_{jm}^{(0)} - p_{nn} a_{nm} + f_{nm}^{(0)} + e_{nm}^{(1)} + d_{nm}^{(2)} = 0 \quad (\text{B-8c})$$

for $n, m \leq \beta$, where $f_{pq}^{(i)} = (2i\omega_n \lambda_n + \mu_n^2) \langle \phi_p | \phi_q \rangle_{\rho_1}^{(i)} - \lambda_n \langle \phi_p | \phi_q \rangle_j^{(i)}$. Notice that a_{nm} for $n, m \leq \beta$ is unknown in both (B-8b,c). Substitute (B-8b) into (B-8c) to eliminate b_{nj} and recall that $[p_{nm}]$ is diagonal for $n, m \leq \beta$. These reduce (B-8b,c) to

$$a_{nm} = \frac{1}{p_{nn} - p_{mm}} \left[\sum_{j=\beta+1}^{\infty} \frac{(e_{nj}^{(0)} + d_{nj}^{(1)} - d_{nn}^{(0)} a_{nj}) d_{jm}^{(0)}}{\omega_j^2 - \omega_n^2} + \sum_{j=\beta+1}^{\infty} a_{nj} p_{jm} + f_{nm}^{(0)} + e_{nm}^{(1)} + d_{nm}^{(2)} \right] \quad (\text{B-9})$$

for $n, m \leq \beta$. If $p_{nn} = p_{mm}$ (i.e. $\lambda_n = \lambda_m$), then a_{nm} is not specified uniquely. Higher order perturbations similar to the one described above can be developed.

Table 1 - Splitting of Eigenvalues in a Circular Plate
by Three Viscoelastic Inclusions

Complex eigenvalue $v_{mn} = v_{mn} \sqrt{\frac{4\rho_0 b^4}{E_0 h^2}}$

Plate: clamping ratio 0.5; $\sigma=0.3$; fixed at inner rim, free at outer rim.
Inclusions extend from $r=0.75b$ to $r=b$; $\epsilon=0.035$.

$\frac{\rho_0'}{\rho_0} = \frac{E_0'}{E_0} = 0.5$; $\sigma_0' = 0.3$; $\xi = \frac{E_0^*}{E_0} \sqrt{\frac{E_0 h^2}{4\rho_0 b^4}} = 0.05$; $\sigma_0^* = 0.3$.

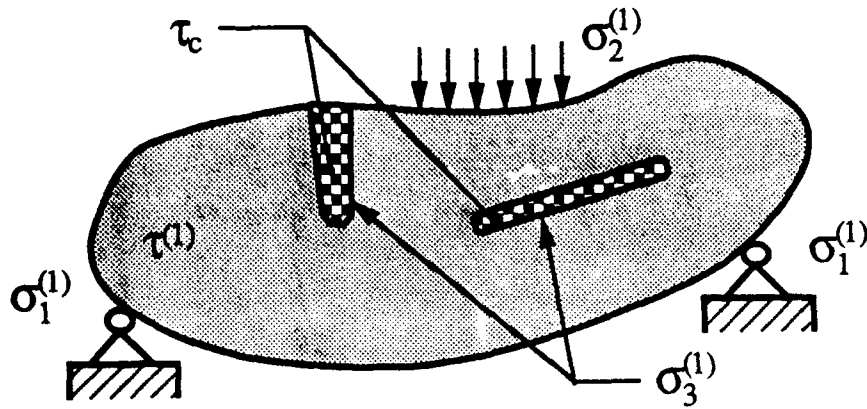
(m, n)	Mode	Eigenvalues Without Inclusions‡	With Three Inclusions†	
			Re[v _{mn}]	Im[v _{mn}]
(0,0)	axisym.	(0, 7.88264)	- 3.5974×10 ⁻³	7.90959
(0,1)	cos	(0, 8.04334)	- 4.0253×10 ⁻³	8.06966
	sin	(0, 8.04334)	- 4.0253×10 ⁻³	8.06966
(0,2)	cos	(0, 8.89915)	- 7.2558×10 ⁻³	8.92844
	sin	(0, 8.89915)	- 7.2558×10 ⁻³	8.92844
(0,3)	cos	(0, 11.23423)	- 1.4344×10 ⁻²	11.31474
	sin	(0, 11.23423)	- 3.1725×10 ⁻²	11.20828
(0,4)	cos	(0, 15.49129)	- 6.4819×10 ⁻²	15.51938
	sin	(0, 15.49129)	- 6.4819×10 ⁻²	15.51938
(0,5)	cos	(0, 21.62483)	- 0.15262	21.66391
	sin	(0, 21.62483)	- 0.15262	21.66391
(0,6)	cos	(0, 29.45800)	- 0.43977	29.63642
	sin	(0, 29.45800)	- 0.18127	29.41778
(0,11)	cos	(0, 90.41296)	- 3.2630	91.58853
	sin	(0, 90.41296)	- 3.2630	91.58853
(0,12)	cos	(0, 106.61302)	- 7.1748	109.84900
	sin	(0, 106.61302)	- 1.8536	106.82114
(0,13)	cos	(0, 124.10038)	- 5.6289	126.72937
	sin	(0, 124.10038)	- 5.6289	126.72937

† Perturbation iteration with error of $|v_{mn}| < 10^{-6}$, and error of norm square $< 10^{-10}$.

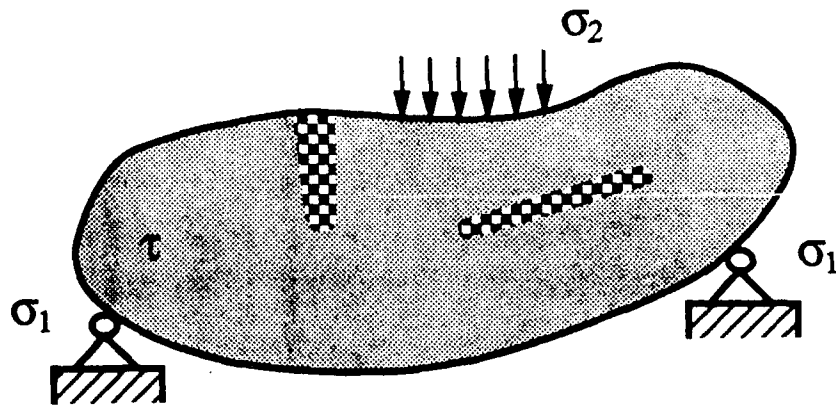
‡ The eigenvalues are represented by complex numbers (a, b), where a and b are real and imaginary parts of the eigenvalues.

References

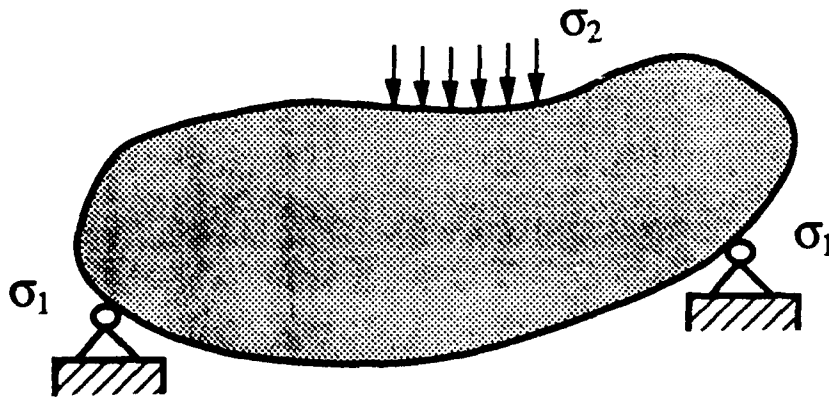
1. Nashif, Ahid D., Jones, David I. G., and Henderson, John P., *Vibration Damping*, John Wiley & Sons, Inc., New York, NY., 1985.
2. Rogers, Lynn, "Vibration Damping as a Design Parameter," *Mechanical Engineering*, vol. 108, pp. 66-69, Jan. 1986.
3. Drake, Michael L., "Passive Damping: Has Its Time Finally Come," *Mechanical Engineering*, vol. 107, pp. 20-24, Dec. 1985.
4. Yamaguchi, H. and Saito, H., "Vibrations of Beams with an Absorber Consisting of a Viscoelastic Solid and a Beam," *Earthquake Engineering and Structural Dynamics*, vol. 12, pp. 467-479, 1984.
5. Snowdon, J. C., "Platelike Dynamic Vibration Absorbers," *Journal of Engineering for Industry*, vol. 97(1), pp. 88-93, Feb. 1975.
6. El-Raheb, M. and Wagner, P., "Damped Response of Shells by a Constrained Viscoelastic Layer," *Journal of Applied Mechanics*, vol. 53, pp. 902-908, Dec. 1986.
7. Torvik, P. J., "The analysis and Design of Constrained Layer Damping Treatments," in *Damping Applications for Vibration Control*, ed. Peter J. Torvik, pp. 85-112, ASME, New York, NY., 1980.
8. Christensen, R. M., *Theory of Viscoelasticity*, Academic Press, Inc., New York, N.Y., 1982.
9. Shen, I. Y. and Mote, C. D. Jr., "Dynamic Analysis of Three Dimensional, Finite, Linear Elastic Solids Containing Small Imperfections: Theory with Application to Asymmetric Circular Plates," *submitted to Journal of Sound and Vibration*.



(a) System 1, λ_0, μ_0, ρ_0 and $\lambda_0^*, \mu_0^*, \rho_0^*, \lambda_0^*, \mu_0^*$

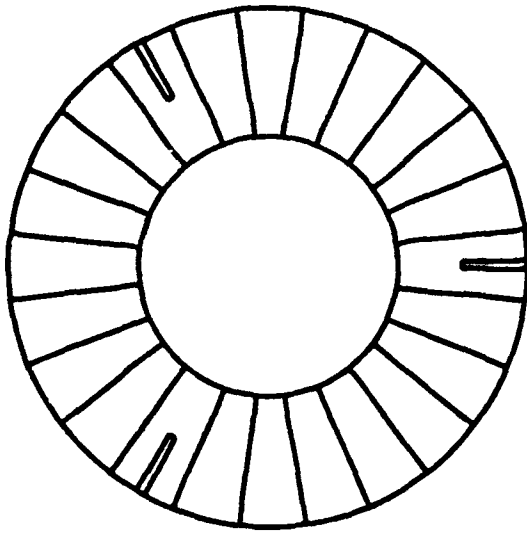


(b) System 2, $\lambda(\mathbf{r}), \mu(\mathbf{r}), \rho(\mathbf{r})$ and $\lambda_0^*(\mathbf{r}), \mu_0^*(\mathbf{r})$

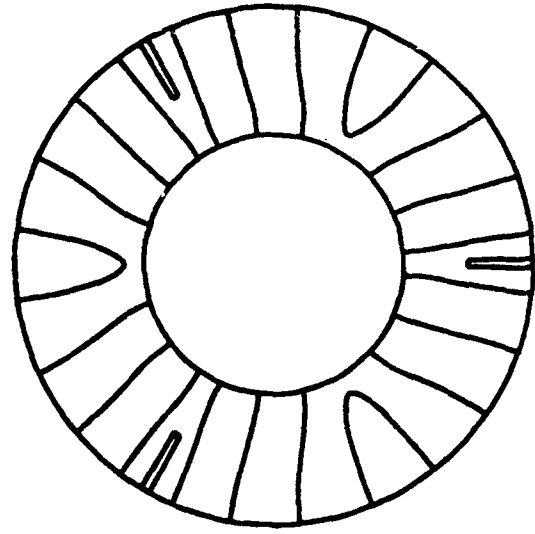


(c) System 3, λ_0, μ_0, ρ_0

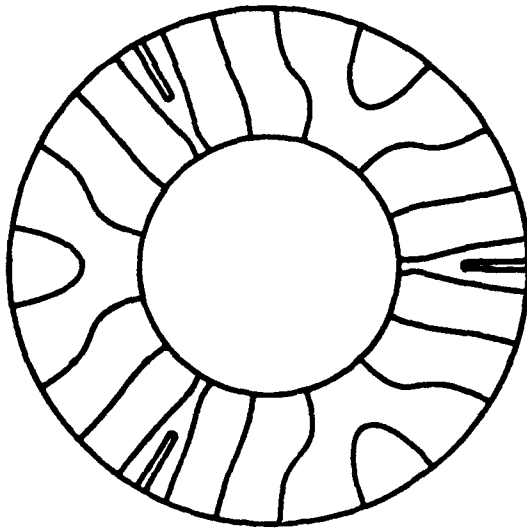
Fig. 1 (a) An Elastic Solid Containing Viscoelastic Inclusions
 (b) The Equivalent Inhomogeneous Viscoelastic Solid
 (c) The Homogeneous Elastic Solid without Inclusions



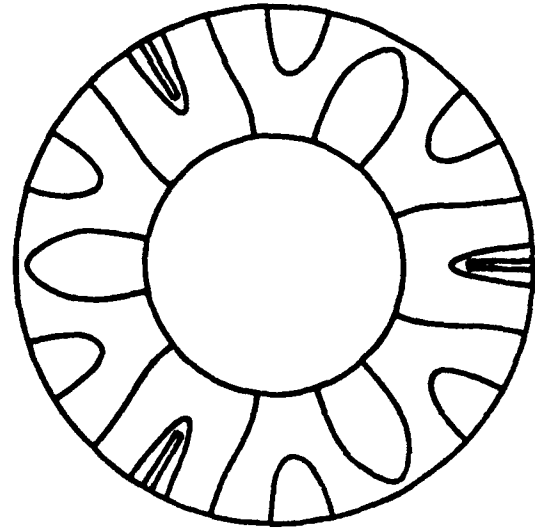
(a) $t=0.0$



(b) $t=0.18$

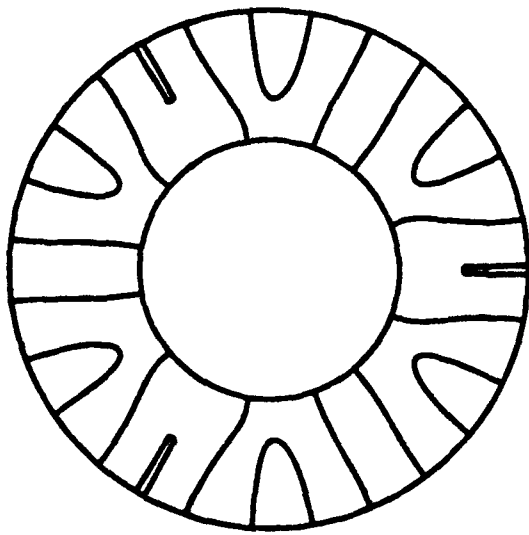


(c) $t=0.22$

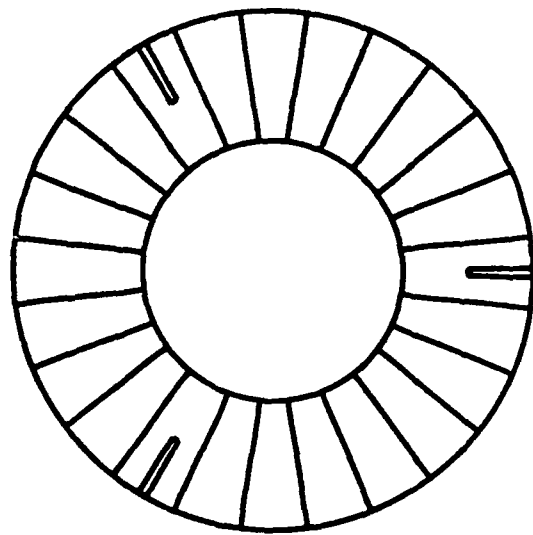


(d) $t=0.25$

Fig. 2 Evolution of Nodal Curves of $(0, 12^C)$



(e) $t=0.30$



(f) $t=0.50$

Fig. 2 (Continued)

Fig. 3 Loci of Eigenvalues \tilde{v}_{mn}

$\xi = 0 - 0.2$ for 5^C , 5^S , 6^C , and 6^S

$\xi = 0 - 0.4$ for 3^C , 3^S , 4^C , and 4^S

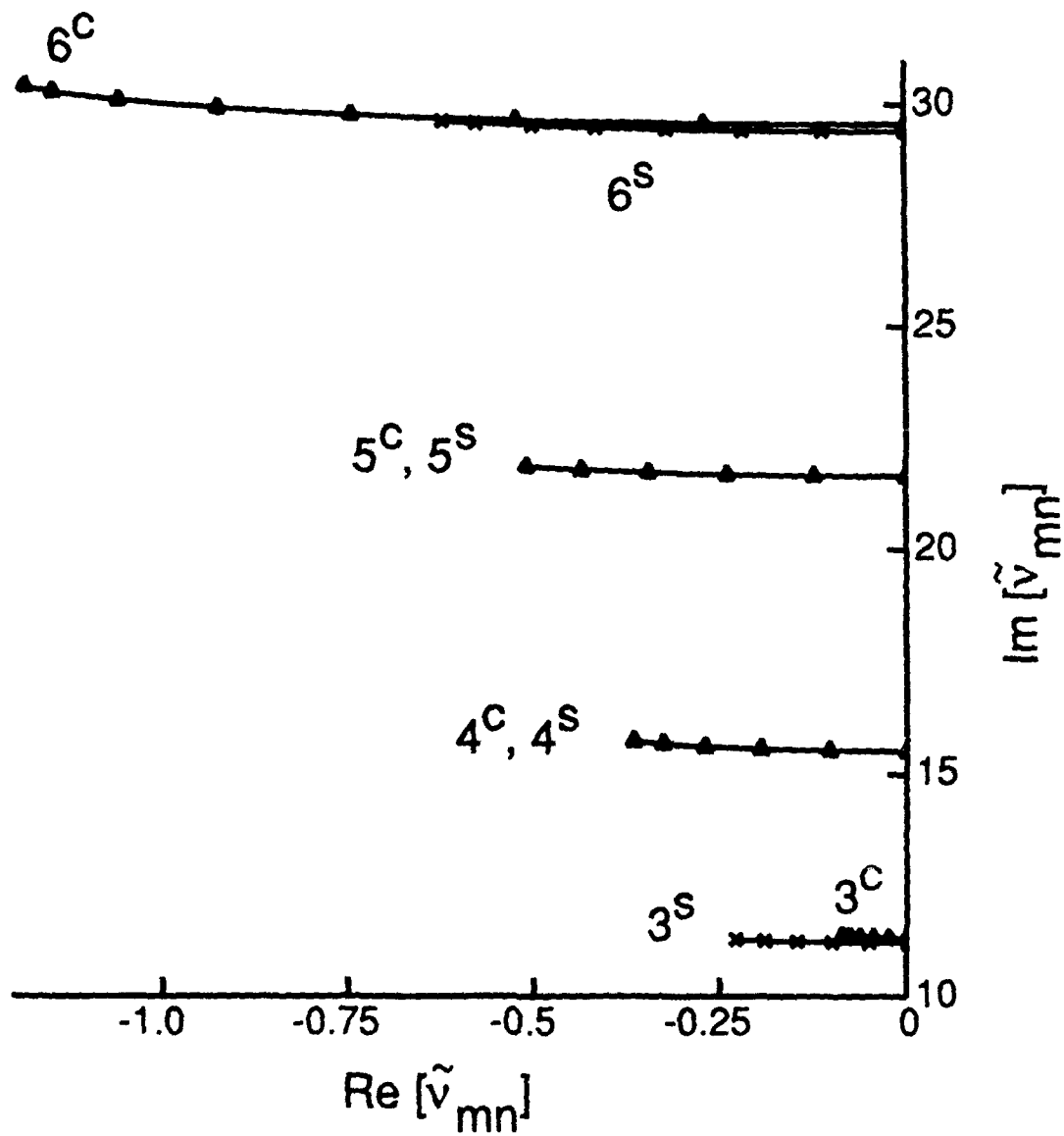


Fig. 4 Displacement Contours of
Green's Function with

$t=0$, $r_0=(b,30^\circ)$, $\tilde{\nu}=6.00$, $\Delta w=0.05$

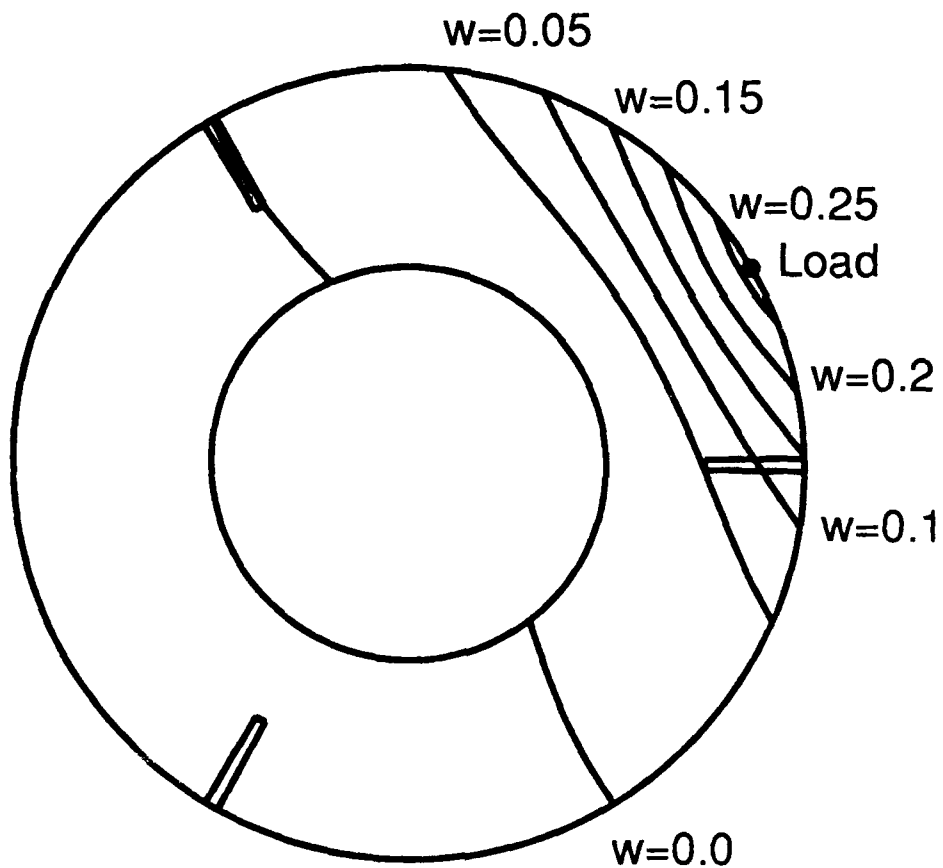
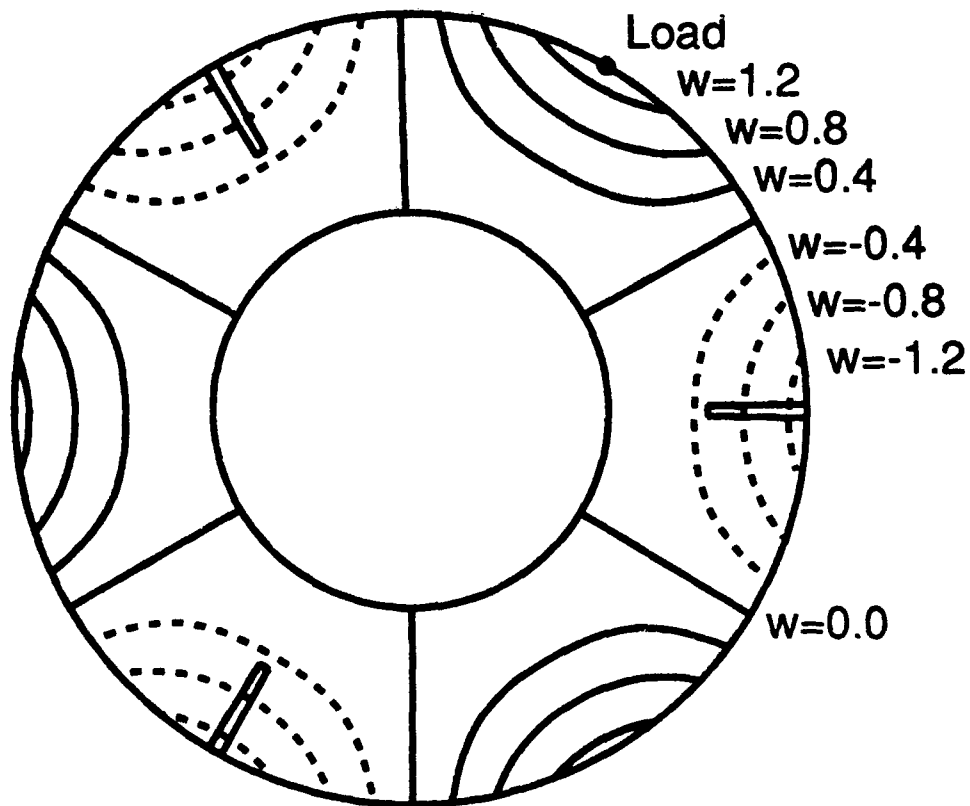


Fig. 5 Displacement Contours of
Green's Function with

$$t=0, r_0=(b, 60^\circ), \tilde{v}=11.40, \Delta w=0.4$$



Modal Analysis of Kelvin Viscoelastic Solids Under Arbitrary Excitation: Circular Plates under Moving Loads

I. Y. Shen †
and
C. D. Mote, Jr.

Department of Mechanical Engineering
University of California, Berkeley
Berkeley, CA 94720
U. S. A.

ABSTRACT

The response of a finite, inhomogeneous, Kelvin viscoelastic solid under arbitrary excitation is determined by modal analysis. Through the reciprocal theorem of viscoelasticity, vibration modes of the Kelvin viscoelastic solid satisfy orthogonality conditions and the system response under any excitation is represented in a modal series. This formulation technique is illustrated on an asymmetric, classical, circular plate containing Kelvin inclusions excited by a constant transverse force rotating at constant speed. The viscosity of the inclusions suppresses the instability excited at supercritical speed in the elastic plate, but it may or may not suppress instability excited at subcritical speed depending on the geometry and location of the Kelvin inclusions.

† (415) 642-6371

1. Introduction

Viscoelastic components are often introduced to elastic structures to suppress excessive vibration and to reduce noise level produced by the structures [1-3]. Instead of adding additional damping material to elastic structures, which is common in damping design such as tuned dampers [4,5] and surface treatments [6,7], viscoelastic components can be introduced as inclusions in the structure [8]. In addition, the location and geometry of the viscoelastic inclusions can be specified to significantly strain the inclusions during particular vibration modes.

In an earlier study [8] eigenfunctions and Green's function have been determined for a three dimensional, finite, elastic solid with Kelvin viscoelastic inclusions through an integral equation and a perturbation iteration method. The purposes of this paper are to develop the orthogonality of the eigenfunctions of the viscoelastic solid and to present the response of the solid to arbitrary excitation.

Following the viscoelastic reciprocal theorem [9], eigenfunctions of the Kelvin viscoelastic solid satisfy orthogonality conditions in a state space representation. Eigenfunction expansion of the response in a modal series then discretizes an action integral whose stationarity governs the response of the viscoelastic solid under arbitrary excitation. Stationarity of the action integral and the state space orthogonality conditions give a set of decoupled equations governing the generalized coordinates of the modal series.

This technique is illustrated on an asymmetric, classical, circular plate containing viscoelastic inclusions excited by a constant transverse force rotating at constant speed. The steady state response of the plate is obtained through the modal analysis.

2. Orthogonality

Consider an inhomogeneous, isotropic, Kelvin viscoelastic solid with Lamé distributions $\lambda(\mathbf{r})$, $\mu(\mathbf{r})$, density distribution $\rho(\mathbf{r})$, and damping distributions $\lambda^*(\mathbf{r})$, $\mu^*(\mathbf{r})$. The solid occupies a three dimensional domain τ with zero displacements on the boundary σ_1 and vanishing traction on boundary σ_2 . The complex-valued eigenfunction $\Psi(\mathbf{r}) \equiv [\Psi^{(1)}(\mathbf{r}), \Psi^{(2)}(\mathbf{r}), \Psi^{(3)}(\mathbf{r})]^T$ and eigenvalue v satisfy

$$\frac{d}{dx_j} [\sigma_{ij}(\Psi(\mathbf{r}), v; \lambda, \mu, \lambda^*, \mu^*)] = v^2 \rho(\mathbf{r}) \Psi^{(i)}(\mathbf{r}), \quad i = 1, 2, 3 \quad (1)$$

with boundary conditions

$$\Psi(\mathbf{r}) = \mathbf{0}, \quad \text{on } \sigma_1 \quad (2a)$$

$$\sigma_{ij}(\Psi(\mathbf{r}), v; \lambda, \mu, \lambda^*, \mu^*) n_j = 0, \quad \text{on } \sigma_2, \quad i = 1, 2, 3 \quad (2b)$$

where

$$\sigma_{ij}(u, v; \lambda, \mu, \lambda^*, \mu^*) = \lambda \delta_{ij} \epsilon_{kk}(u) + 2\mu \epsilon_{ij}(u) + v [\lambda^* \delta_{ij} \epsilon_{kk}(u) + 2\mu^* \epsilon_{ij}(u)] \quad (3)$$

In addition, the divergence theorem [9] gives

$$\int_{\sigma_2} \sigma_{ij}(u, v; \lambda, \mu, \lambda^*, \mu^*) n_j u'_i d^2 \mathbf{r} - \int_{\tau} \frac{d}{dx_j} [\sigma_{ij}(u, v; \lambda, \mu, \lambda^*, \mu^*)] u'_i d^3 \mathbf{r}$$

$$= \int_{\tau} I(u, u'; \lambda, \mu) d^3r + \nu \int_{\tau} I(u, u'; \lambda^*, \mu^*) d^3r \quad (4)$$

with

$$I(u, u'; \lambda, \mu) = \int_{\tau} [\lambda \epsilon_{kk}(u) \epsilon_{kk}(u') + 2\mu \epsilon_{ij}(u) \epsilon_{ij}(u')] d^3r \quad (5)$$

where $u(r)e^{i\omega t}$ and $u'(r)e^{i\omega t}$ are harmonic displacement fields vanishing on σ_1 , and $\epsilon_{ij}(\cdot)$ is infinitesimal strain.

Replace the unprimed and primed u in (4) by $\psi_m(r)$ and $\psi_n(r)$. Since eigenfunctions satisfy (1) and (2a,b), (4) implies

$$-\nu_m^2 \int_{\tau} \rho(r) \psi_m \cdot \psi_n d^3r = \int_{\tau} I(\psi_m, \psi_n; \lambda(r), \mu(r)) d^3r + \nu_m \int_{\tau} I(\psi_m, \psi_n; \lambda^*(r), \mu^*(r)) d^3r \quad (6a)$$

and

$$-\nu_n^2 \int_{\tau} \rho(r) \psi_n \cdot \psi_m d^3r = \int_{\tau} I(\psi_n, \psi_m; \lambda(r), \mu(r)) d^3r + \nu_n \int_{\tau} I(\psi_n, \psi_m; \lambda^*(r), \mu^*(r)) d^3r \quad (6b)$$

Subtract (6a) from (6b), apply the symmetry of I , and normalize

$$(\nu_m + \nu_n) \int_{\tau} \rho(r) \psi_m \cdot \psi_n d^3r + \int_{\tau} I(\psi_m, \psi_n; \lambda^*(r), \mu^*(r)) d^3r = \delta_{mn} \quad (7a)$$

Multiply (7a) by ν_n and add to (6b)

$$-\nu_m \nu_n \int_{\tau} \rho(r) \psi_m \cdot \psi_n d^3r + I(\psi_m, \psi_n; \lambda(r), \mu(r)) d^3r = -\nu_n \delta_{mn}, \quad (n \text{ no sum}) \quad (7b)$$

Orthonormality (7a,b) can also be written in a compact form

$$\langle \Phi_m, \Phi_n \rangle_A = \int_{\tau} \Phi_m^T A \Phi_n d^3r = \delta_{mn} \quad (8a)$$

$$\langle \Phi_m, \Phi_n \rangle_B = \int_{\tau} \Phi_m^T B \Phi_n d^3r = -\nu_n \delta_{mn} \quad (8b)$$

where Φ_m , A , and B are

$$\Phi_m = \begin{bmatrix} \nu_m \psi_m \\ \psi_m \end{bmatrix} \quad (9a)$$

$$A = \begin{bmatrix} 0 & \rho(r) \\ \rho(r) & I(\cdot, \cdot; \lambda^*(r), \mu^*(r)) \end{bmatrix} \quad (9b)$$

$$B = \begin{bmatrix} -\rho(r) & 0 \\ 0 & I(\cdot, \cdot; \lambda(r), \mu(r)) \end{bmatrix} \quad (9c)$$

The first and second entries of I in (9b,c) operate on the premultiplied and postmultiplied functions, respectively.

3. Response Under Arbitrary Excitations

The response $w(r,t)$ of the solid under arbitrary excitation $f(r,t)$ satisfies stationarity of the following action

$$\delta J = \int_{t_1}^{t_2} \left[\delta T - \delta V + \delta W_D + \delta W_F \right] dt \quad (10)$$

where

$$\delta T = \int_{\tau} \rho(\mathbf{r}) \dot{\mathbf{w}}(\mathbf{r}, t) \delta \dot{\mathbf{w}}(\mathbf{r}, t) d^3 \mathbf{r} \quad (11a)$$

$$\delta V = \int_{\tau} I(\mathbf{w}, \delta \mathbf{w}; \lambda(\mathbf{r}), \mu(\mathbf{r})) d^3 \mathbf{r} \quad (11b)$$

$$\delta W_D = - \int_{\tau} I(\dot{\mathbf{w}}, \delta \dot{\mathbf{w}}; \lambda^*(\mathbf{r}), \mu^*(\mathbf{r})) d^3 \mathbf{r} \quad (11c)$$

$$\delta W_F = \int_{\tau} \mathbf{f}(\mathbf{r}, t) \cdot \delta \mathbf{w}(\mathbf{r}, t) d^3 \mathbf{r} \quad (11d)$$

are the variations in the kinetic and strain energies plus the virtual work done in the viscoelastic material and by the external load. By (11a-d), (10) can be rewritten as

$$\delta J = \int_{t_1}^{t_2} \left\{ \int_{\tau} \rho(\mathbf{r}) \frac{d}{dt} [\dot{\mathbf{w}} \delta \mathbf{w}] d\tau - [\langle \dot{\Psi}, \delta \Psi \rangle_A + \langle \Psi, \delta \Psi \rangle_B] + \int_{\tau} \mathbf{F} \cdot \delta \Psi d\tau \right\} dt \quad (12)$$

where

$$\Psi(\mathbf{r}, t) = \begin{bmatrix} \dot{\mathbf{w}}(\mathbf{r}, t) \\ \mathbf{w}(\mathbf{r}, t) \end{bmatrix}, \quad \mathbf{F} = \begin{bmatrix} 0 \\ \mathbf{f}(\mathbf{r}, t) \end{bmatrix} \quad (13)$$

If the eigenfunctions $\Phi_m(\mathbf{r})$ in (9a) are complete, then $\Psi(\mathbf{r}, t)$ allows a representation as an eigenfunction expansion

$$\Psi(\mathbf{r}, t) = \sum_{m=1}^{\infty} q_m(t) \Phi_m(\mathbf{r}) \quad (14)$$

Substitute (14) into (12) and recall the orthogonality (8a,b) to obtain

$$\delta J = \int_{\tau} \int_{t_1}^{t_2} \rho(\mathbf{r}) \frac{d}{dt} [\dot{\mathbf{w}} \delta \mathbf{w}] dt d\tau - \sum_{n=1}^{\infty} \int_{t_1}^{t_2} [\dot{q}_n - \nu_n q_n - Q_n] \delta q_n dt \quad (15)$$

where

$$Q_n(t) = \int_{\tau} \Phi_n^T(\mathbf{r}) \cdot \mathbf{F} d^3 \mathbf{r} = \int_{\tau} \Psi_n^T(\mathbf{r}) \cdot \mathbf{f}(\mathbf{r}, t) d^3 \mathbf{r} \quad (16)$$

The stationarity of J , $\delta J = 0$, and $\delta q_n(t_1) = \delta q_n(t_2) = 0$, $n = 1, 2, \dots$, imply that

$$\dot{q}_n(t) - \nu_n q_n(t) = Q_n(t), \quad n = 1, 2, 3, \dots \quad (17a)$$

with the initial condition

$$q_n(0) = \langle \Phi_n(\mathbf{r}), \Psi(\mathbf{r}, 0) \rangle_A, \quad n = 1, 2, 3, \dots \quad (17b)$$

The complete response is then

$$\mathbf{w}(\mathbf{r}, t) = \sum_{n=1}^{\infty} q_n(t) \Psi_n(\mathbf{r}) = \sum_{n=1}^{\infty} [\langle \Phi_n(\mathbf{r}), \Psi(\mathbf{r}, 0) \rangle_A e^{\nu_n t} + \int_0^t e^{\nu_n(t-\tau)} Q_n(\tau) d\tau] \Psi_n(\mathbf{r}) \quad (18)$$

4. Applications to Asymmetric Circular Plates

The steady state response of a stationary, classical, asymmetric, viscoelastic circular plate under a rotating force is determined by modal analysis. Classical plate theory requires

$$\mathbf{w}(\mathbf{r}, t) = w(\mathbf{r}, t) \hat{k}, \quad \mathbf{f}(\mathbf{r}, t) = f(\mathbf{r}, t) \hat{k}$$

where \hat{k} is the unit vector normal to the middle surface of the plate. The eigenfunctions are

$$\psi_{mn}(\mathbf{r})\hat{k} \quad \text{and} \quad \bar{\psi}_{mn}(\mathbf{r})\hat{k}, \quad m=0, 1, \dots, \quad n=0, \pm 1, \dots$$

where $\psi_{mn}(\mathbf{r})$ and $\psi_{m,-n}(\mathbf{r})$ and their complex conjugates (denoted by the overbar) are four orthonormal complex eigenfunctions of the plate with m nodal circles and n nodal diameters. Therefore, the plate response is

$$w(\mathbf{r}, t) = \sum_{\alpha=1}^2 \sum_{m=0}^{\infty} \sum_{n=-\infty}^{\infty} \psi_{mn}^{(\alpha)}(\mathbf{r}) q_{mn}^{(\alpha)}(t) \quad (19)$$

where $\psi_{mn}^{(1)}(\mathbf{r}) \equiv \psi_{mn}(\mathbf{r})$ and $\psi_{mn}^{(2)}(\mathbf{r}) \equiv \bar{\psi}_{mn}(\mathbf{r})$.

For a unit concentrated force rotating along a circle $r = r_0$ at constant speed Ω ;

$$f(\mathbf{r}, t) = \frac{1}{r_0} \delta(r - r_0) \delta(\theta - \Omega t) \quad (20)$$

the modal response is

$$\dot{q}_{mn}^{(\alpha)}(t) - v_{mn}^{(\alpha)} q_{mn}^{(\alpha)}(t) = \psi_{mn}^{(\alpha)}(r_0, \Omega t) \quad (21)$$

Because $\psi_{mn}^{(\alpha)}(r, \theta)$ is periodic in θ

$$\psi_{mn}^{(\alpha)}(r, \theta) = \sum_{p=-\infty}^{\infty} a_{mn}^{(\alpha)}(r; p) e^{ip\theta}, \quad (22)$$

and the steady state $q_{mn}^{(\alpha)}(t)$ is

$$q_{mn}^{(\alpha)}(t) = \sum_{p=-\infty}^{\infty} \frac{\bar{a}_{mn}^{(\alpha)}(r_0; p)}{ip\Omega - v_{mn}^{(\alpha)}} e^{ip\Omega t} \quad (23)$$

Resonance occurs when $v_{mn} = ip\Omega$ and $a_{mn}^{(\alpha)}(r_0; p)$ is nonzero.

The average strain energy of vibration is

$$\langle E_s \rangle = \frac{1}{T} \int_0^T \int_A I(w, \bar{w}; \lambda, \mu) dA dt, \quad T = \frac{2\pi}{\Omega} \quad (24)$$

Substitute (19) and (23) into (24) to obtain

$$\langle E_s \rangle = - \sum_{\alpha\beta mnkl} \int_A I(\psi_{mn}^{(\alpha)}, \bar{\psi}_{kl}^{(\beta)}; \lambda, \mu) dA \left[\sum_{p=-\infty}^{\infty} \frac{a_{mn}^{(\alpha)}(r_0; p) \bar{a}_{kl}^{(\beta)}(r_0; p)}{(ip\Omega - v_{mn}^{(\alpha)})(ip\Omega + v_{kl}^{(\beta)})} \right] \quad (25)$$

where $\sum_{\alpha\beta mnkl} \equiv \sum_{\alpha=1}^2 \sum_{m=0}^{\infty} \sum_{n=-\infty}^{\infty} \sum_{\beta=1}^2 \sum_{k=0}^{\infty} \sum_{l=-\infty}^{\infty}$. Similarly, total dissipation per cycle is

$$\langle E_d \rangle = \int_0^T \int_A I(\dot{w}, \dot{\bar{w}}; \lambda^*, \mu^*) dA dt \quad (26)$$

Substitute (19) and (22) into (26) to obtain

$$\langle E_d \rangle = - \sum_{\alpha\beta mnkl} \int_A I(\psi_{mn}^{(\alpha)}, \bar{\psi}_{kl}^{(\beta)}; \lambda^*, \mu^*) dA \left[\sum_{p=-\infty}^{\infty} \frac{2\pi\Omega p^2 a_{mn}^{(\alpha)}(r_0; p) \bar{a}_{kl}^{(\beta)}(r_0; p)}{(ip\Omega - v_{mn}^{(\alpha)})(ip\Omega + v_{kl}^{(\beta)})} \right] \quad (27)$$

An averaged loss factor $\langle \eta \rangle$ is [7]

$$\langle \eta \rangle = \frac{\langle E_d \rangle}{\langle E_s \rangle} \quad (28)$$

As a numerical illustration of the moving load instability, consider an uniform, elastic, circular plate with three evenly spaced radial inclusions. Each inclusion spans an angle 0.035 rad ($\approx 2^\circ$) and extends from $r=0.75b$ and $r=b$, where b is the outer radius of the plate. The inclusions considered are elastic or viscoelastic. Material properties of the plate and the inclusions, and plate eigenvalues are described in Table 1. Eigenfunctions $\psi_{mn}(r)$ of the plate are calculated by the method of perturbation iteration [8, 10].

Figure 1 shows the average strain energy of the asymmetric plate. The thin lines are for elastic, and the thick lines are for viscoelastic inclusions. When the inclusions are elastic, resonances occur at $\frac{\Omega}{\omega_{cr}} = \frac{\beta_{mn}}{n}$, where ω_{cr} is the critical speed of the axisymmetric plate without the inclusions and β_{mn} is a natural frequency of the asymmetric plate in Table 1. Increasing modal damping (Table 1) results in greater amplitude reduction in Fig. 1. Figure 2 shows the strain energy of the plate at subcritical speed. Subcritical speed resonances, which do not exist in axisymmetric plates [11], do occur here at rotation speeds

$$\frac{\Omega}{\omega_{cr}} = \frac{\beta_{mn}}{|3j \pm n|}, \quad j = \pm 1, \pm 2, \dots \quad (29)$$

because [10]

$$a_{mn}^{(\alpha)}(r_0; p) \begin{cases} \neq 0, & p = 3j \pm n, \quad j = \pm 1, \pm 2, \dots \\ = 0, & \text{Otherwise} \end{cases} \quad (30)$$

The resonance around $\Omega \approx 0.704\omega_{cr}$ is caused by $\psi_{00}(r)$, and the ones near $\Omega \approx 0.592\omega_{cr}$ and $\Omega \approx 0.829\omega_{cr}$ are caused by the repeated modes $\psi_{04}(r)$ and $\psi_{0,-4}(r)$. The subcritical speed instability may or may not be suppressed by damping in the inclusions depending on the modal damping ζ_{mn} . The resonance by $\psi_{00}(r)$ is slightly suppressed because of the minimal modal damping in $\psi_{00}(r)$ (cf. Table 1).

5. Conclusions

1. For an inhomogeneous, isotropic, Kelvin viscoelastic solid, eigenfunctions $\psi_m(r)$ and $\psi_n(r)$ satisfy orthonormality conditions (8a,b).
2. A lateral force rotating at constant speed will excite asymmetric plates containing elastic or viscoelastic inclusions to subcritical speed resonances that do not exist in axisymmetric plates. The occurrence of the subcritical resonances depends on the plate asymmetry and can be predicted analytically.
3. The viscosity of the inclusions may or may not suppress the subcritical resonances depending on the geometry and location of the inclusions. The suppression of resonances can be predicted by the modal damping of each vibration mode.

Table 1 - Normalized Eigenvalues of a Circular Plate with Three Inclusions

Normalized natural frequencies:

$$\omega_{mn} = \frac{\bar{\omega}_{mn}}{\omega_{cr}} \text{ (axisymmetric plates), } \beta_{mn} = \frac{\bar{\beta}_{mn}}{\omega_{cr}} \text{ (asymmetric plates)}$$

Modal damping ratio: ζ_{mn}

Plate: fixed at inner rim at $0.5b$, free at outer rim at b ; $\frac{W_0}{D_0} = 0.7$.†

Inclusions extend from $r = 0.75b$ to $r = b$; $\epsilon = 0.035$.

For elastic inclusions: $\frac{\rho'_0}{\rho_0} = \frac{D'_0}{D_0} = \frac{W'_0}{W_0} = 0.5$.†

For viscoelastic inclusions: $D_0^* = 0.00489$, $\frac{W_0^*}{D_0^*} = 0.7$; $\frac{\rho'_0}{\rho_0} = \frac{D'_0}{D_0} = \frac{W'_0}{W_0} = 0.5$.‡

(m, n)	Mode	No Inclusions	With Three Inclusions		
		ω_{mn} †	Elastic †	Viscoelastic ‡	
			β_{mn}	ζ_{mn}	β_{mn}
(0,0)	axisym.	2.1050	2.1121	4.5481×10^{-4}	2.1122
(0,1)	cos	2.1479	2.1549	4.9882×10^{-4}	2.1549
	sin	2.1479	2.1549	4.9882×10^{-4}	2.1549
(0,2)	cos	2.3764	2.3842	8.1266×10^{-4}	2.3843
	sin	2.3764	2.3842	8.1266×10^{-4}	2.3843
(0,3)	cos	3.0000	3.0212	1.2677×10^{-3}	3.0215
	sin	3.0000	2.9927	2.8305×10^{-3}	2.9931
(0,4)	cos	4.1368	4.1429	4.1766×10^{-3}	4.1443
	sin	4.1368	4.1429	4.1766×10^{-3}	4.1443

† Converted from Table 1 of [10]

‡ Converted from Table 1 of [8]

References

1. Nashif, Ahid D., Jones, David I. G., and Henderson, John P., *Vibration Damping*, John Wiley & Sons, Inc., New York, NY., 1985.
2. Rogers, Lynn, "Vibration Damping as a Design Parameter," *Mechanical Engineering*, vol. 108, pp. 66-69, Jan. 1986.
3. Drake, Michael L., "Passive Damping: Has Its Time Finally Come," *Mechanical Engineering*, vol. 107, pp. 20-24, Dec. 1985.
4. Yamaguchi, H. and Saito, H., "Vibrations of Beams with an Absorber Consisting of a Viscoelastic Solid and a Beam," *Earthquake Engineering and Structural Dynamics*, vol. 12, pp. 467-479, 1984.
5. Snowdon, J. C., "Platelike Dynamic Vibration Absorbers," *Journal of Engineering for Industry*, vol. 97(1), pp. 88-93, Feb. 1975.
6. El-Raheb, M. and Wagner, P., "Damped Response of Shells by a Constrained Viscoelastic Layer," *Journal of Applied Mechanics*, vol. 53, pp. 902-908, Dec. 1986.
7. Torvik, P. J., "The analysis and Design of Constrained Layer Damping Treatments," in *Damping Applications for Vibration Control*, ed. Peter J. Torvik, pp. 85-112, ASME, New York, NY., 1980.
8. Shen, I. Y. and Mote, C. D. Jr., "Dynamic Analysis of Finite, Three Dimensional, Linear Elastic Solids with Kelvin Viscoelastic Inclusions: Theory with Application to Asymmetrically Damped Circular Plates," *The Journal of the Acoustical Society of America*. (Submitted)
9. Christensen, R. M., *Theory of Viscoelasticity*, Academic Press, Inc., New York, N.Y., 1982.
10. Shen, I. Y. and Mote, C. D. Jr., "Dynamic Analysis of Three Dimensional, Finite, Linear Elastic Solids Containing Small Elastic Imperfections: Theory with Application to Asymmetric Circular Plates," *Journal of Sound and Vibration*. (Submitted)
11. Mote, C. D. Jr., "Stability of Circular Plates Subjected to Moving Loads," *Journal of the Franklin Institute*, vol. 290(4), pp. 329-344, October 1970.

Strain Energy of Asymmetric Plates

— Viscoelastic Inclusions
— Elastic Inclusions

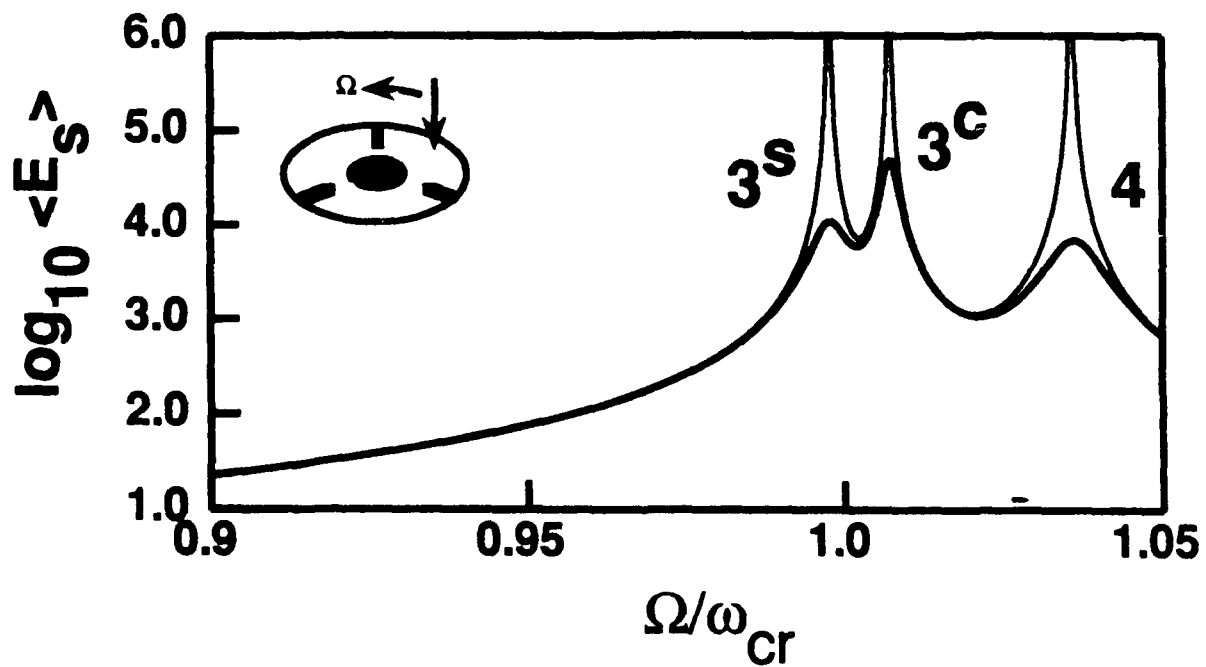
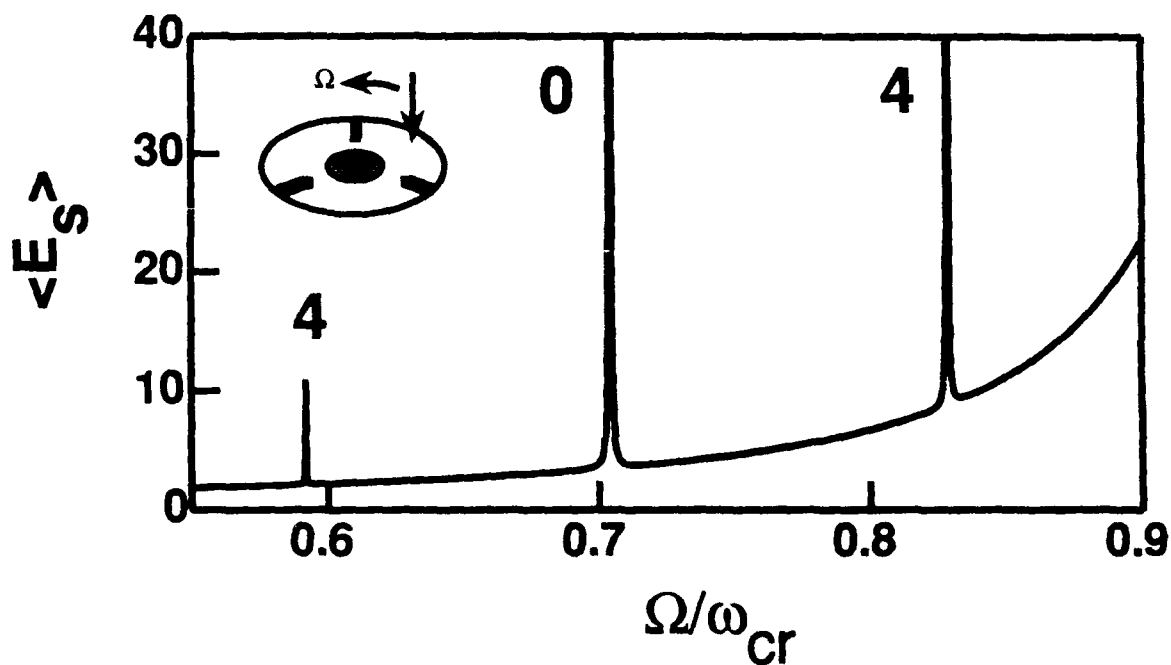


Fig. 1 Average strain energy of asymmetric plates with three elastic or viscoelastic inclusions excited by a rotating force at supercritical speed

Strain Energy of Asymmetric Plates

(a) Plates with Elastic Inclusions



(b) Plates with Viscoelastic Inclusions

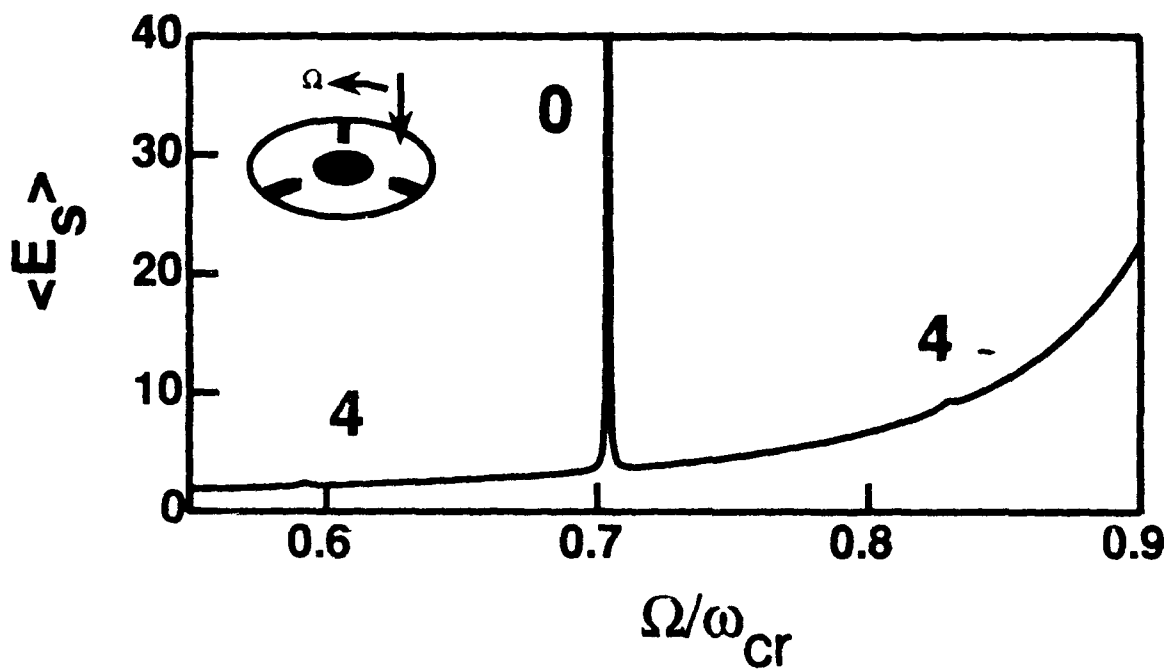


Fig. 2 Average strain energy of asymmetric plates excited by a rotating force at subcritical speed; (a) plate with elastic inclusions, and (b) plate with viscoelastic inclusions

Response of a Circular Plate with Patch Damping

Mahmoud Mezache
Structural Group
Institut National de Génie Mécanique
Bourmerdès
Algeria

Douglas Muster
Department of Mechanical Engineering
University of Houston
Houston, TX
U.S.A.

Gary H. Koopman
Department of Mechanical Engineering
Pennsylvania State University
University Park, PA
U.S.A.

Abstract

Originally, we were interested in minimizing, by a damping treatment, the vibration and acoustical response of a plate-like structure (such as a railroad bridge) to a dynamic force applied at a single point. Often, in practice, a damping treatment is applied to the entire surface of such a structure. We were interested in evaluating the effect of providing selected damping treatments on selected surface areas of the plate-like portions of the structure in order to maximize reducing the responses with minimal amounts of selectively located damping treatment. If information of this kind was available, the cost of applying a damping treatment to a large structure could be reduced. Before we proceeded to the practical problem of treating an actual structure, we sought first to obtain information on the responses of a simple structure, such as a circular thin plate, to damping treatments applied selectively to its surface area. We studied the first three axisymmetric modes of vibration of a thin circular plate by a finite-element approach. The elements of the plate were modeled in terms of their mass, loss factor and flexural rigidity. The measured Q factor for an untreated plate vibrating in its third mode was 425. When 15 percent of the surface area of the plate was covered with a damping treatment, the measured Q factor of the treated plate in the same mode was 40. In general, there is good agreement between the computed and experimental frequencies, mode shapes and motion amplitudes of the untreated plate. As the treated area of the plate was increased, the agreement between computed and experimental results deteriorated, particularly with respect to the motion amplitudes of the higher modes at and near the antinodes. Based on the results obtained from these tests, we have concluded that it should be possible to optimize the amount and location of a surface damping treatment on a large plate-like structure in order to obtain reductions in the acoustic and vibration responses that approach those which can be obtained by applying a damping treatment to the entire structure.

Introduction

Structural vibrations cause noise radiation which can be excessive and objectional under certain circumstances. This occurs particularly when a structure goes into resonance. At this condition, the amplitudes of vibration are large, and must be reduced to a safe level.

The most common means of controlling structural vibrations is by applying damping. If a damping treatment is properly applied, it can prevent the structure from failing, perhaps, catastrophically.

Usually, the form of application of the damping treatment depends on the type of the structural system. It is well known that the response of a coupled lumped-mass system at resonance can be reduced significantly, using viscous dampers in the form of dashpots; while a plate vibrating at resonance in more than one mode should be treated with a continuous damping layer.

The analysis of damped structures is relatively simple if the application of damping is proportional, that is, if the damping matrix is a linear combination of the mass and stiffness matrices. This formulation assumes that the structure is fully coated and the coating is uniform. In this study, a viscoelastic material which provides only damping is used, in which case the term characterizing dry friction damping in the inertial matrix, will not appear. The damping matrix is still a linear function of the stiffness matrix, and the undamped modal matrix may be used to uncouple the equations of motion. The damping parameter is introduced only to calculate the response of the structure.

However, the search for light-weight, rigid structures requires that the external damping treatment be minimized. Then, only selected areas must be treated and, since the damping layer is of the free type, it must be applied to regions of large vibration amplitudes where tensile stresses are highest. This will result in a case of nonproportional damping, because the stiffness matrix will contain real and complex elements pertaining to untreated and treated structural elements, respectively. This type of problem is complex and the response of the corresponding system can not be found from the eigensolution containing no damping.

A numerical model of a circular plate clamped at its center is considered. The plastic is partitioned into annular elements, and only axisymmetric modes are allowed.

Formulation of the Problem

Elastic structures can be analyzed by classical mode superposition methods after evaluating their mass, stiffness and damping matrices. The equation of motion of an n-degree of freedom system with hysteretic damping is

$$[M] \{q\} + [[K] + f [H]] \{q\} = \{Q\}. \quad (1)$$

The damping matrix [H] can be linearly related to [K], depending on the configuration of the coating. If the entire structure is treated, then

$$[H] = f \eta [K], \quad (2)$$

where η is a proportionality constant, referred to as the loss factor of that structure. Introducing Eq. (2), Eq. (1) becomes

$$[M] \{q\} + (1 + f \eta) [K] \{q\} = \{Q\}. \quad (3)$$

Assuming a solution in the form $\{q(t)\} = \{q_0\} \sin \omega t$, the classical eigenvalue problem is obtained. The response in the case of a nonproportionally damped system, as expressed by Eq. (1), is [1]

$$\{q_0\} = \sum_{r=1}^n \frac{\{q\}\{q\}^T\{Q\}}{\omega_r^2 - \omega^2} \quad (4)$$

where the square of ω_r is the r th eigenvalue in the solution of the eigenproblem corresponding to Eq. (1). Both the eigenvalue and the associated eigenvector are complex. In the case of proportional damping, Eq. (4) takes the form

$$\{q_0\} = \sum_{r=1}^n \frac{\{q\}\{q\}^T\{Q\}}{\omega_r^2 (1 + f \eta) - \omega^2} \quad (5)$$

where, now, the eigenvalues and eigenvector are real.

In the above, the stiffness matrix is a function of the equivalent complex modulus of elasticity of the structure, $E^* = (1 + f \eta) E$. In turn, the latter is determined experimentally at given frequencies and temperatures. Therefore, the introduction of hysteretic damping in the equations of motion does not necessarily imply that the damping material used has hysteretic properties. Thus, in general, these equations are only valid at the conditions under which the measured quantities are obtained. In this respect, the complexity of frequency dependence of the treatment material is irrelevant, as long as a different eigenvalue problem would have to be solved at each frequency of interest.

The Damping Model

Among the energy-dissipating mechanisms which have been considered for the design of damped structures, hysteretic damping has been the most widely exploited; particularly in structural configurations incorporating viscoelastic materials, capable of dissipating relatively large amounts of energy. The dissipating capacity of a given material is characterized by the loss factor, defined as the ratio of energy dissipated during one cycle to the total energy stored in the system for the duration of that cycle.

Some viscoelastic materials and most metals possess stress-strain characteristics which deviate from the elliptic shape, exhibiting a nonlinear property. In these cases, compromise is necessary and a linear approximation is used, unless the deviation is unacceptably excessive. The best compromise appears to maintain the loop areas and the amplitudes of the stress and strain [2].

Mathematical models developed to evaluate parameters of linear damping have been reviewed by Bert [3]. Because of their complexity, some of these have no immediate implementation in the general sense. Others are limited in their range of application. A comparison of the various models shows that the difference between them lies only in the way the respective loss factor is expressed in terms of the input variables, such as frequency and temperature.

The work done on the dynamics of beams and plates incorporating continuous damping treatments is well documented [1]. In these models, attempts are made to duplicate the dynamic characteristic of the treated plate using an equivalent angle plate, with the loss factor, the mass and the flexural rigidity remaining constant. These conditions may be expressed as follows, see Fig. 1.

$$\eta = \eta_0, \quad (6)$$

$$\rho t = \rho_1 t_1 + \rho_2 t_2, \quad (7)$$

$$EI = E_1 I_1 + E_2 I_2. \quad (8)$$

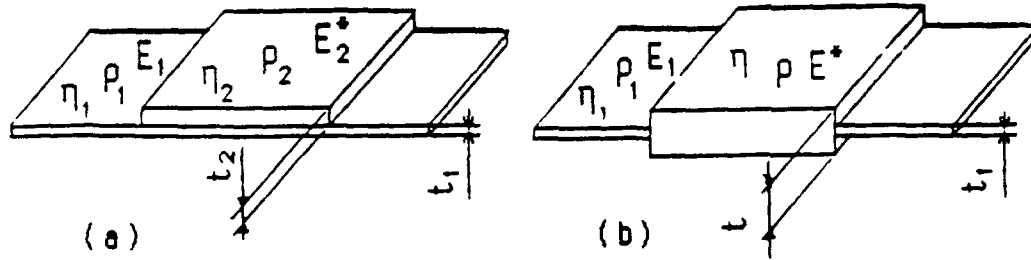


Fig. 1 Transformation of (a) the plate into (b) a singular equivalent plate.

In Eq. (6) it is assumed that the damping of the base plate is negligible. The unknown quantities here being ρ , t , η and E , a fourth equation is required. Since the mass moment of inertia is a function of the material density and the geometry of the composite, it can be used here.

$$J = J_1 + J_2$$

Three of the four unknowns may be calculated using the geometry of the coated plate as shown in Fig. 2, using Eqs. (7) through (9).

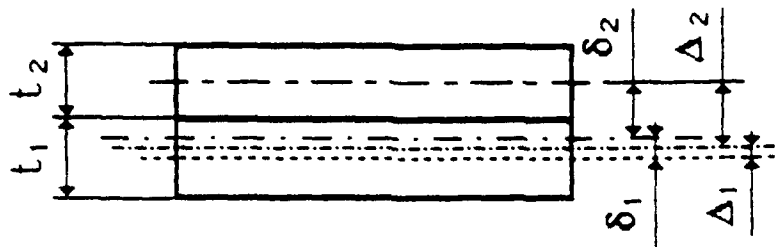


Fig. 2 Cross section of a coated element.

The equivalent loss factor may be determined using different approaches [4,5]. The model due to Cremer *et al.* [4] is used, yielding the following expression for η .

$$\eta = \frac{12\eta_2 E_2 t_2 \Delta_2^2}{E_1 t_1^3 + 12E_2 t_2 \Delta_2^2} \quad (10)$$

Now the four unknowns which define the model of the treated plate completely can be calculated for given a material and thickness of the base plate and the coating. The values of E_2 and η_2 in Eq. (10) are determined experimentally, using the resonant beam method [6]. The inertial and complex matrices of Eqs. (1) and (2) are evaluated from the equivalent parameters obtained for a circular plate clamped at its center. The plate is partitioned into ten annular elements and allowed to vibrate only in its axisymmetric modes.

Experimental Work

The experiments performed in this work may be grouped into two parts. The first part is concerned with the measurement of the loss factor and the storage modulus of the damping material. The resonant-beam technique was used, whereby a carefully machined cantilever beam was coated with a commercial damping material, Type GP-2 supplied by SoundCoat, Inc., New York. The test beam, made of aluminum 66-60, was machined with its root in block to observe the clamped condition.

The coated-beam experiments yielded loss factor values of 0.259 at 76.0 Hz, 0.420 at 136.0 Hz and 0.418 at 758.0 Hz. The two latter frequencies correspond to the second and fourth modes of the composite beam, respectively. According to the recommendations put forth in the measurement method based on its acceptance as ASTM E 756/83, reliable measurements were obtained only if the beam was vibrated at higher modes whose shapes exhibit half wavelengths. The first value of the loss factor was obtained accordingly at the second mode, with a concentrated mass attached to the free end of the beam to lower its resonance frequency to 76.0 Hz, 0.420 at 136.0 Hz, and 0.418 at 758.0 Hz. The two latter frequencies correspond to the second and fourth modes of the composite beam, respectively. According to the recommendations put forth in the measurement method based on its acceptance as ASTM E756/83, reliable measurements are obtained only if the beam is vibrated at higher modes whose shapes exhibit half wavelengths. The first value of the loss factor was obtained accordingly at the second mode, with a concentrated mass attached to the free end of the beam to lower its resonance frequency to 76.0 Hz. The respective values of the storage modulus were found to be 2.50, 2.74 and 2.82 GNm⁻².

Damping due to air resistance was verified by driving the untreated beam into resonance *in vacuo*. The pressure in the vacuum chamber was gradually increased from 18.0 μ mHg to ambient pressure. At 30.0 Hz, the loss factor was found to be 0.0050 at ambient pressure, and 0.0048 at 18 μ mHg. At 216.0 Hz these values were 0.00095 and 0.00086, respectively.

The second part of the experiments consisted in measuring the plate response with different damping treatments. The experimental set-up is shown in Fig. 3, showing a plate, 1.2 mm thick and 286.0 mm in diameter, excited by seven electromagnets placed equidistantly around the circumference. The exciting force was kept constant by fixing the value of the

current in the coils to 200.0 Ma. This value was chosen to avoid saturation of the circuit cores, and to obtain a response large enough to be measured in the cases of heavy damping. The various positions of the damping patches and their areas as a fraction of the total plate area are shown in Figs. 4 and 5 for the second and third mode, respectively.

The plate was first fully coated, then it was gradually uncovered according to Figs. 3 and 4. In the case of the first mode, the damping material was removed from two elements at a time, starting from the circumference.

Since the damping layer is of the free type, the areas to be treated are those in the neighborhood of a displacement antinode, where strain energy is maximal. If the wave neighborhood of a displacement antinode represents also the point with the smallest radius of curvature, where stress and strain are both high. However, in situations where the deformed shape is not symmetric, the treatment is applied in the area with small radii of curvature.

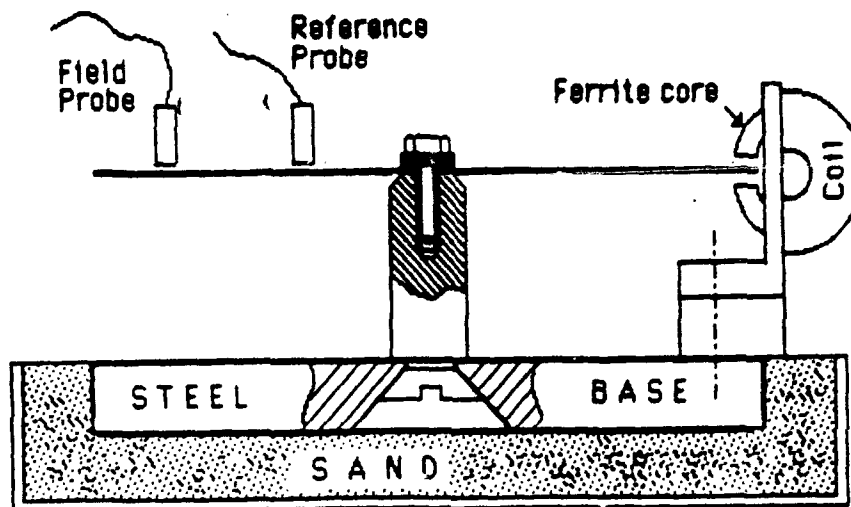


Fig. 3 Experimental set-up for the plate model.

Results and Discussion

The resonance frequencies of the untreated and fully coated plates are given in Table 1.

		Untreated	Fully treated
Mode 1	Calculated	56.3	55.8
	Measured	55.0	54.5
Mode 2	Calculated	329.7	330.7
	Measured	3336.5	3332.0
Mode 3	Calculated	955.9	959.3
	Measured	1016.8	997.7

Table 1 Natural frequencies of the circular plate (Hz).

The measured resonance frequency of the first mode is lower than the calculated value for both the treated and the untreated case. This is consistent with the principle by which the Rayleigh quotient overestimates the natural frequency of a system. In the second and third mode, the measured values are higher. Since the Rayleigh quotient is applicable only to the

fundamental mode, it can not be used to justify this result. However, we believe that the numerical model did not predict the proper ratio of the added mass and stiffness. Also, the damping layer in the experimental model is not constrained at the boundaries. The assumption that the coating does not undergo shear deformation, and the invariance of Poisson's ratio in the calculation of the flexural rigidity of the composite plate have contributed to these discrepancies. These will also affect on the amplitudes and mode shapes.

The Q factor of the plate evaluated at element node 4 is shown in Figs. 6 and 7. The measured and the predicted curves are in good agreement. However, this comparison can not be made for the outer region of the plate described above as it will be seen later in the discussion.

The displacement response for the first three modes is shown in Fig. 8 through 13. A curve fit was performed on each set of data for presentation clarity. A detailed comparison was made between the calculated and experimental results for each damping case. The response of the undamped plate was predicted with an error of less than 1%, evaluated at the free edge. A close agreement is also obtained with coverages up to 36% of the plate surface area. The error at 36% coverage is 8%, while that for a full coating is 6%. This discrepancy, which increases as the treated area is reduced, can be attributed to the unconstrained boundary elements. These, being at the edge of the treated area, are not subject to tensile forces, as is assumed in the numerical model. As the treated area is reduced, the surface area of the boundary element becomes relatively high, and its contribution to the damping of the plate appears to be less significant. An error of 32% was recorded in the 4% and 16% coverage cases.

The results for the second mode are presented in Figs. 10 and 11. The damped waveform exhibits two regions of interest. The first is the region within the nodal circle where the measured values are greater than the predictions. This is consistent with the argument on the boundary element as explained above. The error varies from 28% at 27% coverage to 3% for full coating. The second region of concern is that between the nodal circle and the edge, which behaves simply as an annular plate, simply supported at the inner diameter and free at the outer edge, oscillating without undergoing flexural deformation. The induced tensile stresses in this region are small and, as a consequence, the damping treatment has little effect. The vibration amplitudes are controlled by the inertia of the annular region which may have contributed to an observed progressive shift of the nodal circle in the coating cases above 40% coverage of the plate area.

This behavior is more pronounced in the third mode, shown in Figs. 12 and 13. The results agree in the area within the first nodal circle, where an error of 22% was recorded for a 15% coverage. This error drops to 8% for the fully coated plate. Although the flexing motion of the region located outside the first nodal circle is pronounced, the local antinode is heavily damped.

Conclusion

The dynamic response of a circular plate incorporating patch damping is investigated using a finite-element approach, with only axisymmetric modes being allowed. The predicted response was in reasonable agreement with our experiments at low frequencies, or in the regions where half wavelengths are described. A flexing motion of the outer part of the plate is observed which the numerical model failed to predict.

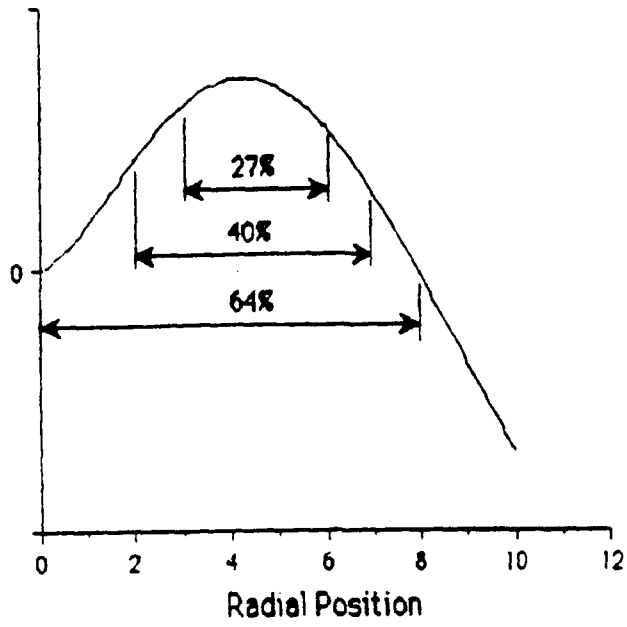


Fig. 4 Different damping treatments in mode 2.

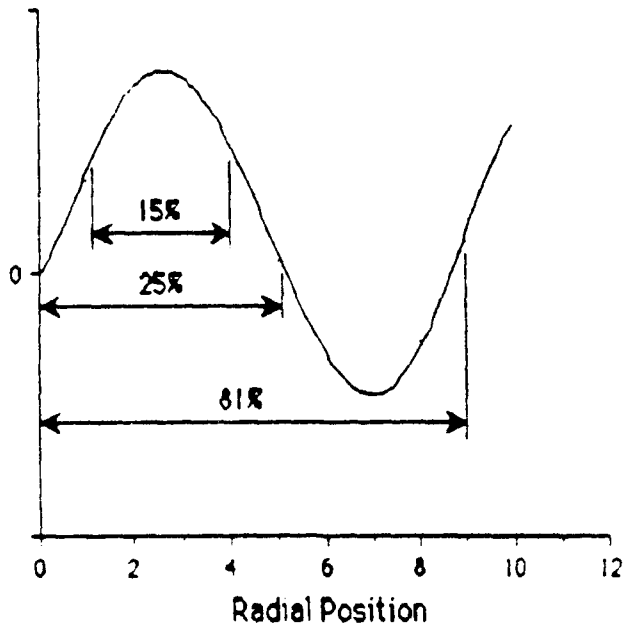


Fig. 5 Different damping treatments in mode 3.

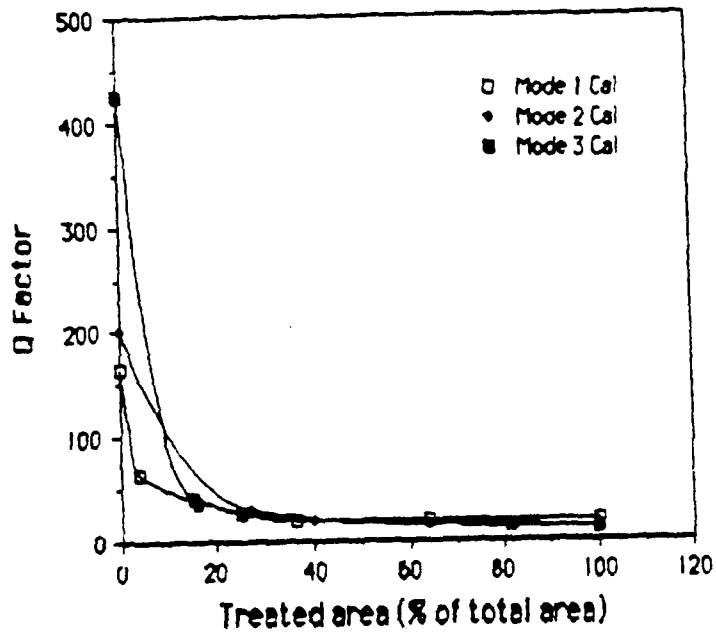


Fig. 6 Calculated Q factor.

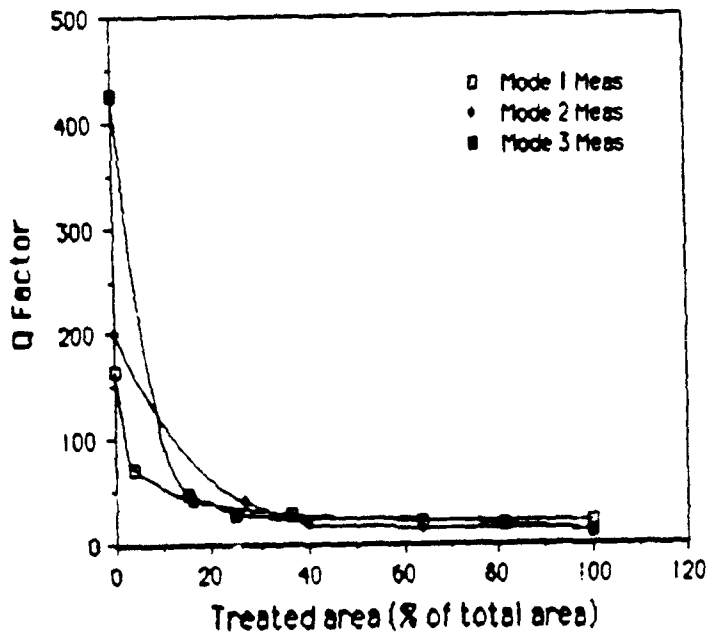


Fig. 7 Measured Q factor

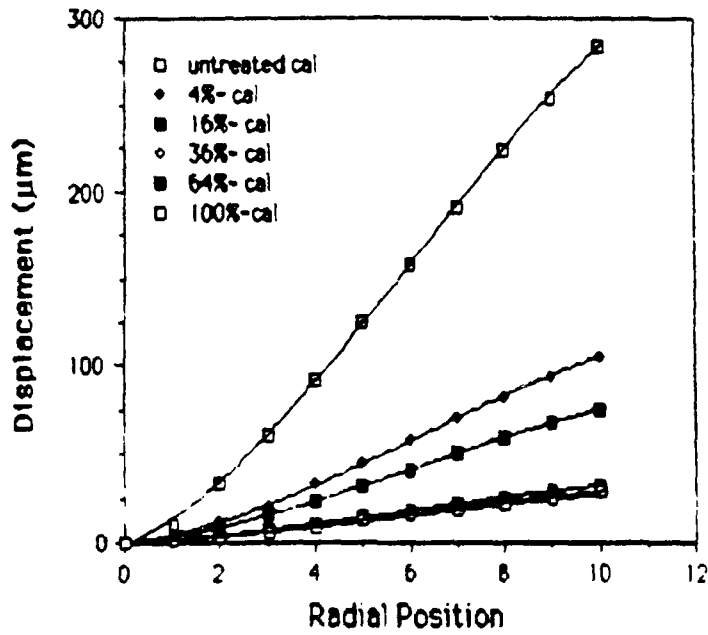


Fig. 8 Mode 1, calculated response.

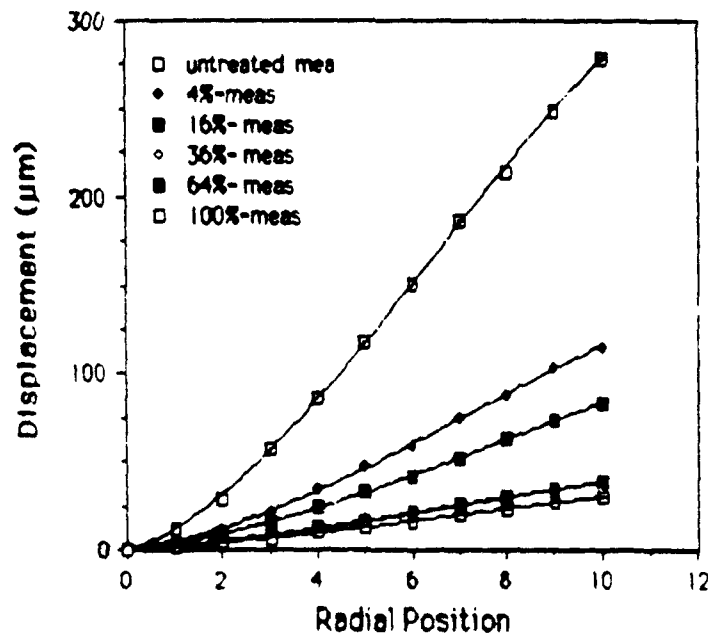


Fig. 9 Mode 1, measured response.

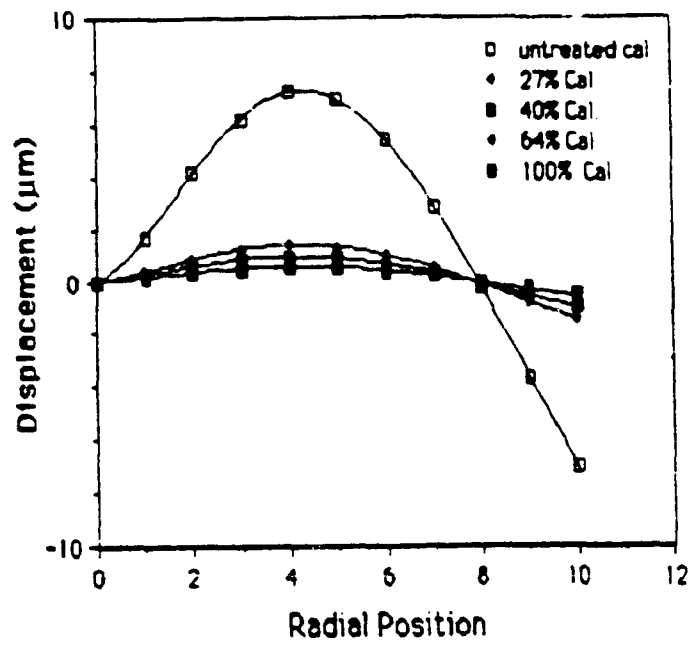


Fig. 10 Mode 2, calculated response.

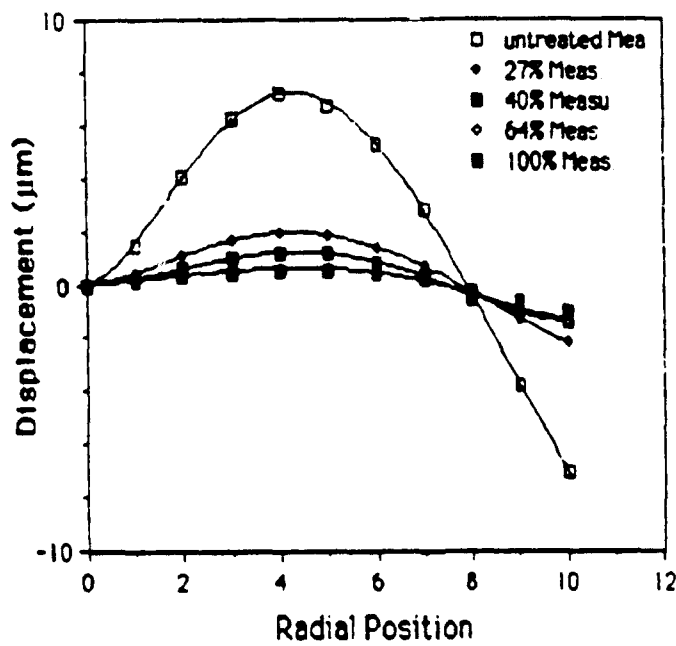


Fig. 11 Mode 2, measured response.

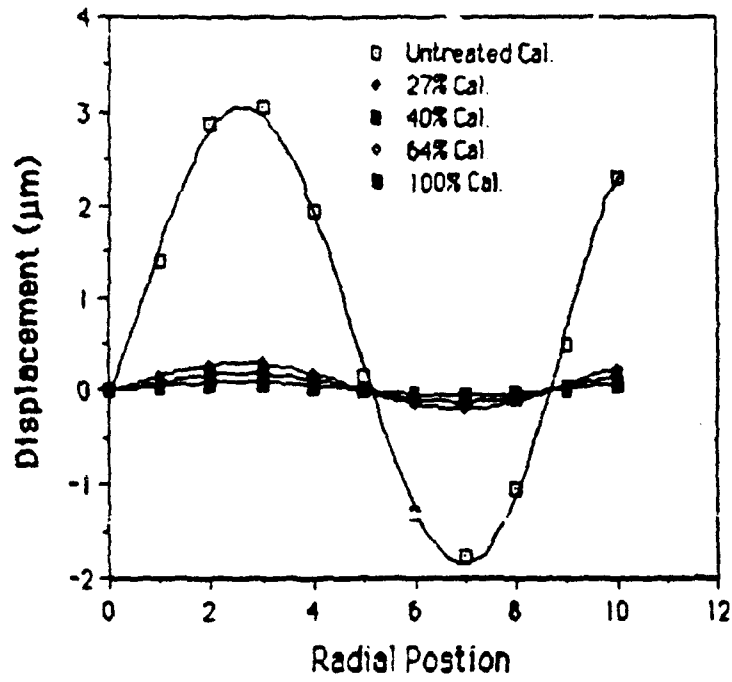


Fig. 12 Mode 3, calculated response.

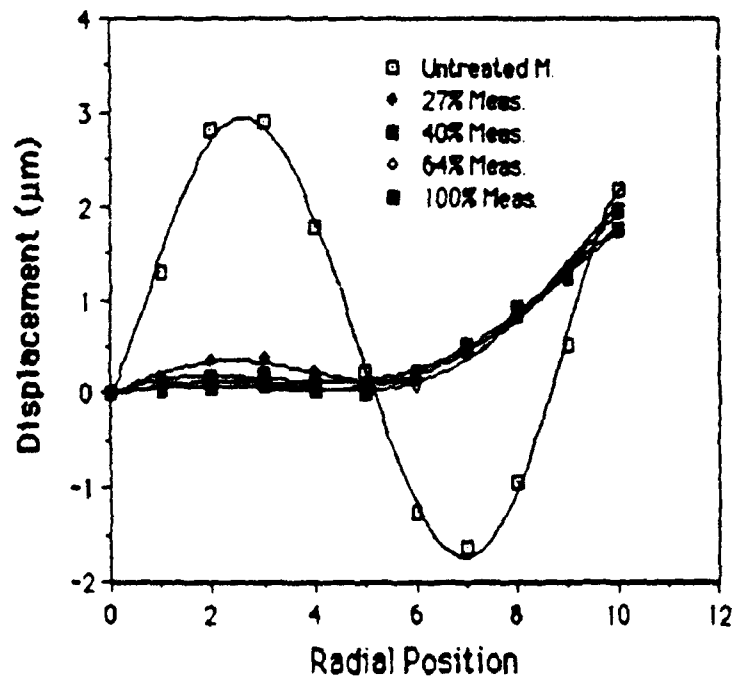


Fig. 13 Mode 3, measured response.

References

1. Mezache, M., "The Dynamics of Circular Plates with Patch Damping: A Numerical and Experimental Study", Ph.D. Dissertation, University of Houston, Texas, U.S.A., Aug. 1988.
2. Ozguven, H.N., "An investigation into the mathematical modeling of damped mechanical structures", Ph.D. Dissertation, UMIST, Manchester, U.K., Aug. 1978.
3. Bert, C.W., "Material damping an introductory review of mathematical models, measures and experimental techniques". J. of Sound and Vibration, 29(2), 129-153, 1973.
4. Cremer, L, M. Heckl, M, and E.E. Ungar; "Structure-Borne Sound", Springer-Verlag, New York, N.Y., 1973.
5. Ditaranto, R.A., and J.R. McGraw, Jr., "Vibratory bending of damped laminated plates", ASME J. Eng. Ind., Nov. 1969.
6. Oberst, H., Acustica 6, Akus. Beih. No. 1, 144-153 (1956).

Acknowledgment

The authors would like to express their gratitude to Mr. Frank Kirschner of the Sound Coat Company for supplying various damping material samples.

DEVELOPMENT OF THE PACOSS D-STRUT™

David C. Cunningham¹
Honeywell Inc., Satellite Systems Operation

ABSTRACT

This paper presents the design optimization procedure that was used to size the D-Struts™ used on the Passive/Active Control of Space Structures (PACOSS) program. While this design uses a diaphragm for the pumping member of the damper, the method can be adapted for other approaches. Fourteen D-Struts are fabricated and extensively characterized using the method of complex mechanical impedance. Performance agrees well with predictions, except that the peak phase lead is low. Additional compliance, which is responsible for this loss in performance, is primarily due to the diaphragm flexing at its inner and outer edges. This paper suggests solutions to improve the diaphragm clamping as well as alternatives to using a diaphragm.

¹Senior Staff Engineer, Honeywell Inc., Satellite Systems Operation,
P.O. Box 52199, Phoenix, AZ 85072, (602) 561-3211

INTRODUCTION

The viscously damped strut, or D-Strut™, was invented by L. Porter Davis and Dr. James F. Wilson to provide damping augmentation in a truss-type structure. The D-Strut consists of two concentric tubes, rigidly fastened together at one end, and connected through a viscous damper at the other. D-Struts can be used selectively in a truss-type structure to provide high damping of specific modes by placing them at locations of high modal strain energy. See the paper "Design, Analysis, and Testing of the PACOSS D-Strut Truss" by D. Morgenthaler in these proceedings for a discussion of this methodology.

THREE PARAMETER MODEL

The simplest dynamic model of the element is shown in Figure 1 and consists of three parameters: a stiffness representing the outer tube, a second stiffness representing the inner tube, and a viscous damper in series with the inner tube stiffness.

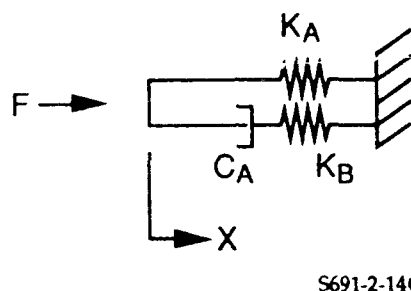


Figure 1. D-Strut Simplified Model

The ratio of force to deflection at one end, with the opposite end fixed, is the mechanical impedance, and it is given by:

$$Z3(s) = KA(1+s/w1)/(1+s/w2) \quad (1)$$

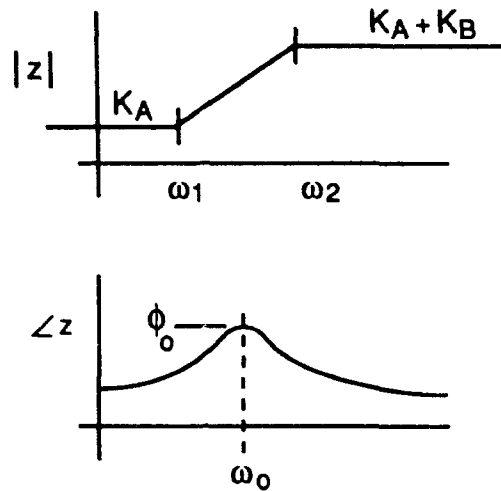
where,

$$\omega_1 = KA KB / (KA + KB) CA \quad (2)$$

$$\omega_2 = KB / CA \quad (3)$$

The magnitude of $Z3$ is plotted against radian frequency in Figure 2. At frequencies below ω_1 , the D-Strut acts like a "soft" spring, while at frequencies above ω_2 , the D-Strut acts like a "stiff" spring. The phase shift follows a bell-shaped curve between ω_1 and ω_2 . The maximum phase lead occurs at the geometric mean frequency:

$$\omega_0 = (\omega_1 \omega_2)^{1/2} \quad (4)$$



S691-2-1*

Figure 2. Mechanical Impedance

Letting α^2 denote the lead/lag separation ratio,

$$\alpha = (\omega_2/\omega_1)^{1/2} \quad (5)$$

the complex impedance at ω_0 is:

$$Z_3(j\omega_0) = K_A[2 + j(\alpha - \alpha^{-1})]/(1 + \alpha^2) \quad (6)$$

The maximum phase lead is:

$$\phi(\omega_0) = \tan^{-1}[(\alpha - \alpha^{-1})/2] \quad (7)$$

When the D-Strut is used in a structure, damping will be proportional to the phase lead at any frequency. Maximum damping then occurs when the frequency of maximum phase lead is made to coincide with the resonant frequency to be damped. For example, if the D-Strut supports a simple mass, M , the damping ratio will be equal to:

$$\zeta = (\alpha - 1)/2 \quad (8)$$

provided that the D-Strut is optimally tuned to the resonant frequency. This is accomplished by selecting the damping constant, C_A , such that:

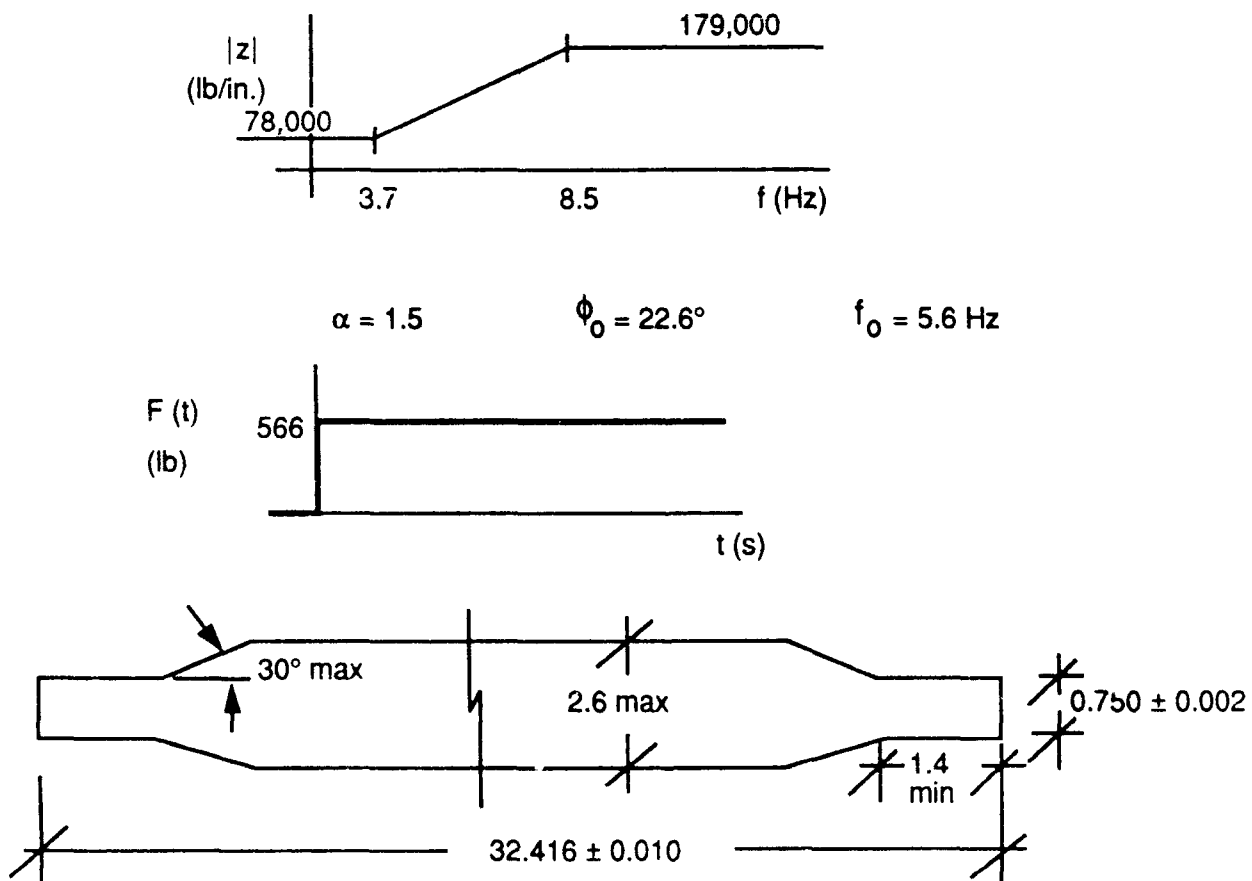
$$\omega_0 = (\alpha K_A/M)^{1/2} \quad (9)$$

PACOSS REQUIREMENTS

For the PACOSS program, D-Strut requirements were defined by the contractor, Martin Marietta, to provide damping of the first two structural frequencies when D-Struts were used as the longerons in the lower 3 bays of an 8-bay truss structure. Figure 3 summarizes these requirements. The static stiffness is 78,000 lb/in., and the dynamic stiffness ($K_A + K_B$) is 179,000 lb/in. Maximum phase lead is 22.6 degrees and occurs at a frequency of 5.6 Hz; this corresponds to a 1.5 separation ratio, α .

The structural design of the D-Strut is based on accommodating a step function of force equal to 566 lb. (This corresponds to the longeron force developed by a 100-lb lateral load at the tip of the truss.)

Finally, the D-Strut is to meet the interface and outline dimensions shown in Figure 3. The maximum diameter indicated is to be minimized.



S691-2-2

Figure 3. PACOSS D-Strut Design Requirements

DESIGN CONFIGURATION

Figure 4 is a conceptual view of the D-Strut showing the selected dimensions that provide the required performance. In this implementation, the viscous damper consists of a circular diaphragm connecting the inner and outer tubes. Viscous fluid is sheared in the orifice of length, L , and diameter, d , when the fluid is pumped by relative motion of the inner and outer tubes. The spring shown on the left provides a preload in the fluid contained by the bellows such that damping will occur in both forward and reverse directions.

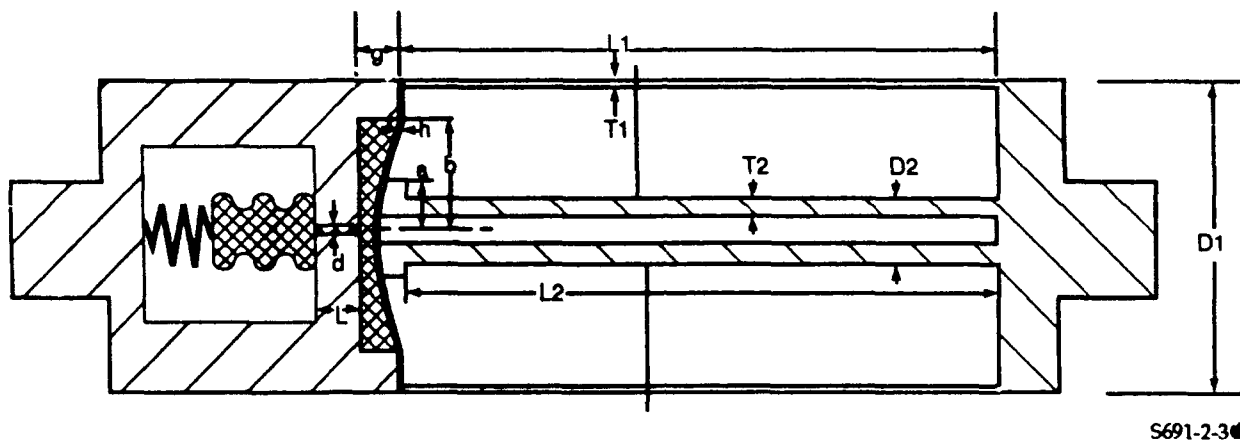


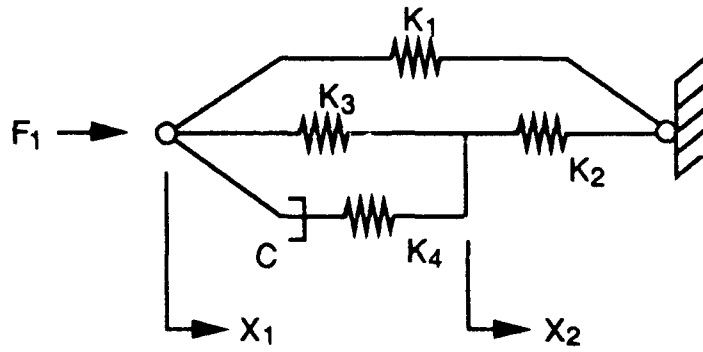
Figure 4. Conceptual D-Strut Design Dimensions

FIVE-PARAMETER MODEL

Analytical models were developed for the stiffness, damping, and stress of each of the components shown in Figure 4. In the case of the tubes, the stiffnesses K_1 and K_2 are simply A_1E_1/L_1 and A_2E_2/L_2 for the respective members. For the diaphragm, however, the static stiffness (K_3) is a complicated function of the dimensions a , b , and h and the diaphragm modulus of elasticity, E_d . Damping (C) is calculated from the fluid viscosity, μ , and orifice dimensions, d and L . An additional stiffness (K_4) is calculated for the diaphragm/fluid cavity to account for the compressibility of the fluid and the finite volumetric stiffness of the diaphragm. This stiffness involves parameters a , b , h , g , the diaphragm modulus of elasticity, E_d , and the fluid bulk modulus, K_f .

A complete dynamic model of this system is indicated in Figure 5. In this model, there are now five parameters: K_1 through K_4 and C . The mechanical impedance of the complete five-parameter model is:

$$Z_5(s) = \frac{F}{X_1} = \frac{(K_1K_2 + K_1K_3 + K_2K_3)K_4 + (K_2K_4 + K_1K_2 + K_1K_3 + K_1K_4 + K_2K_3)Cs}{(K_2 + K_3)K_4 + (K_2 + K_3 + K_4)Cs} \quad (10)$$



S691-2-4

Figure 5. D-Strut Detailed Model

This transfer function is of the form:

$$Z5(s) = K_{EQ}(1+s/\omega_Z)/(1+s/\omega_P) \quad (11)$$

where, $\omega_Z = (K_1K_2+K_1K_3+K_2K_3)K_4/(K_2K_4+K_1K_2+K_1K_3+K_1K_4+K_2K_3)C$ (12)

$$\omega_r = (K_2+K_3)K_4/(K_2+K_3+K_4)C \quad (13)$$

$$K_{EQ} = (K_1K_2+K_1K_3+K_2K_3)/(K_2+K_3) \quad (14)$$

EQUIVALENCE OF THREE- AND FIVE-PARAMETER MODELS

Typically, the stiffness due to fluid compressibility and damping chamber expansion, K_4 , is large, and the stiffness due to diaphragm flexure, K_3 , is small compared to K_1 and K_2 . If $K_4 = \infty$ and $K_3 = 0$ are substituted into (10) through (14), these equations reduce to (1) through (3), with $K_A = K_1$, $K_B = K_2$ and $C = C_A$. However, it is also possible to establish an equivalence between the three-parameter and five-parameter mechanical impedance models with finite, non-zero values for K_3 and K_4 .

Equating the static stiffnesses:

$$K_A = (K_1K_2+K_1K_3+K_2K_3)/(K_2+K_3) \quad (15)$$

Equating the zero and pole frequencies:

$$K_A K_B / (K_A + K_B) C_A = (K_1K_2+K_1K_3+K_2K_3)K_4 / (K_2K_4+K_1K_2+K_1K_3+K_1K_4+K_2K_3)C \quad (16)$$

$$K_B / C_A = (K_2+K_3)K_4 / (K_2+K_3+K_4)C \quad (17)$$

Equations (16) and (17) can be solved simultaneously for the two unknowns K_B and C_A :

$$K_B = K_2^2 K_4 / [(K_2 + K_3 + K_4)(K_2 + K_3)] \quad (18)$$

$$C_A = [K_2 / (K_2 + K_3)]^2 C \quad (19)$$

This equivalence is significant because it allows the three-parameter model to describe the D-Strut dynamics just as accurately as the five-parameter model.

D-STRUT PARAMETER SYNTHESIS

In the above section, it was shown that an equivalent three-parameter model could be used to represent the dynamics of a five-parameter D-Strut. In the detailed design of a D-Strut, however, it is necessary to utilize the five-parameter model, because it is these parameters that can be related to specific physical quantities (tube stiffnesses, diaphragm stiffnesses, etc). The relationship between the three-parameter and five-parameter models is not unique, and this fact may be used to develop a D-Strut optimized for minimum stress or weight without affecting its performance (i.e., its mechanical impedance).

To determine allowable values of the five-parameter D-Strut from the three-parameter description of the mechanical impedance, equations (15), (16), and (17) are solved with two additional constraint equations:

$$N = K_4 / K_3 \quad (20)$$

$$M = K_2 / K_1 \quad (21)$$

In addition to providing a closed solution, these two constraints make intuitive sense. M is the ratio of inner-to-outer-tube axial stiffness, and should generally be in the range $1 \leq M \leq 100$. N is the ratio of series-to-shunt stiffness of the diaphragm/fluid damper. Typically, one would expect N to also lie in the range $1 \leq N \leq 100$. As will be evident, the actual range of M and N to meet a specific mechanical impedance will be less.

The solution of the five equations noted above for the five unknowns is tedious, but there is a closed-form solution. In fact, there are two solutions, both of which are valid:

Letting $a = N(1+M) \quad (22)$

$$b = K_A [\alpha^2 (M-N) - (N+M+NM)] \quad (23)$$

$$c = \alpha^2 K_A^2 N \quad (24)$$

$$K_1 = [-b \pm (b^2 - 4ac)^{1/2}] / 2a \quad (25)$$

$$K_2 = MK_1 \quad (26)$$

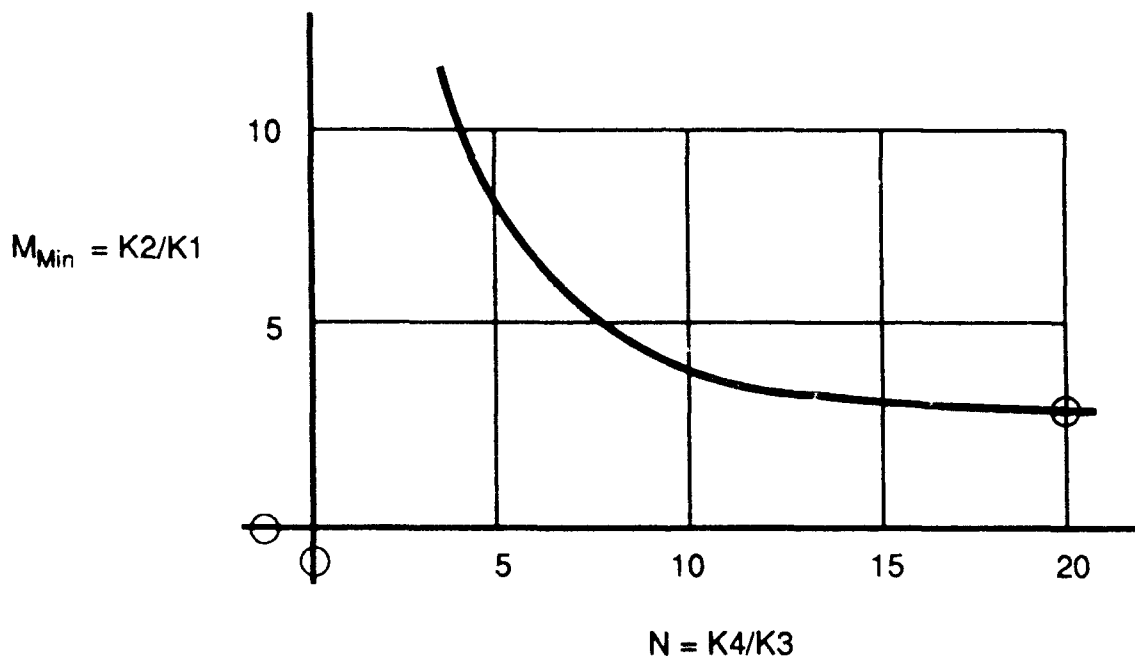
$$K_3 = [K_2(K_A - K_1)] / [K_2 - (K_A - K_1)] \quad (27)$$

$$K_4 = NK_3 \quad (28)$$

$$C = NK_3(K_2 + K_3) / [\omega_2(K_2 + K_3(C + N))] \quad (29)$$

For specific values of K_A , K_B , C_A , N , and M the above equations may produce complex or negative values for K_1 , K_2 , etc; however, where a positive real solution exists, two positive real solutions exist.

In order to minimize the D-Strut weight, M should be made as small as possible. There is, however, a minimum value of M once N is selected. Figure 6 illustrates this relationship for the PACOSS D-Strut case. Clearly, N should be made as high as possible, consistent with practical design and stress considerations. The point circled in Figure 6 shows the value for M and N ultimately selected for the PACOSS design.



S691-2-5

Figure 6. Minimum K_2/K_1 Versus K_4/K_3

D-STRUT FORCES

When sizing the D-Strut mechanical components, the applied forces are required in order to calculate static and dynamic loads, fluid pressures, stresses, etc. Let F_T denote the externally applied axial force. This force divides (dynamically) between the inner and outer tubes. Let F_I denote the force in the inner tube. Referring to Figure 5, $F_I = K_2 X_2$; this leads to the following transfer function:

$$F_I/F_T(s) = K_2 K_3 (1+s/\omega_3) / [(K_2+K_3)K_A(1+s/\omega_1)] \quad (30)$$

where,
$$\omega_3 = K_3 K_4 / [(K_3+K_4)C] \quad (31)$$

The force in the inner tube depends not only on the ratio of stiffnesses, but on the frequency content of the applied force. Two cases are of interest:

- (1) F_T is a sinusoid of magnitude F_T and frequency ω_0 . In this case the magnitude of F_I is obtained by substituting $j\omega_0$ for s in equation (30).
- (2) F_T is a step function of magnitude F_T . The force in the inner tube is then an exponentially decayed step, which has an initial value F_D and a final value F_S (referred to as the dynamic and static forces, respectively). F_S is obtained by setting s to zero in (30), while F_D is obtained by letting s approach infinity.

$$F_S = F_T K_2 K_3 / [K_A (K_2 + K_3)] \quad (32)$$

$$F_D = F_T K_2 K_3 \omega_1 / [K_A (K_2 + K_3) \omega_3] \quad (33)$$

DESIGN OPTIMIZATION PROCEDURE

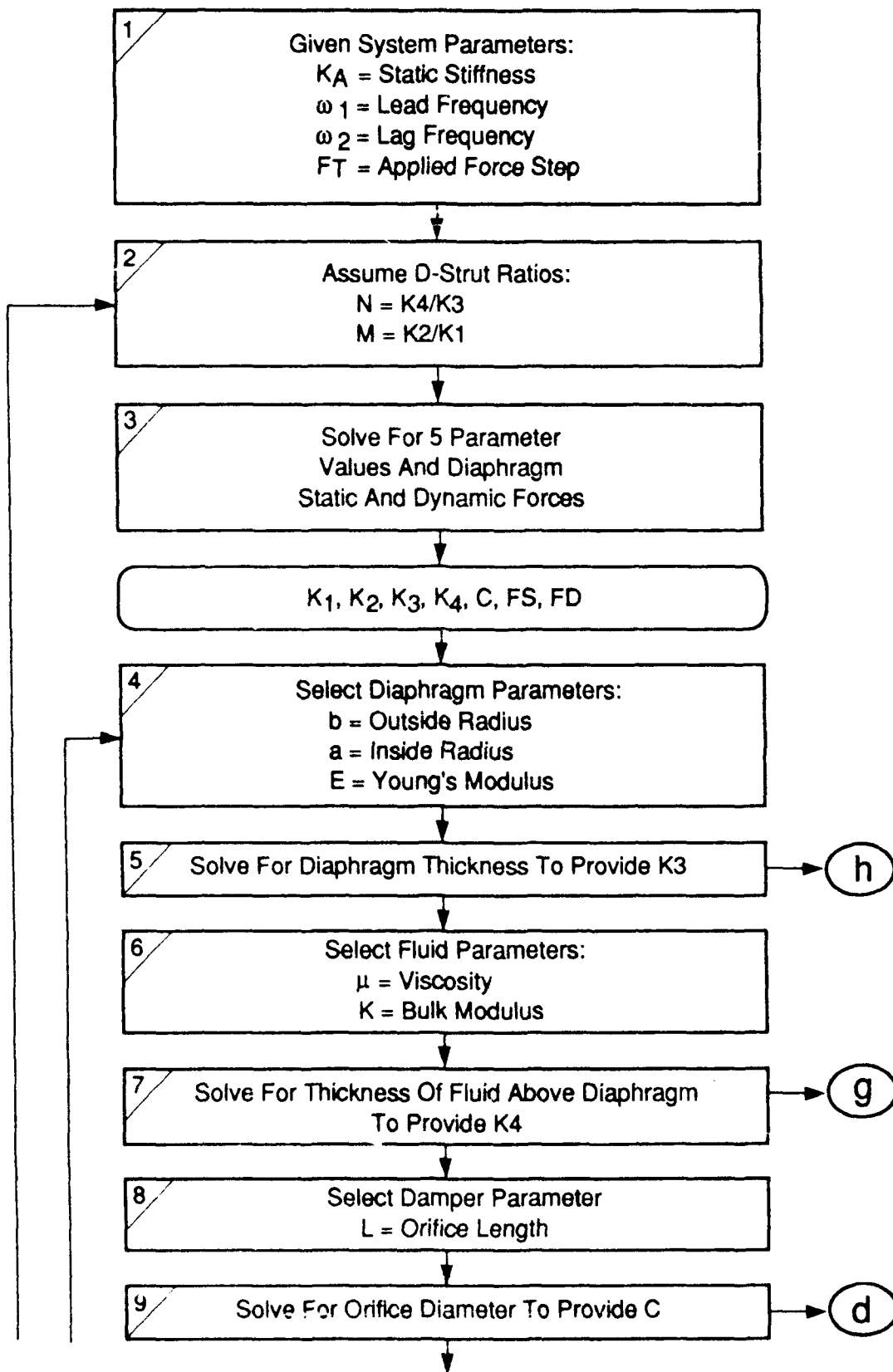
The flow chart shown in Figure 7 summarizes the design procedure.

Steps 1 through 3 determine a set of the five parameter model values meeting the specified requirements. The selection of M and N is arbitrary, but if the limitation shown in Figure 6 is violated, the computed stiffnesses will be imaginary.

Steps 4 through 13 are used to size a diaphragm and damper meeting the required K_3 , K_4 , and C . This is done iteratively for various diaphragm aspect ratios (the ratio of diaphragm outside diameter to inside diameter, η), and the peak stresses and deflections are calculated under the two conditions of peak static and dynamic loads. An optimum design is then selected to provide the minimum peak stress and a peak diaphragm deflection less than the fluid gap.

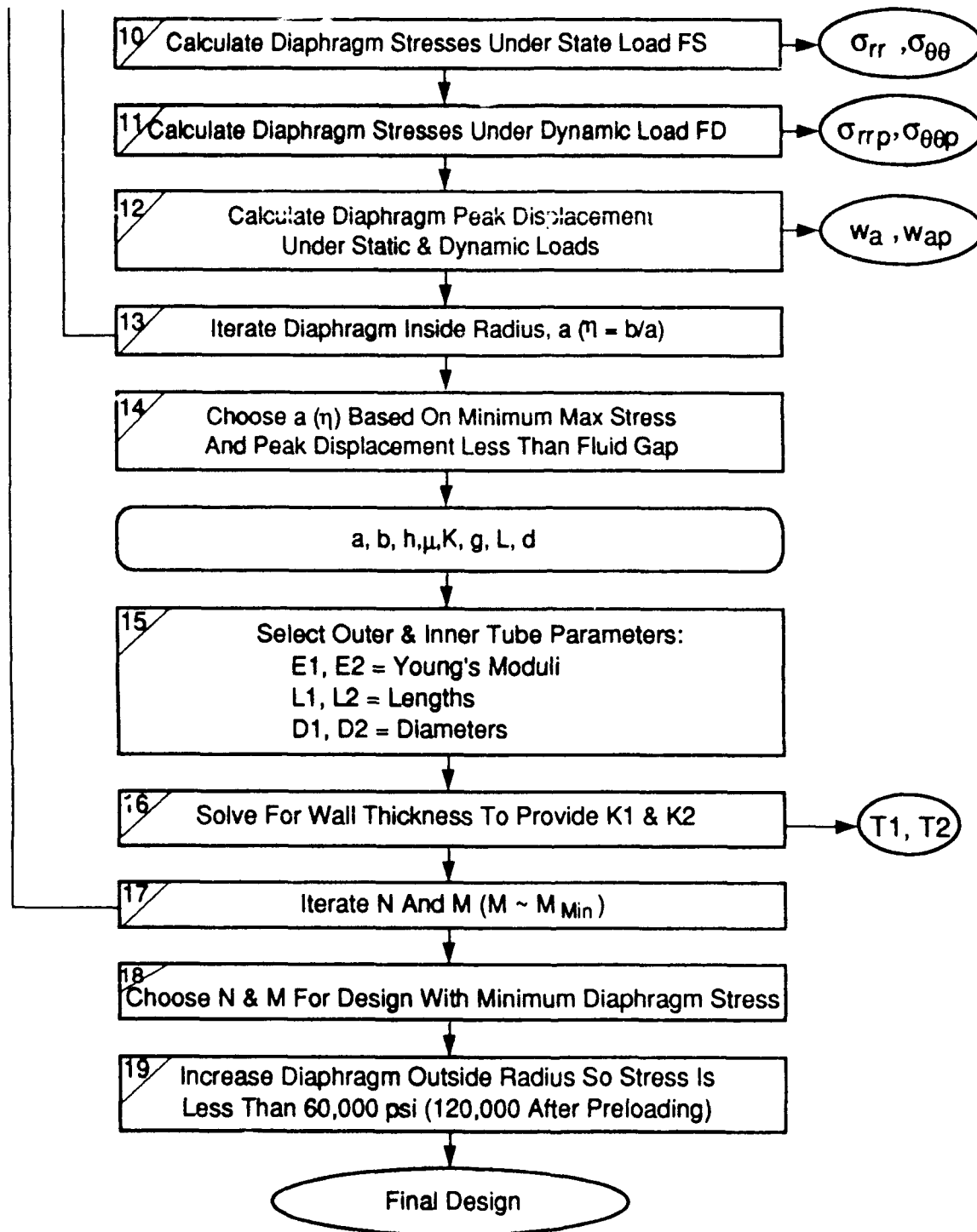
To complete the design, Steps 15 through 17 are used to size the tubing thickness to provide the required K_1 and K_2 . Each design corresponds to one row in Table 1. Steps 4 through 17 must be performed twice for each set of five parameter requirements determined in Steps 1 through 3 because there are two valid solutions for each assumed M and N . In Table 1, the two solutions are distinguished by the notation '+' or '-' under the column "Sln."

In Step 18, the entire process (Steps 1 through 17) is repeated iteratively for alternative values of M and N . In Table 1, the best case (H) is underlined. Most of the cases run assumed the use of titanium for the diaphragm material. Beryllium copper was also evaluated, but found to produce a lower fatigue stress margin of safety.



S691-2-6(1)Ⓢ

Figure 7. Design Optimization Procedure (Sheet 1)



S691-2-6(2)

Figure 7. Design Optimization Procedure (Sheet 2)

The stresses shown in Table 1 do not include the effect of fluid preload. To prevent cavitation when the D-Strut is used in tension rather than compression, the preload is typically selected to equal the peak pressure in the fluid. This has the effect of doubling the stresses in the diaphragm. Therefore, the minimum stress design will be $2 \times 77,000 = 154,000$ psi, which exceeds the 120,000-psi limit for titanium.

Table 1. Optimum Diaphragms for 0.75-inch Outside Radius

N	M	Slr	Mtl	Case	OD/ID	Stress	h	g	wa
297	1.543	—	Ti	G	1.2	117	0.005	0.043	0.007
40	8	—	Ti	X	1.4	136	0.007	0.607	0.007
40	8	·	Ti	Y	1.6	116	0.030	0.010	0.005
40	4	—	Ti	V	1.4	116	0.008	0.471	0.007
40	4	·	Ti	W	1.6	112	0.026	0.016	0.005
20	32	—	Ti	R	1.4	112	0.009	0.851	0.007
20	32	·	Ti	S	2.0	100	0.046	0.010	0.004
20	8	—	Ti	T	1.4	101	0.009	0.720	0.007
20	8	·	Ti	U	2.0	99	0.041	0.014	0.005
20	4	—	Ti	P	1.6	86	0.014	0.357	0.007
20	4	·	Ti	Q	2.2	91	0.038	0.012	0.006
<u>20</u>	<u>3</u>	<u>—</u>	<u>Ti</u>	<u>H</u>	<u>2.0</u>	<u>77</u>	<u>0.021</u>	<u>0.098</u>	<u>0.007</u>
10	8	—	Ti	C	1.8	83	0.019	0.420	0.007
10	8	·	Ti	D	3.2	93	0.056	0.010	0.005
10	4	—	Ti	A	3.0	81	0.038	0.042	0.006
10	4	·	Ti	B	3.0	85	0.041	0.033	0.006
20	4	—	BeCu	P1	1.4	94	0.010	0.530	0.007
20	3	—	BeCu	F1	2.0	86	0.020	0.098	0.007
10	8	—	BeCu	C1	1.8	91	0.018	0.420	0.007
10	4	—	BeCu	A1	3.0	91	0.036	0.042	0.006
7	6	—	BeCu	E1	3.0	93	0.035	0.109	0.007

S691-2-7

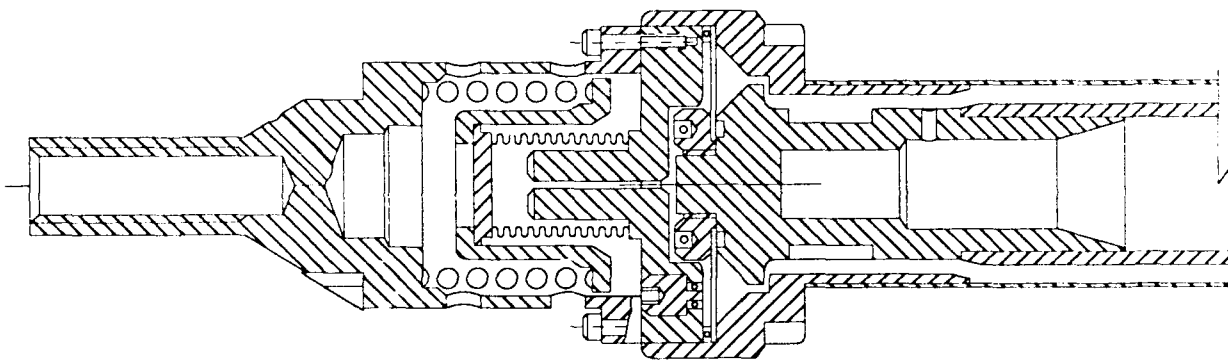
All the cases shown in Table 1 assume a diaphragm outside diameter (OD) of 1.5 inches (because our initial goal was to design a D-Strut having approximately the same OD as the undamped PACOSS struts.) In Table 2, the results of increasing the diaphragm OD are shown. These cases all assume the same optimum ratios for M , N , and η . The final entry shown (Case H4) provides an adequate fatigue stress margin and has a diaphragm OD of 2.0 inches.

Figure 8 is a cross section of the final design, and Figure 9 is a photograph of the prototype.

Table 2. Optimum Diaphragms for N=20, M=3, Sln=-

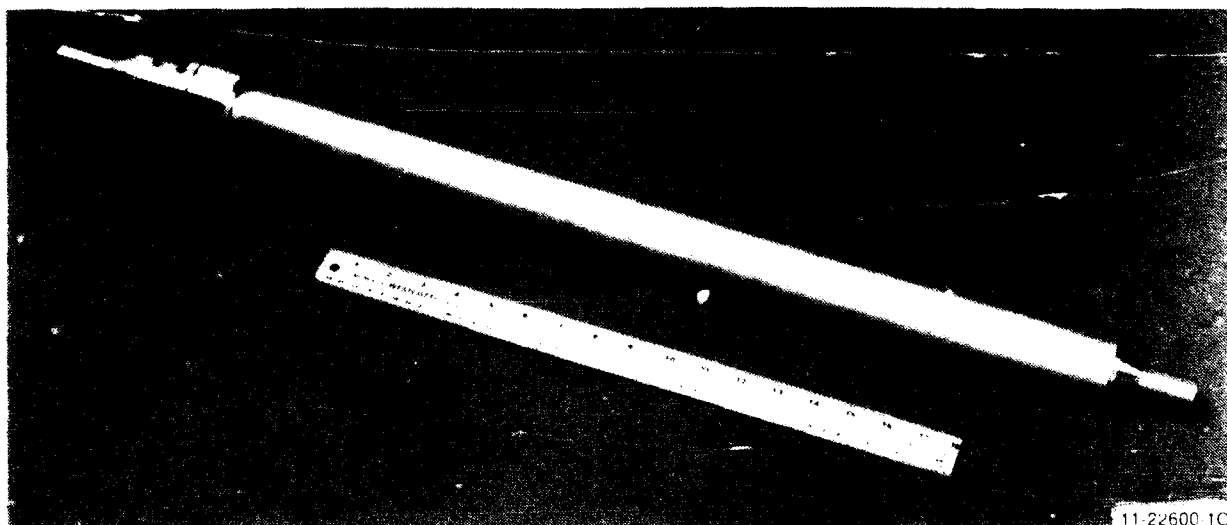
b	Mtl	Case	OD/ID	Stress	h	g	wa	p
0.625	BeCu	F2	2	110	0.018	0.068	0.007	493
0.750	BeCu	F1	2	86	0.020	0.098	0.007	343
0.875	BeCu	F3	2	70	0.022	0.134	0.007	252
1.000	BeCu	F4	2	59	0.025	0.174	0.007	193
1.250	BeCu	F5	2	44	0.028	0.273	0.007	123
1.500	BeCu	F6	2	34	0.032	0.392	0.007	86
0.625	Ti	H2	2	98	0.019	0.068	0.007	493
0.750	Ti	H1	2	77	0.021	0.098	0.007	343
0.875	Ti	H3	2	63	0.024	0.134	0.007	252
1.000	Ti	H4	2	50	0.026	0.174	0.007	193

S691-2-8



S691-2-9

Figure 8. Final Layout of PACOSS D-Strut



11-22600 1C

Figure 9. PACOSS D-Strut

D-STRUT CHARACTERIZATION

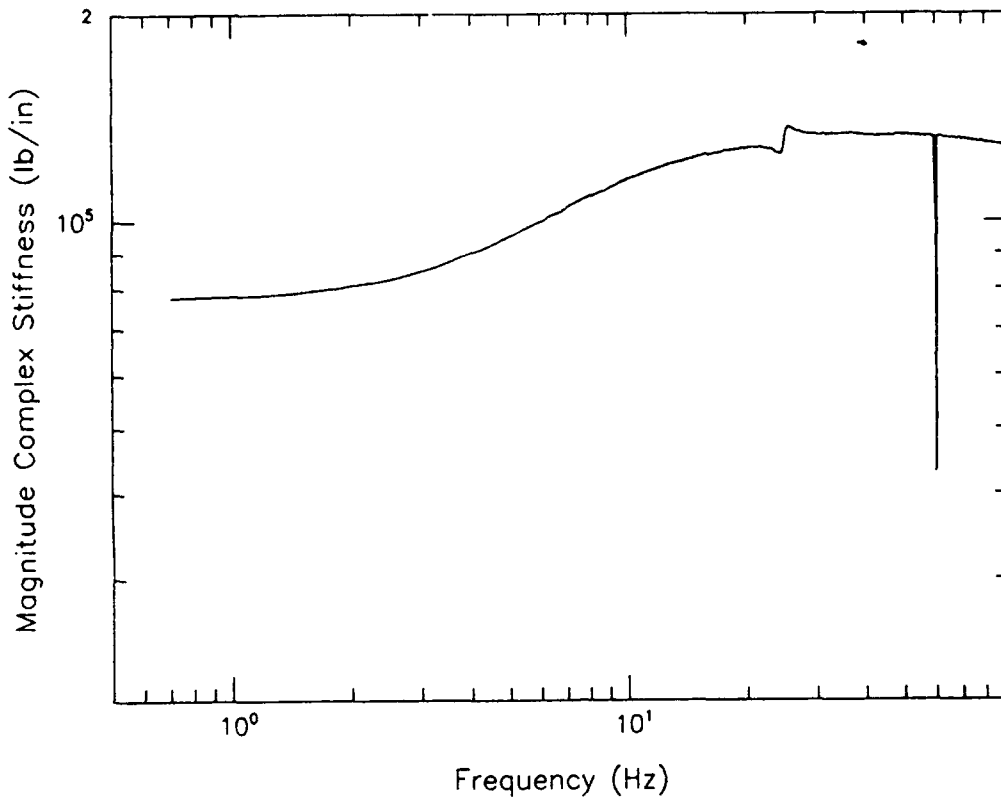
Testing of the D-Struts was conducted at CSA Engineering in Palo Alto, California, between January and April 1990. The mechanical impedance was measured using a shaker driving the D-Strut under test through a load cell with the other end of the D-Strut rigidly grounded. The differential displacement across the D-Strut was measured using a pair of Kaman eddy current proximeters. Calibration was verified with a "dummy" tube consisting of an outer tube (1.5-in. OD x 0.035-in. aluminum wall) mounted between two end fittings, which provided the same overall length and mechanical interface as the deliverable units. Both static and dynamic tests verified that the stiffness was equal to that calculated for the tube alone, and that the phase angle was only a few tenths of a degree.

In the succeeding tests, two basic procedures evolved. Static measurements were made by commanding the shaker with a 20-second period triangle waveform corresponding to ± 500 lb force peak amplitude. The displacement was plotted by the Zonic analyzer against force so that the stiffness (slope), linearity, and hysteresis were readily apparent. Dynamic impedance was measured by applying a random noise having a flat Power Spectral Density (PSD) over a selected bandwidth. The input was controlled by a GenRad Servo Controller that monitored the force transducer output. Peak force and bandwidth can be independently controlled and a constant compressive or tensile force can be superimposed by the shaker amplifier electronics. A crest factor (peak-to-rms ratio) of 3.6 was assumed for adjusting the output of the controller. For dynamic impedance measurement, the Zonic analyzer computes the complex Fast Fourier Transfer (FFT) of the force and differential displacement, then displays the amplitude and phase angle of their ratio. Further details of the testing procedure are given in the paper, "Testing of a Viscous Damped Isolator," by B. Allen, also in these proceedings.

Figures 10 and 11 are plots of the magnitude and phase of the complex mechanical impedance of a typical D-Strut. Analysis of the test data indicates that the peak phase lead is about 16.5 degrees, which is less than the 22.6 degrees desired. Considerable effort was spent in an attempt to identify the source of the added compliance that caused this loss. The results of the development testing program showed that the added compliance was distributed between:

- Diaphragm edge clamping (both inner and outer edges)
- Low modulus in the inner tube aluminum
- Series compliance in the spring housing and end fittings
- Low shear modulus in the epoxy originally used

Alternative designs were also hypothesized, which would replace the diaphragm with (1) a piston, (2) an annular flexure, or (3) a bellows, which might provide a higher phase lead. Unfortunately, the schedule or funding did not permit our pursuing these approaches. These alternatives are discussed further in the paper "Design Trade Data on the Arch-Flexure D-Strut," by L. Porter Davis and Dr. Steve Ginter, also in these proceedings.

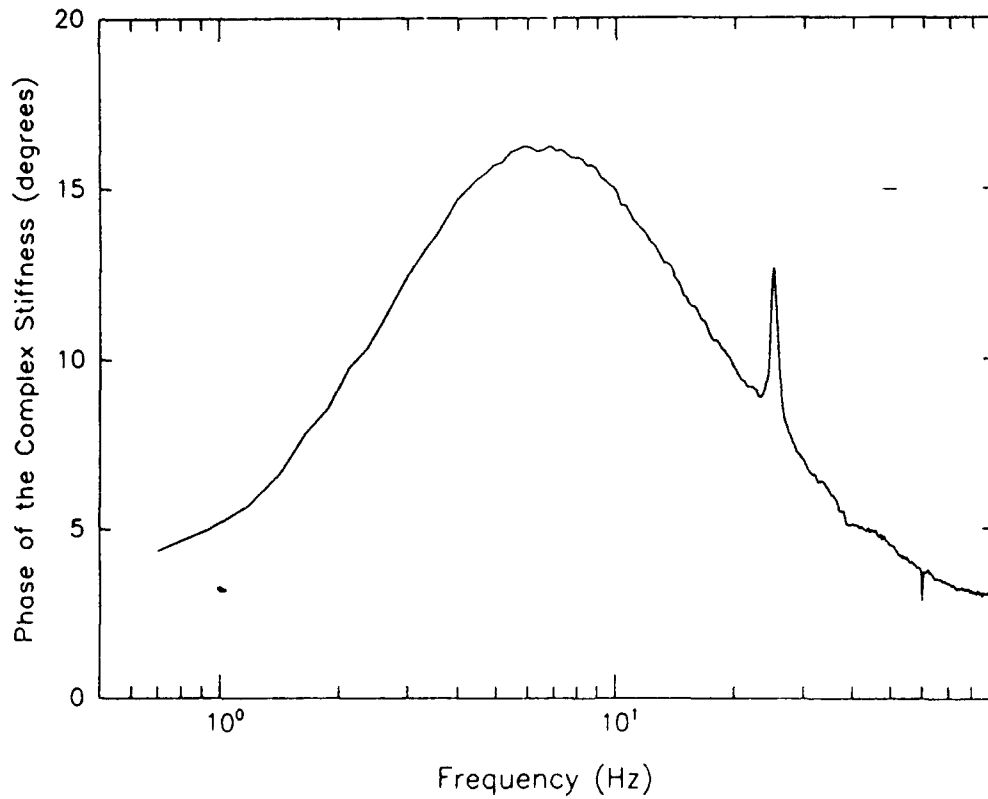


07:06:07
02-MAY-90

USER\$DISK: JE HOQUAL.GPH

S691-2-11

Figure 10. D-Strut 1 Mechanical Impedance - Magnitude



16:16:49
02-MAY-90

USER\$DISK: JE.FORTRAN DG HOQUAL1.GPH

S691-2-12

Figure 11. D-Strut 1 Mechanical Impedance - Phase

A total of 14 D-Struts were built, which incorporated improvements to the diaphragm edge clamping and tube bonding. Results of the characterization testing are listed in Table 3.

Table 3. Test Results

Serial No.	KSTATIC	Hysteresis (%)	ϕ_{PK}	f_0
1	75k	1	16.5	6.5
2	71k	1	13.5	5.0
3	76k	negligible	14.5	5.0
4	74k	1	14.5	4.5
5	74k	1	15.5	6.0
6	69k	1	12.0	6.5
7	74k	1	13.0	6.5
8	71k	1	16.0	5.1
9	77k	negligible	16.7	6.5
10	73k	1	15.7	5.8
11	73k	negligible	16.0	6.2
12	72k	1	15.5	6.5
13	70k	1	15.0	6.0
14	72k	1	15.5	6.5

S691-2-13

CONCLUSIONS

Analytical techniques were developed to optimize the design of a D-Strut that utilized a diaphragm to pump the damping fluid. The optimization minimized the outside diameter of the diaphragm (which determines the OD of the D-Strut). A prototype unit was built and tested, and 14 additional units were fabricated and characterized.

The results were qualitatively very close to those predicted, showing that the dynamic models used to analyze and design the D-Strut were functionally correct. However, the peak phase lead was less than that desired (16 to 18 degrees versus 22.6 degrees desired).

The most significant factor limiting the peak phase lead achievable is the difficulty of obtaining bending rigidity of the diaphragm edges. Some radial compliance must be accommodated to permit differential thermal expansion between the titanium diaphragm and the aluminum housing. An all-titanium machining might provide a better solution for the diaphragm design, but would be expensive to fabricate.

An alternative would be to replace the diaphragm with either a piston, an annular flexure, or a bellows.

Truss testing at Martin has now been completed, and the results indicate that the D-Struts, as delivered, demonstrate a very high damping of the lower frequency truss modes. The design optimizations and testing methodology presented in this paper should be of help in future D-Strut development.

DESIGN, ANALYSIS, AND TESTING OF THE PACOSS D-STRUT TRUSS

Daniel R. Morgenthaler *
Martin Marietta Astronautics Group
Denver, CO

ABSTRACT

Future space systems may be large, lightweight, and flexible. Such systems will often include trusswork due to the high specific strength and stiffness typical of trusses. Damping of these structures will minimize detrimental vibration, which otherwise may reduce system performance to unacceptable levels.

A damping device suitable for application to trusses, which is designated the D-Strut™, has been developed by Honeywell. This paper discusses the further development of the damping member, the derivation of analytic procedures required for efficient integration of these members into truss structures, and the results of testing of a structure which incorporates these damping members.

Following design, prototyping, fabrication, and impedance testing of D-Strut members, a truss structure which includes these members was assembled and subjected to modal testing. Comparisons of the finite element model of the truss with the experimental modal test data show excellent agreement for the first seven modes, and verify damping levels in the fundamental modes of nearly 10% critical.

The D-Struts were compared with viscoelastic extensional damping members designed to produce similar damping levels. These comparisons included weight, temperature stability, strength, etc. Results of the comparisons currently favor the viscoelastic members; however, advances in the design of the viscous device will allow the D-Strut to provide an efficient damping treatment for truss structures of the future.

* Mail Stop H4330
P. O. Box 179
Denver, CO 80201
(303)-971-9387

1.0 Introduction

A goal of the Passive and Active Control of Space Structures (PACOSS) Program is the development and verification of passive damping treatments for application to flexible space structures. An examination of the performance of the Honeywell viscous fluid damping struts (D-Struts) for use in truss structures was completed during the second phase of the PACOSS Program.

At the onset of the investigation, there were considered to be four potential advantages of the D-Strut over other types of damping treatments for truss structures, such as viscoelastic damping members. These potential benefits were reduced temperature dependency, decreased susceptibility to outgassing, higher static loading capability, and the potential for decreased weight as compared to viscoelastic dampers. The objectives of the research were to develop the analytic tools necessary to efficiently design and analyze truss structures including D-Struts, to design and build a structure consistent with goals for the test truss, and to confirm the performance of the members through unit testing and a modal test on the structure with the damping members installed.

To meet these objectives, a truss structure which contains the D-Strut members was designed, fabricated, and tested (Fig. 1). The truss structure was designed and fabricated by Martin Marietta, while the D-Strut members themselves were built by Honeywell. The structure consists of eight bays which are each 34-in. square, with damping members as the longerons for the lower three bays. During the design process, design techniques which allow for the efficient application of D-Strut damping treatments to structures was developed.

Following fabrication of the D-Struts, unit testing of the members, and their integration into the structure, a modal test was performed. The resulting modal parameters were compared with analytic predictions to determine model accuracy and D-Strut performance. Finally, the D-Strut damping members were compared with their viscoelastic counterparts for important properties. This paper discusses the design methodology and analysis techniques which were developed, the results of the D-Strut member design and fabrication, the structure modal test results, and the results of the damping member comparison.

2.0 The D-Strut Member and Viscous Fluid Damping Device

The D-Strut is comprised of a viscous fluid damping device, structural tubing, and end fittings. The tubing attaches to the joints of the structure and supplies the static stiffness of the element, while the damping element is used to attenuate vibration of the structure. A schematic of the damping device as used in the PACOSS D-Struts is provided as Figure 2.

The working elements of the damping device consist of a titanium diaphragm, a small orifice, and a bellows which contains a viscous silicone fluid. When a dynamic load is applied to the member, a portion of the load is transmitted through the inner tube, and a portion is transmitted through the outer tube. The force applied by the inner tube to the damping device bends the circular diaphragm which is connected to

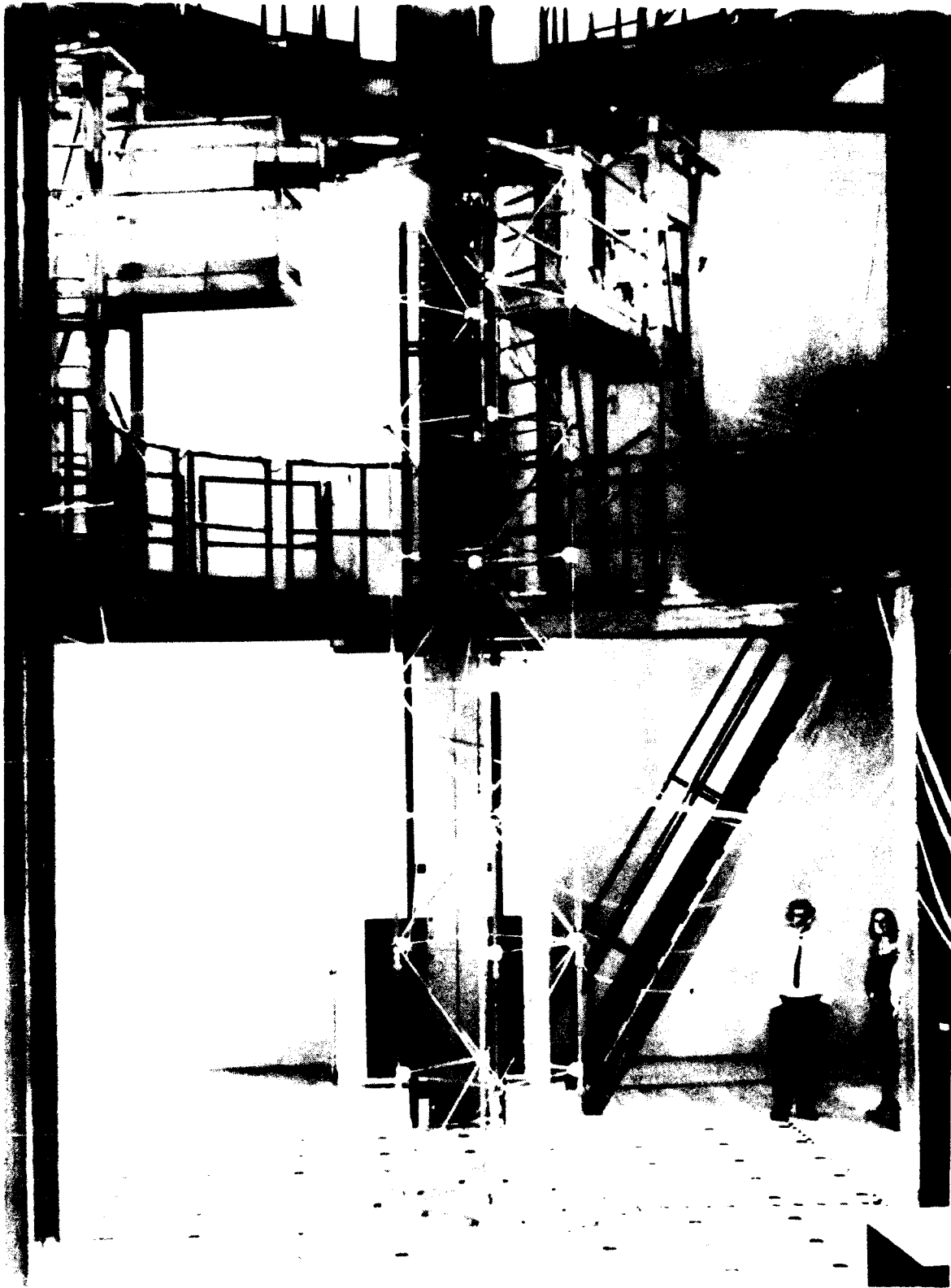


Figure 1 - The D-Strut Test Truss In the Modal Test Configuration

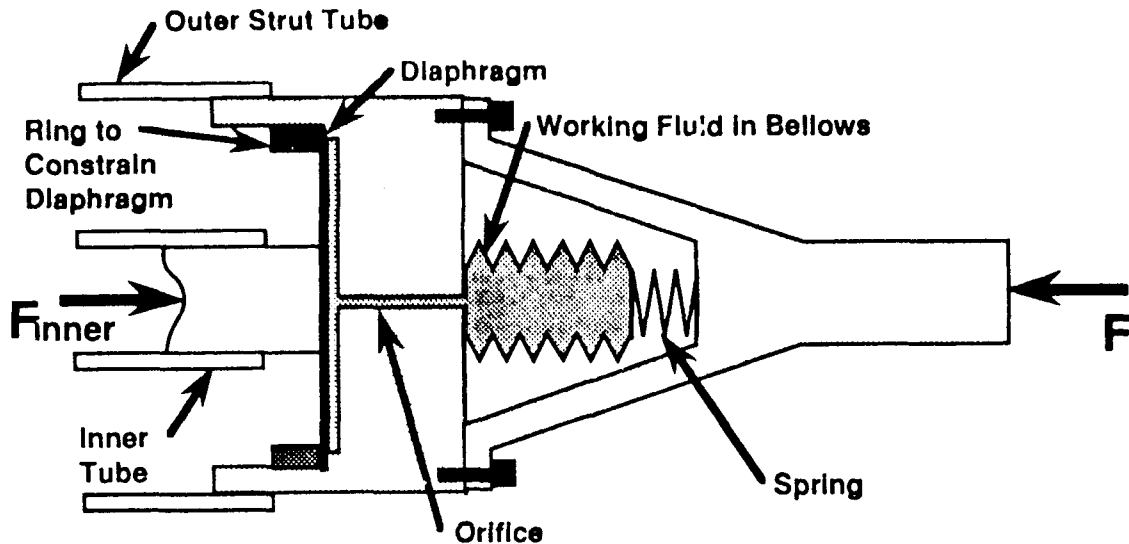


Figure 2 - Schematic of the Honeywell Viscous Fluid Damping Device

a fitting on the inner diameter, and is constrained to move with the damper housing on the outer diameter. The deformation of the diaphragm pressurizes the fluid behind it and forces the fluid through the orifice. The resistance of the fluid flow due to its viscosity creates a damping force which is applied to the structure at the joints. A spring is used to apply static pressure to the fluid to eliminate cavitation of the fluid for dynamic tension loads applied to the damping device. The spring and bellows also allow for expansion and contraction of the fluid with temperature.

Two D-Strut concepts were developed by Honeywell which have been designated the SD and the D1 strut. The SD strut incorporates two tubing members: an outer tube member which connects directly across the span element, and an inner tube which connects to the damping device. The D1 strut is similar. However, a single tube which connects to the end fitting on one side and to the damping device on the other is used. The potential application of both designs was examined during the PACOSS effort.

3.0 D-Strut Modeling Using the Spring / Dashpot Model and Impedance Methods

Design and analysis of truss structures which incorporate D-Struts necessitates models of the damping members. Two methods of modeling the D-Strut were investigated. These methods include modeling of the strut using a spring / dashpot network and modeling using impedance methods.

The D-Strut can be modeled using a series of springs and a dashpot [1], using a network which was previously formulated by Honeywell. The network model of the SD strut is included as Figure 3.

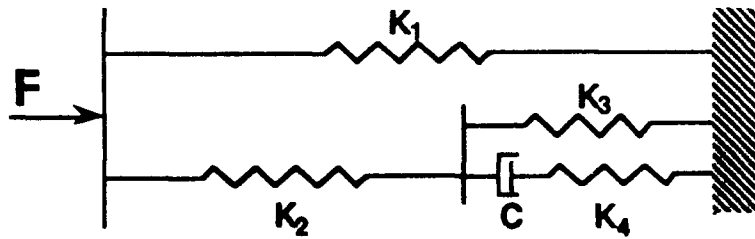


Figure 3 - Spring / Dashpot Model of the SD Strut

The correlation between hardware effects and network parameters is given in Table 1. The 5-parameter spring / dashpot model effectively simulates the dynamic response of the D-Strut, when appropriate values of the model elements are chosen. This analytic model can be directly incorporated into truss models and the matrix equations solved to provide the complex eigenvalues and eigenvectors of the damped structure. However, this method does not provide insight into the best selection of locations for the dampers or effective design of the damping members. Alternative modeling methods can be used to determine the effect of the strut on the dynamics of a structure, and to provide insight into the proper selection of the various strut parameters.

To efficiently model the D-Strut behavior, the impedance of the strut was developed. The impedance of the strut is a frequency-dependent complex number which provides the ratio of the applied force to the resulting displacement across the strut, as well as the phase relationship between them. The strut impedance can be determined by transforming a dynamic load and the resulting dynamic displacement across the member to the frequency domain using the Laplace transform:

$$X(s) = \mathcal{L}(x(t)) \quad F(s) = \mathcal{L}(f(t)) \quad (1)$$

where:

$x(t)$ = the dynamic displacement across the damper
 $f(t)$ = the dynamic force applied

The strut impedance then relates the frequency-dependent force and displacement. However, it is a function of the Laplace variable:

$$F(s) = Z(s) X(s) \quad (2)$$

where:

$Z(s)$ = member impedance function

The impedance can be written in many alternative forms which have utility in different applications. A representation of the impedance which is useful for the analysis of dynamic systems and for optimization of the D-Strut is the complex stiffness representation. The complex stiffness representation can be determined by evaluating the real part of the impedance, and defining the loss factor as the ratio of the imaginary part of the impedance to the real part of the impedance:

Table 1 - Hardware Effects Modeled by Various Springs

Model Parameter	Hardware Effect
K ₁	Outer Tube Axial Stiffness
K ₂	Inner Tube Axial Stiffness
K ₃	Diaphragm Bending Stiffness
K ₄	Fluid Compressibility and Chamber Compliance
C	Orifice Fluid Flow Restriction

$$K_{eq}(s) = \text{Real}(Z(s)) \quad \eta(s) = \text{Imag}(Z(s)) / \text{Real}(Z(s)) \quad (3)$$

When represented in this manner, the frequency-dependent impedance is identical to the "complex stiffness" which is typically used to model viscoelastic damping treatments. Impedance (complex stiffness) models of viscoelastic damping struts were previously used for the design and analysis of the PACOSS Dynamic Test Article (DTA) and were shown to provide a useful representation of the damping elements which allowed the determination of the dynamic properties of the damped structure [2].

To show how the impedance is determined for a simple spring / dashpot network, consider the network in Figure 4. The network consists of a spring which is in parallel with a spring and dashpot in series.

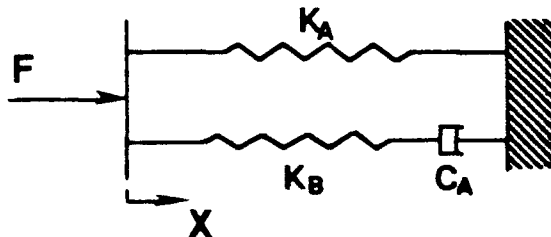


Figure 4 - Simple Spring / Dashpot Network

The impedance of any network can easily be determined using network simplification. The impedance of this network is:

$$Z(s) = K_A + \frac{C_A s K_B}{C_A s + K_B} \quad (4)$$

The strut impedance for sinusoidal inputs as a function of frequency is determined by evaluating along the imaginary axis in the Laplace domain (at $s = i\omega$):

$$K_{eq}(i\omega) = \text{Real}(Z(i\omega)) = \frac{-K_B^3}{C_A^2 \omega^2 + K_B^2} + K_A + K_B$$

$$\eta(i\omega) = \frac{\text{Imag}(Z(i\omega))}{\text{Real}(Z(i\omega))} = \frac{C_A K_B^2 \omega}{C_A^2 \omega^2 (K_A + K_B) + K_A K_B^2} \quad (5)$$

The complex stiffness representation can be plotted versus frequency to show the shape of the impedance function. Figures 5 and 6 provide representative impedance plots for the simple network. The values used to generate the impedance plots were 50,000 lb/in., 100,000 lb/in., and 2,000 lb-s/in. for K_A , K_B , and C_A , respectively. The equivalent stiffness asymptotically approaches the sum of K_A and K_B , while the loss factor displays a distinct peak. The low-frequency stiffness of the network is the stiffness of the shunt spring K_A .

A high loss factor is desirable to provide high damping ratios to the modes of flexible structures [3]. To determine the maximum loss factor of the spring / dashpot network and the frequency of the peak as a function of the network parameters, the derivative of the loss factor equation with respect to frequency is taken, and the frequency ω_{max} is determined:

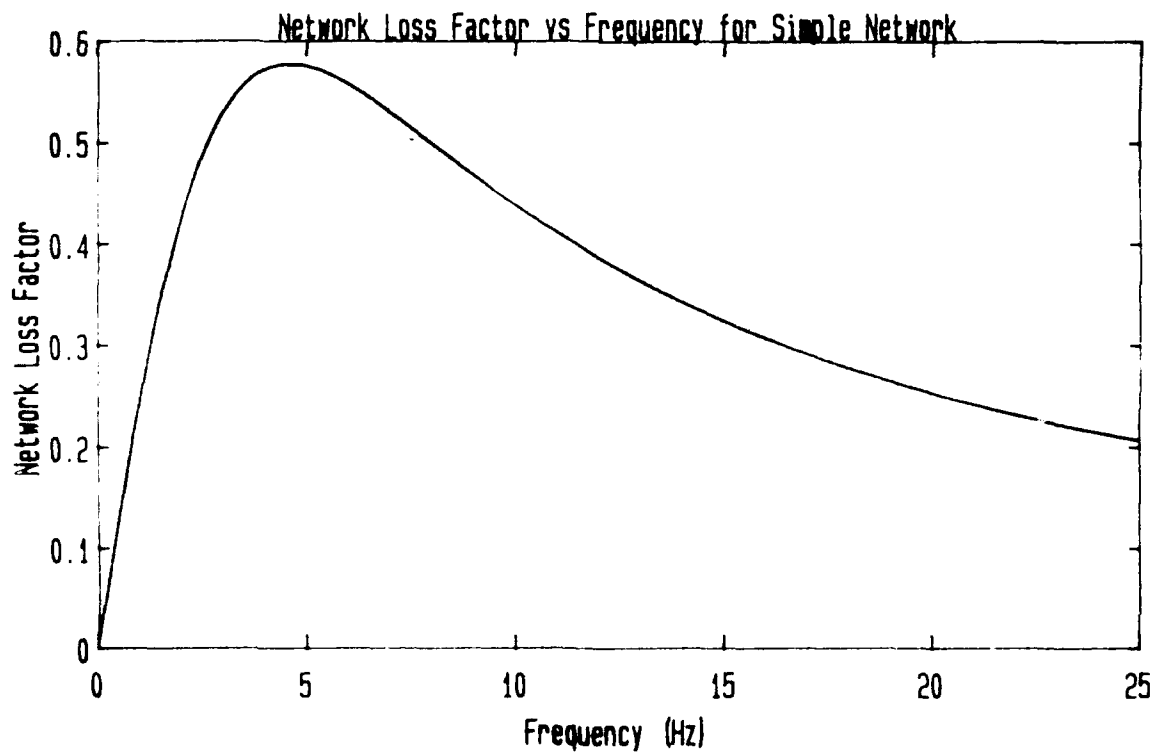
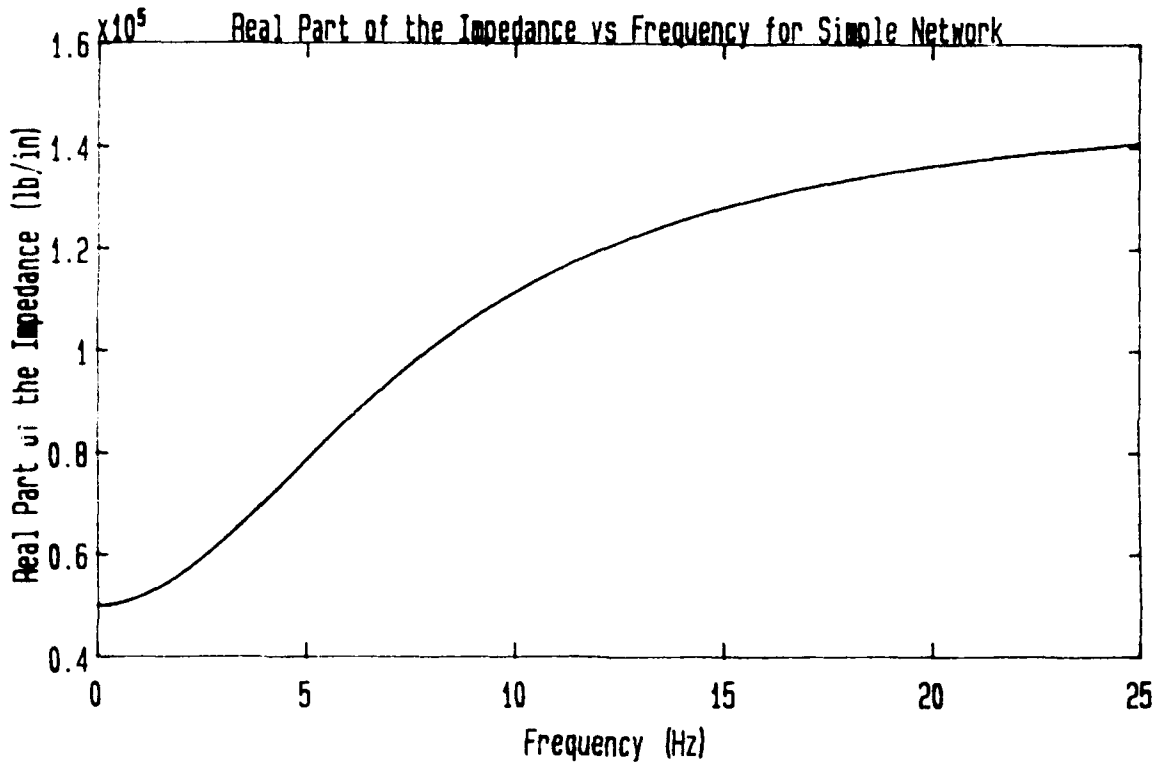
$$\omega_{max} = \frac{K_B}{C_A \sqrt{\frac{K_A + K_B}{K_A}}} \quad (6)$$

Substituting this frequency into the loss factor equation, the peak loss factor is determined to be:

$$\eta_{max} = \frac{K_B \sqrt{\frac{K_A + K_B}{K_A}}}{2(K_A + K_B)} \quad (7)$$

Notice that the value of the peak loss factor is independent of the dashpot value C_A . The peak loss factor is determined by the stiffness ratios in the network, and the value of the dashpot coefficient sets the frequency of the peak. This is counterintuitive to most structural dynamicists, as in most simple dynamic systems it is the stiffnesses which set the frequency and the dashpot value which sets the damping ratio.

Impedance analysis of the D-Strut network model is similar to the simple network. In fact, the 5-parameter network can be converted to an equivalent 3-parameter network which has an identical impedance. The conversion of the 5-parameter model to the 3-parameter model is useful to provide insight into the proper selection of the spring stiffnesses and dashpot values for the more complex



Figures 5 and 6 - Impedance Characteristics of the 3-Parameter Network

network. Solving for the values of K_A , K_B , and C_A of the 3-parameter model in terms of the parameters K_1 , K_2 , K_3 , K_4 , and C of the 5-parameter model yields:

$$\begin{aligned}
 K_A &= \frac{K_1 K_2 + K_1 K_3 + K_2 K_3}{K_2 + K_3} \\
 K_B &= \frac{K_2^2 K_4}{K_2^2 + 2 K_2 K_3 + K_3^2 + K_4 K_2 + K_4 K_3} \\
 C_A &= \left[\frac{K_2}{K_2 + K_3} \right]^2 C
 \end{aligned}
 \tag{8}$$

The 3-parameter network is entirely equivalent to the 5-parameter network with this selection of the parameters, with any internal effects of inertias neglected.

The behavior of the spring / dashpot impedance as a function of frequency is very similar to the impedance characteristics of viscoelastic materials (VEMs). The network stiffness increases monotonically, while the loss factor shows a distinct maximum value. The maximum loss factor occurs in the transition region between soft and stiff behavior. The strut properties, as the viscous dashpot coefficient is altered, can be written in terms of a reduced frequency, which depends on both the forcing frequency and the dashpot coefficient. The similar characteristics of the spring / dashpot network and viscoelastics has previously been used to model viscoelastics materials as networks, as in Maxwell's and other models of damping material behavior.

The impedance representation of the strut properties provides insight into the design and efficient use of D-Strut members. The incorporation of these models into truss structures and evaluation of alternative structural modeling techniques was evaluated for use in the design and analysis of the PACOSS truss.

4.0 Modeling Techniques and Design Methodology for Structures Incorporating D-Struts

For D-Strut members to be used efficiently to provide damping to flexible truss structures, a coherent design methodology is required to provide structural designs which meet requirements with minimal additional weight and system impact. Modeling methods were developed which allow simple calculations to estimate the effects of incorporating D-Struts on system natural frequencies, damping ratios, and mode shapes. These methods were shown to be accurate and allowed the development of a simple design methodology. When applied to a structure, the methodology will provide efficient damping designs without the high cost associated with the solution of large complex eigenproblems.

A preliminary concept which must be developed is the conversion of a viscous system to one with complex stiffnesses (impedances). The concept can be extended to arbitrary systems with many networks and many degrees of freedom. In general, the Laplace transform of the free vibration equations of motion of an arbitrary system with viscous damping are:

$$\left[\mathbf{M}s^2 + \mathbf{C}s + \mathbf{K} \right] \mathbf{X} = 0 \quad (9)$$

where: **M** = system mass matrix
C = system viscous damping matrix
K = system stiffness matrix
X = vector of transformed global displacements

By choosing an initial estimate to the eigenvalue, the transformation from a system with viscous damping to a system with a complex impedance can be obtained:

$$\left[\mathbf{M}s^2 + \mathbf{C}\sigma + \mathbf{K} \right] \mathbf{X} = 0 \quad (10)$$

define: $\mathbf{C}\sigma + \mathbf{K} = \mathbf{Z}_R + \mathbf{I} \cdot \mathbf{Z}_I$
 where: σ is an initial eigenvalue estimate

The impedance matrix can be obtained as shown above, or by the assembly of elemental impedances:

$$\mathbf{Z}(s) = \sum_{j=1}^{NE} \mathbf{Z}_{Rj}(s) + \mathbf{I} \cdot \mathbf{Z}_{Ij}(s) \quad (11)$$

This conversion will typically be performed on an element level prior to assembly of the impedance matrix. The utility of the method is in noting that the impedance matrix has the form of a complex stiffness matrix. If iterations are performed to calculate an eigenvalue and eigenvector from the initial estimate, and the impedance is updated using the result as a new initial eigenvalue guess, the procedure will converge to an exact eigenvalue and eigenvector of the viscously damped system.

The transformation transfers the 2 N-size complex eigenproblem (solution of the 2 N real matrix eigenproblem in state form) to a 1 N-size eigenproblem with a complex matrix which must be solved iteratively. The iteration method can be used efficiently in conjunction with matrix iteration methods such as the inverse power method, since this method converges to a single eigenvalue and eigenvector at a time. In fact, the inverse power iterations performed in MSC/NASTRAN to calculate the complex modes of a viscously damped system are performed essentially by making this substitution and iterating with a shifted dynamical matrix. The real value of the transformation of the eigenproblem, however, is that approximate methods can be used to obtain

modes, natural frequencies, and damping ratios without the solution of a complex eigenproblem.

The modal strain energy (MSE) method is a well known method for approximating the solution of a system with complex stiffness using only real eigenproblems. The MSE method is typically used to approximate the behavior of systems with viscoelastic damping treatments, and was used in previous PACOSS efforts in the design and analysis of the PACOSS DTA [4]. Similar to the D-Strut network, VEMs exhibit frequency-dependent complex stiffness behavior (frequency-dependent shear modulus and loss factor). Therefore, visco-elastic damping problems must also be solved iteratively by supplying an initial estimate to the natural frequency, substituting this value to determine the material complex modulus, and then solving a real eigenproblem to provide approximate mode shapes, frequencies, and damping ratios for modes "nearby" the initial frequency estimate.

Note that the member impedances should be calculated at the system pole (eigenvalue) for the analysis to provide the best approximation. For D-Struts, the impedance can readily be calculated at the system poles using the spring / dashpot network. Computation of the impedance at the system eigenvalue provides a more accurate approximation to the system behavior when used with the MSE method.

Due to the similarity of the D-Strut behavior and the behavior of viscoelastic damping struts, the methods previously developed for viscoelastic damping struts to select damping member locations and provide approximate system behavior can be directly used for the design of D-Strut damping treatments [4]. A simple methodology to be used when designing a truss structure with D-Strut members as a damping treatment is provided in Table 2.

This method allows the designer to achieve a satisfactory design for strength, natural frequencies, and damping ratios using only real eigenproblems, except for complex analyses at the end of the design cycle. It is apparent, when using this method, that the optimum locations for the dampers are areas of high strain energy, and that the sizing of the selected members for damping should be such that the maximum possible strain energy is contained in these members within the constraints of the problem. It is also evident that the damping members should have high loss factors at frequencies of the modes in which they have high strain energy to provide the highest system damping ratios.

A final benefit of the design method is that it allows the number or locations of dampers to be readily changed in the finite element model, since the only difference between the damper modeling and undamped member modeling is the member axial stiffness and member weight. Using this method, the only input data alteration required to change an undamped member to a damping strut is a property designation. With network modeling, a significant effort is required to add and/or remove additional nodes and element connectivities, when a damping element location is changed.

The D-Strut design procedure was exercised on several sample problems using the MSE method, in order to determine its accuracy and applicability for

Table 2 - Design Methodology for Incorporating D-Struts

- 1) Create a finite element model of the undamped structure.
- 2) Determine system natural frequencies and the required modal damping levels through simulation.
- 3) Select favorable damping locations for struts from MSE and loading considerations.
- 4) Size members such that high percentage of MSE is obtained in damping locations without causing an excessive shift in frequencies. Revise damping requirements based on altered mode shapes obtained in this step, if changes in the mode shapes significantly alter the performance.
- 5) Specify maximum additional weight over undamped members for the D-Strut members. Or, alternatively, specify the required D-Strut loss factors, since there is a direct relationship between strut weight and maximum achievable loss factor.
- 6) Specify the minimum static stiffness and strength for the damping struts.
- 7) Design a D-Strut such that the maximum weight is not violated, the designed stiffness and maximum loss factor are achieved at the frequency of highest D-Strut participation, and strength requirements are met. It is possible that all the constraints cannot be met, while simultaneously achieving the desired loss factor. The maximum weight constraint will then have to be relaxed, lower damping levels may be required, or additional damping locations must be selected.
- 8) Estimate the damped eigenvalues using the MSE method.
- 9) Calculate the strut properties at the damped eigenvalues.
- 10) Insert the damper properties into the model as an equivalent bar element; and recalculate system modes, natural frequencies, MSE. (Several runs may be necessary for several frequency and/or damping ratio values.)
- 11) Check the frequency and damping values to be sure that the eigenvalues have not changed significantly and, therefore, damper properties are accurate. Iteration may be required on the strut loss factors and system damping.
- 12) Determine if performance requirements have been met. If not, return to step 3 and select additional damping strut locations or alter D-Strut designs for higher loss factors.
- 13) When the design requirements have been met for all modes, model the dampers as spring / dashpot networks with K_1 and K_2 implemented as bar elements, and solve the complex eigenproblem. This will check the results and allow final complex modes to be used in simulations. Alternatively, use accelerated complex subspace iteration with the dampers modeled as frequency-dependent complex stiffness elements [5].

problems of this type. From these sample problems, several conclusions were drawn. Most importantly, it was shown that for light damping levels the procedure is accurate and effective. For modest damping levels, however, the MSE method often produces approximations which have relatively high error. Therefore, an alternative method of determining the properties of damped structures using real eigenproblems, termed the absolute value modal strain energy method [6], was developed which improves the accuracy of the solution for higher damping levels.

5.0 Preliminary Design of the D-Strut Truss

To ensure the success of the PACOSS D-Strut truss as a verification testbed while providing an economic validation tool, several goals for the structural design were established. The basic configuration selected for the truss consisted of eight bays with a 34-in. bay size.

The fundamental goal was to achieve high modal damping of major structural modes in the frequency range characteristic of future Large Space Structures (LSS). Modal damping levels of 10% critical viscous damping in the fundamental truss modes were selected as a goal for the truss design. This level of damping was to be achieved using 12 D-Strut members in locations selected to achieve the highest damping possible in the fundamental modes.

To provide data in the frequency range characteristic of future LSS, a fundamental frequency of 5.0 Hz was selected for the truss. In addition, a frequency separation of 0.5 Hz for the two fundamental bending modes (bending in two orthogonal planes) was desired, to allow the separation of the modes during the modal test and simplify the modal test data reduction problem.

Hardware design issues, such as joint design and member integrity, were addressed during the preliminary design process. Bonded joints similar to those used on other PACOSS structures were selected [4], primarily since they have been shown to provide strong connections with negligible inherent damping. Aluminum members were selected for the basic truss to provide the greatest economy.

A finite element model of the truss was created to allow for member sizing and preliminary design. A back-to-back K-diagonal pattern was selected to provide a structure with two planes of symmetry. This diagonal pattern results in two separated modes which have their primary motion along 45° axes with respect to the sides of the truss bays. The members were sized so that the major strain energy portions were in the longerons of the structure, as the damper locations were selected to be the lower longeron members due to the high modal strain energy content.

A plate located at the top of the truss was adjusted to achieve the desired 5.0-Hz frequencies; and the desired frequency separation between the fundamental modes of the truss were obtained by replacing the aluminum longerons in two of the vertical sides of the truss with steel members. This nearly achieved the desired 0.5-Hz frequency separation. Member offsets at the joints were included in the model to model the effective free length of the tubes when bonded in place.

An investigation of the effect of various tip weights was also undertaken for the truss. Various tip weights were incorporated into the truss model and analyzed to determine the natural frequencies and damping ratios. With tip weights which were twice the nominal, one-fourth, and without a tip weight, the fundamental modes of the truss could be altered within a range of 3.5 to 11.0 Hz. These values of the tip weight were selected for use on the truss so that the D-Strut members could be validated over a greater frequency range.

A summary of the truss properties following the preliminary design is included in Table 3. Notice that the 5.0-Hz frequencies with 0.5-Hz separation and high strain energy in the dampers were achieved with stock aluminum and steel sections for the members. This design provided an economically-manufactured structure which allows extraction of the two major modes due to the frequency separation and inherent structural symmetry.

Preliminary design for the damping members were generated based on the impedance equations for the strut network. The parameters of the network were selected to provide high damping levels with minimum strut weight. The hydraulic stiffness in the damping device was selected to be as high as was thought to be achievable, and the sizes of the tubing members were selected to provide the required loss factor with minimum weight. The dashpot coefficient was selected to place the peak loss factor at the frequency of the fundamental frequency of 5.0 Hz and, therefore, to supply the peak possible damping. Using the parameters of the preliminary D-Strut design, the damping in the truss was calculated using the MSEI method for both the SD and D1 strut types. The damping ratios using these members are given in Table 4.

6.0 Detail Design, Fabrication, and Impedance Testing of the D-Struts

The preliminary D-Strut parameter selection information was provided to Honeywell to allow them to perform the detail design and fabrication of a prototype D-Strut member [7]. The detail design of the strut members was performed using the member design equations developed by Honeywell in prior internal research efforts.

Table 3 - Summary of D-Strut Truss Natural Frequencies and Strain Energy Distribution Following Preliminary Design

Mode Description	Frequency (Hz)	% Strain in Dampers
1 st Bending Mode (Plane 1)	4.98	61.7
1 st Bending Mode (Plane 2)	5.44	66.0
1 st Torsion Mode	14.26	4.0
2 nd Bending Mode (Plane 1)	28.97	2.6
2 nd Bending Mode (Plane 2)	30.84	1.7
Total Weight including Joints and Tip Weight		267 lb
Tip Plate Weight		113 lb

Table 4 - Modal Damping Levels Using SD and D1 Strut Preliminary Designs

MODE DESCRIPTION	SD STRUT DAMPING	D1 STRUT DAMPING
Plane 1 1 st Bending	13.1	19.1
Plane 2 1 st Bending	14.0	20.4

From the detail design effort, it was apparent that the stresses within the viscous damping device and the achievable values for the device hydraulic stiffness were the major considerations in the design of the damping members. These constraints on the design eliminated the D1 strut from consideration, due to the very high damping element stresses for this configuration.

Due to these design constraints, the prototype design philosophy followed by Honeywell was to match the impedance characteristics of the preliminary design, while minimizing the stresses in the damping device diaphragm under constraints on the overall diameter of the damping device. This allowed the design of the strut to achieve the desired impedance characteristics, however, a significant weight increase over the preliminary design was required to obtain the required loss factor. A prototype of this design was then constructed for evaluation.

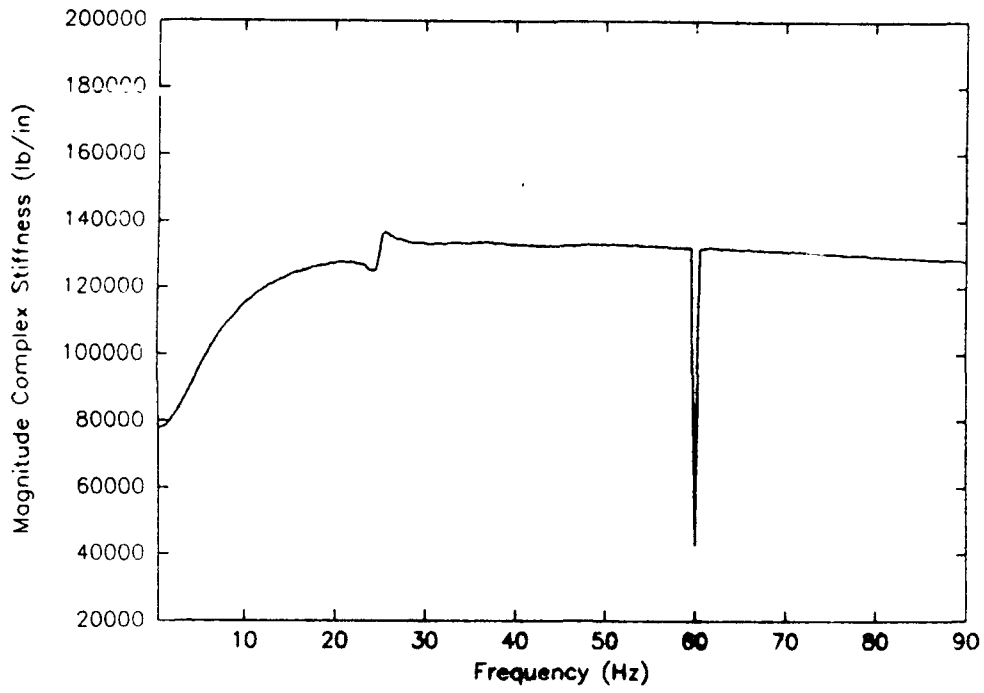
Impedance testing of the strut prototype was performed to verify the design of the member and to provide data which would allow improvement of the design. Tests of the prototype D-Strut showed that the strut possessed good linearity and provided a peak loss factor at the desired frequency. The peak loss factor, however, was lower than expected. The clamping of the diaphragm was suspected as the most probable reason for the degraded performance, although the effects of bonds and low modulus of the aluminum of the inner tubing also contributed to the low performance. Several design/test/build iterations were undertaken, however, the desired performance specifications of the preliminary design were not obtained.

The fabrication of the delivery D-Struts was undertaken using the prototype design with the modified clamping arrangement for the diaphragm which provided the best performance. Fourteen D-Struts were fabricated by Honeywell, and following completion of the member fabrication, each individual strut was tested to verify its strength and impedance characteristics. A typical impedance measurement is provided as Figures 7 and 8. The individual members showed some unit-to-unit variation, however, "average" strut parameters were synthesized for use in the model of the D-Strut truss pretest analysis. The static stiffness, peak loss factor, and peak loss factor frequency of the 14 D-Strut members are given in Table 5. The individual strut impedance data were also fit to determine the parameters which could be used to represent the individual strut members in a refined model for analysis following testing of the actual truss structure.

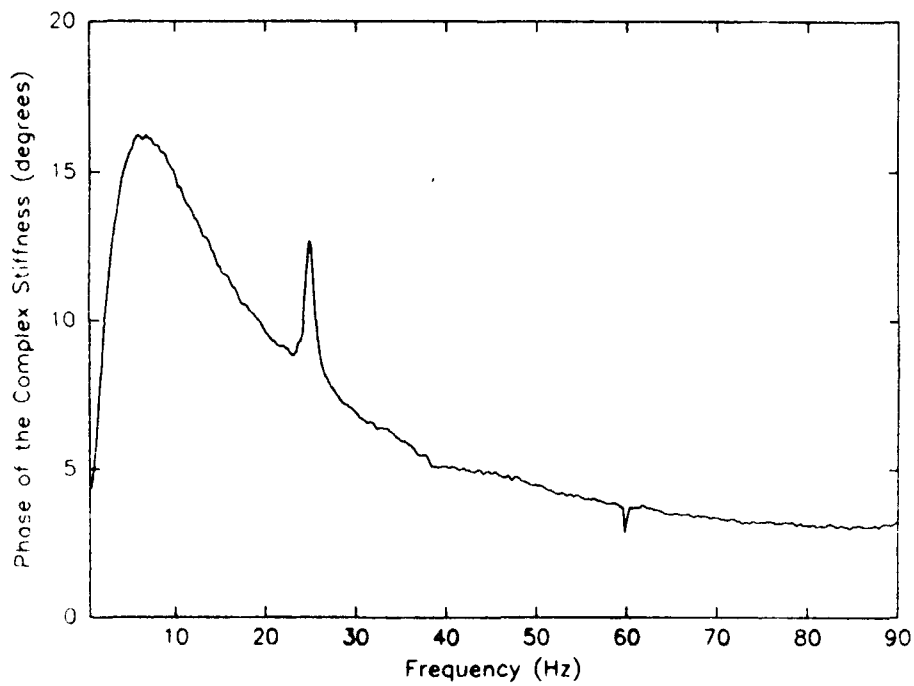
7.0 Modal Testing of the D-Strut Truss

The objectives of the D-Strut truss test were to identify the natural frequencies, mode shapes, and damping ratios of the test truss, and to allow for correlation with the truss modal analysis. The undamped truss assembly was first tested to validate the

Dstrut 1 qualification test



Dstrut 1 qualification test



Figures 7 and 8 - Measured D-Strut Impedance Function

Table 5 - Static Stiffness, Peak Loss Factor, and Peak Loss Frequency as Read from Impedance Plots

Strut No.	Static Stiffness	Peak Loss Factor	Frequency of Peak Loss
1	78,000	0.29	6.2
2	80,000	0.23	4.5
3	83,000	0.26	4.0
4	80,000	0.26	4.5
5	78,000	0.28	6.2
6	80,000	0.20	6.4
7	80,000	0.23	5.2
8	78,000	0.28	4.8
9	80,000	0.30	6.2
10	82,000	0.28	5.2
11	80,000	0.29	6.0
12	77,000	0.28	6.3
13	78,000	0.27	5.8
14	77,000	0.28	6.0

test fixturing and setup and allow the verification of the structural modeling without additional damping treatments. The nominal tip weight was used in the undamped truss test, which caused the fundamental frequencies of the truss to be close to the damped truss fundamental frequency of 5.0 Hz. A full modal survey of the undamped structure was performed to determine the structure natural frequencies, damping ratios, and mode shapes below 45 Hz.

The damped truss assembly was then tested with the nominal tip weight to determine the properties of the damped assembly with the D-Struts as the longerons in the lower three bays. Again, a full modal survey was performed on the truss to determine the modal properties of the damped assembly.

Finally, various tip weights were added to the truss to determine the truss properties over a significant frequency range. Sufficient data were acquired in each configuration to permit the identification of the natural frequencies, damping ratios, and mode shapes of the two lowest frequency structural modes, which are most greatly affected by the D-Strut members.

8.0 Analytic / Test Correlation of the Truss Modal Data

Following completion of the D-Strut truss modal test, correlation with the analytic model was evaluated. The undamped truss test results were initially compared with the analysis, and minor revisions to the model were made to improve the correlation. The model was compared with the test results in terms of the natural frequencies and mode shapes, with excellent agreement found for the modes below 45 Hz. Table 6 provides the analytic / test comparison for the modes of the undamped structure. Note the light damping ratios which were determined by parameter

Table 6 - Undamped Truss Tuned Analysis/Test Comparison

Measured Mode No.	Analytic Frequency (Hz)	Measured Frequency (Hz)	Measured Damping Ratio (%)
1	4.62	4.61	0.07
2	4.78	4.79	0.08
3	13.64	13.72	0.08
4	26.46	27.10	0.08
5	29.32	28.84	0.08
6	31.86	31.55	0.08
7	43.24	43.74	0.11

estimation. Decay measurements of the structure without cabling show damping of 0.01% critical in the fundamental mode.

Following correlation of the undamped structure, the model of the damped assembly was modified to reflect the changes in the undamped portion of the model. The truss properties with the nominal tip weight and each strut modeled as the "average" strut were then computed and compared with the test data. Excellent correlation was found for natural frequencies and mode shapes, and good agreement was found for the damping ratios. One final model modification was made which involved the incorporation of the properties of each individual strut in the proper strut locations, with the individual strut parameters determined from member impedance data. Table 7 provides the comparison of the damped structure modal analytic and test results. With the individual members incorporated, the agreement with the test data showed some improvement over the "average" strut model, although the previous model showed good agreement. Modal orthogonality checks were performed between the analytic and test modes using the analytic mass matrix. Table 8 provides the orthogonality results, which show outstanding agreement between the experimental and analytic mode shapes.

Finally, the refined model of the damped assembly was altered to reflect the various tip weights and reanalyzed to determine the truss properties. Again, these results agreed well with the measured data and verified the performance of the damping members at frequencies other than the peak loss factor location. Table 9 provides the frequency and damping correlation for the various tip weights.

The model correlation showed that accurate modeling of truss structures incorporating D-Struts was achieved using the 5-parameter D-Strut model. However, determination of the model parameters from impedance measurements on the individual struts was required. The test/model correlation of both the damped and undamped structures are excellent, particularly if the highly damped nature of the structure with the D-Strut incorporated is considered, and the difficulty in parameter estimation associated with these high damping ratios is recognized.

Table 7 - Nominal Tip Mass Tuned Analytic/Test Comparison with the D-Struts Modeled Using Parameter Fits

Mode No.	Analytic		Measured	
	Frequency (Hz)	Damping Ratio (%)	Frequency (Hz)	Damping Ratio (%)
1	4.98	7.23	5.00	6.59
2	5.10	9.62	5.25	9.43
3	13.61	<0.1	13.68	0.11
4	26.20	0.72	26.79	0.79
5	28.42	0.28	28.16	0.39
6	30.77	0.49	30.67	0.52
7	40.70	0.22	40.99	0.26

Table 8 - Cross-Orthogonality Matrix for Tuned Analysis of Damped Truss

		Analytic Frequency						
		4.98	5.10	13.61	26.62	28.42	30.77	40.70
5.00		1.00	0.00	0.00	0.00	-0.01	0.03	0.01
5.25		0.00	0.99	0.00	0.00	0.01	0.00	0.00
13.68		0.00	0.00	1.00	0.00	0.00	0.00	0.00
26.79		0.00	0.00	0.00	1.00	-0.03	0.00	0.00
28.61		0.00	0.00	0.00	0.03	1.00	0.02	0.00
30.67		0.00	-0.01	0.00	0.00	-0.02	1.00	-0.01
40.99		0.00	0.00	-0.01	0.00	0.02	0.00	1.00
		Experimental Frequency						

Table 9 - Tuned Analysis/Test Comparison with Various Tip Weights

	Analytic			Measured	
	Measured Mode No.	Frequency (Hz)	Damping Ratio (%)	Frequency (Hz)	Damping Ratio (%)
Twice Nominal Weight	1	3.62	7.17	3.68	6.59
	2	3.70	8.83	3.87	9.39
One-Fourth Nominal	1	7.85	6.17	7.84	6.70
	2	7.98	8.82	8.18	8.67
No Tip Weight	1	10.46	7.40	10.27	7.23
	2	10.45	5.08	10.87	5.91
	3	10.68	4.27	10.97	5.52

9.0 Comparison of Viscoelastic Extensional Shear Dampers and D-Struts for Truss Damping Applications

The PACOSS DTA [2,4] includes damping strut members which were designed and fabricated using VEMs. For treatment of the box truss and equipment platform, viscoelastic extensional shear dampers (VESDs) were designed and incorporated into these truss structures. As the D-Strut is also designed to be used as a damping element for truss structures, a comparison of the state-of-the-art hardware for the two methods of damping treatment is beneficial.

To allow a direct comparison of the properties of these damping members, a viscoelastic damper was designed, which had an identical stiffness and loss factor at the 5.0-Hz frequency of the fundamental modes. Similar elements were designed, built, and tested under the PACOSS Program, and the analytic design equations for these members have been adequately verified. The pertinent properties of the VESD were then compared to those of the D-Strut.

The results of the comparison show that the D-Strut hardware which was developed for the PACOSS truss structure has one advantage over viscoelastic members, and several disadvantages. A comparison of the important characteristics of these two damping members is provided in Table 7. The primary advantage of the D-Strut is its reduced temperature dependency. The D-Strut has a $\pm 40^{\circ}\text{F}$ temperature range for a 10% variation in the impedance, while a similar viscoelastic member has only a $\pm 5^{\circ}\text{F}$ range.

Table 8 - Comparison of Important VESD and D-Strut Properties

	D-Strut	VESD
Peak Loss Factor/Frequency	0.275 / 6.0 Hz	0.285 / 4.0 Hz
Loss Factor at 5.0 Hz	0.270	0.280
Equivalent Stiffness at 5.0 Hz	96,000 lb/in.	94,000 lb/in.
Static Stiffness	78,000 lb/in.	54,000 lb/in.
Static Strength	600 lb	5,700 lb
Damped Element Weight	2.71 lb	1.74 lb
Added Weight / Undamped Weight	2.31	1.13
Required Temperature Control	± 40°F	± 5°F

The viscoelastic member, however, has a much higher load carrying capacity and adds less weight to produce a similar damping ratio. The added weight of the D-Strut member was roughly twice the added weight of a viscoelastic member. This added weight is primarily due to the low hydraulic stiffness (K_4) of the current damping device. The load carrying capacity of the D-Strut is currently very low, due to stress constraints within the damping device. These stresses cause the maximum load capacity of the D-Strut to be approximately a factor of 10 lower than its viscoelastic counterpart.

While, at this time, the comparison favors the viscoelastic member, future advances in the design of viscous damping members should exceed the capabilities of viscoelastic struts. The success of an alternative damping device which can sustain high deflections and has a much larger hydraulic stiffness can cause this comparison to favor the D-Strut. Damping devices which show almost no temperature dependence may be developed, which will eliminate the need for temperature control of the strut members.

10.0 Conclusions

From the PACOSS investigation of the D-Strut, it was determined that efficient MSE techniques in conjunction with member impedances can be used to design both the damped structure and to optimize the characteristics of the damping members. Final analysis of a damped structure can then be performed by incorporating a spring / dashpot model of the damping struts directly into the finite element model.

The D-Strut members which were fabricated and tested qualitatively agreed with the 5-parameter spring / dashpot model developed by Honeywell. Quantitatively, however, the parameters of the model derived from the design equations for the member did not accurately predict the performance of the viscous fluid damping device. In particular, the predicted hydraulic stiffness and the diaphragm stiffness were significantly different from the values predicted by the model. The lower hydraulic stiffness caused the damping of the truss test structure to be approximately 35% lower than anticipated during preliminary design.

Following fabrication and testing of a strut prototype, each individual D-Strut member was dynamically tested to determine its impedance characteristics. Testing of the individual strut members provided data for the determination of the parameters of the strut model which would provide an impedance consistent with the measured data for each unit. The model of the truss was modified to reflect these data.

An undamped lower section of the structure was also fabricated to determine the accuracy of the model of the undamped section and verify that very light inadvertent damping was present. Decay testing of the undamped truss verified an extremely low damping ratio of 0.01% critical, which demonstrates the light damping ratios expected for precision truss structures without damping augmentation. With the D-Strut members incorporated into the truss, the damping ratios of the damped structure were approximately 7.5% and 10.0% critical for the first two structural modes. This represents a 4-order-of-magnitude increase in damping over the undamped structure. Four tip weights were used on the truss, which allowed a significant variation in the fundamental frequencies and verified the performance of the damping members over a significant frequency range.

When the modal data as synthesized from measurements are compared with the analytic data, the correlation is excellent. The first seven natural frequencies of the tuned model of the undamped structure agree with the test data to within 2%, and other measures of model accuracy show good agreement. The model of the damped structure also has similar accuracy in terms of natural frequencies, and all damping ratio predictions agree to within 9% relative error. This agreement verifies that the modal properties of damped structures which incorporate D-Strut members can be accurately predicted with finite element models and the Honeywell 5-parameter model, if the appropriate parameters of the model are determined from member impedance test data.

Finally, a comparison of the D-Strut to the PACOSS VESD was made to determine whether the potential advantages of the D-Strut were achieved. From the comparison, it was concluded that the only current advantage of the D-Strut is its larger temperature range. The current D-Strut design was shown to be heavier than a VESD which was designed to produce identical frequencies and damping ratios when incorporated into the truss. The D-Strut was shown to have only a 600-lb strength (due to the stress limitations of the damping element), while the VESD design had a strength of 5,700 lb. This lower strength of the current D-Strut design may preclude its use in situations where high loads are present.

While the current design of the D-Strut has some deficiencies, alternative designs of the viscous fluid damping device may reduce or eliminate these shortcomings. In particular, if the viscous damping element can be designed to have a much higher hydraulic stiffness than the current device, the weight of the damper for a given performance will be significantly decreased such that it will be lighter than its viscoelastic counterpart. Similarly, if the damping element can be designed to sustain high deflections, the strength of the element will be comparable to the VESD. Future work should be undertaken to investigate alternative designs of the damping element.

The PACOSS investigation has shown that the viscous fluid damping strut can be successful in producing high damping ratios for truss structures. The device can be modeled accurately from impedance test data, and properties of structures which incorporate these devices are predictable. Refinement of the design of the damping element will make the D-Strut concept extremely successful and attractive for incorporation into damped trusses for space applications.

References

- 1) Wilson, J. F., and Davis, L. P., "Very High Damping in Large Space Structures," The Role of Damping in Vibration and Noise Control, ASME Publication, 1987.
- 2) Gehling, R. N., "Large Space Structure Damping Treatment Performance - Analysis and Test Results," The Role of Damping in Vibration and Noise Control, ASME Publication, 1987.
- 3) Johnson, C. D., and Kienholz, D. A., "Finite Element Prediction of Damping in Structures with Constrained Viscoelastic Layers," AIAA Journal, Vol 20, No 9, pp 1284-1290, 1982.
- 4) Morgenthaler, D. R., "Design and Analysis of Passively Damped Large Space Structures," The Role of Damping in Vibration and Noise Control, ASME Publication, 1987.
- 5) Morgenthaler, D. R., "Practical Design and Analysis of Systems with Fractional Derivative Materials and Active Controls," Presented at Damping '91, West Palm Beach, Florida, 12-15 May 1991.
- 6) Morgenthaler, D. R., "The Absolute Value Modal Strain Energy Method," Presented at Damping '91, West Palm Beach, Florida, 12-15 May 1991.
- 7) Cunningham, D. C., "Development of the PACOSS D-Strut," Presented at Damping '91, West Palm Beach, Florida, 12-15 May 1991.

AN ADVANCED D-STRUT™

L. Porter Davis¹
Steven D. Ginter, Ph.D.²
Honeywell Inc., Satellite Systems Operation

ABSTRACT

A viscous-damping technique offering high damping for spacecraft truss structures has been under development since 1986. The technique, known as the D-Strut™, uses a small mechanical viscous damper configured in an inner-outer tube-strut configuration, and replaces the nominal-type strut. The viscous-damped D-Strut has been employed in more compliant isolation systems for space applications, including the Hubble Space Telescope.

The United States Air Force and Jet Propulsion Laboratory have investigated D-Struts for use in high specific-stiffness truss structures. This technique is an attractive means of attaining significant damping levels in space structures.

¹Senior Staff Engineer, (602) 561-3211

²Staff Engineer, (602) 561-3244

Honeywell Inc., Satellite Systems Operation, P.O. Box 52199, Phoenix, AZ 85022

INTRODUCTION

A viscous-damping technique that offers high damping for spacecraft truss structures has been under development now for several years (References [1-3]). The technique, known as the D-Strut™, employs a small, mechanical viscous damper configured in an inner-outer tube-strut configuration. The D-Strut serves as a basic element in a truss structure, replacing the nominal-type strut. The viscous-damping concept, employed in more compliant isolation systems, has been qualified for at least three space applications and is currently flying in the Hubble Space Telescope, where the function is to isolate disturbances emanating from the attitude control reaction wheel assembly (References [4-5]).

The United States Air Force and the Jet Propulsion Laboratory (JPL) have investigated the use of D-Struts in high specific-stiffness truss structures. With considerable development heritage, the viscous D-Strut now provides an attractive means for attaining significant damping levels in space structures. The D-Strut is simple in design and construction, is easy to model, and is readily incorporated into the overall structure design and analysis process.

The advantages of the D-Strut are:

- Very large dynamic range (no rubbing friction or hysteresis)
- Damping independent of stiffness
- High damping
- Low temperature sensitivity compared to viscoelastic materials
- Adjustable performance
- Linear and predictable performance
- Qualified for space application
- Hermetically sealed fluid (fluid exposed satisfies outgassing and mass transfer requirement of NASA)

Design alternatives within the basic concept provide a variety of performance options. Design improvements continue to provide better performance, nearing that of an *ideal damper*. The reference to *ideal* refers to a damper which can be modeled simply as a spring and dashpot in parallel. The following several paragraphs expand on this consideration and develop the necessary mathematics for a more complete understanding. Following that, an improved *arched flexure* design with test results is presented. Finally, a glimpse of future plans is provided.

D-STRUT CONFIGURATION

The first D-Struts built, shown in Figure 1(a), employ three basic elements: a small viscous damper, an inner tube, and an outer tube.

The damper is placed in series with the inner tube and the damper/inner tube is placed in parallel with the outer tube. An axial displacement across the strut produces a

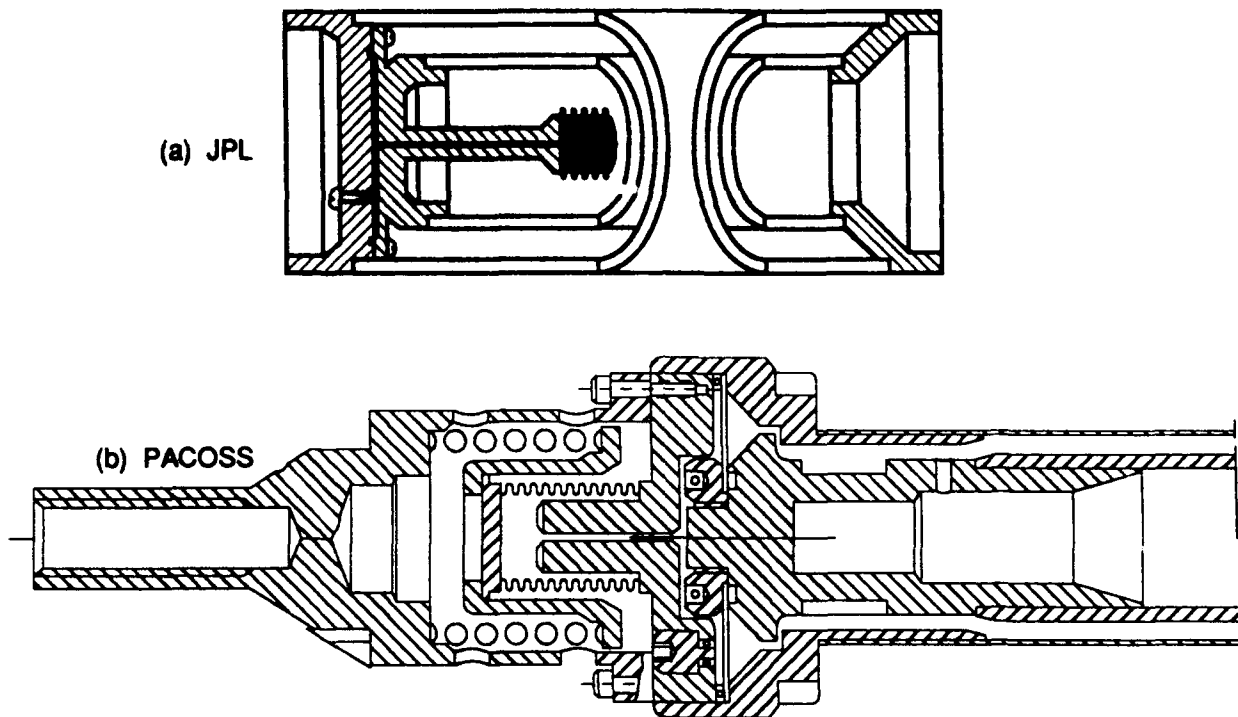


Figure 1. Diaphragm Flexure D-Struts for JPL and PACOSS

displacement across the damper. Under an axial displacement, the damper forces fluid through a small-diameter orifice, thereby causing a shear in the fluid. The fluid shear is proportional to the displacement rate across the damper; thus, a true viscous-damping force is obtained (i.e., a force proportional to velocity).

The compliances of the damper, the inner tube, and the outer tube are key to the damping performance of the D-Strut. The damper is the most-compliant element and the inner tube is the least-compliant element. The outer tube provides the basic static stiffness of the strut and is pertinent to applications where the strut is a critical load-bearing element in the structure. Otherwise, the outer tube is not necessary and can be eliminated with a resulting improvement in damping performance.

The damper element consists of two compliant metal cavities connected by a small-diameter orifice of a certain length. The damper cavities are hermetically sealed to avoid outgassing and fluid loss. The damper is mechanically simple, has no moving parts or wear mechanisms, and is completely tolerant of space vacuum and radiation.

A diaphragm flexure D-Strut tested by JPL is shown in Figure 1(a). A second diaphragm flexure D-Strut was developed for PACOSS program (Reference [3]) and is illustrated in Figure 1(b). Both systems were tested as single elements and as an integral part of a truss structure. Twelve D-Struts were used in the PACOSS structure.

The flexing of a metal diaphragm is the mechanism that forces fluid through the small orifice. The advanced designs replace the diaphragm with a convoluted cylinder or *arched flexure*.

D-STRUT MODEL

A D-Strut is readily modeled by five physically lumped parameters, as indicated by Figure 2. Considerable insight to the damping performance is gained by regarding the D-Strut as a *mechanical impedance*. Mechanical impedance is somewhat analogous to electrical impedance and related, in the frequency domain, the axial force f to the axial displacement x across the strut:

$$z(s) \equiv \frac{f(s)}{x(s)} \quad (1)$$

with s denoting the *Laplace* transform variable. For no damping, the impedance reduces to a standard stiffness. The mechanical impedance is a good characterization of the D-Strut behavior as long as the mass lumped at the internal nodes, labeled N_3 and N_4 in Figure 2, is negligible. This is typically a very good approximation over the frequency range of interest.

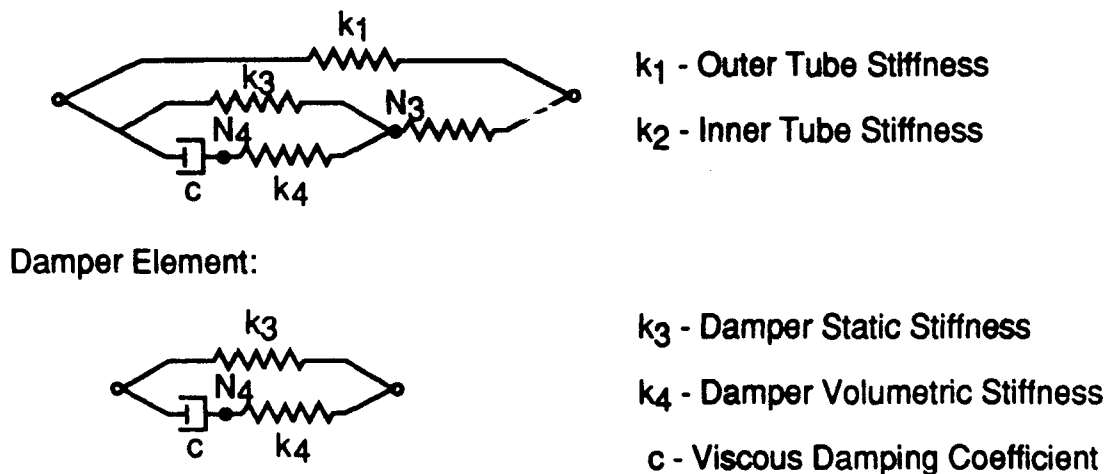


Figure 2. Inner-Outer Tube D-Strut Equivalent Model

The impedance of a D-Strut is a function of three parameters and has a classic *lead-lag* network characteristic:

$$z(s) = k_s \frac{\omega_p s + \omega_z}{\omega_z s + \omega_p} \quad (2)$$

with:

$$k_s = \frac{k_1 k_2 + k_1 k_3 + k_2 k_3}{k_2 + k_3} \quad (3)$$

$$\omega_z = \frac{k_4}{c} \frac{k_1 k_2 + k_1 k_3 + k_2 k_3}{k_1 k_2 + k_1 k_3 + k_1 k_4 + k_2 k_3 + k_2 k_4} \quad (4)$$

$$\omega_p = \frac{k_4}{c} \frac{k_2 + k_3}{k_2 + k_3 + k_4} \quad (5)$$

Because the impedance depends only on three parameters, an equivalent three-parameter physical model of the D-Strut can be obtained, as indicated in Figure 3.

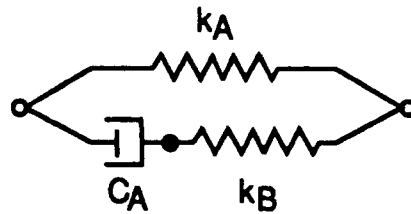


Figure 3. Equivalent D-Strut Model

The equivalent model impedance is:

$$z(s) = k_A \frac{\omega_B s + \omega_A}{\omega_A s + \omega_B} \quad (6)$$

with:

$$\omega_A = \frac{1}{c_A} \frac{k_A k_B}{k_A + k_B} \quad (7)$$

$$\omega_B = \frac{k_B}{c_A} \quad (8)$$

The relation between the parameters $\{k_A, k_B, c_A\}$ and $\{k_1, \dots, k_4, c\}$ is given by:

$$k_A = k_1 \left[1 + \frac{\frac{k_3}{k_1}}{1 + \frac{k_3}{k_2}} \right] \quad (9)$$

$$k_B = k_2 \left[\frac{1}{1 + \frac{k_3}{k_2}} \right] \left[\frac{1}{1 + \frac{k_2 + k_3}{k_4}} \right] \quad (10)$$

$$c_A = c \left[\frac{1}{1 + \frac{k_3}{k_2}} \right]^2 \quad (11)$$

The equivalent model indicates that only three parameters – two equivalent stiffness values and an equivalent dashpot coefficient – are needed to model the D-Strut in overall structure design and analysis. D-Strut testing verifies that this is indeed the case.

The expressions above for $\{k_A, k_B, c_A\}$ show that $k_A \sim k_1$, $k_B \sim k_2$, and $c_A \sim c$. Actually, k_A is larger than k_1 , since its multiplying factor in brackets is larger than 1 and both k_B and c_A are smaller than k_2 , and c , respectively, since their multiplying factors in brackets are smaller than 1. It will be shown momentarily that the maximum damping performance of the D-Strut is established by the ratio k_B/k_A . This ratio depends only on the stiffness elements in the damper and the stiffness of the inner and outer tubes. To maximize the D-Strut damping performance, the damper element should be made to approach the characteristic of an ideal dashpot. This is accomplished by driving $k_3 \rightarrow 0$ and $k_4 \rightarrow \infty$. In this situation $k_A \rightarrow k_1$, $k_B \rightarrow k_2$, and the maximum damping performance are established by the ratio of the inner-to-outer tube stiffness k_2/k_1 . A damper with nonzero stiffness for k_3 and a finite stiffness for k_4 reduces the D-Strut maximum damping performance from the theoretical limit.

D-STRUT PERFORMANCE

The D-Strut damping performance is easily understood under the condition of sinusoidal displacement and forces. If a sinusoidal displacement:

$$x(t) = X \sin \omega t \quad (12)$$

is prescribed across the D-Strut, then the resulting force developed in the strut is also sinusoidal:

$$f(t) = XA(\omega) \sin (\omega t + \phi(\omega)) \quad (13)$$

where $A(\omega)$ and $\phi(\omega)$ are the amplitude and phase angle of the impedance at the frequency ω :

$$z(j\omega) = z_R(\omega) + jz_I(\omega) = A(\omega)e^{j\phi(\omega)} \quad (14)$$

Defining the parameters α as:

$$\alpha \equiv \sqrt{\frac{\omega_B}{\omega_A}} = \sqrt{1 + \frac{k_B}{k_A}} \quad (15)$$

the amplitude and phase of the impedance are given by:

$$A(\omega) = k_A \alpha^2 \frac{\sqrt{1 + (\omega/\omega_A)^2}}{\sqrt{\alpha^4 + (\omega/\omega_A)^2}} \quad (16)$$

$$\tan \phi(\omega) = \frac{(\alpha^2 - 1) (\omega/\omega_A)}{\alpha^2 + (\omega/\omega_A)^2} \quad (17)$$

A typical impedance characteristic is illustrated in Figure 4.

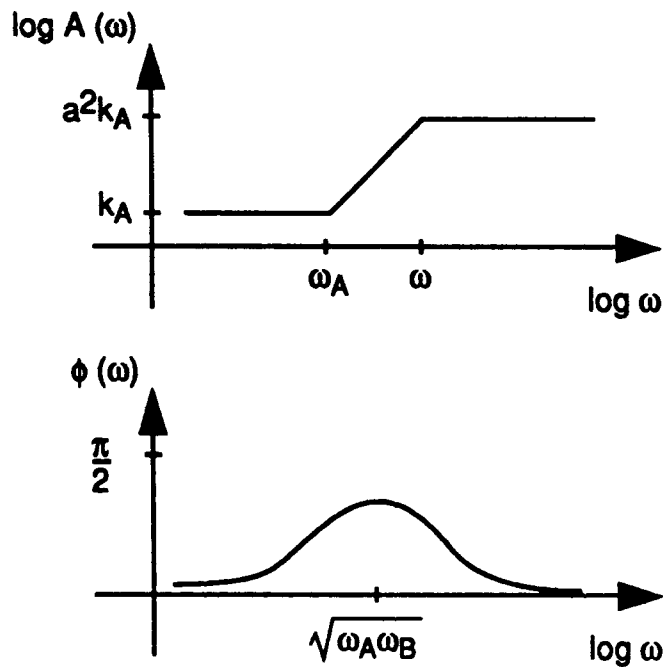


Figure 4. D-Strut Impedance Characteristic

The energy dissipated per cycle due to the damping is determined by $\phi(\omega)$. In fact, using the classical definition of damping loss factor:

$$\eta(\omega) \equiv \frac{1}{2\pi} \frac{\text{energy dissipated / cycle}}{\text{max energy stored / cycle}} \quad (18)$$

then:

$$\eta(\omega) = \tan \phi(\omega) \quad (19)$$

and the impedance can be expressed as:

$$z(j\omega) = z_R(\omega) (1 + j\eta(\omega)) \quad (20)$$

It is easy to demonstrate that the maximum loss factor is given by:

$$\eta^* \equiv \max_{\omega} \eta(\omega) = \frac{1}{2} \frac{\alpha^2 - 1}{\alpha} = \frac{1}{2} \frac{k_B/k_A}{\sqrt{1 + k_B/k_A}} \quad (21)$$

and that η^* occurs at:

$$\omega^* = \sqrt{\omega_B \omega_A} = \alpha \omega_A = 2 \frac{k_A}{c_A} \eta^* \quad (22)$$

The value of $z_R(\omega)$ at ω^* is:

$$z_R(\omega^*) = 2k_A \frac{1 + k_B/k_A}{2 + k_B/k_A} \quad (23)$$

Thus, the maximum loss factor is determined only by the stiffness characteristics of the damper and tubes, not by the damping coefficient c . Since k_A is the strut static stiffness, which is determined by the load capability needed, the damping coefficient c is used to set the frequency at which the maximum loss factor occurs.

The above equations indicate an equivalence between the *physical* parameters $\{k_A, k_B, c_A\}$ and the *performance* parameters $\{\eta^*, \omega^*, z_R(\omega^*)\}$. When *designing* damping performance into a structure, the structure engineer often prefers to work in terms of the performance parameters $\{\eta^*, \omega^*, z_R(\omega^*)\}$. In *analyzing* the damping performance of the structure, the physical parameters $\{k_A, k_B, c_A\}$ are more appropriate.

From the above equations it is clear that η^* is maximized by maximizing k_B/k_A . This ratio is related to the four stiffness parameters $\{k_1, \dots, k_4\}$ by:

$$\frac{k_B}{k_A} = \frac{k_2}{k_1} \frac{1}{1 + \frac{k_3}{k_2} + \frac{k_3}{k_1}} \frac{1}{1 + \frac{k_2}{k_4} + \frac{k_3}{k_4}} \quad (24)$$

It appears from this equation that, to maximize the damping performance, the stiffness ratios k_2/k_1 and k_4/k_3 should be maximized. The first ratio is that of the inner-to-outer tube stiffness and the second ratio is the damper's *static-to-volumetric* stiffness. The damper volumetric stiffness is due to the fluid bulk modulus and the change in cavity volume due to stretching of the metal under fluid pressure.

Thus, from the performance viewpoint, the damper element of a D-Strut should be designed to have as large a ratio of k_4/k_3 as possible. An achievable stiffness ratio for a typical diaphragm flexure, as designed for the PACOSS program, is $k_4/k_3 = 20$. A significant factor preventing a larger ratio for the diaphragm flexure is the difficulty increasing the volumetric stiffness k_4 while not compromising the strut's static deflection capability, which is determined by k_3 . This limiting factor of the diaphragm flexure has led to the development of an improved damper employing an *arched* flexure with the capability of achieving considerably greater ratios of k_4/k_3 . As discussed in a latter section, preliminary testing of several prototype designs has indicated attainable ratios of 50, more than double that for the diaphragm flexure.

D-STRUT DESIGN

Performance is not the only consideration in D-Strut design. Strut weight and load capability are two more important considerations. There are four basic elements contributing to strut weight: the inner tube, outer tube, damper elements, and strut end fittings that interface the strut to the structure. A typical damper element employing an *arched* flexure weighs approximately 0.1 lb. The end fittings also tend to have a rather small, fixed weight. Thus, the inner and outer tubes are the major weight contributors that vary in the design process.

The tube stiffness is AE/L and the tube weight is $AL\rho$, where A , L , E , and ρ are the tube cross sectional area, length, material elastic modulus, and material density, respectively. Thus, for a given tube length and a selected material, the tube weight varies in proportion to its stiffness. Therefore, the sum of the inner and outer tube weights, and thus the strut weight varies as:

$$W_i + W_o \sim k_1 \left(a + \frac{k_2}{k_1} b \right) \quad (25)$$

where a and b are constants. The outer tube stiffness k_1 is now the major factor determining the strut's static stiffness (recall that the strut's static stiffness is k_A , which is proportional to k_1). The strut-load requirement essentially establishes k_1 and the strut weight then varies as the stiffness ratio k_2/k_1 .

The strut load requirement leads to consideration of allowable stresses and strains in the strut elements. The two most important elements in terms of stresses are the outer tube and the damper. Consider a static-load condition. If x denotes the resulting static displacement across the strut (outer tube), y denotes the static displacement across the

inner tube, and β denotes the ratio of the displacement across the damper to the displacement across the strut:

$$\beta \equiv \frac{x-y}{x} \quad (26)$$

then the ratio of the axial stress in the damper to the axial stress in the outer tube is proportional to β . An optimal D-Strut design should tend to have the stresses in the damper and outer tube approximately equal.

Therefore, three important considerations in D-Strut design are performance, weight, and allowable stress in the outer tube and damper. At the first level, D-Strut design involves determining values for the five parameters $\{k_1, \dots, k_4, c\}$ to address performance, weight, and allowable stress. Specification of performance in terms of the three parameters $\{\eta^*, \omega^*, zR(\omega^*)\}$ leads to conditions for determining three of the five parameters $\{k_1, \dots, k_4, c\}$. Conditions for determining the remaining two parameters are derived from weight and stress considerations.

To be specific, let the two parameters M and N be defined by:

$$M \equiv \frac{k_2}{k_1} \quad \text{and} \quad N \equiv \frac{k_4}{k_3} \quad (27)$$

M is indicative of D-Strut weight and N is the ratio of the damper's volumetric stiffness to the static stiffness. D-Strut design addressing performance, weight, and stress can be accomplished via the equation:

$$\frac{k_B}{k_A} = \frac{M}{1 + (1 + M)\delta} \frac{N\delta}{1 + (1 + N)\delta} \quad (28)$$

$$\delta \equiv \frac{1 - \beta}{\beta} \quad (29)$$

and the previous equation relating η^* to k_B/k_A . As an example, Figure 5 shows M as a function of N for various values of η^* and a value of $\beta = 0.95$. This figure clearly illustrates the benefit of maximizing the damper's stiffness ratio N . For a fixed level of performance (η^*), maximizing N tends to minimize the D-Strut weight (M). Conversely, for a fixed weight (M), maximizing N leads to improved damping performance (η^*). The *arched* flexure damper, described next, is able to attain values of N greater than 50, which provides a significant improvement over the diaphragm flexure $N = 20$.

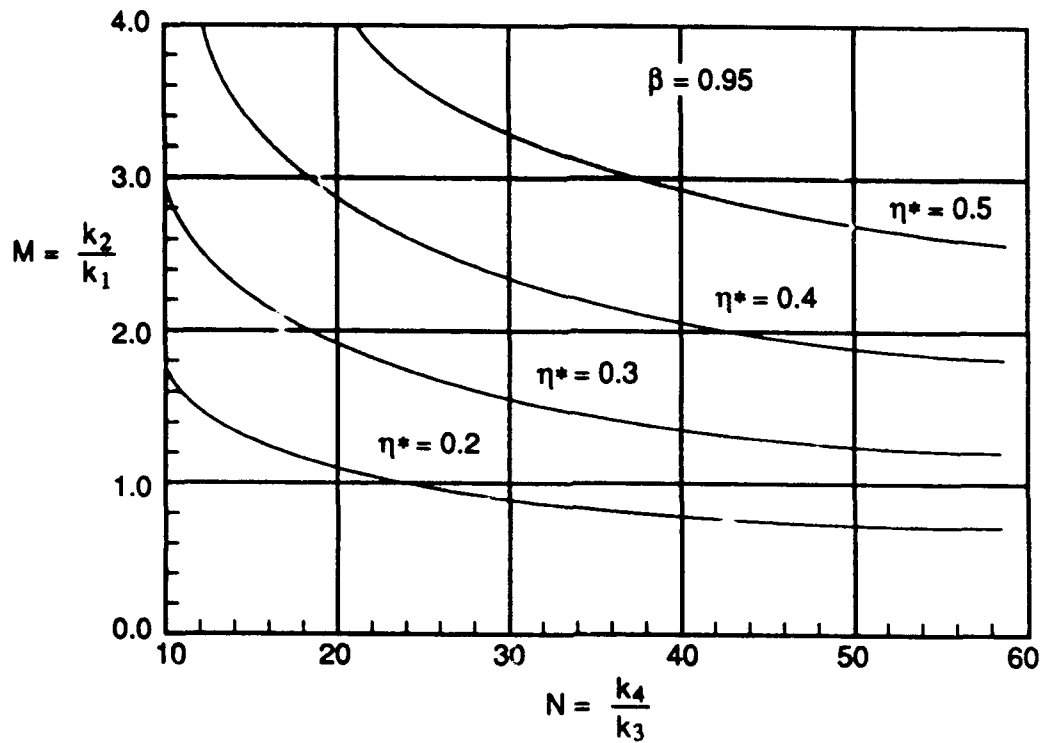


Figure 5. D-Strut Design Curves

ARCHED FLEXURE D-STRUT

The name *arched flexure* was chosen because of the similarity with a two-dimensional semicircular arch. The design is more accurately a convoluted or corrugated cylinder. Figure 6 shows a single-convoluted design and Figure 7 shows a multiconvoluted design.

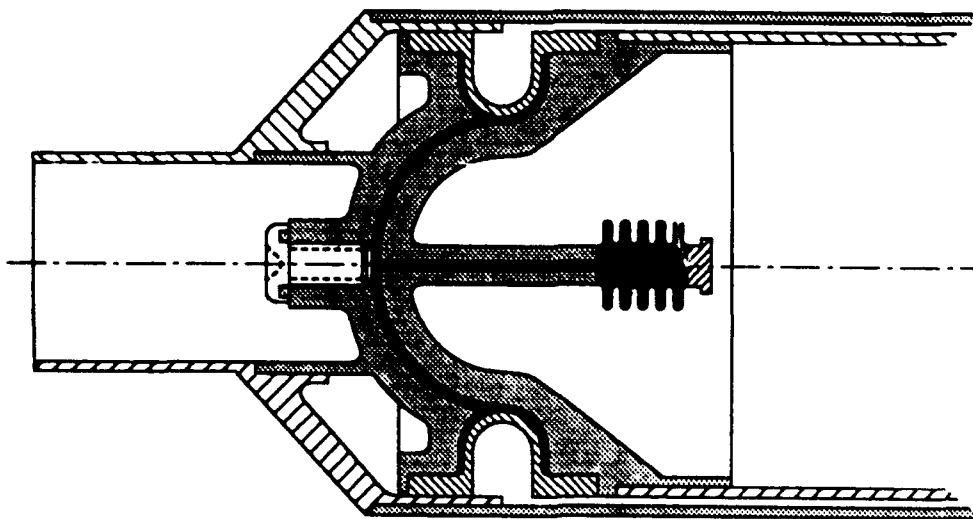


Figure 6. Arched Flexure D-Strut

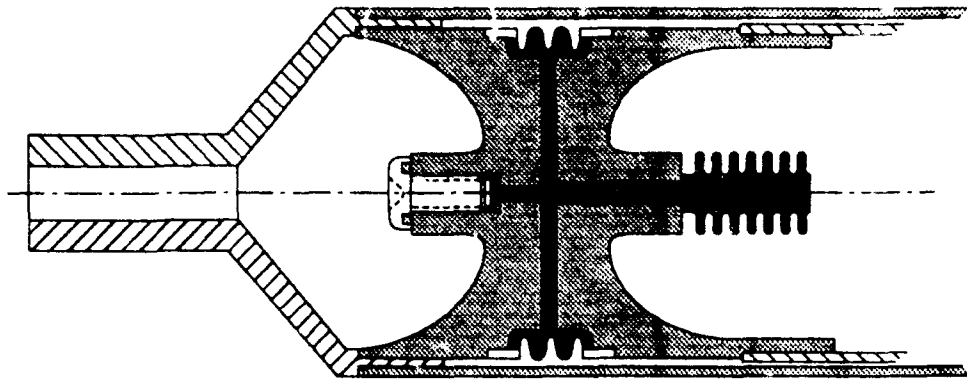


Figure 7. Arched Flexure D-Strut (Multiple Convolutions)

The *arched* flexure configuration was selected because its shape will provide the highest possible ratio of k_4/k_3 , which in turn will minimize the needed ratio of k_2/k_1 . This is equivalent to minimizing k_2 , which will also minimize the weight of the system for a given performance.

The volumetric stiffness, k_4 , can be characterized as a ballooning effect. It specifically is the axial stiffness of the system that would result if the shear annulus were plugged. Both the flexure and the fluid contribute to k_4 . The fluid stiffness is generally not a problem if the depth of the fluid is minimized. The fluid stiffness will range from 1 to 15 million pounds per inch. The D-Strut configuration used in the PACOSS testing, using a diaphragm flexure, typically exhibited a k_3 in the range of 5,000 to 10,000 lb/in. and a k_4 in the range of 100,000 to 250,000 lb/in. The ratio of k_4/k_3 ranged from 20:1 to 25:1.

The *arched* flexure has the potential for much higher values. Several single convoluted systems have been fabricated and tested. The result of the first prototypes was a k_4/k_3 ratio of 52 to 1, or a 2-to-1 improvement over the diaphragm designs. Much higher values are expected with a second-generation design.

The k_4/k_3 ratio of 52 to 1 was obtained by dynamic test methods as opposed to direct static-load testing. In the test setup shown in Figure 8, k_3 was measured by removing the fluid, adapting a known mass, and vibrating the system to determine its resonance. One result of such a test is shown in Figure 9. The resonance was 64.2 Hz. The suspended mass was 23 lb. Thus:

$$k_3 \cong (2 \pi f)^2 \frac{w}{g} = \frac{(2 \pi \times 64.2 \text{ Hz})^2 23 \text{ lb}}{386 \text{ rad/s}^2} = 9686 \text{ lb/in.} \quad (30)$$

To determine k_4 , the fluid cavity was refilled and the annulus plugged. The resulting resonance, shown in Figure 10, is 463 Hz. Thus k_4 is approximated:

$$k_4 \cong (2 \pi f)^2 \frac{w}{g} = \frac{(2 \pi \times 463 \text{ Hz})^2 23 \text{ lb}}{386 \text{ rad/s}^2} = 503,776 \text{ lb/in.} \quad (31)$$

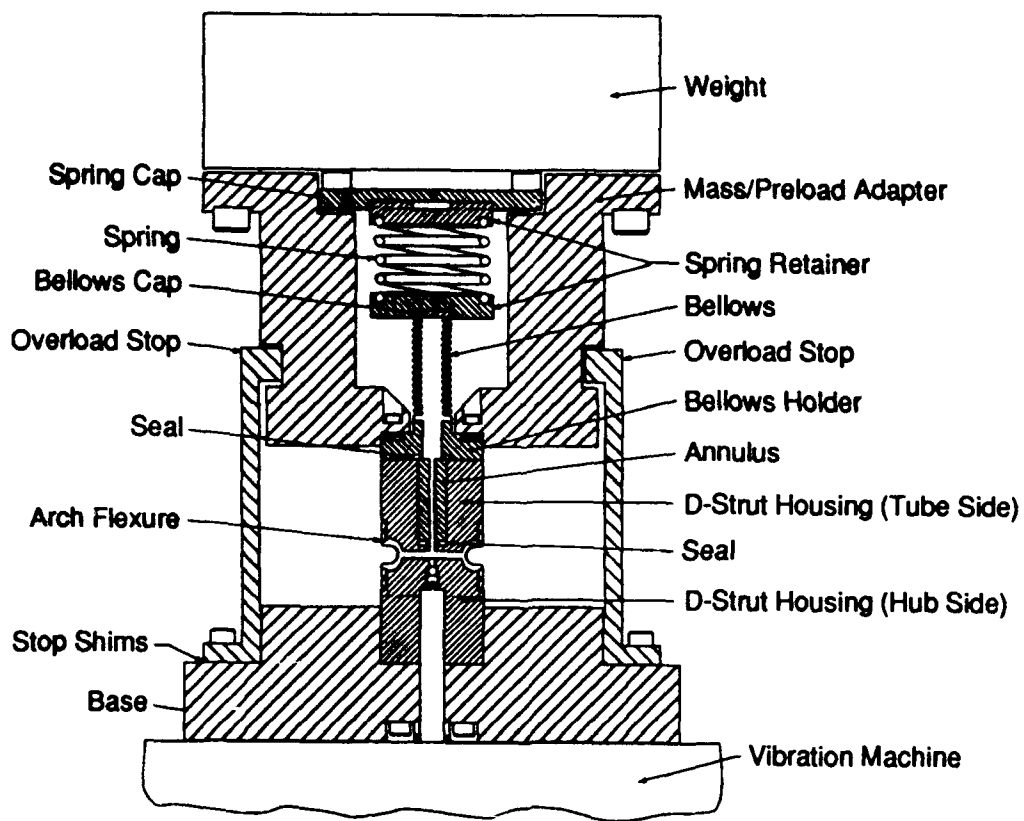


Figure 8. D-Strut Test Setup

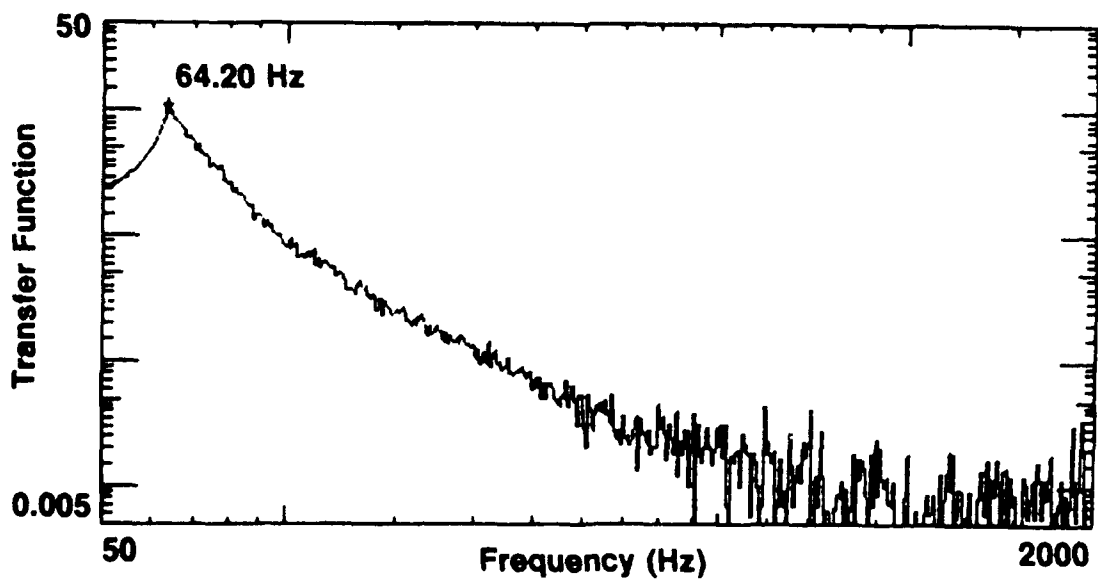


Figure 9. Transfer Function Without Fluid

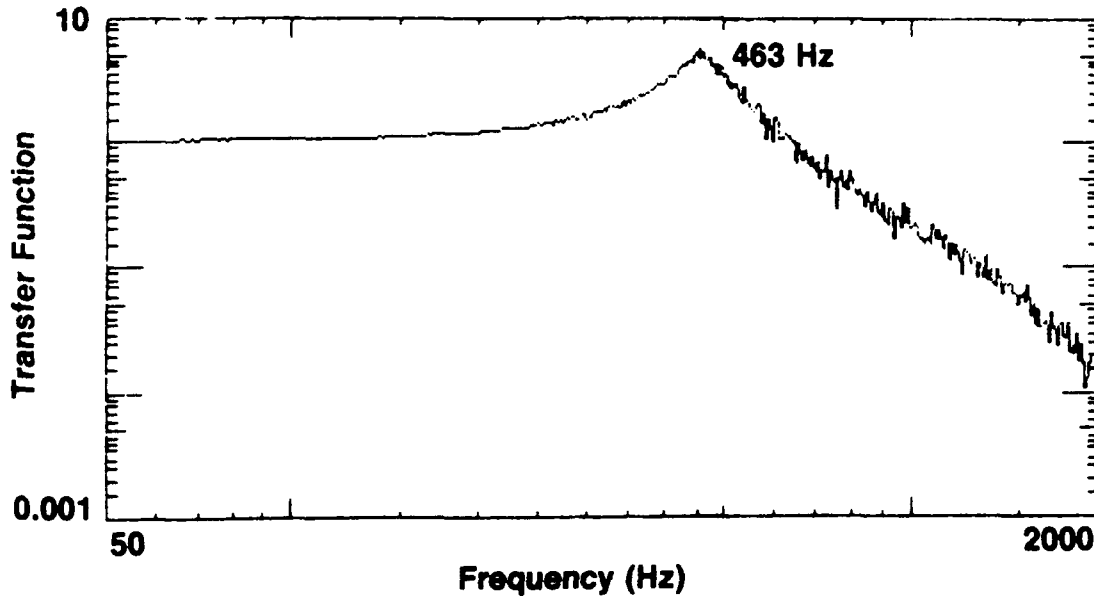


Figure 10. Transfer Function With Annulus Block (With Fluid)

For a ratio:

$$\frac{k_4}{k_3} = \frac{503776}{9686} = 52 \quad (32)$$

Calculations show that the fluid stiffness is 15,000,000 lb/in. Using this value, the metal volumetric stiffness is calculated to be 521,100 lb/in.

Parametric optimization using closed form stiffness equations lead to the conclusion that k_4/k_3 ratios much higher than 52 to 1 can be achieved through parametric optimization. Further, axial strokes can be achieved greater than the deflection capacity of the tubular part of any strut. This means that the addition of a D-Strut element will not reduce the static load capacity of the system. Figure 11 shows a table of *arched* flexure designs that point to these conclusions. Note that design No. 4 approximates the results of the single convoluted design just discussed. This design has one convolution, $N = 1$; the radiu. of the arch is $b = 0.125$ in., the radius of the tube forming the convolute is $a = 0.445$ in.; the OD (outside diameter) of the element is 1.34 in.; the modulus $e = 16$ million lb/in., which corresponds to titanium; the stroke of $s = 0.006$ in. results in a stress of 55,418 psi; $k_3 = 9.68$ klb/in.; $k_4 = 503$ klb/in.; $k_4/k_3 = 52$; the outer tube stiffness $k_1 = 67$ klb/in.; the 3-model equivalent paralleled spring stiffness $k_A = 76$ klb/in.; the inner tube stiffness $k_2 = 165$ klb/in.; and the 3-model equivalent series spring stiffness $k_B = 156$ klb/in. In this case, k_1 and k_2 were somewhat arbitrarily selected to represent the character of the PACOSS structure. k_1 and k_2 were not part of the testing: only the basic D-Strut element was tested. However, previous correlation

between D-Strut element tests and D-Strut tests is evidence that this process is accurate. Notice that the damping loss factor $\text{ETA} = 0.586$ or 58% (in the text ETA is N). Had k_4/k_3 been larger than 52, ETA would have been larger. Also the effective damping constant (C_A) = 1784.5 lb-s/in. would have been closer to the actual damping constant (c_1) = 2000 lb-s/in. Notice further that the range of frequencies where the damping is effective from $\text{OMEGA A} = 4.56$ Hz (minimum) to $\text{OMEGA A}^* = 7.97$ Hz (maximum).

DSGN	(n)	(b)	(a)	(OD)	(t)	(e)	(s)	sigma 1	(k ₃)	(k ₄)	(k ₄ /k ₃)
1	1	0.15	0.445	1.39	0.006	16.00	0.006	49,073	8.06	255	32
2	1	0.125	0.445	1.34	0.012	16.00	0.007	81,497	38.71	1,006	26
3	1	0.125	0.445	1.34	0.015	16.00	0.006	75,260	60.49	1,258	21
4	1	0.125	0.445	1.3	0.01	16.00	0.006	55,418	9.68	503	52
5	1	0.125	0.6	1.65	0.01	16.00	0.006	53,849	26.88	2,425	90
6	2	0.125	0.6	1.65	0.006	16.00	0.014	52,970	4.84	727	150
7	2	0.125	0.8	2.05	0.005	16.00	0.018	52,892	3.36	1,611	480
8	4	0.125	0.8	2.05	0.006	16.00	0.036	56,213	2.42	967	400
9	6	0.1	0.8	2	0.003	16.00	0.06	57,503	0.50	673	1,336
10	10	0.1	0.8	2	0.003	16.00	0.1	57,503	0.30	404	1,336
	(k ₁)	(k _A)	(k ₂)	(k _B)	ALPHA	(ETA)	(c ₁)	(c _A)	OMEGA A	OMEGA B	OMEGA
1	67	75	165	157	1.76	0.598	2000	1817.9	4.44	13.78	7.82
2	67	98	165	134	1.54	0.442	2000	1312.1	6.88	16.22	10.56
3	67	111	165	121	1.44	0.376	2000	1070.9	8.61	17.95	12.43
4	67	76	165	156	1.75	0.586	2000	1785	4.56	13.91	7.97
5	67	90	165	142	1.60	0.491	2000	1478.9	5.93	15.28	9.52
6	67	72	165	180	1.80	0.621	2000	1887.7	4.18	13.52	7.52
7	67	70	165	162	1.82	0.633	2000	1921	4.06	13.40	7.38
8	67	69	165	163	1.83	0.641	2000	1942.6	3.99	13.33	7.29
9	67	68	165	164	1.85	0.657	2000	1987.8	3.83	13.18	7.11
10	67	67	165	165	1.86	0.659	2000	1992.7	3.82	13.16	7.09

Poisson's Ratio (ν)	(b) Arch Radius	(n) Number of Convolutions
Number of Convolutions (n)	(t) Thickness	(OD) Outside Diameter
Stroke (s)	(a) Tube Radius	(k ₁) Outer Tube Stiffness
Validation Factor $4 < u < 40$	(e) Modulus of Elasticity	(k ₂) Inner Tube Stiffness
Load to Produce Deflection (p)	(k ₃) Axial Stiffness of Arch	(c ₁) Two Spring Damping Coef
SIGMA 1 - Stress	(k ₄) Volumetric Stiffness	(c _A) Four Spring Damping Coef
SIGMA 2 - Stress		

Figure 11. Damping Spring Design Alternatives (D-Strut)

Two questions arise, as follows:

- How high must the ratio of k_4/k_3 be to obtain practically ideal performance?
- Once this ratio is known, can the D-Strut be optimized to provide that capability?

To answer these questions, compare the sample designs shown (designs 1 through 10 in Figure 11), and consider the values of k_4/k_3 . Notice that, as the design parameters of the

arched flexure change, substantial improvement in k_4/k_3 is realized, particularly for designs 9 and 10 ($k_4/k_3 = 1,336$). Also notice that, for these designs, $c_1 \approx c_A$, $k_1 \approx k_A$, $k_2 \approx k_B$. Therefore, it is clear that this value of k_4/k_3 results in essentially ideal performance and further increase will not produce additional value. Further analyses of the 10 designs suggest that values of k_4/k_3 above 100 are of little additional benefit. It should also be clear from this data that a second-generation *arched* flexure D-Strut, with better parametric optimization, could easily reach the $k_4/k_3 > 100$ level. The more optimum design would appear to be a multiconvolved design not only because of the better k_4/k_3 ratio, but also because of the large stroke capacity.

The data presented here suggest near-perfect correlation between empirical data and analytical calculations for stiffness. Actually this was not the case; some substantial differences existed. Specifically, the coefficient of the equation for k_3 was factored by 1.156 and for k_4 by 2.35. Therefore, only limited value can be placed on the specific numerical results. The factors were applied to facilitate limited design trades and trend considerations.

The reason for these discrepancies is believed to be primarily the differences between the actual thickness of the flexures manufactured and the intended design thickness. Improved controls are planned for future parts. Some error has likely been contributed due to the limitations of the equations used. We are currently conducting fundamental work to improve these.

FUTURE PLANS

Future plans for the D-Strut involve further improvements in the damper element of the strut, based substantially on the factors and optimization trends discussed in the preceding paragraphs. A multiconvolved design will be a first priority.

Another factor significantly influencing D-Strut performance is the ratio of inner-to-outer tube stiffness. D-Struts fabricated to date have used the same material for inner and outer tubes. The lengths of the two tubes are also approximately equal. Thus, using the same material for both tubes, the only way to increase the stiffness ratio k_2/k_1 is to either decrease the outer tube cross sectional area or increase the inner tube cross sectional area. Decreasing the outer tube area will affect static stiffness requirements, while increasing the inner tube area leads to a considerable weight penalty.

An obvious alternative is to use different materials for the inner and outer tubes. For example, an aluminum outer tube with a metal matrix composite inner tube would give a factor of 2 improvement in the ratio k_2/k_1 , due solely to the difference in the modulus of elasticity. The use of different materials for the inner and outer tubes is an important aspect under investigation.

Of course, for a nonload-bearing strut, the outer tube may be eliminated, providing a significant improvement in damping. Other factors then become important. To date, no D-Struts have been fabricated without an outer tube. There are applications where this will be an important consideration.

REFERENCES

- [1] Davis, L.P. and Wilson, J.F., "Very High Damping in Large Space Structures", ASME Vibrations Conference, Boston, MA, 1987.
- [2] Davis, L.P. and Wilson, J.F., "New Structure Design Criteria Offer Improved Pointing and Lower Weight", 59th Shock and Vibration Symposium, Albuquerque, NM, October 1988.
- [3] Cunningham, D.C., "Final Technical Report PACOSS D-Strut Development", Prepared for Martin Marietta, Honeywell Inc., Satellite Systems Operations, Glendale, AZ, August 1990.
- [4] Roddeb, J.J., Dougherty, H.J., Reschke, L.F., Hasha, M.D., and Davis, L.P., "Line of Sight Performance Improvement with Reaction Wheel Isolation", AAS Guidance and Control Conference, Keystone, CO, February 1986.
- [5] Davis, L.P., Wilson, J.F., and Jewell, R.E., "Workshop on Structural Dynamics and Control Interaction of Flexible Structures", NASA Marshall Space Flight Center, Huntsville, AL, April 1986.

TESTING OF A VISCOUS-DAMPED ISOLATOR

Bradley Allen*
CSA Engineering, Inc.
Palo Alto, CA

David Cunningham
Honeywell Satellite Systems
Glendale, AZ

ABSTRACT

It is essential that accurate methods for testing mechanical properties be employed during the development of precision spacecraft isolation systems. Mechanical properties of the isolator will determine force transmission to the spacecraft; thus they are critical to its performance. This paper documents component-level tests performed on viscous-damped isolators developed by Honeywell Satellite Systems for a spacecraft reaction wheel isolator system.

Two types of component-level tests were performed on the elements: direct stiffness measurements (often called mechanical impedance) and transmissibility tests. Direct stiffness measurements indicated linearity, linear stiffness, damping, and hysteresis. A custom test apparatus was designed for accuracy and repeatability. Stiffness deviations as small as 5 percent could be detected, and loss factors as low as 0.01 could be resolved with the direct stiffness measurements.

Motion transmissibility measurements determined high-frequency isolation and verified stiffness and damping near the predicted resonance of the sprung payload. Although the suspension system consisted of eight isolators, tests were performed on a single unit. Motion was constrained to a single degree of freedom using a system of air bearings sliding on rails. The air bearing design possessed less than 0.4 grams of friction allowing verification of isolation properties to above 300 Hz and enabled transmissibility to be accurately measured over 4 orders-of-magnitude of input excitation.

*CSA Engineering, Inc., 560 San Antonio Road, Suite 101, Palo Alto, CA, (415) 494-7351

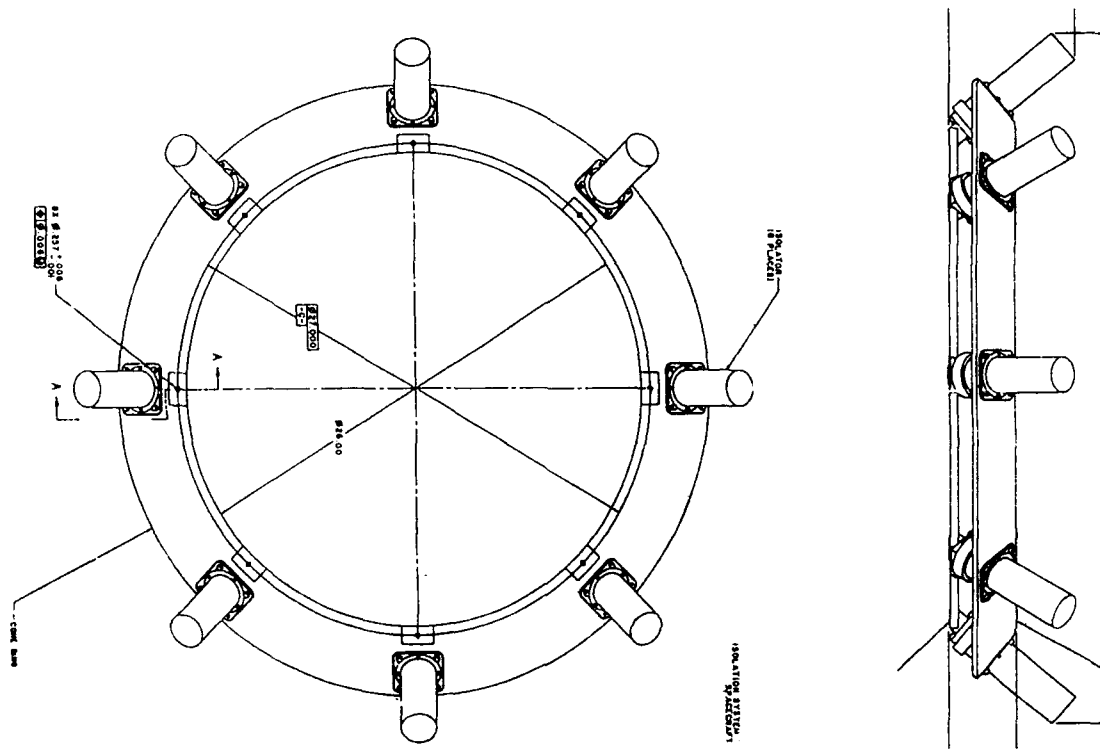


Figure 1. Reaction wheel isolation system

1. Introduction

Viscous damper designs are finding wider applications in spacecraft; demands for lower ambient vibration levels coupled with the predictability and simplicity of viscous dampers make them a good choice for many damping applications in space. This paper addresses test techniques used to characterize the mechanical properties of an isolation system by testing its components: viscous-damped isolators.

The isolators are used to suspend the momentum wheel on a spacecraft. The suspension consists of eight isolators placed symmetrically around the frame of the momentum wheel, as shown in Figure 1. Machined metal springs provide elastic forces with nearly isotropic stiffness, but the damping mechanism applies dissipative forces primarily along the element's axis. These isolators are designed to behave with a linear force-deflection relationship and an axial stiffness of approximately 950 lbf/in up to a stroke limit of 0.044 inches. Mechanical stops dramatically increase the stiffness outside this operational region.

Isolation performance was specified for the system to tolerances that required repeatable and predictable mechanical performance. Transmissibility was specified to 300 Hz, such that modes introduced by the isolators could not obstruct the transmissibility below 300 Hz.

2. Test Method

Tests documented in this paper were performed at the component level. Component or element level testing provides detailed characterization data such as linearity, hysteresis, damping variation with excitation levels and temperature, and other variations in mechanical performance between isolators. Measurements of both axial and radial properties were made. Component-level tests were performed to acquire data necessary for the design of the isolators, and system-level tests subsequently verified that component-level test results could be extrapolated to system level performance.

Two approaches were implemented at the component level: direct complex stiffness (DCS) methods and resonant tests. DCS methods use the force through and displacement across a specimen to calculate the complex stiffness of a specimen directly at frequencies well below the resonances of the test assembly. Under this condition, the elastic stiffness is the real part of the ratio between force and displacement, and damping is calculated from their phase difference. Resonant tests infer the mechanical properties of a resonant system through an analytical model where modal frequencies and damping ratios are inputs, and specimen stiffness and damping are outputs. A single-degree of freedom system was constructed for these tests with a one-eighth-scale mass sprung on one of the eight isolators. The ratio of acceleration across the masses was measured to construct a dimensionless function of frequency known as transmissibility.

DCS tests yielded the majority of the mechanical property data on the isolators. A DCS test assembly was designed which could measure the unidirectional mechanical properties in both the axial and radial directions of the isolator. Figure 2 shows the test assembly for the axial configuration. Motion was constrained to one degree-of-freedom by the pushrod and linear bearings. Measurement bandwidth of the assembly was from DC to 96 Hz, limited on the high end by the resonant frequency of the isolator and sprung fixture.

Transmissibility tests verified high frequency isolation, enabled testing over a wide dynamic range, and provided verification of stiffness and damping at a single frequency for verification of the DCS test results. Isolation performance at high frequency was verified by continuation of transmissibility roll off with increasing frequency.

Transmissibility measurements utilized a test assembly that simulated a single-degree of freedom system. It restricted motion across the isolator to one direction without exerting forces in the unconstrained direction. Figure 3 shows the apparatus while outfitted for axial measurements. The center mass floats on the rails through air bearings. Two center masses were designed for the radial and axial test configurations. The rails and external mass simulate a rigid massive mounting base which translates to provide unidirectional excitation. Transmissibility is measured along the axes of the rails, and is calculated as the ratio of the acceleration seen at the floating mass to that at the base. The center mass was sized to one-eighth that of the system level, since only one of eight isolators was under test at any instant in the component-level tests.

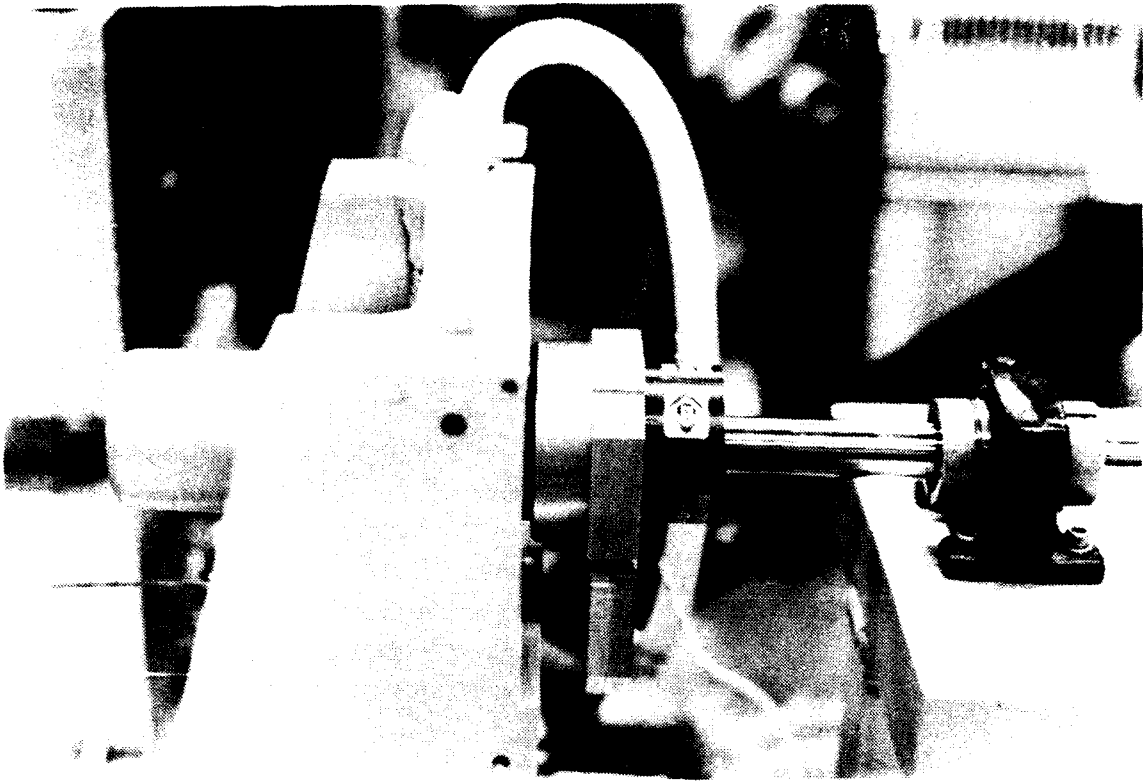


Figure 2. DCS test assembly in the axial configuration

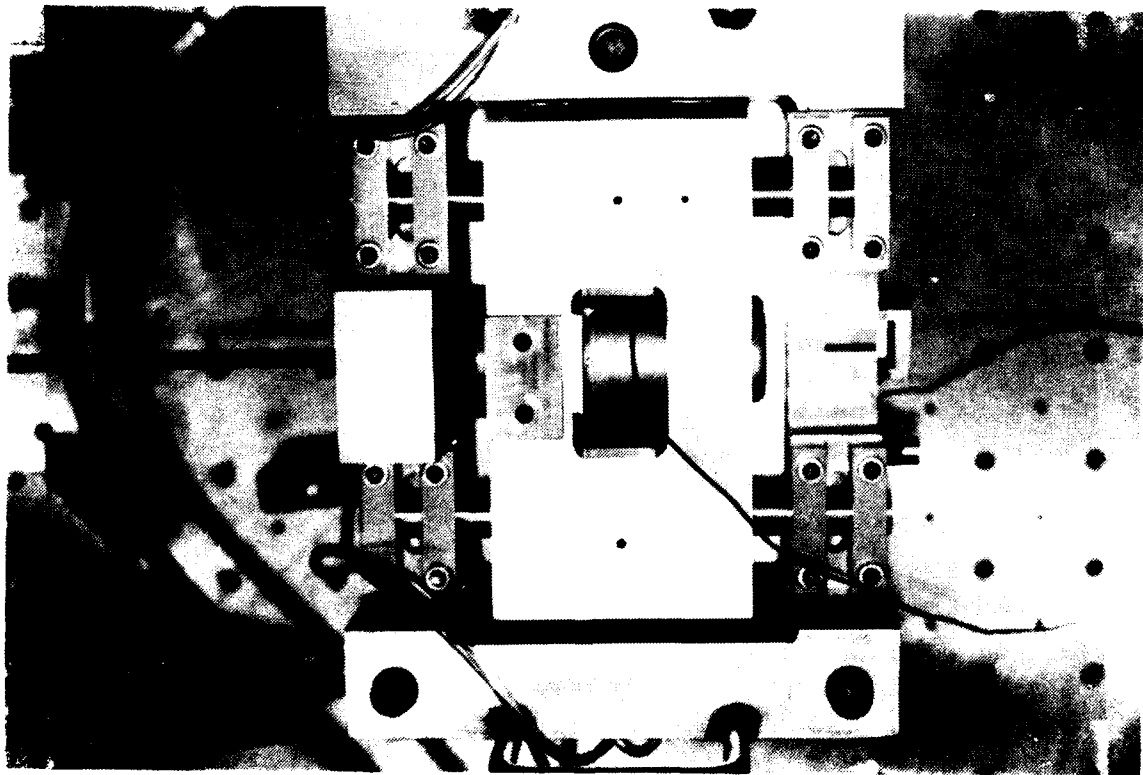
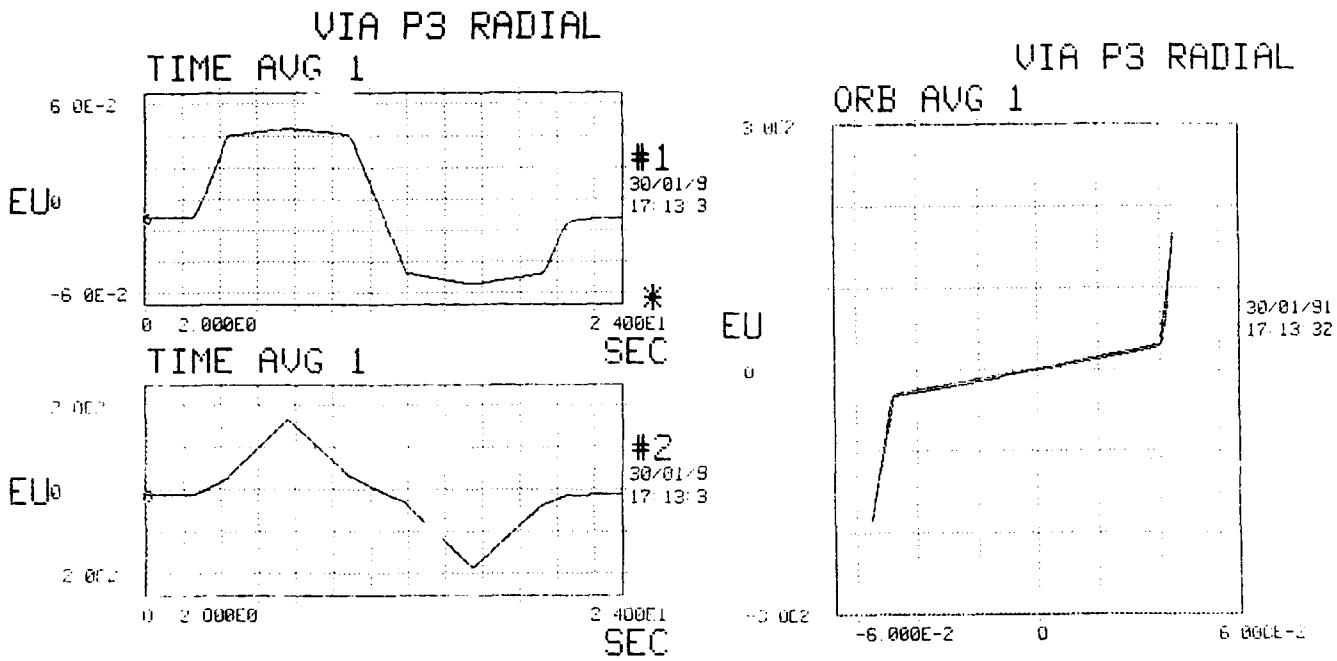
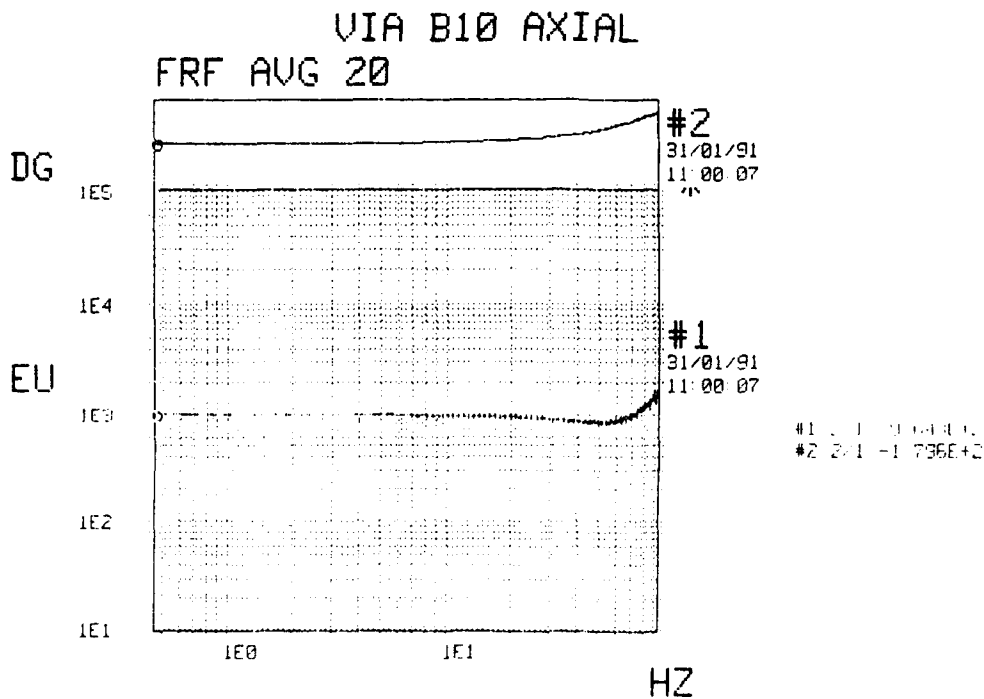


Figure 3. Transmissibility test assembly in the axial configuration



$$x = 2.500E-2$$

Figure 4. Pseudo-static DCS test data.



$$x = 4.688E-1$$

Figure 5. Dynamic DCS test data.

3. Results

DCS tests proved particularly useful for development testing because of the availability of force and deflection as functions of time under various forms of excitation. A sawtooth wave with a period of 20 seconds was applied to obtain the data shown in Figure 4. The plot force versus deflection clearly exhibits a linear relationship up to the stop locations at either end of its stroke. Stop stiffness can also be measured from the graph. One measurement identifies hysteresis, linearity between force and deflection, stiffness, and location of travel restricting stops. Broadband dynamic tests indicated stiffness and damping of isolators. Band-limited white noise excitation and Fast-Fourier Transform methods enabled the instantaneous acquisition of data across an entire measurement bandwidth. Figure 5 shows the resulting curve of complex stiffness. Magnitude and phase are shown, although the elastic stiffness is actually the real part of the magnitude, and the loss factor is the tangent of the phase angle between force and displacement. Deviations from constancy of these parameters above 30 Hz is caused by the mass of the load cell and adapter plate and is not indicative of the isolator stiffness.

Transmissibility data demonstrated the repeatability and precise performance of the viscous damped isolators; however, the rigidity of the test fixture fell short of the specifications requiring a bandwidth of 300 Hz. A sizeable mode appeared to obstruct isolation of the system near 300 Hz. Figure 6 shows a typical transmissibility plot as measured. The base mass was supported on flexures to permit unidirectional motion, and tests mentioned below indicated that an extensional mode of the flexures was partially responsible for the obstruction.

Modal tests were performed on the transmissibility test apparatus to identify the harmful mode and exonerate the isolator. It was removed and small compression springs were installed in the tester to provide a centering stiffness with negligible added mass to the tester frame. Mode shapes for both axial and radial tester configurations are shown in Figure 7. The external box frame represents the outline of the base mass, and the smaller frame outlines the center mass. Shapes from axial and radial tests are nearly identical. Strain energy is concentrated in the flexures that support the base, as evident by the tilting base mass, and somewhat in the flexible mounts of the air bearings as indicated by the relative motion between the two apparently rigid bodies.

The detrimental mode was identified as a property of the test apparatus and subtracted from subsequent transmissibility measurements. It was modeled as a second-order system as is commonly done in test-acquired modal data, and its transmissibility was subtracted from the measured transmissibility. Figures 8 and 9 contain plots of the pre- and post-processed data. The first is an overlay of the raw transmissibility curve and the generated response for the detrimental mode at 280 Hz. Figure 9 is their difference, the post-processed data.

The viscous damped isolators operate in a low-level vibration environment, and tests were performed to verify linearity across a range of excitation levels. Limitations in the test apparatus and instrumentation limited measurements of dynamic range to

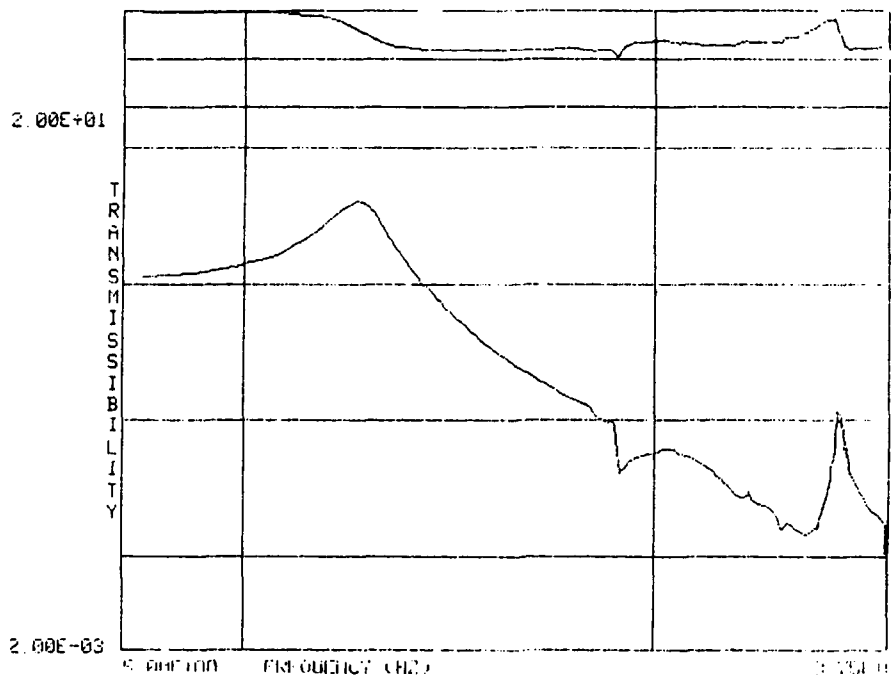
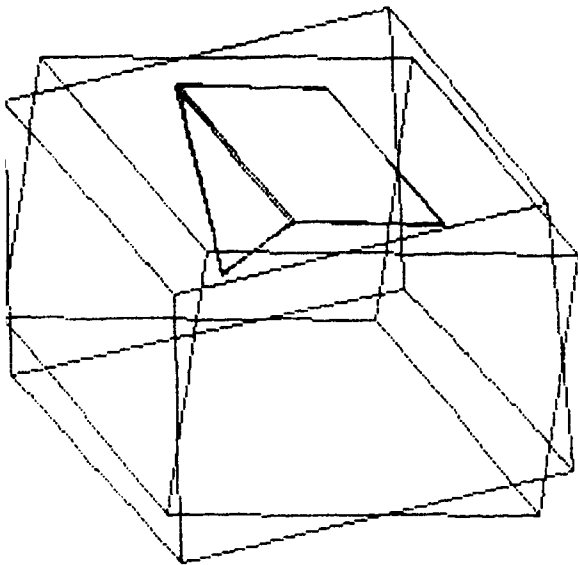
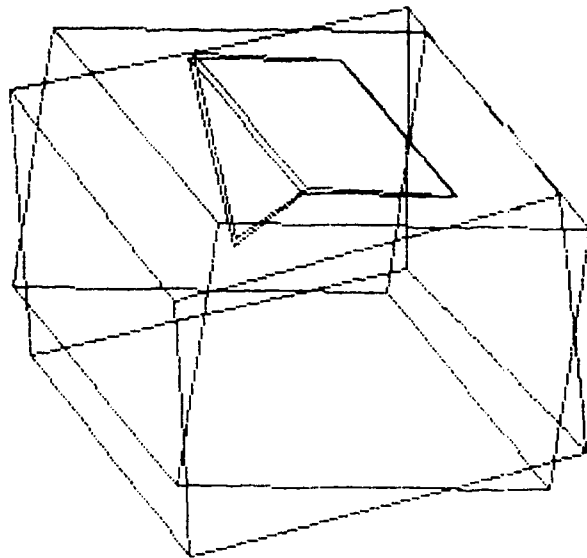


Figure 6. Unprocessed transmissibility data in axial configuration.



Axial Configuration



Radial Configuration

Figure 7. Mode shapes of detrimental resonance for axial and radial test configurations.

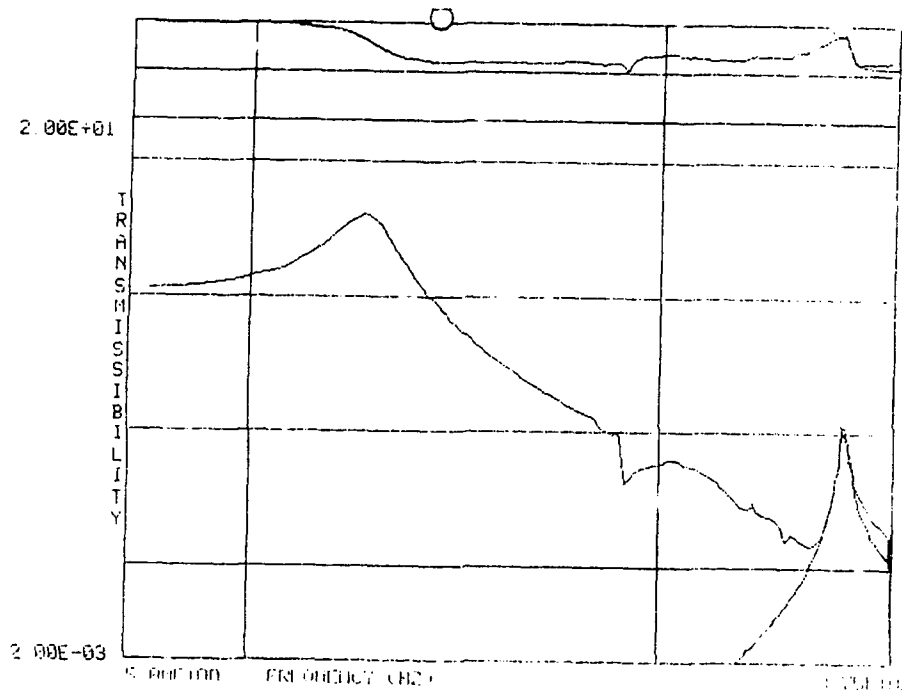


Figure 8. Unprocessed transmissibility overlaid with synthesis of reconstructed mode.

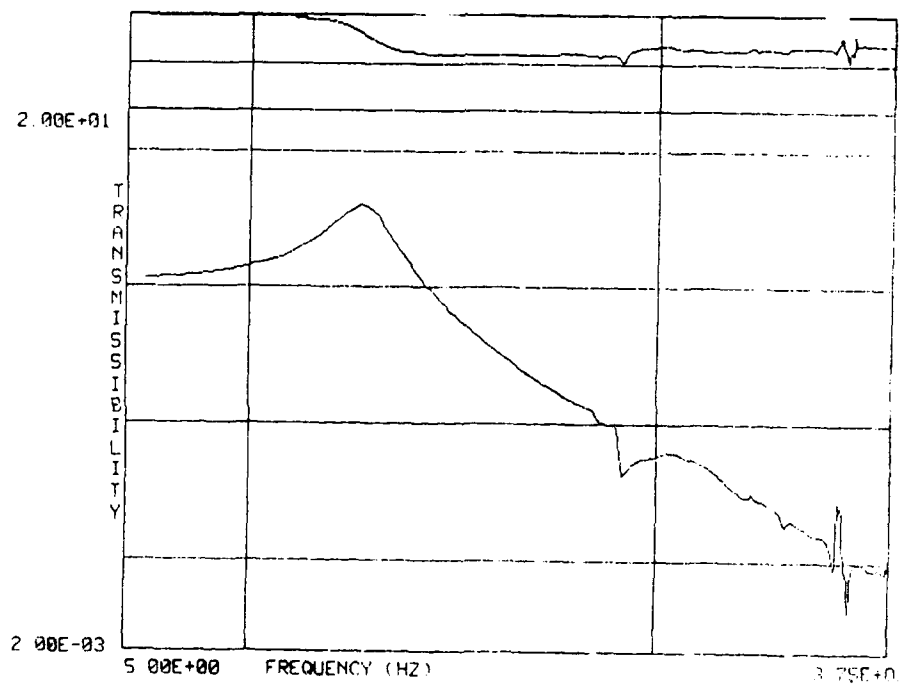


Figure 9. Post-processed transmissibility data.

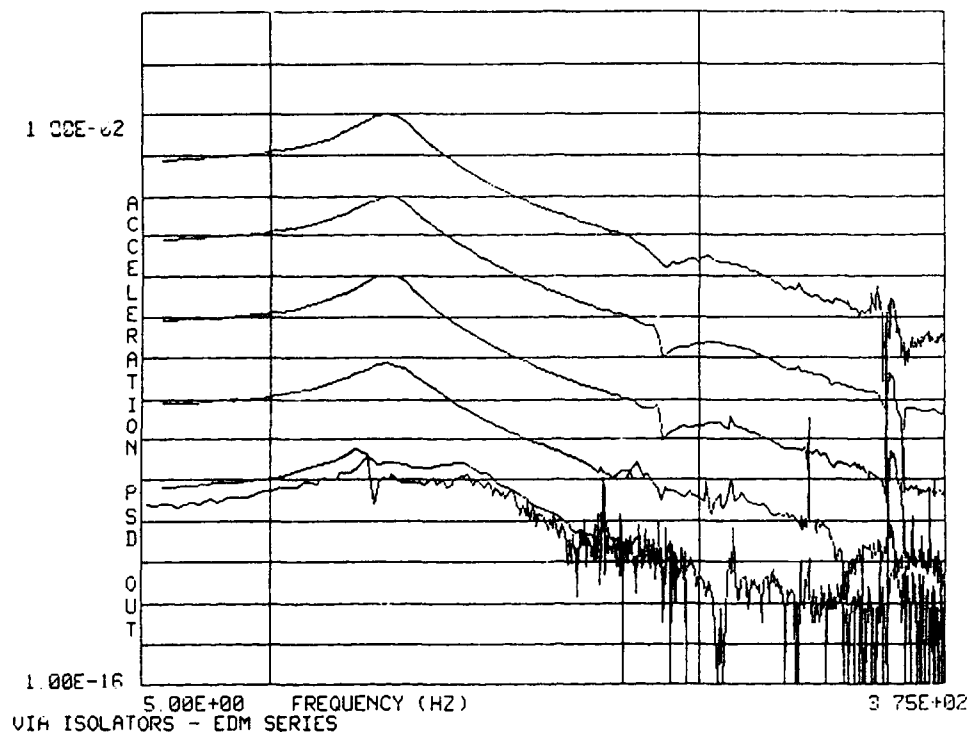


Figure 10. Acceleration Power Spectral Density of Isolated Mass for White Noise Excitation

90 dB, from 25 micro-Gs to 1.5 Gs rms. Figure 10 is a plot of the output acceleration PSD for a white noise input from 1 to 375 Hz. Because white noise is a constant level, the character of the curve is identical to the corresponding transmissibility function at each level. At base acceleration levels of 50 micro-Gs rms and below (lowest level curve), a subtle changes in the shape of the transmissibility function became apparent, and a limited amount of troubleshooting tests were performed. They indicated that restoration force well below 0.04 lbs was being introduced by the tester assembly and is related to the air pressure in the air bearings. Since this level was below the required specifications for the isolator, it was not pursued further.

4. Summary and Conclusions

Component level tests provide accurate characterization of the mechanical properties of the viscous damped isolators. DCS tests were most effective for verification of linearity, static force-deflection information, and stiffness and damping properties at frequencies well below that of the DCS test assembly. Resonant methods proved more effective for examination of the roll off in transmissibility at high frequency and for acquiring data across a wide dynamic range of input excitation levels.

Tests indicated that the viscous damped isolators performed as predicted, with repeatable and precise mechanical properties. They behaved linearly from 25 micro-Gs to 1.5 Gs, with precise stiffness and damping properties.

**THE EFFECT OF SOURCE IMPEDANCE
ON
DAMPING MEASUREMENTS
USING
RESONANCE DWELL TESTING**

by
Ralph E. Tate
LTV Aircraft Products Group
Dallas, Texas

ABSTRACT

J.C. Heine developed a test methodology for evaluating the damping in various materials, particularly metals. LTV employs a resonance dwell technique adapted from that of J.C. Heine, which facilitates the use of a smaller shaker from that normally required. This test apparatus permits the rapid characterization of viscoelastic laminates not only for damping, but also for vibroacoustical fatigue resistance.

During check-out of the modified apparatus, it was found that the behavior of damped specimens differed markedly from prior results. That is, significantly higher values of damping were observed regardless of measurement technique. The author demonstrates, through the use of impedance modeling techniques, that the differences arise from the coupling the specimen to the electrodynamic of the excitation source. A refinement of the test procedure is outlined to remedy the data anomaly and a discussion of the impact on the interpretation of damping data naturally follows.

1.0 INTRODUCTION

Various techniques are employed throughout industry to evaluate the complex modulus of viscoelastic materials. Perhaps, the most common techniques are the "Oberst" beam-type tests that are prescribed in the ASTM standards [1]. The simplicity of the test method affords rapid evaluation of a candidate viscoelastic with a minimal investment in material and equipment.

The cited standard, ASTM E756-83 [1], provides three alternative cantilever beam test specimen configurations, depending on whether shear or tensile modulus is to be measured. The standard presumes base motion acceleration excitation. The standard also provides a set of equations to compute the viscoelastic's material loss factor from the specimen's sample loss factor, based on the Ross-Kerwin-Ungar (RKU) equations for damped laminates.

LTV employs a resonance dwell methodology adapted from that of JC Heine [2], which facilitates the use of a smaller shaker. The test apparatus is depicted in Figure 1. This particular testing apparatus permits evaluation of viscoelastic laminates not only for damping properties, but for vibro-acoustical fatigue resistance, as well. This paper describes the analytical mechanics of this method of resonance dwell testing of constrained layer laminates, based on a motivating example arising from adaption of the test apparatus to perform fatigue testing. Further, comparisons of test results from resonance dwell testing to published nomogram data for viscoelastic materials are discussed .

2.0 "HEINE'S" METHOD

JC Heine developed a test methodology for evaluating the damping in various materials, particularly metals (cf. Figure 1)[2]. A test beam is clamped into the root lever arm. Then, a constant shaker force is applied to the lever near the root of the beam. The shaker force is varied until the tip deflection peaks and the root acceleration simultaneously minimizes. At that frequency, the test beam is said to be at resonance.

The prescription works due to the high stiffness of the lever relative to that of the test specimen. Effectively, the system is rendered mechanically uncoupled; that is, the test beam resonance is identical with that obtained from a cantilever beam under base motion excitation. Given the resonance frequency and tip deflection, the modulus and loss factor for a given material are easily estimated. For a damped constrained layer laminate, the sample loss factor is given by

$$\eta_s = \left(\frac{\phi_n a_R}{\pi^2 V_t f_d^2} \right) \frac{(\sigma_n / \lambda_n)}{[1 - f_0 / f_d]} \left(1 + \frac{L_B}{\sigma_n \lambda_n L_R} \right),$$

and the dynamical shear modulus is given by,

$$G = 4\pi^2 f_d^2 [1 - (f_0 / f_d)^2]$$

$$\times \left(\frac{m_B t_3 L_B^2}{W \sigma_n \lambda_n (2 + \sigma_n \lambda_n) d^2} \right).$$

(variables defined at end of paper)

3.0 TEST RESULTS

Although Heine developed his apparatus to study lightly damped materials such as metals, it is just as applicable to the testing of highly damped laminates. Further, after reduction of the lever arm stiffness, the apparatus can be effectively used to evaluate the vibroacoustical fatigue resistance of damped laminates. It then differs from many similar devices in that it provides levels of stress that are experienced by aircraft structures, while using a smaller and less expensive shaker. It was found that the behavior of the modified apparatus during tests of highly damped specimens differs markedly from its behavior during tests of lightly damped test specimens.

Some typical results of a damped constrained layer test specimen in the adapted Heine test apparatus are depicted in Figure 2. The tip deflection curve in Figure 2 was generated using the procedure developed by Heine. The transfer function shown in that figure was computed between the root acceleration and the tip deflection, as a check on the procedure. The tip deflection indicates a broader damping than the transfer function, based on standard half-power estimates [3]. Further, the tip deflection shows a lower peak frequency, and the acceleration minimized with the transfer function. Since these peculiarities of the transfer function and the base acceleration had not been observed during previous testing of lightly damped specimens, interpretation of the data became ambiguous.

A strain gage was affixed to the root of the test beam, and the test repeated. Figure 3 shows that the tip deflection and the root strain track together. Then a controller was added to maintain a constant root acceleration. Figure 4 shows that the tip deflection (as well as the root strain, not depicted) and the transfer function agree in damping and frequency, when the base acceleration is controlled. This behavior conflicts with the procedure defined by Heine.

Several indications of maximum response for damped test specimens are displayed in Figure 2 through 4. How, then, should the resonant frequency be identified, and how should the damping of the specimen be determined, once the resonant frequency is identified? The mathematical analyses described below were undertaken to answer those questions.

4.0 EQUATIONS OF MOTION

The equations of motion for the resonance dwell apparatus were developed using a standard energy method approach [4,5,6]. The analytical model used the geometry described in Figure 5. That test specimen is a laminate encompassing a constrained layer of viscoelastic damping material, as shown in Figure 6. The assumed deflection of the system is (tensor summation assumed over free subscript indices, 1 to N):

$$v(x,t) = x \alpha(t) \underline{H}(x) + \phi_i(x-L_R) v_i(t) \underline{H}(x-L_R).$$

The virtual work due to bending of the face sheets, as shown in Figure 6, can be computed as:

$$\delta W_B = \int_{L_R}^{(L_R+L_B)} [(EI)_1 + (EI)_2] v'' \delta v'' dx,$$

$$= [(EI)_1 + (EI)_2] \underline{X}_{4,i} v_i \delta v_j,$$

where

$$\underline{X}_{4,i} = \begin{cases} (\beta_i)^4 L_B, & (i=j) \\ 0, & (i \neq j, \text{ orthogonality}). \end{cases}$$

Analogously, the virtual work from lever flexure is:

$$\delta W_R = K_R \alpha(t) \delta \alpha(t).$$

Assuming plane sections of the laminated test specimen remain plane, and given that G^* is the complex shear modulus of the constrained damping material shown in Figure 6, the virtual work due to shearing is [4,7]:

$$\delta W_s = \int_{L_R}^{(L_R+L_B)} t_3 G^* \gamma(x,t) \delta \gamma(x,t) dx,$$

$$= d^2 (G^*/t_3) \underline{X}_{1,j} v_i \delta v_j, \text{ where}$$

$\underline{X}_{1,j}$ is defined as,

$$\begin{cases} \sigma_i \beta_i (2 + \sigma_i \beta_i L_B) & (i=j) \\ \left(\frac{4\beta_i \beta_j}{\beta_i^4 - \beta_j^4} \right) [(-1)^{i+j} (\sigma_j \beta_i^3 - \sigma_i \beta_j^3) - \beta_i \beta_j (\sigma_i \beta_i - \sigma_j \beta_j)] & (i \neq j). \end{cases}$$

The virtual work performed by the inertial forces can be similarly obtained. The virtual work due to acceleration of the lever arm is:

$$\delta W_L = -[J_R + M_R (L_R/2)^2] \ddot{\alpha}(t) \delta \alpha(t)$$

$$= -I_R \ddot{\alpha}(t) \delta \alpha(t).$$

The virtual work due to beam acceleration is ($\mu = [\rho_1 t_1 + \rho_2 t_2 + \rho_3 t_3]$):

$$\delta W_{B2} = -\mu \int_{L_R}^{(L_R+L_B)} \ddot{v}(x,t) \delta v(x,t) dx$$

$$= -\mu [\underline{X}_1 \ddot{\alpha} \delta \alpha + \ddot{\alpha} \underline{X}_{2,i} \delta v_i + \delta \alpha (\underline{X}_{2,i} \ddot{v}_i) + \underline{X}_{3,i} \ddot{v}_i \delta v_i],$$

where

$$\underline{x}_1 = \left[\frac{(L_R + L_B)^3 - L_R^3}{3} \right],$$

$$\underline{x}_{2,i} = \left[\frac{2L_R \sigma_i}{\beta_i} \quad \frac{2}{\beta_i^2} \right],$$

$$\text{and } \underline{x}_{3,i} = L_B.$$

Employing the identical prescription, the virtual work performed by the applied forces becomes, including base motion:

$$\delta W_{nc1} = F L_R \delta \alpha,$$

$$\delta W_{nc2} = \frac{-M_R a_B L_R}{4} \delta \alpha, \text{ and}$$

$$\delta W_{nc3} = \mu a_B [\underline{F}_1 \delta \alpha + \underline{F}_{2,i} \delta v_i].$$

The integrals \underline{F}_1 and $\underline{F}_{2,i}$ are defined as follows:

$$\underline{F}_1 = \left[\frac{(L_R + L_B)^2 - L_R^2}{2} \right] - \left[\frac{(L_R + L_B)^3 - L_R^3}{L_R} \right],$$

and

$$\underline{F}_{2,i} = \frac{2\sigma_i}{\beta_i} - \frac{1}{L_R} \left(\frac{2L_B \sigma_i}{\beta_i} + \frac{2}{\beta_i^2} \right).$$

The equations of motion then can be written as:

$$\begin{aligned} & \delta W_B + \delta W_R + \delta W_S - (\delta W_L + \delta W_{B2}) \\ & - (\delta W_{nc1} + \delta W_{nc2} + \delta W_{nc3}) = 0. \end{aligned}$$

The assembled matrix form of the equations of motion is:

$$[M] \ddot{x} + [K] x = F.$$

The explicit form of the matrices are given in the Appendix.

The topological features are more readily observed in matrix form. The coupling between the beam generalized coordinates is the interesting feature to be observed. The mass matrix is only coupled between each degree of freedom and the lever rotation coordinate. No inertial coupling exists between the generalized coordinates themselves.

The opposite situation is true of the stiffness matrix. The beam generalized coordinates are completely coupled through the shear compliance. Thus, for a highly damped core material, no simple closed form solution can

be obtained [8]. No stiffness coupling exists between the beam coordinates and the lever rotation.

5.0 COUPLED MODE SOLUTION

Figure 7 shows the result of a digital simulation performed incorporating the first two beam generalized coordinates and the lever rotation coordinate. The difference between the peak frequencies of the transfer function and that of the tip deflection in Figure 7 is attributable to inertial coupling of the beam with the lever arm. The coupling of both inertial and elastic structural subcomponents is a well documented phenomenon in structural mechanics [6,9,10].

The rotational stiffness of the lever was lowered to permit testing at higher strain levels approximating service fatigue environments. However, that modification lowered the lever arm resonance to near 100 Hz; that is, in the middle of the desired frequency range for testing (20 Hz to 300 Hz). Thus, the maximum tip deflection occurs at the coupled system resonance, not at the uncoupled specimen resonance. For that reason, the root strain maximizes at the coupled mode resonance, since it is there that the system is at resonance (cf. Figure 3).

The transfer function peaks at the specimen resonant frequency, since that is the relationship from root-to-tip; that is, it reflects the beam properties, per se (Figure 2). The root acceleration minimizes at the uncoupled beam frequency, since at that frequency the system observes the beam as a damper. When the root acceleration is controlled as a constant, the tip deflection and the transfer function indicate the same resonant frequency. That control enforces a base motion excitation, that effectively isolates the beam from the fixture (cf. Figure 4).

The mechanical coupling of the test specimen with the test fixture will cause an error in damping estimates, if Heine's procedure is strictly followed. First, if the frequency of maximum tip deflection is used, the damping estimate will be high, since the estimate is inversely proportional to the frequency squared [2]. Secondly, if the frequency of the minimum of the root acceleration is used, the damping estimate will again be high, since that estimate is inversely proportional to the displacement [2]. Depending on the proximity of the lever resonance to that of the test beam, a considerable error can be realized. The essential point to be considered here is: the test beam must be isolated from the fixture dynamics to obtain reliable damping estimates.

6.0 IMPEDANCE MODEL

Whereas the coupled mode solution partially described the measured frequency behavior data, the simulation did not reflect the measured damping behavior. After repeated attempts to match the difference in damping behavior between the transfer function and the tip deflection, an equivalent circuit impedance model was constructed, using a force-voltage technique (Figure 8) [11,12]. The model retained two degrees of freedom: the first beam generalized coordinate, and the lever rotation coordinate. That model maintained the important relationships between the fixture and the test beam.

The motivation for using an impedance model was the observed influence of source impedance on the electrical duals of mechanical circuits [13,14].

Summing the impedances about each loop (cf. Figure 8) and solving for the transfer impedances:

$$\frac{I_2}{V_s} = \frac{1}{A + B + jC}, \text{ and}$$

$$\frac{I_1}{I_2} = \frac{-j\omega M_{12}}{R_1 + jX_1}, \text{ where}$$

$$A = (R_1 + R_2),$$

$$B = \frac{\omega^2 M_{12}^2 R_1}{R_1^2 + X_1^2},$$

$$C = j \left(X_2 - \frac{\omega^2 M_{12}^2 X_1}{R_1^2 + X_1^2} \right),$$

with reactances defined as,

$$X_1 = \omega L_1 - \frac{1}{\omega C_1} \quad \text{and} \quad X_2 = \omega L_2 - \frac{1}{\omega C_2}.$$

Here, the dependence of the root-to-tip transfer impedance solely on the specimen properties is readily observed. Thus, the system is at resonance when the tip deflection is maximized, but the transfer impedance (or function) possesses the specimen damping property information (cf. Figure 2) [13].

Since the load should appear as a large resistance relative to the fixture, the Thevenin resistance (R) was tuned to nearly 50% percent of the lever arm stiffness. At that level, the analytical simulation converged to that of experiment (Figure 9). The loss factor computed from the transfer function is 0.02 and 0.045 from the tip deflection. Thus, the principal difference between the damping estimates arises from the shaker source impedance inertially coupled to the specimen through the lever arm, that is the back-EMF induces damping [19]!!

6.0 VARIANCES WITH RKU DAMPING ESTIMATES

The Ross-Kerwin-Ungar equations (RKU) were developed to evaluate the response of damped and sandwich beams [15,16] to acoustical excitation. The loss factors measured in the above analytical and measured data are somewhat lower than that expected from RKU estimates and published nomograms for viscoelastic materials. Much of the available nomogram data was developed using the RKU formulations, since those nomograms are for materials that were developed for noise and vibration control, not for sonic fatigue suppression. Based on those nomograms, loss factors at or above 0.1 should be anticipated.

The principal source of disagreement arises from the mode in which the specimen is tested.

The RKU equations assume simply supported boundary conditions [15,16]. Figure 10 shows that the eigenvalues for cantilevered beams converge to within 80% of those of simply supported beams after the third mode. (For instance, Anatrol formulates their nomograms based on the average loss factor measured from the third through sixth modes [17].) Therefore, the loss factors measured from the first or second mode will be as much as one order of magnitude lower than those found in the nomograms, since the shearing strain is concentrated at the root of the beam in those modes. That is, for the higher modes of vibration, the material is being more uniformly worked along the beam length; whereas, the lower modes of vibration only work the material near the root of the beam. This fact illustrates why constrained layer systems are effective on the higher modes, since more wavelengths are shearing the core material.

7.0 SUMMARY/CONCLUSIONS

The mechanics of a widely used resonance dwell test apparatus were developed through an energy method application, with respect to the testing methodology established by Heine using ASTM "Oberst" specimens [1,2]. Test considerations for fixturing and comparison with published data were highlighted through analysis of a practical example. The essential points to be considered are several-fold.

Firstly, the mechanics of an apparently simple apparatus can be quite complex. Failure to comprehend those subtleties can result in the acquisition of irrelevant data, especially when the test apparatus is modified from its original intent. The test procedure and ultimate application of the test data must be wholly consistent with the physical parameters of the test apparatus.

Secondly, the test specimen must be either mechanically or artificially isolated from the fixture dynamics to obtain reliable damping estimates. That is, the fixture must not possess resonances that may couple to the test specimen, or the use of a controller may be required to isolate the specimen artificially. Otherwise, the coupling must be indirectly eliminated in the data reduction, which may be unsatisfying.

Thirdly, the source and test methodology employed to develop any published nomogram data must be consistent with the particular test objectives when comparing measured test data. Lastly, although not a consideration in the above application, the effect of the root restraint should be examined, since the damped boundary condition is very difficult to effect.

Resonance dwell testing is a cost effective method of screening candidate damping materials for noise and vibration control, and sonic fatigue resistance. However, a particular methodology or apparatus cannot be used ad hoc. A short reflection on the desired results and test objectives reaps a great reward in acquiring good, relevant, and inexpensive test data.

NOMENCLATURE

L = lever length
 L^R = beam specimen length
 M^B, J = lever inertias
 W^R = Specimen width
 t_1, t_2 = facesheet thicknesses
 $t_1^1 = t_2^2$ = viscoelastic thickness
 V^3 = specimen tip deflection
 a^t = root acceleration
 a^R = base acceleration
 f^B = bare specimen frequency
 f^0 = damped specimen frequency
 $d^d = t_1 + (t_1 + t_2)/2$
 m = lineal mass density
 G^B = storage modulus
 η = loss factor
 $G^* = G(1 + j\eta)$
 E = facesheet elastic modulus
 $v(x, t)$ = beam displacement
 $\alpha(t)$ = lever rotation
 $v_i(t)$ = generalized beam deflection
 $\phi^i(x-L)$ = mode shape
 $\underline{H}(\cdot)$ = step function
 σ = mode shape parameter
 λ^n = eigenvalue
 $\beta^n = \lambda^n / L$
 μ^n = area mass density
 F = applied shaker force
 ω = angular frequency

REFERENCES

1. Anon. (1983); "Measuring Vibration-Damping Properties of Materials, Standard Method for-", ASTM STD-E756-83.
2. JC Heine(1966); "The Stress and Frequency Dependence of Material Damping Factors for Some Engineering Materials", ScD Dissertation, MIT, Cambridge, MA.
3. RW Clough and J Penzien(1975); Dynamics of Structures, McGraw- Hill, NY.
4. RD Blevins(1979); Formulas for Frequency and Mode Shape, Van Nostrand Rheinhold, NY.
5. HL Langhaar(1962); Energy Methods in Applied Mechanics, John Wiley, NY.
6. RR Craig (1981); Structural Dynamics: An Introduction to Computer Methods, John Wiley, NY.
7. SP Timoshenko and JM Gere (1972); Mechanics of Materials, Van Nosstrand Rheinhold, NY.
8. JC Slater and NH Frank (1947); Mechanics, McGraw-Hill, NY.
9. L Meirovitch (1975); Elements of Vibration Analysis, McGraw-Hill, NY.
10. JS Przemieniecki (1968); Theory of Matrix Structural Analysis, McGraw-Hill, NY.
11. LL Beranek (1955); Acoustics, McGraw-Hill, NY.
12. VH Neubert (1987); Mechanical Impedance: Modelling/Analysis of Structures, Naval Sea Systems Command, Code NSEA-55N, DC.
13. G Koehler (1955); Circuits and Networks, MacMillan, NY.
14. SE Schwarz and WG Oldham (1984); Electrical Engineering: An Introduction, Harper Rheinhardt and Winston, NY.
15. AD Nashif, et.al. (1985); Vibration Damping, John Wiley, NY.
16. L Cremer, Heckl, and EE Ungar (1987); Structure-Borne Sound, 2nd Ed., Springer-Verlag.
17. Personal communication between ML Parin (Anatrol Corporation) and RE Tate (LTV Aircraft Products Group).
18. FF Rudder and HE Plumblee (1975); "Sonic Fatigue Design Guide for Military Aircraft", AFWAL AFFDL-TR-74-112.
19. EL Peterson, WM Rusen, and TA Mouch ; "Modal Excitation - Force Drop-Off at Resonances", Sound and Vibration, April 1990.

APPENDIX

The inertia matrix, stiffness matrix, and force vector were developed by application of energy methods above. The coupled inertia matrix is:

$$\begin{bmatrix} \mu_{3,1} & 0 & 0 & 0 & \dots & 0 & \mu_{2,1} \\ 0 & \mu_{3,2} & 0 & 0 & \dots & 0 & \mu_{2,2} \\ 0 & 0 & \mu_{3,3} & 0 & \dots & 0 & \mu_{2,3} \\ \vdots & \vdots & \vdots & \vdots & \ddots & \vdots & \vdots \\ \mu_{2,1} & \mu_{2,2} & \mu_{2,3} & \dots & \dots & \mu_{2,N} & \mu_{1} + I_R \end{bmatrix},$$

Analogously, the coupled stiffness matrix is:

$$\begin{bmatrix} (EI)\beta_1^4 + G^*X_{1,1} & G^*X_{1,2} & \dots & G^*X_{1,N} & 0 \\ G^*X_{1,2} & (EI)\beta_2^4 + G^*X_{2,2} & \dots & G^*X_{2,N} & 0 \\ \vdots & \vdots & \ddots & \vdots & \vdots \\ G^*X_{1,N} & G^*X_{2,N} & \dots & (EI)\beta_N^4 + G^*X_{N,N} & 0 \\ 0 & 0 & \dots & 0 & K_R \end{bmatrix},$$

Finally, the force vector is:

$$\begin{bmatrix} F_{2,1} \\ F_{2,2} \\ F_{2,3} \\ \vdots \\ \mu a_B \frac{F_1}{4} - M_R \frac{a_B^2 L_R}{4} + F L_R \end{bmatrix},$$

where $G^* = \frac{G^*}{t_3} \left[t_3 + \left(\frac{t_1 + t_2}{2} \right) \right]^2$,
and $EI = [(EI)_1 + (EI)_2]$.

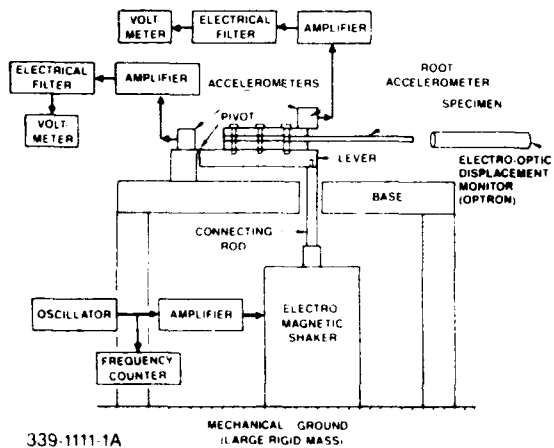


Figure 1 LTV's Resonance Dwell Apparatus

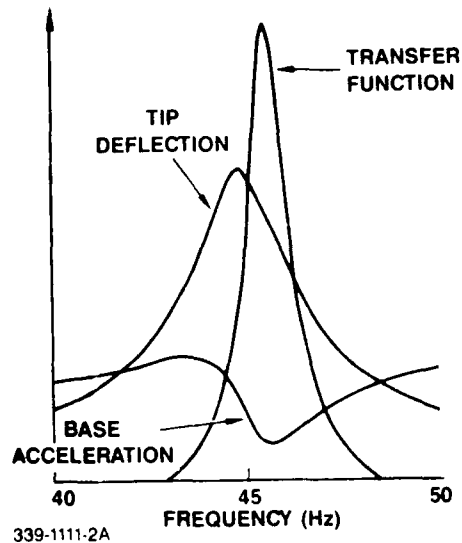


Figure 2 Response of Beam Specimen Depicting Discrepancies Versus Heine Method

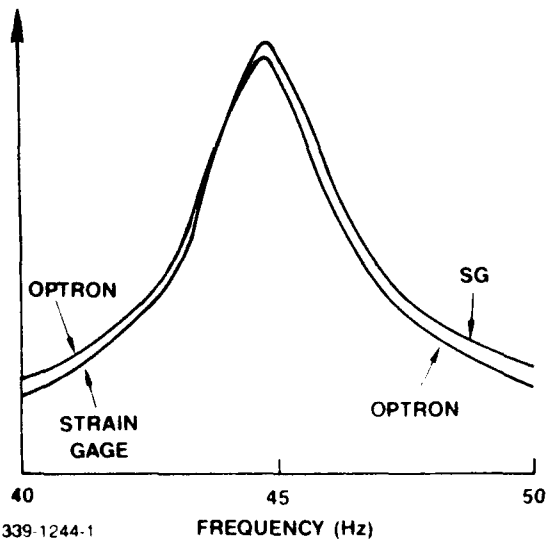


Figure 3 Tip Deflection and Root Strain - Shaker Force Constant

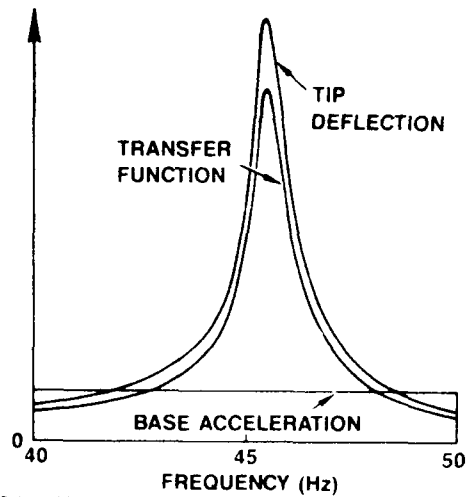


Figure 4 Tip Deflection Versus Transfer Function - Base Acceleration Constant

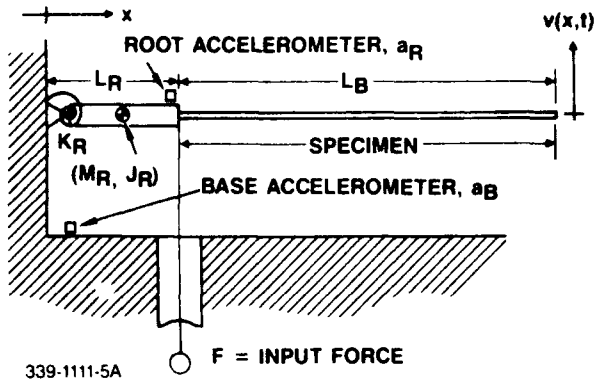


Figure 5 Analytical Geometry of the Resonance Dwell Apparatus; After Heine

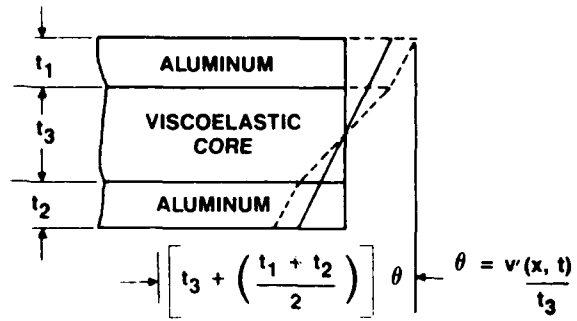


Figure 6 Geometry of Constrained Shear Layer

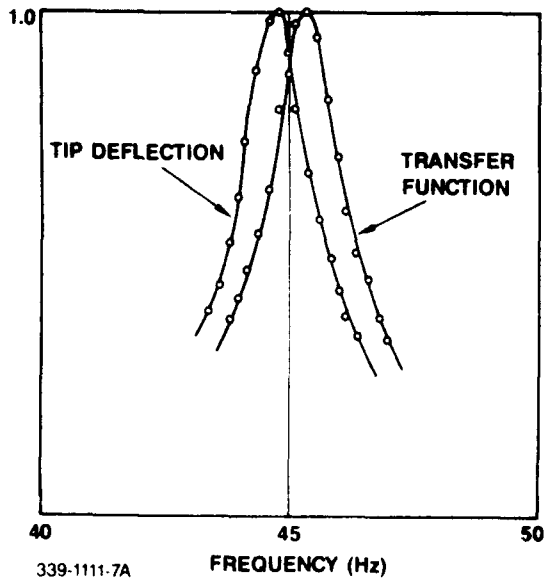


Figure 7 Coupled Response of Beam Test Specimen; Tip Deflection and Transfer Function

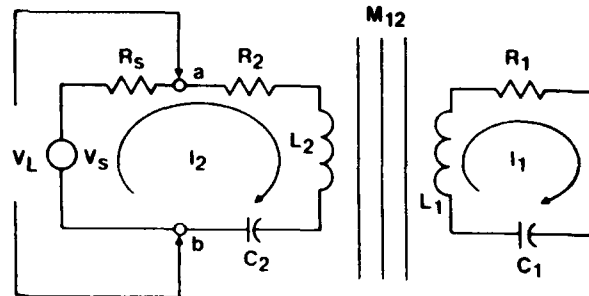
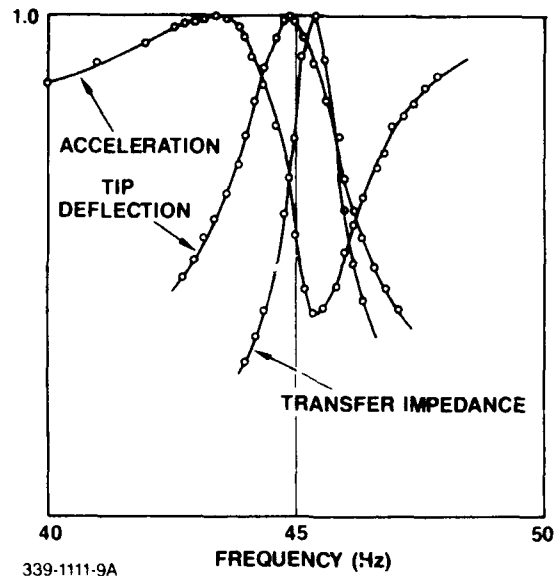
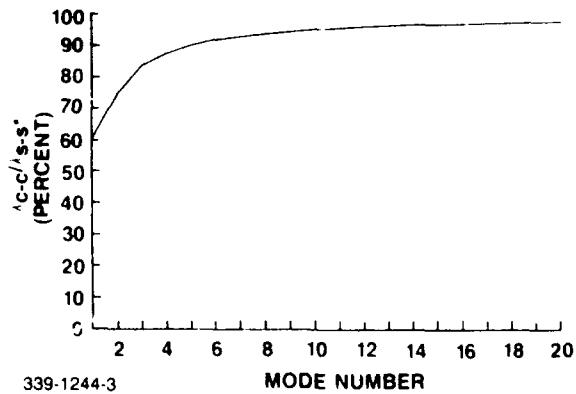


Figure 8 Equivalent Circuit for Lever Rotation (\$I_2\$) and Beam-First Mode Deflection (\$I_1\$)



339-1111-9A

Figure 9 Normalized Acceleration and Transfer Function Depicting Convergence with Test Results



339-1244-3

Figure 10 Convergence of Clamped-Free Eigenvalues to Simply-Supported Eigenvalues Versus Mode Number

THE DEPENDENCY OF VIBRATION ENERGY DISSIPATION ON THE AMPLITUDE OF STRUCTURAL MOTION

Dale L. Jensen¹
Lawndale, CA

ABSTRACT

Quantitative values of structural damping factors for ground launched aerospace vehicles are seldom precisely determinable. This paper presents measured data from a large vibration test program and shows correlation of these data with the amplitude of motion. Experimental structural damping factor values and amplitude of vibratory motion from a vibration test are combined to show the amplitude dependency of structural damping factors. The experimental data show good correlation of structural mode damping factor with the amplitude of vibratory motion. The data were obtained from flight control frequency response testing of shuttle orbiter and ascent vehicles and structural mode damping factors obtained from Ground Vibration Tests, MSFC, Huntsville, Alabama, June 1978 through February 1979.

**FULL PAPER NOT AVAILABLE FOR
PUBLICATION**

¹Consultant, P.O. Box 694, Lawndale, CA 90260, (714) 896-6156

LOW-DEFLECTION LOSS AND HYSTERESIS MEASUREMENTS ON A SPACECRAFT TEST JOINT

Eric M. Austin*
CSA Engineering, Inc.
Palo Alto, California

Timothy L. Flora
Lockheed Missiles and Space Company, Inc.
Sunnyvale, California

James C. Goodding
CSA Engineering, Inc.
Palo Alto, California

ABSTRACT

Passive damping has been demonstrated to be an effective and efficient means for limiting the effects of on-board excitations on the dynamics of space vehicles. High-precision applications require these treatments to both be effective at very low excitation levels and not affect the dimensional stability of the structure under quasi-static and thermal-mechanical loads. This work documents a study of two important issues facing structures damped with viscoelastic materials: hysteresis and loss at low deflection levels.

The test article is an I-beam-like structure designed to simulate an experimental method of fabricating graphite-epoxy/honeycomb structures without using any mechanical fasteners. After identifying the most critical vibrational modes from a separate system-level analysis, a damping treatment was designed for the test joint using standard finite element techniques. A modal test using very low random excitation levels was performed on the resulting damped structure. Statistical methods were used to determine that the maximum displacement level of the free-free structure was of the order of nano-meters. Subsequently, hysteresis tests were performed on the same damped beam. Laser interferometry was used to measure displacements of the joint after undergoing cyclic static loads of varying magnitudes. Percent hysteresis was measured while the joint was loaded in three-point bending. Hysteresis behavior during displacements as small as 150 nano-meters was recorded

*Senior Engineer, 560 San Antonio Road, Suite 101, Palo Alto, CA 94306 (415) 494-7351

1. Introduction and Objectives

Passive damping has been demonstrated to be a vital technology for limiting the effects of on-board excitations on the dynamics of space vehicles. High-precision applications require these treatments to both be effective at very low excitation levels and not affect the dimensional stability of the structure under quasi-static and thermal-mechanical loads. Of equal concern are the damping characteristics of the structure when undergoing very low strain levels. This information is particularly important when performing analysis of the structure to predict response to launch and in-service loads. Since this fabrication technique is new, typical levels of inherent damping are not known. It is also anticipated that passive damping will be incorporated into any design using this construction technique, so it is necessary to test for damping performance at very low levels of response.

For many spacecraft designs it is desirable to predict the magnitude the structure may deform or shift after being launched and placed in service. This deformation can be caused by gravity release or changes to the thermal and moisture environment. However, one of the largest and least understood contributors is hysteresis. Structural hysteresis is the failure of the structure to return to its original position after an external load has been applied and removed. This effect is typically caused by friction effects, slippage of fasteners within their holes, and small viscoelastic properties of most materials. Hysteresis is not to be confused with inelastic behavior of a structure resulting from loads exceeding the yield strength or proportional limit. It is also separated from the predictable effects of both long-term creep, where materials deform slowly due to sustained stresses, and microcreep, which occurs when repeated short-term loading exceeds the material's microyield strength.[1] In essence, hysteresis is treated herein as an accumulation of distortion sources that cannot be accounted for by classical analysis techniques.

Of particular concern is the behavior of dimensionally critical spacecraft structures. Hysteresis predictions of precision composite structures after being launched or after small on-orbit maneuvering loads are applied must be based on limited and mostly irrelevant static test data. The hysteresis of structures constructed using graphite/epoxy parts bonded together with honeycomb core is not well understood. When viscoelastic passive damping materials are applied, the hysteresis of the structure may increase, especially during low-amplitude vibration. The hysteresis test is designed to give insight into these problems and aid in analysis efforts to bound or quantify structural hysteresis behavior. In summary, the objectives of the hysteresis tests are as follows:

1. Measure the amount of hysteresis present in a generic spacecraft joint with a constrained layer passive damping treatment applied.
2. Determine the linearity of hysteresis at low displacement levels.

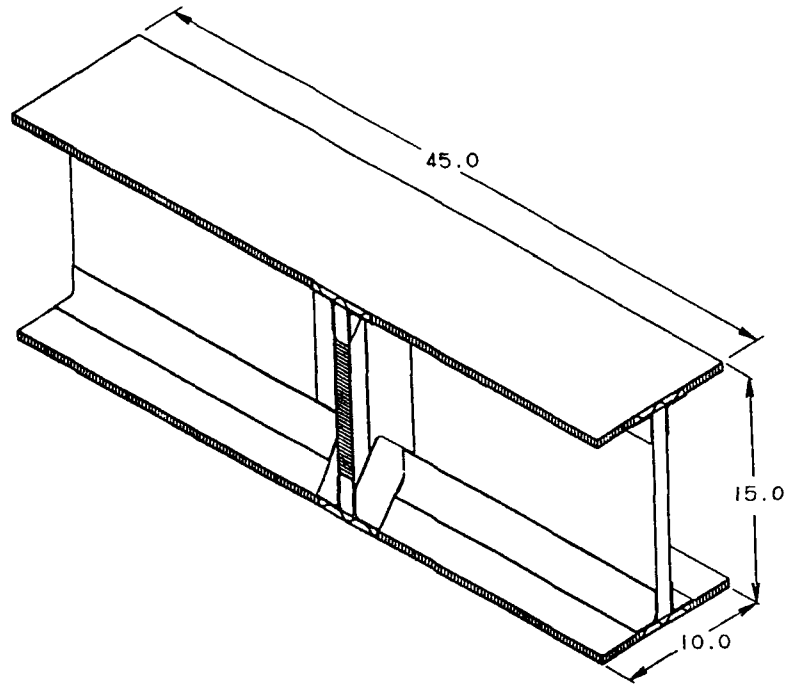


Figure 1. Sketch of the test article

The test article, shown in Figure 1, is designed to simulate an experimental method of fabricating graphite-epoxy/honeycomb structures without the use of any mechanical fasteners. The article is essentially the intersection, a joint, between two composite I-beams at an angle of 60° . The attachments are strengthened with overlapping graphite-epoxy (GR/EP) plates attached solely with high-strength epoxies. The primary mode of interest is the first bending mode of the "I-beam" in its strong direction, since that deflection best simulates operational deflections using this construction.

A secondary objective of this effort was to design and apply an add-on damping treatment that would increase the damping of the test article significantly in the mode of interest. A finite element model was developed to aid in this design. The finite element model was constructed with enough details that it could be used later for failure analysis of some of the internal parts. This configuration was also tested at very low levels of excitation.

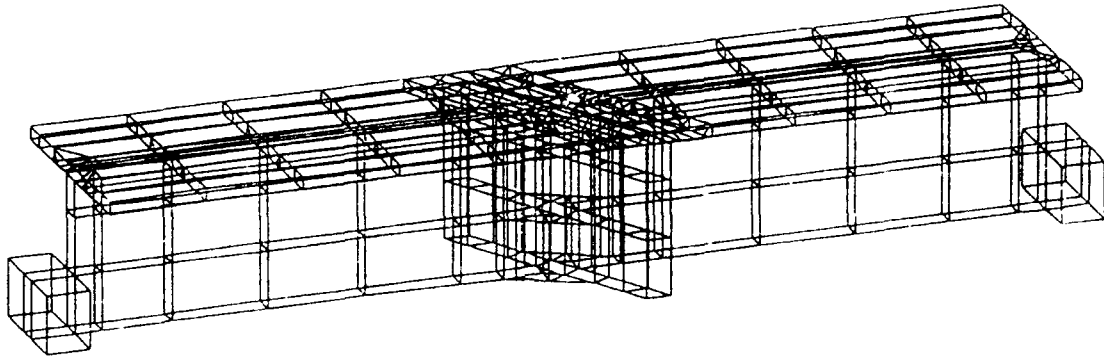


Figure 2. Finite element model of the test joint

2. Analysis and Design of the Damping Treatment

2.1 Finite Element Model

The primary reason for creating the finite element model was to evaluate candidate damping treatments for the test joint. The model was based on drawings supplied by LMSC and was created using I-DEAS pre-processing software. The finished model was translated from I-DEAS to MSC/NASTRAN format for the actual analyses. Figure 2 shows the resulting finite element model. Due to symmetry, only half of the structure was modeled.

2.2 Predicted Baseline Modes

The modes of interest are the first overall mode of the Test Joint and the first bending about its strong axis, shown in Figure 3. The "banana" mode is most representative of a typical troublesome mode in similar structures. Since only half of the test joint was modeled, two runs, one with symmetric and one with asymmetric boundary conditions, are needed to predict all of the structure's modes. Both of the modes of interest are asymmetric with respect to the symmetry plane, so most of the runs were done using only these boundary conditions. Since no other boundary conditions were applied, this predicted free-free modes of the test joint.

The initial run of the test joint model predicted the "banana" mode to be the eleventh elastic mode, at a frequency of slightly more than 1,200 Hz. The high frequency itself is not a problem for testing; however, the bending mode was coupled with local modes of nearly every panel section in the structure. This would have complicated the test greatly, requiring many measurement points in order to identify the proper mode with confidence. Another concern was that the high level of local panel participation might distort the inherent level of damping sought for the pure "banana" mode.

The solution agreed upon by LMSC and CSA engineers was to add some dead weight to the ends and center of the test joint. It was felt that this would bring the

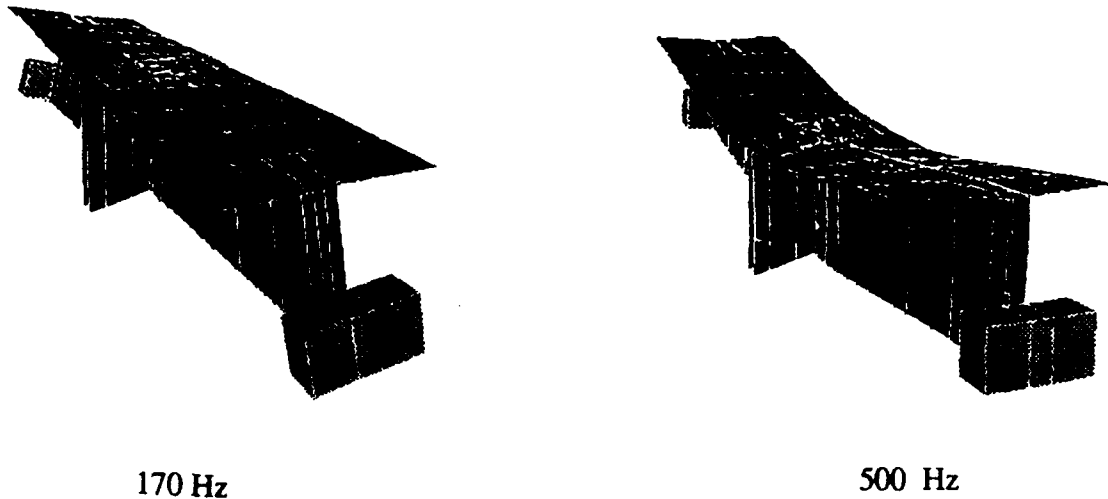


Figure 3. Primary vibration modes of interest

first bending mode down in frequency while not affecting the local panel modes. The finite element model bore this hypothesis out. The solution was to add 10 pounds to each of the ends and the center, a total of 30 pounds of added weight for the half model. The added weight brought the mode of interest down to about 585 Hz, and there was no local panel participation at all.

The frequencies predicted for the baseline undamped structure including the dead weight are given in Table 1.

2.3 Analysis of Damping Treatments

An ideal outcome of the this analysis would be a damping treatment that added significant damping without any additional weight. A more realistic goal is to maximize the damping added to the mode of interest while minimizing the added weight. Though there are many possible weight-efficient damping strategies, most requiring that the VEM be an integral part of the structure. A simple constrained-layer approach was chosen for this work because of hysteresis and creep concerns.

The baseline finite element model including the added weights was altered to add the effects of constrained-layer damping treatments on both the top of the flange and the sides of the webs. The damping was predicted using the Modal Strain Energy Method. Initial runs showed that the modal strain energy (MSE) in the VEM on the sides (web) was much higher than that in the VEM on the top (flange). Thus, the treatment on the flange was removed in order to save weight, and all subsequent iterations were on the web treatment only.

Mode	BC	frequency
1	asym	169 Hz*
2	sym	204 Hz
3	sym	360 Hz
4	sym	423 Hz
5	asym	514 Hz
6	asym	585 Hz†
7	sym	640 Hz
8	asym	675 Hz

* first twisting mode

† first bending, strong direction

Table 1. Predicted elastic modes of the baseline test joint

It is often logical to make the constraining layer from the same material as the base structure, especially when considering thermal expansion. LMSC had some surplus 48-mil-thick GR/EP from the same batch used on the test joint, so this was chosen for the constraining-layer material. It was shown through analysis that increasing the thickness from 48 to 96 mils (milli-inches) did not increase the damping enough to justify the increase in weight. Thus, the final constraining layer was a 18.5-inch-long by 9.5-inch-wide, 0.048-inch-thick sheet of graphite/epoxy, supplied by LMSC.

The next step was to determine the best combination of VEM shear modulus and thickness. The properties (shear modulus and loss factor) of viscoelastic materials vary with both temperature and frequency, and both are important in choosing a good design. The loss factor is essentially the efficiency with which strain energy in the VEM is dissipated, i.e., a low loss factor will result in low damping.

The initial candidate VEM's were chosen for their availability. The properties of these candidate were then evaluated at 585 Hz and 70°F, the approximate temperature of CSA's laboratory. Shear moduli of the VEM's having good loss factors ($\approx > 0.7$) were simulated on the model, and damping was predicted following the MSE method. The viscoelastic material chosen for this application was 3M's Y-9473, a 10-mil-thick double-back adhesive transfer tape. This choice resulted in the most modal strain energy in the VEM given the other factors that were held constant.

The surface area of coverage of the treatment was approximately 700 in² (four sheets at 9.5 x 18.5 inches each), and the VEM has a density of about 0.035 $\frac{lb}{in^3}$. Together with the constraining layer, the added weight is about 2.5 lbs.

2.4 Predicted Levels of Damping

Once the final configuration of the damping treatment was chosen, predictions of damping were made. These damping levels, presented here in terms of viscous damping ($\frac{1}{2Q}$), were calculated using the modal strain energy in the VEM as predicted by the finite element model. The only modes of interest were the first mode overall of the system and the first bending mode in the strong direction ("banana"). From Table 1, the frequencies of these modes were predicted to be 169 and 585 Hz. Since the properties of viscoelastic materials (VEM's) are sensitive to changes in temperature and frequency, two runs had to be made for each set of symmetry conditions: one each with the VEM properties evaluated at 169 and 585 Hz. The shear modulus of the chosen VEM is nearly twice as stiff at 585 Hz as it is at 169 Hz.

The damping predicted for these two modes was 2.3% and 2.4%, respectively. A full summary of the frequencies and damping values will be included in a later section. Note that these predictions are for added damping, and they neglect any damping inherently in the structure.

3. Modal Testing of the Test Joint

3.1 Test Setup

The Test Joint was suspended with steel cables and extension springs to simulate free-free boundary conditions. In order for these boundary conditions to be effective, the rigid-body modes of the structure need to be about ten times lower in frequency than the first elastic mode. Free-free boundary conditions were chosen to reduce the possible effects of fixturing dynamics on the damping measurements. Often times with simply supported or fixed-end boundary conditions, it is difficult, if not impossible, to distinguish between loss from the structure and loss from connections at the boundary conditions. This is particularly important in a precision structure such as this where few mechanical fasteners are used. An additional benefit is that comparisons with finite element models are easier since the dynamics of the supports do not have to be modeled.

The 60 pounds of lead were added by affixing lead blocks to the ends and center of the beam. The center blocks were attached with epoxy, and the end blocks were bolted to an aluminum bar with two 3/8-inch-diameter bolts. The added weights were placed as close as possible to the center line of the Test Joint to avoid affecting twisting modes.

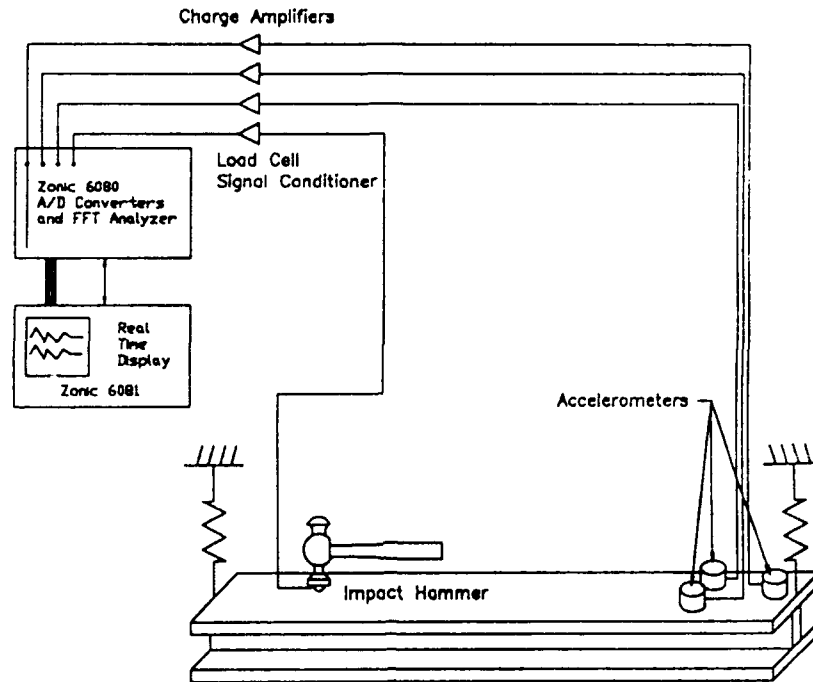


Figure 4. Schematic of test instrumentation

3.2 Instrumentation

The instrumentation for the test consisted of an impact hammer, a signal conditioner for the load cell, three piezoelectric accelerometers, accelerometer charge amplifiers, and a four-channel modal analysis system. An impact hammer was used to excite the Test Joint, since it was adequate for the measurements sought, and it doesn't require any additional fixturing or rigging.

Coupled with the charge amplifiers, the sensitivity of the accelerometers was more than adequate to ensure a good signal-to-noise ratio, even for the low-amplitude measurements. The tip on the impact hammer was chosen to input the most energy over the frequency band of interest. A schematic of the instrumentation is shown in Figure 4.

3.3 Measurements

Two points were used for most of the testing: one on the top of the Test Joint near the center line and one on the vertical web near its intersection with the flange. Two points were used since it was difficult to excite both the lowest mode (a twisting mode) of the structure and the first strong-direction bending with the same excitation, especially when impacting normal to the surfaces of the test joint. Using two

excitation points also simplified the task of data reduction, since few if any of the symmetric modes were excited by the excitation directly on top of the test joint. Recall from Table 1 that both the modes of interest are asymmetric modes.

Impact force and acceleration time records were captured and averaged with a Fast-Fourier-Transform analyzer within the test system. From these, frequency response functions (FRF's) were computed by dividing the accelerations by the excitation force. These FRF's yield insight into the test joint's structural dynamics by depicting the magnitude and phase relationships of the two signals versus frequency. Modal surveys were conducted using two impact points. Each impact point was chosen to excite one of the two modes of interest.

A standard modal analysis curve-fitting technique was used to determine the structure's resonant frequencies, the corresponding mode shapes, and the modal damping from the impact test measurements. This circle-fitting technique estimates the mode shapes by minimizing the least-square error to the FRF displayed in the complex plane. Fast-Fourier-transform zoom techniques were used to provide the very high spectral resolution required for accurate damping measurements from the data.

4. Damping at Low Displacement Amplitudes

After the modal tests had been completed, both the baseline and treated configurations were tested at low excitation levels to determine how damping was effected. The goal was to measure the damping at displacement levels of about 10 nano-meters peak-to-peak. The primary mode of interest for low-amplitude damping was the strong-direction bending ("banana") mode. It was necessary to make certain approximations and assumptions in order to determine the amplitude of the response contributed by this mode.

The test of the baseline undamped structure was done using the same impact-hammer technique used for the modal test, only with much lower impact levels and a higher sensitivity hammer tip. The response measured at the geometric center of the joint on the top surface was used as the maximum displacement. If the structure is excited on the top surface directly over the web, the desired bending mode dominates the response. Thus, it is assumed that the acceleration time history is due solely to the response of the bending mode. This allows the peak-to-peak displacement to be defined as the peak-to-peak acceleration integrated twice, i.e., divided by the square of the frequency of the mode. In order to get the low response levels, the structure was excited near the a node of the bending mode. Even if other modes were excited by the impact, the they would only add to the measured response. Thus, these displacement levels are conservative in the worst case.

After the damping treatment was applied, the excitation for the low-amplitude measurements was changed from an impact hammer to a burst-random signal applied

	Lowest Mode		Bending Mode	
	Freq (Hz)	ζ	Freq (Hz)	ζ
predicted	169	n/a	585	n/a
measured	160	0.26%	508	0.28%

Table 2. Comparison of predicted and measured frequencies and damping for the untreated baseline Test Joint

through a small shaker. The change resulted in much better quality data.

A burst-random signal was used to excite the structure with random levels of energy at all of the frequencies with a specified range. For these tests, the range was set to 160 to 640 Hz. For accuracy, several bursts are averaged to arrive at the final frequency response functions. The major drawback to this method for this application is that there no way to get an exact deterministic output from a random input. There is, however, a method for handling problems such as this. It is based on a statistical relationship between the RMS (root mean square) of a function and its peak value. This factor, sometimes called the *crest factor*, usually has a value between 3.0 and 4.0.[2,3] Additional details about the application of the crest factor for this test will be presented along with the results in the following section.

5. Test Results

After testing with various bolt configurations (different torques, different washers, grease, etc.), the original configuration was maintained for all of the testing.

5.1 Damping Measured in the Baseline Test Joint

A frequency of 160 Hz was measured for the lowest mode. This compares well with the predicted value of 169. For the "banana" mode, the measured frequency was 508 Hz, compared to 585 Hz predicted. This 15% discrepancy is of some concern, but not much since there is high confidence in the actual mode shape. Damping predictions via the modal strain energy method are dependent solely on the system eigenvectors and the structure's stiffness matrix. Of the two, the mode shape is the more important in getting accurate predictions of damping. For this reason, only minimal time was spent trying to match the frequencies of the finite element model to those measured. (A subsequent finite element model built by LMSC was tuned to match both of these modes very well.)

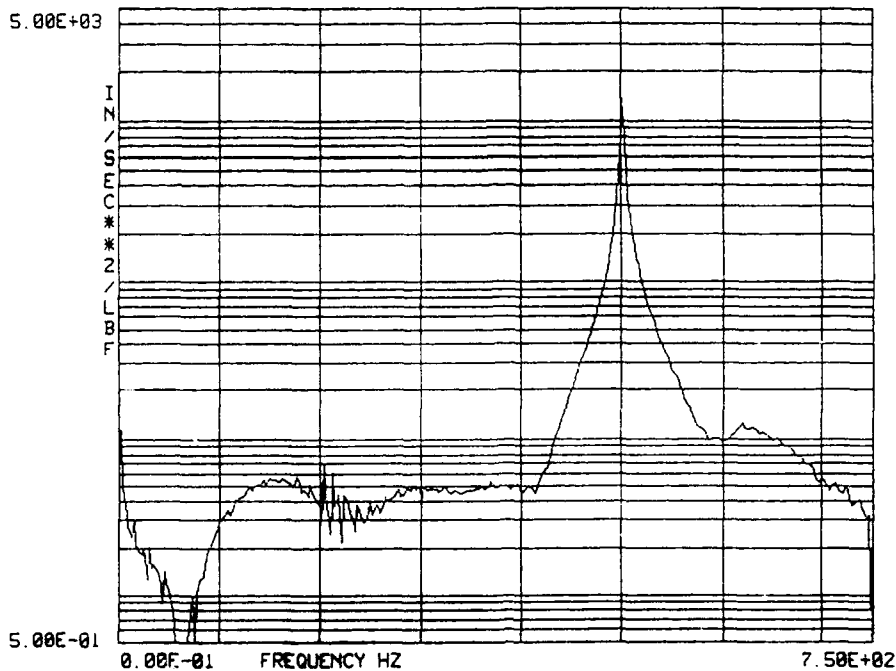


Figure 5. Frequency-response function showing strength of mode at 500 Hz

5.2 Damping Measured in the Treated Test Joint

After the damping treatment was applied, the measurements were repeated, only this time at a smaller subset of the original 32 points. The 500-Hz bending mode is very dominant when impacting the joint in the vertical direction from the top side, so it was not necessary to re-find the mode. This dominance is seen by the relative isolation (as in distance from other modes) of the mode, as shown in Figure 5. A comparison of the measured and predicted frequencies and damping values is given in Table 3. This close agreement between test and analysis damping levels is good considering that the viscoelastic material properties were not verified by test. The model correlates better with the lowest modes than with the target bending mode. Therefore, it is reasonable to expect the damping prediction for this mode to be better.

5.3 Damping Measured at Low Amplitude Levels

5.3.1 Untreated Baseline Structure

In order to produce the low-level responses desired, the Test Joint had to be excited with a light impact hammer to produce very low forces. The untreated Test Joint was excited with two low-level excitations: one producing about 25 nm zero-to-peak displacement and the other about 5 nm. The acceleration time history produced by

	Lowest Mode		Bending Mode	
	Freq (Hz)	ζ	Freq (Hz)	ζ
predicted	170	2.3%	612	2.4%
measured	169	2.5%	530	1.95%

Table 3. Comparison of predicted and measured frequencies and damping for the treated Test Joint

one of the impact forces is shown in Figure 6. The displacement was calculated as follows: The figure shows the zero-to-peak acceleration to be about $2 \frac{\text{in}}{\text{sec}^2}$. Considering the FRF in Figure 5, it can reasonably be asserted that this signal is dominated by the 530-Hz mode, so the zero-to-peak displacement can be calculated to be

$$\begin{aligned}
 \text{displacement} &= \frac{\text{acceleration}}{(2\pi f)^2} = \frac{2.0 \frac{\text{in}}{\text{sec}^2}}{(2\pi 530)^2 \frac{1}{\text{sec}^2}} = \\
 &= 1.804 \times 10^{-7} \text{ inches} \times \frac{0.0254 \times 10^9 \text{ nano-meters}}{1 \text{ inch}} \\
 &= 4.59 \text{ nano-meters}
 \end{aligned}$$

The damping measured for the 5-nm and 25-nm displacements was 0.28% and 0.33%, respectively. These compare very well with the 0.28% from Table 2.

5.3.2 Structure With Damping Treatment

This test used a shaker producing a burst-random signal. The quality and repeatability of the results far exceeded that of the impact hammer. As discussed briefly in an earlier section, a statistical relationship had to be employed in order to infer displacements from the random loading used on the treated structure. Two quantities are needed to determine this *crest factor*: the ratio of the RMS of a power spectral density function (PSD) at a point and the maximum response at that point. For this purpose, the acceleration at the geometric center of the top surface was used. As with the displacements, deterministic accelerations cannot be determined from a random loading. In place of finding the maximum acceleration during the random burst, a limiting value was determined. This was done by placed a limit on the voltage signal output by the accelerometer at the response point. If this limit voltage was exceeded, the ensemble was rejected. Knowing the accelerometer's relationship between acceleration and voltage output, this provides a good, if slightly conservative, measure of the maximum acceleration.

The crest factor was calculated for each excitation level by dividing the upper-limit acceleration by the RMS of the acceleration PSD between 160 and 640 Hz. This ratio was then multiplied by the RMS of the displacement PSD to obtain a statistical

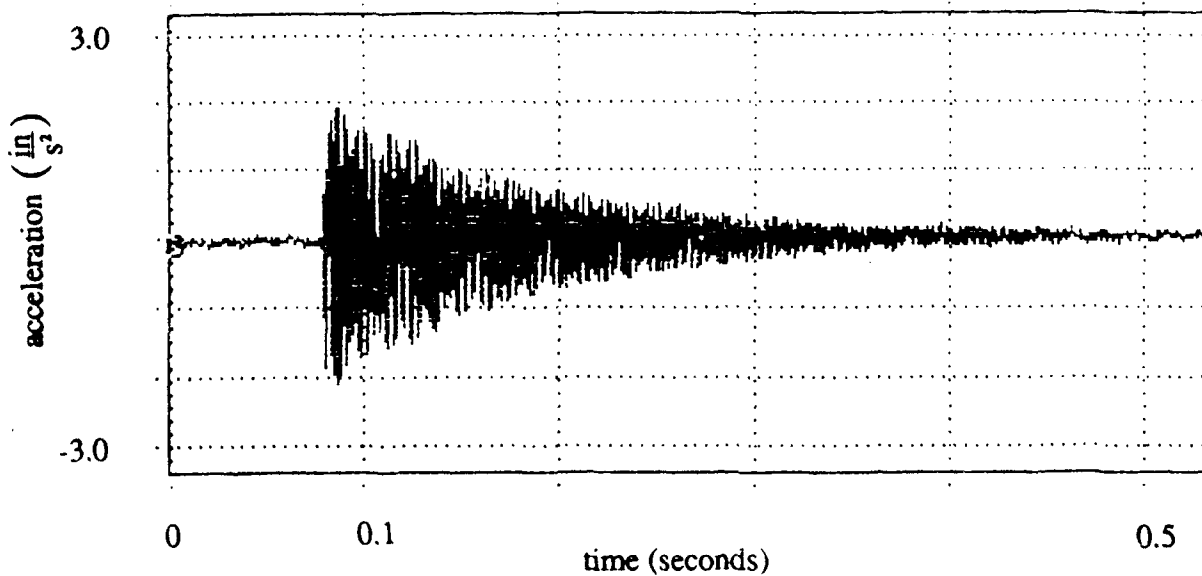


Figure 6. Acceleration time trace of low-level impact in the untreated baseline Test Joint: first strong-direction bending mode

estimate of the maximum displacement. In order to better estimate the maximum displacement of bending mode alone, the displacement RMS was computed between the half-power (3-db down) points. The results are summarized in Table 4.

In two of the measurements (marked by * in Table 4), the random signal was limited to a narrow band around the desired mode. This further ensured that only the bending mode was excited. This is noted because the crest factors for these two cases are lower than the others. In the limit, as the frequency band collapses down to a single frequency, the crest factor approaches the one over the RMS of a simple sinusoid, or $\sqrt{2}$.

a_{limit} (in/s ²)	acceleration RMS (in/s ²)	Crest factor (unitless)	displacement RMS (nano-meters)	d_{limit} 0-pk (nm)	ζ (%)
0.259	0.06317	4.100	0.1042	0.427	1.77
0.386	0.1001	3.856	0.1623	0.626	2.04
0.66	0.1751	3.769	0.2937	1.11	1.95
1.93	0.7039	2.742	1.1784	3.23	1.95
5.8	2.821	2.056*	4.9863	10.25	2.04
9.65	2.538	3.802	4.148	16.8	1.95
19.3	5.043	4.808	9.270	44.57	1.95
38.6	10.99	3.51	20.163	70.82	1.95
58.0	27.75	2.090*	47.90	100.11	1.96

* band-limited signal used

Table 4. Results of test of treated joint at low excitation levels

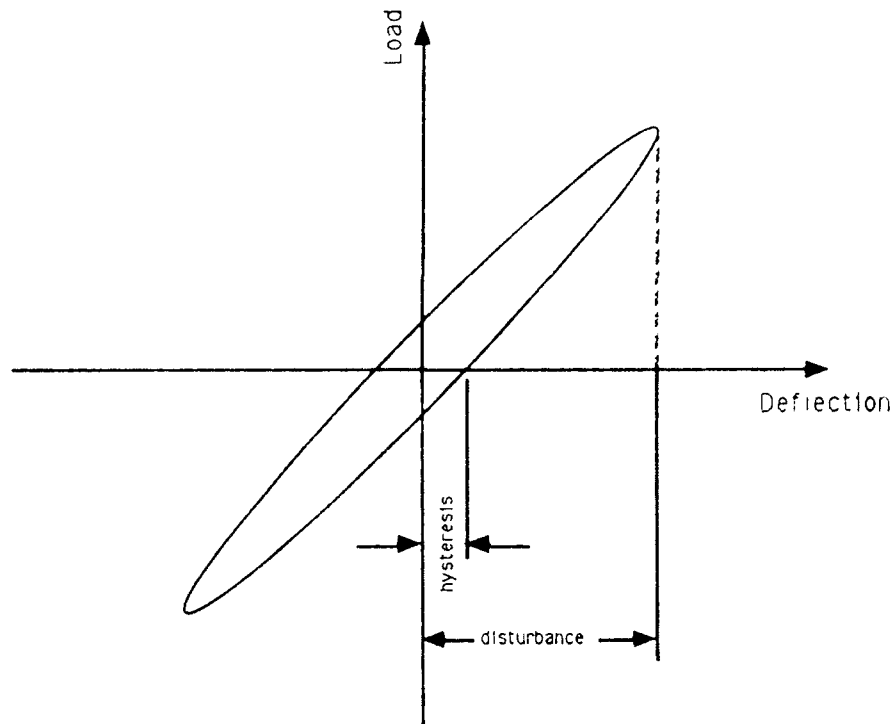


Figure 7. Percent hysteresis taken from ratio of hysteresis over disturbance

6. Hysteresis Testing

Historically on LMSC structures, hysteresis observed in static test programs typically exceeds 10% of their maximum displacements. On structures such as this where dimensional stability is of concern, hysteresis must be reduced by eliminating mechanical fasteners where possible and bonding or welding critical interfaces. Past experience with alignment platforms and other precision structures has shown hysteresis effects reduced to approximately 1% when a large static load is applied.

Quantifying hysteresis as a percent of displacement is the best method of describing the effect. It is not to suggest that hysteresis can be predicted accurately in this manner, rather the effect can be bounded by some \pm percent range. This allows the effect to be accounted for within structural stability budgets.

Duration of the applied loading should not be of importance since creep effects generally take a comparatively large amount of time to accumulate and are treated separately from hysteresis. Figure 7 shows that hysteresis is independent of time. However, because graphite/epoxies respond with small viscous effects, a finite amount of time to settle and take readings was given to allow full recovery. Because of the dynamic and cyclic nature of load conditions of primary interest to spacecraft structures, the viscous behavior is not as critical as it first may seem. At any rate, because of the sensitive nature of the test equipment in use, time dependant effects

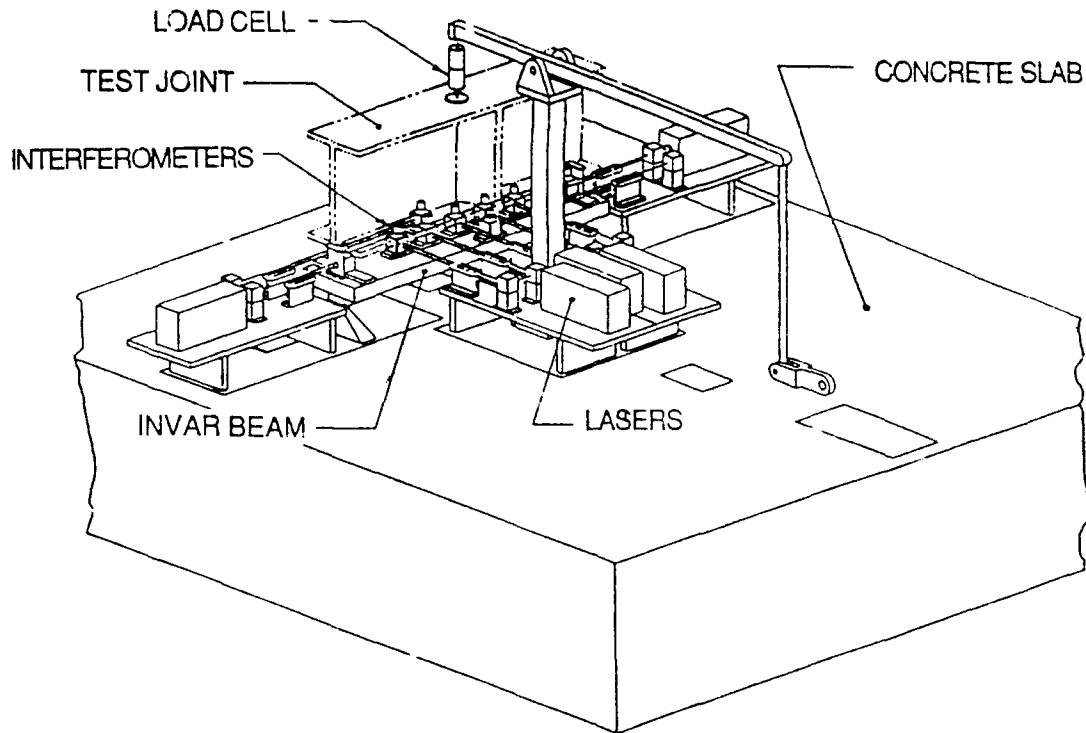


Figure 8. Hysteresis test setup

from suddenly applied and removed loadings are left for future studies.

6.1 Description of Hysteresis Test

The test was conducted at the Laser Interferometer Micro Measurement System (LIMMS) Lab. This lab is capable of measuring small displacements with a resolution of ± 0.6 micro-inches. This is achieved by using a series of Hewlett-Packard laser interferometers mounted on a seismic pad. The lasers were sampled 100 times a second and averaged over one-second intervals to eliminate high-frequency jitter influences. To help minimize temperature effects, the lab uses its own air-conditioner system, steady to $\pm 1^\circ\text{F}$ over 24 hours, and critical fixturing is made from Invar.

The test joint was supported on two blade flexures to simulate a simple support. The load was applied at the mid-span to put the joint into three-point bending. Seven lasers were used to measure displacements at varying locations along the bottom of the joint. Figure 8 is a schematic of the test setup.

Two redundant 10-pound (± 0.01 lb) load cells were used; one calibrated for tension and the other for compression. Both cells were located as close to the joint interface as possible to minimize error caused by fixturing or motor drive slop or relaxation. The load was applied with a 60000-to-1 gear-reduced motor to apply a very smooth and accurate load to the joint.

The test sequence used was to zero the load fixture and take displacement readings. As load was applied laser readings were monitored continuously. When the target load was achieved in the positive direction, the motor drive paused for 10 seconds and unloaded to zero. Another 10-second pause was maintained at zero immediately followed by a negative load application to reverse the target load. The sequence would then pause at this negative load and again at zero. By cycling the load between a positive and negative load, a more realistic load environment where the structure was not allowed to settle in any one direction, was simulated.

6.2 Results of Hysteresis Testing

The test sequence was applied at medium-to-small load levels to determine the beams response at as low of displacement levels as possible. Tests were run at $\pm 1, 5, 10, 25, 50,$ and 100 pounds. Stresses at these load levels never exceed 50 psi, which is two orders of magnitude less than the microyield strength. [4] Deflections used for hysteresis measurements were taken at the mid-span of the joint after subtraction of the end measurements, in effect zeroing any contribution of the test fixturing to deflections or hysteresis. The stiffness of the joint was measured as 142,300 lb/in, so deflections during all test runs were very small.

The data suggests that hysteresis shifts the structure in the direction of the last applied load. This observation is relatively insignificant considering the dynamic disturbance and cyclically decaying response typical of spacecraft structures.

Test runs were repeated up to 50 times each to increase confidence in the results. While every attempt has been made to minimize outside disturbances from influencing test measurements, the scatter of data levels is much greater than the laser resolution would suggest. Data scatter during higher load levels are probably caused by large disturbances such as trucks passing by the building, foot traffic down adjacent hallways, or the air conditioner switching on at an inopportune moment. Scatter in the data during the ± 1 -pound test is much smaller and can be caused by more sources such as load cell resolution, humidity changes and motor vibrations. To minimize the influences from all these error sources, only the data that fits within a one sigma (.68p) distribution is kept for analysis, essentially throwing out the worst one third of the data at each load level.

The remaining data is then averaged and plotted for of the six each load levels. The curve plotted for Figure 9 shows that hysteresis in the joint is typical of precision structures. The composite construction and applied damping treatment have not appreciably increased hysteresis above one percent for large disturbances. However when disturbances are less than about 0.001 inches the test data would suggest that structural hysteresis is nonlinear. The ± 1 sigma error band is included to show test repeatability. Admittedly since the number of perturbing error sources and

significance of test inaccuracies increases at low disturbance levels, one would expect to see a curve shape similar to Figure 9 even if percent hysteresis is linear and constant. However the amount of nonlinearity measured is more than expected by attempting to quantify the test error sources alone.

7. Summary and Conclusions

The viscous damping in the untreated Test Joint was measured to be 0.28% for the strong-direction bending mode and 0.26% in the first twisting mode. The damping of the bending mode was shown to be constant down to a displacement level of about 5 nm zero-to-peak.

A finite element model of the Test Joint was constructed for the purpose of evaluating damping concepts for the Test Joint. Though few attempts were made to tune the model to the test results, the model predicted with good accuracy the damping in the treated Test Joint. The roughly 3-pound damping treatment resulted in about 2% viscous damping in the bending mode and about 2.5% in the lowest twisting mode.

The best quality signals for the low-level damping came from the test of the treated structure. Figure 10 shows the damping measured versus maximum zero-to-peak displacement. It is important to understand that the damping values of 1.95 and 2.04 are virtually the same within the accuracy of the test. With 1024 measurements over the frequency range of 160 to 640 Hz, the modal and half-power frequencies can only be determined to an accuracy of $\frac{(640-160)}{1024} = 0.47$ Hz. The damping is determined by $\frac{\Delta\omega}{\omega_n}$, where $\Delta\omega$ spans the half-power points and ω_n is the center (natural) frequency. Thus, the measurement of damping for the 530-Hz mode can only be resolved to within $\frac{0.47}{530} = \frac{0.47}{530} \approx 0.09\%$ viscous damping. The only deviation comes at the very lowest level, where the load levels were so small that the signal-to-noise ratio was poor; most of the response was attributed to the drive gear in the shaker.

This work demonstrates structural damping using a viscoelastic material (VEM) to be constant with respect to amplitude down to nano-meter levels. It shows that passive damping is a viable means for reducing the response of structures using this construction to external excitations. Finally, the correlation between the analysis and test shows that levels of damping can be predicted with reasonable accuracy. The collimation of the above factors gives engineers a valuable and powerful tool for analysis and design of precision structures.

Structural hysteresis of the test joint is shown in Figure 9. Plus or minus 1% hysteresis can be used as a conservative estimate to bound large-deflection hysteresis of structures using the passively damped composite construction techniques. The hysteresis behavior of these structures appears to be nonlinear at very small displacement levels. For analysis of events which produce disturbances less than one mil, Figure 9 along with an appropriate uncertainty factor can be used as a design guide.

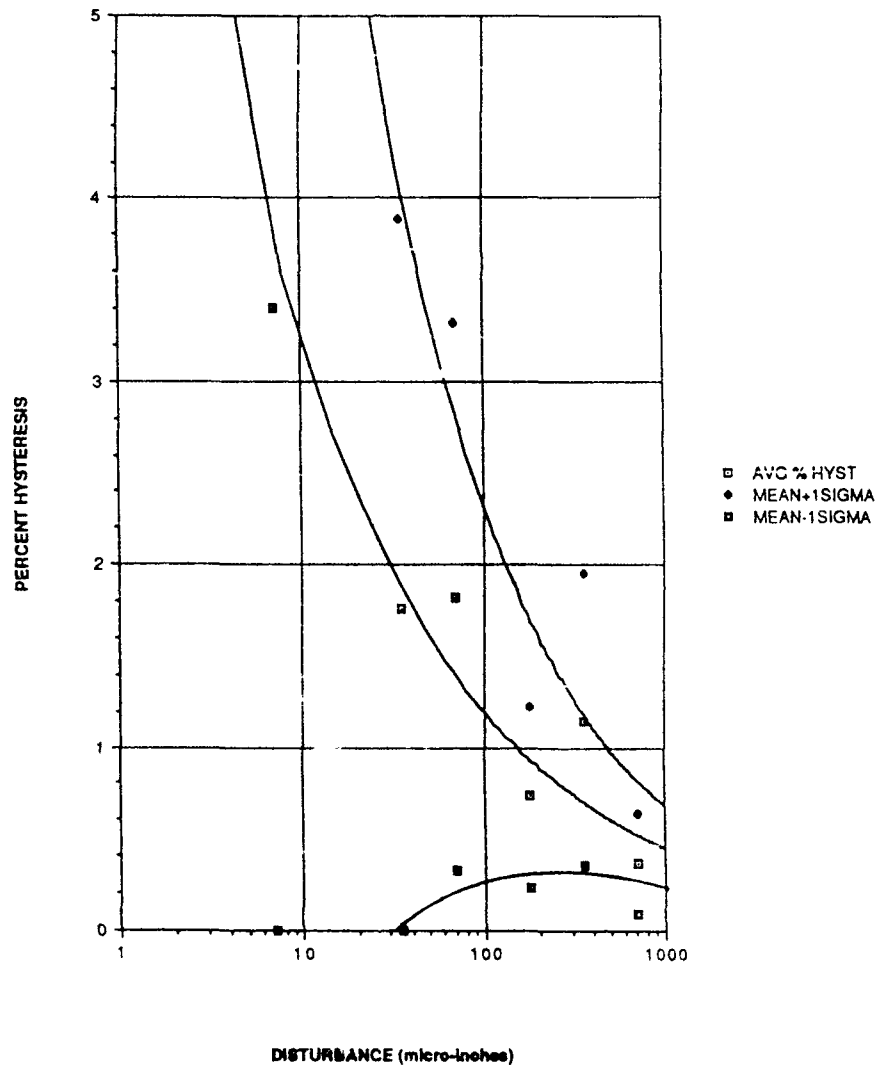


Figure 9. Hysteresis results - one sigma (0.68p)

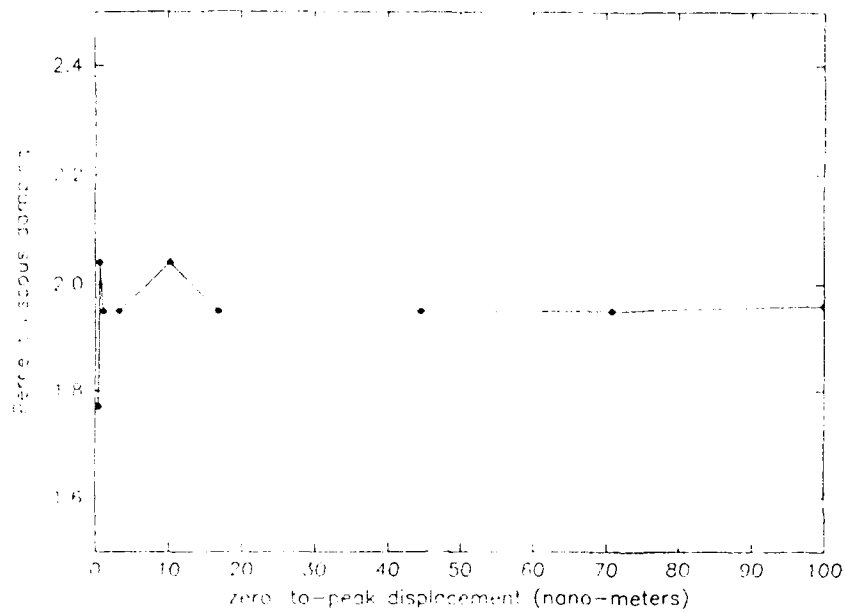


Figure 10. Damping versus maximum displacement for the treated test structure

References

- [1] Lee, Stuart M., Editor, *International Encyclopedia of Composites*.
- [2] Schloss, Fred, "Accelerometer Overload," *Sound and Vibration*, Page 12, January, 1989.
- [3] Harris, C.M., and Crede, C.E. (eds.), *Shock and Vibration Handbook, Second Edition*, Page 22-11, McGraw-Hill, New York, 1976.
- [4] Wolff, E.G. and Crane, S.T., "Prediction of the Microyield Strength of Polymer Matrix Composites," *Journal of Composite Technology & Research*, Vol. 10, No. 4, Winter 1988.

DAMPING RATIO MEASUREMENTS IN KEVLAR SANDWICH SAMPLES

L. Balis-Crema¹
University of Rome
Rome, Italy

A. Agnani
University of Rome
Rome, Italy

A. Castellani
University of Rome
Rome, Italy

ABSTRACT

Unlike some structural aerospace materials, as for instance carbon fibers, Kevlar composites present high damping ratios. This characteristic seems important in the structural design of satellites and large spacecraft. Besides the use of Kevlar sandwich structures is particularly interesting because of their high specific stiffness.

This paper presents the experimental results of damping ratio measurements derived from several sandwich samples, characterized by different skins, fabric and laminate with different lay-up.

Damping ratios are evaluated by using different techniques and a comparison is discussed. The effects of frequency and temperature - in the range from the room value up to 100 Centigrade - on the damping ratio values are also considered.

A model (based on an energetic approach), that permits a theoretical estimate of the damping ratio in sandwich samples is presented. Finally a comparison between the experimental and the predicted values is carried out.

**FULL PAPER NOT AVAILABLE FOR
PUBLICATION**

¹University of Rome, Aerospace Department, Via Eudossiana, 16, 00184 Roma, Italy, (06) 463211

CHARACTERIZATION OF THE DAMPING PROPERTIES OF HIGH-DAMPING ALLOYS

by

I.G. Ritchie* and Z-L. Pan

ABSTRACT

Many problems of noise and vibration reduction cannot be solved by traditional methods using mechanical dampers or high-damping viscoelastic materials (e.g., rubbers, polymers and plastics). Often constraints imposed by the service environment, particularly those of stress, temperature and corrosive atmospheres, will force the design engineer to consider high-damping metals, alloys and composite materials. Unfortunately, characterization of the damping and stiffness properties of promising high damping metals and alloys has hardly ever been carried out in a systematic manner. Consequently, damping data are rarely accessible to the design engineer in a readily usable form. This lack of standard data has resulted in relatively few cases where metals and alloys have been chosen specifically for their high damping properties.

This paper outlines techniques and strategies to characterize the damping properties of high-damping metals and alloys that owe their damping behaviour to the major classes of high-damping mechanisms. The main goal of the characterization is to present the damping data in a form that can be readily used by the design engineer to predict the vibration response of a component fabricated from the high-damping metal or alloy in question.

*Materials and Mechanics Branch
AECL Research
Whiteshell Laboratories
PINAWA, Manitoba, Canada R0E 1L0
(204) 753-1311

the block after casting. The composition of the samples tested is also shown in Table 1.

TABLE 1--Composition ranges of the alloys investigated.

Alloy Designation	Composition (wt%)						
	Zn	Al	Cu	Mg	Si	Fe	C
A380 (SC84A)	3.0	remainder	3.0-4.0	0.1	7.5-9.5	1.3	
#3 (AG40A)	remainder	3.5-4.3	0.25	0.02-0.05	-	0.1	
ZA8	remainder	8.0-8.8	0.8-1.3	0.015-0.030	-	0.1	
ZA12	remainder	10.5-11.5	0.5-1.25	0.015-0.030	-	0.025	
SPZ (ZA22)	78	22		-			
ZA27	remainder	25-28	2.0-2.5	0.010-0.020	-	0.010	
Grey Cast Iron	-	-	-	-	-	96	4
SONOSTON	Mn	Cu	Al	Fe	Ni	C	Si
	55.2	38.3	4.36	3.16	1.42	0.095	0.07

TECHNIQUES

LOW FREQUENCIES (1-10 Hz)

Samples were machined from the as-received, as-cast materials into small rectangular prisms, typically 5 mm x 2.5 mm x 1.0 mm, for testing in a low-frequency, flexure pendulum. The pendulum used in this study as well as its electronic instrumentation is described in detail elsewhere [2].

INTERMEDIATE FREQUENCIES (10-5000 Hz)

Samples in the form of rectangular section bars of various lengths and thicknesses were machined from the as-received materials for testing in both fixed-free (cantilever) and free-free resonant bar equipment [3]. A detailed description of some of these techniques adapted to the narrower goal of the investigation of elastic moduli is given in reference 4.

ULTRASONIC FREQUENCIES (40 kHz and 120 kHz)

Samples in the form of square-section (3 mm x 3 mm) prisms, 60 mm in length, were machined from the as-received materials for testing by the

automated piecework
The basic principle of the
[3.1] system is to
measure the time spent
the individual worker
during the production

DASE - Auto Piecework System

The system is designed to
measure the time spent
on each piece of work
by the individual worker
and to calculate the
piecework rate for each
worker.

The system is designed to
measure the time spent
on each piece of work
by the individual worker
and to calculate the
piecework rate for each
worker.

The system is designed to
measure the time spent
on each piece of work
by the individual worker
and to calculate the
piecework rate for each
worker.

EXPERIMENTAL RESULTS

The results of the
experiment show that
the system is capable of
measuring the time spent
on each piece of work
by the individual worker
and to calculate the
piecework rate for each
worker.

The results of the
experiment show that
the system is capable of
measuring the time spent
on each piece of work
by the individual worker
and to calculate the
piecework rate for each
worker.

1957

1958

1959

1960

1961

1962

1963

1964

1965

1966

1967

1968

1969

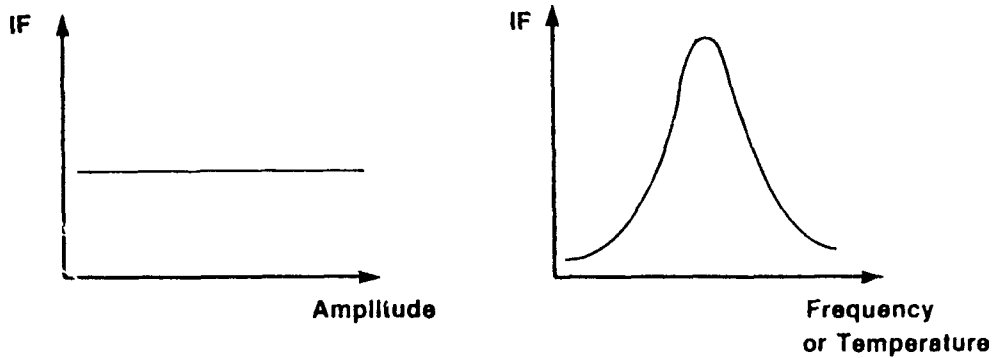
1970

1971

1972

1973

(a) AMPLITUDE INDEPENDENT AND FREQUENCY DEPENDENT



(b) AMPLITUDE DEPENDENT AND FREQUENCY INDEPENDENT

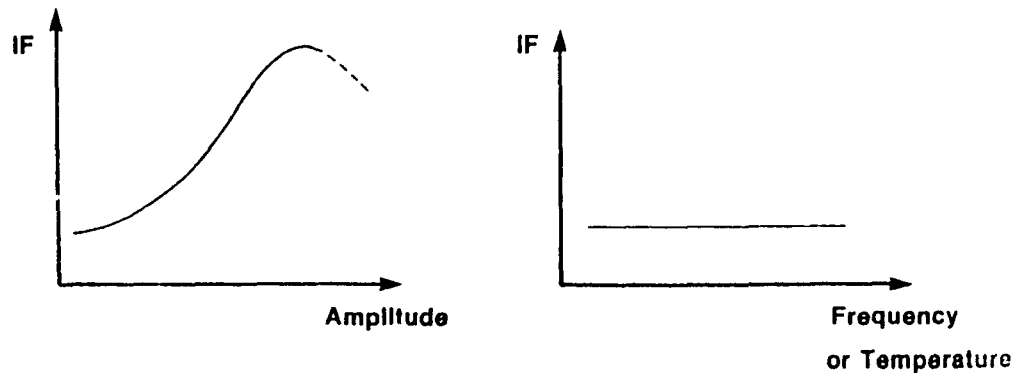


FIGURE 1: Schematic diagrams of internal friction as a function of strain amplitude for (a) amplitude-independent (dynamic hysteresis) and (b) amplitude-dependent (static hysteresis) damping.

RESULTS

ZA ALLOYS

The first flexure pendulum experiments (~ 4 Hz), on any one of the materials, using samples of two different thicknesses immediately revealed a strong dependence of the damping on the thickness in bending. This in turn suggested the existence of a large thermoelastic component, subsequently confirmed by the frequency dependence of the damping of samples of the same thickness and different lengths, and calculations of the thermoelastic damping using Zener's theory [6] and the known thermophysical properties of the materials (Fig.2). Other flexure pendulum measurements established the presence of a large peak as a function of T , culminating in a phase change at about 290°C , as shown in Fig. 3 for SPZ and ZA27. Low-frequency and high-frequency measurements of the low-temperature tail of this peak, as well as the strain amplitude dependence of the IF at ambient temperature ($\sim 20^\circ\text{C}$), are shown in Fig. 4 for ZA27.

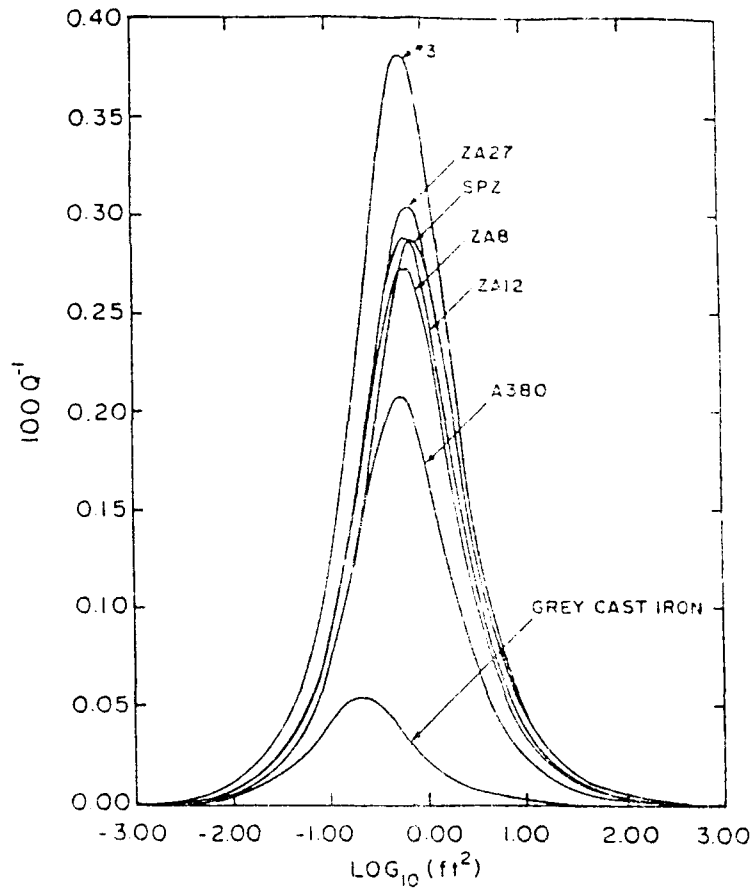


FIGURE 2: Thermoelastic damping peaks plotted as a function of $\log(ft^2)$, where f is the frequency in hertz and t is the specimen thickness in centimetres, for the ZA alloys, A380 and grey cast iron.

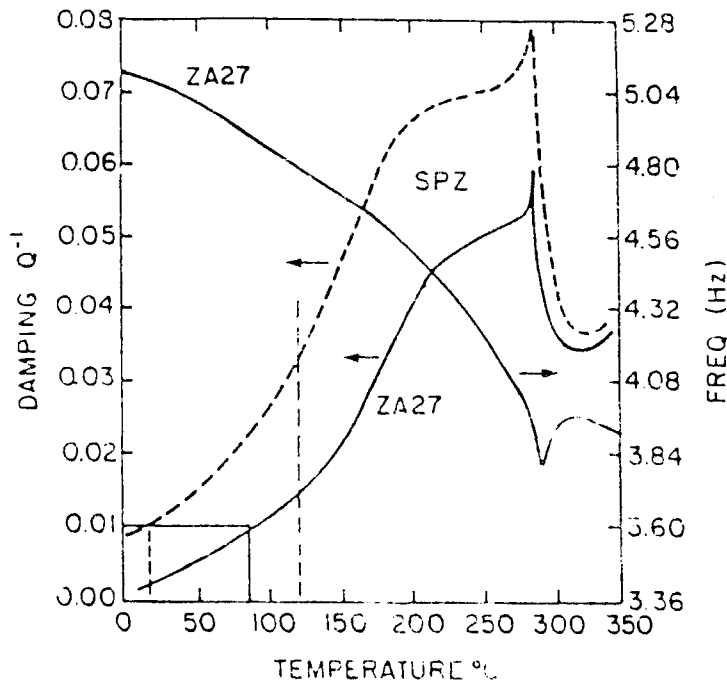


FIGURE 3: Damping, Q^{-1} , and resonant frequency (Hz) as a function of temperature for ZA27 and SPZ. The vertical dotted lines indicate the temperature range of practical interest.

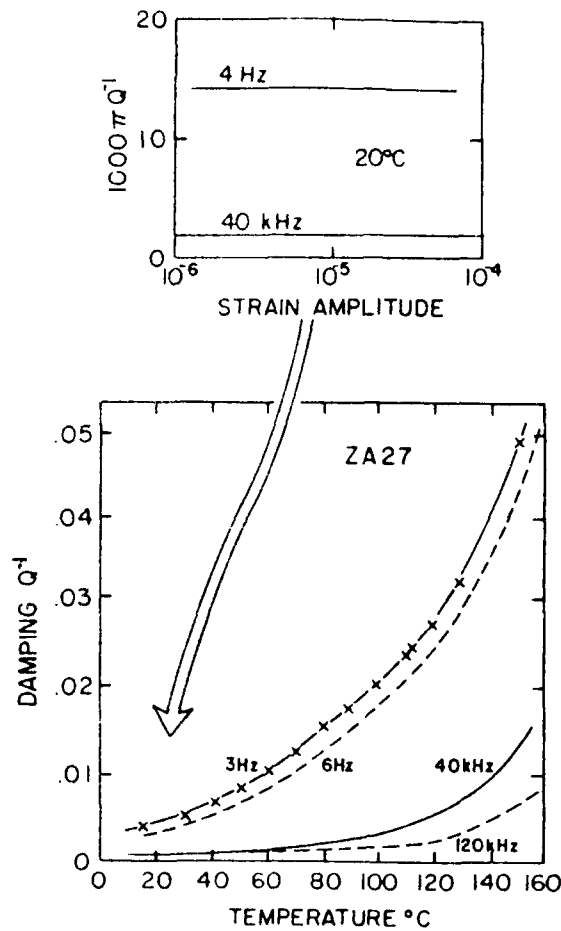


FIGURE 4: Damping, Q^{-1} , as a function of temperature and strain amplitude (at 20°C) for ZA27.

Combining the results of the flexure pendulum and the APUCOT measurements revealed the following important conclusions:

1. The IF and E are amplitude-independent at both high frequencies and low frequencies over the useful temperature range from 20 to 150°C. Such purely linear behaviour of IF and E in a series of alloys is quite unusual and indicates that all of the major components of the IF come from linear, dynamic relaxation mechanisms.
2. One of the mechanisms is thermoelastic damping.
3. The IF increases rapidly with temperature at both low and high frequencies.
4. The IF curves as function of T shift to higher temperatures (without noticeable change in shape) with higher frequencies. This strongly suggests that the major component of the IF comes from a thermally activated relaxation.
5. These results agree with the findings of previous investigations into the SPZ alloy [7-9].

If the IF at both low frequencies and high frequencies can be accurately described by the sum of the two thermally activated processes mentioned above (thermoelastic relaxation and the low temperature tail of a boundary relaxation), then this suggests that no other mechanisms become active at intermediate frequencies. However, to be sure that this is indeed the case, data at the intermediate frequencies must be collected and they too should be described by the sum of the two components.

SEMI-EMPIRICAL DESCRIPTION OF THE IF

The main results of the IF study of the ZA alloys are most easily displayed in a $\log Q^{-1}$ vs. $\log F$ plot, as shown in Fig. 5 for ZA27. The scatter is somewhat large, but not unduly so considering that the samples were cut from commercial die castings with variations in porosity, composition and other microstructural characteristics. Also, it should be noted that each datum is the average of at least three repeat measurements on a separate sample of the same thickness. The IF is highly reproducible for repeat measurements on the same sample, but variable from sample to sample cut from the same die casting.

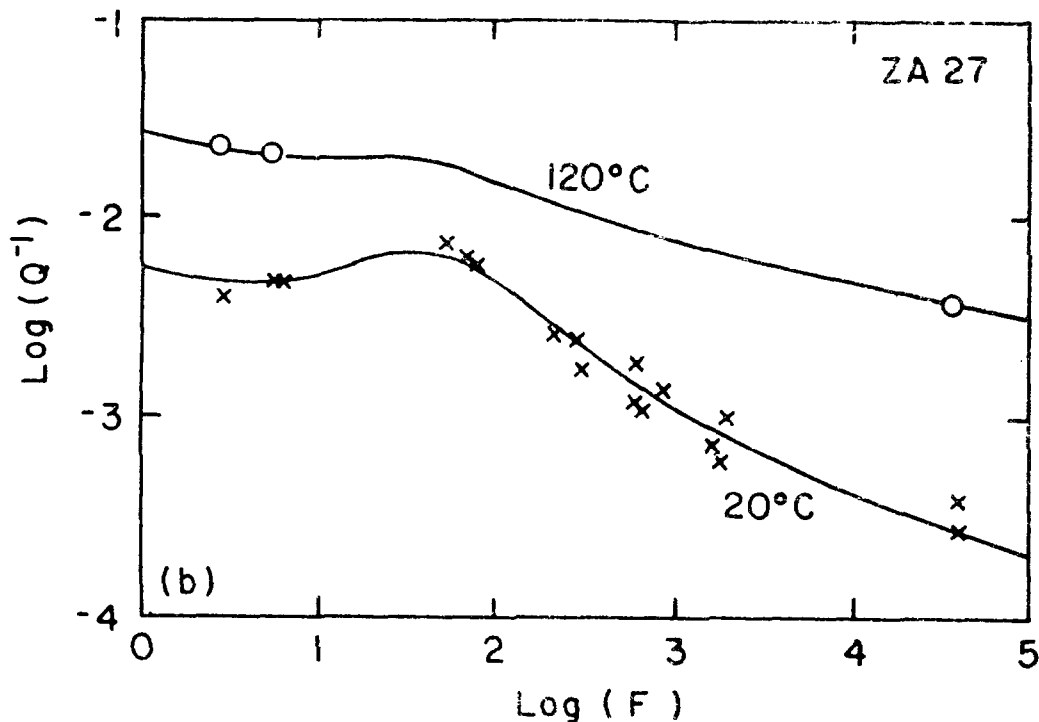


FIGURE 5: Log-log plot of damping Q^{-1} , as a function of frequency, f , for ZA27 at 20°C and 120°C . The full curves were calculated using equation (2) and the data in Table 2.

We expect to be able to describe the data of Fig.5 by an expression of the form

$$Q^{-1}(t, f, T) = \text{Background} + \frac{A}{f^n} \exp\left[-\frac{nH}{kT}\right] - \frac{\Delta_{TE}\omega\tau}{1 + (\omega\tau)^2} \quad (1)$$

where $Q^{-1}(t, f, T)$ is the IF for a sample of thickness t , at frequency f and temperature T . In eqn. (1) the IF is given in terms of three components: (1) a temperature-independent background; (2) the tail of a broadened high-temperature peak, characterized by the exponent n , the activation enthalpy H , and the constant, A ; and (3) the thermoelastic relaxation of strength, Δ_{TE} , and relaxation time τ . $\omega = 2\pi f$ is the radian frequency of the oscillations. Determination of n and H from the experimental results and

Δ_{TE} and τ from a combination of the thermophysical data on the alloys and the experimental results is described in detail in reference 10.

The experimental data obtained for all of the ZA series of alloys obtained over the temperature range from 20 to 150°C and the frequency range from 1 Hz to 120 kHz is well described by the semi-empirical formula derived from eqn. (1):

$$Q^{-1}(t, f, T) = \alpha_1 f^{-m} + \alpha_2 f^{-n} \exp(-\beta/T) + \alpha_3 T(ft^2)/[1 + (\delta_1 ft^2)^2] \quad (2)$$

where the first term represents the f -dependent but T -independent background, the second term is the tail of a broadened high-temperature relaxation and the third term is the thermoelastic component. The constants for the various alloys are tabulated in Table 2. In Fig. 5 it is important to note that the calculated curve at 120°C is in good agreement with the limited IF data obtained at that temperature.

TABLE 2--Data used to describe the thickness, frequency and temperature dependence of the damping in the ZA alloys.

Material	Frequency-Dependent Background		Temperature Dependence			Thermoelastic Damping	
	m	α_1	α_2	n	β	α_3	δ
#3	0.26	$2.90_0 \times 10^{-3}$	5530	0.16	5222	3.963×10^{-5}	1.556
ZA8	0.28	$3.54_8 \times 10^{-3}$	4566	0.16	5106	2.758×10^{-5}	0.911
ZA12	0.29	$4.07_3 \times 10^{-3}$	2937	0.18	4758	2.863×10^{-5}	0.977
SPZ	0.22	$1.17_5 \times 10^{-2}$	16987	0.13	4875	2.335×10^{-5}	0.918
ZA27	0.29	$5.01_2 \times 10^{-3}$	6910	0.16	4990	5.016×10^{-5}	1.495

Young's modulus measured at ambient temperature for the ZA alloys is given in Table 3.

TABLE 3--Young's modulus of the ZA alloys measured at 20°C and 40 kHz.

Material	Young's Modulus (GPa)
#3	93.8
ZA8	91.4
ZA12	89.5
SPZ	91.6
ZA27	78.0

SONOSTON

The IF of a sample of DR-1 as a function of ϵ at ambient temperature is shown in Fig. 6. Also, shown in Fig. 6 is the intrinsic IF of the material calculated from the specimen damping using the known strain distribution in the flexure pendulum sample. Details of this calculation are given elsewhere [11]. Similar experiments carried out on samples of both DR-1 and DR-4 using the APUCOT are shown in Fig. 7. Once again, the IF of the as-received SONOSTON is ϵ -dependent at high amplitudes, but the form of curves at 40 kHz are very different compared with those at low frequencies

The IF and E as a function of temperature for a sample of DR-1 measured at about 4 Hz in the flexure pendulum and at about 40 kHz by APUCOT are compared in Fig. 8. The minima in f^2 (~4 Hz) and E (~40 kHz) mark the Néel temperature for the alloy. At temperatures below the minimum in E the material is antiferromagnetic and the damping contains two components, an ϵ -dependent component and an ϵ -independent component. At temperatures higher than that of the minimum in E , the material is paramagnetic and the IF is ϵ -independent. This is borne out by the sets of Q^{-1} and E vs. T curves for different constant ϵ values shown in Figs. 9 and 10 for samples of DR-1 and DR-4 respectively. Fig. 8 also shows a rather complicated peak structure at low frequencies that shifts to higher temperature and increases in height at higher frequencies. A few tests at intermediate frequencies confirmed this observation. The sharp side or truncation of the high-frequency peak in

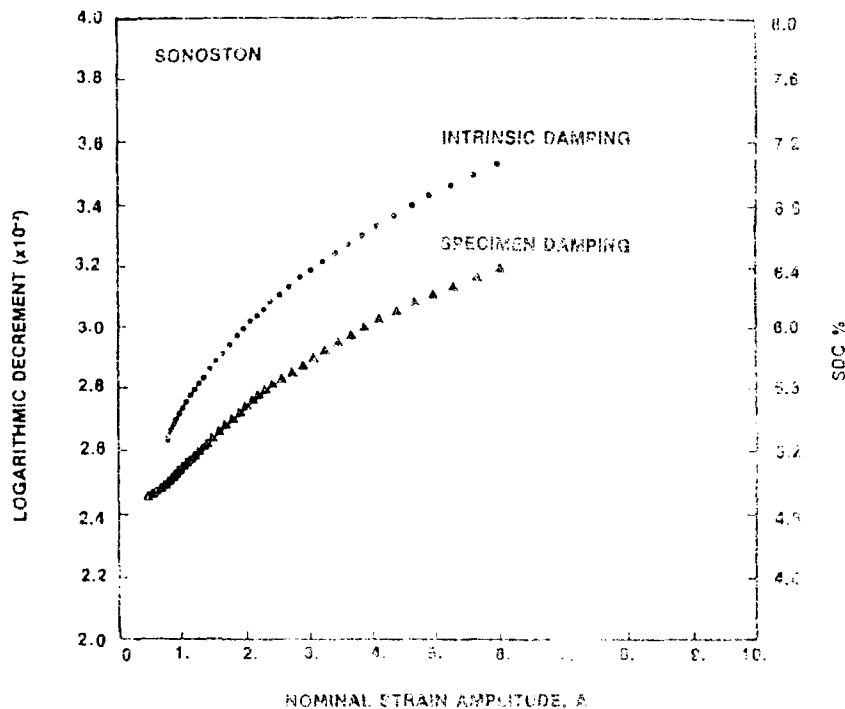


FIGURE 6: Comparison of measured specimen damping and calculated intrinsic damping for a sample of SONOSTON tested in a low-frequency flexure pendulum. The surface strain amplitude is equal to the nominal strain amplitude times 1.5×10^{-5} , while the logarithmic decrement is 10^{-7} and specimen damping coefficient (SDC) in percentage is $2\pi^{-1} \times 100$.

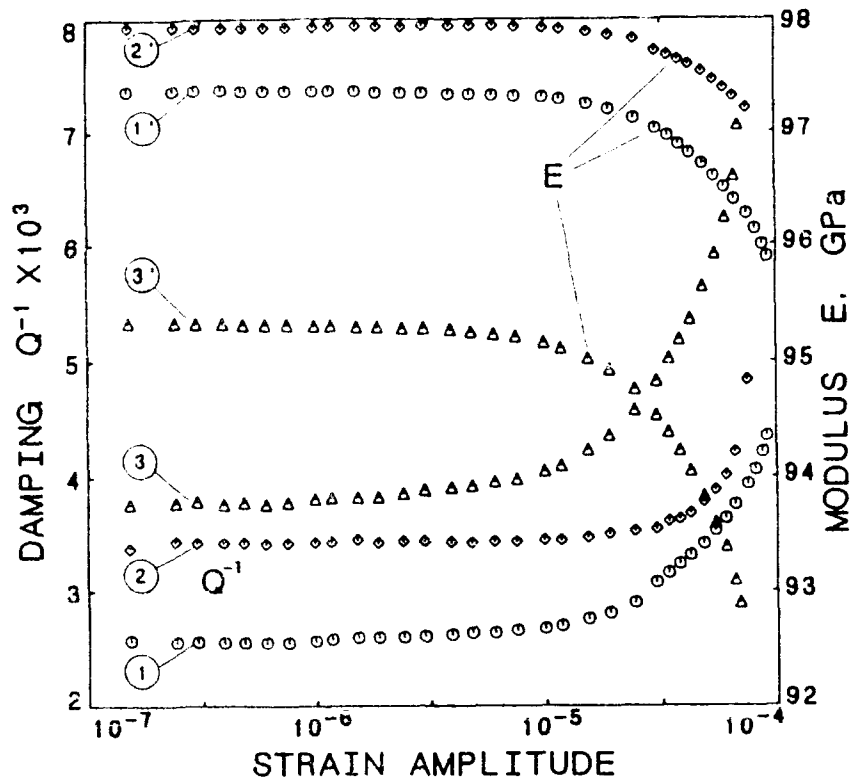


FIGURE 7: Damping and Young's modulus of samples of DR-1 and DR-4 as a function of strain amplitude at 20°C and 40 kHz: 1. as-received DR-4, 2. as-received DR-1, and 3. DR-4 after 2 h at 425°C and furnace cooling.

Fig. 8 is evidence of the fact that the thermally activated processes in the lower-temperature antiferromagnetic phase are shifted to the region of the phase change, but are inoperative in the higher-temperature paramagnetic phase. An important point to note in these results is the substantial differences in the Néel points and the forms of the Q^{-1} vs. T curves for samples of DR-1 and DR-4. These differences come entirely from microstructural differences between parts of the same casting that cooled at different rates. As shown in Figs. 7 and 8 respectively, the highest levels of damping achievable in the SONOSTON were not present in the as-received samples of either DR-4 or DR-1. Even higher damping levels were found at both low and high frequencies in samples heat-treated for 2 h at 425°C and furnace-cooled.

Combining the results of the flexure pendulum and APUCOT measurements revealed the following important conclusions:

1. The IF and E are strongly ϵ -dependent at both low and high frequencies at temperatures below the Néel temperature. At higher temperatures the IF is ϵ -independent.
2. At least one of the mechanisms is thermally activated, since the peak of Q^{-1} vs. T shifts to higher temperatures with higher frequencies. An unexpected feature of these results is that the overall peak height also increases with frequency (see Fig. 8).

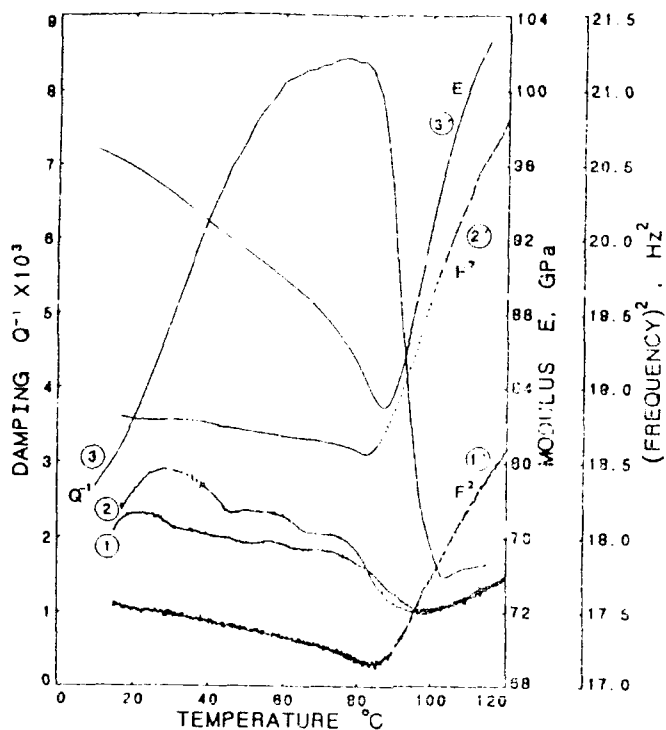


FIGURE 8: Damping and resonant frequency squared as a function of temperature for flexure pendulum tests on a sample of DR-1 before (1) and after (2) 2 h at 425°C. Damping and Young's modulus vs. temperature curves for a sample of DR-1 measured at 40 kHz (3). The strain amplitude in both types of test was 2×10^{-5} .

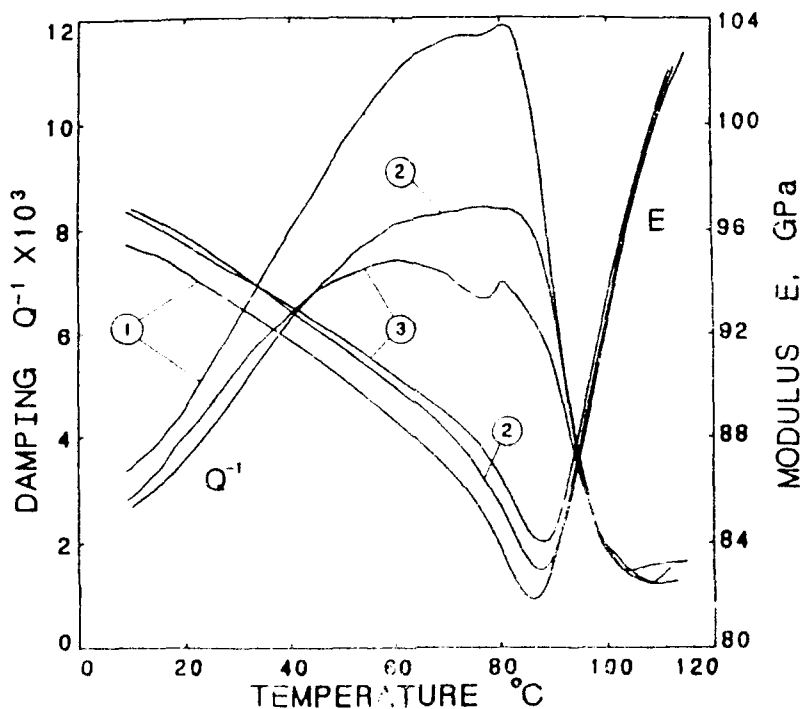


FIGURE 9: Q^{-1} and E vs. T curves for a sample of DR-1 measured at 40 kHz and different strain amplitudes. 1. $\epsilon = 6 \times 10^{-5}$, 2. $\epsilon = 2 \times 10^{-5}$, and 3. $\epsilon = 2 \times 10^{-7}$.

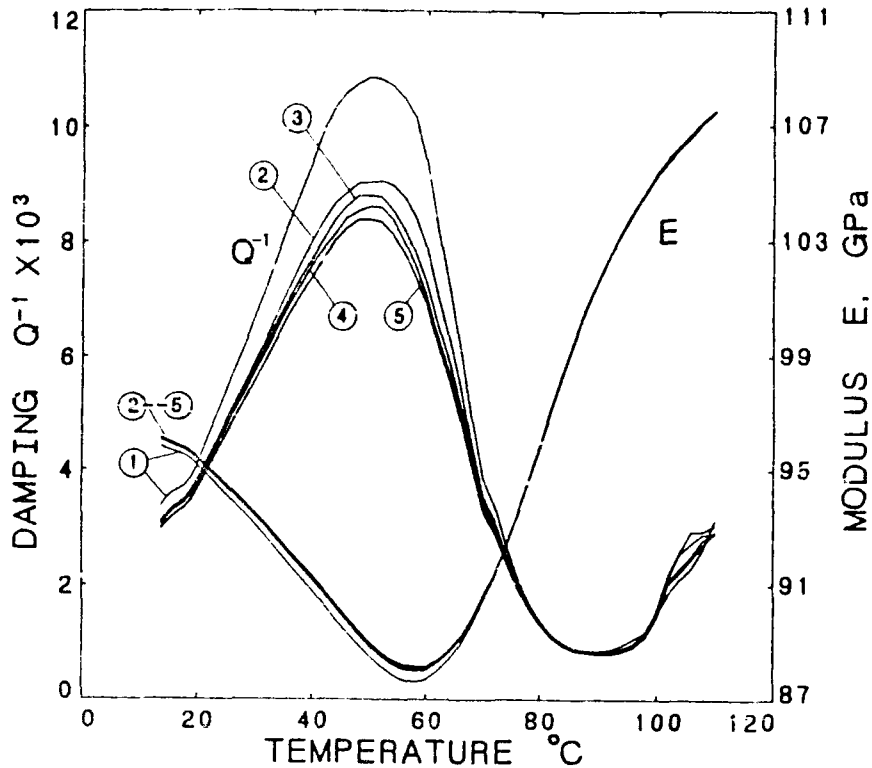


FIGURE 10: Q^{-1} and E vs. T curves for a sample of DR-4 measured at 40 kHz and different strain amplitudes: 1. $\epsilon = 3.5 \times 10^{-5}$, 2. $\epsilon = 1.2 \times 10^{-5}$, 3. $\epsilon = 3.5 \times 10^{-6}$, 4. $\epsilon = 1.2 \times 10^{-6}$, and 5. $\epsilon = 3.5 \times 10^{-7}$.

The difficulties of characterizing the intrinsic ϵ dependence for each of the vibration modes used in our experiments, together with unknown mechanism that causes the increase in Q^{-1} with frequency for the thermally activated mechanism, make a semi-empirical description of the IF, similar to the description given above for the ZA-alloys, almost impossible for SONOSTON. Indeed, at present it is not clear if the same mechanisms are operative at both low and high frequencies in the antiferromagnetic phase. In addition, the variation from place to place in the casting is much too large to ignore in a semi-empirical description of the damping of the whole casting.

DISCUSSION

The characterization of the damping and stiffness properties of commercial HIDAMETS is a difficult and in some cases tedious procedure. We have outlined a method that works reasonably well for ϵ -dependent mechanisms and is not very different from the methods used to characterize viscoelastic materials. However, the majority of commercial HIDAMETS obtain their high-damping properties from ϵ -dependent mechanisms or mechanisms involving aspects of both dynamic and static hysteresis mechanisms that are highly sensitive to small microstructural changes. For such materials, it is a challenge to extract even the intrinsic damping for a given mode of vibration. This does not mean that such materials are not useful in practice, but it does mean that some other method of assessing the usefulness of the damping properties must be employed. A method that we have employed with some success involves the simple substitution of

materials for the component or structure involved, as mentioned in the introduction

The ZA alloys are already used in hundreds of different applications and among these are several where the elevated damping of the alloy in question has proven to be of great benefit. For example, automobile engine mounts have been die-cast from ZA27 [12]. SONOSTON has been used to cast quiet submarine propellers.

CONCLUSIONS

The ZA alloys have elevated damping values at ambient temperatures compared with most of their competitors. This elevated damping is almost always a bonus in practical applications. At temperatures between 60 and 80°C, all of the ZA alloys become HIDAMETS in the sense that $Q^{-1} \geq 10^{-4}$. A characterization of this damping behaviour is given that allows the design engineer to estimate the damping of these alloys in flexure at useful values of thickness, temperature and frequency.

Properly heat-treated SONOSTON is also a HIDAMET at temperatures from about 0°C to the Néel point and high strain amplitudes ($\epsilon > 10^{-4}$). But, because of the complexity of the mechanisms involved, it is not possible to present the damping behaviour in a simple manner (using a semi-empirical description) that will cover wide ranges of temperature, frequency or vibration strain amplitude.

ACKNOWLEDGEMENT

The research reported in this paper on the ZA alloys was funded by the International Lead Zinc Research Organization, Inc.

References

- [1] Sahoo, M., Moore, V.E. and Weatherall, G., Canmet Report MRP/PMRL 84-61 (TR), 1984.
- [2] Sprungmann, K.W. and Ritchie, I.G., "Instrumentation, Computer Software and Experimental Techniques Used in Low-Frequency Internal Friction Studies at WNRE," Atomic Energy of Canada Limited Report, AECL-6438 1980.
- [3] Ritchie, I.G. and Pan, Z-L., "High Damping Metals and Alloys," Metallurgical Transactions A, 22A, 1991. In press.
- [4] Rosinger, H.E., Ritchie, I.G. and Shillinglaw, A.J., "Improved Measurements of Elastic Properties at Acoustic Resonant Frequencies," Atomic Energy of Canada Limited Report, AECL 1114, 1976.
- [5] Robinson, W.H. and Eogar, A., "The Piezoelectric method of Determining Mechanical Damping at 30 KHz," IEEE Transactions of Sonic and Ultrasonics SU-21, 1974, 98-101.
- [6] Zener, C., Elasticity and Anelasticity of Metals, The University of Chicago Press, Chicago, 1949, p. 13.

- [7] Nuttall, K., "The Damping Characteristics of a Superplastic Zn-Al Eutectoid Alloy," *Journal of the Institute of Metals*, 99, 1971, 266-270.
- [8] Kawabi, K., and Kuwahara, K., "High Damping and Modulus Characteristics in a Superplastic Zn-Al Alloy," *Journal de Physique*, 42, 1981, C5-941-C5-946.
- [9] Otani, T., Sakai, T., Hoshino, K. and Kurosawa, T., "Damping Capacity of Zn-Al Alloy Castings", *Journal de Physique*, 46, 1985, C10-417-C10-420.
- [10] Ritchie, I.G., Pan, Z-L. and Goodwin, F.E., "Characterization of the Damping Properties of Die-Cast Zinc-Aluminum Alloys," *Metallurgical Transactions A*, 22A, 1991, in press.
- [11] Ritchie, I.G., Schmidt, H.K. and Sprungmann, K.W., "Non-Linear Internal Friction from Flexure Pendulum Measurements," *Journal de Physique*, 46, 1985, C10-791-C10-794.
- [12] Lyon, R. and Spillane, A.F., "The Development of ZA-27 Engine Mounts by Austin Rover", *Proc. SAE Conf.*, Detroit, Michigan, February 1988.

VISCOELASTIC AND STRUCTURAL DAMPING ANALYSIS

Harry H. Hilton*
University of Illinois at Urbana-Champaign

ABSTRACT

The interrelationships between viscoelastic, Newtonian viscous and structural damping are analyzed in terms of Fourier transforms and complex moduli in the frequency domain and are also interpreted in terms of behavioral responses associated with real material compliances or moduli in the real time plane. It is shown that the correspondence between viscous and elastic structural damping is spurious, severely limited to only harmonic motion and that it does not extend to more complicated viscoelastic materials beyond Newtonian viscous flow dissipation. The dissipation energy generated by viscoelastic and structural damping is also examined. The effects of structural damping on elastic and viscoelastic bending-torsion flutter are evaluated with the help of numerical examples. The material considered is aluminum, but the analysis is general and can be applied to any viscoelastic material. It is shown that the presence of increased structural damping does not necessarily have a stabilizing effect by decreasing the viscoelastic or elastic flutter speed nor are the viscoelastic flutter speeds necessarily lower than the corresponding elastic ones.

INTRODUCTION

In flutter and vibration analysis, it is standard practice to augment elastic effects by the introduction of structural damping coefficients g [1-4], where the latter are essentially measures of losses due to material hysteresis and/or friction in structural joints. In both instances, the fundamental dissipation phenomenon is "dry" solid friction and as such, the associated force and displacement constitutive relations are explicitly independent of frequency and of displacement velocities, accelerations or their higher time derivatives. Analytically, the algebraic Hooke's law is maintained, but the actual, real elastic moduli are replaced by complex

* Professor Emeritus of Aeronautical
and Astronautical Engineering
104 S. Mathews
Urbana, IL 61801-2997
217-333-2653 FAX 217-244-7705
E-mail: HILTON AT UIUCVMC.BITNET

values, i.e., $E = E_0 (1 + ig_1)$, where E_0 is Young's modulus in the absence of structural damping. A similar expression is used for the elastic shear modulus, $G = G_0 (1 + ig_2)$ and for the elastic bulk modulus, $K = K_0(1 + ig_3)$. The three g 's displayed here may or may not be equal depending upon the particular damping encountered in a given structure.

Viscoelastic materials, on the other hand, obey differential and/or integral stresses-strain laws which relate stresses, strains and their time derivatives of various orders [5]. The viscoelastic dissipation process is primarily an involved, highly frequency sensitive, material dependent viscous phenomenon with one or more coefficients of viscosity [5] and, as will be shown, totally unrelated to the structural damping mechanism. Historically, and in this paper as well, the term viscous damping refers to Newtonian flow, where the stresses are proportional to the strain velocities through at most only one coefficient of viscosity for shape changes and no more than one other for volume changes. While the structural damping phenomenon is well understood and experimental values for these damping coefficients are readily available [1-4], its interpretation vis-a-vis viscous damping appears confused [6, 7]. Fung [3], on the other hand, has correctly based his correspondence between viscous and structural damping on harmonic motion, but has restricted his analysis to only motion at the system's natural frequency. Under these conditions he shows that the structural damping coefficient is frequency independent. More recently, Dahl [8] has modeled solid friction damping in mechanical oscillators by using both linear and nonlinear formulations. His models are of interest, since they simulate decay behavioral patterns which approximate (a) Coulomb friction at high amplitudes and low frequencies, (b) viscous damping at mid amplitudes and mid frequencies and, finally, (c) structural damping at small amplitudes and high frequencies. However, these approximate similarities do not imply any relations between fundamental behavioral responses of solid and viscous damping phenomena. Saravanan and Chamis [9] present a hysteric damping analysis for composite laminates and include an extensive bibliography on damping.

Since viscoelasticity includes among other mechanisms both elasticity and viscous damping, i.e. velocity dependent Newtonian viscous dissipation, it can readily serve as a vehicle for the comparison of viscous and structural damping. In this paper, general linear viscoelastic stress-strain relations (including structural and viscous damping) are used to interpret the various damping processes by a critical examination of complex moduli in the frequency domain and of compliances in the real

time plane. Such an approach makes it possible to treat generalized many degree of freedom systems and is not limited to the single mass, spring and damper combinations of References [6] and [7].

ANALYSIS

Flutter and Complex Moduli

The governing elastic equilibrium equations for flexible lifting surfaces, fuselages, etc. subjected to aerodynamic and inertial forces with generalized displacements $q_m(x, t)$, $m=1, 2, \dots, M$, can be expressed in the generalized form

$$\sum_{m=0}^M \left[\sum_{n=0}^N D_{mnk}^e \partial^n q_m(x, t) / \partial x^n \right] = \sum_{n=1}^{N''} L_{mnk} \{V, q_m, \dot{q}_m, \ddot{q}_m\} = F_k \quad (1)$$

$$k = 1, 2, \dots, M; \quad x = \{x_1, x_2, x_3\}$$

where L_{mnk} are differential operators describing inertia and unsteady aerodynamic contributions, V is the flight speed, F_k are generalized forces and the D_{mnk}^e are elastic stiffness terms depending primarily on material properties (i.e., Young's and shear moduli E_0 and G_0), on structural geometry and on mass distributions. The elastic-viscoelastic analogy [5, 10, 11] consists of the application of Fourier transforms (F.T.) to Eqs. (1) and of the subsequent substitution of complex viscoelastic moduli \bar{E} and \bar{G} for the elastic moduli E_0 and G_0 , or essentially replacing the real and frequency independent elastic stiffnesses D_{mnk}^e by complex viscoelastic stiffness functions $\bar{D}_{mnk}(\omega)$. This, then leads to governing viscoelastic relations in the F. T. plane

$$\sum_{m=0}^M \left[\sum_{n=0}^N \bar{D}_{mnk}(x, \omega) \partial^n \bar{q}_m(x, \omega) / \partial x^n \right] = \sum_{n=1}^{N''} \bar{L}_{mnk} \{V, \bar{q}_m, \omega\} = \bar{F}_k(x, \omega) \quad (2)$$

It can be readily shown [5] that for simple harmonic motion the F. T. variable ω is the oscillatory frequency and that in the case of flutter [10, 11] it becomes the flutter frequency, while V plays the role of the flutter speed. The latter two are, of course, pairs of eigenvalues at which a given flight structure can experience harmonic motion. The velocity V can readily be replaced by the flutter Mach number M_f .

response.) Similar, but more involved, expressions may also be written for anisotropic materials [13], but will not be introduced here for the sake of simplicity. They are, however, treated briefly at the end of the next section.

The application of Fourier transforms to Eqs. (3), leads to [5, 10, 11]

$$\bar{\bar{F}}_m = \bar{\bar{E}}_m \bar{\bar{Q}}_m \quad (6)$$

where the $\bar{\bar{E}}_m$ are frequency dependent viscoelastic complex moduli. Note that Eqs. (6) are symbolically equivalent to the F.T. of Eqs. (4) and that the F.T. of the elastic Eqs. (4) gives a complex modulus $\bar{\bar{E}}_m = E_{m0}(1 + ig_m)$ for structural damping, which is frequency insensitive. Since these complex moduli are expressible as $\bar{\bar{E}}_m = E_{mnk}(x, \omega) + iE_{mnl}(x, \omega)$, it follows that the viscoelastic stiffnesses are also complex, i.e., $\bar{\bar{D}}_{mnk}(x, \omega) = D_{mnkR}(x, \omega) + iD_{mnkI}(x, \omega)$, where the E_{mR} , E_{mI} , D_{mnkR} , and D_{mnkI} are all distinct real frequency functions. Such an omega dependence is due to the intrinsic nature of the time differential or integral viscoelastic stress-strain laws of Eqs. (3). It can be readily seen from Eqs. (5), that in the general viscoelastic case, the complex moduli with structural damping are

$$\bar{\bar{E}}_m(x, \omega) = (1 + ig_m)E_{mR}(x, \omega) + iE_{mnl}(x, \omega) = E_{mR}(x, \omega) + iE'_{mnl}(x, \omega) \quad (7)$$

where $E'_{mnl} = g_m E_{mR} + E_{mnl}$.

Furthermore, elastic structural damping is also included in Eqs. (2), by virtue of the complex moduli defined by Eqs. (4), except that then the D_{mnkR} and D_{mnkI} are frequency independent. In any event, the expressions on the right hand sides of Eqs. (2) (i.e., the generalized forces) are unaffected by the nature of the elastic or viscoelastic materials. Therefore, the fundamental difference is that in the elastic case with or without structural damping, D_{mnk}^e are frequency independent, while for viscoelastic materials the stiffness parameters $\bar{\bar{D}}_{mnk}$ are always frequency functions. For nonhomogeneous viscoelastic materials with structural damping, one needs only to replace the elastic stiffnesses in Eqs. (2) with $\bar{\bar{D}}_{mnk}(x, \omega) = D_{mnkR}(x, \omega) + iD'_{mnkI}(x, \omega)$ in the F. T. plane where $D'_{mnkI} = g_m D_{mnkR} + D_{mnkI}$. Again note, that for elastic structural damping, the

stiffness parameters in Eqs. (2) have a form identical to frequency independent viscoelastic ones. Table I illustrates the complex moduli representations in the four combinatorial cases considered.

TABLE I.
Complex Moduli $E = E_R + iE_I$ and Compliances $J_E(t)$

<u>Material</u>	<u>Real Part</u>	<u>Imaginary Part</u>	<u>Compliance $J_E(t)$</u>
Elastic	E_0	0	
Elastic with structural damping	E_0	gE_0	$\delta(t)JE_0/(1 + ig)$
Viscous damping with structural damping	E_0	$gE_0 + c\omega$	$\exp[-(1 + g)t/\tau]/c$
Viscoelastic with structural damping	$E_R(\omega)$	$gE_R(\omega) + E_I(\omega)$	Eq. (14)

The structural damping terms igq may be thought of as out of phase components of the displacements q , and, as such, bear some resemblance to velocity effects, i.e., viscous damping. However, examination of the F. T. of the viscous damping term $c\dot{q}$, in Eqs. (5), clearly shows that it is equal to $i\omega\bar{q}$ for a time independent viscosity coefficient c . Consequently, as long as structural damping coefficients g are frequency independent, they cannot phenomenologically relate to viscous damping, unless one postulates a c inversely proportional to ω - not the ordinary coefficient of viscosity, to be sure. Also note that the F. T. of Eq. (5) for $g = 0$ is $\bar{E} = E_0(1 + i\omega^*/\sqrt{M^*E_0})$, where $\omega^* = \omega/\omega_N$ and the natural frequency $\omega_N^2 = E_0/M^*$, with M^* the system mass. Therefore, the complex modulus for viscous damping is frequency dependent, and only at the natural frequency can a frequency independent correspondence be established between structural and viscous damping when $g = c\sqrt{M^*E_0}$. This relation between the complex moduli applies to any motion, and such a correspondence between g and c is not limited to harmonic motion as has been discussed earlier by Fung [3]. At all other frequencies, of course, the frequency dependent relationship $g = c\omega^*/\sqrt{M^*E_0}$ is valid for any elastic structural or viscous damping complex modulus, but is not physically realistic.

However, while such a proposition satisfies the consistency of expressions in the ω F. T. plane, Eqs. (4) and (5) demonstrate that even an

inversely frequency dependent viscosity coefficient c or a constant one at the natural frequencies cannot restore correspondence in the time plane between the elastic and viscous damping cases for general displacement functions $q(x,t)$ encountered in creep, relaxation and other non-oscillatory motions. As a matter of fact, even in relatively simple motion where q is proportional to a single exponential function $\exp(i\omega t)$, the correspondence between viscous and structural damping is lost in those non mechanical vibration problems, such as for instance flutter, which have highly nonlinear sensitivities to frequency eigenvalues. For convenience and completeness, one usually represents viscoelastic stress and strain behavior in terms of mechanical models, such as, for instance, the generalized Kelvin model (GKM) [5] shown in Fig. 2. Consequently, it follows from Eq. (5) and from an examination of the GKM that viscoelastic damping represents a much more complicated phenomenon than either elastic or viscous structural damping, since the complex compliances $\bar{J}_E = 1/\bar{E}$, $\bar{J} = 1/\bar{G}$, $\bar{J}_v = 1/\bar{K}$, etc. with $\bar{E} = 3\bar{G}/(1 + \bar{G}/\bar{K})$ are of the form

$$\bar{J} = J_0/(1 + ig) + 1/i\omega\eta_{N+1} + \sum_{n=1}^N 1/\{G_n[1 + i(\omega\tau_n + g)]\} \quad (8)$$

with similar relations for the other \bar{J} 's and where the relaxation times $\tau_n = \eta_n/G_n$, η_n and G_n are all material property, temperature sensitive parameters [5] (Fig. 2). Viscoelastic compliances in the absence of structural damping are given by Eq. (8) with $g = 0$. Similarly, the expressions (8) also include viscous damping as a degenerate case of the form $N = 0$, $J_0 = 0$ and with all $G_n = \infty$. The elastic case can be obtained from $\eta_{N+1} = G_n = \infty$.

These two distinct phenomena, i.e., structural and viscoelastic (including viscous) damping, may be interpreted in yet another fashion by examining their complex representations. For each generalized displacement q_m , the corresponding elastic modulus with structural damping can be represented by $E_0(1 + ig) = R_c \exp(i\Delta_c)$ and the expressions $R_c = E_0\sqrt{1 + g^2}$ and $\Delta_c = \tan^{-1}(g)$ are both frequency independent. (For the sake of simplicity of representation, the subscripts m are not included here.) Complex viscoelastic moduli may be written in a similar fashion as seen in Eq. (7) with

$$\bar{E}(\omega) = R_{ve} \exp(i\Delta_{ve}) \quad (9)$$

where

$$R_{ve}(\omega) = E_R(\omega) \{1 + g^2 + 2g E''(\omega) + [E''(\omega)]^2\}^{1/2} \quad (10)$$

and

$$\Delta_{ve}(\omega) = \tan^{-1} [g + E''(\omega)] \quad (11)$$

are both frequency dependent with $E^*(\omega) = E_I(\omega)/E_R(\omega)$. These values are shown in Table II for 2024 aluminum [10, 11]. The $R_{ve_{min}}$ and $R_{ve_{max}}$ values correspond to $\omega = 0$ and ∞ (i.e. $t = \infty$ and 0) respectively and the E_I/E_R peak in the neighborhood of 15 Hz, which is of the order of magnitude of the flutter frequencies for the examples considered in Reference [11]. The R_e vectors for the elastic structural damping at the temperatures of Table II are equal to $R_{ve_{max}}$ and the angles Δ_e are equal to $\Delta_{ve_{min}}$ at all temperatures.

TABLE II.

Viscoelastic Damping Properties of
2024 Aluminum [11]

Temperature °F	Structural Damping Coefficient	(E_I/E_R)	$R_{ve_{max}}$ psi x 10 ⁻⁷	$R_{ve_{min}}$ psi x 10 ⁻⁷	$\Delta_{ve_{max}}$ degrees	$\Delta_{ve_{min}}$ degrees
80	0	.00283	1.070	1.060	.162	0
80	.05	.0528	1.071	1.061	3.02	2.86
200	0	.00585	1.038	1.020	.335	0
200	.05	.0559	1.039	1.021	3.20	2.86
340	0	.0144	.990	.966	.826	0
340	.05	.0644	.991	.967	3.69	2.86
450	0	.0258	.954	.900	1.48	0
450	.05	.0758	.955	.901	4.33	2.86

Since the flutter Eqs. (2) are highly nonlinear functions of ω , an analytical comparison of viscoelastic and structural damping is not feasible. However, a reexamination of the bending-torsion supersonic flutter

problem for a Timoshenko beam previously analyzed in Reference [11] based on the addition of structural damping effects as exemplified by Eqs. (7), leads to the results displayed in Table III.

TABLE III.

Some Flutter Results for
a 2024 AL Wing

g	Elastic		Viscoelastic	
	ω_f	M_f	ω_f	M_f
0	20.0001	1.3037	26.8586	1.5167
.005	19.9737	1.3056	26.8070	1.5081
.01	19.9465	1.3074	26.7550	1.4994
.05	19.7150	1.3239	29.0102	1.9887

These results are typical for metal wings in supersonic flow and fully account for the material property dependence on temperature as the flutter Mach number changes. It is to be noted that as the structural damping g increases the viscoelastic flutter Mach number M_f may increase (destabilizing) or decrease (stabilizing). For an elastic aluminum wing with the same mass distribution, geometry and aerodynamics, the corresponding flutter Mach numbers are smaller than the viscoelastic ones and an increase in structural damping for the elastic wing is destabilizing. Even though the viscoelastic action for 2024 aluminum at elevated temperatures is far from being as pronounced as it is in high polymers and composites, the viscoelastic flutter Mach numbers are significantly different from the corresponding elastic ones. (Table III) This is due to the highly nonlinear dependence on the flutter frequency ω_f and the attendant phase relations which shift in a complicated fashion. In References 10 and 11 it has been previously noted that viscoelastic flutter Mach numbers may be higher or lower than corresponding elastic ones for wings of identical geometry, mass distributions and aerodynamic properties. Dugunji [12] has noted similar behavior due to structural damping in elastic panel flutter.

Dissipation Energy

A comparison of the dissipation energies generated by viscoelastic, viscous and structural damping processes is next in order. They can be considered together by referring to the mechanical models of Fig. 2. For an

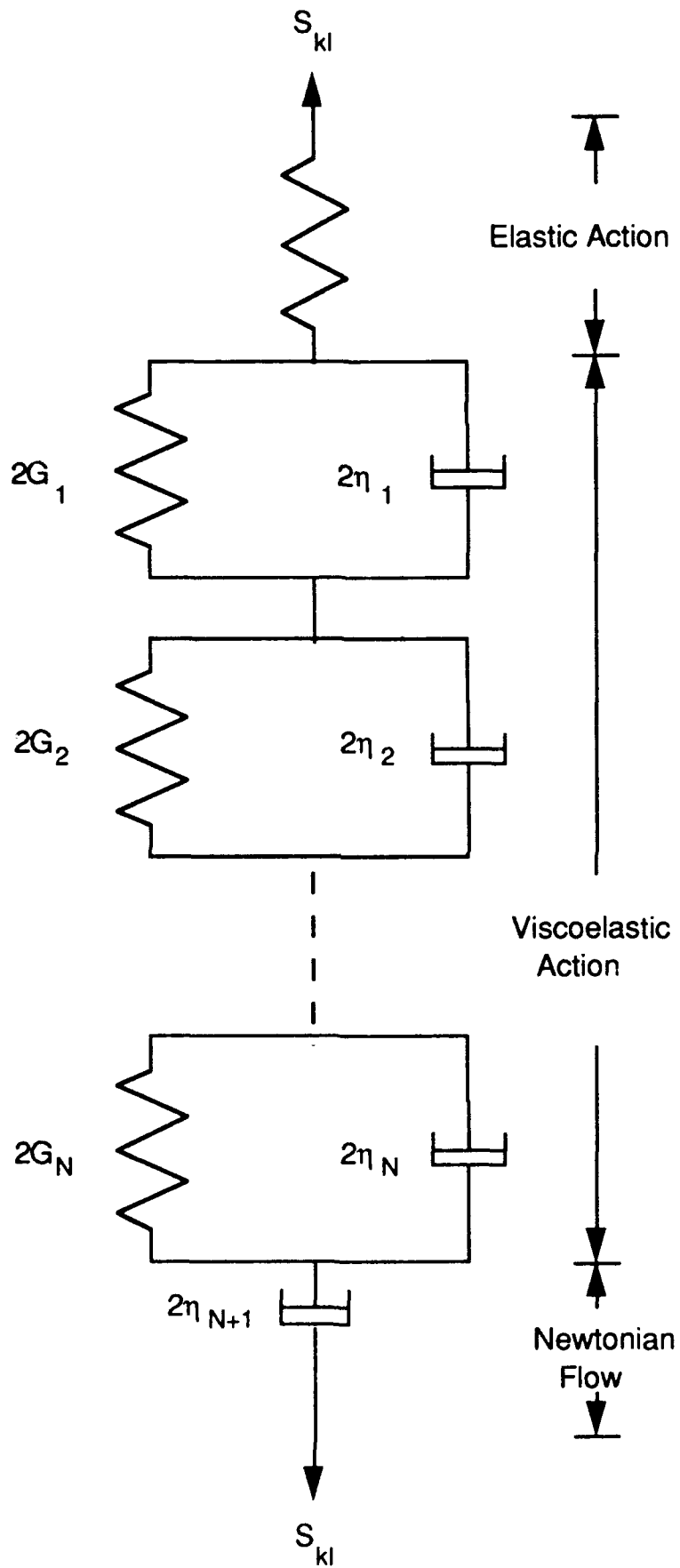


Fig. 2. The Generalized Kelvin Model

isotropic, linear viscoelastic material the stress-strain relations for change in shape and in volume are, respectively [5]

$$2 E_{kl}(x, t) = \int_0^t J(x, t - t') S_{kl}(x, t') dt' \quad (12)$$

$$\epsilon(x, t) = \int_0^t J_v(x, t - t') \sigma(x, t') dt' \quad (13)$$

where S_{kl} and E_{kl} are the stress and strain deviators, ϵ and σ the mean strains and stresses and where the compliances are

$$J(t) = \sum_{n=1}^{N+1} J_n(t) = \delta(t) J_0/(1 + ig) + 1/\eta_{N+1} + \sum_{n=1}^N \exp[-(1 + g)t/\tau_n]/\eta_n \quad (14)$$

and with a similar expression for the volumetric compliance J_v , both of which are obtained by the F.T. inversion of Eq. (8). Note that Eq. (14) defines the general viscoelastic compliances in the presence of structural damping. These compliances may also be written in the manner of Eq. (7), i.e.

$$\bar{J}(\omega) = 1/\bar{G}(\omega) = J_R(\omega) - iJ_I(\omega) = [G_R(\omega) - iG_I(\omega)]/[G_R^2(\omega) + G_I^2(\omega)] \quad (15)$$

As can be seen from Eqs. (5) and (8), the introduction of structural damping effects into viscoelasticity results in changes of $G_n[1 + i(\omega\tau_n + g)]$ in the denominators of the sums of Eq. (5) and in first term multiplication by $1/(1+ig)$. Effectively, upon F.T. inversion, this serves to shift the time to $t+gt$ in the exponential terms of Eq. (14).

The dissipation energy per unit volume at any point $x = (x_1, x_2, x_3)$ and at any time $t > 0$ is

$$DE(x, t) = \int_0^t \sum_{n=1}^{N+1} S_{kl}^{(n)}(x, t') \dot{E}_{kl}^{(n)}(x, t') dt' + \int_0^t \sum_{m=1}^{M+1} \sigma^{(m)}(x, t') \dot{\epsilon}^{(m)}(x, t') dt' \quad (16)$$

where superscripts (n) and (m) denote quantities associated with each dashpot n or m in the Fig. 2 model. The stress-strain relations for each dashpot are given by [5]

$$S_{kl}^{(n)} = 2\eta_n \dot{E}_{kl}^{(n)} \quad (17)$$

and

$$2 E_{kl}^{(m)}(x, t) = \int_0^t J_n(x, t-t') S_{kl}(x, t') dt' \quad (18)$$

where S_{kl} is the total stress deviator in the GKM model and is the sum of $S_{kl}^{(n)}$ of any dashpot and the stress deviator of its corresponding elastic paired spring. Equations similar to (17) and (18) can also be written for volumetric changes.

Differentiation of Eqs. (18) and substitution into (17) gives

$$S_{kl}^{(n)}(x, t) = \eta_n \left\{ \int_0^t \frac{\partial J_n(x, t-t')}{\partial t'} S_{kl}(x, t') dt' + J_n(x, 0) S_{kl}(x, t) \right\} \quad (19)$$

with a similar expression for $\sigma^{(m)}$. Finally, the introduction of Eqs. (17), (18) and (19) into (16) results in

$$\begin{aligned} DE(x, t) = & \int_0^t \left\{ \sum_{n=1}^{N+1} \frac{1}{2\eta_n} \left[\int_0^{t'} \frac{\partial J_n(x, t'-\xi)}{\partial t'} S_{kl}(x, \xi) d\xi \right. \right. \\ & \left. \left. + J_n(x, 0) S_{kl}(x, t') \right] \left[\int_0^{t'} \frac{\partial J_n(x, t'-\xi)}{\partial t'} S_{kl}(x, \xi) d\xi \right. \right. \\ & \left. \left. + J_n(x, 0) S_{kl}(x, t') \right] \right\} dt' + \int_0^t \left\{ \sum_{m=1}^{M+1} \frac{1}{\eta_{vm}} \left[\int_0^{t'} \frac{\partial J_{vm}(x, t'-\xi)}{\partial t'} \sigma(x, \xi) d\xi \right. \right. \\ & \left. \left. + J_{vm}(x, 0) \sigma(x, t') \right] \right\} dt' \end{aligned} \quad (20)$$

The total dissipative energy $DE_T(t)$ is the volume integral

$$DE_T(t) = \int_V DE(x, t) dx_1 dx_2 dx_3 \quad (21)$$

where V is the total volume of the body. It is readily seen that Eqs. (20) and (21) depend both on material properties (J_n, J_{vm}) and the loading process (S_{kl}, σ , i. e. the stresses $\sigma_{kl} = S_{kl} + \delta_{kl}\sigma$). Consequently, Eq. (21) is an extremely useful expression for comparing the dissipation properties of various materials at one or more processes.

In the viscous no structural damping case, Eqs. (12) through (20) simplify to only one term in each of the J 's, i.e.,

$$J = \exp[-(1 + g)t/\tau]/\eta \quad (22)$$

and with a similar v subscripted expression for J_v and where $\tau = \eta/G_0$ and $\tau_v = \eta_v/K_0$ with, of course, the usual coefficient of viscosity c equal to the more general η . For elastic structural damping alone, only the first term of Eq. (14) remains and due to the nature of the Dirac delta functions the stress-strain relations (12) and (13) reduce to the usual algebraic elastic ones. The results are summarized in Table I.

For anisotropic materials, similar but more complicated flutter and dissipation energy expressions can readily be derived. However, they may require as many as 21 complex moduli or compliances (instead of the two isotropic ones used in the foregoing development) to fully describe anisotropic material behavior [13]. The anisotropic relations between stress σ_{kl} and strains ϵ_{kl} now become in the F. T. plane

$$\bar{\bar{\sigma}}_{kl}(x, \omega) = \sum_{m=1}^3 \sum_{n=1}^3 \bar{\bar{B}}_{klmn}(\omega) \bar{\bar{\epsilon}}_{mn}(x, \omega) \quad (23)$$

where $\bar{\bar{B}}_{klmn}$ are complex moduli. For the sake of economy of length, the anisotropic flutter and dissipation energy analysis and results are not included in this paper, however, the previous isotropic analysis can easily be extended to anisotropic materials by rewriting Eq. (3) as [11]

$$P_m \{F_m\} = \sum_{l=1}^6 Q_{ml} \{q_{ml}\} \quad (24)$$

and subsequently redefining each $\bar{\bar{E}}_m, \bar{\bar{D}}_{mnk}$, etc, as $\bar{\bar{E}}_{ml}, \bar{\bar{D}}_{mnkl}$ in the relations following Eqs. (3) with l ranging from 1 to 6. This serves to expand the discussion from each isotropic $\bar{\bar{E}}_m$ to six anisotropic $\bar{\bar{E}}_{ml}$, but does not change any of the fundamental principles and interactions considered above.

Extensive damping properties of real materials may be found in References 14 and 15.

CONCLUSIONS

It is shown that for any general motion there is no relation between elastic structural damping and Newtonian viscous damping except at the natural frequencies of the system. The viscoelastic complex moduli are rederived to include structural damping.

The results indicate that in the presence of structural damping the real part is unaffected but the imaginary part includes effects due to the structural damping coefficient and the usual real and imaginary parts of the complex modulus. The illustrative examples for supersonic flutter of an aluminum wing indicate that an increase in the structural damping coefficient may increase or decrease the viscoelastic flutter speeds and the elastic flutter speeds are not necessarily higher than the corresponding viscoelastic ones. In other words neither structural nor viscoelastic damping necessarily produce stabilizing effects.

REFERENCES

1. Bisplinghoff, R. L., Ashley, H. and Halfman, R. L., *Aeroelasticity*, Addison-Wesley, N.Y., 1955.
2. Bisplinghof, R. L. and Ashley, H., *Principles of Aeroelasticity*, John Wiley and Sons, N.Y., 1962, p. 381.
3. Fung, Y. C., *An Introduction to the Theory of Aeroelasticity*, John Wiley and Sons, N.Y., 1955, pp. 477-479.

4. Scanlon, R. H., and Rosenbaum, R., *Introduction to the Study of Aircraft Vibration and Flutter*, Macmillan, N.Y., 1951, pp. 85-88, 196, 209-210, 341.
5. Hilton, H. H., "An Introduction to Viscoelastic Analysis," *Engineering Design for Plastics*, Reinhold Publ. Corp., N.Y., 1964, pp. 199-276.
6. Soroka, W. W., "Note on the Relation Between Viscous and Structural Damping Coefficients," *Journal of the Aeronautical Sciences*, Vol. 16, July 1949, pp. 409-410, 448.
7. Pinstler, W., "Structural Damping," *Journal of the Aeronautical Sciences*, Vol. 16, Nov. 1949, p. 699.
8. Dahl, P. R., "Solid Friction Damping of Mechanical Vibrations," *AIAA Journal*, Vol. 14, Dec. 1976, pp. 1675-1682.
9. Saravanos, D. A. and Chamis, C. C., "Mechanics of Damping for Fiber Composite Laminates Including Hygrothermal Effects," *AIAA Journal*, Vol. 28, 1990, pp. 1813-1819.
10. Hilton, H. H., "Pitching Instability of Rigid Lifting Surfaces on Viscoelastic Supports in Subsonic and Supersonic Potential Flow," *Proc. of Third Midwestern Conf. on Solid Mechanics*, 1957, pp. 1-19.
11. Vail, C. F. and Hilton, H. H., "Bending-Torsion Flutter of Linear Viscoelastic Wings in Two Dimensional Flow" *University of Illinois Technical Report AAE 76-1*, 1976. Submitted for publication to *AIAA Journal*.
12. Durunji, J., "Theoretical Considerations of Panel Flutter at High Supersonic Mach Numbers," *AIAA Journal*, Vol. 4, 1966, pp. 1257-1266.
13. Hilton, H. H., and Dong, S. B., "An Analysis for Anisotropic, Nonhomogeneous, Linear Viscoelasticity Including Thermal Stresses," *Development in Mechanics*, Pergamon Press, N.Y., 1964, pp. 58-73.
14. Lazan, B. J., *Damping of Materials and Members in Structural Mechanics*, Pergamon Press, N.Y., 1968.
15. Nashif, A. D., Jones, D. I. G. and Henderson, J. P., *Vibration Damping*, John Wiley & Sons, N.Y., 1985.

ANALYSIS OF STRAIN DEPENDENT DAMPING IN METALS VIA MODELING OF MATERIAL POINT HYSTERESIS

by

Edward J. Graesser* and Catherine R. Wong

David Taylor Research Center
Ship Materials Engineering Department
Bethesda, Maryland, 20084-5000

ABSTRACT

In strain dependent (or nonlinear) high damping metals, measured values of damping vs. strain are often inconsistent for different damping test configurations. To better understand the nature of such inconsistencies shear and bending test configurations were modeled analytically. A hysteretic material point stress-strain relationship was used for each modeling configuration. This model is similar to established constitutive laws of viscoplastic behavior and has been adapted especially for the study of nonlinear hysteresis and the problem of strain dependent damping. Analytical material response analyses of bending and torsion samples indicated that when the damping of a single nonlinear material is plotted against the one-dimensional local strain of the sample, highly discrepant results are produced. However, when the same results are plotted against an invariant measure of three-dimensional local distortion the agreement improves considerably. The method can also be applied to homogeneous isotropic nonlinear damping materials that are not metallic (such as amorphous nonlinear high damping polymers).

* Presenting author, ONR/ASEE Postdoctoral Fellow, Business Telephone: (301) 267-2835

INTRODUCTION

In addition to well known plating techniques currently being used in the Navy, material damping is being investigated as a potential means of further reducing machine vibration, noise, and sound emission (in starting, etc.). Ideally a high damping structural material provides a sufficient amount of both stiffness and damping so as to be used as a sole machine part or vibrating element without added treatments. Such materials are most useful for oscillating parts or elements that cannot be treated by conventional external treatments. Also these materials can be useful in situations where other environmental factors (e.g. moisture, corrosion) have to be considered. This approach is also useful in damping longitudinal vibrations which cannot be effectively controlled by external treatments.

Because high stiffness and strength are required in many important applications, metals which possess a high natural damping capacity have been extensively sought [1,2]. Some specific applications include gears and gear webs, pump castings, engine parts, propellers, and others (see [1]). High damping materials are also used as plug inserts and cladding, and such applications can provide a reduction of resonant amplification factors as well as the attenuation of fatigue [1].

Generally, high damping in metal is a measured peak loss factor or phase lag with a value of 10^{-3} or higher. In fact, many compositions have been studied and found to possess such levels of damping (e.g. see [3,4]). Mechanisms that give rise to damping in metals include: movement of point defects, dislocations, or domain walls. These effects give rise to macroscopic hysteresis and thus damping. For example, in Cu-Mn high damping alloys straining the material induces movement of twin boundaries in the antiferromagnetic matrix, even at low strain levels (10^{-2} to 10^{-4}) [3]. High damping metals possess strain dependent characteristics because the primary damping mechanism is function over a finite range of strain. For example, in magnetostrictive materials, a low strain is necessary to move magnetic domain boundaries away from their primary position and thus activate the damping mechanism. However, once a maximum strain is reached which induces full alignment of the magnetic domains the boundaries can no longer move and the primary damping mechanism is saturated. Such effects are apparent by a finite strain defined peak in the plot of measured damping vs. specimen strain. Examples of magnetostrictive metallic materials exhibiting strain-dependent damping are given in Fig. 2. Because the measured damping data varies with changes in specimen strain, a plot of the damping of this type of response is called nonlinear. A generalized stress-strain diagram corresponding to such nonlinear damping mechanisms is illustrated in Fig. 3. It is important to note that the response that is hysteretic with a damping mechanism that occurs over a finite strain of ϵ_p .

The damping behavior of a nonlinear strain dependent material in different test configurations is often investigated. Data for resonance bending and torsion tests [3] given in Fig. 3 shows this effect. It is important to note that the torsional tests produce significantly higher values of damping than the bending tests. However it is important to note that the strains on the plots are not axial strains in the case of torsional data and axial strains in the case of bending data. The consequences of this are not equivalent and the consequence of plotting damping vs. $1/\text{strain}$ in the frequency plots is discussed in the analysis section of this paper.

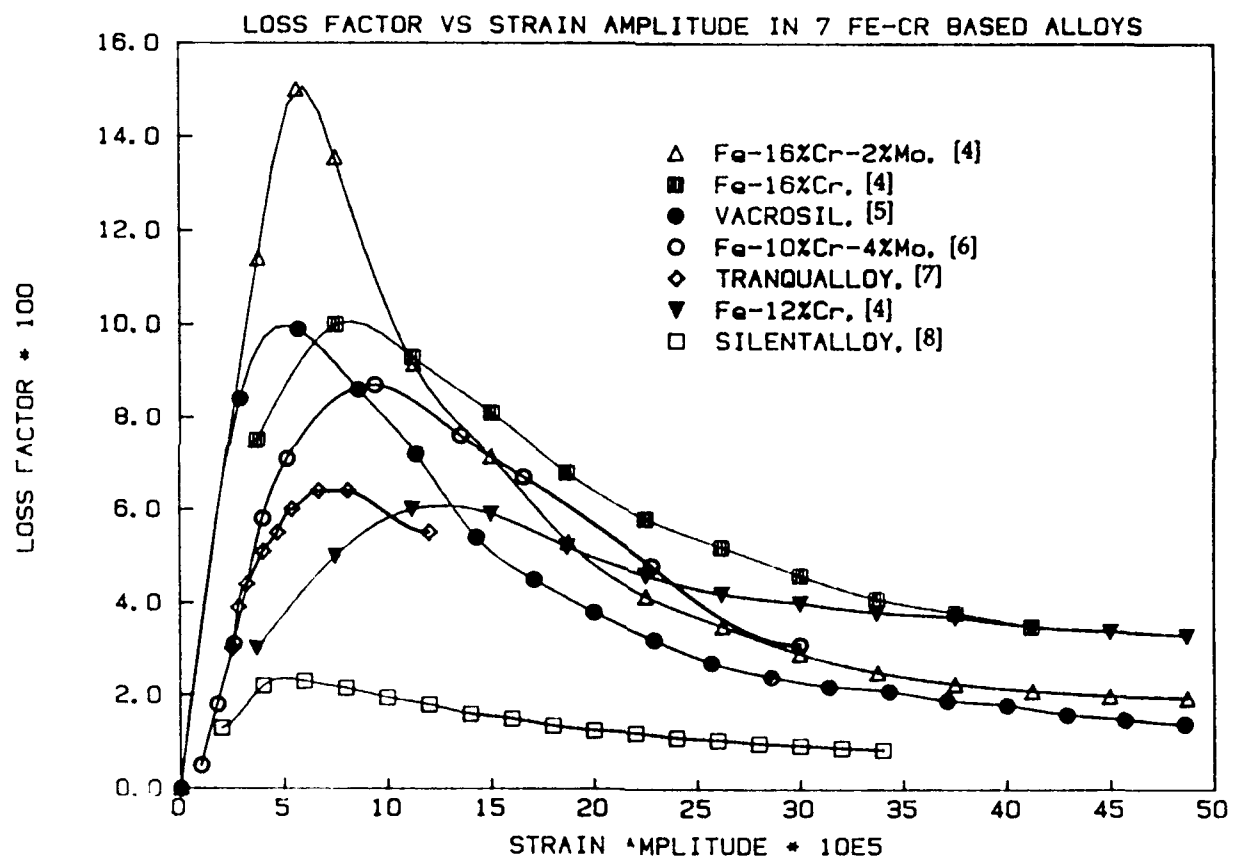


Figure 1: Strain Amplitude Dependent Damping in Fe-Cr Based High Damping Alloys

Cyclic σ - ε with a Saturated Damping Mechanism Outside ε_0

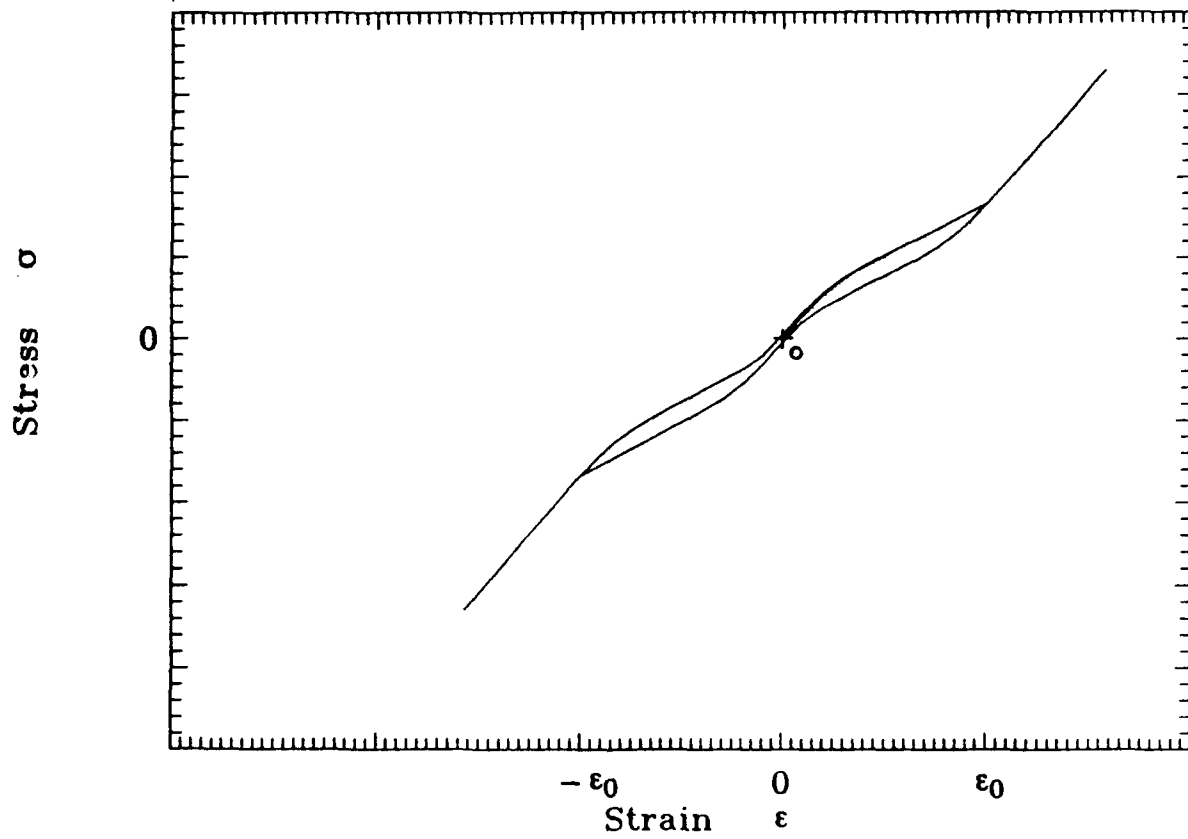


Figure 2: Generalized Macroscopic Hysteresis of Nonlinear Damping Materials

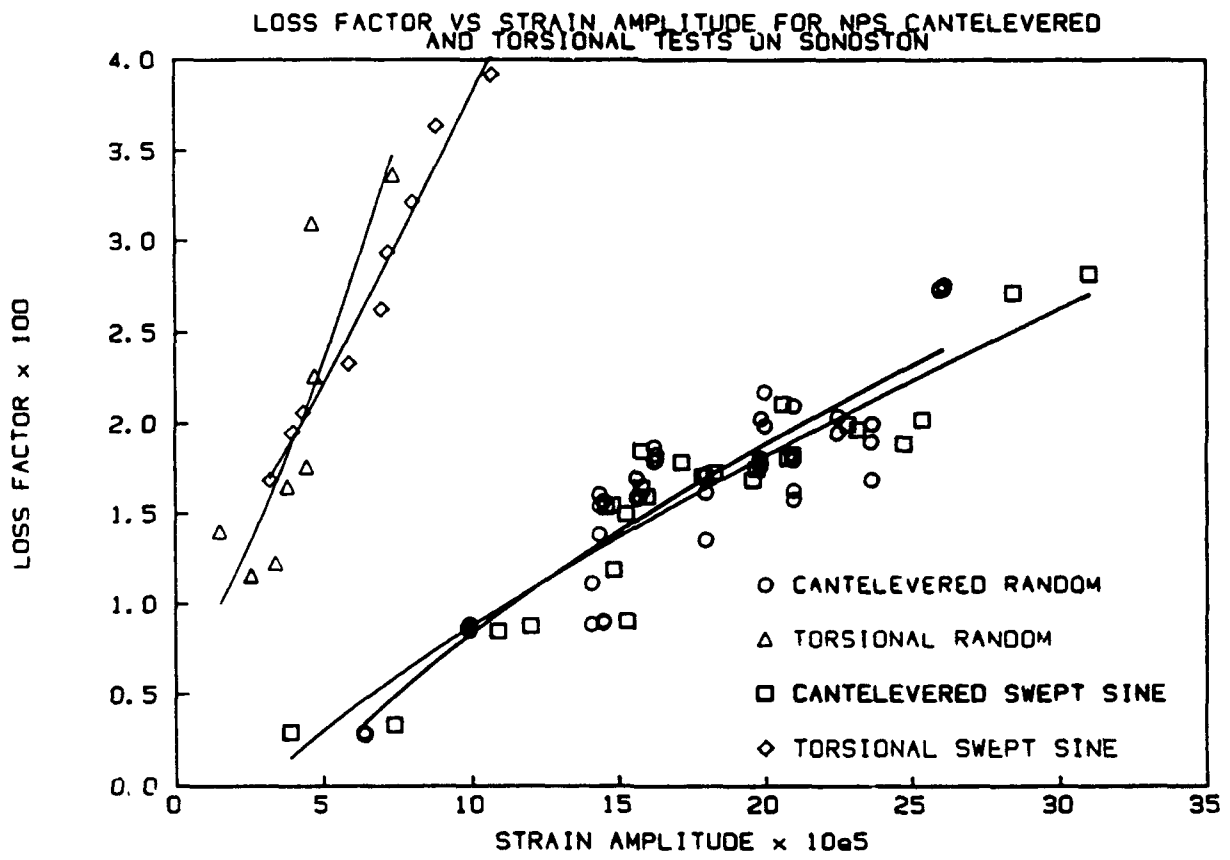


Figure 3: Strain Dependent Damping of Cu-Mn in Separate Bending and Torsion Tests [3]

Strain dependent materials are, at best, difficult to model analytically because of their nonlinear characteristics. Early work in this area concentrated on evaluating the damping of members by combining material energy absorbing properties with geometric and stress distribution factors [9,10]. Another approach is to use a constitutive law which describes nonlinear material behavior and hysteresis at a point, and this approach will be used here. Many such laws exist (e.g. see [11,12]), but these are usually specific to postyielding viscoplastic behavior and large strain levels. In this paper a proposed constitutive law [13] for the stress-strain behavior of shape memory alloys is adapted to the case of nonlinear damping. The equations of this law were applied to the cases of simple uniaxial tension-compression and shear loading, and then were expanded to analyze beam and shaft test samples in bending and torsion respectively. The strain dependent nature of each test configuration was computed, and because this behavior was of primary interest, temperature and frequency effects were not considered.

ANALYSIS

In order to make a useful study of strain dependent damping, a three-dimensional constitutive law of hysteretic material behavior was used in analyses. The law, which is of the viscoplastic type, was originally developed to model the large strain hysteretic behavior of shape memory alloys [13], and especially superelastic behavior. This choice of modeling schemes was pursued because the hysteretic response of superelastic materials is similar in character to that high damping metals (see Fig. 2), except that the stress and strain levels are different by many orders of magnitude. This does not prevent the use of the constitutive law, however, as long as the material properties of the law can be scaled to accommodate the lower stress and strain levels associated with the dissipative mechanisms in the damping material.

The constitutive law is for homogeneous and isotropic material behavior and is based upon a separation of strain and strain rate into elastic and inelastic components:

$$\epsilon_{ij} = \epsilon_{ij}^{el} + \epsilon_{ij}^{in} \quad (1a)$$

$$\dot{\epsilon}_{ij} = \dot{\epsilon}_{ij}^{el} + \dot{\epsilon}_{ij}^{in} \quad (1b)$$

Here an overhead dot represents ordinary time differentiation. Thus ϵ_{ij} and $\dot{\epsilon}_{ij}$ are the three-dimensional tensors of strain and strain rate, and the superscripts "el" and "in" designate the respective elastic and inelastic components of each. The elastic component follows directly from the theory of elasticity [14]:

$$\epsilon_{ij}^{el} = \frac{1+\nu}{E} \sigma_{ij} - \frac{\nu}{E} \sigma_{kk} \delta_{ij} \quad (2)$$

where σ_{ij} is the stress tensor, δ_{ij} is the Kronecker delta,¹ and where E and ν are the elastic material constants.

¹ $\delta_{ij}=1$ if $i=j$, $\delta_{ij}=0$ if $i \neq j$, $i,j=1,2,3$

The basic equations for the evolution of inelastic strain were taken from a model of shape memory alloy behavior [13]. In this model the growth of inelastic strain is a function of backstress β_{ij} , which is a variable that accounts for internal stress fields in the material. In order to model the saturation of damping mechanisms a unit step function was included to stop the growth of inelastic strain after a limiting value of distortion. This resulted in the following set of equations:

$$\dot{\epsilon}_{ij}^{in} = \sqrt[+]{3K_2} \left[\sqrt[+]{3J_2} \right]^{n-1} \left[\frac{s_{ij} - b_{ij}}{Y} \right] \left\{ u \left[\sqrt[+]{3I_2} - \sqrt[+]{3I_2} \right] \right\} \quad (3)$$

$$b_{ij} = \frac{2}{3} E\alpha \left[\epsilon_{ij}^{in} + f_T \frac{e_{ij}}{\frac{2}{3} \sqrt[+]{3I_2}} \operatorname{erf} \left[\frac{2}{3} \sqrt[+]{3I_2} \right] \left\{ u \left[-I_2 \right] \right\} \right] \quad (4)$$

where e_{ij} , s_{ij} , and b_{ij} are the deviatoric tensors of strain, stress and backstress respectively; the difference $s_{ij} - b_{ij}$ is often referred to as the effective stress. The quantities I_2 , J_2 , and K_2 are the second order invariants of the deviatoric tensors of strain, dimensionless effective stress, and strain rate, respectively. All these quantities are formally described below:

$$\begin{aligned} e_{ij} &= \epsilon_{ij} - \frac{1}{3} \epsilon_{kk} \delta_{ij} \quad , & I_2 &= \frac{1}{2} e_{ij} e_{ij} \quad , & K_2 &= \frac{1}{2} \dot{\epsilon}_{ij} \dot{\epsilon}_{ij} \\ s_{ij} &= \sigma_{ij} - \frac{1}{3} \sigma_{kk} \delta_{ij} \\ b_{ij} &= \beta_{ij} - \frac{1}{3} \beta_{kk} \delta_{ij} \quad , & J_2 &= \frac{1}{2} \frac{s_{ij} - b_{ij}}{Y} \frac{s_{ij} - b_{ij}}{Y} \end{aligned}$$

Thus the growth of inelastic strain is a function of stress, backstress, and strain rate. Note that plus sign appearing with the radical sign of the square root of the invariants in Eqs. (3)-(4) indicates that the square root, once taken, is to be positive (i.e. the absolute value of the square root). Also, I_2 represents a measure of volumetric distortion that is invariant with respect to coordinate transformations, and this will be an important quantity in the forthcoming discussion.

To summarize, the material constants in Eqs. (2)-(4) are:

- E: Axial elastic modulus
- ν : Poisson ratio of elastic material
- Y: Axial stress level where the damping mechanism is activated thus giving rise to an inelastic response²
- α : Constant determining the slope of the inelastic region
= $E_y / (E - E_y)$, where E_y is the inelastic slope

² The material constant Y, as it is used here, corresponds to a stress whereupon the slope of the axial stress-strain curve is lowered to accommodate the activation of internal damping mechanisms. Therefore Y represents a material constant that is analogous to the yield stress of large strain plastic behavior (indeed for the constitutive law in [11] Y does represent the yield stress) and above this stress the inelastic response is important.

- n: Constant controlling the sharpness of transition from elastic to inelastic behavior
- f_T : Constant controlling the size of the hysteresis loop
- a: Constant controlling the amount of elastic recovery during unloading

Also, Eqs. (3) and (4) contain two special functions: the error function, $\text{erf}(\cdot)$, and the unit step function, $\{u(\cdot)\}$. Simply stated the purpose of the error and unit step functions contained in Eq. (4) is to allow for the recovery of accumulated inelastic strain during unloading, and thus simulate the unique behavior of superelastic materials [13]. As stated earlier the consequence of the unit step function in Eq. (3) is to eliminate inelastic growth outside a limiting value of volumetric distortion.

Let us take a moment to explain the role of the inelastic response in the modeling of strain dependent damping. The inelastic component of strain is responsible for the dissipation of energy that takes place in cyclic loading. Equations (1)-(4) have been used to represent the macroscopic stress-strain behavior of shape memory alloys, and especially superelastic materials [13]. The hysteretic character of superelasticity is macroscopically similar to that of nonlinear anelasticity except that the respective stress and strain levels of each type of response are different by many orders of magnitude. Therefore, the inelastic response governed by Eqs. (3)-(4) can be used to macroscopically represent the effect of a nonlinear anelastic damping mechanism.

By using Eqs. (1)-(4), a number of special cases can be considered. First let us consider the cases of uniaxial tension-compression and pure shear loading. The state of uniaxial loading (superscript u) is described by:

$$\epsilon_{ij}^u = \begin{bmatrix} \epsilon & 0 & 0 \\ 0 & -\mu\epsilon & 0 \\ 0 & 0 & -\mu\epsilon \end{bmatrix} \quad \dot{\epsilon}_{ij}^u = \begin{bmatrix} \dot{\epsilon} & 0 & 0 \\ 0 & -\rho\dot{\epsilon} & 0 \\ 0 & 0 & -\rho\dot{\epsilon} \end{bmatrix} \quad \sigma_{ij}^u = \begin{bmatrix} \sigma & 0 & 0 \\ 0 & 0 & 0 \\ 0 & 0 & 0 \end{bmatrix} \quad \beta_{ij}^u = \begin{bmatrix} \beta & 0 & 0 \\ 0 & 0 & 0 \\ 0 & 0 & 0 \end{bmatrix}$$

Here ϵ , σ , and β are the axial strain, stress, and backstress in the x direction of Cartesian space, respectively. Also the lateral strain and strain rate induced by the Poisson effect ($-\mu\epsilon$ and $-\rho\dot{\epsilon}$) are associated with the coefficients μ and ρ respectively. Because of the nonlinear effect induced by the damping mechanism μ and ρ are neither constant nor equal. In order to evaluate these factors the lateral strain and strain rate are decomposed into elastic and inelastic parts. The total lateral strain is decomposed in the same way. The elastic component is related to the elastic axial strain by the elastic Poisson ratio ν , and the inelastic component is related to the axial inelastic response in an incompressible manner (recall that the Poisson ratio associated with incompressible behavior is .5) [14]. Therefore we have $-\mu\epsilon = -\nu\epsilon^{el} - .5\epsilon^{in}$. Similarly, the lateral strain rate is $-\rho\dot{\epsilon} = -\nu\dot{\epsilon}^{el} - .5\dot{\epsilon}^{in}$. Using these relations one can deduce that μ and ρ are both variable and different from one another in the following manner:

$$\mu = \frac{1}{2} - \frac{1}{E} \left(\frac{1}{2} - \nu \right) \frac{\sigma}{\epsilon}$$

$$\rho = \frac{1}{2} - \frac{1}{E} \left(\frac{1}{2} - \nu \right) \frac{d\sigma}{d\epsilon}$$

If the behavior is only a small departure from elasticity then $\mu \approx \rho \approx \nu$; conversely if a condition of strain and strain rate exists where inelastic behavior dominates and where $\sigma/\epsilon \ll E$ and $d\sigma/d\epsilon \ll E$ then the response is essentially incompressible with $\mu \approx \rho \approx .5$.

For the state of shear loading (superscript s) we have:

$$\epsilon_{ij}^s = \begin{bmatrix} 0 & \frac{\gamma}{2} & 0 \\ \frac{\gamma}{2} & 0 & 0 \\ 0 & 0 & 0 \end{bmatrix} \quad \dot{\epsilon}_{ij}^s = \begin{bmatrix} 0 & \frac{\dot{\gamma}}{2} & 0 \\ \frac{\dot{\gamma}}{2} & 0 & 0 \\ 0 & 0 & 0 \end{bmatrix} \quad \sigma_{ij}^s = \begin{bmatrix} 0 & \tau & 0 \\ \tau & 0 & 0 \\ 0 & 0 & 0 \end{bmatrix} \quad \beta_{ij}^s = \begin{bmatrix} 0 & \xi & 0 \\ \xi & 0 & 0 \\ 0 & 0 & 0 \end{bmatrix}$$

Here γ and $\dot{\gamma}$ are the engineering shear strain and strain rate, τ is the shear stress, and ξ is the shear backstress in the xy plane of Cartesian space.

By using the appropriate stress, backstress, and strain tensors, as well as their respective deviators and associated invariants, Eqs. (1)-(4) produce the following uniaxial equations:

$$\dot{\sigma} = E \left[\dot{\epsilon} - \frac{2(1+\rho)}{3} |\dot{\epsilon}| \left| \frac{\sigma - \beta}{Y} \right|^{n-1} \left[\frac{\sigma - \beta}{Y} \right] \{u(\epsilon_0 - |\epsilon|)\} \right]$$

$$\beta = E\alpha \left[\epsilon - \frac{\sigma}{E} + f_T \operatorname{erf} \left[\frac{2(1+\mu)}{3} a\epsilon \right] \{u(-\epsilon\dot{\epsilon})\} \right]$$

Note that ϵ_0 is the limiting strain for inelastic growth. At strains above ϵ_0 the damping mechanism is saturated and elastic behavior prevails. Also, $|\epsilon|$ is the absolute value of ϵ . These equations can be further simplified by taking the total material response to be incompressible in the inelastic region (i.e. when $Y/E \leq \epsilon \leq \epsilon_0$). This simplification does not greatly affect the overall dissipative character of the axial response. Thus by setting $\mu = \rho = .5$ in the nonlinear inelastic response terms we obtain:

$$\dot{\sigma} = E \left[\dot{\epsilon} - |\dot{\epsilon}| \left| \frac{\sigma - \beta}{Y} \right|^{n-1} \left[\frac{\sigma - \beta}{Y} \right] \{u(\epsilon_0 - |\epsilon|)\} \right] \quad (5)$$

$$\beta = E\alpha \left[\epsilon - \frac{\sigma}{E} + f_T \operatorname{erf}(a\epsilon) \{u(-\epsilon\dot{\epsilon})\} \right] \quad (6)$$

Following the same process, the shear equations are:

$$\dot{\tau} = G \left[\dot{\gamma} - |\dot{\gamma}| \left| \frac{\tau - \xi}{Y_s} \right|^{n-1} \left(\frac{\tau - \xi}{Y_s} \right) \{u(\gamma_0 - |\gamma|)\} \right] \quad (7)$$

$$\xi = \frac{E\alpha}{3} \left[\gamma - \frac{\tau}{G} + \sqrt{3} f_T \operatorname{erf} \left(\frac{a\gamma}{\sqrt{3}} \right) \{u(-\dot{\gamma})\} \right] \quad (8)$$

where

$$\gamma_0 = \frac{2(1 + \nu)}{\sqrt{3}} \epsilon_0 \quad \text{is strain limiting inelastic growth in shear}$$

$$G = \frac{E}{2(1 + \nu)} \quad \text{is the elastic shear modulus}$$

$$Y_s = \frac{Y}{\sqrt{3}} \quad \text{is the shear stress whereupon the damping mechanism is activated}$$

Note that Y_s falls out of the formulation automatically in a manner that is consistent with the theory of maximum distortional strain energy [15]. This is because Eq. (3) is dependent on the stress gradient of a potential function [13] that contains a von Mises type condition for the onset of the inelastic damping mechanism. Later the cases of bending and torsion will be modeled using finite difference geometries in conjunction with the above equations.

Now let us examine the results produced by numerical integration of Eqs. (5)-(6) and (7)-(8); a sinusoidal history of strain input was specified with strain amplitudes of ϵ_p in the axial case and γ_p in the shear case. These amplitudes were specified to be greater than the limiting strains so that the full character of the predicted response could be displayed in illustrative plots. The results of calculations for the axial and shear loading conditions are given in Figs. 4 and 5 respectively. Both figures possess the same characteristics: elastic behavior dominates in the region of the origin as well as outside the limiting strain, and a hysteresis loop is manifested in the full cycle of strain application. The area enclosed by the hysteresis loop represents the energy absorbed by the material undergoing cyclic oscillation. The elastic modulus of $E = 28.5 \times 10^6$ psi and limiting strain of $\epsilon_0 = .0001$ were selected based on the elastic modulus and approximate strain of peak damping in Fe-Cr alloys (see Fig. 1). The remaining material constants used in the calculations that generated Figs. 4 and 5 were not selected to reproduce the behavior of any specified damping material; rather they were selected to approximate the general character of a nonlinear damping metal and allow for some investigative analyses. It should be noted that the results generated by the constitutive equations are numerically stable and insensitive to the rate of strain input [13]. Also the elastic and inelastic material properties (i.e. E , E_y , and Y) are accurately reproduced in numerical calculations [13].

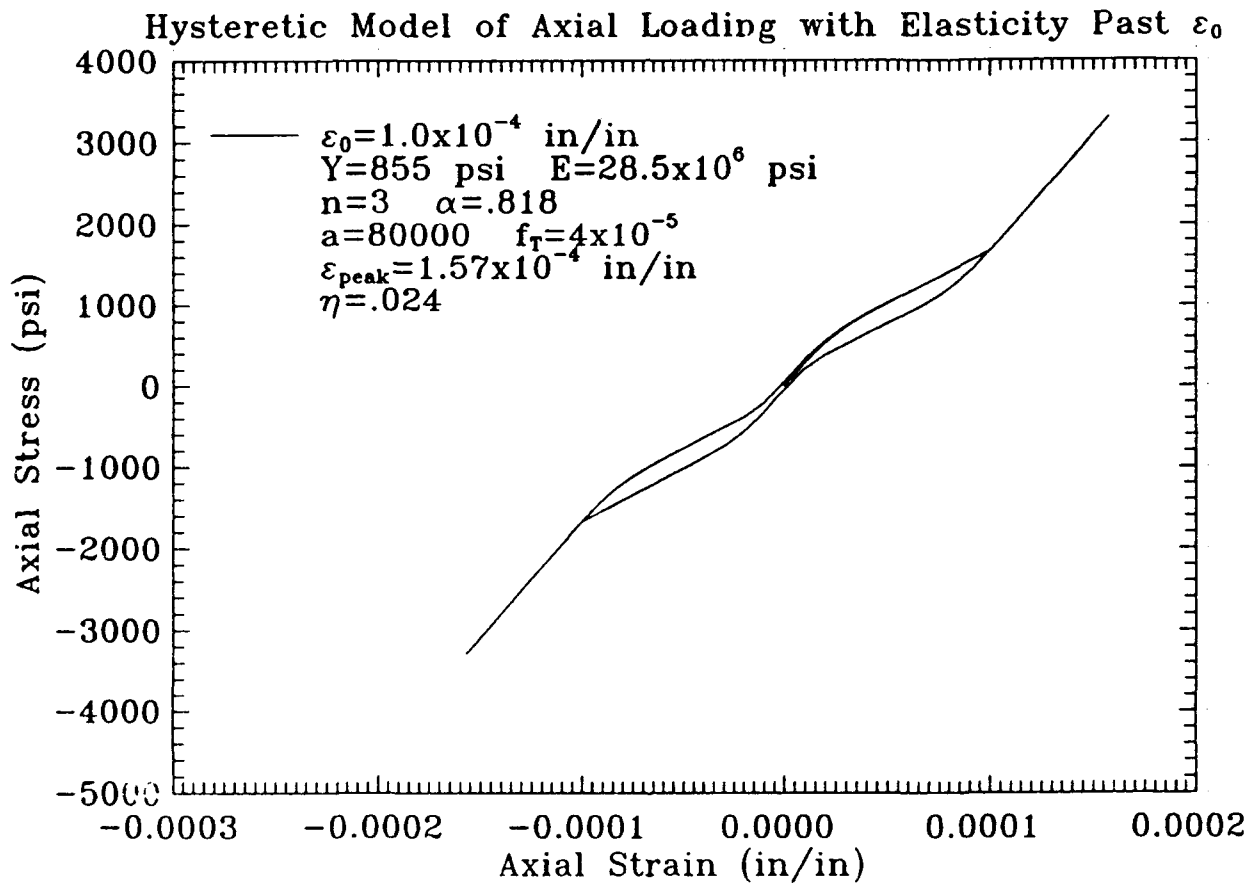


Figure 4: Hysteretic Behavior Calculated for Pure Axial Loading

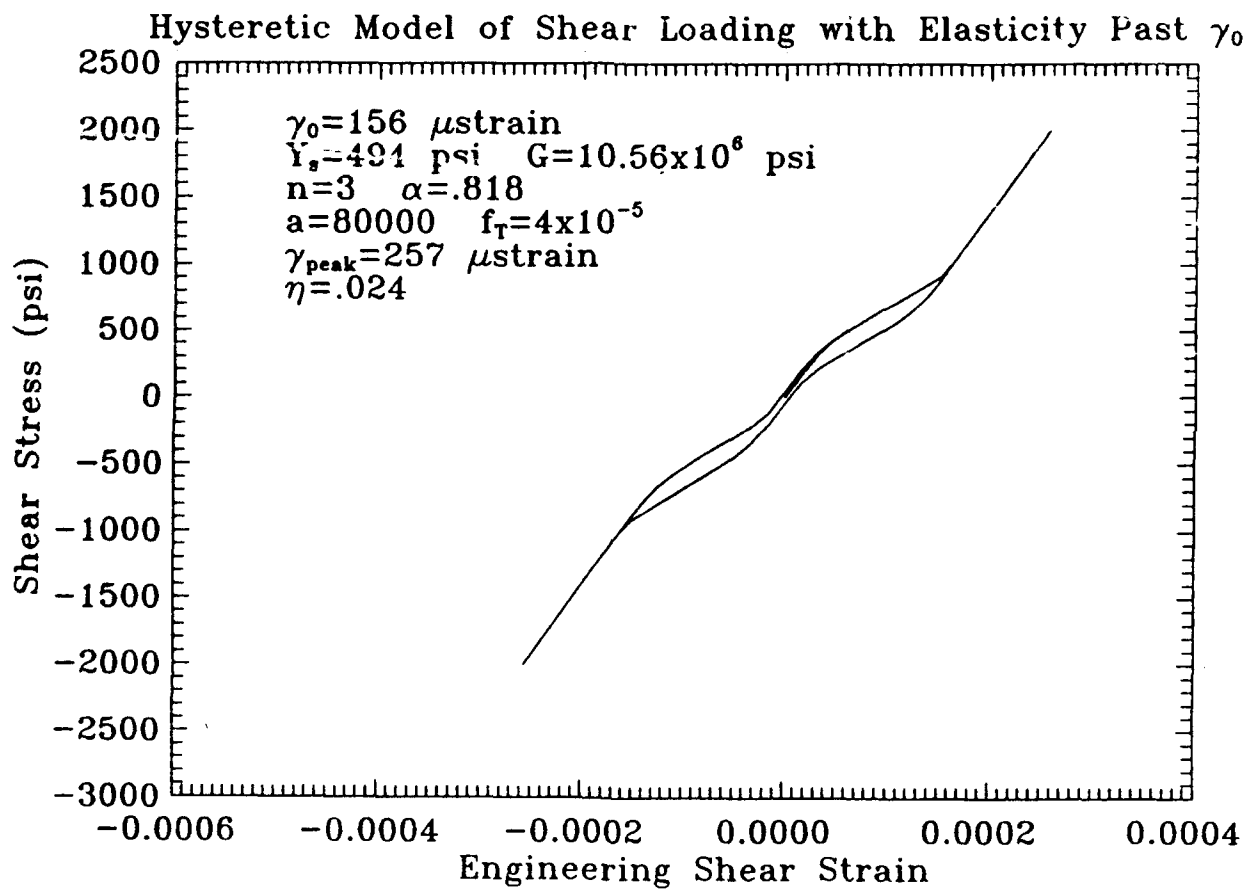


Figure 5: Hysteretic Behavior Calculated for Pure Shear Loading

By having numerical results of the type just presented, it is possible to numerically calculate the energy absorbed per cycle. We can then compute the material damping by dividing this energy by the product of 2π and an energy storage term. This corresponds to the measure of damping known as the loss factor η

$$\eta = \frac{\Delta W}{2\pi W} \quad (9)$$

In Eq. (9) ΔW is the energy absorbed due to damping and W is a measure of stored energy, often selected as

$$W = \frac{1}{2} \varepsilon_{\max} \sigma \Big|_{\varepsilon_{\max}} \quad (10)$$

When the damping mechanism is linear rather than nonlinear W represents the energy stored in a linear elastic material at peak strain. Also, for linear materials the loss factor is constant over a wide range strain because ΔW and W are proportional to one another. This is not the case for nonlinear materials. By using Eqs. (5)-(6) and (7)-(8) in calculations for the cyclic material response over a range of peak axial and shear strains, and computing the loss factor associated with each peak strain according to Eqs. (9) and (10), the general character of the damping vs. strain diagram of nonlinear materials was produced; this is shown in Fig. 6. Note that both curves possess the characteristic damping peak associated with nonlinear damping materials.

However the separate curves in Fig. 6 that represent axial and shear loading differ significantly with respect to one another. The cause of this difference was first investigated by evaluating the amount of energy absorbed in each loading configuration. The amount of energy absorbed, plotted as a function of peak strain, is given in Fig. 7. Above the respective limiting axial and shear strains the amount of energy absorbed by the material is essentially the same for both loading configurations, their difference being less than 1%. Therefore the difference in the character of the two separate responses must be due to other factors.

It turns out that the plots given in both Figs. 6 and 7 are misleading because the abscissa of these figures represents values of strain associated with separate axial and shear loading conditions, and the strains associated with these separate conditions are not equivalent. Therefore another measure of deformation equivalent to both types of loading needs to be employed. One such possibility is to use a measure of local distortion experienced by the strained material. Let us define an equivalent strain $\bar{\varepsilon}$ as follows:

$$\bar{\varepsilon} = \sqrt{3I_2} \quad (11)$$

This measure is similar to the effective plastic strain in plastically deforming materials [14]. It is clear that $\bar{\varepsilon}$ has a physical meaning that is independent of the choice of coordinate axes since it is based on the invariant I_2 , which is the I_2 is the second invariant of the deviatoric strain e_{ij} (also

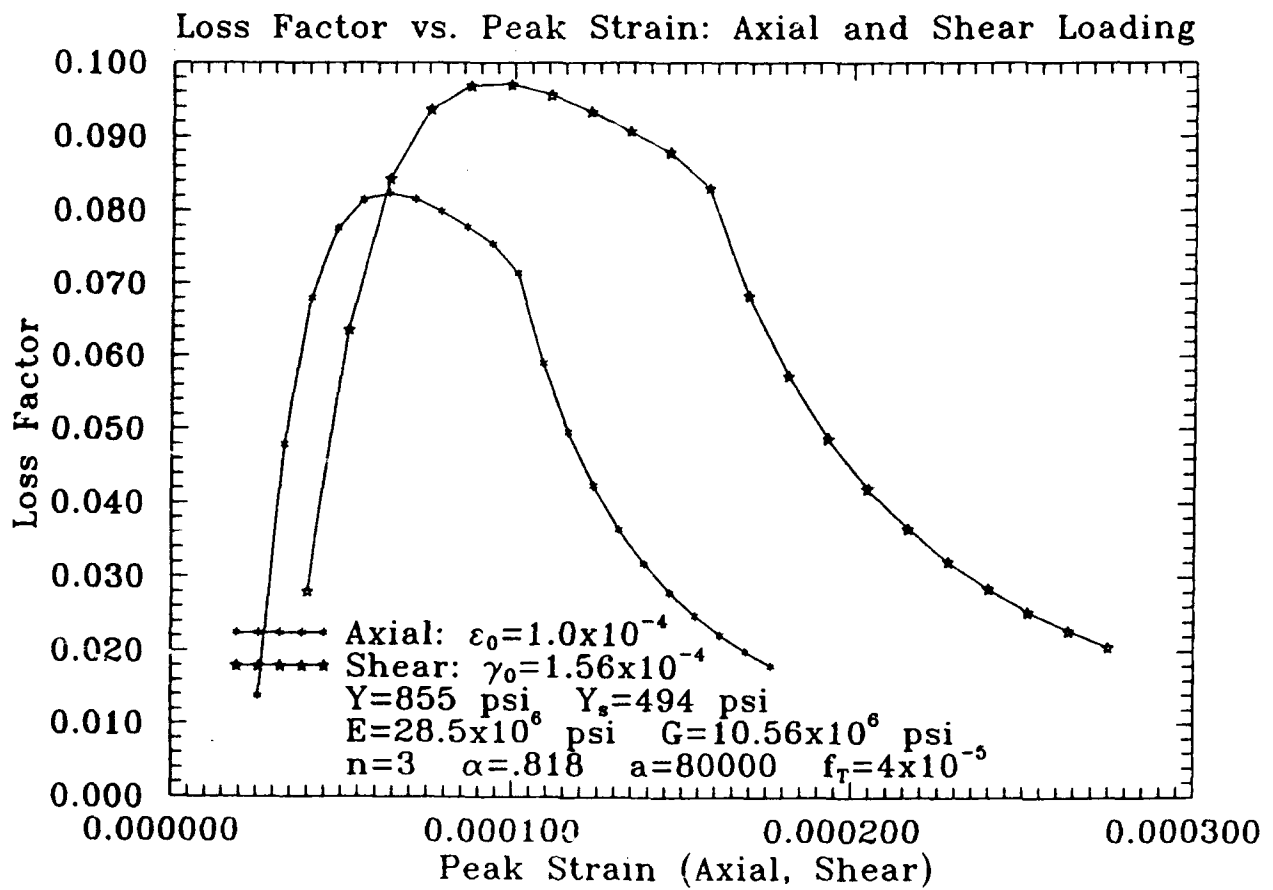


Figure 6: Strain Amplitude Depending Damping for Pure Axial and Shear Loading

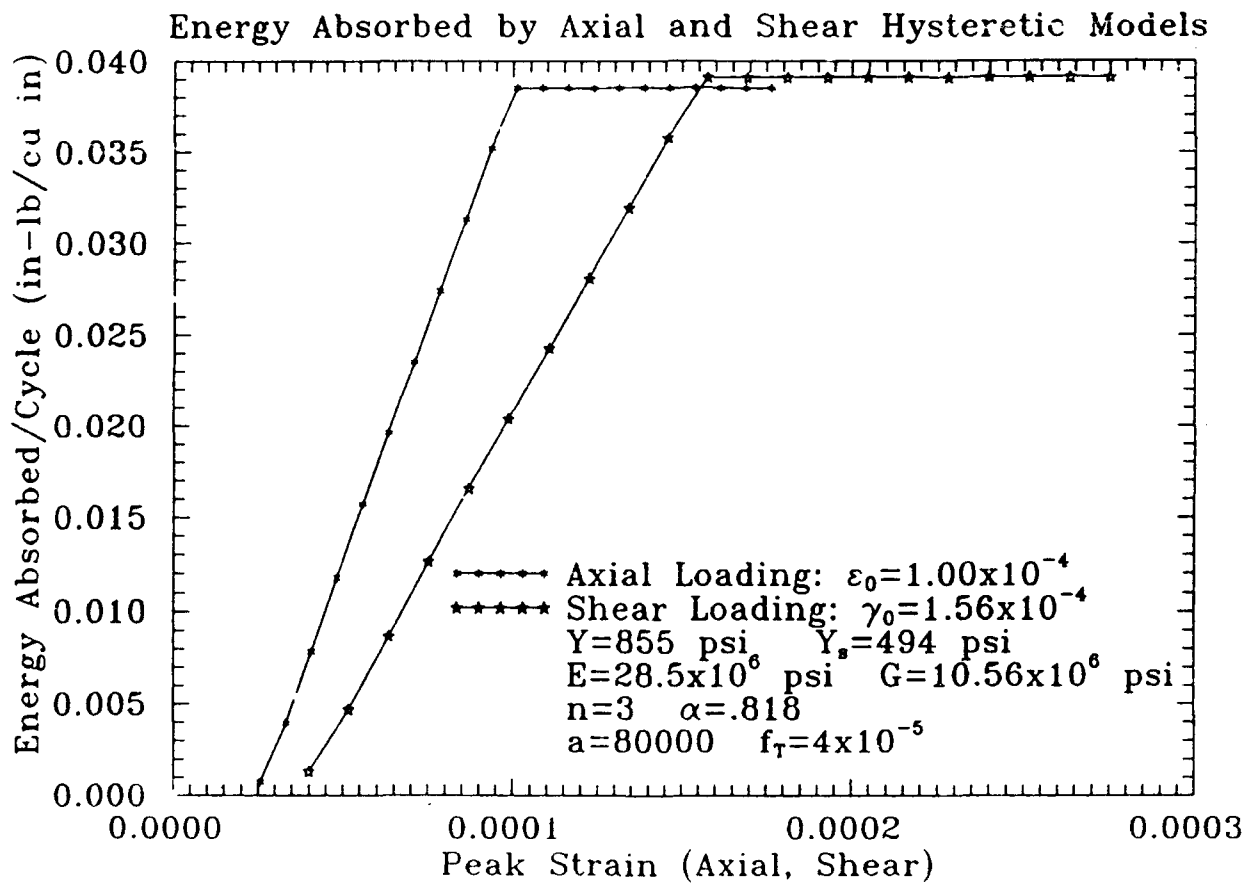


Figure 7: Energy Absorbed in Axial and Shear vs. Peak Axial and Shear Strains

called the distortional component of strain³). Therefore $\bar{\epsilon}$ is an invariant measure of the local distortion.

By considering the separate states of axial and shear strain, and by taking the Poisson ratio to be the simple constant ν for axial case, one deduces that the equivalent strains for each state of strain are as follows:

$$\bar{\epsilon}^u = (1 + \nu) \epsilon \quad (\text{uniaxial loading})$$

$$\bar{\epsilon}^s = \frac{\sqrt{3}}{2} \gamma \quad (\text{shear loading})$$

By using the peak equivalent strains of axial and shear loading in place of the peak strains used in Figs. 6 and 7 a more consistent pattern of results is developed. This is first done for the amount of energy absorbed as shown in Fig. 8. Note from this figure that for both cases the energy absorbed as a function of the distortion is in very good agreement along the entire abscissa. In Fig. 9 the loss factors of the axial and shear loading cases are also plotted against the peak equivalent strain. The results in this figure are now also much more consistent than before; indeed the breadth of each damping curve spans the same values of equivalent strain and the peak of each damping curve occurs at approximately the same level of distortion.

The only inconsistency that now remains is in the value of the peak loss factor of each separate curve and this is simply due to the occurrence of different values of stored energy being produced by the separate loading conditions. Indeed, because the modulus of the material in shear is lower than that of the same material under axial loading, the value of peak shear stress will also be lower than the peak axial stress at equivalent levels of distortion. Consequently, at equal levels of distortion, the measure of stored energy W will be larger in axial loading than in shear and this will cause the loss modulus in shear to be greater than the loss modulus in axial loading.

Because bending and torsion are common damping test configurations lets us next proceed to the following cases: bending of a solid beam having length L and rectangular cross-section of width b and thickness h , and torsion of a solid shaft having length L and circular cross-section of radius R . Even though the stress-strain response is nonlinear we can consider both cases in a simple fashion without needing to consider residual stresses or movement of the neutral axis of the beam. This is because the response takes place in a manner which gives symmetric behavior for positive and negative strains, and the response is hysteretic with essentially no residual strain. When considering bending and torsion problems with more pronounced inelastic behavior and residual stresses then special considerations must be made when computing the acting moments [16].

³ The tensor e_{ij} is known as the distortional component of strain because, by definition, it subtracts the dilatational component of deformation out of the strain tensor ϵ_{ij} .

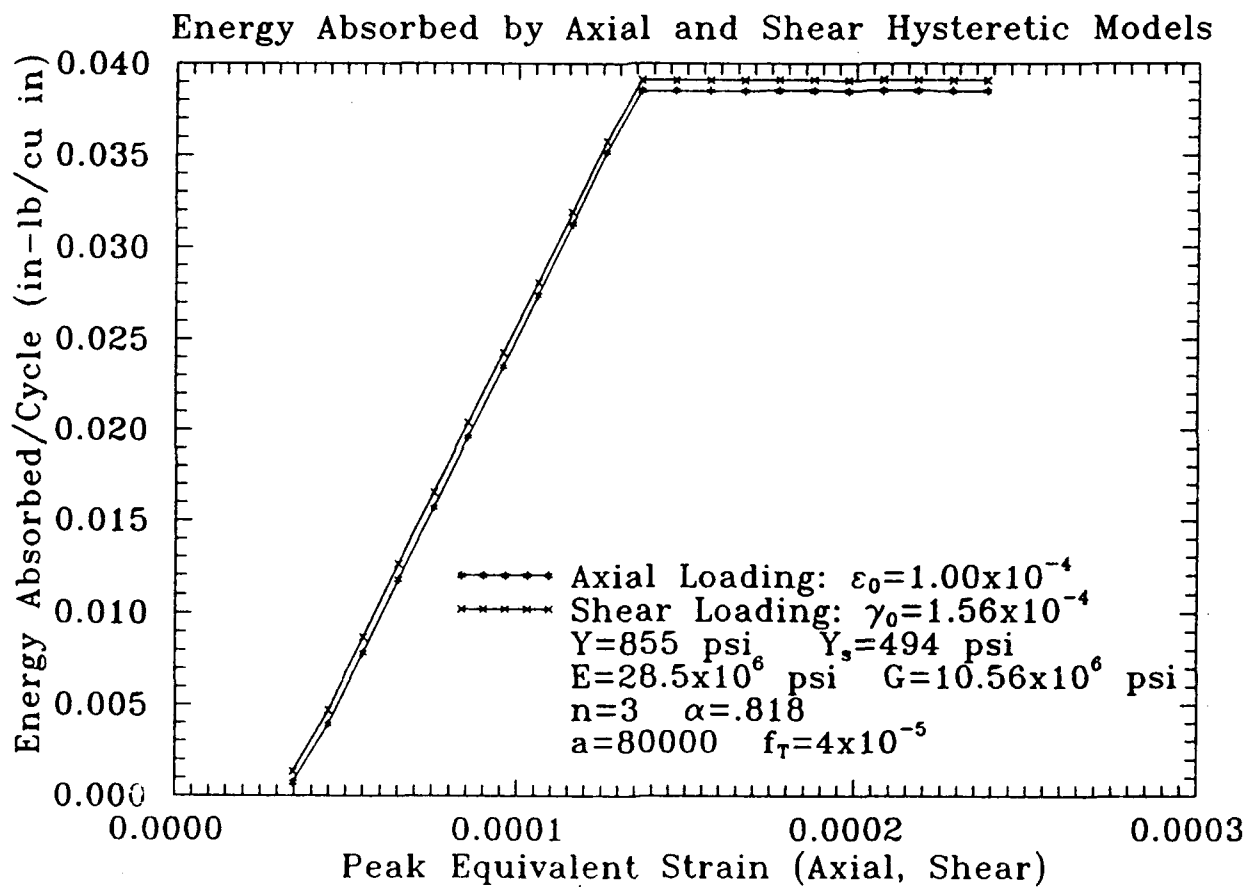


Figure 8: Energy Absorbed in Axial and Shear vs. Peak Equivalent Strain

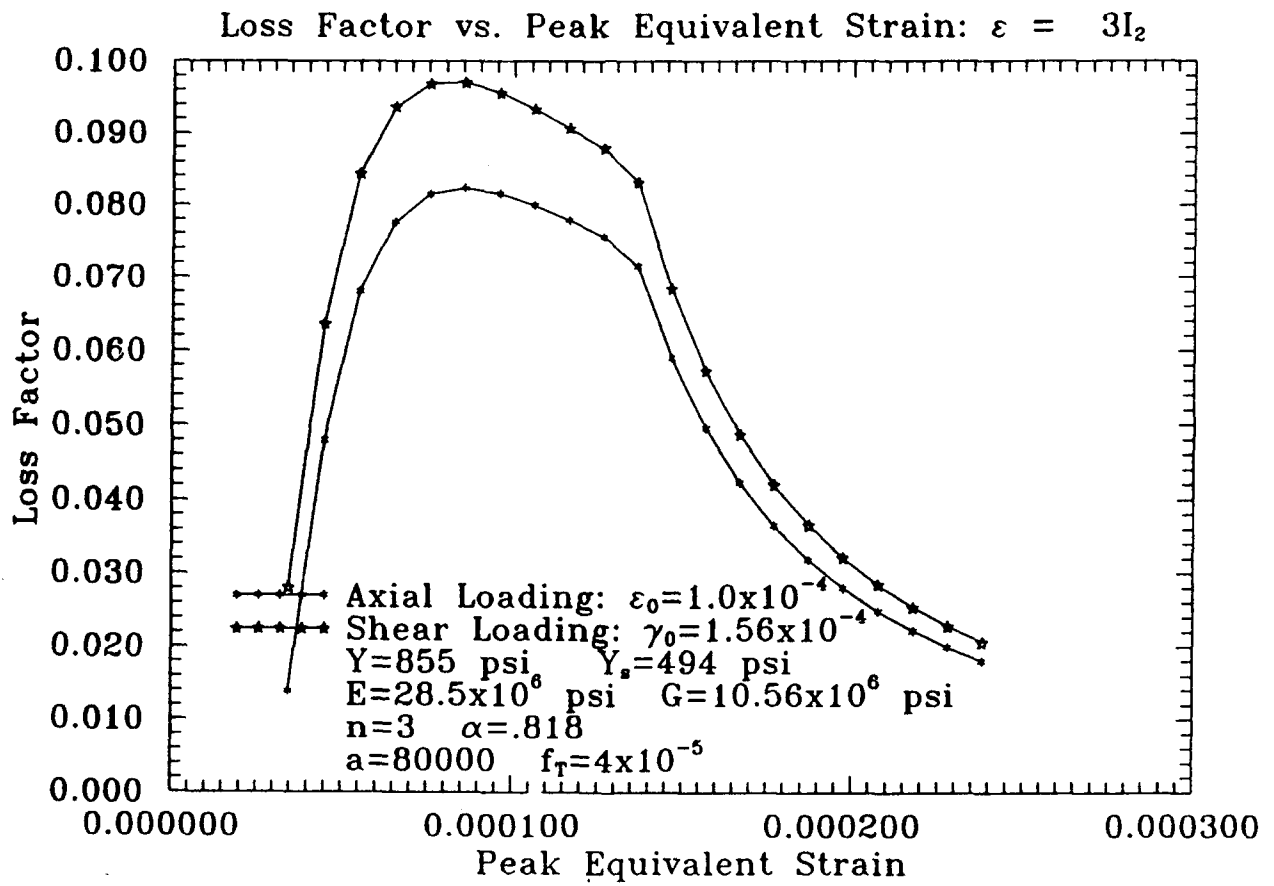


Figure 9: Amplitude Dependent Damping in Axial and Shear vs. Peak Equivalent Strain

Schematic illustrations of the bending and torsion cases are shown in Fig. 10. Note that the strain profiles in each geometry are linear, passing through zero at the position of the neutral axis of the beam and starting at zero at the center of the shaft. Also note that ϵ_p is the value of the axial strain at the beam surface while γ_p is the value of the engineering shear strain at the shaft surface. Because the problems under consideration involve only small strain, the following simple relations can be used to compute the moments and angular displacements for the beam and shaft geometries respectively:

$$M = - \int_A y \sigma \, dA \quad \text{and} \quad \theta = \frac{\epsilon_p L}{h} \quad (\text{beam})$$

$$T = \int_A r \tau \, dA \quad \text{and} \quad \phi = \frac{\gamma_p L}{R} \quad (\text{shaft})$$

Here y is the vertical distance from the neutral axis of the beam cross-section, σ is the axial stress in the longitudinal fibers of the beam, M is the resultant moment bending the beam, and θ is the beam rotation; for the shaft r is the distance from the center of the circular cross-section, τ is the shear stress due to torsion, T is the resultant torque twisting the shaft, and ϕ is the angle of twist. In both cases A denotes the area of cross-section.

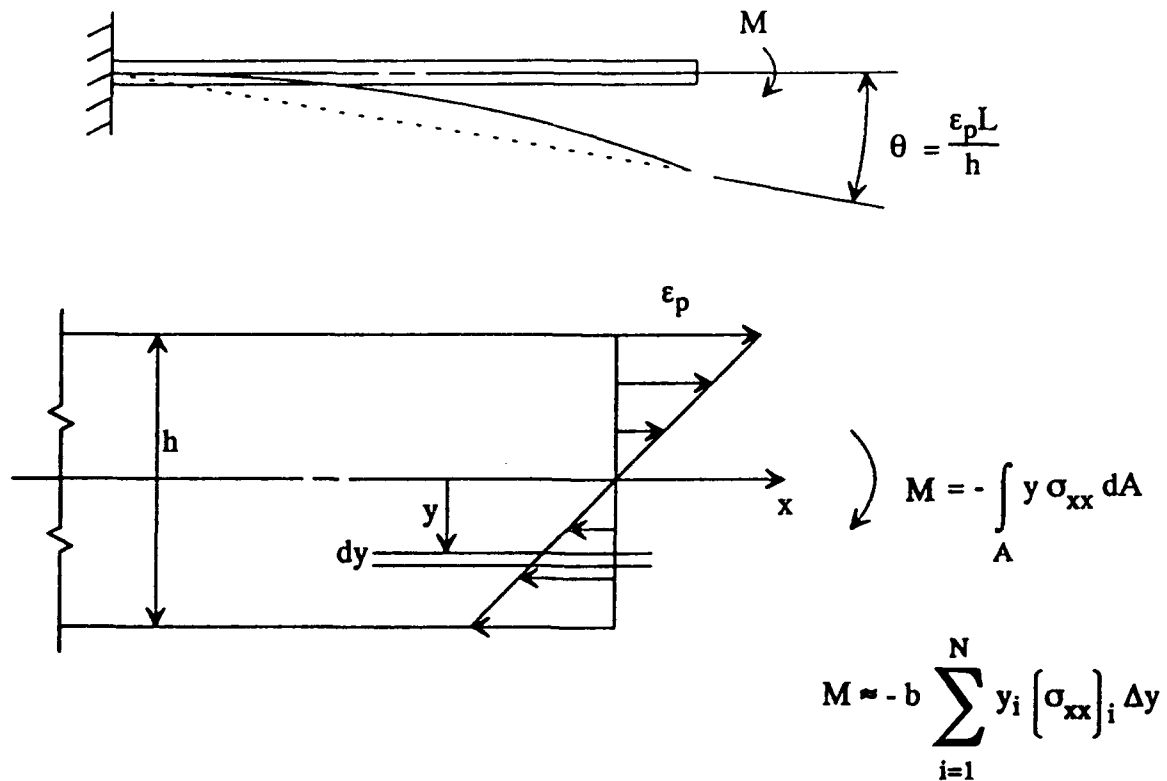
In analyses the surface strains of each geometry were specified to act sinusoidally in time. In addition each geometry was subdivided into a large number of finite, but thin, subsections; i.e. the infinitesimal distances dy and dr in Fig. 10 were replaced by small but finite distance Δy and Δr respectively. Also, the strain distribution for each finite subsection was assumed to be constant over the subsection thickness and the value of the strain was taken as the value of the strain profile at the center of the subsection. Having knowledge of the strain profile of the cross-section of each geometry, specifying the surface amplitudes and a sinusoidal history for each one, the stress history for each subsection of the geometry was computed numerically. Specifically, Eqs. (5)-(6) were integrated to give the stress profile time history of the bending beam and (7)-(8) were integrated for the shear stress profile time history of the shaft. Then the following formulas were used to compute the resultant moment and torque histories of the beam and shaft respectively:

$$M = -b \sum_{i=1}^N y_i \sigma_i \Delta y$$

$$T = 2\pi \sum_{i=1}^N (r_i)^2 \tau_i \Delta r$$

where N is the number of subdivisions making up the cross-sectional geometry and where the subscript i indicates reference to the location of a single subsection.

Bending Beam (Length: L , Width: b , Thickness: h)



Twisting Shaft (Length: L , Radius R)

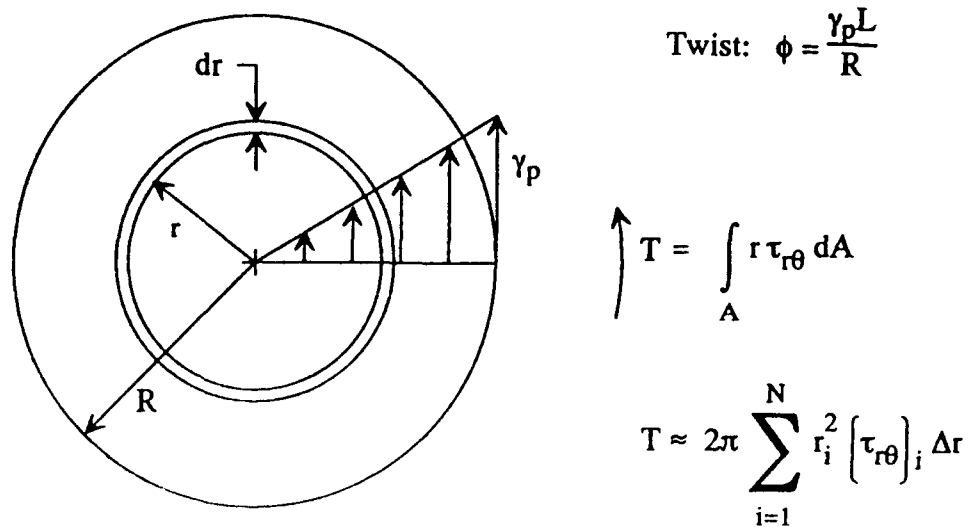


Figure 10: Schematic Drawing of Strain Profile in Bending and Torsion Geometries

The loss factor of each sample geometry was then calculated for a specified value of surface strain amplitude according to Eq. (9) where ΔW was determined by the area enclosed by the resultant moment vs. angular displacement hysteretic response and W was determined by

$$W = \frac{1}{2} \theta_{\max} M \Big|_{\theta_{\max}} \quad (\text{beam})$$

$$W = \frac{1}{2} \phi_{\max} T \Big|_{\phi_{\max}} \quad (\text{shaft})$$

The damping values which were computed in this way were found to be independent of sample geometry, i.e. for a given surface amplitude the ratio of ΔW to W remained constant for changes in cross-sectional size, sample length or both.

By repeating the calculations over a range of surface amplitudes the loss factor was plotted against the surface amplitude for both the bending and torsion cases as shown in Fig. 11. Note that the character of the damping vs. surface amplitude curves are vastly different with respect to one another. This is analogous the trend shown earlier in Fig. 6 for one dimensional behavior. Also, by comparing Fig. 11 to Fig. 6 it is clear that the character of the damping vs. peak strain curve of each sample is quite different than that corresponding to the respective one-dimensional material point responses. This is because of the strain dependent nature of the damping and the fact that strain is distributed throughout the sample; therefore some regions of the geometry may be contributing significantly to the overall damping of the solid sample while others are not.

As was done earlier, the inconsistent nature of the results given in Fig. 11 can be improved by making use of the peak equivalent strain $\bar{\epsilon}$ at the surface rather than the surface strain amplitude alone. Using Eq. (11) to calculate the amounts of peak equivalent strain at the surface of the bending and torsion samples, and plotting the corresponding loss factors of each sample against these values produces the curves given in Fig. 12. This figure shows that the use of peak equivalent strain for the finite sized geometries of bending and torsion samples gives an improved measure of correlation in the same manner that was exhibited earlier for the one-dimensional cases.

Thus presentation of nonlinear damping data as a function of equivalent strain rather than as a function of sample strain can be very useful. It is probably most useful in comparing damping data obtained by different test methods. It may also be useful in design work where the dynamic strains in a vibrating part or member are known. To show this let us consider an example where a designer wishes to use a high damping, but nonlinear, material in an application where bending is the primary mode of deformation, and suppose that damping data is available only from torsional tests. If the vibrational strain levels to be expected in service can be deduced from load and design analyses, then these strain levels can be converted to the measure of equivalent strain introduced in this paper. Applying the same conversion to the peak shear

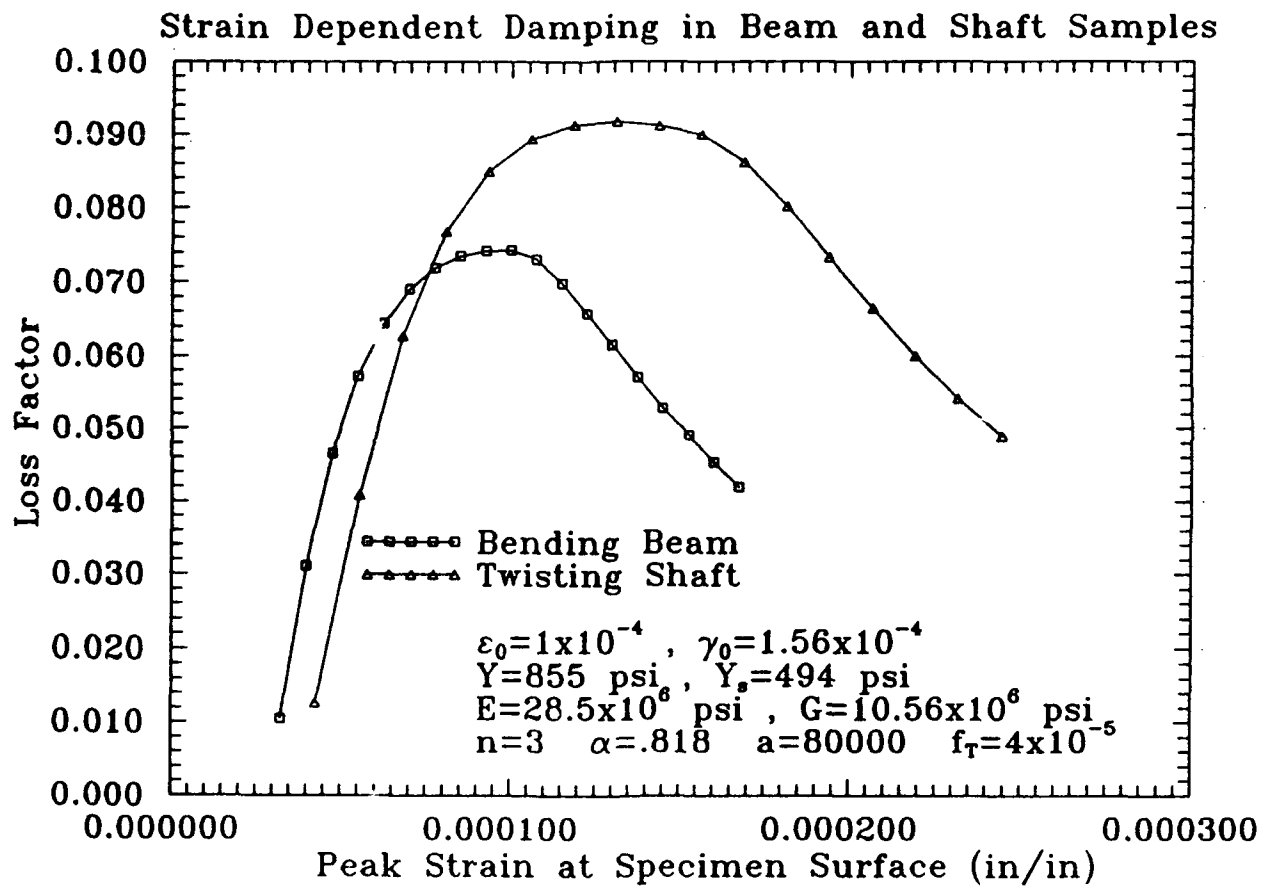


Figure 11: Amplitude Dependent Damping in Bending and Torsion vs. Peak Surface Strain

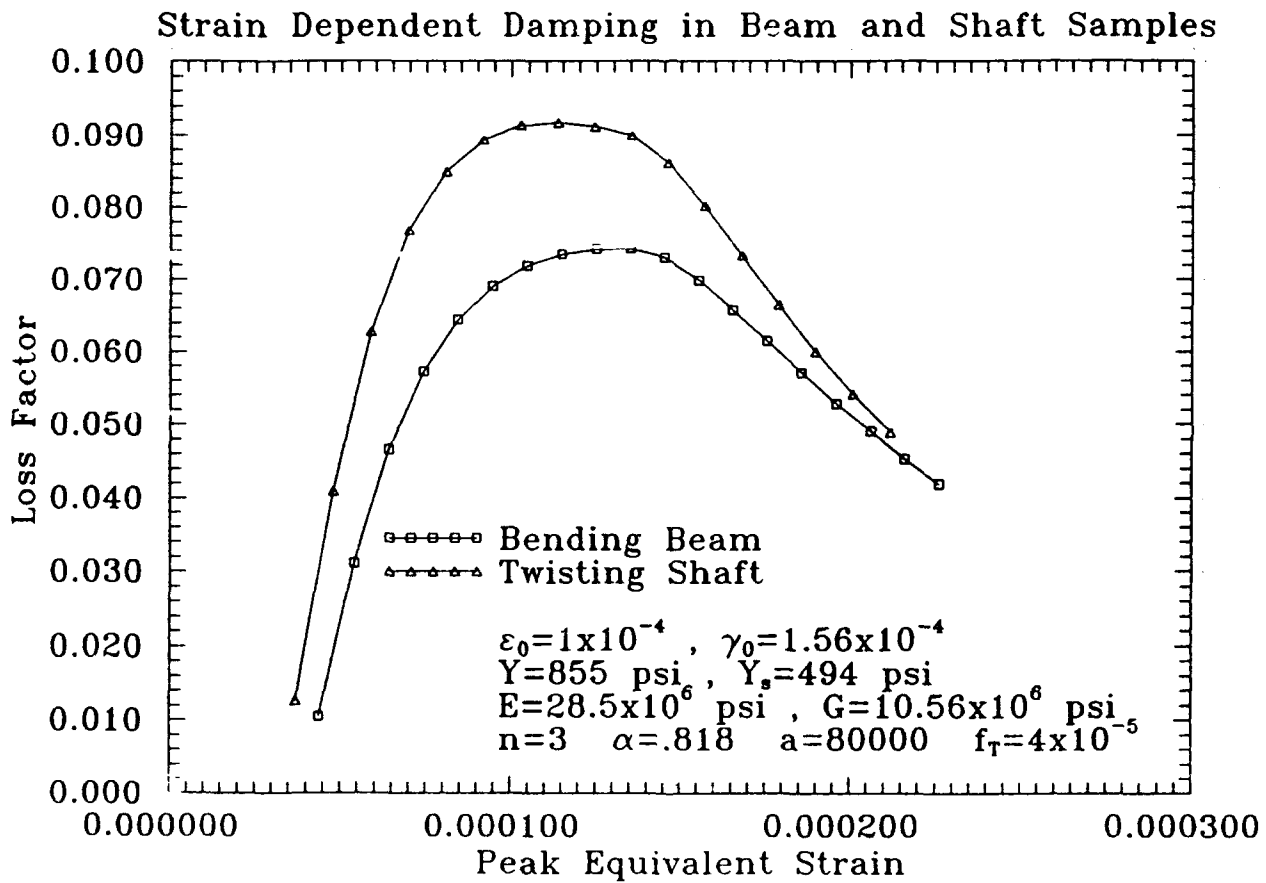


Figure 12: Amplitude Dependent Damping in Bending and Torsion vs. Peak Equivalent Strain

strains of the torsional damping data the designer would then be able to estimate whether or not the material damping will be in a range of peak performance for the application of interest.

SUMMARY

The work presented in this paper includes two major aspects; 1) modeling of nonlinear (or strain dependent) damping behavior via constitutive equations and 2) a way of improving correlation of nonlinear damping data via use of equivalent measures of distortion. These efforts were conducted in order to gain a better understanding of macroscopic nonlinear high damping material behavior and also to obtain a means in which to better correlate existing discrepancies in reported data for high damping materials. The modeling scheme applies to homogeneous isotropic materials and is adapted from a viscoplastic law through incorporation of material constants that correspond to small strain damping mechanisms. Also the law was modified to include damping mechanisms that become saturated after a given amount of strain. Analyses were made to calculate the loss factor of the common damping test configurations of bending and torsion. To do this material point relationships were used at each point in the cross-sectional geometry. In this way it was possible to relate the damping of the material to the damping of the specimen. The results did not depend on the relative dimensions of the sample geometry; rather the calculated loss factors depended only on the mode of deformation. The results showed that the strain dependent damping associated with each test were vastly different when plotted solely against the peak surface strain of the sample geometry. This is because the peak strains that correspond to each of these test configurations, namely axial and shear strain, are not equivalent to one another. However if an invariant measure of peak sample distortion is used in place of peak sample strain, then the correlation of the nonlinear damping of separate bending and torsion samples is predicted to improve considerably. Such an improved capacity for the correlation of nonlinear damping data may be very useful in comparing data obtained from different tests. Future research will include the modeling of specific nonlinear damping data. Also, constitutive law material parameters that are physically motivated by the microstructure will be studied.

ACKNOWLEDGEMENT

This research described in this paper was performed at David Taylor Research Center, and was supported in part by an Office of Naval Technology (ONT) postdoctoral fellowship under the administration of the American Society for Engineering Education (ASEE). Also, the research was supported by the Quiet Alloys Program which is part of the Functional Materials Block Program sponsored by Mr. Ivan Caplan.

REFERENCES

1. Perkins, A.J., Edwards, G.R., and Hills, N.A., "Materials Approaches to Ship Silencing," Report No. NPS-59Ps74061, Naval Postgraduate School, Monterey, California, June, 1974.
2. Schetky, L.M. and Perkins, J., "The 'Quiet' Alloys," *Machine Design*, April 6, 1978, pp. 202-206.

3. Dew, D., "Strain Dependent Damping Characteristics of a High Damping Manganese-Copper Alloy," Report No. NPS69-86-007, Naval Postgraduate School, Monterey, California, September, 1986.
4. Suzuki, K., Fujita, T., and Hasebe, M., "Damping Capacity and Mechanical Properties of Sintered Fe-Cr-Mo High Damping Alloys," *Proceedings of the 6th International Conference on Internal Friction and Ultrasonic Attenuation in Solids*, Hasiguti, R. and Mikoshiba, N. (ed.), University of Tokyo Press, 1977, pp. 757-761.
5. Schneider, W., Schrey, P., Hausch, G., and Török, E. "Damping Capacity of Fe-Cr and Fe-Cr Based High Damping Alloys," *Journal De Physique*, Colloque C5, Supplément au n° 10, Tome 42, October, 1981, pp. C5-635 - C5-639.
6. Masumoto, M., Hinai, M., and Sawaya, S., "Damping Capacity and Pitting Corrosion Resistance of Fe-Mo-Cr Alloys," *Transactions of the Japan Institute of Metals*, Vol. 25, No. 12, 1984, pp. 891-899.
7. Nippon Kokan K.K., *Tranqaloy Data Sheets*, 1981.
8. Kawabe, H. and Kuwahara, K., "A Consideration of the Strain Dependent Damping and Modulus in Ferromagnetic Metals," *Transactions of the Japan Institute of Metals*, Vol. 22, No. 5, 1981, pp. 301-308.
9. Lazan, B.J., "Effect of Damping Constants and Stress Distribution on the Resonance Response of Members," *Journal of Applied Mechanics*, Transactions of the ASME, Vol. 75, 1953, pp. 201-209.
10. Cochardt, A.W., "A Method for Determining the Internal Damping of Machine Members," *Journal of Applied Mechanics*, Transactions of the ASME, Vol. 76, 1954, pp. 257-262.
11. Krempl, E., "Models of Viscoplasticity: Some Comments on Equilibrium (Back) Stress and Drag Stress." *Acta Mechanica*, Vol. 69, 1987, pp. 25-42.
12. Miller, A.K. (ed.), *Unified Constitutive Equations for Creep and Plasticity*, Elsevier Applied Science, 1987.
13. Graesser E., "Multi-Dimensional Modeling of Hysteretic Materials Including Shape Memory Alloys: Theory and Experiment," Ph.D. Dissertation, Dept. of Mechanical and Aerospace Engineering, State University of New York at Buffalo, Buffalo, New York, February, 1990.
14. Shames, I.H. and Cozzarelli, F.A., *Elastic and Inelastic Stress Analysis*, Prentice-Hall, 1991.
15. Shames, I.H., *Introduction to Solid Mechanics*, Prentice-Hall, 1975.
16. Timoshenko, S.P. and Goodier, J.N., *Theory of Elasticity*, Third Edition, McGraw-Hill, 1970.

NON-OBSTRUCTIVE PARTICLE DAMPING TESTS ON ALUMINUM BEAMS

H. V. Panossian, Ph.D*
Principal Engineer, Control Structure System Dynamics
Rockwell International Corporation, Rocketdyne Division

ABSTRACT

Presented in this paper is a novel passive vibration damping technique referred to as "Non-Obstructive Particle Damping (NOPD)." The NOPD technique consists of making small diameter holes (or cavities) at appropriate locations inside the main load path of a vibrating structure and filling these holes to appropriate levels with particles that yield the maximum damping effectiveness for the desired mode (or modes). Metallic or nonmetallic particles in powder, spherical, or liquid form (or mixtures) with different densities, viscosities, and adhesive or cohesive characteristics can be used.

Two 24- by 3- by 3/4-in. aluminum beams were used and thirteen 2-mm diameter, equidistant cross-holes (along the width) in one, and seven 2-mm diameter, equidistant longitudinal holes (along the length) in the other, were drilled. These holes were partially filled with tungsten and zirconium oxide powder and steel (spherical) particles and the beams were tested under different conditions. Modal tests under free-free and clamped conditions indicated an increase in damping ratios from 0.02% without particles to about 10% with tungsten. Moreover, damping of specific modes by placing particles at various locations of high kinetic or strain energies were also carried out with remarkable effects. This paper will discuss the test results and will evaluate various methods of damping estimation.

INTRODUCTION

Damping in vibrating structures is described with various terms: loss factor, quality factor, reverberation time, etc. The interconnections between these various descriptions are discussed in Reference 1. One of the major concerns in vibration control problems is the response prediction of a structure excited by an external force. The reason for this concern is the difficulty in accurately determining the damping factor required for response prediction in analyses. Several different techniques are utilized for damping measurements that entail vibration decay rate, "one-half power point" at resonances, and steady-state input and stored energy measurements, among others. All of these methods involve the generation of frequency response functions (FRFs) and some curve fitting techniques that require knowledge of input amplitude and corresponding vibration measurements at various locations of a structure. Fraction of critical damping (the minimum viscous damping required in a vibrating structure for it to return to its initial position without oscillations) is the most common measure used to express the response characteristics of a structure, referred to as damping ratio.

The NOPD technique entails making small holes (or cavities) at analytically determined (and, when possible, experimentally verified) locations inside the main load path of a vibrating structure in appropriate areas and filling these holes to proper levels with such particles as to yield maximum damping effectiveness. A specific vibration mode, or

*6633 Canoga Avenue
Canoga Park, CA 91303
(818) 773-5533

several modes, can be addressed in a given structure. Powders, spherical, metallic, non-metallic, or liquid (or even mixtures) with different densities, viscosities, and adhesive or cohesive characteristics can be used.^[2,3]

This new approach has a great deal of potential applications under cryogenic, high-temperature, high-flow, or high-pressure environments. It does not affect the mass or the performance of the structure (on the contrary, it often reduces it). The only drawback, when applied to an existing structure, is the creation of stress concentrations when making the holes. However, this concern can be greatly reduced by making the size of the holes small compared to the material thickness and by using less destructive manufacturing techniques. In addition, the particles can be embedded inside a structure as a part of the manufacturing process, thus avoiding the previously mentioned negative effects.^[4]

NOPD involves the potential of energy absorption or dissipation via friction, momentum exchange between the moving particles and the vibrating walls, heat, and viscous and shear deformations. It offers benefits in vibration reduction of rotating machinery, lasers, rotorcraft, aircraft, spacecraft, automotive, and civil structures, among others, through the decreasing of structural fatigue and associated savings in cost or extension of system life cycles.

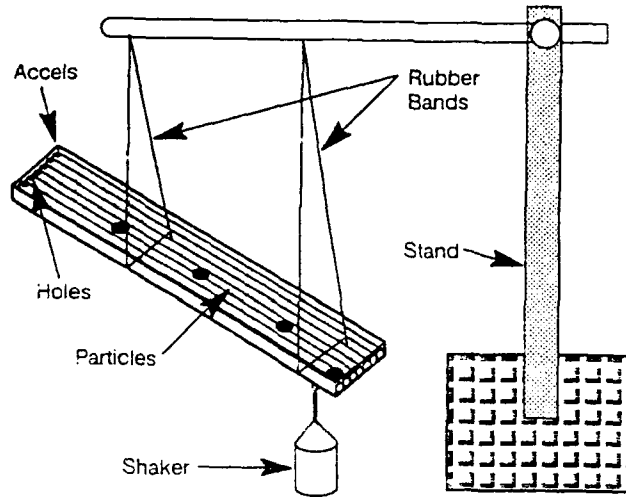
MODAL SURVEY TESTS

Experimental modal survey tests were carried out in the Rocketdyne Engineering Development Laboratory (EDL) on two 24- by 3- by 3/4-in. aluminum beams under free-free conditions, and various modal and vibration data were generated. Acceleration measurements were taken on five equidistant points on each beam. One of the beams had seven 2-mm diameter holes along the length, and the other had thirteen 2-mm diameter holes along the width. The holes were filled with various particles and tested for damping effectiveness.

The tests were performed by suspending each beam from two rubber bands and exciting it, via an impact hammer and an electromechanical exciter with load cells at their tips, near one of its ends (Fig. 1). Five acceleration measurements were taken at equidistant points on the beam with the two accelerometers placed at the opposite corners of both ends. Frequency response functions (FRFs), power spectral densities (PSDs), time histories, and other appropriate data were evaluated to study the damping ratios, mode shapes, and frequencies.

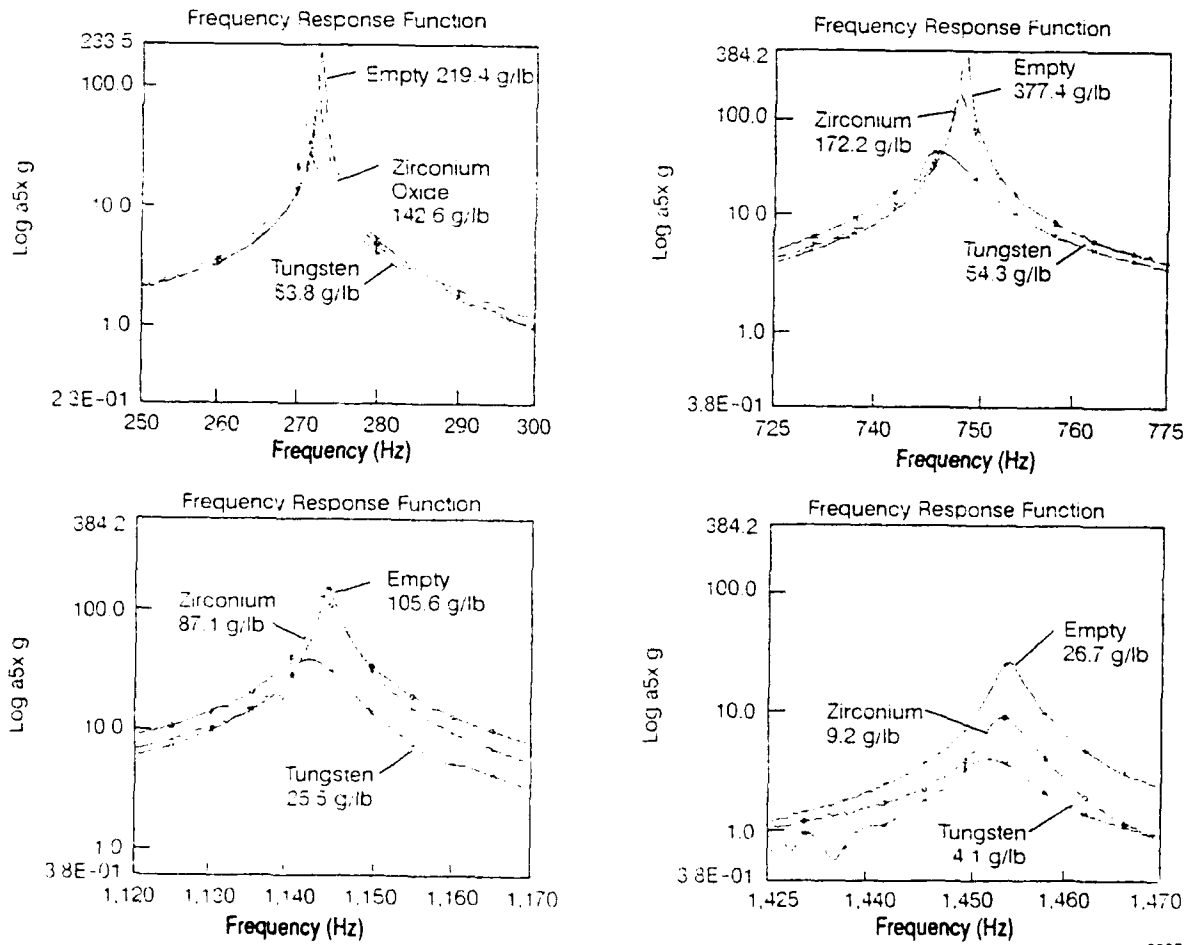
The 13 equidistant 2-mm diameter holes drilled across the width of the first aluminum beam were partially filled (about 75%) with tungsten powder, zirconium oxide powder, and steel shots (0.011 in. diameter). The beam was excited with a shaker (with flat random inputs between 10 to 1,600 Hz) and an impact hammer (both applied to one of the corners of the beam) from the opposite side of the accelerometer. The FRFs were generated under empty and filled conditions and overlaid for each of the first four vibration modes (Fig. 2). The first plot is that of the first bending mode at about 273 Hz when empty; the second at 749 Hz is the second bending mode; the third at about 1,145 Hz is the first torsional mode; and the last one at 1,455 Hz is the third bending mode. The overall FRF up to 1,600 Hz is shown in Fig. 3.

All of the seven 2-mm diameter longitudinal holes were filled with tungsten and zirconium oxide powder, and steel shots separately, and tested under (about) 90% full. Moreover, the beam was also tested with empty holes, and the FRFs were compared by overlaying the peaks of each of the first four vibration modes under a free-free test



6297-1

Figure 1. Free-free beam tests in air



6297-2

Figure 2. Free-free cross-holed beam vibration FRFs in air

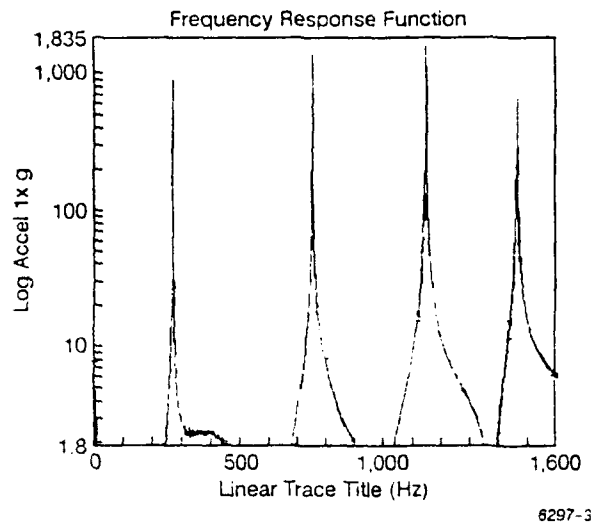


Figure 3. FRF of empty cross-holed beam free-free in air

condition with flat random (shaker) and hammer input excitations. The dramatic decay rate provided by the presence of tungsten powder (see Fig. 4) caused some difficulty in calculating the damping values and various approaches were used to derive the damping ratios for each mode. The overlays of each mode, both empty and filled with different particles, are shown in Fig. 5. The first mode decreased in amplitude from 911.7 g/lb down to 14.9 g/lb by more than a factor of 61.

DISCUSSION

Table 1 summarizes the damping ratios estimated under various damping particle treatments and with different estimation techniques. In all cases, it is apparent that damping effectiveness with such a minute particle amount is dramatic. The total mass of the aluminum beam was 5.4 lb, while the total mass of the heaviest particles used (tungsten)

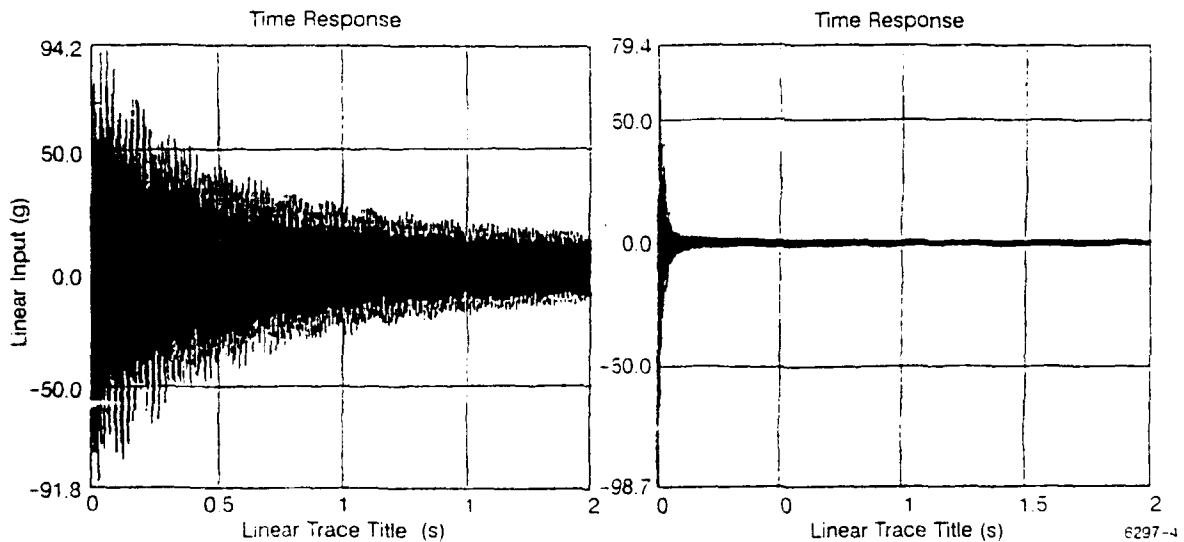
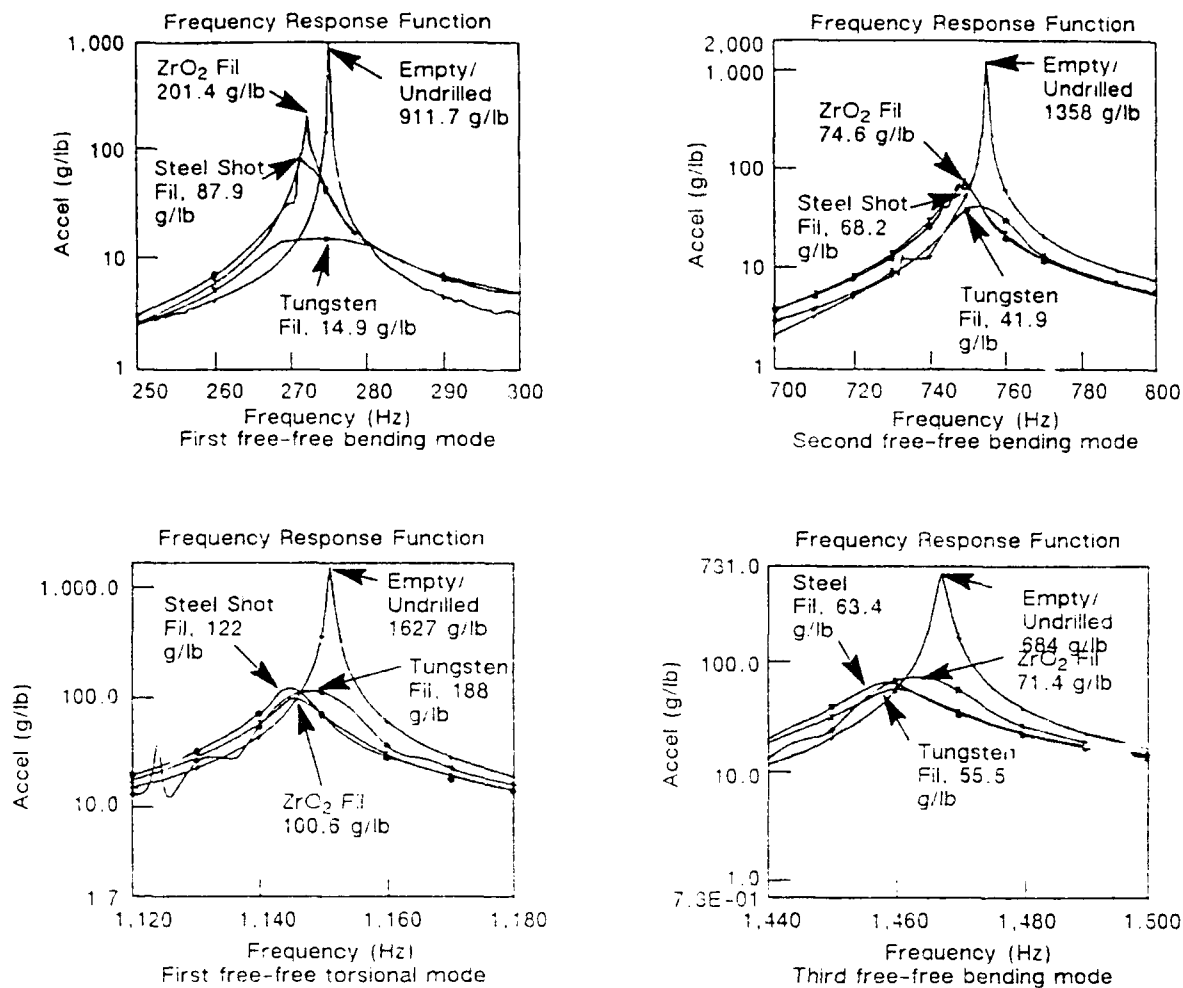


Figure 4. Time histories of aluminum beam empty (right) and with tungsten powder (right) in air



6297-5

Figure 5. FRF overlays of first four free-free in air vibration modes of longitudinal-holed beam with different particles

was only 0.3 lb in the longitudinal-holed beam (about 5%). The damping estimates were derived by using curve fitting, one-half power point calculation, and fast Fourier transform (FFT) decay rate methods. There are discrepancies in the damping ratios, especially when particles provide high damping values (Table 1). The reason for this is the fact that all the curve fitting routines used consider structures with low damping values, thus making provisions for approximations and losing accuracy. The most reliable damping estimation technique for highly damped systems is probably the log decrement (or the FFT decay rate) for each mode. Thus, FFTs are used to generate the time history of each resonant peak in a waterfall pattern and then take the log decrement of each mode (Fig. 6). The damping ratios were calculated by the following formula:

$$\zeta = \frac{D}{8.69\omega} \quad (1)$$

where ζ is the damping ratio, D is the decay rate in dB/s, and ω is the natural frequency.

**Table 1. Damping Ratios With Different Estimation Methods
for Longitudinal-Holed Aluminum Beam**

Mode Number	Particle/Condition	Frequency (Hz)	Peak Amplitude (2/lb)	Damping Ratios		
				Curve Fit	One-Half Power Point	FFT Decay Rate
1	Holes empty	275.45	911.7	0.000148	0.000272	0.00046
	0.011-in. steel shots	271.7	87.9	0.00415	0.00391	0.00253
	Zirconium oxide powder	272.6	201.4	0.00154	0.00142	0.00111
	Tungsten powder	272.67	14.9	0.109	0.0912	0.0875
2	Holes empty	755.2	1,358	0.000135	0.000342	0.00090
	0.011-in. steel shots	749	68.2	0.0146	0.0156	0.00942
	Zirconium oxide powder	749.2	74.6	0.00442	0.00541	0.00365
	Tungsten powder	753.45	41.9	0.0143	0.0275	0.00998
3	Holes empty	1,151.4	1,627	0.000277	0.000344	0.000443
	0.011-in. steel shots	1,144.8	122	0.00325	0.00415	0.00311
	Zirconium oxide powder	1,145.6	100.6	0.0033	0.00536	0.00315
	Tungsten powder	1,148	188	0.0085	0.0091	0.0069

DS45-0012

CONCLUSIONS

Extensive modal testing on two aluminum beams (one with thirteen 2-mm diameter holes along the width and the other with seven 2-mm diameter holes along the length) provided significant data regarding the effectiveness of NOPD. Moreover, different characteristics and key parameters that influence NOPD performance were identified. The main objective of this program, to assess the applicability of NOPD at low frequencies, was achieved. Further studies are needed to evaluate the subtle influences exerted by various test conditions, materials, holes, and structural characteristics.

It is especially remarkable to achieve over 60 times vibration amplitude reduction by minute amounts of particles placed inside small cavities in a beam. The practical issues related to implementation of NOPD remain to be tackled. However, the effectiveness of NOPD over a wide range of frequencies undoubtedly opens new avenues for further research and even applications.

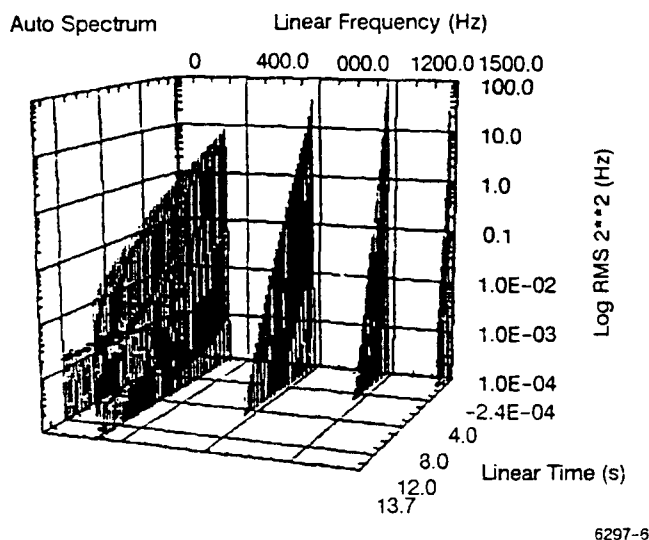


Figure 6. FETs of free-free beam in air

REFERENCES

1. Svend Gade and Henrik Herlufsen, "Digital Filter vs FFT Techniques for Damping Measurements," *Sound and Vibration Magazine*, V. 24, No. 3, pp. 24-32, 1990.
2. H. V. Panossian, "Structural Damping Optimization via Non-Obstructive Particle Damping Technique," in the proceedings of the Third Air Force/NASA Symposium on Recent Advances in Multidisciplinary Analysis and Optimization, pp. 7-15, San Francisco, CA, 24-26 September 1990.
3. H. V. Panossian, "Structural Damping/Acoustic Attenuation Optimization via Non-Obstructive Particle Damping," presented in the JANNAF propulsion meeting, Anaheim, CA, 2-4 October 1990.
4. H. V. Panossian and D. L. Bice, "Low Frequency Applications of Non-Obstructive Particle Damping," in the proceedings of the 61st Shock and Vibration Symposium, pp. 41-51, Pasadena, CA, 16-18 October 1990.

COMPLEX DYNAMIC MODULUS OF NITINOL-REINFORCED COMPOSITES

J. Gilheany¹

The Catholic University of America
School of Engineering and Architecture, Washington, DC

R. Deigan

The Catholic University of America
Washington, DC

A. Baz

The Catholic University of America
Washington, DC

ABSTRACT

Shape memory fibers, made of a Nickel-Titanium alloy (NITINOL), are embedded into fiberglass/polyester resin composites in order to control their dynamic characteristics over wide frequency and temperature ranges. The characteristics of the resulting NITINOL-reinforced composites can be tuned and controlled adapt to changes in the loading and operating conditions. Such adaptive characteristics can be utilized in controlling the shape and vibration of composite structures.

The dynamic characteristics of this class of NITINOL-reinforced composites are quantified by measuring the complex dynamic modulus. The modulus is determined using the Dynamic Mechanical Thermal Analyzer (DMTA) over a temperature range from 0 to 100°C and over the frequency range from 0.3 to 30 Hz. The effects of shape memory and initial pre-strain of the NITINOL fibers on the complex modulus are also determined over the same temperature and frequency ranges. The measured characteristics are compared with those of unreinforced fiberglass/polyester resin composites as well as with those of pure NITINOL. It is observed that the continuously decaying storage modulus of the fiberglass composite with increasing temperature, near the glass transition region, can be compensated for by the increased storage modulus of the activated NITINOL fibers. With proper control of the initial pre-strain and activation temperature of the NITINOL fibers, the characteristics of the composite can be tailored for loading and environmental conditions.

**FULL PAPER NOT AVAILABLE FOR
PUBLICATION**

¹Assistant Dean, The Catholic University of America, 620 Michigan Avenue, NE, Washington, DC 20064 (202) 319-5170

ESTIMATION OF NONPROPORTIONAL DAMPING FROM EXPERIMENTAL MEASUREMENTS

T. K. Hasselman¹
Engineering Mechanics Associates, Inc.
Torrance, CA

Jon D. Chrostowski
Engineering Mechanics Associates, Inc.
Torrance, CA

ABSTRACT

The full modal damping matrix (both diagonal and off-diagonal terms) is required to synthesize the modal damping of a structural system from substructure tests, and may be used to estimate the distribution of damping in a structure.

A method for determining a full modal damping matrix from experimental measurements was published by the first author in 1972. The method was applied with limited success, the problem being that complex modes were very difficult to obtain from the analog sine-dwell modal test data which were available at the time. Since then, several modal identification methods have been developed which derive complex modes from digitally recorded and processed vibration test data. Only the real parts of these complex modes are used, however; the small imaginary parts so far have been ignored.

This paper presents methods which have been developed to condition the experimental complex mode data obtained by the ERA method for purposes of estimating the full modal damping matrix. Practical application of these methods using experimental data from truss-beam type structures are presented.

**FULL PAPER NOT AVAILABLE FOR
PUBLICATION**

¹President, 3820 Del Amo Boulevard, Suite 318, Torrance, CA 90503 (213) 370-2551

Load Unit Deflection Correction
for
Forced Vibration Test System

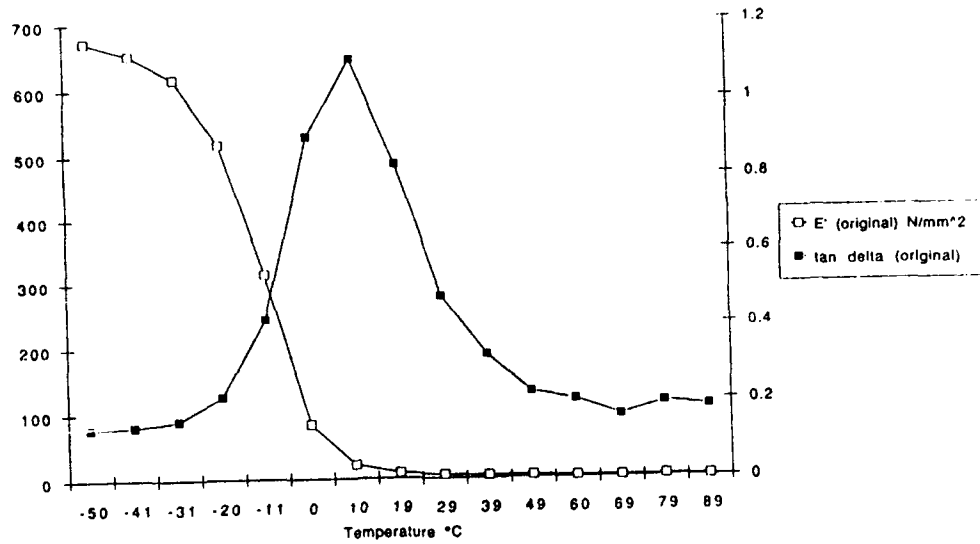
Author: Kirk K. Biegler MTS Systems Corporation

ABSTRACT

A correction for the errors due to load unit deflection is presented and examples are given that show the effectiveness of the correction on typical data. Displacement errors are typically induced through deflections of the load cell, extension rods, and fixtures, with the load frame contributing a very small effect. With this correction, forced vibration test systems can be used over a wide range of frequencies, amplitudes and temperatures to give accurate material dynamic characterization data for specimens in shear, compression, tension, or bending with minimal changes in specimen geometry or fixtures. Work so far has been conducted on metallic samples. Work remaining includes collection of data on samples to be included in the Damping Technology round robin.

MTS Systems Corporation
Box 24012
Minneapolis, Minnesota 55424

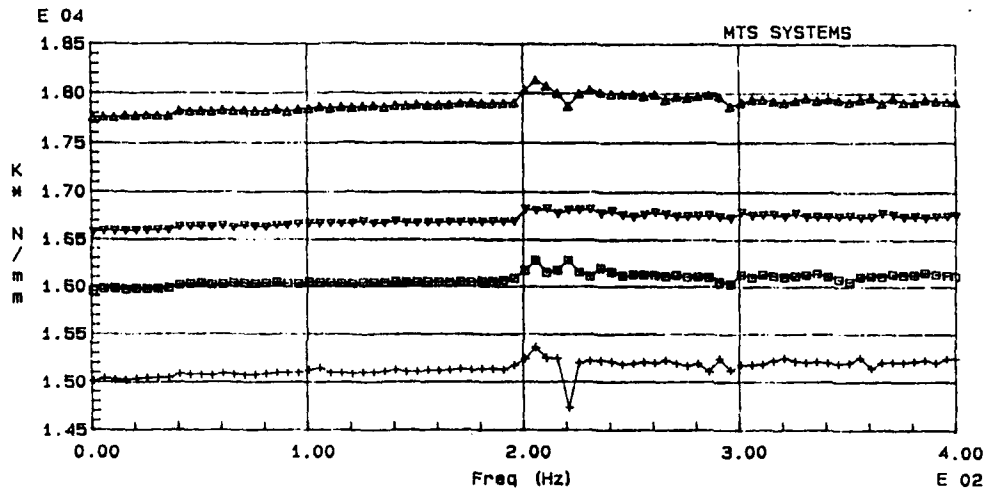
E' and tan delta vs Temperature(original data)



This is the original data submitted to the round robin. The specimen was a 25 mm diameter by 12.5 mm high compression button. Test conditions were 10 hz constant frequency with an expected 2% prestrain and a dynamic strain of 0.1%. One sample and one set of transducers was used to collect all the data. System full scales are $\pm 10,000$ N and ± 25 mm. Data "looks good", but modulus at cold temperature was reported to be low.

Load Unit Deflection Correction
MTS Systems Corporation
Box 24012
Minneapolis, Minnesota 55424

K* vs Freq

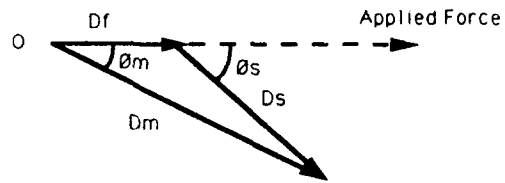


Test	Proc	Mean (N)	Amp (mm)
▲	SHAT01 STUBE1	-1400	.06
▼	SAT31 STUBE1	-1400	.06
□	SAT51 STUBE1	-1400	.06
+	SAT81 STUBE1	-1400	.06

This is an example of data taken on a metallic spring with different length extension rods added to the loading path. It shows very clearly the errors due to ignoring the load unit deflections.

Load Unit Deflection Correction
 MTS Systems Corporation
 Box 24012
 Minneapolis, Minnesota 55424

LOAD UNIT DEFLECTION CORRECTION



D_f = frame deflection

D_m = measured deflection

D_s = actual specimen deflection

θ_m = measured phase angle

θ_s = actual specimen phase angle

DISPLACEMENT CORRECTION

$$D_s = \sqrt{D_m^2 + D_f^2 - 2D_m D_f \cos \theta_m}$$

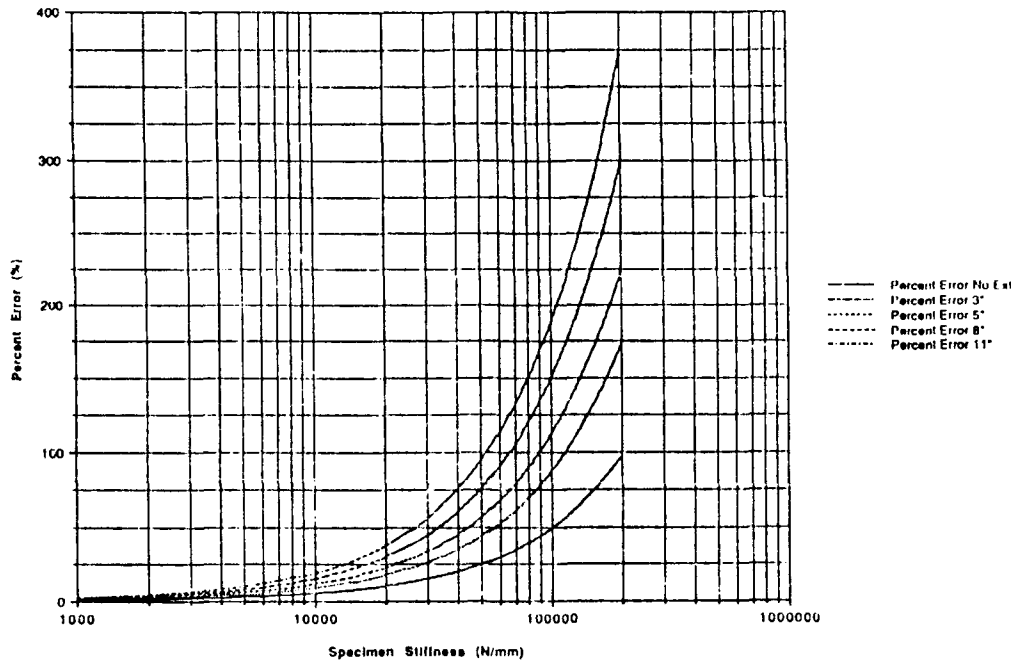
PHASE ANGLE CORRECTION

$$\theta_s = \tan^{-1} \left(\frac{\sin \theta_m}{\cos \theta_m - D_f / D_m} \right)$$

This is the mathematical formula for the load unit deflection correction as we have implemented it on our systems for dynamic mechanical analysis. It was provided to MTS by one of our customers and agrees well with theoretical and experimental results.

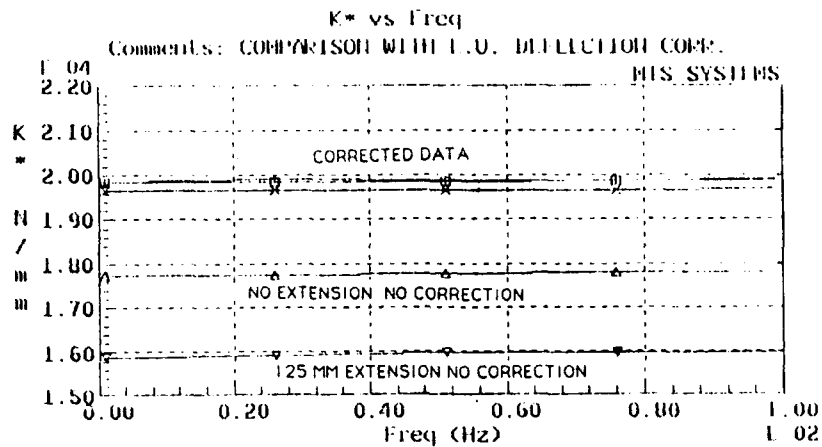
Load Unit Deflection Correction
 MTS Systems Corporation
 Box 24012
 Minneapolis, Minnesota 55424

Frame Deflection Errors



This graph gives typical errors for a forced vibration test system. We have used hollow extension rods to minimize moving mass errors and allow dynamic property measurements at frequencies up to 1000 hz. The error with no extension is due to load cell deflections. A combination of strain gaged load cell and piezoelectric device is used to measure long term mean levels and high resolution dynamic amplitudes

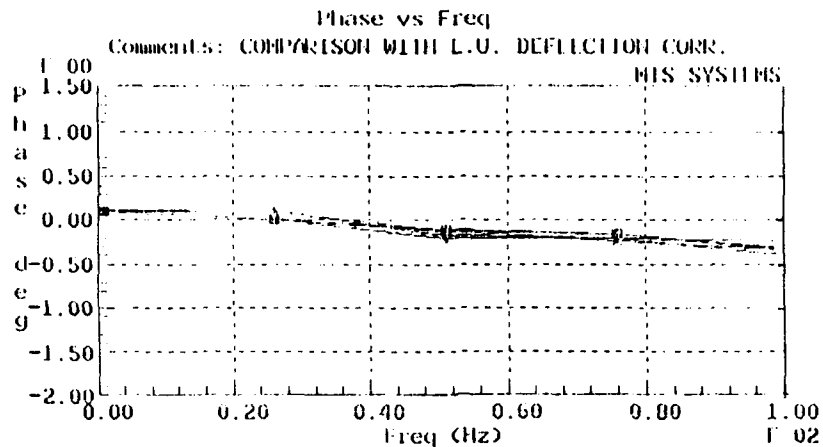
Load Unit Deflection Correction
MIS Systems Corporation
Box 24012
Minneapolis, Minnesota 55424



Test	Proc	Mean (N)	Amp (mm)
Δ SIRT02	STUBL	-1400	.06 NO EXTENSION NO CORRECTION
∇ SRT52	STUBE	-1400	.06 125 MM EXTENSION NO CORRECTION
□ STIFF1	TUBE	-1400	.06 NO EXTENSION WITH CORRECTION
+ STIFF1	TUBE	-1400	.06 75 MM EXTENSION WITH CORRECTION
× STIFFK	TUBE	-1400	.06 125 MM EXTENSION WITH CORRECTION

This graph compares the data collected on a metallic spring with no correction and with the proposed correction. This shows a dramatic improvement from 20% error to less than 1%. The system LVDT is used to measure the errors and the specimen deflections

Load Unit Deflection Correction
 MTS Systems Corporation
 Box 24012
 Minneapolis, Minnesota 55424

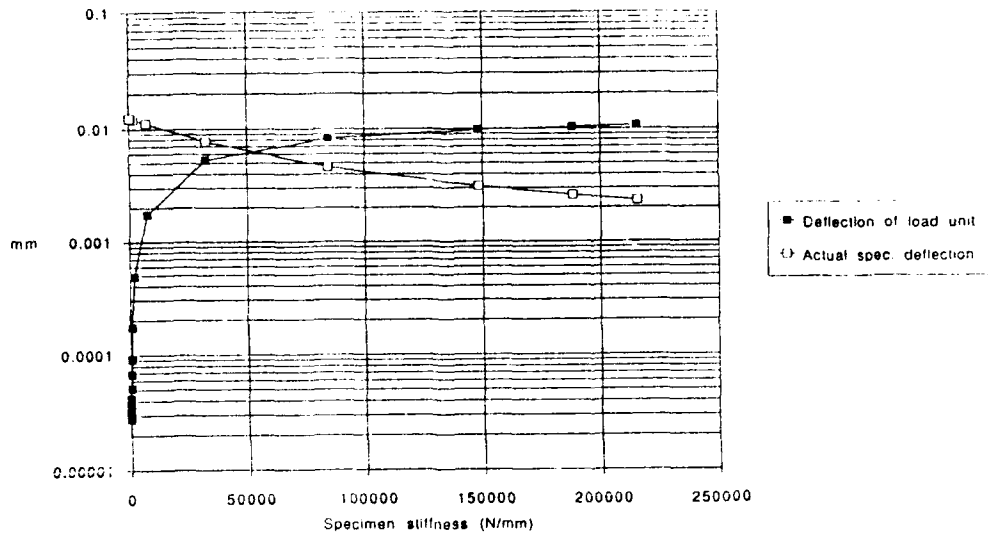


Test	Proc	Mean (N)	Amp (mm)	
△	SIRT02	STUBE	-1400	.06 NO EXTENSION NO CORRECTION
▽	SRT52	STUBE	-1400	.06 125 MM EXTENSION NO CORRECTION
□	STIFF1	TUBE	-1400	.06 NO EXTENSION WITH CORRECTION
+	STIFF1	TUBE	-1400	.06 75 MM EXTENSION WITH CORRECTION
x	STIFFK	TUBE	-1400	.06 125 MM EXTENSION WITH CORRECTION

This graph compares the data collected on a metallic spring with no correction and with the proposed correction. This shows no effect on phase angle measurements. There was some concern that the correction would increase the scatter in the phase angle since there is division by numbers close to zero and multiplication of numbers close to zero.

Load Unit Deflection Correction
 MTS Systems Corporation
 Box 24012
 Minneapolis, Minnesota 55424

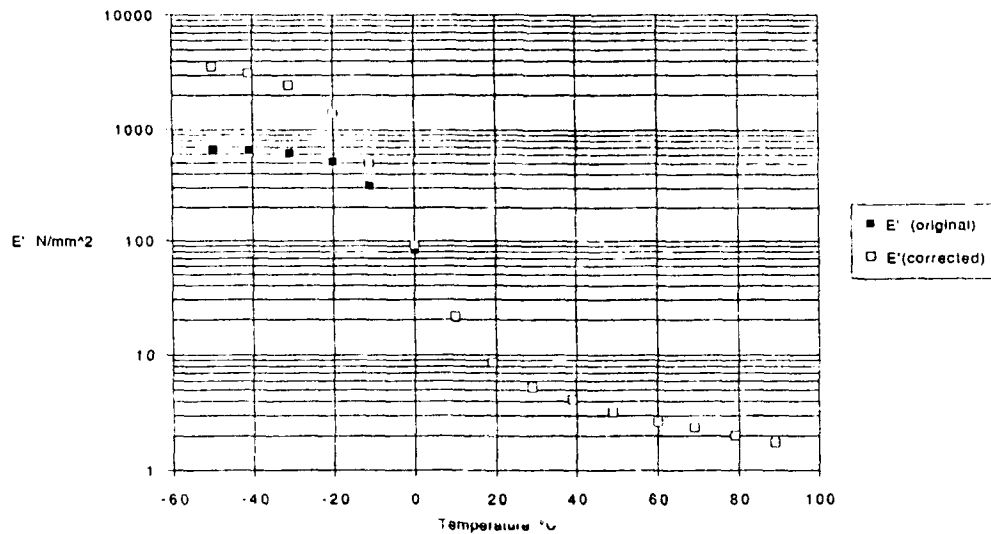
Specimen deflection errors



This graph shows the tradeoff between specimen deflections and load unit deflections for the test setup we have used for temperature property measurement. If the accuracy of the load unit deflection correction is questioned, solid extension rods can be used as long as test frequencies are low.

Load Unit Deflection Correction
MTS Systems Corporation
Box 24012
Minneapolis, Minnesota 55424

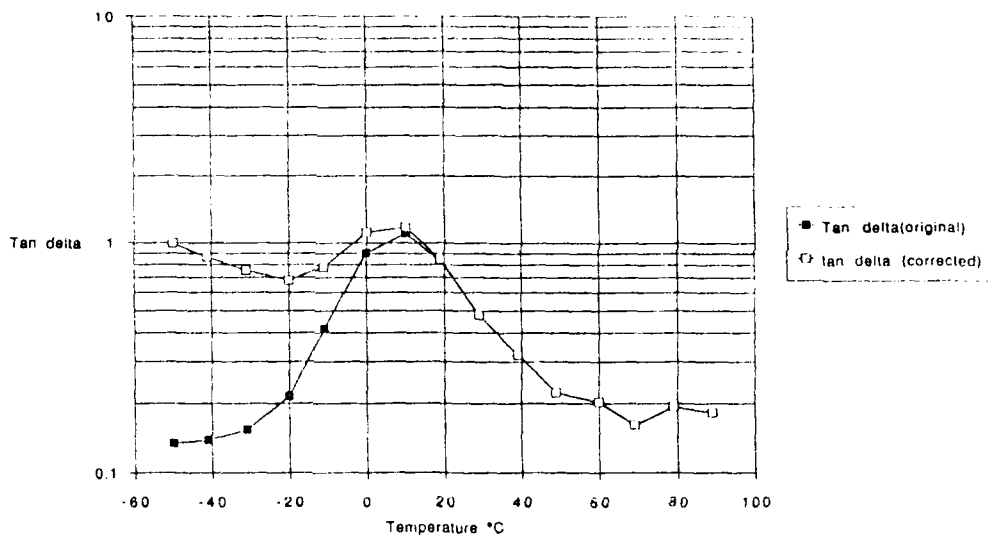
Modulus correction for WP round robin data



This graph compares the data before and after the correction has been applied. The correction is made to existing data so actual specimen dynamic strains were lower than expected. Original measured maximum modulus was 700 N/mm², corrected modulus is 3600 N/mm² in compression compared to a reported 4200 N/mm² in tension. The reduction in modulus could be due to the manner of loading or the low strain amplitudes. Further work will be done to collect extensional modulus data with full strain amplitudes.

Load Unit Deflection Correction
MIS Systems Corporation
Box 24012
Minneapolis, Minnesota 55424

Tan Delta correction for WP round robin data



This graph compares the data before and after the correction has been applied. The correction is made to existing data so actual specimen dynamic strains were lower than expected. This may explain the strange tan delta behavior at low temperatures. Additional work will be done to verify the low temperature tan delta measurements on the round robin material.

Load Unit Deflection Correction
MT. Systems Corporation
Box 24012
Minneapolis, Minnesota 55424

AN ANALYTICAL APPROACH TO DESIGNING FRICTION DAMPERS IN TURBOMACHINERY BLADING

Josef Panovsky¹, Analytical Engineer

David G. Hendley, Staff Design Engineer

Raymond A. MacKay, Senior Staff Aeromechanical Engineer

GE Aircraft Engines
Cincinnati, Ohio and Lynn, Massachusetts

ABSTRACT

Aircraft engine turbomachinery blading operates in an environment that induces vibration which can lead to failure through high-cycle fatigue. This vibration can often be reduced to acceptable levels by friction dampers, which dissipate energy by capitalizing on the resulting relative motion between the blade and a motionless structure or adjacent vibrating blades. The key to optimizing a given damper design is to determine the dynamic weight at which the maximum energy is dissipated without locking the blade at the damper contact point. As the design of turbomachinery blading progresses towards higher-loaded stages with more complex geometry, vibratory modes beyond the primary beam bending become more prominent. This paper will discuss the development of an analytical method to predict damper effectiveness for any blade mode. The analysis is based on a component mode method, and includes provisions for modeling stick-slip at the friction contact. Multiple damper contact points can be evaluated, and the damper design can be blade-to-ground or blade-to-blade with arbitrary phase angle. The results of a series of lab tests with simple beam specimens to evaluate the principal damper design variables will be presented along with the corresponding analytical predictions.

1. GE Aircraft Engines, 1 Neumann Way, M/D A334, Cincinnati, Ohio 45215. Tel (513) 583-5117.

1 INTRODUCTION

Dampers for turbomachinery blading have traditionally been designed through the use of experience and lab testing. Until recently, there was little analytical support available because of the complexity of the governing equations, which are nonlinear due to the friction forces present at the blade-damper contact points. The solution is also complicated by the requirement to know all three spatial components of the relative motion at these contact points. Recent development efforts, however, have resulted in analytical methods which can be used to evaluate the effectiveness of the damper in reducing blade vibration.

There are certain basic characteristics that qualitatively describe the effects of a damper on the vibratory motion of a blade. The most important characteristic is the existence of an optimal friction force for a given excitation. As the damper weight is varied, a value can be found which minimizes the blade response, and increasing or decreasing the damper weight from this value will cause the vibratory response of the blade to increase. Variables such as shank-to-airfoil stiffness ratio can modify this optimum weight. A damper also causes the vibratory mode shape to change, and in the extreme a very heavy damper can reduce the relative motion to a point that the airfoil is vibrating alone without any mechanical damping. As a result of the damper and the mode shape change, the resonant frequency will increase, and the change may be quite significant in some cases. An example of a blade and damper along with the nomenclature that will be used in this paper is shown in Figure 1.

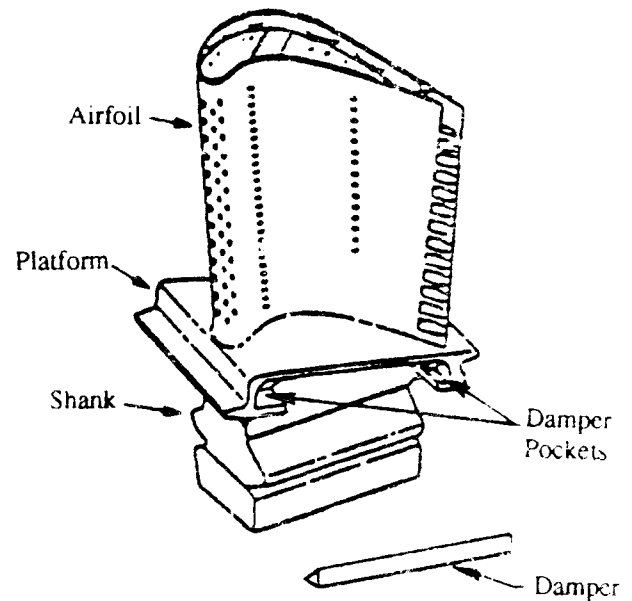


Figure 1. Typical turbine blade with self-centering damper. The damper rides under the platform and contacts adjacent blades.

The methodology to be used follows the references [1] through [5]. The main emphasis of this paper is the extension of these methods to efficiently analyze self-centering blade-to-blade dampers, which are characterized by the relative motion of adjacent blades. Engine rotation causes the centrifugal forces, which load the blades, to be constant, and the design of the dampers is such that they always contact the same adjacent blade, hence the term "self-centering". To begin, the typical blade-to-blade damper is considered to introduce the methodology which will be used.

2 ANALYTICAL MODEL

2.1 BLADE-TO-BLAD DAMPERS. Because of the complexity of the geometry of turbomachinery blades, a direct analytical method such as three-dimensional finite element analysis is required to accurately assess the natural frequencies and their associated mode shapes. Since frequency analysis is nearly always utilized as a part of the blade design process, it is assumed that such a model exists

and the governing equations will be used as a starting point. The equations of motion for the blade are then

$$[m]\{\ddot{u}\} + [c]\{\dot{u}\} + [k]\{u\} = \{P\} - \{F\} \quad (1)$$

where

- u = displacement of each degree of freedom
- m = mass matrix
- c = viscous damping matrix (assumed proportional)
- k = stiffness matrix
- P = driving force
- F = friction force.

For typical turbine blade models, (1) represents a very large set of equations, which are all coupled through the mass, stiffness, and damping matrices. While P will be specified, the F are nonlinear functions, so the equations cannot be solved directly. One approach to dealing with this set of equations is to turn to a modal method, where it is assumed that the natural frequencies and mode shapes have been previously determined by solving the eigenvalue problem,

$$[m]\{\ddot{u}\} + [k]\{u\} = \{0\} . \quad (2)$$

An important mathematical property of the mode shapes is that they form an orthogonal set, which is relevant because the mode shapes can then be used as coordinates to describe the motion. The physical displacements can be represented as a superposition of the mode shapes,

$$\{u\} = [\Phi]\{q\} \quad (3)$$

where

- Φ = matrix of mode shapes, ϕ_i
- q = modal amplitudes.

Note that the physical displacements are a function of position and time, while the mode shapes are a function of position only and the modal amplitudes are a function of time only. This can be substituted into (1), and after pre-multiplying by the transpose of $[\Phi]$,

$$M_i[\ddot{q}_i + 2\zeta_i\omega_i\dot{q}_i + \omega_i^2q_i] = Pp_i - Fa_i \quad (4)$$

where

- M_i = modal mass of i^{th} mode
- ω_i = natural frequency
- ζ_i = viscous damping
- p_i = mode shape component at the location of the excitation force for the i^{th} mode
- a_i = mode shape component at the location of the friction damper for the i^{th} mode.

The mass, stiffness, and damping matrices have been diagonalized due to the orthogonality of the modes, meaning the left-hand sides of (4) are completely de-coupled. Any physical quantity can be described in terms of the modal amplitudes by using (3), and in particular, the physical displacement at the damper contact is given by

$$\xi = \sum_{i=1}^n a_i q_i . \quad (5)$$

The equations of motion will be simplified through the use of the method of harmonic balance. The displacements and forces are assumed to be of the form

$$\begin{aligned} q_i &= q_i^c \cos \Omega t + q_i^s \sin \Omega t \\ P &= P^c \cos \Omega t + P^s \sin \Omega t \\ F &= F^c \cos \Omega t + F^s \sin \Omega t \\ \xi &= \xi^c \cos \Omega t + \xi^s \sin \Omega t \end{aligned} \quad (6)$$

where Ω is the driving frequency. Note that the damper displacement, for example, can also be written in terms of its magnitude and phase,

$$\xi = \bar{\xi} \sin(\Omega t + \psi) . \quad (7)$$

By applying the harmonic balance method to (4), expressions for the modal amplitudes can be determined,

$$\begin{aligned} q_i^c &= \frac{(P^c p_i - F^c a_i)(\omega_i^2 - \Omega^2) - (P^s p_i - F^s a_i)(2\xi_i \omega_i \Omega)}{M_i[(\omega_i^2 - \Omega^2)^2 + (2\xi_i \omega_i \Omega)^2]} \\ q_i^s &= \frac{(P^c p_i - F^c a_i)(2\xi_i \omega_i \Omega) + (P^s p_i - F^s a_i)(\omega_i^2 - \Omega^2)}{M_i[(\omega_i^2 - \Omega^2)^2 + (2\xi_i \omega_i \Omega)^2]} \end{aligned} \quad (8)$$

Substituting these into (5), then using (6) and equating like terms,

$$\begin{aligned} \xi^c &= A1 P^c - A2 F^c - A3 P^s + A4 F^s \\ \xi^s &= A1 P^s - A2 F^s + A3 P^c - A4 F^c \end{aligned} \quad (9)$$

where

$$\begin{aligned} A1 &= \sum_{i=1}^n \frac{p_i a_i (\omega_i^2 - \Omega^2)}{\gamma_i} & A3 &= \sum_{i=1}^n \frac{p_i a_i (2\xi_i \omega_i \Omega)}{\gamma_i} \\ A2 &= \sum_{i=1}^n \frac{a_i a_i (\omega_i^2 - \Omega^2)}{\gamma_i} & A4 &= \sum_{i=1}^n \frac{a_i a_i (2\xi_i \omega_i \Omega)}{\gamma_i} \end{aligned}$$

and

$$\gamma_i = M_i[(\omega_i^2 - \Omega^2)^2 + (2\xi_i \omega_i \Omega)^2] .$$

Following [2], the damper is taken to be a Coulomb friction element and a spring in series, so that slip occurs in the friction element when the spring force reaches a value of μN . Lab measurements have shown this to be a good idealization of the behavior of the damper. The damper displacement and the resulting friction force are defined in Figure 2, and it is noted that the displacement can be written

$$\xi = \bar{\xi} \cos \theta \quad (10)$$

and the start of slip in the half-cycle $0 < \theta < \pi$ can be determined to be

$$\Theta = \cos^{-1} \left(1 - \frac{2\mu N}{k\bar{\xi}} \right) . \quad (11)$$

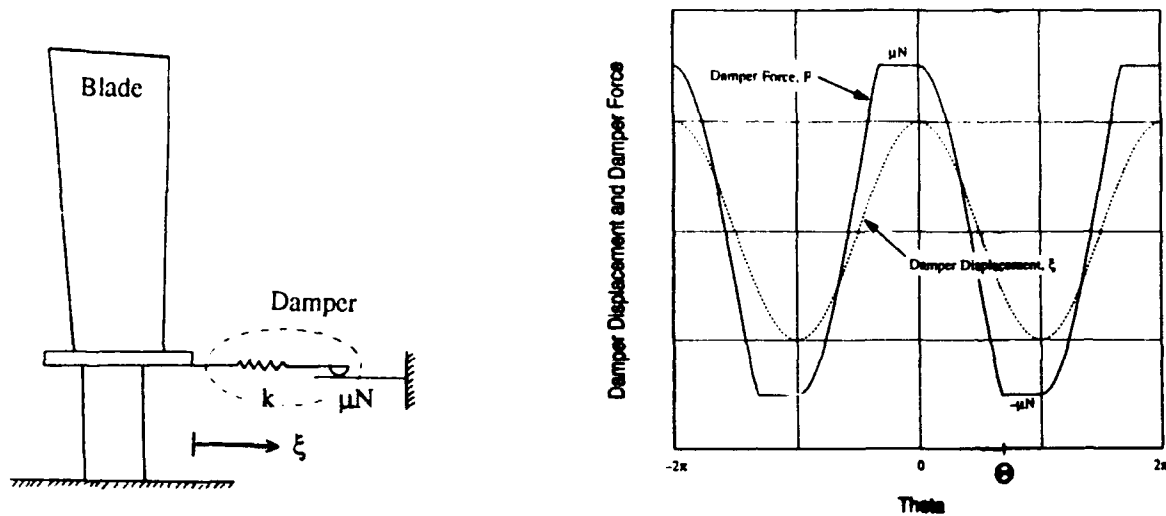


Figure 2. Behavior of friction interface. The friction element, shown schematically with the blade, behaves as a spring until the slip value is attained.

The damper force is expanded in a Fourier series and truncated after the fundamental harmonic terms, resulting in

$$F = G1 \bar{\xi} \cos \theta + G2 \bar{\xi} \sin \theta \quad (12)$$

where

$$G1 = \frac{k}{\pi} \left(\Theta - \frac{1}{2} \sin 2\Theta \right)$$

$$G2 = -\frac{k}{\pi} \sin^2 \Theta .$$

Comparing (6), (7), and (10), this equation becomes

$$F^c = G1 \xi^c - G2 \xi^s \quad (13)$$

$$F^s = G1 \xi^s + G2 \xi^c .$$

This is substituted into (9), which is rearranged to give

$$E1 = -D1 \xi^c + D2 \xi^s \quad (14)$$

$$E2 = D1 \xi^s + D2 \xi^c$$

where

$$D1 = 1 + A2 G1 - A4 G2$$

$$D2 = A2 G2 + A4 G1$$

$$E1 = A1 P^c - A3 P^s$$

$$E2 = A1 P^s + A3 P^c .$$

Equation (14) can be solved to give

$$\bar{\xi} = \sqrt{\frac{E1^2 + E2^2}{D1^2 + D2^2}} \quad (15)$$

$$\tan \psi = \frac{D1 E1 + D2 E2}{D1 E2 - D2 E1}$$

Because $D1$ and $D2$ are transcendental functions of Θ , iteration is required to solve (15). A simple bisection method is utilized because Θ is bounded by $0 < \Theta < \pi$. Once ξ is known, substitution into (13) gives all the forces acting on the blade. The modal amplitudes q_i are then determined using (8), and any physical displacement or stress of interest can then be obtained by following (3).

A common approach to assess the effectiveness of a given damper design is to repeat the solution for a range of driving frequencies, determining the displacement and/or stress at key locations on the blade. By varying the friction or driving forces, a parametric study can be conducted as shown in Figure 3. From this information, which includes the resonant stress, frequency, and log decrement, the optimum damper weight can be determined.

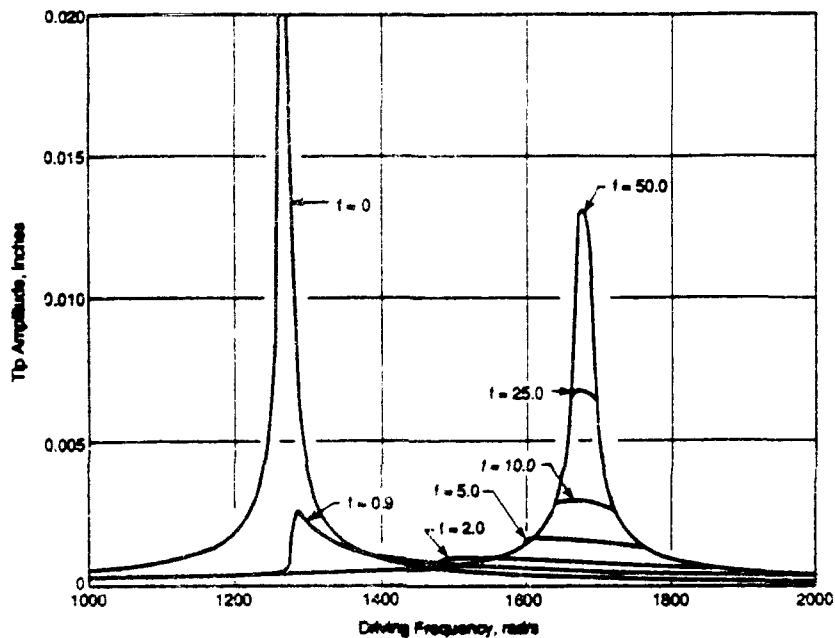


Figure 3. Frequency response for various friction forces. By using a series of driving frequencies, the maximum response for a given friction force can be found.

2.2 BLADE-TO-BLADE DAMPERS. A common design approach for blade dampers is to place the damper between two blades, so that centrifugal forces cause the damper to remain in contact with the platform of each blade as they vibrate. Because of the free-floating nature of the damper, its relative motion along each face of the blade platform must be determined. Simply knowing the absolute motion of the damper is not sufficient. It is assumed that these vibratory motions are small enough so that the scrubbing surfaces move in translation only, that the centrifugal force will cause the damper to move radially outward as far as the platforms allow, and this motion will be continuous sliding. These assumptions are consistent with good damper design practices.

The damper is shown schematically in Figure 4. With the assumptions made for damper motion, the damper position is known once the motions of the two blades have been specified. Motion out of this plane is considered separately because its effect on damping depends on the physical damper restraints, and in addition, this component is usually not a source of reliable damping. If an oblique coordinate system is placed along the contact surfaces as shown, with the origin at the damper apex, determination of the relative motion becomes much easier. The transformation equations to obtain

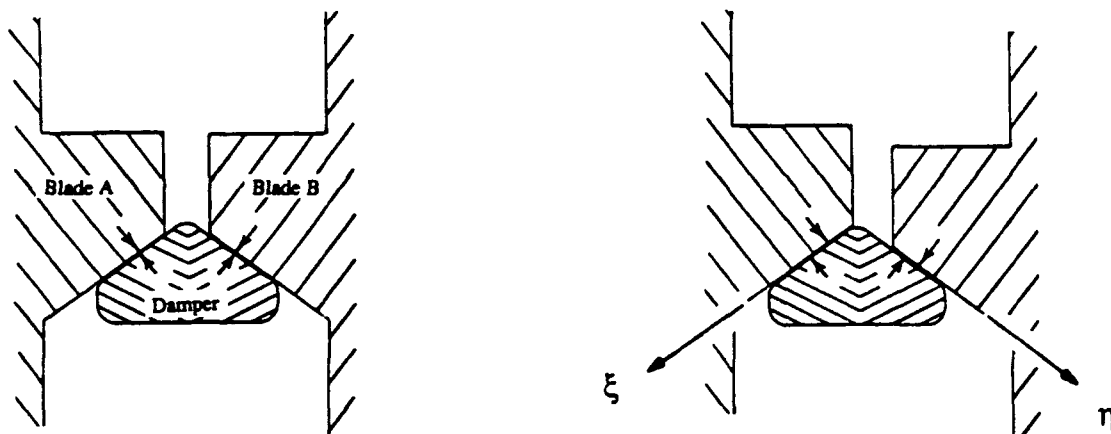


Figure 4. Blade-to-Blade Damper. The motion of the damper is shown schematically. Note that the location of the damper is determined by the location of the contact points on the blades.

the vibratory motions in terms of the oblique coordinates from the usual Cartesian reference frame can be found in [8]. Because rotations of the blade contact surfaces are ignored, the A-blade damper surface will move along lines parallel to ξ , while the B-blade moves parallel to η . The absolute damper motion is seen to correspond to the ξ -motion of B and the η -motion of A, and the relative motion along each face of the damper is given directly by

$$\begin{aligned}\xi &= \xi_{abs}^B - \xi_{abs}^A \\ \eta &= \eta_{abs}^B - \eta_{abs}^A\end{aligned}\quad (16)$$

In this equation, the "abs" subscript indicates absolute components of motion while the lack of a subscript indicates a relative term. For clarity, the discussion will be limited to motion in the ξ direction; similar results would be applicable to the η component. Replacing the blade displacement in (16) with the modal components,

$$\xi = \sum_{i=1}^n a_i q_i^A - \sum_{i=1}^n b_i q_i^B \quad (17)$$

where

a_i = mode shape in the ξ direction for the i^{th} mode at the damper contact of blade A

q_i^A = modal amplitude of blade A

b_i = mode shape in the ξ direction for the i^{th} mode at the damper contact of blade B

q_i^B = modal amplitude of blade B.

Now assume that blades A and B have identical responses with the exception of an interblade phase angle, Φ . Again assuming harmonic motion, the modal amplitude can be written

$$\begin{aligned}q_i^A &= q_i^c \cos \Omega t + q_i^s \sin \Omega t \\ q_i^B &= q_i^c \cos(\Omega t + \Phi) + q_i^s \sin(\Omega t + \Phi)\end{aligned}\quad (18)$$

where the cosine and sine terms on the right-hand side of both equations refer to blade A.

Expanding and substituting into (17),

$$\xi^c = \sum_{i=1}^n (a_i - b_i \cos \Phi) q_i^c - \sum_{i=1}^n (b_i \sin \Phi) q_i^s \quad (19)$$

$$\xi^s = \sum_{i=1}^n (a_i - b_i \cos \Phi) q_i^s + \sum_{i=1}^n (b_i \sin \Phi) q_i^c .$$

The relations given by (8) still apply, and substituting into (19) leads to

$$\begin{aligned} \xi^c &= C1 P^c - C2 F^c - C3 P^s + C4 F^s \\ \xi^s &= C1 P^s - C2 F^s + C3 P^c - C4 F^c \end{aligned} \quad (20)$$

where

$$C1 = A1 - B1 \cos \Phi - B3 \sin \Phi$$

$$C2 = A2 - B2 \cos \Phi - B4 \sin \Phi$$

$$C3 = A3 - B3 \cos \Phi + B1 \sin \Phi$$

$$C4 = A4 - B4 \cos \Phi + B2 \sin \Phi$$

and

$$B1 = \sum_{i=1}^n \frac{p_i b_i (\omega_i^2 - \Omega^2)}{\gamma_i}$$

$$B3 = \sum_{i=1}^n \frac{p_i b_i (2\zeta_i \omega_i \Omega)}{\gamma_i}$$

$$B2 = \sum_{i=1}^n \frac{a_i b_i (\omega_i^2 - \Omega^2)}{\gamma_i}$$

$$B4 = \sum_{i=1}^n \frac{a_i b_i (2\zeta_i \omega_i \Omega)}{\gamma_i} .$$

The forces contributed by the damper are still given by (12), where it is understood that ξ is the motion of the blade relative to the damper at the contact point. Then (20) is identical in form to (9), the only difference in the equations being in the C -coefficients. In fact, (9) can be obtained by taking the b_i to be zero. The solution can then proceed in a manner identical to the blade-to-ground damper, iterating on (15) to find the relative displacement.

2.3 MULTIPLE DAMPERS. The analysis is now extended to the case of multiple damper locations with multiple excitation forces. Because the blade-to-blade analysis will easily degenerate to the blade-to-ground case, only these results are derived here. Also, because the approach taken is identical to that for a single damper, detail will be kept to a minimum.

The equations of motion are generalized to

$$M_i [\ddot{q}_i + 2\zeta_i \omega_i \dot{q}_i + \omega_i^2 q_i] = \sum_l P_l p_{li} - \sum_j F_j a_{ji} \quad (21)$$

where

P_l = excitation force at l^{th} location

p_{li} = mode shape component at the l^{th} location for the i^{th} mode

F_j = friction force at the j^{th} damper location

a_{ji} = mode shape component at the j^{th} damper for the i^{th} mode for blade A.

The relative motion at the j^{th} damper, obtained by starting with (17), assuming harmonic motion,

and substituting for the q_i , is given by

$$\begin{aligned}\xi_j^c &= \sum_I C1_{jI} P_I^c - \sum_J C2_{jJ} F_J^c - \sum_I C3_{jI} P_I^s + \sum_J C4_{jJ} F_J^s \\ \xi_j^s &= \sum_I C1_{jI} P_I^s - \sum_J C2_{jJ} F_J^s + \sum_I C3_{jI} P_I^c - \sum_J C4_{jJ} F_J^c\end{aligned}\quad (22)$$

where

$$\begin{aligned}C1_{jI} &= A1_{jI} - B1_{jI} \cos \Phi - B3_{jI} \sin \Phi \\ C2_{jJ} &= A2_{jJ} - B2_{jJ} \cos \Phi - B4_{jJ} \sin \Phi \\ C3_{jI} &= A3_{jI} - B3_{jI} \cos \Phi + B1_{jI} \sin \Phi \\ C4_{jJ} &= A4_{jJ} - B4_{jJ} \cos \Phi + B2_{jJ} \sin \Phi\end{aligned}$$

and

$$\begin{aligned}A1_{jI} &= \sum_{i=1}^n \frac{a_{ji} p_{li} (\omega_i^2 - \Omega^2)}{\gamma_i} & B1_{jI} &= \sum_{i=1}^n \frac{b_{ji} p_{li} (\omega_i^2 - \Omega^2)}{\gamma_i} \\ A2_{jJ} &= \sum_{i=1}^n \frac{a_{ji} a_{Ji} (\omega_i^2 - \Omega^2)}{\gamma_i} & B2_{jJ} &= \sum_{i=1}^n \frac{b_{ji} a_{Ji} (\omega_i^2 - \Omega^2)}{\gamma_i} \\ A3_{jI} &= \sum_{i=1}^n \frac{a_{ji} p_{li} (2\xi_i \omega_i \Omega)}{\gamma_i} & B3_{jI} &= \sum_{i=1}^n \frac{b_{ji} p_{li} (2\xi_i \omega_i \Omega)}{\gamma_i} \\ A4_{jJ} &= \sum_{i=1}^n \frac{a_{ji} a_{Ji} (2\xi_i \omega_i \Omega)}{\gamma_i} & B4_{jJ} &= \sum_{i=1}^n \frac{b_{ji} a_{Ji} (2\xi_i \omega_i \Omega)}{\gamma_i}\end{aligned}$$

Because the force at each damper is only a function of the relative motion at that location, (12) still applies for each damper, and (22) becomes

$$\begin{aligned}E1_j &= \sum_J D1_{jJ} \xi_j^c - \sum_J D2_{jJ} \xi_j^s \\ E2_j &= \sum_J D1_{jJ} \xi_j^s + \sum_J D2_{jJ} \xi_j^c\end{aligned}\quad (23)$$

where

$$\begin{aligned}D1_{jI} &= \delta_{jI} + \sum_J C2_{jJ} G1_J - \sum_J C4_{jJ} G2_J & E1_j &= \sum_I (C1_{jI} P_I^c - C3_{jI} P_I^s) \\ D2_{jJ} &= \sum_J C2_{jJ} G2_J + \sum_J C4_{jJ} G1_J & E2_j &= \sum_I (C1_{jI} P_I^s + C3_{jI} P_I^c)\end{aligned}$$

where δ_{jI} is defined to be the Kronecker delta. The displacements at the various dampers are coupled through the D -matrices so the result is a set of coupled, nonlinear algebraic equations, with one equation for each damper location and direction. The solution method employed for a single damper can no longer be used and is replaced by a method based on Newton-Raphson iteration. This algorithm, though, cannot guarantee convergence, and in practice assumptions are made to reduce the system to a single equivalent damper whenever possible.

3 EXPERIMENTAL VERIFICATION OF ANALYTICAL METHOD

Verification of the preceding analytical methods by laboratory experiments was deliberately planned to take place in several stages, beginning with a simple beam model and eventually leading to actual turbine blade geometry. This paper shows analytical comparisons with experimental re-

sults for simple beam models of various geometries. Specimens were constructed with a simulated airfoil, platform, and shank region as shown in Figure 5. A number of different specimen geometries were tested and the effects of the most significant variable, shank thickness, are illustrated for blade-to-ground, blade-to-blade, and multiple damper test configurations.

3.1 BLADE-TO-GROUND DAMPER. The first specimens were tested with a blade-to-ground arrangement as shown in Figure 5. This arrangement allowed the normal load on the damping surface to be varied and the resulting dynamic friction force to be measured. Excitation was provided by a shaker table. Strain gages were placed on the specimens to monitor the vibration as a result of the action of the bar damper.

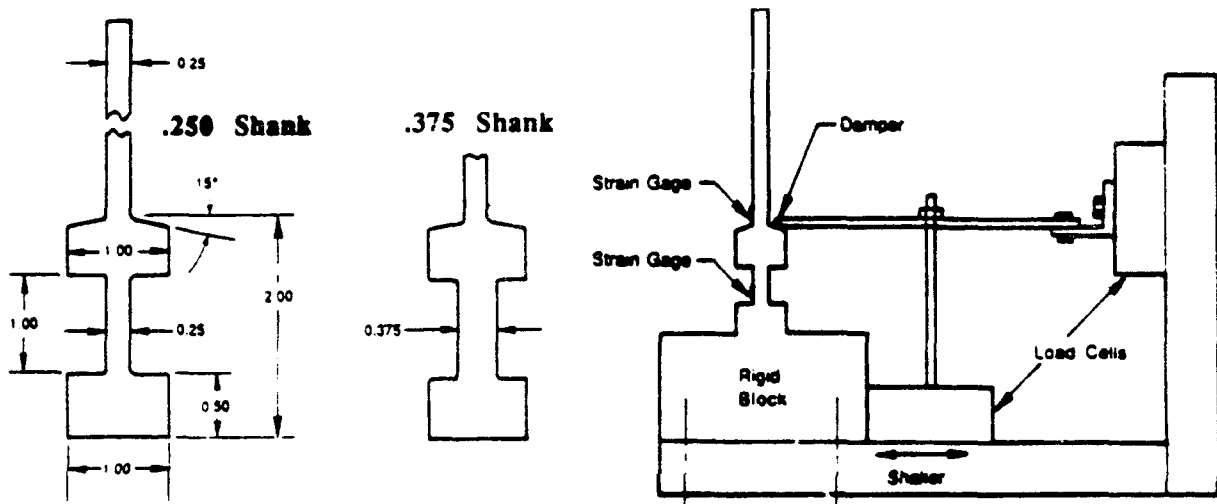


Figure 5. Simple Beam Model and Associated Test Apparatus.

The vibratory response of the simple beam model in terms of airfoil root stress versus damper load is shown in Figure 6. The effect on the first flexural (primary) frequency with increasing damper load is also shown. Each set of data for the two different shank thicknesses shows very good correlation to the analytical method.

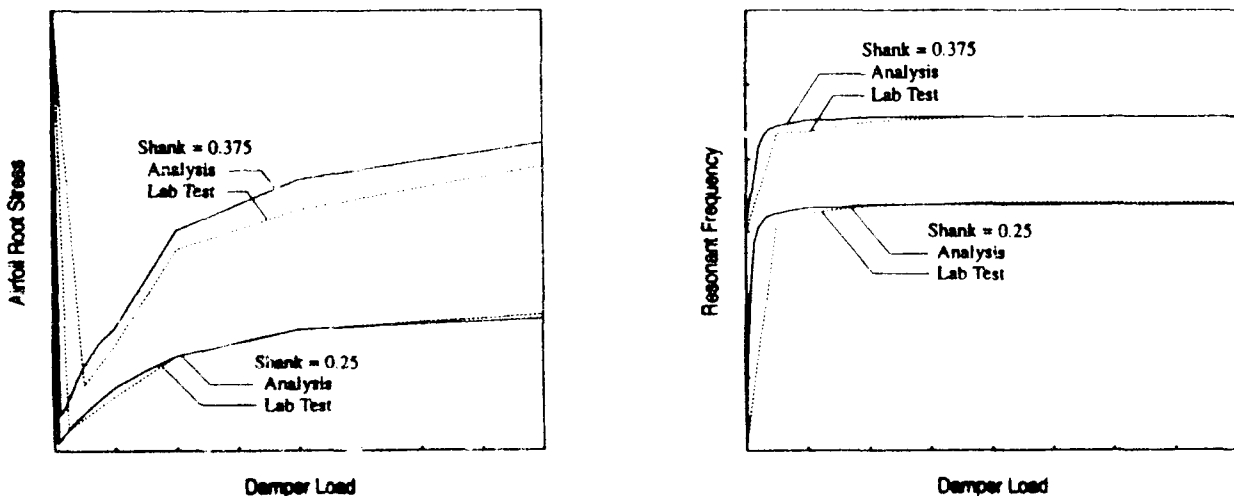


Figure 6. Comparison of Analytical Method with Test Data for Blade-to-Ground Damper.

3.2 BLADE-TO-BLADE DAMPER. Testing of a blade-to-blade configuration was conducted using the apparatus shown in Figure 7. Two identical simple beam models were clamped in a fixture with a damper supported between adjacent platforms and loaded by means of a wire attached to a pulley. The damper load was varied over a wide range by applying varying tensile loads in the wire. Excitation was provided by means of a pulsing air jet (siren), exciting the specimens in the first flexural mode of vibration. The level of excitation was controlled by the air jet supply pressure, and the frequency was controlled by the speed of the air jet rotor.

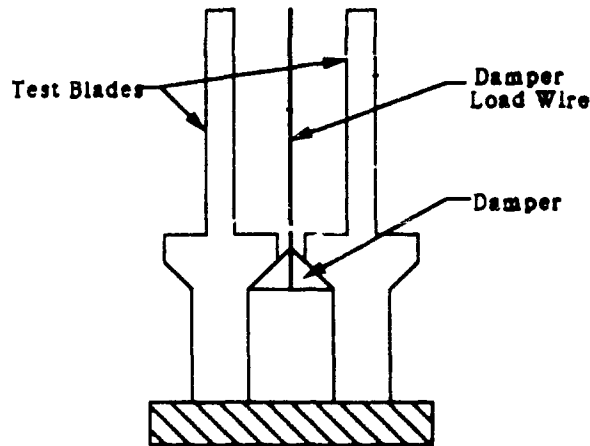


Figure 7. Blade-to-Blade Damper Test Apparatus.

Vibratory stresses were measured at the airfoil root, the top of the blade shank, and at the bottom of the blade shank. Two different levels of excitation were used, and results were obtained for in-phase and out-of-phase blade motions.

Results for the in-phase and out-of-phase damper tests are shown in Figures 8 and 9, respectively. The averages of several experimental data sets are shown and compared with analytical predictions. Airfoil root stress at the two levels of excitation and resonant frequency predictions at the lower level are given.

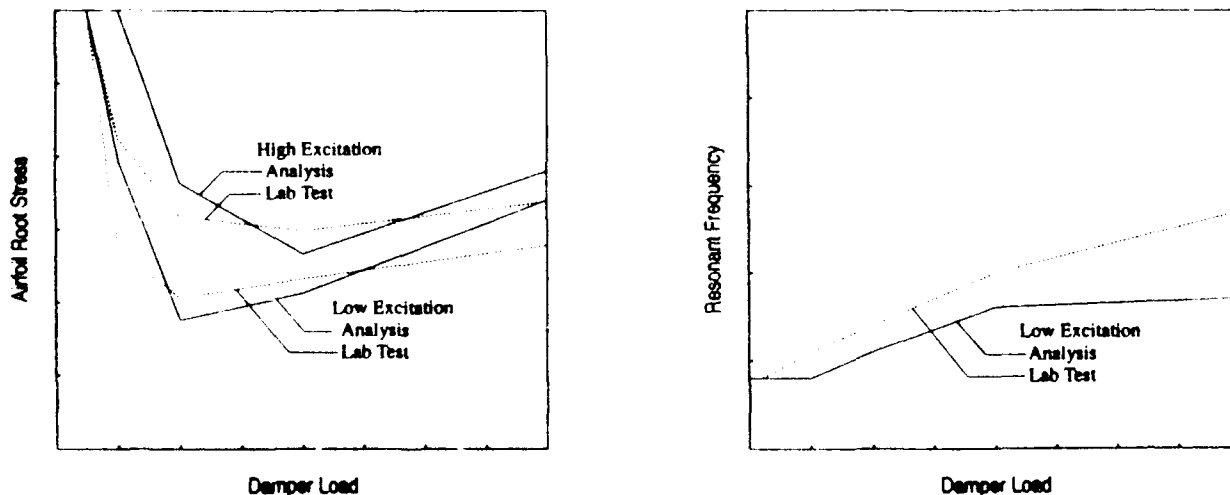


Figure 8. Blade-to-Blade Damping Results: In-Phase Vibration.

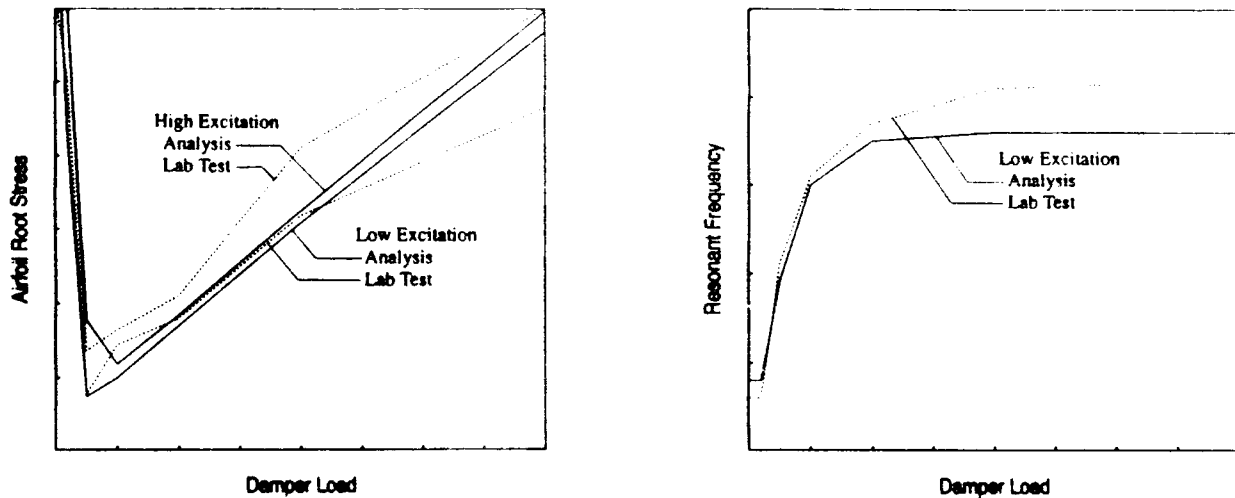


Figure 9. Blade-to-Blade Damping Results: Out-of-Phase Vibration.

The analytical predictions for both levels of excitation show good agreement with the experimental data for in-phase and out-of-phase vibration. Prediction of frequency change as a result of increasing damper load also shows good agreement.

3.3 TYPICAL DAMPER EFFECTIVENESS TEST. The final stage of experimental testing was designed to duplicate a typical set-up used in the laboratory to conduct damper effectiveness testing on actual engine hardware. The testing on model blades was conducted using a damper positioned either side of a test blade with the dampers retained by two additional blades with airfoils removed, as shown in Figure 10. The test blade was excited by means of the air siren, but the "dummy" blades do not vibrate because of the removal of their airfoil. Again several variables were examined, and the tests were repeated to obtain an average for each setting.

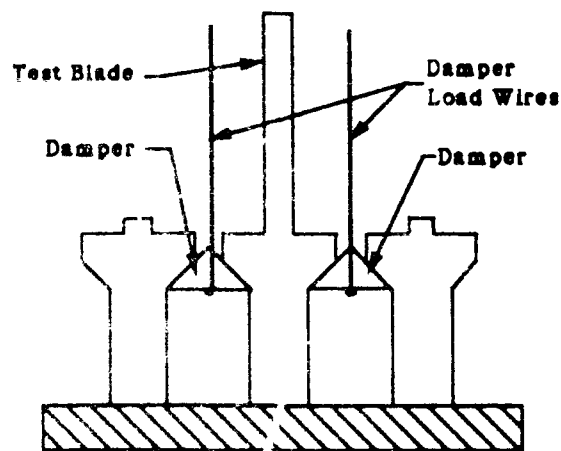


Figure 10. Experimental Set-up for Typical Damper Effectiveness Test.

Figure 11 shows the airfoil root stress and resonant frequency change plotted against damper load for three shank thicknesses compared to analytical results. There is good agreement between the

analytical results and the experimental data. This again supports the use of this analytical technique to predict the optimum damper weight to ensure maximum damper effectiveness.

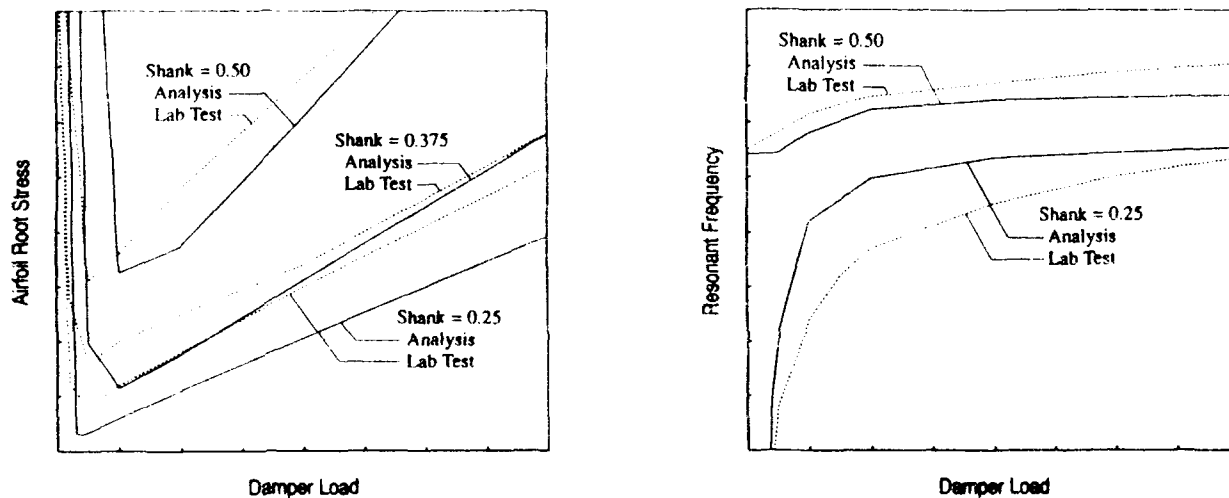


Figure 11. Comparison of Analytical Method with Test Data for Damper Effectiveness Test.

4 DISCUSSION OF RESULTS

A full range of experimental testing has been carried out examining variables such as damper-to-platform contact angle, platform width, and shank thickness. Various excitation levels were used, and results were plotted for an average of each data set. It was decided to present the results for the variation in shank thickness because these illustrated the most pronounced effect on blade damping, and it has been demonstrated within this paper that the analytical method was able to predict the results for this variable accurately. Predictions for other variables were also good although not shown here for brevity. It should be noted that, while comparison of the analytical method with experimental results has been presented for only the primary bending mode, the method is capable of predicting the damper effectiveness for any mode of interest.

The analytical method is able to determine the "optimum" damper weight by predicting the actual decrease and increase in vibratory response as the damper load is increased. The optimum theoretical weight of the damper is that weight which, when converted into an equivalent load at engine speed, produces the minimum vibratory response.

A damper can increase the frequency of the blade by significantly high percentages. For first flexural modes this can be as large as 25% for a cooled turbine blade. It is, therefore, important to be able to predict this increase accurately as it has a pronounced significance when considering resonances with stimuli that could produce detrimental responses of the blades. The analysis has demonstrated its ability to predict this frequency increase accurately for the test cases presented and offers a means of correcting for damping effects when assessing resonances in engines.

The analysis was able to predict the point at which the damper load becomes so high that it prevents motion in the shank and causes the airfoil to vibrate in an undamped mode. This condition is potentially dangerous for the airfoil because of the high vibratory stresses involved.

5 CONCLUSIONS

- A new analytical method has been developed which enables a blade designer to pre-determine the effectiveness of a damper design prior to manufacture and bench test.
- The method is able to predict the optimum damper load for maximum effectiveness and the point at which the damper is so heavy that it effectively "locks-up" the airfoil at the platforms so that it is virtually undamped.
- Comparisons made between the analytical method and experimental data generated by using simple beam models confirms the accuracy of the tool for design use.
- Future work will be centered around developing this analytical method for use with actual cooled turbine blade geometry and applying it to a rotating system of blades to predict damped responses compared to engine blade strain gage data.

6 ACKNOWLEDGEMENTS

The authors wish to acknowledge the contributions of R.O. Brooks and V.C. Gallardo towards the development of this damping methodology. Appreciation is also expressed to A. Rotsko, J. Miller, L. Joyce, and W. Day for the experimental work and to others at GEAE who have supported this effort.

REFERENCES

1. Dowell, E.H., "The Behavior of a Linear Damped Modal System with a Non-linear Spring-Mass-Dry Friction Damper System Attached," *Journal of Sound and Vibration*, Vol. 89, 1983, pp. 65-84.
2. Griffin, J.H., "Friction Damping of Resonant Stresses in Gas Turbine Engine Airfoils," *ASME Journal of Engineering for Power*, Vol. 102, Apr. 1980, pp. 329-333.
3. Menq, C.-H., and Griffin, J.H., "A Comparison of Transient and Steady State Finite Element Analyses of the Forced Response of a Frictionally Damped Beam," *ASME Journal of Vibration, Acoustics, Stress, and Reliability in Design*, Vol. 107, Jan. 1985, pp. 19-25.
4. Cameron, T.M., Griffin, J.H., Kielb, R., and Hoosac, T.M., "An Integrated Approach for Friction Damper Design," *ASME Bound Volume DE-5*, Sept. 1987, pp. 205-212.
5. Tongue, B.H., and Dowell, E.H., "Component Mode Analysis of Nonlinear, Nonconservative Systems," *ASME Journal of Applied Mechanics*, Vol. 50, Mar. 1983, pp. 204-205.
6. den Hartog, J.P., "Forced Vibrations with Combined Coulomb and Viscous Friction," *Trans ASME*, Paper APM-53-9, 1931, pp.107-115.
7. Goodman, L.E. and Klumpp, J.H., "Analysis of Slip Damping With Reference to Turbine Blade Vibration," *ASME Journal of Applied Mechanics*, Sept. 1956, pp. 421-429.
8. Arfken, G., *Mathematical Methods for Physicists*, 2nd ed., Academic Press, New York, 1970.

MICRO SLIP DAMPING MECHANISM IN BOLTED JOINTS

M. Groper¹
Western Michigan University
Kalamazoo, MI

ABSTRACT

In bolted structural connections the dissipation of energy/damping depends on the magnitudes of the frictional force and of the relative slide between the joined parts. However, in a joint with a large number of bolts, the magnitude of the relative slide (slip) cannot be large as the bolt hole is not much larger than the bolt diameter and, thus, some bolts may be sheared at the onset of slip. As the clamping pressure decreases with the distance away from the bolt the magnitude of slip will be larger in regions more distanced from the bolt hole. If the applied tangential load is not large enough to establish slip in an adjoining annulus to the bolt's hole there will be some slip in more remote regions of the contact surface due to the elastic deformation of the joined parts, but the joint will not fully slip. As the tangential load is increased the joint might slip completely.

As the stage of loading before gross slips occurs in the joint was less studied, the paper presents an analysis of the mechanism of frictional damping for the partial slip stage of loading. The factors which influence partial slip friction, and the distributions of the clamping pressure, coefficient of friction and slip with the distance away from the bolt are considered in a model of energy dissipation. The proposed model is then compared with the experimentally obtained hysteresis loops.

**FULL PAPER NOT AVAILABLE FOR
PUBLICATION**

¹Professor, Department of Mechanical Engineering, Western Michigan University, Kalamazoo, MI 49008, (616) 387-3380

ON A THEORY OF COMPLEX DAMPING

Z. Liang, G. C. Lee, and M. Tong

412 Bonner Hall
State University of New York at Buffalo
Amherst, NY 14260
Tel. (716) 636-2771

ABSTRACT

In non-proportionally damped structures, both energy dissipation and energy transformation exist. To characterize such aspects, in this paper, a new concept of complex damping ratio is introduced by means of generalizing the concept of Rayleigh quotient. The real part of this new quantity is the traditionally defined damping ratio, which reflects the modal energy dissipation per cycle; whereas, the imaginary part describes a ratio of energy transformation of a virtual mode per cycle. With this new concept, modal equations are set up and other relevant theoretical results are developed. Such a theory of complex damping is not only an alternative way to describe the phenomena of complex modes, but also a useful tool, with strong physical meaning, for solving many theoretical and engineering problems of non-proportionally damped systems.

1 INTRODUCTION

In recent years considerable progress has been made in the field of mechanical vibrations and structural dynamics. However, many important questions remain to be answered in particular concerning non-proportionally damped systems. For example, using proportional damping to describe real structures may result in severe errors (see Sigh 1986). Under what conditions do we have to change our models, Where do these errors come from and how can we minimize these errors? These questions are often asked in considering whether the structure responses should be calculated or estimated in the design of dampers; in the measurement of the damping matrix to evaluate the capability of energy dissipation of structures and in the construction of a valid damping matrix in finite element modeling. In the area of modal testing, we also face similar questions when we deal with damping ratios and with the measurement of damping matrix (see Liang and Lee 1991). Most of these unanswered questions are due to the lack of knowledge on energy relationship in non-proportionally damped structures. They may be systemically answered by using a theory of complex damping introduced in this paper. This theory unifies energy dissipation and energy transformation by means of one complex quantity. The real part of this complex quantity is the traditional damping ratio, describing the ratio of energy dissipation in a period; The imaginary part is the ratio of energy transmission in the same period.

One important advantage of using complex damping theory is as follows: When a structure is in vibration, the energy dissipation and transmission often bring the same results to a local region. Therefore, they are difficult to be distinguished. Traditionally, these energy terms are thought to be undecoupleable for a general damped system in N-dimensional space. We can now introduce a complex valued quantity, the complex damping ratio, to study each specific mode of the system. In so doing, we also may realize the physical meanings of the quantities.

2 CONCEPT OF COMPLEX DAMPING RATIOS, MATHEMATICAL TREATMENT

2.1 INTRODUCTION OF COMPLEX DAMPING COEFFICIENT

In this section we will introduce the quantity of complex damping coefficient. The equation of motion for a general MDOF system can be written as

$$\mathbf{M} \mathbf{X}''(t) + \mathbf{C} \mathbf{X}'(t) + \mathbf{K} \mathbf{X}(t) = \mathbf{F}(t)$$

without loss of generality, consider the monic homogeneous form:

$$\mathbf{I} \mathbf{X}''(t) + \tilde{\mathbf{C}} \mathbf{X}'(t) + \tilde{\mathbf{K}} \mathbf{X}(t) = 0$$

with order n .

The above equation has eigenvalue matrix

$$\Lambda = \text{diag}(\lambda_1) = \text{diag}(-\xi_1 \omega_1 + j \sqrt{1-\xi_1^2} \omega_1)$$

and eigenvector matrix \mathbf{P}_1 . Then we have

$$\mathbf{P}_1 \Lambda^2 + \tilde{\mathbf{C}} \mathbf{P}_1 \Lambda + \tilde{\mathbf{K}} \mathbf{P}_1 = 0 \quad (1)$$

$$\tilde{\mathbf{K}} = \mathbf{Q} \Lambda_k \mathbf{Q}^T \quad (2)$$

$$\Lambda_k = \text{diag}(\omega_{ni}^2) \quad (3)$$

Pre-multiplying \mathbf{Q}^T of equation (1) results in

$$\mathbf{R} \Lambda^2 + \mathbf{Q}^T \tilde{\mathbf{C}} \mathbf{P}_1 \Lambda + \Lambda_k \mathbf{R} = 0$$

where

$$\mathbf{R} = \mathbf{Q}^T \mathbf{P}_1 = \begin{bmatrix} r_{11} & r_{12} & \dots & r_{1n} \\ r_{21} & r_{22} & \dots & r_{2n} \\ \vdots & \vdots & \vdots & \vdots \\ r_{n1} & r_{n2} & & r_{nn} \end{bmatrix}$$

So, using the notations (1) and (2), we

can have the following expression of equations for the ii^{th} entries, that is,

$$\lambda_1^2 r_{11} + \mathbf{Q}_1^T \tilde{\mathbf{C}} \mathbf{P}_{11} \lambda_1 + \omega_{ni}^2 r_{11} = 0 \quad (4)$$

where \mathbf{Q}_1 and \mathbf{P}_1 are the i^{th} column of matrices \mathbf{Q} and \mathbf{P}_1 respectively.

Note that,

$$r_{11} = \mathbf{Q}_1^T \mathbf{P}_{11}$$

If the system is proportionally damped, r_{11} must not be zero. We can also show that at least two of the terms r_{1j} , $i = 1, \dots, n$, are not equal to zero for at least one \mathbf{P}_j in the case of non-proportionally damped system.

With

$$\omega_{ni}^2 \mathbf{Q}_1 = \tilde{\mathbf{K}} \mathbf{Q}_1 \quad \text{or} \quad \mathbf{Q}_1^T = \frac{1}{\omega_{ni}^2} \mathbf{Q}_1^T \tilde{\mathbf{K}}$$

we have

$$r_{11} = \frac{1}{\omega_{n1}^2} Q_1^T \tilde{K} P_{11} \quad (5)$$

Suppose $r_{11} \neq 0$. Letting equation (4) be divided by r_{11} yields

$$\lambda_1^2 + d_1 \lambda_1 + \omega_{n1}^2 = 0 \quad (6)$$

Define the term

$$(Q_1^T \tilde{C} P_{11}) / Q_1^T P_{11} = \mathfrak{R}_{11} \quad (7)$$

to be a *generalized Rayleigh quotient*.

Since P_{11} is generally a complex vector, so is the generalized Rayleigh quotient $\omega_{n1}^2 (Q_1^T \tilde{C} P_{11}) / (Q_1^T \tilde{K} P_{11})$. We therefore use a complex number $d_1 = a_1 + j b_1$ to describe this quantity,

$$d_1 = a_1 + j b_1 = \omega_{n1}^2 (Q_1^T \tilde{C} P_{11}) / (Q_1^T \tilde{K} P_{11}) \quad (8)$$

For convenience, equation (7) and its corresponding differential equation

$$u_1'' + (a_1 + j b_1) u_1' + u_1 = 0 \quad (9)$$

is called the characteristic equation and differential equation of the i^{th} *virtual mode*.

Now consider the physical meaning of Pre-multiplying Q^T of equation (b). We may call the term $P_1 \Lambda^2$, $\tilde{C} P_1 \Lambda$ and $\tilde{K} P_1$ the inertial force, damping force and spring force respectively. (see Clough, 1985). Therefore $Q^T P_1 \Lambda^2$, $Q^T \tilde{C} P_1 \Lambda$ and $Q^T \tilde{K} P_1$ are the virtual work done along the virtual displacement Q . Under this consideration, the quantity d_1 is a kind of ratio of damping virtual work ($Q_1^T \tilde{C} P_{11}$) and inertial virtual work ($Q_1^T P_{11}$) or spring virtual work ($Q_1^T \tilde{K} P_{11}$). In a later section, we will see that, the quantity d can play an important role the vibration analyses, we therefore name d_1 to be the i^{th} *complex damping coefficient*.

2.2 SOME CHARACTERISTICS OF COMPLEX DAMPING

Substituting notations of λ_1 and λ_1^2 into equation (7) and rearranging the results in two equations, for the real part, we have:

$$(\zeta_1^2 - 1) \omega_1^2 + \omega_{n1}^2 = \xi_1 \omega_1 a_1 + \sqrt{1 - \xi_1^2} \omega_1 b_1 \quad (10a)$$

and for the imaginary part, we have:

$$-2 \xi_1 \sqrt{1 - \xi_1^2} \omega_1^2 = -\sqrt{1 - \xi_1^2} \omega_1 a_1 + \xi_1 \omega_1 b_1 \quad (10b)$$

Combining the above two equations yields

$$a_1 = \frac{\xi_1}{\omega_1} (\omega_{n1}^2 + \omega_1^2) \quad (11a)$$

$$b_1 = \frac{\sqrt{1 - \xi_1^2}}{\omega_1} (\omega_{n1}^2 - \omega_1^2) \quad (11b)$$

From equation (11a), it is easy to see that, a_1 is always greater than zero if ξ_1 is non-zero. However, b_1 appears to be undefined. We will show that, for a given M-C-K system, the sign of b_1 is uniquely determined

Taking the complex conjugate of equation (9), we have

$$d_i^* = a_i - jb_i = \omega_{n1}^2 (Q_1^T \tilde{C} P_{11}^e) / (Q_1^T \tilde{K} P_{11}^*) \quad (12)$$

Therefore, the sign of b_1 is completely determined by the i^{th} eigenvector P_{11} . In other words, only one of the i^{th} complex conjugate pair of the i^{th} eigenvectors can give the correct value of b_1 . We thus define this eigenvector as the i^{th} principal eigenvector of the M-C-K system, and define the corresponding eigenvalue the i^{th} principal eigenvalue of the M-C-K system. We also define the eigen-matrix which consists of all n principal eigenvectors and eigenvalues the *principal eigen-matrix*.

2.3 CRITERIA FOR PROPORTIONAL DAMPING, FIRST APPLICATION OF THE COMPLEX DAMPING THEORY

It is easy to show that b_1 can be used as an index to calculate the difference between the undamped natural frequency of the system, ω_1 , and that of corresponding non-proportionally damped system, ω_{n1} . In fact, we have the following theorem:

Theorem 1: The following facts are equivalent:

1) The system has proportional damping, that is,

$$C M^{-1} K = K M^{-1} C \quad \text{or} \quad \tilde{C} \tilde{K} = \tilde{K} \tilde{C}$$

2) The eigen-matrix has following properties:

$$\text{Re}(\mathbf{A}) \text{Im}(\mathbf{A}) = \text{Im}(\mathbf{A}) \text{Re}(\mathbf{A})$$

$$\mathbf{A} \text{Re}(\mathbf{A}) = \text{Re}(\mathbf{A}) \mathbf{A}$$

3) The system has only normal mode, (all eigenvectors of system are weakly complex) that is, $P = Q \mathbf{A}$.

- 4) The undamped natural frequencies of the system and the corresponding eigenvalues of the generalized stiffness \tilde{K} are all equal. Namely, $\omega_i = \omega_{ni}$, $i = 1, \dots, n$
- 5) All the imaginary parts of the generalized Rayleigh quotient κ_{ij} are zero. That is, $b_i = 0$, $i = 1, \dots, n$

Since statements 1) and 2) 3) are well established, (see the paper "A Strong Criterion For Testing Proportionally Damped Systems", Theorem 6 and Corollary 6) we will only prove 4) and 5).

PROOF:

If a system has no complex mode, then b_i 's must be zero. This is an obvious sufficient condition. From the condition, all the P_{ii} 's must be all non-complex valued, that is,

$$Q_i = P_{ii}, \quad i = 1, \dots, N$$

Then it is easy to see, from equation (9), d_i is a real scalar, or, $b_i = 0$; Also, from the argument $Q_i = P_i$ we know that other generalized Rayleigh Quotient κ_{ij} 's, $j \neq i$, are zero.

Next, consider the the necessary condition. It is clear from equation (10b), that this condition is equivalent to the following:

$$\omega_i = \omega_{ni}, \quad i = 1, \dots, n \quad (12)$$

Or, in this case, we have

$$\Lambda \Lambda^* = Q^T \tilde{K} Q = \Lambda_k \quad (13)$$

We know that, (see the paper "A Strong Criterion of Proportionally Damped Systems" by the same authors) for an M-C-K system, if equation (12) holds, it has real-valued eigenvector matrix. Therefore, we know the necessary condition is also true here. ■

Theorem 1 is important. It provides two new criteria to judge whether a system is proportionally damped. Namely, if all the imaginary part of $\kappa_{ij} = 0$ or if $\omega_{ni} = \omega_i$, $i = 1, \dots, n$. In addition it confirms the sufficient and necessary relationship between the complex damping coefficient and the damping property of the system. Also, from the equation (10b), we have a simple but import corollary.

Corollary 1: For a damped system, if its i^{th} complex damping coefficient is real, its i^{th} undamped natural frequency is equal to that of

corresponding proportionally damped system.

2.4 INVARIANTS OF SYSTEMS

A general damping matrix can always be written as

$$C = C_p + C_n \quad (14)$$

where C_p contains all the exact damping ratios of the system, ξ_1 's, by means of the relationship

$$\xi_1 = \frac{d_{11}}{2|\lambda_1|} = \frac{d_{11}}{2\omega_1} \quad (15)$$

where d_{11} is the ii^{th} entry of matrix $Q^T C_p Q$, which is a real number.

Now, consider the i^{th} eigenvalue of the system with damping C , denoted by $\lambda_1(C)$, and that of the system with damping C_p , denoted by $\lambda_1(C_p)$, both systems have the same generalized stiffness matrices \tilde{K} . For convenience, the second system is called the *corresponding proportionally damped system* or simply the *corresponding system*, of the first system,; and denote the first system by $H(C)$ and the corresponding system by $H(C_p)$. If $b_1 = 0$, or $\omega_{n1} = \omega_1$, for all $i = 1, \dots, N$, the system $H(C)$ and the corresponding proportionally damped system $H(C_p)$ will have the same eigenvalue matrices.

Next let us consider some invariants of system $H(C)$ by comparing with its corresponding system $H(C_p)$ where $H(\cdot)$ is the state matrix of the system, i.e.

$$H = \begin{bmatrix} -M^{-1}C & -M^{-1}K \\ I & 0 \end{bmatrix}$$

First, consider the proportionally damped system, we have the following corollary:

Corollary 2: For a M-C-K system with proportional damping, no matter how the damping matrix C changes, as long as the system is proportionally damped, all undamped natural frequencies remain unchanged. That is,

$$\omega_1 = \text{constant} \quad i = 1, \dots, N \quad (16)$$

This corollary is a direct deduction from theorem 1, condition (4). From this fact, we can state, for any proportionally damped system, if the mass and stiffness matrices remain unchanged but only the damping matrix

varies, that system will have the invariant in undamped natural frequencies. Otherwise, we know that, equation (16) will be no longer valid if the system becomes non-proportionally damped. However, we have:

Lemma 1: The determinant of the state matrix and the corresponding generalized stiffness matrix are identical. That is,

$$\det(H) = \det(\tilde{K}) \quad (17)$$

From the second formula of H matrix given on the previous page, using simple manipulation of linear algebra, we can easily establish this lemma.

Theorem 2: For a M-C-K system, if only the damping matrix C changes while both M and K matrices remain unchanged, the product of all undamped natural frequencies also remains unchanged. That is,

$$\prod_{i=1}^{2N} \omega_i = \text{constant} \quad (18)$$

With the help of lemma 1. this result is quite clear, since

$$\prod_{i=1}^{2N} \omega_i = \det(H) = \det(\tilde{K})$$

These invariants will play an important role in the energy analysis of the damped systems. The energy analysis will, in turn, help us to understand the physical meanings of these invariants, and also give the physical meaning of the complex damping coefficients.

3 ENERGY METHODS AND DYNAMICS MEANINGS

In the above section, we mathematically pointed out that the quantity d_1 can describe the complex property of a system. We now try to interpret its physical meaning by the simplest case of SDOF system.

3.1 ENERGY DISSIPATION

Consider a SDOF system with free decay vibration:

$$m x'' + c x' + k x = 0$$

where m, c, and k are all real scalars. We can rewrite this equation in another form:

$$x'' + 2\xi\omega x' + \omega^2 x = 0 \quad (19)$$

where ξ and ω have the same standard meaning in vibrational analysis. Solution of Eq (1a) requires certain initial conditions. For example, we

can have

$$x = \exp(\lambda t) \quad (20)$$

Now, consider the work done by the inertial force, denoted by W_m , by the damping force, denoted by W_c , and by the spring force, denoted by W_k . Since the displacement (20) is in general complex valued, so will be the work done. It is important to know that, the work done can also be considered as virtual work, because the displacement x is in fact the virtual displacement. For convenience, we may call it *the complex virtual work* or simply the *complex work*. Consider the work done in one cycle, with period of $T = 2\pi/\omega$. We have

$$\left. \begin{aligned} W_m &= \int_0^{2\pi/\omega} x'' x \, dt = \frac{\lambda}{2} \eta \\ W_c &= \int_0^{2\pi/\omega} 2\xi\omega x' x \, dt = 2\xi\omega \eta \\ W_k &= \int_0^{2\pi/\omega} k x x \, dt = \frac{\omega^2}{2\lambda} \eta \end{aligned} \right\} \quad (21)$$

where η is a complex number

$$\eta = (\exp(2\lambda T) - 1) \quad (22)$$

Now denote η by equation (23)

$$\eta = \eta_0 e^{j\phi} \quad (23)$$

in the normal complex plane, denoted by $C_p^{(n)}$. This complex work is shown in Fig. 1. If a number is mapped onto this normal complex plane, its module will be multiplied by η_0 with an angle ϕ of rotation counterclockwise. To simplify the matter, we may use a modified complex plane $C_p^{(m)}$ with units measured by η_0 and x-axis coincident with a line of angle ϕ in $C_p^{(n)}$. In this plane, we have

$$\left. \begin{aligned} W_m &= \frac{\lambda}{2} = \frac{1}{2} (-\xi\omega + j\sqrt{1-\xi^2}\omega) \\ W_c &= \xi\omega \\ W_k &= \frac{\omega^2}{2\lambda} = \frac{1}{2} (-\xi\omega - j\sqrt{1-\xi^2}\omega) \end{aligned} \right\} \quad (24)$$

The energy equation (24) satisfies the law of conservation of energy, or the law of virtual work. That is,

$$W_m + W_c + W_k = 0$$

Furthermore, the dissipated energy, W_c , is real-valued. In other words, W_c lies along the x-axis of the $\mathbb{C}_p^{(m)}$ plane. However, both W_m and W_k are complex work done. The sum of their real parts, $\xi\omega$, are just the energy given from the system in the specific circle to the damper. The damper dissipates the exact amount of energy $\xi\omega$. Both W_m and W_k will have an angle γ to the x-axis, which is called the *loss angle*. If the damping ratio ξ is small enough, we can have the following relation:

$$\gamma = \xi = \tan\left(\frac{\text{Im}(\lambda)}{\text{Re}(\lambda)}\right) = \tan\left[\frac{\text{Im}(W_m)}{\text{Re}(W_m)}\right] = \tan\left[\frac{\text{Im}(W_k)}{\text{Re}(W_k)}\right] \quad (25)$$

where the least three tangent forms are called *loss tangent*.

Theorem 3: For a SDOF system with real valued damping coefficient, denoted by (19), its damping ratio equals to the ratio of work done by damping force and the geometric sum of work done by inertia and spring forces during a cycle. That is,

$$\xi = \frac{W_c}{2 \sqrt{W_m W_k}} \quad (26)$$

Equations (25) and (26) can be also be obtained in figure 1.

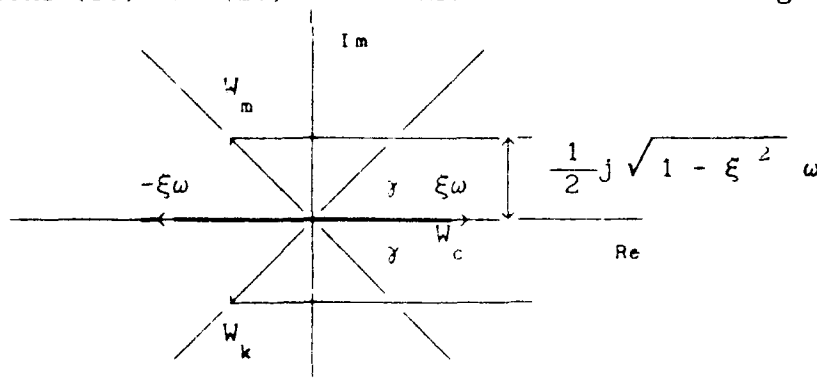


Figure 1 complex $\mathbb{C}_p^{(m)}$ plane

The module of the complex work W_m (or W_k) is equal to ω . If we return to the $\mathbb{C}_p^{(n)}$ plane, and suppose at the beginning of the circle, the amplitude of the displacement is one, then, the quantity ω represents the amount of the kinetic energy at this moment. So, for convenience, we also call the undamped natural frequency *virtual energy*, denoted by δ_v and have the following corollary.

Corollary 3: For a SDOF system with real valued damping coefficient, denoted by (19), its virtual energy equals the square root of generalized

stiffness,

$$\delta_v = \sqrt{m^{-1}k} = \sqrt{\omega^2} = \omega \quad (27)$$

Compare corollary 1 with corollary 3, we see that, the virtual energy of system (19) is an invariant. In other words, for a system (19), no matter how the damping coefficient c changes, the virtual energy remains unchanged. Also, an MDOF proportionally damped system can be decoupled into n -real modes of n -individual equations, like equation (19), as stated by the following corollary.

Corollary 4: If an MDOF system with proportional damping is decoupled into n real modes, then each mode has invariant virtual energy, regardless whether or not the damping matrix changes.

Now, consider the imaginary parts of the complex work W_m and W_k . The work done by the inertial and the spring force contains the real part, the energy to have been dissipated, contains the imaginary part. Only when this latter part is included, the virtual energy is equal to ω . And this amount of energy is the conservative portion of the energy during this circle, (from kinetic energy to potential energy). If the damping is equal to zero, the conservative portion of the energy is equal to ω . However, as the damping ratio ξ becomes larger, this amount of energy will become smaller by the factor $\sqrt{1 - \xi^2}$, because a certain amount energy is dissipated. The interesting thing is, the portion of energy or work done, under the notation of complex work or the $\mathbb{C}_p^{(m)}$ plane, is perpendicular to W_c . This important conclusion also holds for MDOF system.

3.2 ENERGY TRANSMISSION

Now, let us consider the imaginary coefficient of the velocity term in the equation of motion

$$m \ddot{x} + j c \dot{x} + k x = 0$$

Or, in a more familiar form,

$$\ddot{x} + 2j \zeta \omega \dot{x} + \omega^2 x = 0 \quad (28)$$

where m , c and k are real scalars. In practice, equation (28) has no real meaning, if it describes a SISO system. However, it will have clear

physical meaning if it is used to express a virtual mode of a MDOF system. Suppose the solution to equation (28) is

$$x = \exp(\nu t),$$

then

$$x' = \nu \exp(\nu t) \quad \text{and} \quad x'' = \nu^2 \exp(\nu t)$$

Therefore we have the characteristic equation as follows

$$\nu^2 + 2 j \zeta \omega \nu + \omega^2 = 0 \quad (29)$$

The solution of equation (28) is given by

$$\nu = j \omega (- \zeta \pm \sqrt{1 + \zeta^2})$$

Without loss of generality, we may write

$$\nu = j \omega (- \zeta + \sqrt{1 + \zeta^2})$$

The solution does not have real part.

Again using the concept of a modified $C_p^{(m)}$ plane, with the complex number, $\eta = (\exp(2\nu T) - 1)$, we may obtain the work done for one cycle $T = 2\pi/\omega$:

$$W_m = \frac{\nu}{2} = \frac{1}{2} j \omega (-\zeta + \sqrt{1 + \zeta^2})$$

$$W_c = j \zeta \omega$$

$$W_k = \frac{\omega^2}{2\nu} = \frac{1}{2} j \omega (-\zeta - \sqrt{1 + \zeta^2})$$

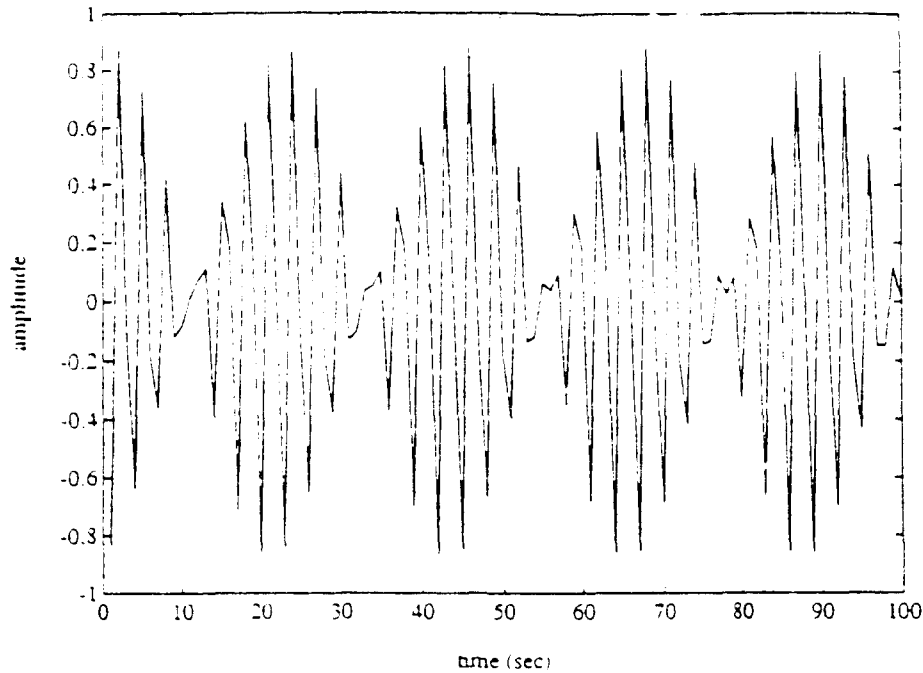
} (30)

The above quantities expressed in equations (30) satisfy the law of conservation of energy or the law of virtual work. That is,

$$W_m + W_c + W_k = 0$$

In addition, these work done quantities are all imaginary. Thus, during a cycle, no energy is dissipated. Figure 2 gives a typical response time history of system (28) subjected to an impulse. It is seen that, without real part of the damping coefficient the amplitude of vibration will not decrease. In other words, no energy is dissipated. The above described impulse response does not behave like a SDOF system. Rather, it behaves like an MDOF system with some more natural frequencies, (see figures 2). In a certain cycle the amplitude seems to decrease whereas in a different cycle it increases. It is easy to understand that, during a certain cycle, the energy, which is proportional to the square of the amplitude, is

Fig. 2 Time History of Imaginarily Damped System



different from that in another cycle. Energy changes or transfers from time to time. The interesting thing is, energy is also transferred within a system with real-valued damping. But the energy-transfer is essentially different from the case where the damping is only imaginary-valued.

Energy dissipation in real-valued and imaginary-valued systems are different. The portion of energy transferring between kinetic energy and potential energy is included in both the first case (24) and second case (30). In the first case it is the part of

$$\pm \frac{1}{2} j \omega \sqrt{1 - \xi^2}; \text{ and in the second case, it is the part}$$

$$\pm \frac{1}{2} j \omega \sqrt{1 + \zeta^2}.$$

In the first case, the energy transfers or dissipates to the the damper is represented by the part $\xi\omega$. The energy transferred to an "imaginary" device in the second case is represented by the part $j\zeta\omega$. The major difference here is that the energy quantity $\xi\omega$ is changed from mechanical work to another type of energy, in most cases thermal energy, while the quantity $j\zeta\omega$ remains in the form of mechanical work. We may think of this energy is transferred to somewhere and stored there for a period of time

and then it may be transferred back to the mass-spring system at a later time. Based on this concept we may call the quantity $j2\zeta\omega$ the *imaginary damping coefficient* and the quantity ζ the *imaginary damping ratio*. This is stated in the following theorem.

Theorem 4: For an imaginary damped system, denoted by (28), the imaginary damping ratio equals the absolute ratio of work done by the imaginary damping force and the geometric sum of work done by the inertia and spring force in a circle. That is,

$$\zeta = \left| \frac{W_c}{2 \sqrt{W_m W_k}} \right| \quad (31)$$

In this paper we refer to the change of energy of $\xi\omega$ the *energy dissipation*, and the change of $j\zeta\omega$ the *energy transformation*. It is interesting to note that, with a given amount energy transferred, the virtual energy, ξ_v , i.e. the "undamped" natural frequency $|\nu|$, is no longer equal to ω . It is modified by the factor

$$(-\zeta \pm \sqrt{1 + \zeta^2})$$

This tells us that, with the energy transformation, the total energy during cycles changes. It also suggests, that for a SDOF system, there appears to have two different values of virtual energy. But for a SDOF system, equation (28) does not have real meaning, neither does the virtual energy of SDOF system have real meaning. In fact, we refer a "SDOF system" to be a virtual mode of an MDOF system. For any given MDOF system, its N-undamped natural frequencies are uniquely determined. Therefore, we have the following corollary.

Corollary 5: A given N-dimensional MDOF system has and only has N-virtual energy. That is,

$$\xi_{v_i} = \omega_i \quad \text{for } i = 1, \dots, N$$

Typically, "virtual energy" is not used in energy considerations of a SDOF system. However, for convenience, we state the following corollary using the virtual energy of SDOF system to actually express the energy relationship between different modes of an MDOF system.

Corollary 6: For a SDOF system (28) with an imaginary damping coefficient $j\zeta$, if the value of $j\zeta$ changes, the virtual energy of the system will also be changed.

3.3 COMPLEX WORK DONE

Consider now the case when a SDOF system has both real and imaginary damping coefficient,

$$x'' + 2(\xi + j\zeta)\omega x' + \omega^2 x = 0 \quad (32)$$

That is, the system has complex damping ratio. From theorems 4 and 5, it is not difficult to qualitatively understand the results of complex work done. Complex work done consists both energy dissipation and energy transformation. And, its virtual energy, or undamped natural frequency will not be an invariant. Also, we know that, an MDOF system can only be "decoupled" with the form (32). Therefore, each equation (28) will no longer have invariant virtual energy. On the other hand, from theorem 3, we know that, the product of total virtual energy is still an invariant. Fig.3 shows the typical time history of complex damped systems, Fig. 4(a) is a real structure, one of its time histories is given in Fig 4(b) which shows the complex damping effects.

To quantitatively describe the complex work done and all its implications is rather complicated. However, it is possible for special cases. One example is the complex damping of lightly damped structures (see the paper "Lightly Damped Systems" by the same authors). Figure 3 (a) gives a response of the complex damped system. Figure 3(b) shows a time history of a real structure.

CONCLUSIONS

1) If a vibrational structure is non-proportionally damped, there exist both energy dissipation and energy transformation resulted by damping effects. The energy transformation is essentially the conservative energy. If the non-proportionality is heavy, this amount energy cannot be simply neglected nor be mistaken as dissipative energy. Otherwise severe errors may be caused.

2) To describe both the energy dissipation and the energy transformation quantitatively, a complex-valued generalized Rayleigh quotient can be used, which is obtained from natural parameters of the structure. This quantity is called complex damping, whose real part is traditional damping

Fig. 3(a) Time History of Complex Damped System

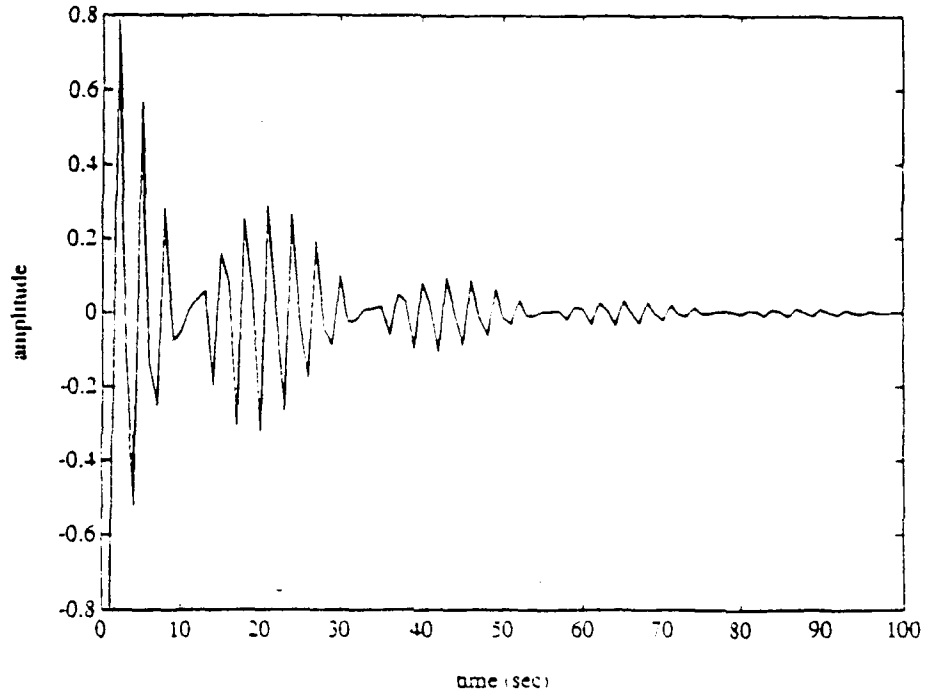


Fig. 3(b) Free response of Real Structures

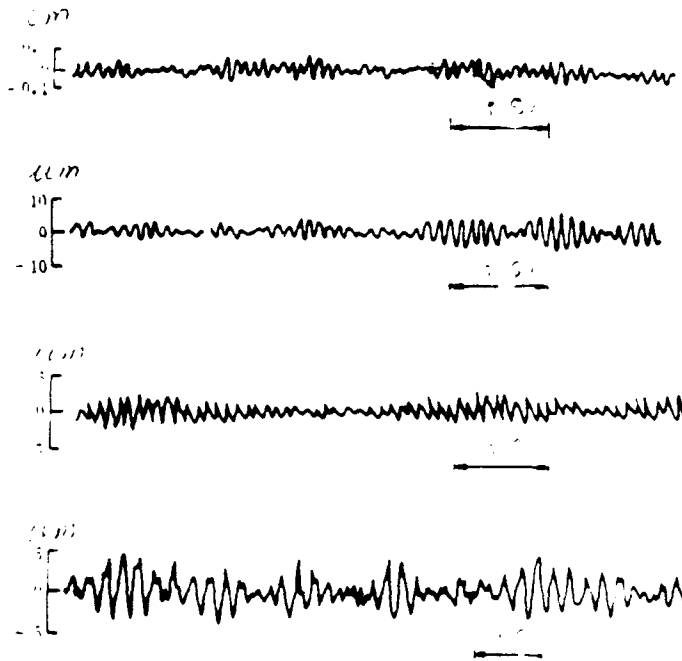


Fig. 4(a) 5-Floor Structure

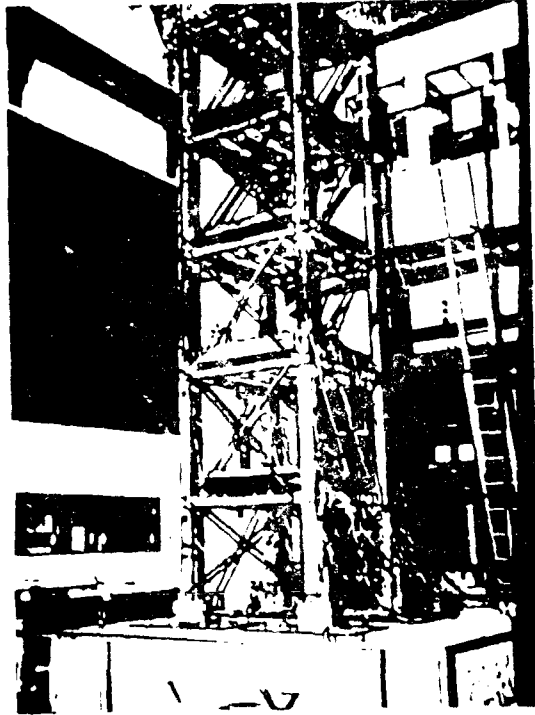
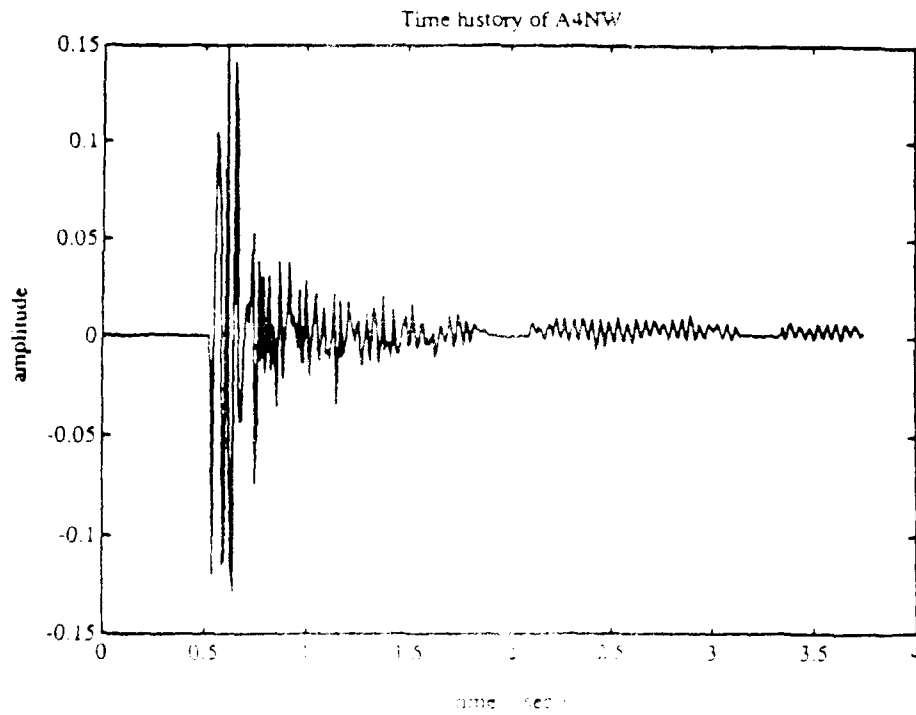


Fig. 4(b) Acceleration Time History (4th floor, north-west)



ratio and imaginary part stands for the ratio of energy transformation.

3) With the help of complex damping, the energy relationship of modal equation, the energy based invariants of systems, and therefore the physical meanings of complex damping itself are explained by the theory of complex damping described by this paper.

ACKNOWLEDGEMENT

Funding for the research reported in this paper has been provided jointly by the State University of New York at Buffalo and the National Science Foundation through the National Center for Earthquake Engineering Research under master contract number ECE86-07591.

REFERENCES

- Caughey, T.K. and O'Kelly, M.M.J. "Classical Normal Mode in Damped Linear Dynamic Systems" J. of Appl. Mech. ASME Vol 32, pp.583-588, 1965.
- Clough, R. W. and Penzien, "Dynamics of Structures," McGraw-Hill, New York, 1975.
- Ewins, D.J "Modal Testing, Theory and Practice" Research Studies Press LTD. England (1986).
- Ibrahim, S.R., Mikulcik, E.C. "A Method for the Direct Identification of Vibration Parameters from the Free Response", the shock & Vib. bulletin 47 Sept. 1977.
- Inman, D. "Vibration with Control, Measurement and Stability", Prentice-Hall, Englewood Cliffs, 1989.
- Juang, J-N.; Pappa, R.S. " An Eigensystem Realization Algorithm (ERA) for Modal Parameter Identification and Model Reduction" presented at NASA/JPL workshop on identification and control of flexible space structures, J. of Guidance, Control and Dynamics, Vol. 8, No. 5, Sept-Oct. 1985, pp.620-627.
- Kozin, F. and Natke, H.G. (1986). "System Identification Techniques", Structural Safety, Vol.#, pp.269-316.
- Lancaster. P. "Lambda-Matrices and Vibrating Systems" (1966) Pergamon Press.
- Liang, Z. and Lee, G.C. "On Complex Damping of MDOF Systems" Proc. of IMAC-8, 1990, pp.1048-1055.
- Liang, Z. and Lee, G.C. "Representation of Damping Matrix", J. of Eng.

Mech. ASCE., May 1991 (to appear).

Liang, Z., Lee, G.C. and Tong, M. (1991) "A Strong Criterion For Testing Proportionally Damped Systems" Proc. of Damping '91, Feb. 13-15 1991, San Diego, CA., Sponsored by Wright Laboratory, Flight Dynamics Directorate, Wright-Patterson Air force Base.

Liang, Z., Lee, G.C. and Tong, M. (1991) "On A Linear Property of Lightly Damped Systems" Proc. of Damping '91, Feb. ' 1991, San Diego, CA., Sponsored by Wright Laboratory, Flight Dynamics Directorate, Wright-Patterson Air force Base.

Lin, R.C., Liang, Z., Soong, T.T. and Zhang, R.H. "An Experimental Study of Seismic Structural Response With Added Viscoelastic Dampers", Technical report NCEER-88-0023. 1988.

Natke, H.G., Yao, J.T-P. (1986)"System Identification Approach in Structural Damage Evaluation", ASCE Structures Congress '86, Preprint 17-1.

Natke, H.G. "Updating Computational Models in the Frequency domain Based on Measured Data: A Survey", Probabilistic Engineering Mech. Vol. 3, No.1 1988.

Shinozuka, M., Yun, C-B. and Imai, H. (1982). "Identification of Linear Structural Dynamic Systems", J. of Structural Engineering, ASCE, Vol. 108, No. EM6, pp.1371-1390.

Singh, M. D. and Ghafory-Ashtiani, M. (1986) "Modal Time History of Non-classically Damped Structures For Seismic Motions". Earthquake Engineering and Structural Dynamics, Vol 13. pp133-146.

Tong, M., Liang, Z. and Lee, G. C. (1991) "On an Application of Complex Damping Coefficients" Proc. of Damping '91, Feb. 13-15 1991, San Diego, CA., Sponsored by Wright Laboratory, Flight Dynamics Directorate, Wright-Patterson Air force Base.

Tong, M., Liang, Z and Lee, G.C.(1991) "Techniques in Design and Using VE Dampers" Proc. of Damping '91, Feb. 13-15 1991, San Diego, CA., Sponsored by Wright Laboratory, Flight Dynamics Directorate, Wright-Patterson Air force Base.

Vold, H; Rocklin, G. " The Numerical Implementation of a Multi-Input Modal Estimation Method for Mini-Computer," Proc. of IMAC-1, 1982, pp.542-548.

**AN ITERATIVE METHOD IN DYNAMIC STRUCTURAL ANALYSES
WITH NONPROPORTIONAL DAMPING**

Wan T. Tsai¹, Joseph T. Leang²

ABSTRACT

A new method in dynamic analyses of structures with non-proportional damping is proposed. By decomposing the non-proportional damping matrix into two portions, the diagonal and off-diagonal, the iterative technique can be employed through use of the classic method of solving a large dynamic structural system with real modal coordinates. Explicitly, the diagonalized damping matrix is retained to form a system of discrete differential equations with proportional damping. The off-diagonal portion of damping forces is treated as a correcting forcing function. The iteration is to use the off-diagonal damping induced forces for the load correction in the subsequent computational step. This enables the structural responses to be simply determined while the effect of off-diagonal damping forces is included.

¹MTS, Dynamic Loads, Rockwell Int'l, 12214 Lakewood Blvd., Mail Code AD88, Downey, CA 90241, (213) 922-0570. Also, Adjunct Professor, Mechanical Engineering Dept., Calif. State Univ., Long Beach.

²MTS, Dynamic Loads, Rockwell Int'l, 12214 Lakewood Blvd., Mail Code AD88, Downey, CA 90241, (213) 922-5794.

AN ITERATIVE METHOD IN DYNAMIC STRUCTURAL ANALYSES WITH NONPROPORTIONAL DAMPING

Wan T. Tsai, J. F. Leang
Dynamic Loads, Rockwell International, Downey, CA

INTRODUCTION

This article presents a new method in dynamic analyses of structures with non-proportional damping. Computed iteratively, this method ensures highly accurate responses yet low cost analyses when the structures are subjected to dynamic forcing functions.

In dynamic analyses of space vehicles, the mass and stiffness matrices of each substructure are usually generated by different contractors. Each substructure may contain its own component modal damping acquired from component testing or empirical data. When all substructures are coupled together into a system for dynamic analyses, a difficulty arises. Generally, the system damping matrix cannot be transformed into a diagonal matrix by using the same transformation matrix as for generalizations of the system mass and stiffness matrices. Since the transformed damping matrix is not diagonalized, the structural responses cannot be determined by taking the advantage of using the real mode superposition technique. In order to avoid this difficulty, the off-diagonal elements of the transformed damping matrix are usually neglected in the wake of their smallness compared to the corresponding diagonal elements. Known as triple-matrix-product (TMP) method in the aerospace industry, this approach has been widely employed as a standard method in analyses of space vehicles. Using this approach, the interface loads are usually accurate for design purposes. However, the responses in some payload components may be grossly incorrect when the full scale payload-orbiter coupled systems are exercised.

The proposed iterative method is to improve the accuracy of payload responses yet to retain the advantage of using the modal superposition technique for cost saving. This method decomposes the transformed system modal damping matrix into two portions, a diagonal damping matrix and an off-diagonal damping matrix. The damping force induced by the off-diagonal damping elements are treated as a correcting force vector to modify the applied forcing function. This correction can be repeatedly applied until the results are within an acceptable range of error. Using this iterative approach, the desired goal can be reached and the impact to the currently applied TMP method can be minimized.

The iterative method in treating the nonproportional damping matrix has been applied by the first author of this paper to analyze small scale of structures since 1988. Independently, the same method given by Udvardi and Esfandiari (1990), may be the first article related to this method published in the open literature. The convergent characteristics of the method is the primary emphasis

of the article. Prior to using the iterative method, several approaches have been proposed in treating structural systems with non-proportional damping. Primarily due to the development of nuclear power plants in the 1970s, replacements of the non-proportional damping matrix with diagonal matrix have been extensively investigated. Those which have been more commonly employed are: (1) using the diagonal elements of the non-proportional damping matrix, i.e., the triple-matrix-product (TMP) method, (2) replacing the non-proportional damping matrix by a diagonal matrix containing each element with a factor of the critical damping to each mode, i.e., the system damping method, and (3) obtaining each diagonal damping element by using the algebraic sum of the corresponding row of the non-proportional damping matrix. Errors acquired from these approximations had also been examined. Those who had been involved in these methodology developments included Clough and Mojtahedi (1976), Cronin (1976), Duncan and Taylor (1979), Hasselman (1976), Thompson, Calkin, and Caravani (1974), and Warburton and Soni (1977.) A different approach in synthesizing the diagonal system damping elements from the component modal testing was given by Tsai (1989.) It is known that a non-proportionally damped system can be completely generalized through the complex mode transformations. Many investigators have been involved in developments of this method, for instance, Beliveau and Soucy (1985), and Veletsos and Ventura (1986.) Although, the complex mode transformation is the exact method in treating non-proportionally damped structural systems, the real mode transformation seems to be still more favorable to most application engineers for two reasons: (1) It is less costly in the full scale transient analysis when an approximate method is employed. (2) It is easier to capture the image of physical behavior when the real mode transformation is applied. Therefore, the approximations developed in the 1970s are still favorably used. The TMP and the system damping approaches have been particularly favored in the aerospace industry.

In addition to the derivation of the iterative method, this paper emphasizes on case applications of the method to a full scale payload/orbiter dynamic analysis, i.e., the IUS/TDRS payload for the 26th space transportation system (STS-26) manifest. The direct integration method is employed as the basis to substantiate the validity of the new method. The reason that the TMP method is inadequate for payload response computations is extensively discussed. Recommendations in transient analyses for non-proportionally damped structures are provided.

ITERATIVE METHOD

Let M , C , and K be the physically coupled mass, damping, and stiffness matrices, P the applied forcing vector, X the response vector, and dots the derivatives with respect to time; the governing

differential equation of the dynamic system is given by

$$M\ddot{X} + C\dot{X} + KX = P \quad (1)$$

Eq. (1) can be solved in a simple manner by transforming the physical response coordinates X into a system of generalized response coordinates x by introducing a transformation matrix ϕ . Namely

$$X = \phi x \quad (2)$$

Through use of Eq. (2), along with the correlations

$$m = \phi^T M \phi, \quad c = \phi^T C \phi, \quad k = \phi^T K \phi, \quad p = \phi^T P \quad (3a, b, c, d)$$

Eq. (1) then reduces to

$$m\ddot{x} + c\dot{x} + kx = p \quad (1')$$

where, m is a unit matrix, c is a fully populated matrix, k is a diagonal matrix containing eigenvalues in the diagonal elements, and p is a generalized forcing vector.

Eq. (1') could be easily solved by using the real mode superpositions if c were a diagonal matrix. In order to take the advantage of expressing all responses with the superpositions of real modes, let c be expressed by the sum of a diagonal matrix c_d and an off-diagonal matrix c_o . Namely,

$$c = c_d + c_o \quad (4)$$

Eq. (1') can then be rewritten by

$$m\ddot{x} + c_d\dot{x} + kx = p - c_o\dot{x} \quad (5)$$

Thus, all the coefficient matrices on the left hand side of Eq. (5) are diagonal. The contribution of each generalized mode can be directly determined without coupling with the other modes. The technique of modal superpositions can then be applied to simplify the analysis inasmuch as the forcing function vector on the right hand side is explicitly given. The industrial practices generally assume that the effect of c_o is negligible since its elements are generally smaller than the corresponding elements of c_d . The approach using this assumption is the method commonly referred in the aerospace industry as the triple-matrix-product (TMP). In fact, the words triple-matrix-product (TMP) does not comprise any meaning of stripping the off-diagonal damping elements. Nevertheless, this article uses the commonly accepted definition that the TMP method implies the applications of the diagonalized damping matrix.

Now, the iterative method comes to play by treating the response vector x on both sides of Eq. (5) as if they were independent at different stages of computations, x_n and x_{n+1} , where n is the number of iterations. Eq. (5) is then rewritten into the form

$$\ddot{x}_n + c_d \dot{x}_n + kx_n = p - c_o \dot{x}_{n-1}, \quad n = 0, 1, 2, \dots \quad (6)$$

The left hand side represents the classic modal system of equations whereas the right hand side is the forcing function corrected by the off-diagonal damping induced forces. Using this system of equations, the modal DOFs can be easily determined since every equation is associated with a single DOF.

In Eq.(6), $\dot{x}_{-1}=0$ when $n=0$. The response x_0 is the TMP result. The off-diagonal damping force obtained from the TMP result is applied to modify the applied force and the first iterative response x_1 for $n=1$ is then determined from Eq.(6). Analogously, the second iterative response x_2 for $n=2$ is computed by using the correcting force obtained from the x_1 response. This procedure can be repeatedly applied until the n th iterative response x_n reaches an acceptable accuracy.

The iteration can be stopped when the response converges to a desired accuracy. Using various examples of three degree-of-freedom, Udwadia and Esfandiari showed that the results of six iterations were almost identical to the exact solutions. For practical applications, such a highly accurate result may not be necessary. The analysis may be terminated by setting an accuracy criterion that the converging rate of the modal accelerations is within a specified admissible error, ϵ . Namely,

$$\left| \frac{\ddot{x}_{n-1}}{\ddot{x}_n} - 1 \right| \leq \epsilon, \quad n = 1, 2, \dots \quad (7)$$

For most design purposes, the modal accelerations may be accurate enough to assume an admissible error of 5% (0.05). This value is suggested on the basis of common practices, not a sophisticatedly computed number. Experiences indicate that responses may generally be converged to $\epsilon < 0.05$ when two iterations are performed.

It must be noted that the provided error limit for the modal accelerations does not assure of the physical accelerations to be always within the same limit. However, their limits are generally agreeable to each other in most applications. It must also be noted that the error determined by Eq.(7) is to judge the acceleration computed in the $(n-1)$ th iterative analysis with the n th iterative acceleration as the basis. In fact, when the result of the n th iteration is used for final response evaluation, the accuracy is higher than the specified admissible error since the updated result is supposed to be judged with the $(n-1)$ th iterative values.

APPLICATIONS OF ITERATIVE METHOD

The dynamic liftoff analysis for the STS-26 flight manifest was used to demonstrate applications of the iterative method. The manifest consists of the substructures: tracking data relay

satellite (TDRS), inner upper stage (IUS) booster, orbiter, solid rocket booster (SRB), and external tank (ET). The spacecraft TDRS was integrated to the IUS which was in turn secured to the orbiter cargo bay through payload trunnions. The primary purpose of this flight was to deploy the payload IUS/TDRS.

Originally, all components were individually modeled as substructures, each was represented by hundreds or thousands of degree-of-freedom (DOFs). After several stages of substructural coupling and condensations, the final model used for the lift-off dynamic analyses was 520 DOFs. The system was subjected to a dynamic forcing function, LR1200, one of the conditions being used for lift-off transient analyses. The analysis was performed over a range of 11 seconds to cover the complete lift-off event. To assure of obtaining an accurate result, the small time interval of 0.001 seconds was used over the entire time span of transient analyses. In the dynamic loads analysis, 1% of the critical damping was assumed for all the IUS/TDRS payload modes. For the orbiter, 1% for frequencies below 10Hz and 2% for frequencies above 10Hz were assumed. No damping was assumed at the payload/orbiter interface DOFs. The analyses were performed by using various approaches for comparisons. The results are summarized in Tables 1-5 in which column 1 represents the items of interest. Columns 2-5 represent the minimum and maximum values obtained from various methods of transient analyses.

Initially, the dynamic system was analyzed by using the TMP method. The results are summarized in column 2 of Tables 1-5 for various component responses. The accelerations along the X-direction at the tip of SA antenna ribs (node 115) was excessively high, a minimum of -25.7g and a maximum of 27.2g as shown in column 2 of Table 1. Since this result was not acceptable and such a strong response was very unusual, a similar analysis was performed by using 1% of the critical system damping. As shown in column 5 of Table 1, the response for the same item reduces significantly to a minimum of -9.6g and a maximum of 9.2g. Clearly, the comparison between these two sets of results indicates a controversial conclusion that the system with a higher damping value has a stronger response than the one with a lower damping value. This conclusion violates the nature of mechanics that a structure has less responses with higher damping.

When the iterative method is applied, the peak accelerations of the same item become -6.6g and 7.4g for one iteration, and -7.2g and 7.7g for two iterations. These results are respectively shown in columns 3 and 4 of Table 1. They are significantly different from that of the TMP method. The responses of several other items are also significantly changed between the TMP and iterative methods. For instance, the Y-acceleration of the C-band reflector CG in Table 1 and the member force at the LTM row 149 in Table 2, their responses using the iterative method appear to be less than one-half the TMP results. The difference between these selected items reveal a fundamentally severe deviation between the TMP and iterative

methods, although the responses of many other items are in good agreement. Physically, the results obtained from the iterative method make better sense than from the TMP method when they are compared to those using the system damping method, as shown in column 6 of Tables 1-5.

To make sure that the iteratively computed results are reasonably accurate, the first iterative result is compared to the second one, i.e., column 3 compared to column 4 of Tables 1-5. Among all interested items, the maximum difference between these two iterative analyses is only 4.6% occurred in the X-acceleration at the tip of SA antenna ribs. Furthermore, in order to assure of correct results obtained from the iterative analyses, a direct integration method using the fully populated damping matrix is also performed. The results are shown in column 5 of Tables 1-5. All iterative responses are in very good agreement with the direct integration results. In general, the results of the second iteration are much closer to that of the direct integration than those of the first iteration. In certain particular items such as the tip of SA antenna ribs, the second iterative value has slightly more deviation than the first iterative result when both are compared to the direct integration result. It just happens on the way of converging process to the final result, but does not indicate any inaccuracy in the iterative method.

A question has been raised regarding the magnitude of the interface loads between using the system damping and iterative methods. Specifically, the load of -8909 lbs in the 1% system damping analysis appear to be weaker than -9024 lbs of the iterative analysis for the X-interface load at X=1155.53 inches (node 43.) This may not be surprised since the damping matrix established for the iterative method is more complex than that for the system damping matrix. The one for the iterative analysis consists of zero damping value at the interface nodes as well as 1% and 2% for the Craig-Bampton form of substructure modelling. But the 1% system damping implicitly include damping values at the interface nodes as well as the other DOFs, as shown in the reversed expression of Eq.(3b). This explains the reason that some of the interface loads are stronger in the iterative analyses than in the analysis of using 1% system damping. The discrepancy for most of other quantities appears to be in the right order that the responses using the system damping method (1% damping) is slightly greater than those using the iterative method (1% and 2% damping for orbiter.)

REASONS FOR THE RESPONSE DISCREPANCY OF TMP METHOD

The reason for such a significant deviation in the TMP method has been interpreted as the consequence of modal response superpositions from two modes that have two closely spaced modes. This can be explained by considering the modal contribution for an item at a particular time slice. For instance, the modal contributions

of the acceleration at the tip of SA antenna ribs at $t=3.3$ second are shown in Figures 1 and 2 respectively for the TMP and one-iterative analyses. Although both modal contribution plots appear to be different, the major contributions occur at the same frequency of 25.4Hz in either analyses. Near the interested frequency, the contributions from Figure 1 of the TMP approach are both negative whereas the contributions from Figure 2 of the iterative method are mixed with a negative and a positive value. Owing to this type of misrepresentation in the TMP modal contributions, the TMP computed responses become significantly different from those of the iterative analysis.

Although the above interpretation is mathematically correct, there remains a clout regarding the true driving source that causes such a strong impact to the component responses in the present illustration. A careful study indicates that the light weight flexible components are driven by wrong forces when the TMP approach is applied. That is the true reason to induce such a significant impact at the component responses. This can be directly interpreted by using Eq. (5). Since the generalized mass m is a unit matrix, Eq. (5) can be rewritten into an alternate form to express the acceleration in terms of p , k , c_0 , c_1 , x , and \dot{x} . The acceleration for the i th modal DOF is given by

$$\ddot{x}_i = p_i - k_i x_i - (c_d)_i \dot{x}_i - \sum_j (c_o)_{ij} \dot{x}_j \quad (3)$$

In the TMP analysis, the last term associated with c_o has been entirely neglected. This may be justified when the applied force p_i , stiffness force $k_i x_i$, and diagonal damping force $(c_d)_i \dot{x}_i$ are much greater than the total off-diagonal damping force. For the internal components of a payload, the DOFs are generally not subjected to any directly applied forces. Instead, the component DOFs are driven by the combined action of stiffness and damping forces. When the stiffness is relatively small like the SA antenna ribs¹, the associated stiffness force is small and the damping force becomes an important part of the driving force. Furthermore, the off-diagonal damping force becomes the dominated portion in the total driving force. Specifically, the sum of several hundreds of off-diagonal damping force components may override the stiffness and diagonal damping forces to influence the final responses of the transient analysis, although each off-diagonal damping force component may be small compared to the counterpart of the stiffness and diagonal damping forces.

¹The component stiffness is small compared to the other portion of the structural system. However, the component frequency may not be small since the corresponding component mass is usually small too.

The above interpretation can be substantiated by the TDPS member loads shown in Table 2. The item at the LTM row 149 has a peak member force reduced from 21.7 lbs in the TMP approach down to 11.9 lbs in the one-iterative analysis. Similarly, the small IUS motor (node 3457) has the peak Y-acceleration changed from 0.42g to 0.23g as shown in Table 4. The changes are up to 100%. On the contrary, the changes in the interface loads at the bridge points between the IUS/TDRS and orbiter as shown in Table 3 and the orbiter bridge acceleration as shown in Table 5 are much less, a maximum of 13% only. Therefore, the TMP may still be applicable if all substructural components are stiff. However, when the component is flexible, it may be subjected to a wrong driving force when the off-diagonal damping force is neglected. As a result, the component response is incorrect. It is particularly sensitive to the component of small mass since it is more responsive to any variation of the driving force.

CONCLUSIONS

1. The commonly referred TMP method has assumed that the off-diagonal damping elements are small and negligible; and that uses of the diagonal damping elements are sufficient to capture accurate component responses of structures. This has been proved to be incorrect. In fact, the TMP method may produce a structural response totally different from the true result. Therefore, the currently applied TMP method should not be used.

2. A new method using iterative procedure is proposed for transient analyses of dynamic structures with non-proportional damping. This method can provide an accurate result within small number of iterations. The validity of this method has been substantiated by using the direct integration method through the illustrative analyses for the STS-26 flight.

3. The proposed iterative method is cost effective. On the basis of analyses for various structure sizes, the cost of using each additional iteration is about 15% more than the cost of using the TMP approach. Generally, two iterations may result in an accurate response for design purposes. If two iterations are used, the expected computing cost may increase about 30%. This cost is not a significant impact when it can assure of obtaining a reliable response in all payload components. Therefore, the iterative method is a viable approach for transient analyses when the transformed system damping matrix is non-proportional.

RECOMMENDATIONS

To ensure accurate component responses of structures, the off-diagonal damping elements must not be neglected. In order to retain the off-diagonal damping without significantly increasing computational cost, the iterative method may be used.

ACKNOWLEDGMENT

The authors wish to thank Dr. R. S. Chao for his encouragement in preparation of this article. They are also grateful for the reference search and technical discussions of Dr. H. T. Tang of Electric Power Research Institute and Dr. C. S. Lin of the Aerospace Corporation.

REFERENCES

- Beliveau, J. G., Soucy, Y., 1985, "Damping Synthesis Using Complex Substructure Modes and A Hermitian System Representation," AIAA 26th Structures, Structural Dynamics, and Material Conference, paper No. 85-0785, pp. 581-586.
- Clough, R. W., Mojtahedi, S., 1976, "Earthquake Response Analysis Considering Non-Proportional Damping," Earthquake Engineering and Structural Dynamics, Vol. 4, pp. 489-496.
- Cronin, D. L., 1976, "Approximation for Determining Harmonically Excited Response of Non-Classically Damped Systems," ASME J. Engineering for Industry, pp. 43-47.
- Duncan, P. E., Taylor, R. E., 1979, "A Note on The Dynamic Analysis of Non-Proportionally Damped Systems," Earthquake Engineering and Structural Dynamics, Vol. 7, pp. 99-105.
- Hasselmann, T. K., 1976, "Modal Coupling in Lightly Damped Structures," AIAA J., Vol. 14, pp. 1627-1628.
- Thompson, W. T., Calkins, T., Caravan, P., 1974, "A Numerical Study of Damping," Earthquake Engineering and Structural Dynamics, Vol. 3, pp. 97-103.
- Tsai, W., 1989, "Considerations of Synthesized System Damping in Dynamic Analysis of Space Structures," Proceedings of Damping'89, 8-10, February 1989, West Palm Beach, Fl., pp. DBE.1-DBE.13.
- Udwadia, F. E., Esfandiari, R. S., 1990, "Nonclassically Damped Dynamic System: An Iterative Approach," J. Appl. Mech., Vol. 57, pp. 423-432.
- Veletsos, A. S., Ventura, C. E., 1986, "Model Analysis of Non-Classically Damped Linear Systems," Earthquake Engineering and Structural Dynamics, Vol. 14, pp. 217-243.
- Warburton, G. B., Soni, S. R., 1977, "Errors in Response Calculations for Non-Classically Damped Structures," Earthquake Engineering and Structural Dynamics, Vol. 5, pp. 365-376.

TABLE 1 STS-26 TDRS ACCELERATION (g)

ITEMS	Diagonal TMP		1 Iteration		2 Iterations		Full Damp-Matrix		1% System Damping	
	Min	Max	Min	Max	Min	Max	Min	Max	Min	Max
SGL Antenna # 13 X	-1.869	2.678	-1.842	2.812	-1.830	2.830	-1.836	2.831	-1.742	2.823
SGL Antenna # 13 Y	-2.732	2.759	-2.755	2.818	-2.759	2.824	-2.761	2.825	-2.729	2.782
SGL Antenna # 13 Z	0.300	3.355	0.220	3.288	0.216	3.290	0.216	3.289	0.189	3.352
SGL Feed # 15 X	-2.868	3.590	-2.850	3.774	-2.842	3.782	-2.843	3.789	-2.798	3.652
SGL Feed # 15 Y	-2.192	2.694	-2.226	2.128	-2.233	2.137	-2.236	2.139	-2.181	2.057
SGL Feed # 15 Z	-2.380	4.475	-2.298	4.353	-2.306	4.350	-2.309	4.351	-2.317	4.394
C-Band Antenna # 17 X	-4.607	4.534	-4.067	3.831	-3.973	3.785	-4.012	3.800	-3.952	3.905
C-Band Antenna # 17 Y	-1.628	1.618	-1.208	1.240	-1.207	1.240	-1.207	1.239	-1.217	1.249
C-Band Antenna # 17 Z	-2.883	5.601	-0.532	3.593	-0.524	3.602	-0.532	3.605	-0.564	4.039
C-Band Reflector CG # 18 Y	-5.371	5.482	-2.297	2.268	-2.300	2.275	-2.301	2.282	-2.652	2.941
Top C-Band Antenna # 20 X	-17.004	15.478	-14.429	13.682	-14.471	13.738	-14.391	13.689	-14.779	14.034
Top C-Band Antenna # 20 Y	-7.164	7.223	-4.977	5.120	-5.002	5.144	-5.002	5.138	-5.034	5.261
Top C-Band Antenna # 20 Z	-5.117	8.104	-1.120	4.128	-1.134	5.935	-1.135	3.786	-1.769	5.133
Propellant Tank CG # 75 X	-0.814	1.028	-0.730	0.912	-0.728	0.911	-0.728	0.911	-0.721	0.917
Propellant Tank CG # 75 Y	-0.510	0.453	-0.405	0.378	-0.416	0.379	-0.422	0.380	-0.505	0.477
Propellant Tank CG # 75 Z	0.160	3.347	0.160	3.354	0.157	3.360	0.158	3.358	0.130	3.442
+Y Solar Panel Hinge # 83 X	-4.582	3.507	-3.064	2.399	-3.001	2.377	-2.898	2.370	-3.557	3.091
+Y Solar Panel Hinge # 83 Y	-2.762	2.802	-2.153	1.643	-2.157	1.643	-2.157	1.602	-2.285	1.981
+Y Solar Panel Boom # 84 X	-1.114	1.191	-0.996	1.193	-0.993	1.202	-0.991	1.204	-1.118	1.269
+Y Solar Panel Boom # 84 Y	-0.630	0.632	-0.514	0.540	-0.504	0.534	-0.503	0.537	-0.550	0.577
+X SA Antenna Ribs #114 X	-15.354	16.508	-8.434	10.605	-8.486	10.607	-8.503	10.605	-8.686	11.969
+X SA Antenna Ribs #114 Y	-10.779	11.661	-13.079	11.731	-13.151	11.865	-13.198	11.948	-20.363	20.347
+X SA Antenna Ribs #115 X	-25.678	27.177	-6.820	7.402	-7.152	7.748	-7.010	7.303	-9.588	9.243
+X SA Antenna Ribs #115 Y	-11.695	12.841	-12.517	14.087	-12.565	14.248	-12.590	14.302	-15.463	15.945

TABLE 2 STB-26 TDRS MEMBER FORCES (lbs)

ITEMS	2		3		4		5		6	
	Diagonal IMP	1 Iteration	2 Iterations	Full Damp-Matrix	1' System Damping	Min	Max	Min	Max	
LTM Row 7	-31.352	167.415	0.742	157.726	0.716	158.092	0.617	158.080	-2.211	161.663
LTM Row 8	-96.063	97.823	-87.604	88.290	-87.553	88.306	-87.588	88.383	86.971	86.844
LTM Row 9	-239.302	248.886	-244.731	251.355	-244.525	250.255	-244.563	250.720	-248.846	247.068
LTM Row 10	-3779.852	4048.862	-3714.292	3640.342	-3695.735	3621.714	-3698.991	3629.298	-3790.617	3638.845
LTM Row 11	-15316.294	15094.602	-15324.817	15111.364	-15323.642	15106.433	-15319.220	15105.144	-1511.047	14984.546
LTM Row 12	-6588.836	5736.225	-6561.235	5739.295	-6563.184	5741.535	-6563.380	5742.944	-6565.495	5721.129
LTM Row 13	-18.031	180.071	-16.874	172.224	-16.880	172.217	-17.039	172.166	-17.373	173.739
LTM Row 14	-138.362	133.735	-139.851	131.548	-140.204	131.659	-140.250	131.769	-38.204	132.125
LTM Row 15	-100.012	141.493	-99.980	150.813	-100.441	151.302	-100.627	151.444	95.802	149.997
LTM Row 16	-2302.582	2691.156	-2302.934	2720.638	-2306.025	2709.896	-2306.691	2710.974	-2266.597	2597.696
LTM Row 17	-9965.971	6880.373	-10251.104	6822.615	-10267.150	6790.424	-10270.888	6801.434	-10180.191	6558.322
LTM Row 18	-12220.455	10234.987	-12191.952	10223.477	-12203.518	10212.594	-12209.673	10212.579	-12132.624	10284.899
LTM Row 49	-910.043	1097.881	-912.467	1100.754	-912.520	1101.126	-912.640	1101.521	-903.279	1093.266
LTM Row 50	-26.328	81.262	-24.331	80.765	-24.317	79.826	-24.691	79.748	-29.942	81.354
LTM Row 51	-80.621	92.894	-79.501	93.739	-79.559	93.806	-79.628	94.043	-81.248	94.451
LTM Row 52	-135.642	149.803	-136.405	144.737	-136.593	145.011	-137.038	145.010	-139.581	149.702
LTM Row 53	-201.294	397.658	-190.031	403.868	-190.372	404.094	-190.581	404.592	-194.017	397.817
LTM Row 54	-140.504	126.025	-132.522	120.977	-132.493	121.681	-131.217	121.498	-146.011	133.610
LTM Row 55	-123.781	77.939	-136.341	67.925	-137.451	68.019	-137.441	68.392	-147.906	71.118
LTM Row 56	-6.905	9.548	-6.711	9.667	-6.701	9.695	-6.668	9.694	-7.013	9.579
LTM Row 57	-959.580	1150.629	-967.793	1163.026	-967.470	1162.230	-967.944	1162.744	-955.373	1152.610
LTM Row 58	-129.890	107.954	-125.973	110.180	-127.025	109.513	-127.377	109.769	-130.990	107.068
LTM Row 59	-125.672	130.057	-121.905	125.346	-122.312	125.712	-122.174	125.777	-131.460	130.171
LTM Row 60	-10.191	13.442	-9.569	13.204	-9.566	13.240	-9.524	13.222	-9.852	13.088
LTM Row 61	-82.391	106.257	-78.834	104.746	-78.594	104.871	-78.735	104.794	-78.305	103.591
LTM Row 62	-24.076	121.615	-23.033	112.885	-23.030	112.838	-23.201	112.810	-23.362	113.540
LTM Row 63	-72.986	80.180	-74.006	79.146	-74.254	79.043	-74.308	79.096	-73.436	77.057
LTM Row 64	-2733.788	1981.400	-2768.411	1955.748	-2778.460	1962.435	-2779.020	1969.346	-2696.461	1998.610
LTM Row 65	-1986.944	2390.924	-1993.430	2403.396	-1989.133	2392.075	-1988.896	2393.278	-1955.770	2286.105
LTM Row 66	-997.770	1339.519	-892.050	1186.780	-890.659	1199.413	-894.419	1204.604	-807.017	1233.651
LTM Row 149	-20.623	21.690	-9.954	11.891	-9.766	11.829	-9.916	11.700	-11.832	14.085
LTM Row 150	-83.035	81.520	-81.647	52.603	-82.227	57.756	-81.261	59.241	-81.855	71.202
LTM Row 151	-16.768	13.490	-9.358	6.927	-9.768	7.056	-9.832	6.998	-11.200	10.020
LTM Row 152	-194.704	230.869	-160.975	157.300	-159.737	153.479	-159.591	148.885	-171.957	172.856
LTM Row 153	-91.644	131.848	-94.615	115.442	-96.752	115.962	-97.676	114.795	-114.314	137.597
LTM Row 154	-101.074	77.361	-83.852	61.391	-69.744	62.328	-71.259	61.854	-81.486	86.363
LTM Row 155	-37.265	49.875	-27.195	37.518	-26.767	37.609	-26.729	37.616	-36.476	45.999
LTM Row 156	-17.823	24.791	-16.363	19.037	-16.361	19.045	-16.262	18.948	-21.151	23.945

TABLE 3 STS-26 PAYLOAD/ORBITER INTERFACE LOADS (lbs)

ITEMS	2		3		4		5		6	
	Diagonal TWP	1 Iteration	2 Iterations	Full Damp-Matrix	1% System Damping	Min	Max	Min	Max	
X=1061.13 RHS Long 8000 X	-2999.701	1267.436	-3057.462	1352.655	-3082.049	1367.236	-3083.571	1367.911	-3792.084	2126.967
X=1061.13 RHS Long 8000 Z	-4003.971	7727.583	-4010.486	7748.758	-4009.231	7741.651	-4007.610	7745.237	-3924.981	7627.289
X=1155.53 RHS Long 43 X	-59543.562	-8938.251	-59761.283	-9024.557	-59758.595	-9024.424	-59763.502	-9028.895	-59733.092	-8909.008
X=1155.53 RHS Long 43 Z	-5003.924	563.117	-4994.387	569.692	-4994.234	565.773	-4991.766	566.079	-5010.085	576.838
X=1165.36 RHS Long 131 Y	-1830.120	4965.188	-2032.299	4792.680	-2021.604	4804.361	-2022.277	4803.494	-2360.679	5478.094
X=1216.50 RHS Long 132 Y	-3400.066	2104.577	-3184.771	2227.027	-3210.368	2223.260	-3206.910	2224.188	-3357.255	2215.780
X=1226.50 RHS Long 39 Z	-3742.837	587.852	-3738.841	592.606	-3736.534	589.249	-3736.319	589.928	-3726.953	582.139
X=1061.13 LHS Long 8250 X	-2900.900	1420.706	-2861.693	1444.388	-2864.546	1451.309	-2865.230	1451.446	-3891.571	1977.441
X=1061.13 LHS Long 8250 Z	-3491.037	8789.977	-3478.651	8811.324	-3484.214	8812.158	-3482.048	8811.452	-3505.514	8698.271
X=1155.53 LHS Long 124 X	-58111.550	-7810.329	-58197.228	-7630.843	-58199.854	-7624.490	-58198.757	-7622.496	-58203.158	-7822.706
X=1155.53 LHS Long 124 Z	-5216.399	964.893	-5198.748	956.545	-5198.593	954.800	-5196.326	955.384	-5204.973	950.756
X=1165.36 LHS Long 135 Y	-4103.196	1731.748	-4086.695	1573.935	-4083.623	1574.735	-4080.749	1575.901	-4679.327	1836.701
X=1216.50 LHS Long 136 Y	-2056.957	3773.966	-2001.451	3668.729	-2002.433	3676.866	-2002.596	3677.055	-2261.874	4056.924
X=1226.33 LHS Long 128 Z	-3799.106	918.146	-3802.587	913.438	-3803.697	911.633	-3802.116	911.518	-3800.477	905.737
X=1061.13 C/L Keel 8050 X	-2066.167	975.528	-2053.556	1056.768	-2053.922	1059.102	-2053.671	1059.239	-2295.171	1283.621
X=1061.13 C/L Keel 8050 Y	-2454.776	5073.594	-2460.642	4932.092	-2461.763	4947.572	-2461.972	4934.895	-2408.746	4939.606

TABLE 4 STS-26 IUS MOTOR ACCELERATIONS (g)

ITEMS	2		3		4		5		6	
	Diagonal TMP Min	Max	1 Iteration Min	Max	2 Iterations Min	Max	Full Damp-Matrix Min	Max	1% System Damping Min	Max
Small IUS Motor #3457 X	0.101	3.091	0.119	3.123	0.118	3.124	0.119	3.125	0.060	3.156
Small IUS Motor #3457 Y	-0.342	0.417	-0.188	0.228	-0.188	0.235	-0.181	0.238	-0.267	0.243
Small IUS Motor #3457 Z	-0.450	0.629	-0.470	0.610	-0.469	0.610	-0.470	0.611	-0.473	0.621
Small IUS Motor #3457 Rx	-1.916	1.726	-1.201	1.206	-1.192	1.267	-1.201	1.277	-1.735	1.590
Small IUS Motor #3457 Ry	-5.630	5.509	-5.889	4.998	-5.905	5.022	-5.903	5.012	-6.454	5.528
Small IUS Motor #3457 Rz	-1.849	1.439	-1.706	1.310	-1.753	1.420	-1.756	1.444	-2.410	1.950
Large IUS Motor #1331 X	0.423	2.735	0.416	2.754	0.416	2.754	0.416	2.754	0.418	2.727
Large IUS Motor #1331 Y	-0.183	0.319	-0.147	0.246	-0.149	0.244	-0.146	0.242	-0.195	0.281
Large IUS Motor #1331 Z	-0.510	0.506	-0.518	0.510	-0.518	0.510	-0.518	0.510	-0.514	0.500
Large IUS Motor #1331 Rx	-1.255	1.236	-1.269	1.433	-1.261	1.456	-1.258	1.458	-1.345	1.742
Large IUS Motor #1331 Ry	-2.246	2.395	-2.332	2.421	-2.321	2.416	-2.319	2.427	-2.596	2.714
Large IUS Motor #1331 Rz	-4.069	4.315	-2.261	2.384	-2.270	2.423	-2.179	2.313	-4.045	4.218

TABLE 5 STS-26 PAYLOAD/ORBITER INTERFACE ACCELERATIONS (g)

ITEMS	1		2		3		4		5		6	
	Min	Max										
X=1061.13 RHS Long 8000 X	-2.537	-0.451	-2.533	-0.475	-2.532	-0.474	-2.532	-0.474	-2.532	-0.474	-2.762	-0.342
X=1061.13 RHS Long 8000 Z	-1.518	1.618	-1.510	1.591	-1.509	1.593	-1.510	1.592	-1.510	1.592	-1.611	1.844
X=1155.53 RHS Long 43 X	-2.390	-0.303	-2.318	-0.299	-2.318	-0.299	-2.319	-0.299	-2.319	-0.299	-2.601	-0.199
X=1155.53 RHS Long 43 Z	-1.214	1.257	-1.216	1.187	-1.216	1.193	-1.215	1.190	-1.215	1.190	-1.705	1.915
X=1165.36 RHS Long 131 Y	-2.735	2.437	-2.669	2.500	-2.672	2.498	-2.671	2.498	-2.671	2.498	-2.807	2.651
X=1216.50 RHS Long 132 Y	-3.480	3.396	-3.461	3.359	-3.465	3.365	-3.464	3.364	-3.464	3.364	-3.988	3.914
X=1226.33 RHS Long 39 Z	-1.267	1.401	-1.242	1.323	-1.234	1.328	-1.234	1.326	-1.234	1.326	-2.061	2.227
X=1061.13 LHS Long 8250 X	-2.799	-0.346	-2.752	-0.367	-2.756	-0.366	-2.755	-0.366	-2.755	-0.366	-3.085	-0.217
X=1061.13 LHS Long 8250 Z	-1.466	1.534	-1.452	1.519	-1.453	1.521	-1.452	1.521	-1.452	1.521	-1.555	1.771
X=1155.53 LHS Long 124 X	-2.535	-0.190	-2.524	-0.220	-2.526	-0.219	-2.526	-0.219	-2.526	-0.219	-2.776	-0.108
X=1155.53 LHS Long 124 Z	-1.097	1.275	-1.035	1.236	-1.043	1.237	-1.042	1.237	-1.042	1.237	-1.788	1.962
X=1165.36 LHS Long 135 Y	-2.426	2.570	-2.328	2.509	-2.333	2.510	-2.333	2.510	-2.333	2.510	-2.659	2.555
X=1216.50 LHS Long 136 Y	-3.045	3.427	-2.870	3.321	-2.888	3.326	-2.886	3.326	-2.886	3.326	-3.457	3.790
X=1226.33 LHS Long 128 Z	-1.130	1.353	-1.043	1.272	-1.058	1.288	-1.057	1.286	-1.057	1.286	-2.056	2.100
X=1061.13 C/L Keel 8050 X	-6.632	3.514	-6.497	3.577	-6.507	3.594	-6.507	3.595	-6.507	3.595	-8.257	5.201
X=1061.13 C/L Keel 8050 Y	-0.292	0.318	-0.294	0.303	-0.292	0.301	-0.292	0.300	-0.292	0.300	-0.326	0.436

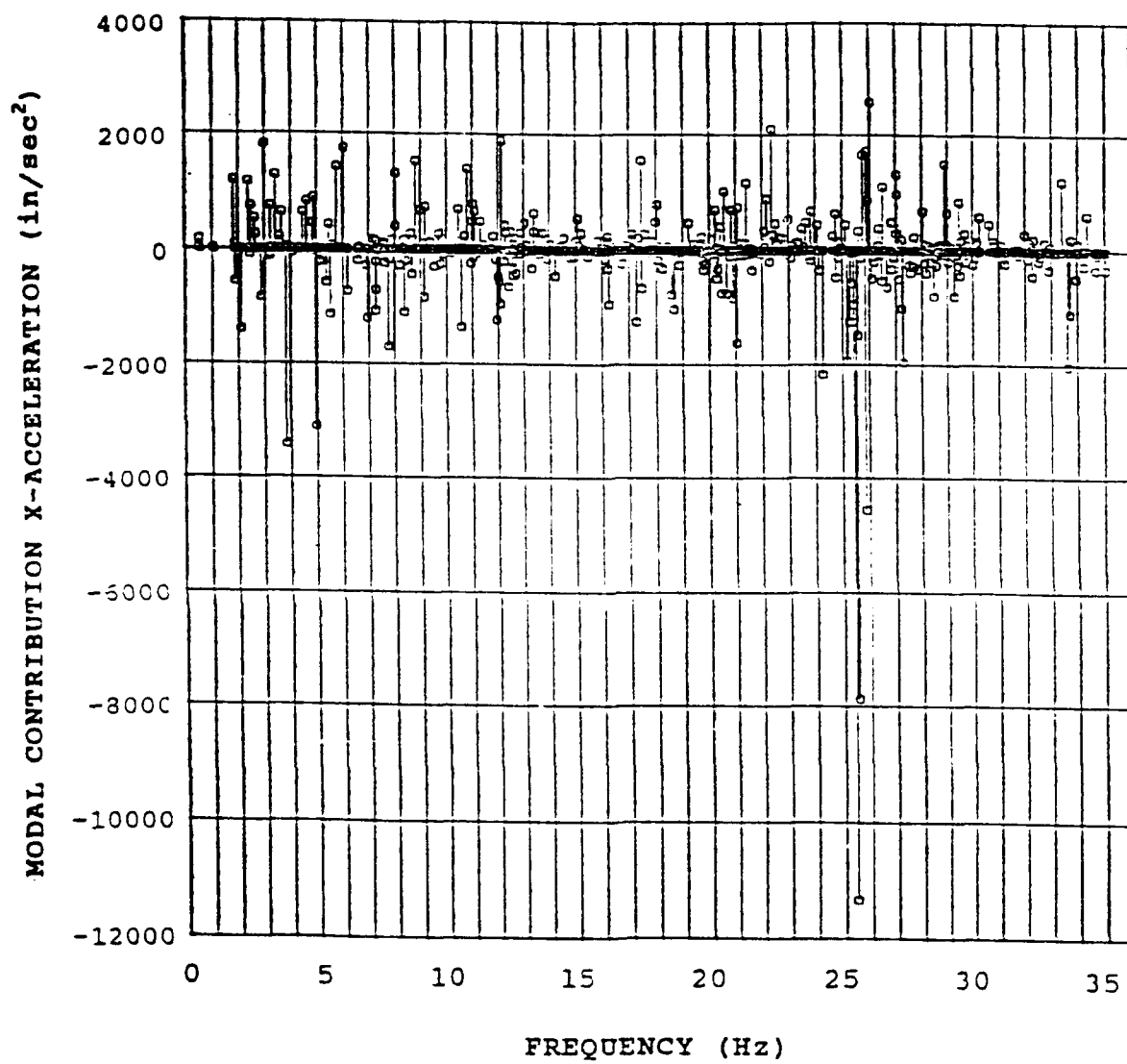


Figure 1 MODAL CONTRIBUTIONS FOR X-ACCELERATION (in/sec²) OF STS-26 SA ANTENNA RIBS USING TMP METHOD, t=8.3 sec.

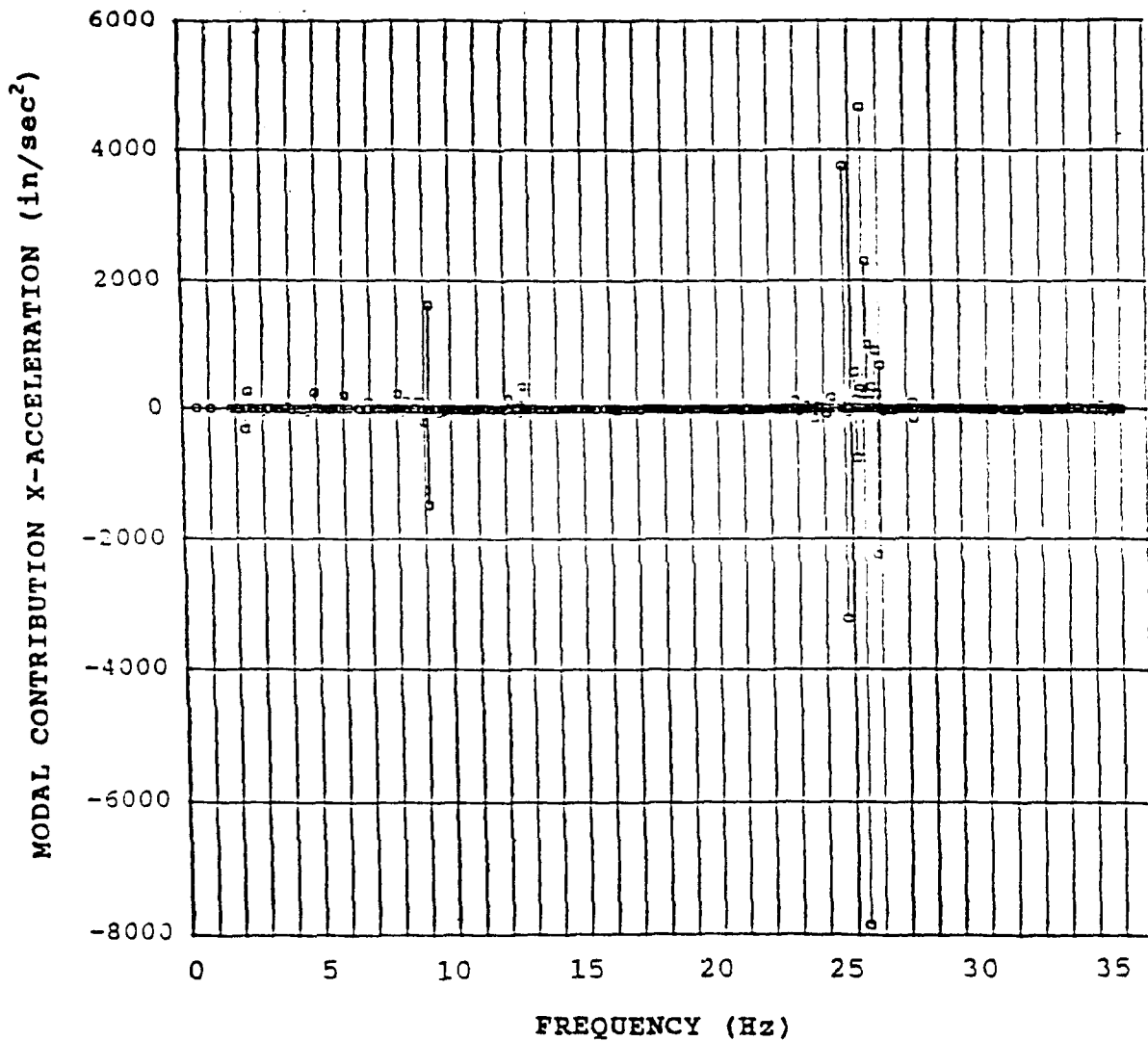


Figure 2 MODAL CONTRIBUTIONS FOR X-ACCELERATION (in/sec²) OF STS-26 SA ANTENNA RIBS USING ITERATIVE METHOD t=8.3 sec.